Transactions of the ASME®

Technical Editor, LEON M. KEER

The Technological Institute
Northwestern University
Evanston, IL 60201

APPLIED MECHANICS DIVISION

Chairman, THOMAS L. GEERS
Secretary, S. LEIBOVICH
Associate Editors,
D. B. BOGY
R. M. CHRISTENSEN
R. J. CLIFTON
R. L. HUSTON
W. D. IWAN
L. M. KEER
W. G. KNAUSS
F. A. LECKIE
J. T. C. LIU
R. M. McMEEKING
FRANCIS C. MOON
A. K. NOOR
J. W. NUNZIATO
R. H. PLAUT
J. G. SIMMONDS
K. R. SREENIVASAN
Z. WARHAFT
L. T. WHEELER

BOARD ON COMMUNICATIONS
Chairman and Vice-President
K. N. REID, JR.

Members-at-Large
J. T. COKONIS
M. FRANKE
M. KUTZ
F. LANDIS
J. R. LLOYD
T. C. MIN
R. E. NICKELL
R. E. REDER
R. ROCKE
F. W. SCHMIDT
W. O. WINER

President, R. ROSENBERG
Exec. Dir.
D. L. BELDEN
Treasurer, ROBERT A. BENNETT

PUBLISHING STAFF
Mng. Dir., Publ., JOS. SANSONE
Managing Editor,
CORNELIA MONAHAN
Production Editor, JUDY SIERANT
Prod. Asst., MARISOL ANDINO

Transactions of the ASME, Journal of Applied Mechanics (ISSN 0021-8936) is published quarterly (Mar., June, Sept., Dec.) for $115 per year by The American Society of Mechanical Engineers, 345 East 47th Street, New York, NY 10017. Second class postage paid at New York, NY and additional mailing offices. POSTMASTER: Send address changes to The Journal of Applied Mechanics, c/o THE AMERICAN SOCIETY OF MECHANICAL ENGINEERS, 22 Law Drive, Box 2300, Fairfield, NJ 07007-2300.

CHANGES OF ADDRESS must be received at Society headquarters seven weeks before they are to be effective. Please send old label and new address.

PRICES: To members, $27.00, annually; to nonmembers, $115.00. Add $12.00 for postage to countries outside the United States and Canada.

STATEMENT from By-Laws. The Society shall not be responsible for statements or opinions advanced in papers or . . . printed in its publications (B7.1, Par. 3).

COPYRIGHT © 1988 by the American Society of Mechanical Engineers. Reprints from this publication may be made on condition that full credit be given the TRANSACTIONS OF THE ASME, JOURNAL OF APPLIED MECHANICS, and the author, and date of publication be stated.

INDEXED by Applied Mechanics Reviews and Engineering Information, Inc.

Journal of Applied Mechanics

Published Quarterly by The American Society of Mechanical Engineers

VOLUME 55 • NUMBER 2 • JUNE 1988

259 In Memoriam

TECHNICAL PAPERS

260 Some Exact and Approximate Solutions for the Modified von Mises Yield Criterion (88-WA/APM-22)
J. H. Lee

267 Analysis of a Power-Law Material Containing a Single Hole Subjected to a Uniaxial Tensile Stress Using the Complex Pseudo-Stress Function (88-WA/APM-19)
Y. S. Lee and L. C. Smith

275 Dynamic Spherical Cavity Expansion in a Compressible Elastic-Plastic Solid (88-WA/APM-24)
M. J. Forrestal and V. K. Luk

280 Mechanical Modeling of Material Damage
S. Murakami

287 Nonlocal Continuum Damage, Localization Instability and Convergence (88-WA/APM-18)
Z. P. Bazănt and G. Pijaudier-Cabot

294 Creep Rupture of Shell Structures Subjected to Cyclic Loading (88-WA/APM-30)
A. C. F. Cocks and F. A. Leckie

299 Elastic-Plastic Analysis of Cracks on Bimaterial Interfaces: Part 1—Small Scale Yielding
C. F. Shih and R. J. Asaro

317 On the Mechanical Modeling of the Interfacial Region in Bonded Half-Planes (88-WA/APM-25)
F. Delale and F. Erdogan

325 A Crystallographic Model for Nickel Base Single Crystal Alloys
L. T. Dame and D. C. Stouffer

332 Finite Axisymmetric Deformation of Rubber-Like Shells of Revolution
W. J. Keppel and D. A. DaDeppo

341 The Linear Elastic Properties of Open-Cell Foams (88-WA/APM-20)
W. E. Warren and A. M. Kraynik

347 Bounds on the Effective Transport and Elastic Properties of a Random Array of Cylindrical Fibers in a Matrix
S. Torquato and F. Lado

355 Inclusion and Misfit Effects in Hydrostatic Tension (88-WA/APM-38)
B. Wilner

361 The Singularity at the Apex of a Rigid Wedge Embedded in a Nonlinear Material (88-WA/APM-21)
J. M. Duva

365 Determining the Stress Distributions in Wound Reels of Magnetic Tape Using a Nonlinear Finite-Difference Approach
M. S. Willett and W. L. Poesch

372 Thermal Stresses Due to a Plane Crack in General Anisotropic Material (88-WA/APM-16)
F. A. Sturla and J. R. Barber

377 Generalized Coupled Transient Thermoelastic Plane Problems by Laplace Transform/Finite Element Method (88-WA/APM-29)
T.-C. Chen and C.-I. Weng

383 Partial Release and Relocking of a Frictionally Locked Crack Due to Moving Tensile Loads (88-WA/APM-27)
D. A. Mendelsohn and K. H. Whang

389 Three-Dimensional Analysis of Laminates With Cross Cracks (88-WA/APM-36)
J. Aboudi, S. W. Lee, and C. T. Herakovich

398 The Wavefield Radiated Into an Elastic Half-Space by a Transducer of Large Aperture
J. G. Harris

405 Scattering From Three-Dimensional Planar Cracks by the Boundary Integral Equation Method
D. E. Budreck and J. D. Achenbach

413 The Optimal Version of Reissner's Theory
P. Ladevèze and F. Pécastaings

419 Bending of Sandwich Plates of Variable Thickness (88-WA/APM-40)
N. Paydar and C. Libove

425 Buckling of Locally Loaded Isotropic, Orthotropic, and Composite Cylindrical Shells
W. Xiao and S. Cheng

430 Unbonded Contact of a Square Plate on an Elastic Half-Space or a Winkler Foundation (88-WA/APM-28)
H. Li and J. P. Dempsey

437 Axisymmetric Free Vibration Problems by Boundary Element Method
H.-C. Wang and P. K. Banerjee

443 Construction of a Consistent Damping Matrix
K. J. Buhariwala and J. S. Hansen

(Contents continued on Inside Book Cover)

Downloaded 04 May 2010 to 171.66.16.49. Redistribution subject to ASME license or copyright; see http://www.asme.org/terms/Terms_Use.cfm

CONTENTS (Continued)

448 **Transient Dynamic Analysis of Rotors Using the Combined Methodologies of Finite Elements and Transfer Matrix**
R. Subbiah, A. S. Kumar, and T. S. Sankar

453 **A Fast Eigenfunction Approach for Computing Spinning Disk Deflections** (88-WA/APM-26)
K. A. Cole and R. C. Benson

458 **Stochastic Sample Stability of Oscillatory Systems**
S. T. Ariaratnam and W.-C. Xie

461 **Interpolated Cell Mapping of Dynamical Systems** (88-WA/APM-17)
B. H. Tongue and K. Gu

467 **Experimental Investigation of Liquid Sloshing Under Parametric Random Excitation** (88-WA/APM-23)
R. A. Ibrahim and R. T. Heinrich

474 **A Practical One-Parameter Integral Method for Laminar Incompressible Boundary Layer Flow With Transpiration** (88-WA/APM-15)
L. C. Thomas and W. L. Amminger

482 **Effect of Entrance Region on Laminar Startup Flow in Pipes** (88-WA/APM-39)
H. I. Andersson and R. Kristoffersen

BRIEF NOTES

Stress Concentration Around a Pair of Circular Holes in Hydrostatically Stressed Elastic Sheet
R. W. Zimmerman 487

On the Theory of Gyroelasticity
G. M. T. D'Eleuterio 488

Inverse Problem Solutions Via Plate Theory With Applications to Position and Force Sensing
P. P. Lin and P. Datseris 489

491 Unstable Elastic Materials and the Viscoelastic Response of Bars in Tension
R. Abeyaratne and J. K. Knowles

492 Diffusion of Self-Equilibrating End Loads in Elastic Solids
D. Durban and W. J. Stronge

495 Transversely Isotropic Medium With a Rigid Spheroidal Inclusion Under an Axial Pull
A. H. Zureick

DISCUSSION

498 **Discussion on a previously published paper by Y. Yong and Y. K. Lin**

499 **Discussion on a previously published paper by S. C. Cowin**

BOOK REVIEWS

500 ***Thermomechanical Coupling in Solids*** **by H. D. Bui and Q. S. Nguyen** . . . Reviewed by **T. Mura**

500 ***A First Look at Perturbation Theory*** **by J. G. Simmonds and J. E. Mann** . . . Reviewed by **L. Sanders, Jr.**

501 ***Stochastic Methods in Structural Dynamics*** **edited by G. I. Schueller and M. Shinozuka** . . . Reviewed by **R. B. Corotis**

501 Books Received by the Office of the Technical Editor

503 *Worldwide Mechanics Meeting List*

505 Errata

505 Change of Address Form

316 8th Annual Conference on Failure Prevention and Liability

367 IUTAM Symposium

388 Announcement—Conference of the Society of Applied Mathematics and Mechanics

418 ASME Junior Awards

279, 324, 452, 486 Applied Mechanics Symposium Proceedings

Downloaded 04 May 2010 to 171.66.16.49. Redistribution subject to ASME license or copyright; see http://www.asme.org/terms/Terms_Use.cfm

In Memoriam
Raymond D. Mindlin

RAYMOND D. MINDLIN, who came to be recognized as the world's leader in the broad field of elasticity during a professional life of some 63 years, died on November 22, 1987 in Hanover, N.H., at the age of 81.

Born in New York on September 17, 1906, he began his 62-year long association with Columbia University when he enrolled there as an 18-year old freshman, subsequently receiving four degrees from that institution: the B.A. in 1928, the B.S. in 1931, the professional C.E. in 1932, and the Ph.D. in 1936. His Ph.D. dissertation presaged his future exemplary work in elasticity, since it presented the solution of what became known as the "Mindlin Problem," namely that of the effect of a concentrated force in the interior of a semi-infinite solid. He had begun teaching while still a doctoral student, however, and can be credited with pioneering graduate instruction and research in mechanics in the early 1930s. This field of endeavor remained close to his heart throughout his academic career as a professor at Columbia, winning him the Great Teacher Award in 1960, and gaining for him lasting appreciation and affection from each of his 30 doctoral students.



Raymond D. Mindlin

Under his leadership the scope of the theory of elasticity grew to encompass bordering areas of electrical, thermal, optical and acoustical phenomena. His work was fundamental and applied, in the best engineering tradition. His extensive research into vibrations and waves in elastic bars and crystal plates led to the development and design of delay lines and electromechanical filters which are today still in use. His collaboration with Hans Bleich on the interaction of an elastic shell with a surrounding fluid is central to the analysis of the shock response of submarine hulls. His pioneering inquiry into pressure and friction in solid contact surfaces has been applied to the design of relay contacts and ball bearings. His microstructural theories of solids illuminated the transition between continuum and discrete descriptions of solid behavior.

Among the honors he received, one should mention the Medal of Merit in 1946 for his part in the development of the radio proximity fuse, and the National Medal of Science in 1979 for is contributions to applied mechanics and mathematics. He was a member of the National Academy of Sciences, the National Academy of Engineering, and a fellow of the American Academy of Arts and Sciences, the American Society of Mechanical Engineers, and the American Acoustical Society. His deep involvement with experimental elasticity is underscored by the fact that he was a founder and president of the Society for Experimental Stress Analysis, which bestowed on him the Frocht Medal in 1974. He was awarded an honorary doctor of science degree from Northwestern University in 1975, the Thomas Egleston Medal from Columbia in 1971, the Timoshenko Medal from ASME in 1964, and the von Karman Medal from ASCE in 1961. He was chairman of the Applied Mechanics Division of ASME in 1955–1956.

Twice in his life he endured the loss of a devoted companion: his first wife, the former Elizabeth Roth, died in 1950, and his second, the former Patricia Kaveney, in 1976. In the face of personal grief and public acclaim alike, Ray Mindlin preserved the gentle good humor and steadfastness of judgment that had earned him the love and respect or students, colleagues and friends over the years. They will long remember him, and mourn his passing—and his influence on the field will long abide. Love noted the "significant fact that most great advances in Natural Philosophy have been made by men who had a first-hand acquaintance with practical needs and experimental methods": Mindlin's place among them is secure.

Bruno A. Boley
Columbia University

Copyright © 1988 by ASME
Downloaded 03 May 2010 to 171.66.16.21. Redistribution subject to ASME license or copyright; see http://www.asme.org/terms/Terms_Use.cfm

Some Exact and Approximate Solutions for the Modified von Mises Yield Criterion

J. H. Lee
Assistant Professor,
Department of Mechanical Engineering,
University of Alaska Fairbanks,
Fairbanks, AK 99775
Assoc. Mem. ASME

The effects of Strength Differential (SD) and plastic compressibility for materials obeying the modified von Mises yield criterion were exemplified by solving two boundary-value problems. The assumptions of associated plasticity (leading to maximum plastic volume increase) and nonassociated plasticity (leading to zero plastic volume increase) were used for comparative studies on the effects of plastic compressibility. The solutions for compression processes showed that SD effects increased the pressure at initial yielding and at failure, as well as increased the capacity of the materials to withstand plastic deformations. The opposite was true for tension processes. For associated and nonassociated plasticity, upper and lower bounds for stresses and strains for load and stroke-controlled situations were indicated. The results also showed unrealistic restrictions on the Poisson's ratio and C/T for nonassociated plasticity under certain conditions. Hence, plastic volume increase, although small, should be incorporated into a more realistic plasticity model.

Introduction

Recently, photoplasticity was applied to three-dimensional upsetting and rolling processes (Gomide and Burger, 1981; Burger and Gomide, 1982). In order to check the validity of the photoplastic experiments, macroscopic yield conditions of photoplastic materials need to be studied. Made of blends of polyester resins, the photoplastic model materials generally follow the modified von Mises (MVM) yield criterion (Zachary and Riley, 1977; Freire and Riley, 1980), where yielding is influenced by hydrostatic pressure. Known as the Strength Differential (SD) effect (Drucker, 1973), the dependence on pressure gives rise to different yield strengths in tension and compression. The true SD effect is, however, distinct from anisotropy and Bauschinger effect (Drucker, 1973; Freed and Sandor, 1986), and should persist over the entire strain range.

Although experimental evidence clearly indicates that initial yield surfaces for photoplastic materials follow the MVM yield criterion, the situation is less clear about subsequent yield surfaces and plastic potentials. Specifically, we are not clear about the effects of SD and plastic compressibility on the macroscopic responses of photoplastic model materials in particular and of polymers in general.

It is, then, the purpose of this paper (in the spirit of Hill, 1949; and Drucker and Prager, 1952) to characterize the implications of the SD and plastic compressibility effects by obtaining exact and approximate solutions of some boundary-value problems (based on certain assumptions). These solutions can further be used as "exact" solutions for the validation of elastoplastic finite-element codes.

Caddell and coworkers in a series of studies (for example, Raghava and Caddell, 1973; Raghava, et al., 1973) showed that, for initial yielding, the MVM yield criterion is suitable for a wide range of crystalline and amorphous polymers. For several plastics, Whitney and Andrews (1967) obtained initial yield surfaces and measured volume *increases* before and during yielding. They indicate that there is negligible plastic volume increase after yielding such that the normality rule is not followed.

Spitzig and Richmond (1979) found plastic volume increases for polyethylene, but the observed volume expansion is only about one-sixth of that predicted from the normality rule. Furthermore, they found that plastic volume decreases for polycarbonate.

Recent studies (Spitzig, et al., 1975, 1976) showed that some high strength steels also exhibit SD effects. The dependence of hydrostatic pressure on yielding for metal is, however, generally less pronounced than that for plastics. However, the volume change predicted from the normality rule (Spitzig, et al., 1976; Gupta, 1977; Casey and Jahedmotlagh, 1984) is much larger than the observed change. Spitzig, et al. (1976) suggested that the normality rule may not hold, and density changes can be ignored. On the other hand, Gupta (1977) remarked that normality should not be ruled out since there is not yet experimental evidence on subsequent yield surfaces.

A re-examination of the data of Whitney and Andrews (1967), to be discussed later, showed that the deviation of the

Contributed by the Applied Mechanics Division for presentation at the Winter Annual Meeting, Chicago, IL, November 28 to December 2, 1988, of The American Society of Mechanical Engineers.

Discussion on this paper should be addressed to the Editorial Department, ASME, United Engineering Center, 345 East 47th Street, New York, N.Y. 10017, and will be accepted until two months after final publication of the paper itself in the JOURNAL OF APPLIED MECHANICS. Manuscript received by ASME Applied Mechanics Division, February 9, 1987; final revision, December 8, 1987.

Paper No. 88-WA/APM-22.

Copyright © 1988 by ASME
Downloaded 03 May 2010 to 171.66.16.21. Redistribution subject to ASME license or copyright; see http://www.asme.org/terms/Terms_Use.cfm

calculated plastic volume expansion (based on the normality rule) for plastics is not as large as the deviation for high strength steels.

In this paper, we will adopt the perfectly plastic MVM yield criterion, which is suitable for photoplastic model materials. One should note that the MVM yield criterion is only one of a family of pressure-sensitive yield criteria (Nemat-Nasser and Shokooh, 1980). While the following discussions may also apply to metals, the main exposition will be for photoplastic model materials.

For a detailed stress and strain analysis, the ultimate objective of plasticity, explicit stress-strain rate relationships are needed. As a definite, unique flow rule is not yet available, we will assume both associated and nonassociated plasticity.

For the nonassociated plasticity, the classic von Mises yield criterion will be used as the flow potential such that there is zero plastic volume change (Fig. 1). For the associated plasticity, maximum plastic volume increase is predicted (Fig. 1). These two simplified assumptions fall into the general plastic compressibility conditions as proposed by Nemat-Nasser and Shokooh (1980).

In the following sections, the MVM yield criterion with associated and nonassociated flow rules will first be presented. Then two boundary-value problems, plane-strain uniform deformations and thick-walled cylinders under internal pressure, are solved to show the general characteristics of SD and plastic compressibility effects. Since the possibility of bifurcation is not considered, the solutions obtained should be interpreted as the fundamental solutions. Also, the term "failure" used later in discussions should be interpreted as *limit* conditions.

Yield Criterion and Flow Rules

The yield criterion for MVM materials is a paraboloid (Tschoegl, 1971) in the six-dimensional space of stresses

$$F=\frac{1}{2}\{(\sigma_x-\sigma_y)^2+(\sigma_y-\sigma_z)^2+(\sigma_z-\sigma_x)^2+6\tau_{xy}^2$$

$$+6\tau_{yz}^2+6\tau_{zx}^2\}+(\sigma_x+\sigma_y+\sigma_z)(C-T)-CT=0 \qquad (1)$$

where C and T are the absolute yield strengths in compression and tension, respectively. When $C=T$, the traditional von Mises (VM) yield criterion results.

The flow rule can be expressed as

$$\dot{\epsilon}_{ij}^p=\dot{\lambda}\frac{\partial Q}{\partial\sigma_{ij}} \qquad (2)$$

where $\dot{\epsilon}_{ij}^p$ is the plastic strain rate; $\dot{\lambda}$ is a nonnegative parameter; Q is the flow potential. When Q is the same as the yield criterion, we have associated plasticity. Otherwise, the nonassociated plasticity results.

Associated Flow Rules. Substituting equation (1) into equation (2) for the associated plasticity yields

$$\dot{\epsilon}_{ij}^p=\dot{\lambda}\left(\sigma_{ij}'+\delta_{ij}\frac{C-T}{3}\right) \qquad (3)$$

where σ_{ij}' is the deviatoric stress defined as $\sigma_{ij}'=\sigma_{ij}-\sigma_{ij}/3\ \delta_{ij}$, and δ_{ij} is the Kronecker delta.

Obviously, $\dot{\epsilon}_{ii}^p=\dot{\lambda}(C-T)$ is no longer zero (i.e., incompressibility in the plastic range does not hold). For uniaxial tests, we can express the slope of the curve of the plastic volume change versus the axial plastic strain rate($\dot{\epsilon}_1^p$)

$$\gamma^p=\frac{\dot{\epsilon}_{ii}^p}{\dot{\epsilon}_1^p} \qquad (4)$$

Substituting equation (3) into equation (4), one gets

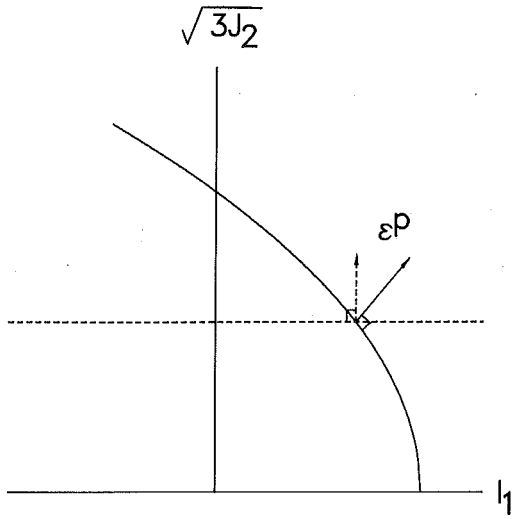


Fig. 1 Modified von Mises yield criterion with associated (solid lines) and nonassociated (dashed lines) flow rules

$$\gamma^p=\frac{3(C-T)}{2\sigma_1+(C-T)} \qquad (5)$$

For polystyrene, using data at yield point (Fig. 1 and Table 1 of Whitney and Andrews, 1967), γ^p is about $0.3\sim0.37$ as predicted from equation (5), while the observed value is about 0.17. As mentioned in the Introduction, the deviation of γ^p for plastics is generally smaller than that for metals. Although Whitney and Andrews fit their data using a modified Mohr-Coulomb criterion, the data can also be fit with the MVM criterion (Christiansen, et al., 1971).

Now we define the von Mises equivalent stress σ_e and the deviatoric equivalent plastic strain rate $\dot{\epsilon}_e^p$ as

$$\sigma_e=\frac{1}{\sqrt{2}}\{(\sigma_x-\sigma_y)^2+(\sigma_y-\sigma_z)^2$$

$$+(\sigma_z-\sigma_x)^2+6(\tau_{xy}^2+\tau_{yz}^2+\tau_{zx}^2)\}^{1/2} \qquad (6)$$

$$\dot{\epsilon}_e^p=\frac{\sqrt{2}}{3}\{(\dot{\epsilon}_x^p-\dot{\epsilon}_y^p)^2+(\dot{\epsilon}_y^p-\dot{\epsilon}_z^p)^2+(\dot{\epsilon}_z^p-\dot{\epsilon}_x^p)^2$$

$$+6[(\dot{\epsilon}_{xy}^p)^2+(\dot{\epsilon}_{yz}^p)^2+(\dot{\epsilon}_{zx}^p)^2]\}^{1/2} \qquad (7)$$

Combining equations (6) and (7), $\dot{\lambda}$ becomes

$$\dot{\lambda}=\frac{3}{2}\frac{\dot{\epsilon}_e^p}{\sigma_e} \qquad (8)$$

Nonassociated Flow Rule. By using equation (6) as the flow potential Q, the familiar Prandtl-Reuss equations result

$$\dot{\epsilon}_{ij}^p=\dot{\lambda}\sigma_{ij}' \qquad (9)$$

where $\dot{\lambda}$ can also be expressed by equation (8). Since $\dot{\epsilon}_e^p$ is the equivalent deviatoric plastic strain, the classical slip-line theory can be extended (cf., equations (38) and (39)).

Even though $\dot{\lambda}$ for both associated and nonassociated cases can be expressed by equation (8), one should note that, in view of equations (3) and (9), $\dot{\epsilon}_e^p$ is different for the associated and nonassociated cases.

Plane Strain Uniform Deformation

Plane-strain uniform deformation is one of the few problems which admits a closed-form solution for the VM criterion

Downloaded 03 May 2010 to 171.66.16.21. Redistribution subject to ASME license or copyright; see http://www.asme.org/terms/Terms_Use.cfm

(Hill, 1950; Alexander, 1959). A closed-form solution for the MVM criterion with associated plasticity is, however, also possible. The solution for the VM criterion is valid for both tension and compression processes (Hill, 1950). However, for the MVM criterion, due to the preference of compression over tension, the solution shows certain restrictions for tension processes.

Associated Plasticity. Let the 3-axis be normal to the planes of flow and the 1-axis be the direction of the compression (or tension). For frictionless, uniform deformation, σ_{12} and ϵ_{12} vanish; also, σ_2 and ϵ_3 are zero. For a given pressure σ_1, the objective is to find the rest of the nonzero strain components.

For elastic regions, it is easily shown that

$$\epsilon_2^e = \frac{-\nu(1+\nu)}{E}\sigma_1 \tag{10}$$

$$\epsilon_1^e = \frac{(1-\nu^2)}{E}\sigma_1$$

where E and ν are the Young's modulus and Poisson's ratio, respectively. The initial pressure for yielding $\sigma_{1(0)}$ can be obtained by substituting equation (8) into equation (1) and solving the resulting quadratic equation

$$\sigma_{1(0)} = \frac{-(C-T)(\nu+1) \pm \sqrt{(C-T)^2(1+\nu)^2 + 4CT(1-\nu+\nu^2)}}{2(1-\nu+\nu^2)} \tag{11}$$

The negative root is for compression and the positive one is for tension; also, $\sigma_{3(0)} = \nu\sigma_{1(0)}$.

For the elastic-plastic region, since $\dot{\sigma}_2 = 0$, the elastic strain rates are

$$\dot{\epsilon}_1^e = \frac{1}{E}\{\dot{\sigma}_1 - \nu\dot{\sigma}_3\}, \quad \dot{\epsilon}_2^e = \frac{-\nu}{E}\{\dot{\sigma}_1 + \dot{\sigma}_3\}$$

$$\dot{\epsilon}_3^e = \frac{1}{E}\{\dot{\sigma}_3 - \nu\dot{\sigma}_1\} \tag{12}$$

Although ϵ_3 and $\dot{\epsilon}_3$ are zero, the elastic and plastic strain rates are not

$$\dot{\epsilon}_3 = \dot{\epsilon}_3^e + \dot{\epsilon}_3^p = 0 \tag{13}$$

We can obtain $\dot{\lambda}$ by substituting equations (3) and (12) into equation (13)

$$\dot{\lambda} = \frac{-1/E(\dot{\sigma}_3 - \nu\dot{\sigma}_1)}{\sigma_3' + \frac{C-T}{3}} \tag{14}$$

Also, $\dot{\sigma}_3$ can be expressed in terms of $\dot{\sigma}_1$ by differentiating equation (1).

$$\dot{\sigma}_3 = \frac{-(2\sigma_1 - \sigma_3 + C - T)}{-\sigma_1 + 2\sigma_3 + C - T}\dot{\sigma}_1 \tag{15}$$

and σ_3 can be expressed in terms of σ_1 by solving equation (1).

$$\sigma_3 = \frac{\sigma_1 - (C-T) + \sqrt{(C-T)^2 - 3\sigma_1^2 - 6\sigma_1(C-T) + 4CT}}{2} \tag{16}$$

where the *positive* root is taken, such that, at initial yielding, σ_3 as obtained from equation (16) agrees with $\sigma_{3(0)} = \nu\sigma_{1(0)}$.

We first evaluate ϵ_1 by decomposing its rate into elastic and plastic components

$$\dot{\epsilon}_1 = \dot{\epsilon}_1^e + \dot{\epsilon}_1^p \tag{17}$$

Substituting equations (3) and (12) into equation (17), also using equations (14)–(16), and after lengthy but straightforward integration, we obtain

$$\epsilon_1 = \frac{1}{E}\left\{\frac{3(C-T)^2 + 3CT}{4\sqrt{3}\{CT + (C-T)^2\}^{1/2}} \times \ln\left[\frac{C - T + \frac{2}{\sqrt{3}}\{CT + (C-T)^2\}^{1/2} + \sigma_1}{-(C-T) + \frac{2}{\sqrt{3}}\{CT + (C-T)^2\}^{1/2} - \sigma_1}\right]\right\}$$

$$+ \frac{(1-2\nu)}{E}\sigma_3 + \text{constant} \tag{18}$$

where the constant can be evaluated from the conditions at initial yielding.

We can evaluate ϵ_2 by using first the *elastic* compressibility relationship

$$\frac{\dot{\epsilon}_1^e + \dot{\epsilon}_2^e + \dot{\epsilon}_3^e}{3} = \frac{1-2\nu}{E}\frac{\dot{\sigma}_1 + \dot{\sigma}_3}{3} \tag{19}$$

Furthermore,

$$\dot{\epsilon}_1 + \dot{\epsilon}_2 + \dot{\epsilon}_3 = \dot{\epsilon}_1 + \dot{\epsilon}_2 = \dot{\epsilon}_1^e + \dot{\epsilon}_2^e + \dot{\epsilon}_3^e + \dot{\epsilon}_1^p + \dot{\epsilon}_2^p + \dot{\epsilon}_3^p \tag{20}$$

Integrating equation (20), and invoking equations (3) and (19), we have

$$\epsilon_1 + \epsilon_2 = \int\dot{\lambda}(C-T) + \frac{1-2\nu}{E}\int(\dot{\sigma}_1 + \dot{\sigma}_3) + \text{constant} \tag{21}$$

Finally, by substituting equations (14)–(16) into equation (21) and integrating, we find

$$\epsilon_2 = -\epsilon_1 + (C-T)\frac{3}{E}\left\{-1/4\ln\{(C-T)^2 - 3\sigma_1^2 - 6\sigma_1(C-T) + 4CT\} + \frac{1/2-\nu}{\sqrt{3}}\sin^{-1}\left[\frac{-3\sigma_1 - 3(C-T)}{[12\{(C-T)^2 + CT\}]^{1/2}}\right]\right\} + \frac{1-2\nu}{E}(\sigma_1 + \sigma_3) + \text{constant} \tag{22}$$

The constant can again be evaluated from known conditions at initial yielding. Obviously, in the absence of SD effect ($C = T$), equations (18) and (22) are reduced to the known solutions (Alexander, 1959) of VM yield criterion.

Nonassociated Plasticity. Using the von Mises yield surface as the flow potential, ϵ_1 can be obtained by substituting equations (9) and (12) into equation (17) and invoking equations (15) and (16). No closed-form solutions are possible, so the results are obtained by numerical integration.

We can find ϵ_2 easily from the elastic compressibility equation as

$$\epsilon_2 = \frac{1-2\nu}{E}(\sigma_1 + \sigma_3) - \epsilon_1 \tag{23}$$

Thick-walled Pressure Vessel Under Internal Pressure

The incremental finite-difference method of Chu (1972), developed for VM criterion, is adopted for this problem. The advantage of this method is that incremental stresses and strains are used directly as variables such that no differentiation of displacement is necessary. Consequently, unlike the finite-element method, one need not take special care to satisfy the conditions of plastic incompressibility (Nagtegaal, et al., 1974). Errors by Chu (1972), however, will be corrected and an improved analysis is used. Furthermore, we will assume the generalized plane-strain condition (i.e., ϵ_z is a nonzero constant).

Downloaded 03 May 2010 to 171.66.16.21. Redistribution subject to ASME license or copyright; see http://www.asme.org/terms/Terms_Use.cfm

The incremental Hooke's laws, relating stress increment to elastic strain increment, are well known.

$$\Delta\sigma_r - \nu(\Delta\sigma_\theta + \Delta\sigma_z) = E\Delta\epsilon_r^e, \ \ldots \text{ etc.} \tag{24}$$

For the associated plasticity in the elastic-plastic region, two independent equations can be obtained from the flow rules, equation (3), by using equation (24) and the decomposition of strain components: $\Delta\epsilon_{ij} = \Delta\epsilon_{ij}^e + \Delta\epsilon_{ij}^p$.

$$\frac{-1}{E}\{3\sigma_z' + C - T + \nu(3\sigma_r' + C - T)\}\Delta\sigma_r + \frac{1}{E}\{\nu(3\sigma_z' + C\text{-}T)$$

$$-\nu(3\sigma_r' + C - T)\}\Delta\sigma_\theta + \frac{1}{E}\{\nu(3\sigma_z' + C - T)$$

$$+3\sigma_r' + C - T\}\Delta\sigma_z + \{3\sigma_z' + C - T\}\Delta\epsilon_r = \{3\sigma_r' + C - T\}\Delta\epsilon_z \tag{25}$$

$$\frac{1}{E}\{\nu(3\sigma_z' + C - T) - \nu(3\sigma_\theta' + C - T)\}\Delta\sigma_r$$

$$+\frac{1}{E}\{-(3\sigma_z' + C - T) - \nu(3\sigma_\theta' + C - T)\}\Delta\sigma_\theta$$

$$+\frac{1}{E}\{\nu(3\sigma_z' + C - T) + 3\sigma_\theta' + C - T\}\Delta\sigma_z$$

$$+\{3\sigma_z' + C - T\}\Delta\epsilon_\theta = \{3\sigma_\theta' + C - T\}\Delta\epsilon_z \tag{26}$$

Differentiating equation (1), the incremental consistency equation becomes

$$\{3\sigma_r' + C - T\}\Delta\sigma_r + \{3\sigma_\theta' + C - T\}\Delta\sigma_\theta + \{3\sigma_z' + C - T\}\Delta\sigma_z = 0 \tag{27}$$

Furthermore, the equilibrium equation is

$$d\sigma_r/dr = (\sigma_\theta - \sigma_r)/r \tag{28}$$

Differentiating equation (28) with respect to a timelike parameter, one gets

$$d\Delta\sigma_r/dr = (\Delta\sigma_\theta - \Delta\sigma_r)/r \tag{29}$$

Using a modified Euler's procedure (Gerald, 1970), equation (29) becomes

$$(\Delta\sigma_r)_i\left(\frac{h}{2r_i} - 1\right) + (\Delta\sigma_r)_{i+1}\left(1 + \frac{h}{2r_{i+1}}\right)$$

$$-\frac{h}{2r_i}(\Delta\sigma_\theta)_i - \frac{h}{2r_{i+1}}(\Delta\sigma_\theta)_{i+1} = 0 \tag{30}$$

where i is a typical grid point, r is the radial coordinate of the grid point and $h = r_{i+1} - r_i$.

The compatibility equation can be obtained by substituting σ_r for ϵ_θ, and substituting σ_θ for ϵ_r in equations (28)–(30).

The governing equations for the elastic region are the three incremental equations for Hooke's laws, equation (24), with the equilibrium, equation (30), and compatibility equation. For the plastic zones, plasticity equations (25)–(27) are used instead of equation (24).

For nonassociated plasticity, the $(C - T)$ terms in equations (25)–(26) are omitted.

The modified Euler's method used in deriving equation (30) is more accurate (Gerald, 1970) than the Euler's method used by Chu (1972). Moreover, the derivations of equations (9) and (10) by Chu are not correct (i.e., the right-hand sides of those equations should be equal to zero). Details of the step-by-step implementations of the finite-difference method can be found in Chu, so they will not be repeated.

Results of Plane-Strain Uniform Deformations

The stresses plotted in all the figures are normalized against the initial yield strength in tension (T). The strains are normalized against the initial yield strain T/E. For compression, σ_1 and σ_3 are negative, ϵ_1 is negative, and ϵ_2 is positive. For tension, the signs of all stresses and strains are reversed. Absolute values of stresses and strains are used for plotting, and are referred to in subsequent discussions. The applied pressure is $p = |\sigma_1|$. Both associated and nonassociated results are presented for comparison. The Poisson's ratio is 0.3; also, the SD effect and C/T are related through

$$\text{SD} = \frac{2(C/T - 1)}{C/T + 1} \tag{31}$$

Figures 2–4 show results for plane-strain compressions. Figure 2 gives the pressure at initial yielding, equation (11), and the pressure at failure $(p_1)_{\max}$ (to be discussed later) against C/T. For $C/T = 1.5$, Fig. 3 relates the histories of strains to the applied pressure, p, in the plastic region; also, for $C/T = 1.5$, Fig. 4 shows the relationship between the normal (ϵ_1) and longitudinal (ϵ_2) strains.

For plane-strain tension and a maximum allowable $C/T = 1.1$, the initial pressure at yielding and the pressure at failure are plotted in Fig. 6. For comparison, results for the plane-strain compression case are superposed in Fig. 6. Note that a C/T around 1.1 is typical of high strength steels (Spitzig, et al., 1975, 1976) and of certain plastics (Spitzig and Richmond, 1979; Freire and Riley, 1980).

The following discussion will focus first on the compression process.

Initial Yielding and Failure. As shown in Fig. 2, the pressure at initial yielding increases dramatically (and approximately linearly) with C/T. Consequently, unless C/T is small, it is not practical to compare results of the von Mises yield criterion with those of the modified von Mises yield criterion. Obviously for compression processes, since hydrostatic pressure inhibits shear deformation, much higher pressure is required for initial yielding.

The pressure at failure (to be interpreted as *limit* conditions) for the associated case (Fig. 2) can be found in several ways. In equation (16), when the square-root term becomes negative, σ_1 becomes

$$\sigma_1 = -(C - T) - \frac{2}{\sqrt{3}}\{(C - T)^2 + CT\}^{1/2} \tag{32}$$

equation (32) is equivalent to

$$\sigma_3 = \{\sigma_1 - (C - T)\}/2 \tag{33}$$

which can also be expressed as

$$\frac{\sigma_3}{\sigma_1} = \frac{1}{2} - \frac{C - T}{\sigma_1} = \nu^* \tag{34}$$

Here ν^* can be considered as an effective Poisson's ratio which is greater than 1/2 for a compression process and less than 1/2 for tension processes.

Furthermore, writing equation (13) explicitly, we have

$$\dot\epsilon_3 = 0 = \dot\lambda\left(\frac{2\sigma_3 - \sigma_1}{3} + \frac{C - T}{3}\right) + \frac{1}{E}(\dot\sigma_3 - \nu\dot\sigma_1) \tag{35}$$

At failure, however, equation (35) requires $\sigma_3/\sigma_1 = \nu$, which is incompatible with equation (34).

By the same token, for the nonassociated case, maximum pressure (Fig. 2) will occur at

$$\sigma_3 = \sigma_1/2 \tag{36}$$

or, from equation (16)

$$\sigma_1 = -(C - T) - \left\{(C - T)^2 + \frac{4}{3}CT\right\}^{1/2} \tag{37}$$

Downloaded 03 May 2010 to 171.66.16.21. Redistribution subject to ASME license or copyright; see http://www.asme.org/terms/Terms_Use.cfm

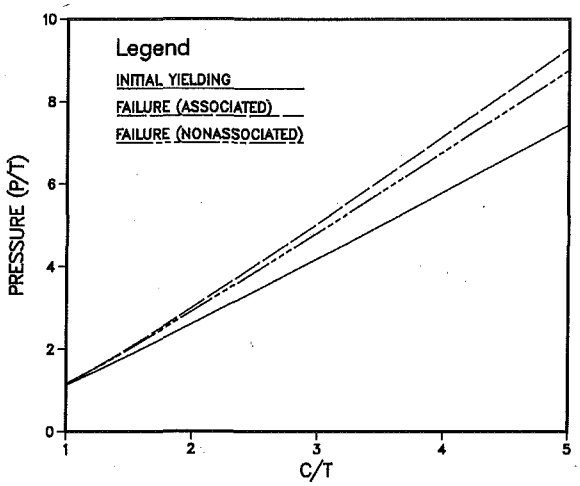


Fig. 2 Pressures at initial yielding and failure versus C/T for plane-strain compression, for associated and nonassociated cases

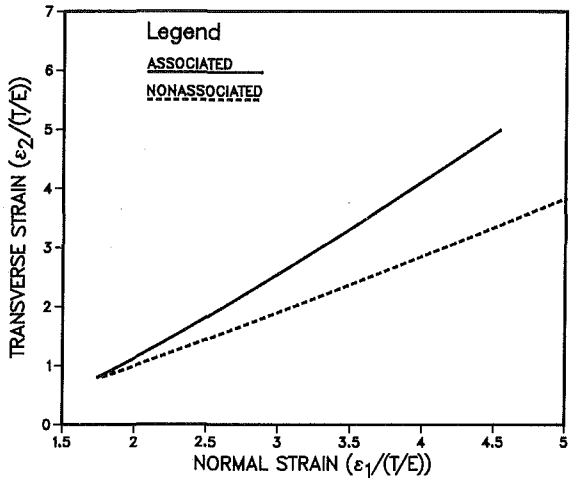


Fig. 4 ϵ_1 versus ϵ_2 for plane-strain compression for associated (solid line) and nonassociated (dashed line) cases $C/T = 1.5$

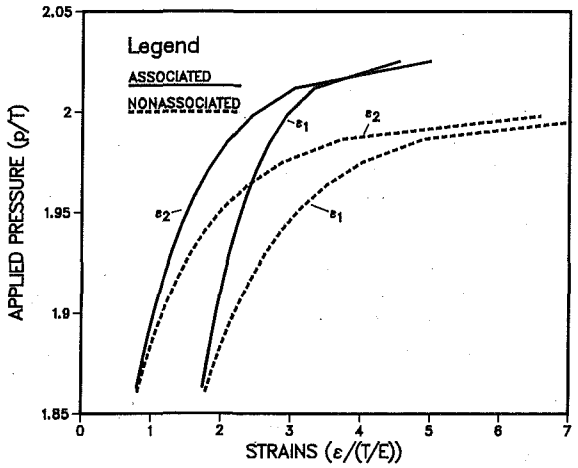


Fig. 3 ϵ_1 and ϵ_2 versus applied pressure for plane-strain compression, for associated (solid lines) and nonassociated (dashed lines) cases, $C/T = 1.5$

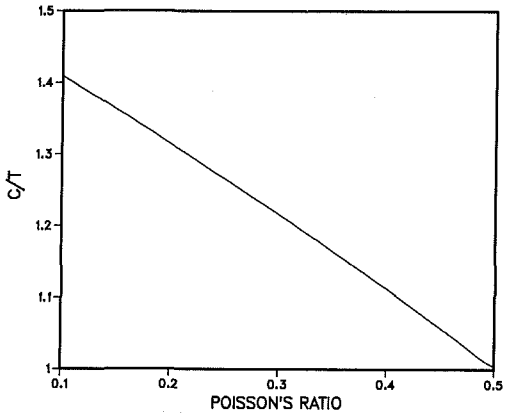


Fig. 5 Maximum allowable C/T versus ν for nonassociated plane-strain tension

Hence, for plane-strain condition, a complete solution is not required to determine pressures at failure. Since $(p_1)_{max}$ calculated from equation (37) is smaller than that calculated from equation (32), the associated case predicts a higher failure pressure than the nonassociated case.

Indeed, for plane-strain conditions, we can generalize equations (33) and (36) for the associated and nonassociated cases, respectively, as

$$\sigma_3 = \frac{1}{2}(\sigma + \sigma_2) - \frac{1}{2}(C - T) \tag{38}$$

$$\sigma_3 = \frac{1}{2}(\sigma_1 + \sigma_2) \tag{39}$$

These results are direct consequences of the assumed flow rules, equations (3) and (9). Note that, since equation (39) is a result of the Prandtl-Reuss flow rules, it applies also to the von Mises yield criterion (Hill, 1949, 1950).

Since $(C - T)$ is assumed to be constant, equation (38) suggests that the classical slip-line theory probably can be extended to MVM materials. Indeed, such an extension has recently been formulated (Inoue, 1986).

Additionally, the vertical distance between the curve of pressure at initial yielding, and the curve of pressure at failure indicates the capacity of the materials to withstand plastic deformation. Since this distance increases with C/T (Fig. 2), the SD effect increases the capacity of the material to withstand plastic deformation.

Bounds of Stresses and Strains. A distinct feature of the nonassociated case is that, for a given pressure, it always predicts much higher (absolute) strains than the associated case (Fig. 3). In other words, when the process is load-controlled, at a given pressure, the nonassociated case gives an upper-bound solution in strains. Note, however, near collapse pressure (Fig. 3), the strains predicted by the associated case are much higher than those of the nonassociated case. This is because the collapse pressure for the associated case is higher than the nonassociated case, and because the strains increase without bound at failure. The same phenomenon is also observed in the numerical studies of associated and nonassociated plasticity for soils (Zienkiewicz, et al., 1975).

For stroke-controlled processes, the opposite is true. As can be seen from Fig. 3, at a given ϵ_1, the nonassociated case predicts a lower pressure than the associated case, so it provides a lower-bound solution in (absolute) stresses.

Under stroke-control, at a given ϵ_1, the nonassociated case also gives a lower strain ϵ_2; hence, it provides an upper-bound solution in the strain components (other than the controlled one), Fig. 4. Generally speaking, for the stroke-controlled case, when the strain components are negative, the nonassociated case will predict higher (absolute) strains than the associated case. On the other hand, when the strain components are positive, the nonassociated case will predict a lower (absolute) strain than the associated case. This is a direct

Downloaded 03 May 2010 to 171.66.16.21. Redistribution subject to ASME license or copyright; see http://www.asme.org/terms/Terms_Use.cfm

ENGINEERING SOCIETIES LIBRARY
JUL 11 1988

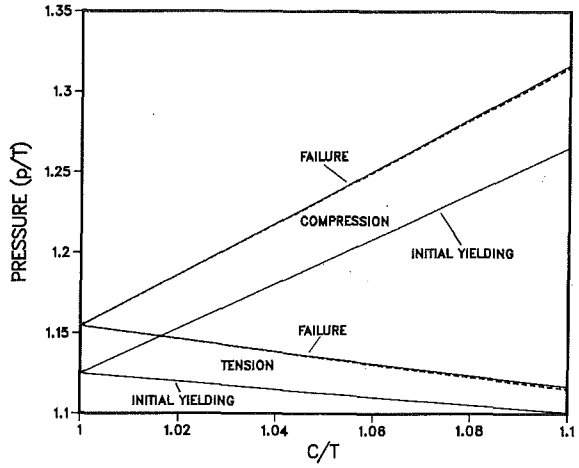


Fig. 6 Pressures at initial yielding and failure versus C/T for plane-strain tension and compression, for associated (solid lines) and nonassociated (dashed lines) cases, $\nu = 0.3$

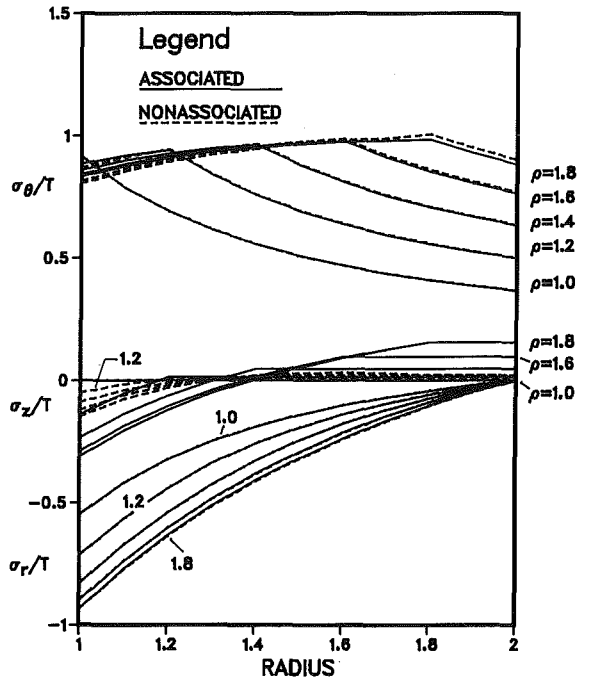


Fig. 7 Radial, tangential and axial stresses for a partly plastic thick-walled cylinder for associated (solid lines) and nonassociated (dashed lines) cases, $C/T = 2$

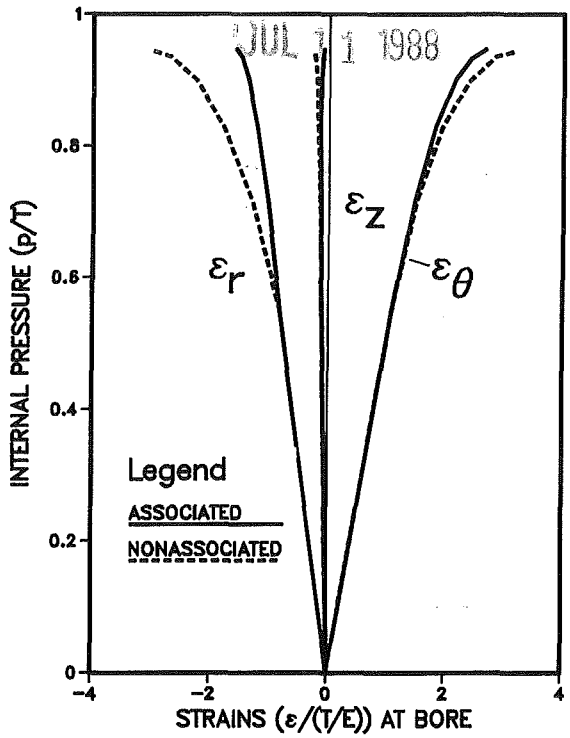


Fig. 8 Radial, tangential and axial strains at the bore versus internal pressure of the completely yielded thick-walled cylinder for associated (solid lines) and nonassociated (dashed lines) cases, $C/T = 2$

consequence of the fact that the plastic volumetric strain components for the associated case are *always positive*; see Fig. 1 and equation (3).

For plane strain *tension*, the pressure at initial yielding (Fig. 6) is again given by equation (11). Using similar arguments for the compression process, the pressures at failure (Fig. 6) for the associated and nonassociated cases, respectively, are

$$\sigma_1 = -(C-T) + \frac{2}{\sqrt{3}}\{(C-T)^2 + CT\}^{1/2} \tag{40}$$

$$\sigma_1 = -(C-T) + \{(C-T)^2 + \frac{4}{3}CT\}^{1/2} \tag{41}$$

However, for the nonassociated case, at a given Poisson's ratio, there is an upper limit on C/T which eliminates the case where the $(p)_{max}$ calculated from equation (41) is less than the initial pressure at yielding, equation (16). This phenomenon seems to indicate the destabilizing effect of nonassociated plasticity. However, since bifurcation is not considered, the possibility of failure before initial yielding shall not be ruled out. No such restrictions exist for the associated case.

The maximum allowable C/T for a given Poisson's ratio is plotted in Fig. 5. If plastic compressibility is to be ignored—for a Poisson's ratio of 0.3, for example—the maximum allowable C/T is only about 1.22 (SD is about 20 percent). While this restriction may have no significance on metals (where the SD effect is generally less than 10 percent), it seems unrealistic for plastics when C/T can be much higher. Plastic compressibility then needs to be incorporated into more realistic constitutive models.

Therefore, with increasing C/T, the range of absolute pressure between initial and final pressure decreases (Fig. 6). As would be expected, this indicates the detrimental effect of hydrostatic pressure for tension processes. Other features of the plane-strain tension process are similar to the compressive one; hence they will not be elaborated.

Results of Thick-Walled Pressure Vessels

For the results of thick-walled cylinders under internal pressure, the ratio of the outer diameter to the inner diameter is 2. Poisson's ratio $\nu = 0.3$. Ten radial segments are used in the solution. Small increments of pressure, $\Delta p/T = 0.0023$, are used.

Typical distributions of stresses at different stages of deformation, for $C/T = 2$, are given in Fig. 7 for both associated and nonassociated cases. These distributions exhibit the familiar patterns of the von Mises yield criterion.

In the plastic region, for a given internal pressure, the nonassociated case predicts lower (absolute) stresses than the associated case. The same trend was also observed by Zienkiewicz, et al. (1975) for soils.

For the problem of plane-strain uniform compression, all the elements of the body yield at the same time, but, for the problem of the thick-walled cylinder, there exists an elastic-

Downloaded 03 May 2010 to 171.66.16.21. Redistribution subject to ASME license or copyright; see http://www.asme.org/terms/Terms_Use.cfm

plastic boundary during deformations. It is interesting that the elastic-plastic boundary for the associated case (with the present numerical scheme and discretization) coincides with the nonassociated one as deformation proceeds. Again, this trend agrees with Zienkiewicz, et al. (1975). However, one should not expect the same to hold for general three-dimensional situations.

The strain distributions versus internal pressure from initial pressurization to complete yielding of the cylinder are given in Fig. 8. Although the states of stresses and strains are more complex than the plane-strain uniform deformation problem, the general trends observed there also hold. The same bounds on stresses and strains as discussed previously for plane-strain deformation apply. Hence, the trends predicted by these two boundary-value problems seem to have more general implications, at least for the essentially one-dimensional plane-strain conditions.

Conclusions

For the pressure modified von Mises yield criterion, under the assumptions of associated and nonassociated plasticity, two boundary-value problems were solved analytically and numerically to assess the SD and plastic compressibility effects.

From the analytical solutions of plane-strain deformations, pressures at initial yielding and at failure, as well as histories of strains were obtained. The pressure at failure, however, was inferred from the flow rules without a full solution. The SD effect increased the pressures at initial yielding and at failure for the compression process. The SD effect also increased the capacity of the materials to withstand plastic deformation for compression processes. The opposite was true for plane-strain tension. Furthermore, unrealistic restriction on the Poisson's ratio and C/T was shown for plane-strain tension and nonassociated plasticity. This implies that the plastic volume increase, albeit small, should be incorporated into a more realistic plasticity theory.

In the comparative study of associated and nonassociated plasticity, upper and lower bounds for stresses and strains for load and stroke-controlled situations were indicated.

For the numerical (finite-difference) solution of a thick-walled pressure vessel, the spread of yield zone and the pressure at full yielding were almost the same for both associated and nonassociatd cases.

Finally, the general trend observed for the plane-strain deformations also applied to the thick-walled cylinder problem. Hence, it is felt that these predictions may apply to more general situations.

Acknowledgments

The author would like to thank Prof. G. J. Weng and the reviewers for their helpful comments and suggestions on the manuscript.

References

Alexander, J. M., 1959, "An Analysis of the Plastic Bending of Wide Plate and the Effect of Stretching on Transverse Residual Stresses," *Proceedings of the Institution of Mechanical Engineers*, Vol. 173, pp. 73–96.

Burger, C. P., and Gomide, H. A., 1982, "Three-Dimensional Strain Field for a Hot Rolled Billet by Photoplastic Simulation," *Experimental Mechanics*, Vol. 22, pp. 441–447.

Casey, J., and Jahedmotlagh, H., 1984, "The Strength-Differential Effect in Plasticity," *International Journal of Solids and Structures*, Vol. 20, pp. 377–393.

Christiansen, A. W., Baer, E., and Radcliffe, S. V., 1971, "The Mechanical Behaviour of Polymers Under High Pressure," *Philosophical Magazine*, Vol. 24, pp. 451–467.

Chu, S. C., 1972, "A More Rational Approach to the Problem of an Elastoplastic Thick-Walled Cylinder," *Journal of the Franklin Institute*, Vol. 294, pp. 57–65.

Drucker, D. C., 1973, "Plasticity Theory, Strength-Differential (S-D) Phenomenon, and Volume Expansion in Metals and Plastics," *Metall. Trans.*, Vol. 4, pp. 667–673.

Drucker, D. C., and Prager, W., 1952, "Soil Mechanics and Plastic Analysis or Limit Design," *Quarterly of Applied Mathematics*, Vol. 10, pp. 157–165.

Freed, A. D., and Sandor, B. I., 1986, "The Plastic Compressibility of 7075-T652 Aluminum-alloy Plate," *Experimental Mechanics*, Vol. 26, pp. 119–121.

Freire, J. L. F., and Riley, R. F., 1980, "Yield Behavior of Photoplastic Materials," *Experimental Mechanics*, Vol. 20, pp. 118–125.

Gerald, C. F., 1970, *Applied Numerical Analysis*, 1st Ed., Addison-Wesley Publishing Co.

Gomide, H. A., and Burger, C. P., 1981, "Three-Dimensional Strain Distribution in Upset Rings by Photoplastic Simulation," *Experimental Mechanics*, Vol. 21, pp. 361–369.

Gupta, Y. M., 1977, "Pressure-Dependent Yield and Plastic Volume Change in High Strength Steels," *Acta Metallurgica*, Vol. 25, pp. 1509–1513.

Hill, R., 1949, "General Features of Plastic-Elastic Problems as Exemplified by Some Particular Solutions," ASME JOURNAL OF APPLIED MECHANICS, Vol. 71, pp. 295–300.

Hill, R., 1950, *The Mathematical Theory of Plasticity*, Clarendon Press, Oxford.

Inoue, N., 1986, "Plane Strain Slip Lines Fields for Polymer Deformation Processes," *JSME*, Vol. 29, pp. 408–415.

Nagtegaal, J. C., Parks, D. M., and Rice, J. R., 1974, "On Numerically Accurate Finite Element Solutions in the Fully Plastic Range," *Comp. Meth. Apply. Mech. Eng.*, Vol. 4, pp. 153–177.

Nemat-Nasser, S., and Shokooh, A., 1980, "On Finite Plastic Flows of Compressible Materials with Internal Friction," *International Journal of Solids and Structures*, Vol. 16, pp. 495–514.

Raghava, R. S., and Caddell, R. M., 1973, "A Macroscopic Yield Criterion for Crystalline Polymers," *International Journal of Mechanical Sciences*, Vol. 15, pp. 967–974.

Raghava, R. S., Caddell, R. M., and Yeh, G. S. Y., 1973, "The Macroscopic Yield Behavior of Polymers," *Journal of Materials Science*, Vol. 9, pp. 225–232.

Spitzig, W. A., and Richmond, O., 1979, "Effect of Hydrostatic Pressure on the Deformation Behavior of Polyethylene and Polycarbonate in Tension and in Compression," *Polymer E. and Sci.*, Vol. 19, pp. 1129–1139.

Spitzig, W. A., Sober, R. J., and Richmond, O., 1975, "Pressure Dependence of Yielding and Associated Volume Expansion in Tempered Martensite," *Acta Metallurgica*, Vol. 23, pp. 885–893.

Spitzig, W. A., Sober, R. J., and Richmond, O., 1975, "The Effect of Hydrostatic Pressure on the Deformation Behavior of Maraging and HY-80 Steels and Its Implications for Plasticity Theory," *Metall. Trans.*, Vol. 7A, pp. 1703–1710.

Tschoegl, N. W., 1971, "Failure Surfaces in Principal Stress Space," *Journal of Polymer Science Sym.*, Vol. 32, pp. 239–267.

Whitney, W., and Andrews, R. D., 1967, "Yielding of Glassy Polymer: Volume Effects," *Journal of Polymer Science*, Part C, Vol. 16, pp. 2981–2990.

Zachary, L. W., and Riley, W. F., 1977, "Optical Response and Yield Behavior of a Polyester Model Material," *Experimental Mechanics*, pp. 321–326.

Zienkiewicz, O. C., Humpheson, C., and Lewis, R. W., 1975, "Associated and Nonassociated Visco-plasticity and Plasticity in Soil Mechanics," *Geotechnique*, Vol. 25, pp. 671–689.

Downloaded 03 May 2010 to 171.66.16.21. Redistribution subject to ASME license or copyright; see http://www.asme.org/terms/Terms_Use.cfm

Analysis of a Power-Law Material Containing a Single Hole Subjected to a Uniaxial Tensile Stress Using the Complex Pseudo-Stress Function

Y. S. Lee
Mem. ASME

L. C. Smith

Power Systems Business Unit,
Westinghouse Electric Corporation,
P.O. Box 2728,
Pittsburgh, PA 15230

The two-dimensional compatibility equation for time-dependent materials described by the power law is expressed in terms of the second derivative of the stress function with respect to complex conjugate variables. The equation is solved by introducing the pseudo-stress function which satisfies the biharmonic equation resulting from the compatibility equation. The relationship between the second derivative of the stress function and the pseudo-stress function is established. The mixed derivative of the stress function associated with the dilatational stress is expressed by an integral of the complicated pseudo-stress function. The velocity and strain-rate components are expressed in terms of the pseudo-stress function. Therefore, responses of power-law creep materials subjected to various boundary conditions can be obtained. Using the pseudo-stress function, the stress distribution in power-law materials, containing a single hole under plane strain and subjected to a uniaxial tensile stress, is found. The Stress Concentration Factors (SCF) on the hole surface, obtained by using the pseudo-stress function, are compared with those under plane stress obtained by another investigator. The results show that the SCF under plane stress is approximately 8 percent higher than that obtained by using the analysis techniques described herein. The maximum tangential stress for $m < 0.5$ is obtained away from the hole whereas for $0.5 \leq m \leq 1$ the maximum stress is found at the hole for $\theta = \pi/2$.

1 Introduction

This analysis includes a representation of the dilatational stress expressed in terms of the integral form of the second derivative of the pseudo-stress function. The velocity, strain rate and stress components are expressed by the pseudo-stress function. The Stress Concentration Factor (SCF) on the hole surface obtained is compared with the results of Hwang (1972). Results (Hwang, 1972) obtained by assuming plane stress are on the average 8 percent higher than those obtained by the analysis described herein. The maximum tangential stress was found to be parallel to the direction of the applied force for all m ($0.1 \leq m \leq 1.0$) and the maximum stress for $0.1 \leq m \leq 0.5$ was found to be in the region away from the hole. The maximum stress location shifts toward the hole surface, and finally, the peak stress is found on the hole for $1.0 \geq m \geq 0.5$. From this, it is determined that the location of flaw initiation is the region away from the hole. This is consistent with experimental observations.

The cavity growth is predicted by using the present results. Three distinct cavity growth configurations are noticed. If $m > 0.25$, the cavity grows elliptically with elongation in the direction of the applied tensile stress. If $m < 0.25$, the cavity also grows elliptically with elongation in the direction perpendicular to the applied tensile stress direction. If $m = 0.25$, the cavity grows essentially like a circle. Similar results were obtained by Anderson (1977) and Budiansky, et al. (1982).

2 Analysis

A method to perform stress analysis associated with power-law materials is described in this section. The procedures of the analyses are very similar to those given in the linear elasticity theory written by Muskhelishvili (1963). The employed assumptions are as follows: (1) The material is homogeneous and isotropic; (2) plane strain; (3) isothermal; (4) incompressible; (5) the constitutive equation is

Contributed by the Applied Mechanics Division for presentation at the Winter Annual Meeting, Chicago, IL, November 28 to December 2, 1988, of The American Society of Mechanical Engineers.

Discussion on this paper should be addressed to the Editorial Department, ASME, United Engineering Center, 345 East 47th Street, New York, N.Y. 10017, and will be accepted until two months after final publication of the paper itself in the JOURNAL OF APPLIED MECHANICS. Manuscript received by ASME Applied Mechanics Division, June 8, 1987; final revision, November 25, 1987.
Paper No. 88-WA/APM-19.

Copyright © 1988 by ASME
Downloaded 03 May 2010 to 171.66.16.21. Redistribution subject to ASME license or copyright; see http://www.asme.org/terms/Terms_Use.cfm

described by the power law. The analyses are performed based on total deformation theory. The constitutive equation of a steady-state creep material is given by

$$\bar{\sigma} = \sigma_0 \dot{\bar{\epsilon}}^m \tag{1}$$

where $\bar{\sigma}$ is the effective stress, $\dot{\bar{\epsilon}}$ is the effective strain rate and m is the strain-rate-hardening exponent which is less than or equal to one. The constitutive equation for the stress components in two-dimensional space under plane strain is given as

$$\dot{\epsilon}_{ij} = \dot{\lambda}(\sigma_{ij} + \sigma_p \delta_{ij}) \tag{2}$$

where σ_p is the hydrostatic pressure (dilatational stress) and $\dot{\lambda} = (3/2)(\dot{\bar{\epsilon}}/\bar{\sigma})$.

Under the incompressible and plane-strain conditions, the effective stress $\bar{\sigma}$ is found to be

$$\bar{\sigma} = \frac{\sqrt{3}}{2}[(\sigma_x - \sigma_y)^2 + 4\sigma_{xy}^2]^{1/2} \tag{3}$$

Using the definition of the Airy stress function in the complex plane, equation (3) can be expressed as

$$\begin{aligned} \bar{\sigma} &= 2\sqrt{3}(\partial^2 U/\partial z^2 \partial^2 U/\partial \bar{z}^2)^{1/2} \\ \dot{\lambda} &= k(m)(\partial^2 U/\partial z^2 \partial^2 U/\partial \bar{z}^2)^{(1-m)/2m} \end{aligned} \tag{4}$$

where $K(m) = (\sqrt{3}/4)(2\sqrt{3}/\sigma_0)^{1/m}$. Let

$$\begin{aligned} (\partial^2 U/\partial z^2 \partial^2 U/\partial \bar{z}^2)^{(1-m)/2m} \partial^2 U/\partial z^2 &= \partial^2 \Lambda/\partial z^2 \\ (\partial^2 U/\partial z^2 \partial^2 U/\partial \bar{z}^2)^{(1-m)/2m} \partial^2 U/\partial \bar{z}^2 &= \partial^2 \Lambda/\partial \bar{z}^2 \end{aligned} \tag{5}$$

If $\partial^2 U/\partial z^2$ and $\partial^2 U/\partial \bar{z}^2$ exist, then $\partial^2 \Lambda/\partial z^2$ and $\partial^2 \Lambda/\partial \bar{z}^2$ exist unless $\partial^2 U/\partial z^2$ or $\partial^2 U/\partial \bar{z}^2$ have singularities in a domain or a boundary. In that case, those locations are deleted in the analysis since $\partial^2 \Lambda/\partial z^2$ and $\partial^2 \Lambda/\partial \bar{z}^2$ do not exist. The strain-rate components can be expressed in terms of $\partial^2 \Lambda/\partial z^2$ and $\partial^2 \Lambda/\partial \bar{z}^2$ by using equations (2) and (5)

$$\begin{aligned} \dot{\epsilon}_x &= -\dot{\epsilon}_y = -K(m)(\partial^2 \Lambda/\partial z^2 + \partial^2 \Lambda/\partial \bar{z}^2) \\ \dot{\epsilon}_{xy} &= -iK(m)(\partial^2 \Lambda/\partial z^2 - \partial^2 \Lambda/\partial \bar{z}^2) \end{aligned} \tag{6}$$

Substituting equation (6) into the compatibility equation the resulting equation is shown to be the biharmonic equation

$$\partial^4 \Lambda/\partial^2 z \partial^2 \bar{z} = 0 \tag{7}$$

Therefore, equation (5) should be restrained as per equation (7). The solution of equation (7) is given as

$$2\Lambda = \bar{z}\phi(z) + \chi(z) + z\bar{\phi}(z) + \bar{\chi}(z) \tag{8}$$

where $\phi(z)$, $\chi(z)$ are holomorphic functions of z. Solving equation (5) with respect to $\partial^2 U/\partial z^2$ and $\partial^2 U/\partial \bar{z}^2$ the second derivative of the Airy's stress function with respect to the complex conjugate are expressed in terms of $\partial^2 \Lambda/\partial z^2$ and $\partial^2 \Lambda/\partial \bar{z}^2$, which are known. The resulting equation is

$$\begin{aligned} \partial^2 U/\partial z^2 &= (\partial^2 \Lambda/\partial z^2 \partial^2 \Lambda/\partial \bar{z}^2)^{(m-1)/2}(\partial^2 \Lambda/\partial z^2) \\ \partial^2 U/\partial \bar{z}^2 &= (\partial^2 \Lambda/\partial z^2 \partial^2 \Lambda/\partial \bar{z}^2)^{(m-1)/2}(\partial^2 \Lambda/\partial \bar{z}^2) \end{aligned} \tag{9}$$

Since Λ is a known and is a differentiable real function, $\partial^2 U/\partial z^2$ and $\partial^2 U/\partial \bar{z}^2$ can be obtained.

The velocity components u and v in the directions of the x and y-axis, respectively, can be obtained by using similar methods as given in Muskhelishvili (1963). The velocity components are given as

$$u + iv = K(m)[\phi(z) - z\bar{\phi}'(z) - \bar{\psi}(z)] \tag{10}$$

where $\psi(z) = \chi'(z)$ in equation (8). The detailed derivation is given by Lee and Gong (1987).

It is now time to define the pseudo-stress function Λ. The pseudo-stress function is defined as differentiable in a domain as well as on a boundary and it is a real-valued function satisfying the biharmonic equation and equations (6), (9), and (10). When a material is perfectly viscous ($m = 1.0$), the pseudo-stress function is identical to the Airy stress function. It is noted that equations (6) and (10) are easy to misunderstand in that the expressions are independent of the strain-rate-hardening exponent. However, the constants contained in the holomorphic conjugate functions, $\phi(z)$, $\psi(z)$, can be a function of the strain-rate-hardening exponent depending on the boundary conditions.

The stress components can also be expressed by the pseudo-stress function

$$\sigma_y - \sigma_x + 2i\sigma_{xy} = 4(\partial^2 \Lambda/\partial z^2 \partial^2 \Lambda/\partial \bar{z}^2)^{(m-1)/2}(\partial^2 \Lambda/\partial z^2) \tag{11}$$

The dilatational stress is given in terms of the pseudo-stress function by using the definition of the total differential of the differentiable function $\partial^2 U/\partial z \partial \bar{z}$,

$$\begin{aligned} \int_{\alpha_1}^{\alpha_2} d(\sigma_p) = 4\int_{\alpha_1}^{\alpha_2} \Bigg[&\frac{\partial}{\partial \bar{z}}\left\{\left(\frac{\partial^2 \Lambda}{\partial z^2}\frac{\partial^2 \Lambda}{\partial \bar{z}^2}\right)^{\frac{m-1}{2}}\left(\frac{\partial^2 \Lambda}{\partial z^2}\right)\right\} dz \\ &+ \frac{\partial}{\partial z}\left\{\left(\frac{\partial^2 \Lambda}{\partial z^2}\frac{\partial^2 \Lambda}{\partial \bar{z}^2}\right)^{\frac{m-1}{2}}\left(\frac{\partial^2 \Lambda}{\partial \bar{z}^2}\right)\right\} d\bar{z}\Bigg] \end{aligned} \tag{12}$$

Since the integrand on the right-hand side of equation (12) is exact in a given region, equation (12) is independent of the integration path C joining an arbitrary pair of points in the region R (Appendix A).

Transforming equation (12) into polar coordinates the resulting equation is

$$\begin{aligned} &\sigma_p(\alpha_2) - \sigma_p(\alpha_1) \\ &= 4\left(\frac{1}{2}\right)^m \int_C \eta^{m-1}\Bigg[\left\{\left(m\frac{\partial \eta}{\partial r} - \frac{\eta}{r}\frac{\partial \Delta}{\partial \theta}\right)\cos(\Delta + 2\theta)\right. \\ &\quad \left. - \left(\eta\frac{\partial \Delta}{\partial r} + \frac{m}{r}\frac{\partial \eta}{\partial \theta}\right)\sin(\Delta + 2\theta)\right\} dr \\ &\quad - \left\{\left(\eta\frac{\partial \Delta}{\partial r} + \frac{m}{r}\frac{\partial \eta}{\partial \theta}\right)\cos(\Delta + 2\theta)\right. \\ &\quad \left. + \left(m\frac{\partial \eta}{\partial r} - \frac{\eta}{r}\frac{\partial \Delta}{\partial \theta}\right)\sin(\Delta + 2\theta)\right\} r d\theta\Bigg] \end{aligned} \tag{13}$$

where $\eta = (\mathrm{Re}^2 + \mathrm{Im}^2)^{1/2}$, $\Delta = \tan^{-1}\dfrac{\mathrm{Im}}{\mathrm{Re}}$,

$$\begin{aligned} \eta &= |\partial^2 \Lambda/\partial z^2| \\ &= \frac{1}{2}\left|\bar{z}\frac{\partial \Phi}{\partial z} + \Psi\right| \end{aligned}$$

$$\begin{aligned} \frac{\partial \eta}{\partial r} &= \frac{1}{\eta}\left(\mathrm{Re}\frac{\partial \mathrm{Re}}{\partial r} + \mathrm{Im}\frac{\partial \mathrm{Im}}{\partial r}\right), \\ \frac{\partial \eta}{\partial \theta} &= \frac{1}{\eta}\left(\mathrm{Re}\frac{\partial \mathrm{Re}}{\partial \theta} + \mathrm{Im}\frac{\partial \mathrm{Im}}{\partial \theta}\right) \\ \frac{\partial \Delta}{\partial r} &= \frac{1}{\eta^2}\left(\mathrm{Re}\frac{\partial \mathrm{Im}}{\partial r} - \mathrm{Im}\frac{\partial \mathrm{Re}}{\partial r}\right), \\ \frac{\partial \Delta}{\partial \theta} &= \frac{1}{\eta^2}\left(\mathrm{Re}\frac{\partial \mathrm{Im}}{\partial \theta} - \mathrm{Im}\frac{\partial \mathrm{Re}}{\partial \theta}\right) \end{aligned} \tag{14}$$

Also, equation (13) can be expressed in terms of the complex variables by using equation (12)

Downloaded 03 May 2010 to 171.66.16.21. Redistribution subject to ASME license or copyright; see http://www.asme.org/terms/Terms_Use.cfm

$$\frac{\partial^2 U}{\partial z \partial \bar{z}}\Big|_A^B = \left(\frac{1}{2}\right)^m \left[\int_A^B \frac{m+1}{2}\,(PQ)^{\frac{m-1}{2}}\left(\frac{\partial P}{\partial \bar{z}}\,dz + \frac{\partial Q}{\partial z}\,d\bar{z}\right)\right.$$

$$\left. + \int_A^B \frac{m-1}{2}\,(PQ)^{\frac{m-3}{2}}\left(P^2\,\frac{\partial Q}{\partial \bar{z}}\,dz + Q^2\,\frac{\partial P}{\partial z}\,d\bar{z}\right)\right] \quad (15)$$

where $P = 2\partial^2\Lambda/\partial z^2 = \bar{z}\partial\Phi/\partial z + \partial\Psi/\partial z$ and $Q = \bar{P}$; A is a fixed point and B is an arbitrary point on a given contour. The detailed derivation in the analysis is given by Lee and Gong (1987) which has been accepted for publication.

3 Boundary-Value Problem

Using the results obtained in the previous section, the boundary-value problem involving a single hole buried in an infinite power-law material subjected to pure tension is solved. The boundary conditions of the problem are

$$\sigma_x = p,\ \sigma_y = 0 \text{ and } \sigma_{xy} = 0 \text{ at } r \to \infty$$

$$\sigma_r = 0 \text{ and } \sigma_{r\theta} = 0 \text{ at } r = R \text{ on the hole surface} \quad (16)$$

where R is the radius of a hole.

Since a single hole is associated with an infinite medium, the holomorphic functions containing the pseudo-stress function, are considered to be

$$\phi'(z) = \Phi = a_0 + \sum_{k=2} \frac{a_k}{z^k} \text{ and } \psi' = \Psi = a_0' + \sum_{k=2} \frac{a_k'}{z^k} \quad (17)$$

The constants a_1 and a_1' are deleted in order to satisfy uniqueness of the displacement

$$a_1 = 0 \text{ and } a_1' = 0 \quad (18)$$

The second derivative of the pseudo-stress function with respect to the complex variable z is given as

$$\frac{\partial^2\Lambda}{\partial z^2} = \frac{1}{2}\left(\bar{z}\,\frac{\partial\Phi}{\partial z} + \Psi\right)$$

$$= \frac{1}{2}\left\{-\sum_{k=2} \frac{k a_k}{r^k}\,e^{-i(k+2)\theta} + \sum_{k=2} \frac{a_k'}{r^k}\,e^{-ik\theta} + a_0'\right\} \quad (19)$$

and

$$\sigma_\theta - \sigma_r + 2i\sigma_{r\theta} = 4(\partial^2\Lambda/\partial z^2 \cdot \partial^2\Lambda/\partial \bar{z}^2)^{(m-1)/2}(\partial^2\Lambda/\partial z^2)e^{2i\theta}$$

$$= 4(1/2)^m \eta^{m-1}(\eta e^{i\Delta})e^{2i\theta}$$

The hydrostatic pressure, σ_p at $z \to \infty$, can be obtained by using equations (15) and (17). σ_p is constant at $z \to \infty$

$$\sigma_p(B) = \sigma_p(A) = 4\left(\frac{1}{2}\right)^m (m+1)\,|a_0'|^{m-1}a_0 \quad (20)$$

The deviatoric stress component at $z \to \infty$ can be obtained from equations (11) and (17)

$$\sigma_y - \sigma_x + 2i\sigma_{xy} = 4\left(\frac{1}{2}\right)^m |a_0'|^{m-1}a_0' \quad (21)$$

From equations (20) and (21)

$$\sigma_x = p = 2\left(\frac{1}{2}\right)^m |a_0'|^{m-1}\{(m+1)a_0 - a_0'\} \quad (22)$$

$$\sigma_y = 0 = 2\left(\frac{1}{2}\right)^m |a_0'|^{m-1}\{(m+1)a_0 + a_0'\}$$

Solving equation (22)

$$a_0 = -a_0'/m + 1, \quad |a_0'|^{m-1}a_0' = -2^m(P/4) \quad (22a)$$

Therefore, a_0' should be a negative real-valued constant

$$a_0' = -2(p/4)^{1/m}, \quad a_0 = (2/1+m)\,(p/4)^{1/m} \quad (23)$$

The right-hand side of the second equation of equation (19) should be a real-valued function based on the boundry condition and Δ should be -2θ on $r = R$. Using the real-valued condition on $r = R$, the following relations are obtained

$$a_3' = 0,$$
$$a_0' + 2a_2/R^2 - a_4'/R^4 = 0, \quad (24)$$
$$Ka_k - a_{k+2}'/R^2 = 0 \quad (K \geq 3).$$

Also, from the condition, $\sigma_r - i\sigma_{r\theta} = 0$ on $r = R$, it can be shown that

$$a_{k+2}'/R^2 = 0 \text{ for } K \geq 3 \quad \text{(Appendix } B\text{)} \quad (25)$$

The derivative $2\partial^2\Lambda/\partial z^2$ is given as

$$2\partial^2\Lambda/\partial z^2 = \eta e^{i\Delta} = \bar{z}\partial^2\phi/\partial z^2 + \psi' \equiv \text{Re} + i\ \text{Im} \quad (26)$$

where

$$\text{Re} = (-2a_2/r^2 + a_4'/r^4)\cos 4\theta + a_2'/r^2\cos 2\theta + a_0'$$
$$\text{Im} = -\{(-2a_2/r^2 + a_4'/r^4)\sin 4\theta + a_2'/r^2 \sin 2\theta\} \quad (27)$$

Equation (27) has two unknowns a_2 and a_2'. They can be determined from the boundary conditions at $r = R$. The dilatational stress is given in equation (13). The first integration path follows from ($\theta = 0$, $r \to \infty$) to ($\theta = 0$, $r \to R$) and the next integration path is considered to be ($r = R$, $\theta = 0$) to ($r = R$, $\theta = \theta$). The resulting equation for the previously described paths is given as follows

$$\sigma_p(R,\theta) = \sigma_p(\infty,0) + 4\left(\frac{1}{2}\right)^m \int_{\theta=0}^{\infty} \eta^{m-1}\left\{\cos\Delta\left(m\,\frac{\partial\eta}{\partial r} - \frac{\eta}{r}\,\frac{\partial\Delta}{\partial\theta}\right) - \sin\Delta\left(\eta\,\frac{\partial\Delta}{\partial r} + \frac{m}{r}\,\frac{\partial\eta}{\partial\theta}\right)\right\}dr$$

$$-4\left(\frac{1}{2}\right)^m \int_{r=R}^{0} \eta^{m-1}\left\{\cos(\Delta+2\theta)\left(\eta\,\frac{\partial\Delta}{\partial r} + \frac{m}{r}\,\frac{\partial\eta}{\partial\theta}\right) + \sin(\Delta+2\theta)\left(m\,\frac{\partial\eta}{\partial r} - \frac{\eta}{r}\,\frac{\partial\Delta}{\partial\theta}\right)\right\}rd\theta$$

$$= \sigma_p(\infty,0) + I_R(R) - I_\theta(\theta) \quad (28)$$

Equation (14) can be found by using equation (27) and the calculation of I_R and I_θ in equation (28) can be performed. The third term on the right-hand side of equation (28) is given as

$$I_\theta = \int_0^\theta \Omega\,\eta^{m-1}\left\{\frac{a_2}{R^2} + (1-m)a_0'\right\}4\sin 2\theta d\theta, \quad \text{on } r = R$$

where

$$\Omega = 4\left(\frac{1}{2}\right)^m \quad (29)$$

Substituting equation (29) into equation (28), the dilatational stress, $\sigma_p\ (R, \theta)$, is given by

$$\sigma_p(R,\theta) = \sigma_p(\infty,0) + \int_{\infty,\theta=0}^{R} \Omega\,\eta^{m-1}\left(m\,\frac{\partial\eta}{\partial r} - \frac{\eta}{r}\,\frac{\partial\Delta}{\partial\theta}\right)\cos\Delta dr$$

$$+\frac{1}{ma_0'}\left\{\frac{a_2}{R^2} + (1-m)a_0'\right\}\left[|2a_0'\cos 2\theta + \frac{a_2'}{R^2}|^m - |2a_0'\right.$$

$$\left. + \frac{a_2'}{R^2}|^m\right]\Omega \quad (30)$$

Downloaded 03 May 2010 to 171.66.16.21. Redistribution subject to ASME license or copyright; see http://www.asme.org/terms/Terms_Use.cfm

for $2a_0' \cos 2\theta + \frac{a_2'}{R^2} \geq 0$ and

$$\sigma_p(R,\theta) = \sigma_p(\infty,0) + \int_{\infty,\theta=0}^{R} \Omega\, \eta^{m-1} \left(m \frac{\partial \eta}{\partial r} - \frac{\eta}{r} \frac{\partial \Delta}{\partial \theta} \right) \cos\Delta dr$$

$$- \frac{1}{m a_0'} \left\{ \frac{a_2}{R^2} + a_0'(1-m) \right\} \left[\left| -\frac{a_2'}{R^2} - 2a_0' \cos 2\theta \right|^m - \left| \frac{-a_2'}{R^2} - 2a_0' \right|^m \right] \Omega \tag{31}$$

for $2a_0' \cos 2\theta + \frac{a_2'}{R^2} \leq 0$.

The second term on the right-hand side of equation (13) can be simplified by using equation (13) and equation (27)

$$\left(m \frac{\partial \eta}{\partial r} - \frac{\eta}{r} \frac{\partial \Delta}{\partial \theta} \right) \cos\Delta = \left(m \frac{\partial \mathrm{Re}}{\partial r} - \frac{1}{r} \frac{\partial \mathrm{Im}}{\partial \theta} \right)$$

since

$$2(\sigma_r - i\sigma_{r\theta}) = 4 \left(\frac{\partial^2 U}{\partial z \partial \bar{z}} - \frac{\partial^2 U}{\partial z^2} e^{2i\theta} \right) \tag{32}$$

and it is noted that the second term on the right-hand side of equation (32) at $r = R$ is given by

$$4 \frac{\partial^2 U}{\partial z^2} e^{2i\theta} = 4 \left(\frac{\partial^2 \Lambda}{\partial z^2} \frac{\partial^2 \Lambda}{\partial \bar{z}^2} \right)^{\frac{m-1}{2}} \frac{\partial^2 \Lambda}{\partial z^2} e^{2i\theta}$$

$$= \Omega \eta^{m-1} (2a_0' \cos 2\theta + a_2'/R^2)$$

$$= -\Omega \eta^m \text{ for } 2a_0' \cos 2\theta + a_2'/R^2 \leq 0.$$

Equation (32) can be simplified as

$$\int_{\theta=0}^{\infty} \Omega \eta^{m-1} \left(m \frac{\partial \mathrm{Re}}{\partial r} - \frac{1}{r} \frac{\partial \mathrm{Im}}{\partial \theta} \right) dr + \sigma_p(\infty,0) + \frac{1}{m a_0'} \left\{ \frac{a_2}{R^2} + (1-m) a_0' \right\} \left| -\frac{a_2'}{R^2} - 2a_2' \right|^m \Omega + \frac{1}{m a_0'} \left\{ (2m-1) a_0' - \frac{a_2}{R^2} \right\} \eta^m(R,\theta) \Omega = 0 \tag{33}$$

for all θ in $[0, 2\pi]$ and on $r = R$.

Therefore the fourth term on the left-hand side of equation (33) should disappear at $r = R$ (Appendix *B*) and the new notation as shown next is introduced

$$a_2 = (1-2m)(-a_0')R^2, \quad A_2 R^2 = (1-2m)R^2 = a_2/-a_0'$$
$$a_4' = (1-4m)(-a_0')R^4, \quad A_4' R^4 = (1-4m)R^4 = a_4'/-a_0'$$
$$A_2' R^2 = a_2'/-a_0' \tag{34}$$

Equation (33) can be simplified as

$$\int_{\theta=0}^{\infty} \Omega \eta^{m-1} \left(m \frac{\partial \mathrm{Re}}{\partial r} - \frac{1}{r} \frac{\partial \mathrm{Im}}{\partial \theta} \right) dr + \sigma_p(\infty,0) + \left| -2a_0' - \frac{2a_2'}{R^2} \right|^m \Omega = 0 \tag{35}$$

for $2a_0' \cos 2\theta + a_2'/R^2 \leq 0$.

Equation (35) can be used if $2a_0' \cos 2\theta + a_2'/R^2 \leq 0$ for all θ. If $2a_0' \cos 2\theta + a_2'/R^2 \leq 0$ at $[0, \theta_1]$ and if $2a_0' \cos 2\theta + a_2'/R^2 \geq 0$ at $[\theta_1, \theta]$; then equations (34) and (35) are still valid expressions. The unknown constants a_0', a_2 and a_4' are given in equations (22*a*) and (34), respectively.

The next step is to determine I_r given in equation (28). It can be calculated using the equations (14) and (27) including new notations given in equation (34) if a_2' is known. Equation (35) at $\theta = 0$ is

$$m \frac{\partial \mathrm{Re}}{\partial r} - \frac{1}{r} \frac{\partial \mathrm{Im}}{\partial \theta} = \{ 2(m-1)x^3 (2A_2 - 2A_4' x^2 - A_2') - 4A_2 x^3 \} \left(\frac{-a_0'}{R} \right)$$

and

$$\eta = [A_4' x^4 + x^2 (A_2' - 2A_2) - 1] |a_0'|,$$
$$\xi = \{ 2(m-1)x^3 (-2A_4' x^2 + 2A_2 - A_2') \} \left(\frac{-a_0'}{R} \right) \tag{36}$$

where $x = R/r$.

If $2a_0' \cos 2\theta + a_2'/R^2 \leq 0$ for all θ or $2a_0' \cos 2\theta + a_2'/R^2 \leq 0$ for $0 \leq \theta \leq \theta_1$ and $2a_0' \cos 2\theta + a_2'/R^2 \geq 0$ for $\theta_1 \leq \theta \leq \pi/2$; then a_2' is determined using the condition

$$\int_0^1 \Omega \eta^{m-1} R \left(m \frac{\partial \mathrm{Re}}{\partial r} - \frac{1}{r} \frac{\partial \mathrm{Im}}{\partial \theta} \right) \left(-\frac{dx}{x^2} \right) + \sigma_p(\infty,0) + \left| -\frac{a_2'}{R^2} - 2a_0' \right|^m \Omega = 0 \tag{37}$$

If $2a_0' \cos 2\theta + \frac{a_2'}{R^2} \geq 0$ for all θ then a_2' is determined using

$$\Omega \int_0^1 \eta^{m-1} R \left(m \frac{\partial \mathrm{Re}}{\partial r} - \frac{1}{r} \frac{\partial \mathrm{Im}}{\partial \theta} \right) \left(-\frac{dx}{x^2} \right) + \sigma_p(\infty,0) - \left| 2a_0' + \frac{a_2'}{R^2} \right|^m \Omega = 0 \tag{38}$$

The unknown constant $A_2' R^2 = a_2'/2\,(P/4)^{1/m}$ can be determined by using equations (37) and (38) and a numerical iteration method. The dilatational stress σ_p at $r = R$ can be found using the conditions from equations (37) and (38) and by using equations (30) and (31); σ_p at $r = R$ is given

$$\sigma_p/P = \sigma_p' = |A_2' - 2\cos 2\theta|^m \text{ for } 2a_0' \cos 2\theta + a_2'/R^2 \geq 0,$$
$$\sigma_p/P = \sigma_p' = -|2\cos 2\theta - A_2'|^m \text{ for } 2a_0' \cos 2\theta + a_2'/R^2 \leq 0. \tag{39}$$

Singularities. The equation associated with the dilatational stress given in equation (28) contains η^{m-1} in the integrand. If $\eta = 0$, then equation (28) involves a singularity which should be deleted from the proper integration path. The integration is possible if the singularities are deleted. Therefore, the existence of singularities must be determined before the integration is performed; η becomes zero if and only if Re = 0 and Im = 0 at the same time. Re and Im for the present boundary conditions are given in equation (27). As mentioned earlier, considering $A_i' R^i = a_i'/2(P/4)^{1/m}$ $(i = 2, 4)$ and $A_i R^i = a_i/2(P/4)^{1/m}$ $(i = 2)$, equation (27) is given as

$$\mathrm{Re} = \{ (A_4' x^4 - 2A_2 x^2) \cos 4\theta + A_2' x^2 \cos 2\theta - 1 \} (-a_0')$$
$$\mathrm{Im} = \{ (-A_4' x^4 + 2A_2 x^2) \sin 4\theta - A_2' x^2 \sin 2\theta \} (-a_0') \tag{40}$$

The values of x and θ to satisfy Re = Im = 0 can be found from equation (40)

Downloaded 03 May 2010 to 171.66.16.21. Redistribution subject to ASME license or copyright; see http://www.asme.org/terms/Terms_Use.cfm

$$\text{Im} = \sin 2\theta\{2(-A_4'x^2 + 2A_2)x^2 \cos 2\theta - A_2'x^2\} = 0$$

$$\theta = 0,\ \pi/2 \text{ or } \cos 2\theta = A_2'/2(-A_4'x^2 + 2A_2) \tag{41}$$

$$\text{Re} = (A_4'x^4 - 2A_2x^2) + A_2'x^2 - 1 = 0 \text{ for } \theta = 0$$

$$\text{Re} = (A_4'x^4 - 2A_2x^2) - A_2'x^2 - 1 = 0 \text{ for } \theta = \pi/2$$

if $\theta \neq 0,\ \pi/2$, then

$$x = 1/\sqrt{1-4m} \text{ or } x = 1. \tag{42}$$

Substituting $x = 1/\sqrt{1-4m}$ into equation (41) results in

$$\cos 2\theta = A_2'/2(1-4m) \tag{43}$$

It is known that m should be <0.25 in equation (42). If $A_2' > 2$, no θ exists to satisfy equation (43). If $A_2' = \pm 2$, then singularities exist at $\theta = \pi/2, 0$ and $x = 1$, on the hole surface. If $A_2' > 2$ and $m < 0.25$, there are no singularities in the domain except at $\theta = 0$ and $\pi/2$. Therefore, movable singularities exist with the location depending on the value of A_2'. The singularities at $x = 1$ are clearly $\cos 2\theta = A_2'/2$ for $A_2' \leq 2$. If $A_2' > 2$, then there is no singularity on $x = 1.0$. Next, the singularities at $\theta = 0$ are considered; x is chosen such that Re $= 0$ at $\theta = 0$; x can be found by the solving equation

$$\text{Re} = A_4'x^4 - (2A_2 - A_2')x^2 - 1 = 0 \tag{44}$$

Since A_4' and A_2 are known, the domain A_2' can be determined by using the conditions: (1) x in equation (44) should have a real positive root and (2) x should be in [0, 1].

As a summary, if $A_2' \leq 2$, then there is a singularity at $r = R$, and the location of the singularity is given by $\cos 2\theta = A_2'/2$ ($R = 1.0$).

If $A_2' > 2$, then there is a singularity at $\theta = 0$ an if $A_2' = 2$, then the singularity is at $r = R = 1.0$ and $\theta = 0$. The location of the singularity is required in order to choose the integration path and to find the A_2'-value. For numerical convenience, the present integration to find the stress components is terminated at $\theta = 89°$. Since the values A_2' are obtained numerically, minor deviations in A_2' and the stress components are expected.

Stress Components Calculation. The constants in equation (27), a_0', a_2, a_2' and a_4' are determined. The hydrostatic pressure, $\sigma_r + \sigma_\theta$ can be determined by using equations (14), (27), and (28) following the integration path from $r \to \infty$ to r at $\theta = 0$ and from $\theta = 0$ to θ at given r. The hydrostatic pressure, $\sigma_r + \sigma_\theta$, at any point in the domain is found by using equation (28) and replacing R into equation (28) by r

$$\sigma_p(r,\theta) = \sigma_p(\infty,0) + I_r(r) - I_\theta(\theta) = \sigma_r + \sigma_\theta \tag{45}$$

where

$$I_r(r) = \int_\infty^r \eta^{m-1}\left\{\cos(\Delta + 2\theta)\left(m\frac{\partial \eta}{\partial r} - \frac{\eta}{r}\frac{\partial \Delta}{\partial \theta}\right) - \sin(\Delta + 2\theta)\left(\eta\frac{\partial \Delta}{\partial r} + \frac{m}{r}\frac{\partial \eta}{\partial \theta}\right)\right\}dr$$

at $\theta = 0$ and

$$I_\theta(\theta) = \int_0^\theta \eta^{m-1}\left\{\cos(\Delta + 2\theta)\left(\eta\frac{\partial \Delta}{\partial r} + \frac{m}{r}\frac{\partial \eta}{\partial \theta}\right) + \sin(\Delta + 2\theta)\left(m\frac{\partial \eta}{\partial r} - \frac{\eta}{r}\frac{\partial \Delta}{\partial \theta}\right)\right\}rd\theta$$

and where

$$\cos(\Delta + 2\theta) = \frac{\text{Re}}{\eta}\cos 2\theta - \frac{\text{Im}}{\eta}\sin 2\theta$$

$$\sin(\Delta + 2\theta) = \frac{\text{Im}}{\eta}\cos 2\theta + \frac{\text{Re}}{\eta}\sin 2\theta$$

Re and Im are given in equation (27) and

$$\sigma_\theta - \sigma_r + 2i\sigma_{r\theta} = \eta^{m-1}\Omega\{(\text{Re}\cos 2\theta - \text{Im}\sin 2\theta) + i(\text{Re}\sin 2\theta + \text{Im}\cos 2\theta)\} \tag{46}$$

As mentioned earlier in equation (28), the total stress components are normalized by the applied stress, p. Solving equations (45) and (46), stress components σ_r, σ_θ, and $\sigma_{r\theta}$ are obtained

$$\sigma_r/p = \frac{1}{2}\{\sigma_p(r,\theta) - \eta^{m-1}(\text{Re}\cos 2\theta - \text{Im}\sin 2\theta)\}\Omega$$

$$\sigma_\theta/p = \frac{1}{2}\{\sigma_p(r,\theta) + \eta^{m-1}(\text{Re}\cos 2\theta - \text{Im}\sin 2\theta)\}\Omega \tag{47}$$

$$\sigma_{r\theta}/p = \frac{1}{2}\eta^{m-1}(\text{Re}\sin 2\theta + \text{Im}\cos 2\theta)\Omega$$

Strain Rates and Velocity Components Calculation. Using equation (6), the complex representation of the strain rates, $\dot{\epsilon}_r$, $\dot{\epsilon}_\theta$ and $\dot{\epsilon}_{r\theta}$, is given by

$$\dot{\epsilon}_\theta - \dot{\epsilon}_r + 2i\dot{\epsilon}_{r\theta} = 4K(m)\frac{\partial^2 \Lambda}{\partial z^2}e^{2i\theta} \tag{48}$$

and

$$\partial^2\Lambda/\partial z^2 = \frac{1}{2}\left(\bar{z}\frac{\partial \Phi}{\partial z} + \Psi\right) = \frac{1}{2}\eta e^{i\Delta} \equiv \frac{1}{2}(\text{Re} + i\,\text{Im})$$

$$\partial\phi/\partial z = \Phi = a_0 + \sum_{k=2} a_k/z^k = a_0 + \frac{a_2}{z^2} \tag{49}$$

$$\partial\psi/\partial z = \Psi = a_0' + \sum_{k=2} a_k'/z^k = a_0' + \frac{a_2'}{z^2} + \frac{a_4'}{z^4}$$

for these boundary conditions.

Substituting equations (49) into (48)

$$\dot{\epsilon}_\theta - \dot{\epsilon}_r + 2i\dot{\epsilon}_{r\theta} = 2k(m)2(P/4)^{1/m}(\text{Re} + i\,\text{Im})e^{2i\theta}$$

where

$$\text{Re} = (-2a_2/r^2 + a_4'/r^4)\cos 4\theta + a_2'/r^2\cos 2\theta + a_0'$$
$$= [\{-2(1-2m)R^2/r^2 + (1-4m)R^4/r^4\}\cos 4\theta + A_2'R^2/r^2\cos 2\theta - 1]$$

$$\text{Im} = -(a_4'/r^4 - 2a_2/r^2)\sin 4\theta - a_2'/r^2\sin 2\theta$$
$$= [-\{(1-4m)R^4/r^4 - 2R^2(1-2m)/r^2\}\sin 4\theta - A_2'R^2/r^2\sin 2\theta]$$

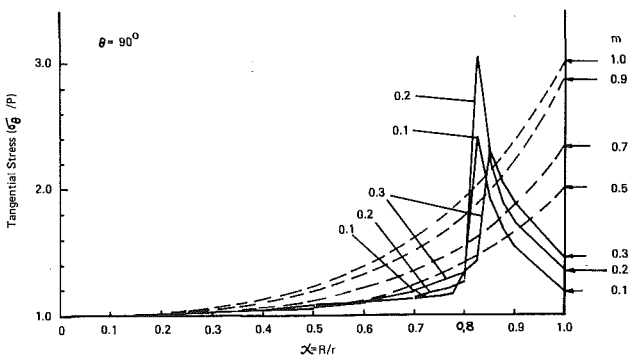


Fig. 1 Tangential stress distribution with respect to various $\chi = R/r$ and strain-rate-hardening exponent at $\theta = 90°$

Downloaded 03 May 2010 to 171.66.16.21. Redistribution subject to ASME license or copyright; see http://www.asme.org/terms/Terms_Use.cfm

and A_2' is strongly dependent on the strain-rate-hardening exponent.

Using the incompressible condition under the plane-strain condition

$$\dot{\epsilon}_\theta = 2(P/4)^{1/m} k(m)\{(A-1)\cos 2\theta + B\} = -\dot{\epsilon}_r$$

$$\dot{\epsilon}_{r\theta} = -2(P/4)^{1/m} k(m)(A+1)\sin 2\theta \tag{50}$$

where

$$A = (1-4m)R^4/r^4 - 2(1-2m)R^2/r^2; \quad B = A_2' R^2/r^2$$

Velocity components u_r and V_θ can be obtained from equations (10) and (49). Equation (10) is

$$u_r + iV_\theta = k(m)\{\phi - z\bar{\phi}'(z) - \bar{\psi}(z)\}e^{-i\theta} \tag{10}$$

Integrating equation (49) with respect to z

$$\phi(z) = a_0 z - \frac{a_2}{z} \text{ and } \psi(z) = a_0' z - \frac{a_2'}{z} - \frac{a_4'}{3z^3} \tag{51}$$

since

$$a_0 = -a_0'/1 + m = 2(P/4)^{1/m}(1/1+m)$$

$$u_r + iV_\theta = 2(P/4)^{1/m} k(m)(\mathrm{Re} + i\ \mathrm{Im})e^{-i\theta} \tag{52}$$

where

$$\mathrm{Re} = \{r - 2(1-2m)R^2/r + (1-4m)R^4/3r^3\}\cos 2\theta + A_2' R^2/r$$

$$\mathrm{Im} = -\{r - (1-4m)R^4/3r^3\}\sin 2\theta$$

$$u_r = 2(P/4)^{1/m} k(m)[\{r - 2(1-2m)R^2/r + (1-4m)R^4/3r^3\}\cos 2\theta + A_2' R^2/r]$$

$$V_\theta = -2(P/4)^{1/m} k(m)[r - (1-4m)R^4/3r^3]\sin 2\theta \tag{53}$$

Equations (47), (50) and (53) describe the stress, the strain rate and the velocity distributions when a single hole buried in power-law materials is subjected to uniaxial tension. The results and discussion are in the next section. It should be mentioned that the constants contained in the holomorphic conjugate functions $\phi(z)$, and $\psi(z)$ in equations (6) and (10) can be a function of the strain-rate-hardening exponent.

4 Results and Discussion

The applications of the pseudo-stress function associated with a power-law material are described. The stress analyses of a simple boundary-value problem for a single hole buried in an infinite power-law material subjected to a simple tension is performed.

The stress distribution obtained by using the analysis described herein are shown in Figs. 1–5. Figure 1 shows the tangential stress distribution for various strain-rate-hardening exponents (m) in the radial direction at $\theta = 89°$. These stress values are considered approximately as stress at $\theta = 90°$. Maximum values at $\theta = 90°$ occur for specific radii, $x = R/r$. The peak tangential stress for $m < 0.5$ occurs in the region away from the hole surface and the location of the peak stress moves toward the hole surface with increasing m-values. When $m = 0.5$, the maximum stress ($\sigma_{\theta\max}$) is on the hole surface and the locations of the maximum stress ($\sigma_{\theta\max}$) for $0.5 \le m \le 1.0$ does not change ($\theta = 90°$ and $x = 1.0$). $\sigma_{\theta\max}$ for $1 \ge m \ge 0.5$ increases with m on the hole surface. However, $\sigma_{\theta\max}$ does not have a monotonic tendency with respect to the variations of m in this ($0.1 \le m < 0.5$) region; σ_θ on the hole surface for $0.1 \le m < 0.5$ increases with m. Therefore, it can be said that σ_θ on the hole surface (at $\theta = 90°$ and $x = 1.0$) increases with m-values. Figure 2 illustrates the Stress Concentration Factor (SCF) that gives the maximum stress in the tangential direction at $\theta = \pi/2$ for all values of m. It includes the results obtained by Hwang (1972), Neuber (1961) and Stowell (1950) under plane stress and used the interpolation method proposed by Calladine (1963–1964). The figure also shows the tangential stress at $\theta = \pi/2$ and $x = 1.0$ for $0.2 \le m \le 0.5$. The maximum SCF under simple tension occurred in the region away from the hole for low strain-rate-hardening exponents.

It is interesting to note that the SCF for $m = 0.2$ is greater than for $m = 1.0$. Therefore, the SCF of a power-law material under the present boundary conditions cannot be predicted by an interpolation, for example, the SCF for the balanced biaxial tension under plane-stress conditions (SCF $= 1 + m$). Figure 3 illustrates the effective stress distributions in the radial direction at given θ and m-values. The effective stress ($\bar{\sigma}$) at $\theta = 89°$ ($= 90°$) decreases with x for all m-values while σ_θ for $m = 0.1$, 0.2, 0.3, and 0.4 have peak values in the region away from the hole. For $0.5 \le m \le 1.0$ σ_θ is maximum on the hole surface. This unusual result may be due to the hydrostatic pressure associated with low m-values. A minimum point of $\bar{\sigma}$ occurs in the radial direction for $0.7 \le m$

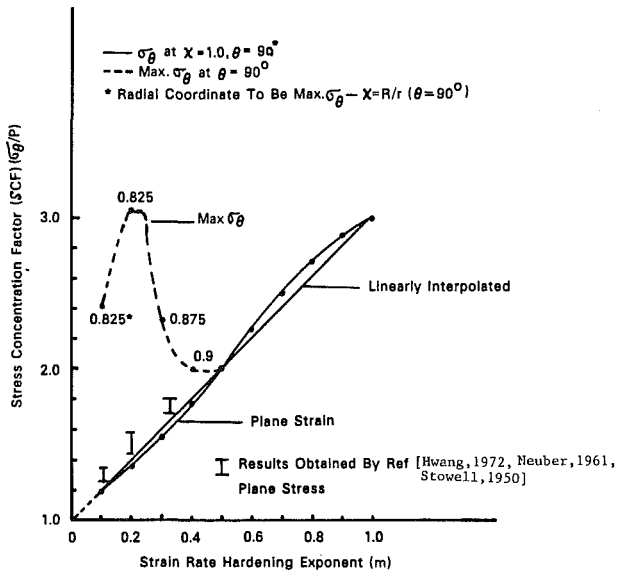


Fig. 2 Stress Concentration Factor (SCF) for various strain-rate-hardening exponent (m) at $\theta = 90°$

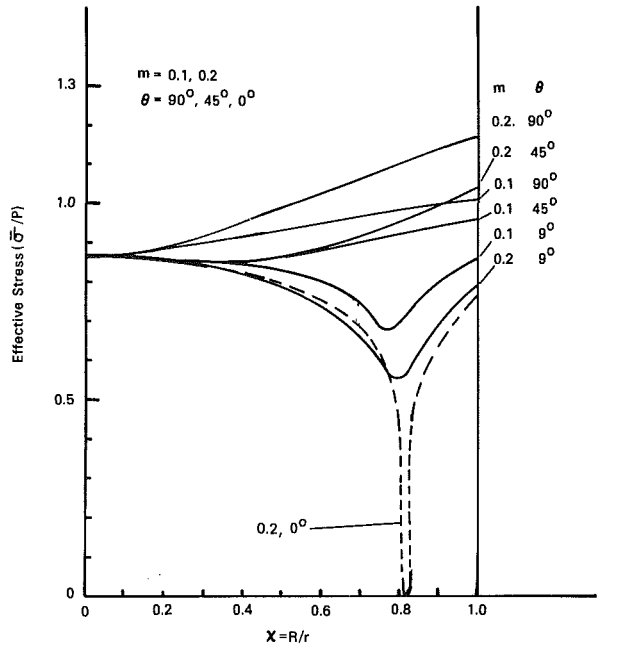


Fig. 3 Effective stress distribution with respect to various $\chi = R/r$ and strain-rate-hardening exponents; $m = 0.1$, 0.2 at given $\theta = 90°$, 45°, 9°, 0°

Downloaded 03 May 2010 to 171.66.16.21. Redistribution subject to ASME license or copyright; see http://www.asme.org/terms/Terms_Use.cfm

≤ 1.0 at $\theta = 9°$ whereas for $m = 0.6$ and 0.5 $\bar{\sigma}$ monotonically increases with decreasing x. For $0.1 \leq m \leq 0.4$, a minimum point for $\bar{\sigma}$ again is predicted. The location of $\bar{\sigma} = 0$ at $\theta = 0$ shifts toward the hole when m is increased (for $0.1 \leq m \leq 0.4$) and $\bar{\sigma}$ for $m = 0.5$ becomes zero at $x = 1.0$. $\bar{\sigma}$ variation with respect to x for $m = 0.2$ and $\theta = 0$ is significantly sharper than for $m = 0.4$ (Fig. 3). Figure 4 illustrates hydrostatic pressure distributions in the radial direction at given θ-values. The location of the maximum $\bar{\sigma}_p$ for $m = 0.1$ and 0.2 coincide with the x-value at which $\bar{\sigma} = 0$ at $\theta = 0$ and it occurs in the region away from the hole surface at $\theta = 90°$.

The σ_p variation with respect to θ on the hole ($x = 1.0$) for $m \leq 0.5$ is always positive whereas σ_p changes from a negative to a positive value for $0.5 \leq m \leq 1.0$. From the stress distributions, shown in Figs. 1-4, it can be concluded that there are two kinds of stress distribution patterns. One for $m < 0.5$ and one for $0.5 \leq m \leq 1.0$. Therefore, the unusual hydrostatic pressure distribution may affect the stress distribution for low m-values. This may be responsible for the unusual stress distribution, especially the stress components related to the hydrostatic pressure.

Experimental results that indicate a void cluster or a flaw in the region away from the hole when a single hole buried in a power-law material is subjected to simple tension were found by Manjoine (1977). Many metallic materials with $T > 0.4$ Tm (Tm is the melting temperature) have strain-rate-hardening exponent of $0 < m < 0.5$ in the steady-state creep region. Hence, the present analysis can be verified by experimental results of Manjoine (1977).

Damage Under Creep. Manjoine (1977) proposed that the ductility of a material in a given metallurgical state is its ability to deform and distribute the strains, which are concentrated in local grains, to adjacent grains without exceeding the strain limit of the grains forming cell volume. The method for evaluating this strain limit has been described by Manjoine (1975). The work of Davis and Connelly (1959) suggested that the ductility of a strain-hardening material such as Type 304 stainless steel is a function of the normal stress on the octahedral plane and the octahedral shearing stress. They proposed a triaxiality factor (T.F.) based on these stresses which are normalized to a value of unity for simple tension.

$$\text{T.F.} = \sigma_p / \bar{\sigma}$$

where

$$\sigma_p = \frac{1}{3}\sigma_{kk};\ \bar{\sigma} = \frac{\sqrt{3}}{2}\{(\sigma_r - \sigma_\theta)^2 + 4\sigma_{r\theta}^2\}^{1/2}$$

under plane strain.

Manjoine (1977) proposed that the ductility is a function of T.F. and the relationship between multiaxial and simple tension strain limit is given for a range of 0.3 to 3.0 of T.F.

Strain limit for multiaxial stress =

Strain limit for simple tension/T.F.

The consumed ductility under the present analysis is obtained by using (strain for multiaxial stress) × (T.F.) or ($\dot{\bar{\epsilon}}$ × T.F.). The consumed ductility for various m at $\theta = 90°$ (89°) is shown in Fig. 5 and it can be used for the explanation of the void formation in the region away from the hole qualitatively even though T.F. for the present analysis exceeds 3.0. The large amount of exhausted ductility for $m = 0.2$ and 0.4 occurs in the region away from the hole whereas for $m = 0.6$ and 1.0 it occurs on the hole (Fig. 5). When the exhausted ductility on the left-hand side region of the peak location is compared with that on the right-hand side obviously the exhausted ductility on the left-hand side is higher. Therefore, the first location to form a flaw could be the location of the maximum exhausted ductility and the next location is the left of the peak location rather than to the right of the peak location. Thus the flaw initiated at the location shown in Fig. 5 would connect with the other flaw produced on the left-hand side of the location. It is obvious that the flaw initiated at the peak location can grow toward the hole because the ligament of the hole side is small and that region is weak. However, it is not expected that the flaw is initiated in the region away from the hole.

The foregoing statement is a conjecture based on Fig. 5 since the present analysis is invalid just after a flaw or a void forms in a material. The statement associated with the triaxiality factor agrees with results obtained from experiment (Manjoine, 1977).

The cavity growth rate can be obtained by using equation (53). Two distinct cavity configurations are observed. The cavity grows faster in the direction of the applied stress and elongates in the applied stress direction for high m-values as expected. However, it grows faster in a direction perpendicular to the applied stress direction for low m-values such as $m = 0.1$ and $m = 0.2$. This is unexpected and similar results are obtained by Anderson (1977) and Budiansky, et al. (1982).

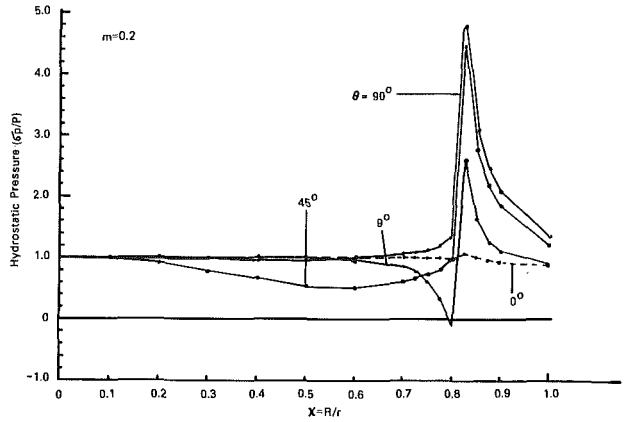


Fig. 4 Hydrostatic pressure distribution with respect to various $\chi = R/r$ for $m = 0.2$ and at a given $\theta = 90°, 45°, 9°, 0°$

References

Anderson, H., 1977, "Analysis of a Model for Void Growth and Coalescence Ahead of a Moving Crack Tip," *Journal of Mechanics and Physics of Solids*, Vol. 25, p. 217.

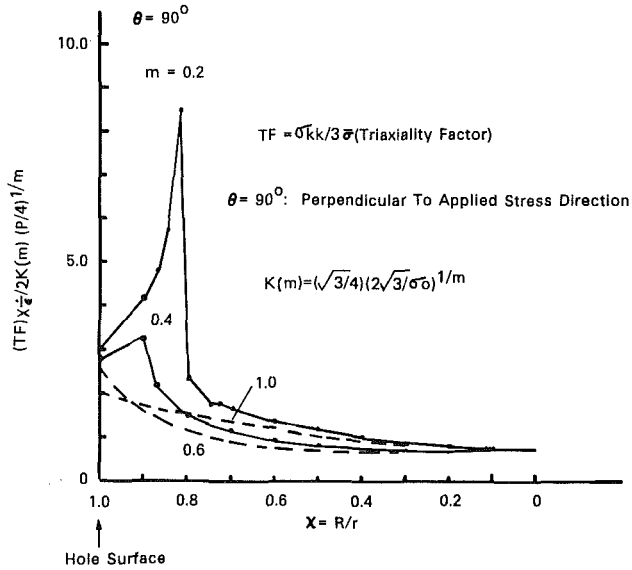


Fig. 5 Triaxiality factor times effective strain-rate distribution with respect to $\chi = R/r$ at $\theta = 90°$

Downloaded 03 May 2010 to 171.66.16.21. Redistribution subject to ASME license or copyright; see http://www.asme.org/terms/Terms_Use.cfm

Budiansky, B., and Hutchinson, J. W., and Slutsky, S., 1982, "Void Growth in Viscous Solids," *Mechanics of Solids*, The Rodney Hill 60th Anniversary Volume, Eds., Hopkinson, H. G., and Sewell, M. J., Pergamon Press, New York, p. 13.

Calladine, C. R., 1963–1964, "A Rapid Method for Estimating the Greatest Stress in a Structure Subject to Creep," *Proceedings of the Institution of Mechanical Engineering*, Vol. 178, p. 198.

Davis, E. A., and Connelly, F. M., 1959, "Stress Distribution and Plastic Deformation in Rotating Cylinder of Strain Hardening Material," *ASME Transaction*, Vol. 81, Series E, p. 25.

Hwang, W. C., 1972, "Theoretical Study of Stress Concentration at Circular Holes and Inclusion in Strain Hardening Materials," *International Journal of Solids and Structures*, Vol. 8, p. 149.

Lee, Y. S., and Gong, H., 1987, "Application of Complex Variables and Pseudo-Stress Function to Power Law Materials and Stress Analysis of Rigid Inclusion in Power Law Materials Subjected to Simple Tension and Pure Shear," *International Journal of Mechanical Sciences*, accepted.

Manjoine, M. J., 1977, "Basic Creep-Rupture Testing at 1100 F, (593 C) of Type 304 Stainless Steel for Uniaxially Loaded Specimens with Stress and Strain Gradients," Topical Report, WARD-HT-3045-26, Distribution Category UC-79h, prepared for the U.S. Energy Research and Development Administration.

Manjoine, M. J., 1975, "Ductility Indices at Elevated Temperatures," *ASME Transaction*, Vol. 97, Series H, p. 156.

Muskhelishvili, N. I., 1963, "*Some Basic Problems of the Mathematical Theory of Elasticity*," P. Noordhoff Ltd., 4th Ed., Groningen, The Netherlands, pp. 107–112 and p. 206.

Neuber, H., 1961, "Theory of Stress Concentration for Shear-Strained Prismatical Bodies With Arbitrary Nonlinear Stress Strain Law," ASME JOURNAL OF APPLIED MECHANICS, Vol. 28, p. 544.

Stowell, E. Z., 1950, "Stress and Strain Concentration at a Circular Hole in an Infinite Plate," National Advisory Committee For Aeronautics-TN2073.

APPENDIX A

Equation (12) can be derived by using the definition of total differential of the differentiable function $\partial^2 U/\partial z\partial\bar{z}$

$$d(\sigma_p) = 4d(\partial^2 U/\partial z\partial\bar{z}) = 4\left\{\frac{\partial}{\partial z}\left(\frac{\partial^2 U}{\partial z\partial\bar{z}}\right)dz + \frac{\partial}{\partial\bar{z}}\left(\frac{\partial^2 U}{\partial z\partial\bar{z}}\right)d\bar{z}\right\} \tag{A-1}$$

$$= 4\left\{\frac{\partial}{\partial\bar{z}}\left(\frac{\partial^2 U}{\partial z^2}\right)dz + \frac{\partial}{\partial z}\left(\frac{\partial^2 U}{\partial\bar{z}^2}\right)d\bar{z}\right\} \tag{A-2}$$

Equation (A-2) can be expressed as shown in equation (12) by using equation (9); also, the validity of interchanging the operators into equation (A-2) can be shown by using the equilibrium equations and $\sigma_y - \sigma_x + 2i\sigma_{xy} = 4\,\partial^2 U/\partial z^2$.

APPENDIX B

Substituting equation (17) into (15) and using equation (24), equation (28), and $\sigma_r - i\sigma_{r\theta} = 0$ on $r = R$, the following equation is obtained

$$I_R(R) + \sigma_p(\infty,0) - \Omega\left|\frac{a_2'}{R^2} + 2a_0'\right|^m + \frac{1}{ma_0'}\left\{\frac{a_2}{R^2} + (1-2m)a_0'\right\}\Omega\int_0^\theta \eta^{m-1}(-4ma_0'\sin 2\theta)\,d\theta$$

$$-\int_0^\theta\left\{\sum_{k=3}\eta^{m-1}\Omega(2\,a_{k+2}'/R^{k+2})\sin k\theta\, d\theta\right\} = 0 \tag{B-1}$$

for all θ in $[0, 2\pi]$ on $r = R$ and for $a_2/R^2 + 2\,a_0'\cos 2\theta \geq 0$.

Equation (B-1) is of the form

$$\text{const} + \sum_{k=2}\int_0^\theta \Omega\eta^{m-1}(R,\theta)A_k\sin k\theta\, d\theta = 0 \tag{B-2}$$

or const $+ F(\theta) - F(0) = 0$ where $A_k = -2a_{k+2}/R^{k+2}$ ($k \geq 3$) and $F(\theta)$ is the primitive function of the integrand on the left-hand side of equation (B-2).

Therefore,

$$F'(\theta) = \sum_2 \eta^{m-1}\Omega A_k \sin k\theta = 0 \text{ for all } \theta \text{ in } [0,2\pi] \text{ and on } r = R.$$

Since

$$\eta^{m-1}(R,\theta) = \left|\frac{a_2'}{R^2} + 2a_0'\cos 2\theta\right|^{m-1} \neq 0$$

for all θ in $[0, 2\pi]$

$$\sum_2 A_k \sin k\theta = 0.$$

Fourier coefficients are linearly independent and $A_k = 0$ for $k \geq 2$; also const $= 0$.

Downloaded 03 May 2010 to 171.66.16.21. Redistribution subject to ASME license or copyright; see http://www.asme.org/terms/Terms_Use.cfm

M. J. Forrestal
Fellow ASME

V. K. Luk
Mem. ASME

Advanced Projects Division II,
Division 9122,
P.O. Box 5800,
Sandia National Laboratories,
Albuquerque, NM 87185

Dynamic Spherical Cavity-Expansion in a Compressible Elastic-Plastic Solid

We developed an analytical model for the elastic-plastic response of a compressible material from the uniform expansion of a spherically symmetric cavity. Previous models consider the material as incompressible. Numerical results from both models showed the effect of compressibility.

Introduction

Hopkins (1960) presents an extensive review on the dynamic expansion of spherical cavities in elastic-plastic materials. That paper summarizes much of the pioneering work conducted during or shortly after the Second World War at the Armament Research Department at Fort Halstead, England. Because of the pressure at that time to produce immediate practical results, much of the original work appears in unpublished reports. Hopkins not only presents mathematical models, but also details the problems that motivated the models. Applications include the response of metals and geological materials from spherical cavity formation produced by high-explosive detonations. In addition, Hill (1980) summarizes an account of some of his work conducted at Fort Halstead during the Second World War. In that paper, Hill applies cavity-expansion methods to investigate armor penetration by nondeforming projectiles.

As discussed by Hopkins (1960), models for the dynamic expansion of spherical cavities assume the material as incompressible. In this paper, we developed a model that included compressibility. Numerical results from both models showed the effect of compressibility.

Compressible Elastic-Plastic Material

A spherically symmetric cavity is expanded from zero, initial radius at constant velocity V. As shown in Fig. 1, this expansion produces plastic and elastic response regions. The plastic region is bounded by the radii $r = Vt$ and $r = ct$, where r is the radial, Eulerian coordinate, t is time, and c is the elastic-plastic, interface velocity. Similarly, the elastic region is bounded by $r = ct$ and $r = c_d t$, where c_d is the elastic, dilatational velocity.

The material in the plastic region is described with a linear, pressure-volumetric strain relation and the Tresca yield criterion. Thus

$$p = K\eta = K(1 - \rho_0/\rho) \tag{1a}$$

$$p = \frac{1}{3}(\sigma_r + \sigma_\theta + \sigma_\phi); \quad \sigma_\phi = \sigma_\theta \tag{1b}$$

$$\sigma_r - \sigma_\theta = Y \tag{1c}$$

where p is hydrostatic pressure; K is bulk modulus; η is volumetric strain; ρ_0 and ρ are the densities in undeformed and deformed configurations; σ_r, σ_θ, and σ_ϕ are the radial, hoop, and meridianal components of Cauchy stress taken positive in compression, $\sigma_\phi = \sigma_\theta$ from symmetry, and Y is the flow stress. The elastic region has bulk modulus K and Poisson's ratio ν.

Plastic Response. Equations of momentum and mass conservation in Eulerican coordinates are

$$\frac{\partial \sigma_r}{\partial r} + \frac{2(\sigma_r - \sigma_\theta)}{r} = -\rho \frac{Dv}{Dt} \tag{2a}$$

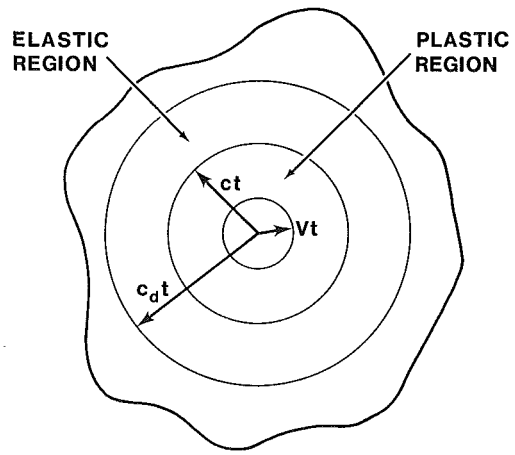


Fig. 1 Response regions

Contributed by the Applied Mechanics Division for presentation at the Winter Annual Meeting, Chicago, IL, November 28 to December 2, 1988, of The American Society of Mechanical Engineers.

Discussion on this paper should be addressed to the Editorial Department, ASME, United Engineering Center, 345 East 47th Street, New York, N.Y. 10017, and will be accepted until two months after final publication of the paper itself in the JOURNAL OF APPLIED MECHANICS. Manuscript received by ASME Applied Mechanics Division, March 31, 1987.

Paper No. 88-WA/APM-24.

Copyright © 1988 by ASME
Downloaded 03 May 2010 to 171.66.16.21. Redistribution subject to ASME license or copyright; see http://www.asme.org/terms/Terms_Use.cfm

$$\rho\left(\frac{\partial v}{\partial r}+\frac{2v}{r}\right)=-\frac{D\rho}{Dt} \tag{2b}$$

where v is the radial, particle velocity (positive outward), and

$$\frac{D}{Dt}=\frac{\partial}{\partial t}+v\frac{\partial}{\partial r} \tag{2c}$$

The nonlinear equations for the plastic region are combined to eliminate σ_θ, ρ resulting in two equations in σ_r, v.

$$\frac{\partial \sigma_r}{\partial r}+\frac{2Y}{r}=\frac{-\rho_0}{(1-\eta)}\cdot\frac{Dv}{Dt} \tag{3a}$$

$$\frac{\partial v}{\partial r}+\frac{2v}{r}=\frac{-1}{K(1-\eta)}\cdot\frac{D\sigma_r}{Dt} \tag{3b}$$

Postanalysis numerical evaluation showed that η is small, and $(1-\eta)$ is taken as unity. The dimensionless variables

$$S=\sigma_r/K,\quad T=Y/K,\quad U=v/c,\quad \epsilon=V/c \tag{4a}$$

and the similarity transformation

$$\xi=r/ct \tag{4b}$$

are introduced. With (4*a*,*b*), equations (3*a*,*b*) transform to

$$\frac{dS}{d\xi}+\frac{2T}{\xi}=\beta^2(\xi-U)\frac{dU}{d\xi} \tag{5a}$$

$$\frac{dU}{d\xi}+\frac{2U}{\xi}=(\xi-U)\frac{dS}{d\xi} \tag{5b}$$

in which

$$\beta=c/c_p,\quad c_p^2=K/\rho_0 \tag{5c}$$

The boundary condition at the cavity wall is

$$U(\xi=\epsilon)=\epsilon \tag{6a}$$

and boundary conditions at the elastic-plastic interface are

$$S(\xi=1)=S_2 \tag{6b}$$

$$U(\xi=1)=U_2 \tag{6c}$$

where S_2, U_2 will be determined from the elastic-plastic interface conditions.

Equations (5*a*,*b*) are solved approximately and later compared with the full, nonlinear solution that requires numerical evaluation of differential equations (Longcope, 1987). First, we neglect the nonlinear terms in (5*a*,*b*) and obtain an equation for $U(\xi)$

$$(1-\beta^2\xi^2)\frac{dU}{d\xi}+\frac{2U}{\xi}=-2T \tag{7}$$

The solution for (7) that satisfies the boundary condition (6*c*) is

$$U(\xi)=\frac{(U_2\beta^2+T)(1-\beta^2\xi^2)}{\beta^2\xi^2(1-\beta^2)}-\frac{T}{\beta^2\xi}+\frac{T(1-\beta^2\xi^2)}{2\beta^3\xi^2}\ln\left[\frac{(1+\beta\xi)(1-\beta)}{(1-\beta\xi)(1+\beta)}\right],$$

$$\epsilon<\xi<1 \tag{8a}$$

Next, substitute (8*a*) into (5*a*) and integrate to obtain $S(\xi)$. Integration of the last term in (5*a*) is made convenient by noting that $U\cdot dU/d\xi=1/2\ d[U^2]/d\xi$, and the integration constant is evaluated from (6*b*). Thus

$$S(\xi)=S_2-\beta^2(U^2-U_2^2)/2+\frac{2(U_2\beta^2+T)(1-\xi)}{\xi(1-\beta^2)}-2T\ln\xi+T\ln\left(\frac{1-\beta^2\xi^2}{1-\beta^2}\right)+\frac{T}{\beta\xi}\ln\left[\frac{(1+\beta\xi)(1-\beta)}{(1-\beta\xi)(1+\beta)}\right],\quad \epsilon<\xi<1 \tag{8b}$$

As discussed by Longcope and Forrestal (1983), the elastic-plastic, interface velocity $c(\beta=c/c_p)$ depends on the cavity-expansion velocity $V(\beta\epsilon=V/c_p)$. This interface velocity is obtained from (8*a*) and (6*a*) and given by the transcendental equation

$$T\beta\epsilon+\beta^3\epsilon^3-\frac{\beta(U_2\beta^2+T)(1-\beta^2\epsilon^2)}{(1-\beta^2)}-\frac{T(1-\beta^2\epsilon^2)}{2}\ln\left[\frac{(1+\beta\epsilon)(1-\beta)}{(1-\beta\epsilon)(1+\beta)}\right]=0 \tag{8c}$$

In this solution procedure, we first obtained an approximate solution for $U(\xi)$ by neglecting nonlinear terms in (5*a*,*b*). However, $U(\xi)$ given by (8*a*) satisfies the boundary conditions exactly. It will be shown later that results from this approximate solution are in excellent agreement with the full, nonlinear results for a practical range.

Interface Conditions. The plastic and elastic regions of response are linked through the Hugoniot jump conditions that conserve mass and momentum across the elastic-plastic interface. In terms of the dimensionless variables

$$U_2=1-(\rho_1/\rho_2)(1-U_1) \tag{9a}$$

$$S_2=S_1+\beta^2(\rho_1/\rho_0)(1-U_1)(U_2-U_1) \tag{9b}$$

where the subscript 2 refers to quantities in the plastic region at the interface ($\xi=1$), and the subscript 1 refers to quantities in the elastic region at $\xi=1$. The Tresca yield criterion and pressure-volumetric strain relations (1*a*,*c*) apply on either side of the elastic-plastic interface. The dimensionless, radial, interface stresses are

$$S_2=2T/3+(1-\rho_0/\rho_2) \tag{9c}$$

$$S_1=2T/3+(1-\rho_0/\rho_1) \tag{9d}$$

Eliminating ρ_1, ρ_2 from (9*a*–*d*) shows there are no jumps in stress and particle velocity across the interface. Thus

$$U_2=U_1,\quad S_2=S_1 \tag{10}$$

Elastic Response. The elastic region is governed by the wave equation (neglecting the convective term)

$$\frac{\partial^2 u}{\partial r^2}+\frac{2}{r}\frac{\partial u}{\partial r}-\frac{2u}{r^2}=\frac{1}{c_d^2}\frac{\partial^2 u}{\partial t^2} \tag{11a}$$

$$c_d^2=\frac{E(1-\nu)}{(1+\nu)(1-2\nu)\rho_0} \tag{11b}$$

and the stress-displacement relations

$$\sigma_r=-\frac{E}{(1+\nu)(1-2\nu)}\left[(1-\nu)\frac{\partial u}{\partial r}+2\nu\frac{u}{r}\right] \tag{11c}$$

$$\sigma_\theta=-\frac{E}{(1+\nu)(1-2\nu)}\left(\nu\frac{\partial u}{\partial r}+\frac{u}{r}\right) \tag{11d}$$

Stress components are positive in compression, u is radial displacement measured positive outward, and E is Young's modulus.

The similarity transformation and dimensionless displacement are introduced

$$\xi=r/ct,\quad \bar{u}(\xi)=u/ct \tag{12}$$

With (12), the wave equation (11*a*) transforms to

$$(1-\alpha^2\xi^2)\frac{d^2\bar{u}}{d\xi^2}+\frac{2}{\xi}\frac{d\bar{u}}{d\xi}-\frac{2}{\xi^2}\bar{u}=0 \tag{13a}$$

$$\alpha=c/c_d \tag{13b}$$

Equation (13*a*) can be reduced to a first-order differential equation in $F(Z)$ with the successive transformations: $Z=\alpha\xi$, $\bar{u}=Z\phi$, $F=d\phi/dZ$. Integration yields

Downloaded 03 May 2010 to 171.66.16.21. Redistribution subject to ASME license or copyright; see http://www.asme.org/terms/Terms_Use.cfm

$$\bar{u} = A\alpha\xi - B\left(\frac{1-3\alpha^2\xi^2)}{3\alpha^2\xi^2}\right) \tag{14a}$$

The constants A, B are evaluated from

$$\bar{u}(\xi = 1/\alpha) = 0 \tag{14b}$$

$$\sigma_r(\xi = 1) - \sigma_\theta(\xi = 1) = Y \tag{14c}$$

where (14*b*) requires zero displacement at the elastic wave front, and (14*c*) satisfies the yield criterion at the elastic-plastic interface. In summary,

$$\frac{u}{ct} = \frac{T(1+\nu)(1-\alpha\xi)^2(1+2\alpha\xi)}{9(1-2\nu)(1-\alpha^2)\xi^2}, \quad 1 < \xi < 1/\alpha \tag{15a}$$

$$\frac{1}{c}\frac{du}{dt} = \frac{T(1+\nu)(1-\alpha^2\xi^2)}{3(1-2\nu)(1-\alpha^2)\xi^2}, \quad 1 < \xi < 1/\alpha \tag{15b}$$

$$\frac{\sigma_r}{K} = \frac{2T(1-\alpha\xi)[(1-2\nu)(1+\alpha\xi)+(1+\nu)\alpha^2\xi^2]}{3(1-2\nu)(1-\alpha^2)\xi^3}, \quad 1 < \xi < 1/\alpha \tag{15c}$$

$$\frac{\sigma_\theta}{K} = \frac{-T[(1-2\nu)-3\alpha^2\xi^2+2(1+\nu)\alpha^3\xi^3]}{3(1-2\nu)(1-\alpha^2)\xi^3}, \quad 1 < \xi < 1/\alpha \tag{15d}$$

As indicated by (8*a–c*) and (10), dimensionless particle velocity and radial stress at $\xi = 1$ are required for response in the plastic region. From (10) and (15*b*, *c*)

$$U_2 = \frac{T(1+\nu)}{3(1-2\nu)} \tag{16a}$$

$$S_2 = \frac{2T}{3}\left[1 + \frac{(1+\nu)\alpha^2}{(1-2\nu)(1+\alpha)}\right] \tag{16b}$$

Quasi-Static Response. For very small, cavity-expansion velocity, inertial terms can be neglected and the response is quasi-static. As discussed by Hill (1950), a finite pressure is required to open a spherical hole from zero, initial radius. Thus, for an infinitesimal, cavity-expansion velocity V, there is a finite pressure on the cavity wall given by

$$\sigma_s = \frac{2Y}{3}\left\{1 + \ln\left[\frac{\mathrm{E}}{3(1-\nu)Y}\right]\right\} \tag{17a}$$

In terms of the dimensionless variables used in this study

$$S_s = \frac{2T}{3}\left\{1 + \ln\left[\frac{(1-2\nu)}{(1-\nu)T}\right]\right\} \tag{17b}$$

Response Equations. Radial stress in the plastic region is given by (8*b*) and requires expressions for U_2, S_2, and β. U_2 and S_2 are given explicitly by (16*a*,*b*) and $\beta = c/c_p$ is given by the transcendental equation (8*c*). Radial stress in the elastic region is given by (15*c*) and requires values of α. Since $\alpha = c/c_d$ and $\beta = c/c_p$,

$$\alpha = (c_p/c_d)\beta = [(1+\nu)/3(1-\nu)]^{1/2}\beta \tag{18}$$

Non-Negative Plastic Work. As discussed by Hunter (1957) and Hopkins (1960), we must also show that work performed in the plastic region is everywhere non-negative. From the procedure outlined in Hopkins (1960), this condition is given by

$$\frac{U}{\xi} - \frac{\partial U}{\partial \xi} \geq 0 \quad \text{for} \quad \epsilon < \xi < 1 \tag{19}$$

We show later that this criterion is satisfied for the applications of this study.

Incompressible Elastic-Plastic Material

As pointed out by Hopkins (1960), Hill (1948) first considered the dynamic, spherical, cavity-expansion problem. His model assumes the material as incompressible in both plastic and elastic regions. Hopkins presents an equation from Hill's unpublished report for pressure on the expanding cavity. Since we chose to compare stress profiles from both compressible and incompressible models, we now summarize results from our derivation for the incompressible solution using the methods outlined in the previous section. For the incompressible model, we normalize stresses by Y, and other dimensionless quantities remain the same.

Plastic Region. The equation of mass conservation for an incompressible material reduces to

$$\partial U/\partial \xi + 2U/\xi = 0 \tag{20a}$$

which integrates to

$$U = \epsilon^3/\xi^2 \tag{20b}$$

with the application of the boundary condition at the cavity wall (6*a*). Substitution of (20*b*) into (5*a*) and integrating gives

$$S_i = \frac{\sigma_r}{Y} = -2\ln\xi + \frac{2\epsilon^3\rho c^2}{Y\xi} - \frac{\epsilon^6\rho c^2}{2Y\xi^4} + B \tag{20c}$$

where the interface velocity c and integration constant B will be determined from the interface conditions (10), and the subscript i denotes incompressible.

Elastic Region. The equation of mass conservation for the elastic region reduces to

$$d\bar{u}/d\xi + 2\bar{u}/\xi = 0 \tag{21a}$$

which integrates to

$$\bar{u} = A/\xi^2 \tag{21b}$$

For an incompressible, elastic material, Hooke's law is $\mathrm{E}u/r = (\sigma_r - \sigma_\theta)/2$, and the equation of motion becomes

$$\frac{dS_i}{d\xi} + \frac{4\mathrm{E}\bar{u}}{Y\xi^2} = -\frac{\rho c^2\xi^2}{Y}\frac{d^2\bar{u}}{d\xi^2} \tag{22a}$$

Substitution of (21*b*) into (22*a*) and integrating gives

$$S_i = \frac{2}{3\xi^3} + \frac{3\rho c^2}{\mathrm{E}\xi}, \quad \xi > 1 \tag{22b}$$

where the integration constant is set to zero, so $S_i(\xi \to \infty) = 0$; A is evaluated by satisfying the yield criterion at $\xi = 1$.

Response Equations. The interface velocity c is obtained by equating particle velocities at the interface ($\xi = 1$). Thus

$$c = (2\mathrm{E}/3Y)^{1/3}V \tag{23}$$

The integration constant in (20*c*) is obtained by equating radial stresses at the interface, and $B = 2/3$. Thus radial stress in the plastic region is

$$S_i = \frac{2}{3} - 2\ln\xi + \frac{2\epsilon^3\rho c^2}{Y\xi} - \frac{\epsilon^6\rho c^2}{2Y\xi^4}, \quad \epsilon < \xi < 1 \tag{24}$$

With c defined by (23), the radial stresses in the elastic and plastic regions are given by (22*b*) and (24), respectively.

The cavity wall is at $\xi = \epsilon = V/c$, and from (23) and (24)

$$S_i(\epsilon) = \frac{2}{3}\left[1 + \ln\left(\frac{2E}{3Y}\right)\right] + \frac{3}{2}\frac{\rho V^2}{Y} \tag{25}$$

which agrees with Hill's result for a uniformly expanding cavity (Hopkins, 1960).

Numerical Results and Discussion

For the compressible solutions derived in this paper, the elastic response is exact; however, the response solution for the plastic region is approximate. To show the accuracy of the approximate, compressible solution, we compare our results with those from the full, nonlinear solution that requires

Downloaded 03 May 2010 to 171.66.16.21. Redistribution subject to ASME license or copyright; see http://www.asme.org/terms/Terms_Use.cfm

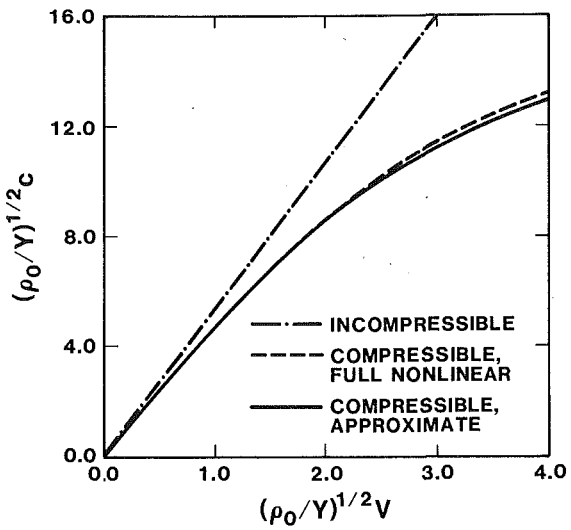


Fig. 2 Elastic-plastic inteface velocity versus cavity-expansion velocity for 6061-T6 aluminum

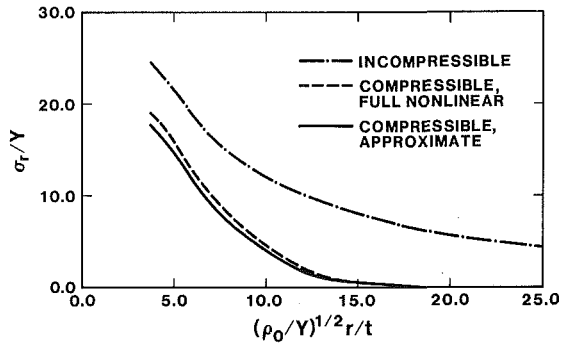


Fig. 3 Radial stress profiles for 6061-T6 aluminum with $(\rho_0/Y)^{1/2}V = 3.70$

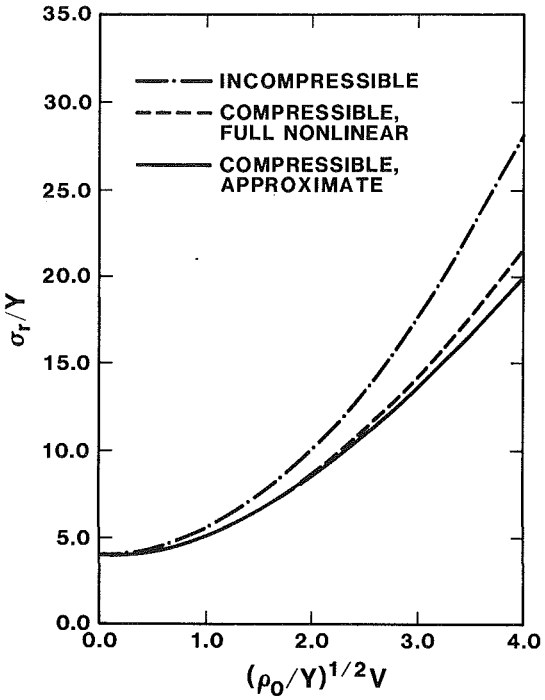


Fig. 4 Radial stress on the cavity wall versus cavity-expansion velocity for 6061-T6 aluminum

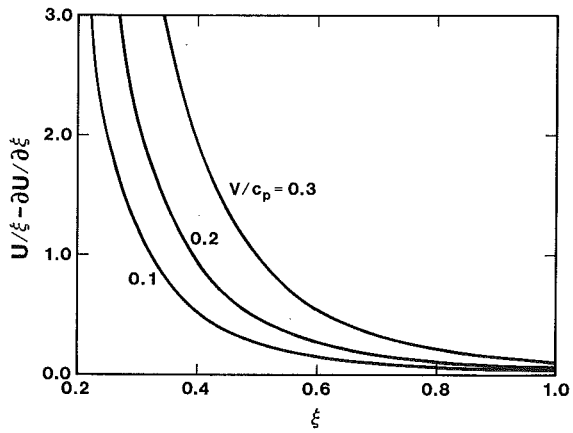


Fig. 5 Criterion for non-negative work in the plastic region for 6061-T6 aluminum

numerical evaluations of differential equations[1] (Longcope, 1987). In addition, we compare our results with the incompressible model to show the effect of compressibility.

We present numerical results in Figs. 2–4 for the compressible solution with $Y/K = 0.00435$ and $\nu = 1/3$. These material parameters correspond to 6061-T6 aluminum with $Y = 300$ MPa. Figure 2 shows the elastic-plastic, interface velocity c versus the expansion velocity V. The models that include compressibility are in excellent agreement, and c asymptotically approaches c_p as the expansion velocity V increases. By contrast, the interface velocity for the incompressible model is proportional to the expansion velocity; see (23).

In Fig. 3, we compare radial stress profiles from the compressible[2] and incompressible models for $(\rho_0/Y)^{1/2}V = 3.70$. For 6061-T6 aluminum, this dimensionless, expansion velocity corresponds to $V = 1.23$ km/s. As shown in Fig. 3, stress profiles from the compressible models are in good agreement, while the incompressible model predicts higher stresses. As previously mentioned, stresses predicted by the compressible models are continuous at the elastic-plastic interface, $(\rho_0/Y)^{1/2}r/t = 12.4$, and at the elastic wave front, $(\rho_0/Y)^{1/2}r/t = 18.6$. As indicated by (22*b*), elastic stresses for the incompressible model decay as ξ increases, but there is no elastic wave front. The elastic-plastic interface for the incompressible model is at $(\rho_0/Y)^{1/2}r/t = 19.7$.

Figure 4 shows radial stress at the cavity wall versus expansion velocity. For $(\rho_0/Y)^{1/2}V = 3.70$, the approximate, compressible model predicts a radial stress that is 6 percent lower than the full, nonlinear solution; whereas, the incompressible model predicts a radial stress that is 29 percent higher than the full, nonlinear solution. In our approximate, compressible model, we take $(1-\eta) = 1$ in the equations of motion and mass conservation (3*a*,*b*). From (1*a*–*c*), $\eta = S - 2T/3$. For $(\rho_0/Y)^{1/2}V = 3.70$, $\eta = 0.073$. So as the volumetric strain η increases, the approximate model deviates from the full, nonlinear solution.

Figure 5 shows that the criterion for non-negative plastic work (19) is satisfied.

In summary, we developed an accurate, approximate model for a spherically expanding cavity in a compressible, elastic-plastic material. The effect of compressibility on radial stress is shown in Figs. 3 and 4. The incompressible model overpredicts radial stress, and the approximate, compressible

[1] This numerical procedure is similar to that presented by Longcope and Forrestal, 1983.

[2] For Figs. 3 and 4, the compressible, radial stresses are normalized by Y rather than K.

Downloaded 03 May 2010 to 171.66.16.21. Redistribution subject to ASME license or copyright; see http://www.asme.org/terms/Terms_Use.cfm

model is in good agreement with the full, nonlinear solution for a practical range of expansion velocities.

Acknowledgments

This work was supported by the U.S. Department of Energy. The authors thank Dr. D. B. Longcope for the full, nonlinear results in the figures.

References

Bishop, R. F., Hill, R., and Mott, N. F., 1945, "The Theory of Indentation and Hardness Tests," *The Proceedings of the Physical Society*, Vol. 57, Part 3, pp. 147–159.

Hill, R., 1948, Unpublished Report.

Hill, R., 1950, *The Mathematical Theory of Plasticity*, Oxford, London.

Hill, R., 1980, "Cavitation and the Influence of Headshape in Attack of Thick Targets by Non-Deforming Projectiles," *Journal of the Mechanics and Physics of Solids*, Vol. 28, pp. 249–263.

Hopkins, H. G., 1960, "Dynamic Expansion of Spherical Cavities in Metals," Chapter III, *Progress in Solid Mechanics*, Vol. 1, Eds., Sneddon, I. N., and Hill, R., North-Holland Publishing Company, Amsterdam, New York.

Hunter, S. C., 1957, "The Propagation of Spherically Symmetric Disturbances in Ideally Plastic Materials," *Proceedings of the Conference on the Properties of Materials at High Rates of Strain*, London, The Institution of Mechanical Engineers, pp. 147–155.

Longcope, D. B., and Forrestal, M. J., 1983, "Penetration of Targets Described by a Mohr-Coulomb Failure Criterion with a Tension Cutoff," ASME JOURNAL OF APPLIED MECHANICS, Vol. 105, pp. 327–333.

Longcope, D. B., 1987, "The Prediction of Loads on Penetrators Into Rock Via the Spherical Cavity-Expansion Approximation," SAND 87-0959, Sandia National Laboratories, Albuquerque, NM.

Downloaded 03 May 2010 to 171.66.16.21. Redistribution subject to ASME license or copyright; see http://www.asme.org/terms/Terms_Use.cfm

Mechanical Modeling of Material Damage

S. Murakami
Professor,
Department of Mechanical Engineering,
Nagoya University,
Furo-cho, Chikusa-ku,
Nagoya 464-01, Japan

A systematic theory to describe the anisotropic damage states of materials and a consistent definition of effective stress tensors are developed within the framework of continuum damage mechanics. By introducing a fictitious undamaged configuration, mechanically equivalent to the real damaged configuration, the classical creep damage theory is extended to the general three-dimensional states of material damage; it is shown that the damage state can be described in terms of a symmetric second rank tensor. The physical implications, mathematical restrictions, and the limitations of this damage tensor, as well as the effects of finite deformation on the damage state, are discussed in some detail. The notion of the fictitious undamaged configuration is then applied also to the definition of effective stresses. Finally, the extension of the effective stresses incorporating the effects of crack closure is discussed. The resulting effective stress tensor is employed to analyze the stress-path dependence of the elastic behavior of a cracked elastic-brittle material.

1 Introduction

Proper understanding and the mechanical description of the damage process of materials brought about by the internal defects are of vital importance in discussing the mechanical effects of the material deterioration on the macroscopic behavior of materials, as well as in elucidating the process leading from these defects to the final fracture. A systematic approach to these problems of distributed defects can be provided by continuum damage mechanics (Chaboche, 1981; Hult, 1979; Kachanov, 1986; Krajcinovic, 1984; Lemaitre and Chaboche, 1978, 1985; Murakami, 1983). The fundamental notion of this theory, attributable originally to Kachanov (1958) and modified somewhat by Rabotnov (1969), is to represent the damage state of materials characterized by distributed cavities in terms of appropriate mechanical variables (internal state variables), and then to establish mechanical equations to describe their evolution and the mechanical behavior of damaged materials.

The nucleation and the growth of voids observed in the process of material damage depend significantly on the direction of the applied stress or strain and, hence, are essentially anisotropic. The generalization of Kachanov-Rabotnov's notion (Kachanov, 1958; Rabotnov, 1969) to multiaxial states of damage, therefore, necessitates the proper description of the oriented features of material damage. Thus considerable efforts have been done to find rational modeling of anisotropic damage phenomena (Betten, 1983; Chaboche, 1984; Cordebois and Sidoroff, 1982; Hayhurst and Storåkers, 1976; Leckie and Onat, 1981; Kachanov, M., 1980; Krajcinovic, 1983; Murakami and Ohno, 1981; Vakulenko and Kachanov, M., 1971; Onat and Leckie, 1988). The damage variables to model such material damage should have not only clear physical implication, but also have appropriate mathematical and mechanical properties. As regards this point, previous modeling of material damage needs further refinement.

The present paper is concerned with a systematic modeling of material damage and the extension of the aforementioned Kachanov-Rabotnov notion to the general three-dimensional anisotropic damage. By postulating that the material damage can be characterized mainly by the decrease of load-carrying effective area caused by the development of microscopic cracks and cavities, the state of material damage is described by introducing a fictitious deformation gradient from the current damaged configuration B_t of the material element to the corresponding fictitious undamaged configuration B_f with the decreased net area due to damage; two kinds of damage tensors $\mathbf{D}$ and $\tilde{\mathbf{D}}$ are defined to represent the damage state with respect to the current damaged configuration B_t and to the elastically unloaded damaged configuration $\tilde{B}_t$. Then, the relations between the damage tensors $\mathbf{D}$ and $\tilde{\mathbf{D}}$ as well as their mathematical restrictions are elucidated; they are shown to be second rank symmetric tensors. The mechanical interpretation of these damage tensors and the definition of the related effective stress also are discussed. Finally, the proposed theory is extended to incorporate the effects of the microcrack closure and is applied to analyze the elastic behavior of a cracked elastic-brittle material under combined hydrostatic pressure and shear.

2 Mechanical Description of Damage States

2.1 Fictitious Undamaged Configuration and Fictitious Deformation Gradient. Let us first take a tensile bar of Fig. 1. We denote its cross-sectional area in the undamaged initial state and that in the current damaged state under stress σ by A_0 and A, respectively. According to the classical damage

Contributed by the Applied Mechanics Division for publication in the JOURNAL OF APPLIED MECHANICS.
Discussion on this paper should be addressed to the Editorial Department, ASME, United Engineering Center, 345 East 47th Street, New York, N.Y. 10017, and will be accepted until two months after final publication of the paper itself in the JOURNAL OF APPLIED MECHANICS. Manuscript received by ASME Applied Mechanics Division, May 27, 1987; final revision, October 20, 1987.

Copyright © 1988 by ASME
Downloaded 03 May 2010 to 171.66.16.21. Redistribution subject to ASME license or copyright; see http://www.asme.org/terms/Terms_Use.cfm

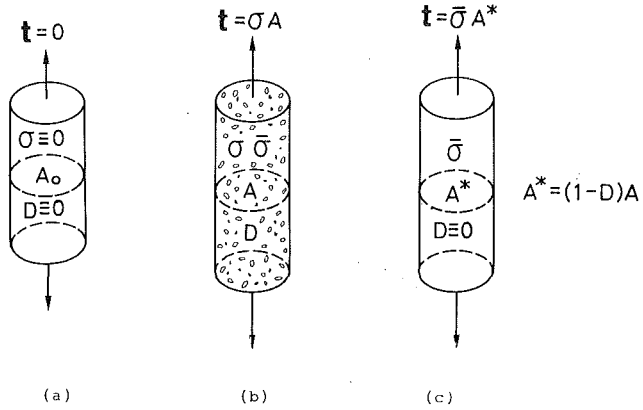


Fig. 1 Damage of a bar under uniaxial tension; (*a*) Initial undamaged state; (*b*) Current damaged state; (*c*) Fictitious undamaged state

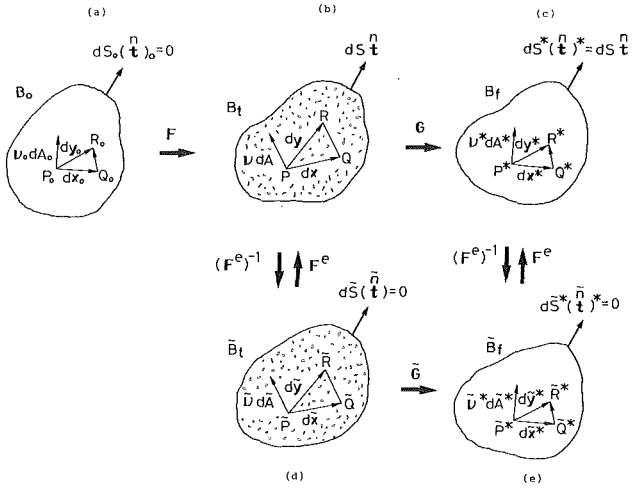


Fig. 2 Definition of three-dimensional states of damage; (*a*) Initial undamaged configuration; (*b*) Current damaged configuration; (*c*) Fictitious undamaged configuration; (*d*) Elastically unloaded damaged configuration; (*e*) Elastically unloaded fictitious undamaged configuration

theory of Kachanov-Rabotnov (Kachanov, 1958; Rabotnov, 1969), the damage state of Fig. 1(*b*) can be represented by a damage variable (internal state variable) D $(0 \le D \le 1)$ specified as follows

$$D = 0 \text{ (initial undamaged state)} \tag{1a}$$

$$D = 1 \text{ (final ruptured state)} \tag{1b}$$

The damage variable D of equation (1) is often interpreted as the *effective area* (*net area*) *reduction* caused by the distributed microscopic cracks and cavities due to material damage (Hult, 1979; Kachanov, 1986; Lemaitre and Chaboche, 1985); namely, it is assumed that the load-carrying net area of the bar of Fig. 1(*b*) is decreased from A to a certain smaller value A^* because of the formation of distributed cavities, and the damage variable D is related to A^* as follows

$$1 - D = A^*/A \tag{2}$$

This reduction of load-carrying net area magnifies the effects of stress σ induced by the external load t; in view of equation (2), the magnified stress is given as follows

$$\bar{\sigma} = t/A^* = \sigma/(1-D) \tag{3}$$

and is usually called *net stress* or *effective stress*.

The notion of Kachanov-Rabotnov's theory expressed by equations (1)–(3) has provided an important basis for the subsequent development of continuum damage mechanics, and considerable efforts have been made in order to extend the theory to the general multiaxial states of damage (Chaboche, 1981; Hult, 1979; Kachanov, 1986; Krajcinovic, 1984; Lemaitre and Chaboche, 1985; Murakami, 1983). However, the extension of the notion of equation (2) to model more general states of damage has always been accompanied by significant difficulties of the proper description of anisotropic damage states induced by the three-dimensional distribution of microscopic cracks and cavities.

In the one-dimensional case of Fig. 1, A^* of equation (2) implies the effective load-carrying area of the current damaged state (*b*). Thus we can assume a fictitious undamaged bar subject to the applied load t with the cross-sectional area A^*, mechanically equivalent to the current damaged state (*b*) as shown in Fig. 1 (*c*); we call it the *fictitious undamaged state*. Then, the damage variable D, namely the damage state of Fig. 1(*b*), can be readily defined by equation (2), if the relation between the areas A and A^* of the two mechanically equivalent states is specified in some way.

2.2 Representation of Damage States With Respect to the Current Damaged Configuration. By assuming that the principal effect of the material damage consists of the net area decrease due to three-dimensional distribution of microcracks or microvoids, let us now extend the argument in the previous section. For this purpose, we will take an area element PQR of an arbitrary orientation in the damaged material as shown in Fig. 2(*b*), and call it the *current* (*actual*) *damaged configuration* B_t. Then, let us assume that the states of stress, strain, and damage are uniform in B_t, and represent the line elements PQ, PR and the area of PQR by the vectors $d\mathbf{x}$, $d\mathbf{y}$ and $\boldsymbol{\nu} dA$ in the three-dimensional Euclidean vector space $\mathbf{E}$. We further take the initial undamaged configuration of the element by B_0 [Fig. 2(*a*)], and denote the corresponding vectors by $d\mathbf{x}_0$, $d\mathbf{y}_0$ and $\boldsymbol{\nu}_0 dA_0$, respectively. The deformation gradient from B_0 to B_t is represented by $\mathbf{F}$.

Because of the three-dimensional distribution of microcavities, the load-carrying net area of PQR will be decreased. Then, as in the one-dimensional case of the preceding section, we postulate that there exists a *fictitious undamaged configuration*[1] B_f [Fig. 2(*c*)] mechanically equivalent to B_t, and that the load-carrying net area of PQR is equivalent to the surface element $P^*Q^*R^*$ in B_f. The segments P^*Q^*, P^*R^* and the area of $P^*Q^*R^*$ will be designated by the vectors $d\mathbf{x}^*$, $d\mathbf{y}^*$ and $\boldsymbol{\nu}^* dA^*$ in the vector space $\mathbf{E}$. Since the net area reduction due to damage is brought about not only in the plane PQR but also in the planes of other orientations, the direction of the vectors $\boldsymbol{\nu} dA$ and $\boldsymbol{\nu}^* dA^*$ do not always coincide with each other.

According to the notion of equation (2), the damage variable $\mathbf{D}$ for general damage states can be defined properly, if the transformation between $\boldsymbol{\nu} dA$ and $\boldsymbol{\nu}^* dA^*$ of the two configurations B_t and B_f of Fig. 2 is specified in some way. This transformation between the area vectors of these two configurations can be identified by introducing a fictitious deformation at point P from the current damaged configuration B_t to the corresponding fictitious undamaged configuration B_f. If we represent the fictitious deformation gradient from B_t to B_f by $\mathbf{G}$, the segments $d\mathbf{x}^*$ and $d\mathbf{y}^*$ in B_f are given as follows

$$d\mathbf{x}^* = \mathbf{G} d\mathbf{x}, \quad d\mathbf{y}^* = \mathbf{G} d\mathbf{y} \tag{4}$$

In view of Nanson's theorem, the area vector $\boldsymbol{\nu}^* dA^*$ in B_f is related to the vector $\boldsymbol{\nu} dA$ in B_f as follows

[1] Fictitious undamaged configuration defined in Fig. 2 is similar to the *physical configuration* proposed by Stolz (1984) when he discussed the deformation of materials with microstructure.

Downloaded 03 May 2010 to 171.66.16.21. Redistribution subject to ASME license or copyright; see http://www.asme.org/terms/Terms_Use.cfm

$$\nu^* dA^* = (1/2) d\mathbf{x}^* \times d\mathbf{y}^* = (1/2)(\mathbf{G} d\mathbf{x}) \times (\mathbf{G} d\mathbf{y}) = K(\mathbf{G}^{-1})^T (\nu dA), \quad K = \det \mathbf{G} \tag{5}$$

where $(\ )^T$ denotes the transpose of the second rank tensor.

The argument developed so far implies that the damage state of B_t can be described by the linear transformation $K(\mathbf{G}^{-1})^T$ of equation (5). By introducing a new tensor $(\mathbf{I}-\mathbf{D})$ to represent the tensor $K(\mathbf{G}^{-1})^T$ in the form of

$$K(\mathbf{G}^{-1})^T = \mathbf{I} - \mathbf{D} \tag{6a}$$

or

$$\mathbf{G} = K[(\mathbf{I}-\mathbf{D})^T]^{-1} = K(\mathbf{I}-\mathbf{D})^{-T}, \tag{6b}$$

equation (5) can be written as follows

$$\nu^* dA^* = (\mathbf{I}-\mathbf{D})(\nu dA) \tag{7}$$

where $\mathbf{I}$ denotes the unit tensor of rank two. Thus the second rank tensor $\mathbf{D}$ of equation (7) is an internal state variable representing the general damage state (anisotropic damage) of materials, and will be called the *damage tensor* with respect to the current damaged configuration B_t.

2.3 Representation of a Damage State With Respect to the Elastically Unloaded Damaged Configuration. The foregoing discussion is concerned with the configuration B_t and, therefore, the material is subject to damage and macroscopic deformation at the same time. Namely, the damage tensor $\mathbf{D}$ defined by equation (7) depends also on the current state of deformation. This means that the tensor $\mathbf{D}$ can no more describe properly the internal state of damage in the case of large macroscopic deformation.

Concerning the damage state of the material element in the current configuration B_t, only the irreversible change of internal structure caused in the process from B_0 to B_t is essential. Thus we take the elastically unloaded configuration $\tilde{B}_t$ from B_t as shown in Fig. 2(*d*), and denote the elastic deformation gradient from B_t to $\tilde{B}_t$ by $(\mathbf{F}^e)^{-1}$. We further assume that the load carrying net area of the area element $\tilde{P}\tilde{Q}\tilde{R}$ of $\tilde{B}_t$ is decreased because of void formation, and that the net area is mechanically equivalent to the area element $\tilde{P}^*\tilde{Q}^*\tilde{R}^*$ of the corresponding fictitious undamaged configuration $\tilde{B}_f$ [Fig. 2(*e*)]. By taking account of the equivalence between the configurations B_t and B_f, the elastic deformation gradient corresponding to the unloading from B_f to $\tilde{B}_f$ is given by $(\mathbf{F}^e)^{-1}$, as before.

According to a similar procedure as in the preceding section, the relation between the area vectors $\tilde{\nu} d\tilde{A}$ and $\tilde{\nu}^* d\tilde{A}^*$ is specified by introducing a fictitious deformation gradient $\tilde{\mathbf{G}}$ from $\tilde{B}_t$ to $\tilde{B}_f$. Then, a similar operation as in equations (4) and (5) furnishes the following relations

$$d\tilde{\mathbf{x}}^* = \tilde{\mathbf{G}} d\tilde{\mathbf{x}}, \quad d\tilde{\mathbf{y}}^* = \tilde{\mathbf{G}} d\tilde{\mathbf{y}} \tag{8}$$

$$\tilde{\nu}^* d\tilde{A}^* = (1/2) d\tilde{\mathbf{x}}^* \times d\tilde{\mathbf{y}}^* = \tilde{K}(\tilde{\mathbf{G}}^{-1})^T (\tilde{\nu} d\tilde{A}), \quad \tilde{K} = \det \tilde{\mathbf{G}} \tag{9}$$

By introducing a new tensor $\tilde{\mathbf{D}}$ to represent the second rank tensor $\tilde{K}(\tilde{\mathbf{G}}^{-1})^T$ as follows

$$\tilde{K}(\tilde{\mathbf{G}}^{-1})^T = \mathbf{I} - \tilde{\mathbf{D}}, \tag{10}$$

equation (9) leads to an alternative form

$$\tilde{\nu}^* d\tilde{A}^* = (\mathbf{I}-\tilde{\mathbf{D}})(\tilde{\nu} d\tilde{A}). \tag{11}$$

Unlike the tensor $\mathbf{D}$, the tensor $\tilde{\mathbf{D}}$ represents the damage state of B_t independently of the elastic deformation in B_t; i.e., it represents the reduction of net area caused by the development of microscopic voids. Hereafter, the tensor $\tilde{\mathbf{D}}$ will be called a *damage tensor* or a *damage tensor with respect to the elastically unloaded configuration* $\tilde{B}_t$.

If we note the deformation from the configuration B_t to $\tilde{B}_t$, together with that from B_f to $\tilde{B}_f$, we have the following relations between $\tilde{\mathbf{G}}$ and $\mathbf{G}$, and $\tilde{\mathbf{D}}$ and $\mathbf{D}$:

$$\tilde{K}(\tilde{\mathbf{G}}^{-1})^T = (\mathbf{F}^e)^T [K\mathbf{G}^{-1}]^T (\mathbf{F}^e)^T \tag{12a}$$

$$\tilde{\mathbf{D}} = (\mathbf{F}^e)^T \mathbf{D} (\mathbf{F}^e)^{-T} \tag{12b}$$

By representing the principal values and the corresponding principal directions of the tensors $\tilde{\mathbf{D}}$ and $\mathbf{D}$ by $\tilde{D}$, $\tilde{\nu}$ and D, ν, respectively, we have the proper equations of $\tilde{\mathbf{D}}$ and $\mathbf{D}$ as follows

$$(\tilde{\mathbf{D}} - \tilde{D}\mathbf{I})\tilde{\nu} = 0 \tag{13a}$$

$$(\mathbf{D} - D\mathbf{I})\nu = 0 \tag{13b}$$

Substitution of equation (12*b*) into equation (13*a*) gives

$$(\mathbf{D} - \tilde{D}\mathbf{I})[(\mathbf{F}^e)^{-T}\tilde{\nu}\,] = 0 \tag{14}$$

Comparison between equations (14) and (13*b*) furnishes the relation between principal directions of $\tilde{\mathbf{D}}$ and $\mathbf{D}$:

$$\tilde{\nu} = (\mathbf{F}^e)^T \nu / \| (\mathbf{F}^e)^T \nu \| \tag{15}$$

where $\| \ \|$ represents the norm of a vector in the Euclidean vector space $\mathbf{E}$.

As mentioned already, damage states should be identified by the tensor $\tilde{\mathbf{D}}$ unless the elastic deformation is small. However, the tensors $\tilde{\mathbf{D}}$ and $\mathbf{D}$ are related by equation (12*b*), and coincide with each other particularly when the elastic part $\mathbf{F}^e$ of the deformation gradient $\mathbf{F}$ is small.

2.4 Restriction and Interpretation of Damage Tensors. We have shown that a damage state in general can be described by the tensor $\tilde{\mathbf{D}}$ of equation (11). Let us now discuss the mathematical restrictions on $\tilde{\mathbf{D}}$.

The vector $\tilde{\nu}^* d\tilde{A}^*$ of equation (11) is the equivalent area vector in $\tilde{B}_f$ transformed from $\tilde{\nu} d\tilde{A}$ in $\tilde{B}_t$ as a result of the net area decrease due to cavity distribution [Fig. 2 (*d*, *e*)], and thus the scalar product of $\tilde{\nu}^* d\tilde{A}^*$ and $\tilde{\nu} d\tilde{A}$ should be positive, i.e.

$$(\tilde{\nu}^* d\tilde{A}^*) \cdot (\tilde{\nu} d\tilde{A}) > 0, \ [\text{for } \forall\ \tilde{\nu} d\tilde{A} \in \mathbf{E}] \tag{16}$$

Substitution of equation (13) into equation (16) gives

$$[(\mathbf{I}-\tilde{\mathbf{D}})(\tilde{\nu} d\tilde{A})] \cdot \tilde{\nu} d\tilde{A}) > 0, \ [\text{for } \forall\ \tilde{\nu} d\tilde{A} \in \mathbf{E}] \tag{17}$$

which means that the tensor $(\mathbf{I}-\tilde{\mathbf{D}})$ is a positive tensor.

Let us further take the Cartesian decomposition of the tensor $(\mathbf{I}-\tilde{\mathbf{D}})$

$$(\mathbf{I}-\tilde{\mathbf{D}}) = (\mathbf{I}-\tilde{\mathbf{D}})^S + (\mathbf{I}-\tilde{\mathbf{D}})^A \tag{18}$$

where $(\mathbf{I}-\tilde{\mathbf{D}})^S$ and $(\mathbf{I}-\tilde{\mathbf{D}})^A$ stand for the symmetric and the antisymmetric part of $(\mathbf{I}-\tilde{\mathbf{D}})$. In view of the contribution of $(\mathbf{I}-\tilde{\mathbf{D}})^A$ in the transformation (11), we have the relation

$$(\tilde{\nu}^* d\tilde{A}^*) \cdot (\tilde{\nu} d\tilde{A}) = [(\mathbf{I}-\tilde{\mathbf{D}})^A (\tilde{\nu} d\tilde{A})] \cdot (\tilde{\nu} d\tilde{A}) = -(\tilde{\nu} d\tilde{A}) \cdot [(\mathbf{I}-\tilde{\mathbf{D}})^A (\tilde{\nu} d\tilde{A})] = 0 \tag{19}$$

This relation implies that the tensor $(\mathbf{I}-\tilde{\mathbf{D}})^A$ transforms the area vector $\tilde{\nu} d\tilde{A}$ of an arbitrary surface element in a damaged material into the equivalent surface element $\tilde{\nu}^* d\tilde{A}^*$ which is always perpendicular to $\tilde{\nu} d\tilde{A}$ independently of the direction of $\tilde{\nu} d\tilde{A}$; i.e., this tensor $(\mathbf{I}-\tilde{\mathbf{D}})^A$ is physically irrelevant as a transformation which represents the net area reduction due to damage. Therefore, the antisymmetric part $(\mathbf{I}-\tilde{\mathbf{D}})^A$ of equation (18) can be excluded from the following discussion, and then we can assume symmetry of the damage tensor $\tilde{\mathbf{D}}$. Thus the tensor $\tilde{\mathbf{D}}$ always has three orthogonal principal directions $\tilde{\mathbf{n}}_i$ $(i=1, 2, 3)$ and the corresponding principal values $\tilde{D}_i$, and can be expressed in the canonical form

$$\tilde{\mathbf{D}} = \sum_{i=1}^{3} \tilde{D}_i \tilde{\mathbf{n}}_i \otimes \tilde{\mathbf{n}}_i \tag{20}$$

In order to examine the properties of $\tilde{\mathbf{D}}$, let us take two sets of principal coordinates systems $O\tilde{x}_1\tilde{x}_2\tilde{x}_3$ and $\tilde{O}^*\tilde{x}_1\tilde{x}_2\tilde{x}_3$ of the tensor $\tilde{\mathbf{D}}$ which pass the points $\tilde{P}$, $\tilde{Q}$, $\tilde{R}$ and $\tilde{P}^*$, $\tilde{Q}^*$, $\tilde{R}^*$ in $\tilde{B}_t$ and $\tilde{B}_f$ in Fig. 2. Then we construct two tetrahedra $\tilde{O}\tilde{P}\tilde{Q}\tilde{R}$ and

Downloaded 03 May 2010 to 171.66.16.21. Redistribution subject to ASME license or copyright; see http://www.asme.org/terms/Terms_Use.cfm

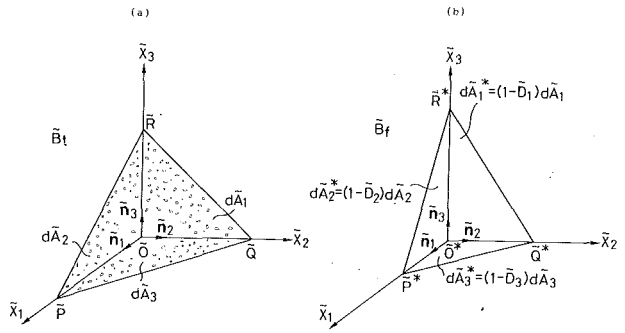


Fig. 3 Interpretation of the damage tensor $\tilde{\mathbf{D}}$; (*a*) Elastically unloaded damage configuration; (*b*) Elastically unloaded fictitious undamaged configuration

$\tilde{Q}^*\tilde{P}^*\tilde{Q}^*\tilde{R}^*$ as shown in Fig. 3(*a*, *b*) which consist of the area elements $\tilde{P}\tilde{Q}\tilde{R}$, $\tilde{P}^*\tilde{Q}^*\tilde{R}^*$ and the facets perpendicular to the principal coordinates axes $\tilde{x}_1$, $\tilde{x}_2$, and $\tilde{x}_3$. Substitution of equation (11) into equation (20) furnishes

$$\tilde{\nu}^* d\tilde{A}^* = \sum_{i=1}^{3} (1-\tilde{D}_i)\, d\tilde{A}_i \tilde{\mathbf{n}}_i$$

$$= \tilde{\mathbf{n}}_1\, d\tilde{A}_1^* + \tilde{\mathbf{n}}_2 d\tilde{A}_2^* + \tilde{\mathbf{n}}_3 d\tilde{A}_3^* \qquad (21a)$$

$$d\tilde{A}_i^* = (1-\tilde{D}_i) d\tilde{A}_i \quad \text{(no sum on } i;\ i = 1, 2, 3) \qquad (21b)$$

where $d\tilde{A}_i = \tilde{\nu}_i d\tilde{A}$ and $d\tilde{A}_i^* = \tilde{\nu}_i^* d\tilde{A}^*$ ($i = 1, 2, 3$) signify the facet areas of the tetrahedra on the coordinate planes in $\tilde{B}_t$ and $\tilde{B}_f$, respectively; see Fig. 3(*a*, *b*). According to equation (20), the principal values $\tilde{D}_i$ of the tensor $\tilde{\mathbf{D}}$ can be interpreted as the net area reductions or the effective void area densities on the three principal planes of $\tilde{\mathbf{D}}$ in $\tilde{B}_t$ and $\tilde{B}_f$, as shown in Fig. 3.

The preceding arguments apply also to the damage tensor $\mathbf{D}$ in B_t; namely, the tensor $(\mathbf{I}-\mathbf{D})$ is a positive tensor, and equations (20) and (21) have the following forms in this case

$$\mathbf{D} = \sum_{i=1}^{3} D_i \mathbf{n}_i \otimes \mathbf{n}_i \qquad (22)$$

$$\nu^* dA^* = \sum_{i=1}^{3} (1-D_i) dA_i \mathbf{n}_i$$

$$= \mathbf{n}_1 dA_1^* + \mathbf{n}_2 dA_2^* + \mathbf{n}_3 dA_3^* \qquad (23a)$$

$$dA_i^* = (1-D_i)\, dA_i \quad \text{(no sum on } i;\ i = 1, 2, 3) \qquad (23b)$$

where $dA_i = \nu_i dA$ and $dA_i^* = \nu_i^* dA^*$ designate the facet areas of the tetrahedra in B_t and B_f; see, Fig. 4 (*b*, *c*).

So far it has been elucidated that, as far as the material damage is characterized by the net area reduction due to distributed cracks and cavities, the damage state corresponding to arbitrary distribution of these voids, however complicated it may be, can be described by the second rank symmetric tensor $\tilde{\mathbf{D}}$ defined by equation (20), or by the tensor $\mathbf{D}$ of equation (22); in these cases, equations (20) and (22) provide general description of damage states. The canonical expressions (20) or (22), on the other hand, imply that the tensors $\tilde{\mathbf{D}}$ and $\mathbf{D}$ cannot describe the damage states which have more complicated symmetry than orthotropy.

When Murakami and Ohno (1981) developed an anisotropic damage theory of creep, they derived the second rank symmetric tensor $\mathbf{D}$ of equation (22) with regards to B_t, by representing the effects of microscopic grain-boundary cavities in terms of a dyadic product of the unit normal vector to the relevant boundary. They discussed also the net area reduction from the Cauchy tetrahedron in a damaged material to that in the equivalent fictitious undamaged material, and showed the relation of equation (7). A similar damage tensor was employed also by M. Kachanov (1980) to develop a continuum model of cracked elastic materials. Contrary to Murakami and Ohno, Betten (1983), thereafter, started from the transformation of a Cauchy tetrahedron in the current damaged configuration to that in the corresponding fictitious undamanged configuration to define the damage variable, and derived equation (22) by postulating the existence of a specific plane in the material, which does not change its direction by damage. In the present paper, on the other hand, we employed a less restrictive assumption that the damage states in materials can be characterized by the reduction of effective load-carrying area caused by the distributed microscopic cracks and cavities, and developed a systematic theory of general material damage caused by distributed cavities.

3 Definition of Effective Stresses

3.1 Effective Stress in Regards to Current Damaged Configuration. By use of the damage tensor $\tilde{\mathbf{D}}$ of equation (20) [or tensor $\mathbf{D}$ related to $\tilde{\mathbf{D}}$ by equation (12*b*)], as an internal state variable for material damage, the constitutive equation and the evolution equation of damaged materials can be established in the framework of the ordinary theory of inelasticity. In the usual procedure of continuum damage mechanics, however, the magnified effects of stress due to damage are often represented by the notion of an effective stress, i.e., the constitutive equation of a damaged material is derived from that of the undamaged material (Lemaitre, 1985; Lemaitre and Chaboche, 1978, 1985) by replacing the Cauchy stress in the equation with the corresponding effective stress on the basis of the *hypothesis of strain equivalence* (Lemaitre and Chaboche, 1978, 1985). The effective stress is applied also to formulate the evolution equation of damage.

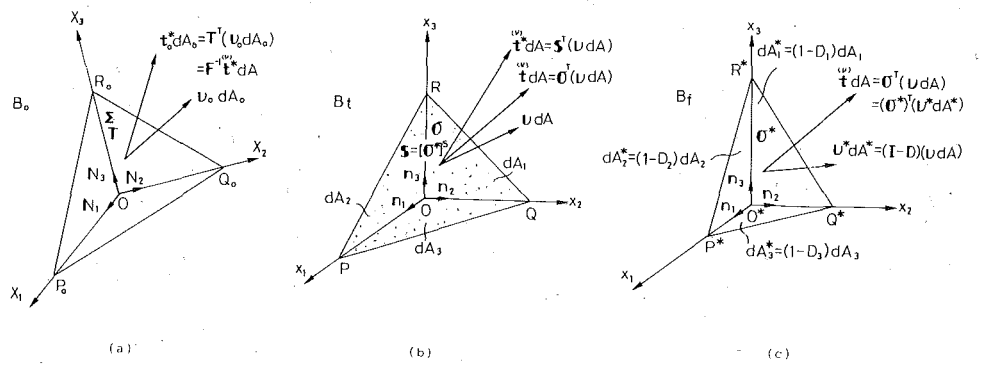


Fig. 4 Effective stress tensors with respect to current and initial configurations; (*a*) Initial undamaged configuration; (*b*) Current damaged configuration; (*c*) Fictitious undamaged configuration

Downloaded 03 May 2010 to 171.66.16.21. Redistribution subject to ASME license or copyright; see http://www.asme.org/terms/Terms_Use.cfm

According to the notion of effective stress of equation (3), the effective stress with reference to the current damaged configuration B_t (i.e., effective stress for the Cauchy stress σ) for the general states of damage can be defined as a stress σ^* which would be induced in the tetrahedron $O^*P^*Q^*R^*$ in B_f [Fig. 4(*c*)], when the surface element $P^*Q^*R^*$ is subject to the indentical force vector $\mathbf{t}^{(\nu)}\,dA$ to that on the element PQR in B_t, Fig. 4(*b*). This stress σ^* corresponds exactly to the first Piola-Kirchhoff stress tensor concerning the reference configuration B_f, and is given as follows

$$\sigma^* = K^{-1}\mathbf{G}\sigma \tag{24}$$

In view of equation (6), this equation can be written in an alternative form

$$\begin{aligned}\sigma^* &= K^{-1}K[(\mathbf{I}-\mathbf{D})^{-T}]\sigma \\ &= (\mathbf{I}-\mathbf{D})^{-1}\sigma\end{aligned} \tag{25}$$

where we have employed the symmetry of $\mathbf{D}$ discussed in the preceding section. Figure 4(c) shows a mechanical interpretation of σ^*.

The effective stress σ^* of equation (25) is asymmetric. Since it is inexpedient to formulate constitutive and evolution equations of damaged materials by using the asymmetric tensor σ^*, we need to symmetrize it in some appropriate way. One possible way is to adopt the symmetric part of the Cartesian decomposition of σ^*

$$\mathbf{S} = [\sigma^*]^S = (1/2)\,[(\mathbf{I}-\mathbf{D})^{-1}\sigma + \sigma[\mathbf{I}-\mathbf{D})^{-1}] \tag{26}$$[2]

So far we have assumed that the mechanical state of the material in the current damaged configuration B_t is equivalent to that in the fictitious undamaged configuration B_f. Thus we can interpret that the mechanical effect of the Cauchy stress σ in B_t is magnified to the effective stress $\mathbf{S}$ of equation (26) as a result of the effective area reduction due to damage.

3.2 Effective Stress in Regards to Initial Undamaged Configuration. Similarly to the second Piola-Kirchhoff stress tensor with respect to the initial undamaged configuration B_0

$$\Sigma = J\mathbf{F}^{-1}\sigma(\mathbf{F}^{-1})^T, \quad J = \det\,\mathbf{F} \tag{28}$$

we can define the effective stress concerning B_0.

The magnified effect of stress in B_t has been given by the effective stress $\mathbf{S}$. We now introduce a stress vector corresponding to $\mathbf{S}$ as shown in Fig. 4(*b*)

$$\overset{(\nu)}{\mathbf{t}}{}^*\,dA = \mathbf{S}^T(\nu dA) \tag{29}$$

Then, we will make a similar assumption to that for the stress Σ, and postulate that the surface element $P_0Q_0R_0$ in B_0 of Fig. 4(*a*) is subject to the force vector transformed from equations (29)

$$\overset{(\nu)}{\mathbf{t}}{}_0{}^*\,dA_0 = \mathbf{F}^{-1}\overset{(\nu)}{\mathbf{t}}{}^*\,dA \tag{30}$$

Denoting the effective stress concerning the configuration B_0 by $\mathbf{T}$, we have Cauchy's formula for B_0

$$\overset{(\nu)}{\mathbf{t}}{}_0{}^*\,dA_0 = \mathbf{T}^T(\nu_0 dA_0) \tag{31}$$

By using Nanson's formula together with equations (30) and (31), the effective stress concerning B_0 is given by the following relation

$$\mathbf{T} = J\mathbf{F}^{-1}\mathbf{S}(\mathbf{F}^{-1})^T \tag{32}$$

which is similar to equation (28).

The effective stress $\mathbf{S}$ and $\mathbf{T}$ are fictitious stresses which represent the magnified effect of stress due to damage.

[2]Other ways of symmetrization are possible. Cordebois and Sidoroff (1982) for example, proposed the following effective stress

$$\mathbf{S} = (\mathbf{I}-\mathbf{D})^{-1/2}\sigma(\mathbf{I}-\mathbf{D})^{-1/2} \tag{27}$$

which gives the elastic potential of damaged materials by replacing the Cauchy stress σ in the corresponding elastic potential of undamaged materials.

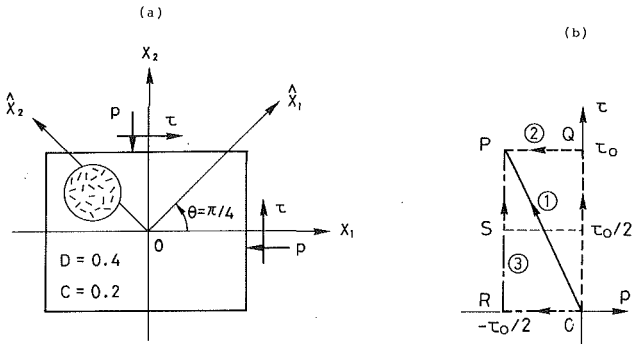


Fig. 5 Cracked elastic material and stress path; (*a*) Two-dimensional elastic material with randomly distributed microscopic cracks; (*b*) Stress path

Therefore, it should be noted that these stresses do not satisfy the equilibrium condition in the relevant configuration.[3]

4 Application to Problems With Crack Closure

4.1 Extension of Effective Stress. In the case of small elastic deformation, the states of material damage can be described by a second rank symmetric tensor $\mathbf{D}$, and the magnified effect of stress is expressed by the effective stress tensors S of equations (26) and (27).[4] So far, it has been assumed that microscopic cavities characterizing damage do not transmit force through their surfaces.

However, when damage is brought about by a set of microscopic penny-shaped cracks in the material, and inelastic deformation as well as elastic deformation is small, the effects of crack closure under compressive stress are often important and not negligible (Horii and Nemat-Nasser, 1983; Kyoya, et al., 1985; Ladeveze and Lemaitre, 1984). This phenomenon is observed, e.g., in the differences in tensile and compressive properties in fracture strength and elastic moduli of brittle materials such as concrete and rocks, or in the mean-stress dependence of fatigue strength of metals. The damage theory discussed so far can be extended to these problems if we define a new effective stress by incorporating the effect of closure of microcracks.

As was done by Ladeveze and Lemaitre (1984), let us first decompose the Cauchy stress σ as follows

$$\sigma = \langle\sigma\rangle - \langle -\sigma\rangle \tag{33a}$$

$$[\langle\sigma\rangle] = \begin{bmatrix} \langle\sigma_1\rangle & 0 & 0 \\ 0 & \langle\sigma_2\rangle & 0 \\ 0 & 0 & \langle\sigma_3\rangle \end{bmatrix} \tag{33b}$$

[3]Effective stresses of $\mathbf{S}$ and $\mathbf{T}$ discussed in Sections 3.1 and 3.2 represent the magnified effects of stress induced by the load-carrying net area due to the damage. Strictly speaking, therefore, these effective stresses should be related to local decohesion effects such as damage and fracture. Deformation of material in general depends not only on the cavity distribution in specific planes but also on the spatial distribution of cavities. Thus, as regards deformation, it is sometimes more reasonable to define effective stresses other than $\mathbf{S}$ and $\mathbf{T}$. This problem was discussed by Murakami and Imaizumi (1982), Murakami and Ohno (1981) and Murakami, et al. (1986).

[4]The damage tensor $\mathbf{D}$ of equation (22) and the effective stress $\mathbf{S}$ of equations (26) and (27) have been applied mainly to damage problems of metals; i.e., the anisotropic damage of creep (Murakami and Ohno, 1981; Murakami, et al., 1986); the effects of prior plastic damage on the subsequent creep damage process (Murakami and Sanomura, 1986); creep crack growth under nonproportional loading (Murakami, Kawai, and Rong, 1988); the change of elastic moduli caused by plastic damage (Cordebois and Sidoroff, 1982); etc.

Downloaded 03 May 2010 to 171.66.16.21. Redistribution subject to ASME license or copyright; see http://www.asme.org/terms/Terms_Use.cfm

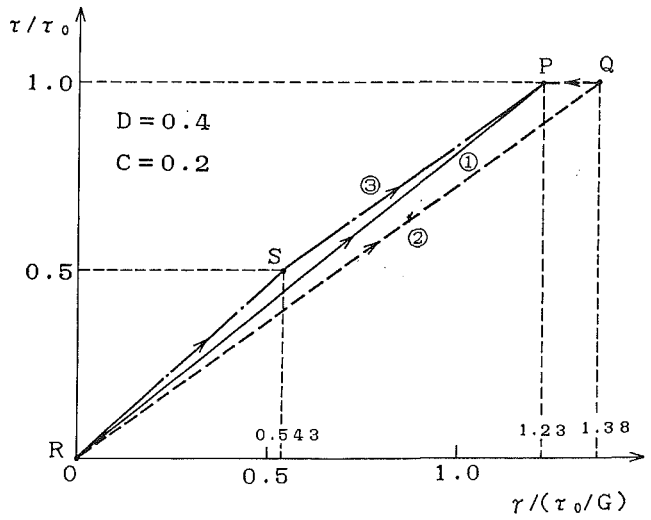


Fig. 6 Elastic behavior of cracked material under combined hydrostatic pressure and shear

$$[\langle -\sigma \rangle] = \begin{bmatrix} \langle -\sigma_1 \rangle & 0 & 0 \\ 0 & \langle -\sigma_2 \rangle & 0 \\ 0 & 0 & \langle -\sigma_3 \rangle \end{bmatrix} \tag{33c}$$

where $\langle\ \rangle$ is the Macauley bracket, and σ_i $(i=1, 2, 3)$ represent principal values of $\boldsymbol{\sigma}$. Because of the effects of crack closure, the effective area reduction due to $\mathbf{D}$ under compressive stress is smaller than that under tensile stress. Denoting this relation by a parameter $C(0<C<1)$ and, in view of equation (33), equation (26) can be extended as follows

$$\mathbf{S} = (1/2)[(\mathbf{I}-\mathbf{D})^{-1}\langle\boldsymbol{\sigma}\rangle + \langle\boldsymbol{\sigma}\rangle(\mathbf{I}-\mathbf{D})^{-1}] - (1/2)[(\mathbf{I}-C\mathbf{D})^{-1}\langle -\boldsymbol{\sigma}\rangle + \langle -\boldsymbol{\sigma}\rangle(\mathbf{I}-C\mathbf{D})^{-1}] \tag{34}$$

where $C = 0$ and $C = 1$ correspond to the case of perfect closure of cracks (unilateral condition) and the case without crack closure (bilateral condition), respectively.

4.2 Elastic Deformation of Elastic-Brittle Materials Containing Distributed Microcracks. As an application of equation (34), let us now analyze the two-dimensional elastic deformation of a cracked body as shown in Fig. 5. The elastic body is in the state of plane stress and subject to combined hydrostatic pressure p and shear stress τ according to the stress paths of Fig. 5(*b*). If the body contains a number of randomly distributed microscopic penny-shaped cracks, the damage state is isotropic and can be described by a damage tensor

$$\mathbf{D} = D\mathbf{I} = D[\mathbf{n}_1 \otimes \mathbf{n}_1 + \mathbf{n}_2 \otimes \mathbf{n}_2] \tag{35}$$

Let us first consider the stress path ① in Fig. 5(*b*). The components of the stress tensor with respect to the coordinate systems Ox_1x_2 and $O\hat{x}_1\hat{x}_2$ are

$$[\boldsymbol{\sigma}] = \begin{bmatrix} -p & \tau \\ \tau & -p \end{bmatrix} = \begin{bmatrix} -(k/2)\tau_0 & k\tau_0 \\ k\tau_0 & -(k/2)\tau_0 \end{bmatrix} \qquad 0 \le k \le 1;\ k = \tau/\tau_0 \tag{36}$$

$$[\hat{\sigma}] = \begin{bmatrix} (k/2)\tau_0 & 0 \\ 0 & -(3k/2)\tau_0 \end{bmatrix} = [\langle\hat{\sigma}\rangle - \langle -\hat{\sigma}\rangle] \tag{37a}$$

$$[\langle\hat{\sigma}\rangle] = \begin{bmatrix} (k/2)\tau_0 & 0 \\ 0 & 0 \end{bmatrix} \tag{37b}$$

$$[\langle -\hat{\sigma}\rangle] = \begin{bmatrix} 0 & 0 \\ 0 & (3k/2)\tau_0 \end{bmatrix} \tag{37c}$$

Substitution of equations (35) and (37) into equation (34) gives the components of effective stress $\hat{S}_{ij}$ in the coordinate system $O\hat{x}_1\hat{x}_2$. Applying further a coordinate transformation to $\hat{S}_{ij}$, we have the component of the effective stress $\mathbf{S}$ in the system Ox_1x_2 as follows

$$[\mathbf{S}] = (k\tau_0/4) \times \begin{bmatrix} 1/(1-D)-3/(1-CD) & 1/(1-D)+3/(1-CD) \\ 1/(1-D)+3/(1-CD) & 1/(1-D)-3/(1-CD) \end{bmatrix} \tag{38}$$

If we employ the hypothesis of strain equivalence (Lemaitre, 1985; Lemaitre and Chaboche, 1985), the elatic deformation of the cracked body is furnished by Hooke's law by replacing the Cauchy stress in it with the effective stress of equation (38) as follows

$$\gamma/(\tau_0/G) = (1/4)[1/(1-D)+3/(1-CD)](\tau/\tau_0) \tag{39}$$

The solid line in Fig. 6 shows the results of equation (39) for the case of $D=0.4$, $C=0.2$. The dashed line and the chain line in the figure, furthermore, are the results of the similar analyses for the stress paths ② and ③ in Fig. 5(*b*). As observed in Fig. 6, in the case of the proportional stress path ①, both the closed cracks and the open cracks exist throughout the whole process of loading, and the final state P is attained. For path ②, a larger number of cracks than for path ① remain open up to point Q, and thus we have larger strain than ①. However, after point Q, cracks start to close with the increase of hydrostatic pressure and the shear strain decreases. For stress path ③, on the other hand, only hydrostatic pressure acts up to point R, and no shear deformation occurs. For the subsequent path RS, since all cracks remain closed, we have the smallest rate of strain increase among these paths. Finally, after point S, part of cracks start to open and the increase of strain is accelerated. Similar results to Fig. 6 have been obtained by Horii and Nemat-Nasser (1983), when they analyzed the overall elastic moduli and the load-induced anisotropy of an elastic body containing uniformly distributed microscopic cracks by means of self-consistent methods of micromechanics.[5]

5 Conclusions

A continuum theory was developed for the systematic modeling of general three-dimensional anisotropic states of material damage.

Directional features of material damage are especially important in many engineering problems, ranging from creep damage, fatigue damage and spall damage in metals to elastic-brittle damage in geological materials and concrete. The present paper provides a consistent framework to analyze these problems from a continuum damage mechanics point of view.

Acknowledgment

The present paper is the outcome of discussions made during the author's stay at Université Paris 6 from April through July, 1986. The author is grateful to his host, Prof. Jean Lemaitre of Université Paris 6, for his hospitality and his stimulating discussions. This work was supported in part by the Ministry of Education of Japan under the Grant-in-Aid for Scientific Research A (No., 61420024) for the fiscal year of 1986.

[5] They assumed a two-dimensional state of plane strain.

Downloaded 03 May 2010 to 171.66.16.21. Redistribution subject to ASME license or copyright; see http://www.asme.org/terms/Terms_Use.cfm

References

Betten. J., 1983, "Damage Tensors in Continuum Mechanics," *Journal de Mécanique Théorique et Appliquée*, Vol. 2, pp. 13–32.

Chaboche, J. L., 1981, "Continuous Damage Mechanics – A Tool to Describe Phenomena Before Crack Initiation," *Nuclear Engineering and Design*, Vol. 64, pp. 233–247.

Chaboche, J. L., 1984, "Anisotropic Creep Damage in the Framework of Continuum Damage Mechanics," *Nuclear Engineering and Design*, Vol. 79, pp. 309–319.

Cordebois, J. P., and Sidoroff, F., 1982, "Damage Induced Elastic Anisotropy," *Mechanical Behavior of Anisotropic Solids,* Boehler, J. P., ed., Martinus Nijhoff, The Hague, pp. 761–774.

Hayhurst, D. R., and Storakers, B., 1976, "Creep Rupture of the Andrade Shear Disk," *Proceedings of the Royal Society of London*, Series A, No. 349, pp. 369–382.

Horii, H., and Nemat-Nasser, S., 1983, "Overall Moduli of Solids With Microcracks: Load-Induced Anisotropy," *Journal of Mechanics and Physics of Solids*, Vol. 31, pp. 155–171.

Hult, J., 1979, "CDM-Capabilities, Limitations and Promises," *Mechanisms of Deformation and Fracture*, Easterling, K. E., ed., Pergamon, Oxford, pp. 233–247.

Kachanov, L. M., 1958, "On Rupture Time Under Condition of Creep," *Izvestia Akademi Nauk SSSR, Otd. Tekhn. Nauk*, No. 8, pp. 26–31 (in Russian).

Kachanov, L. M., 1986, *Introduction to Continuum Damage Mechanics*, Martinus Nijhoff, Dordrecht.

Kachanov, M. L., 1980, "Continuum Model of Medium with Cracks," *Journal of the Engineering Mechanics Division, Proceeding of ASCE*, EM5, pp. 1309–1051.

Krajcinovic, D., 1983, "Constitutive Equations for Damaging Materials," ASME JOURNAL OF APPLIED MECHANICS, Vol. 50, pp. 355–360.

Krajcinovic, D., 1984, "Continuum Damage Mechanics," *Applied Mechanics Reviews*, Vol. 37, pp. 1–6.

Kyoya, T., Ichikawa, Y., and Kawamoto, T., 1985, "A Damage Mechanics Theory for Discontinuous Rock Mass," *Numerical Methods in Geomechanics*, Kawamoto, T., and Ichikawa, Y., eds., A. A. Balkema, Rotterdam, pp. 469–480.

Ladeveze, P., and Lemaitre, J., 1984, "Damage Effective Stress in Quasi-Unilateral Conditions," The 16th International Congress of Theoretical and Applied Mechanics, Lyngby, Denmark.

Leckie, F. A., and Onat, E. T., 1981, "Tensorial Nature of Damage Measuring Internal Variables," *Physical Non-Linearities in Structural Analysis*, Hult, J., and Lemaitre, J., eds., Springer, Berlin, pp. 140–155.

Lemaitre, J., 1985, "Continuum Damage Mechanics Model for Ductile Fracture," *ASME Journal of Engineering Materials and Technology*, Vol. 107, pp. 83–89.

Lemaitre, J., and Chaboche, J. L., 1978, "Aspect Phénoménologique de la Rupture par Endommagement," *Journal de Mécanique Appliquée*, Vol. 2, pp. 317–365.

Lemaitre, J., and Chaboche, J. L., 1985, *Mécanique des Matériaux Solides*, Dunod, Paris.

Murakami, S., 1983, "Notion of Continuum Damage Mechanics and Its Application to Anisotropic Creep Damage Theory," *ASME Journal of Engineering Materials and Technology*, Vol. 105, pp. 99–105.

Murakami, S., Kawai, M., and Rong, H., 1988, "Finite Element Analysis of Creep Crack Growth by Local Approach," *International Journal of Mechanical Sciences*, (in print).

Murakami, S., and Imaizumi, T., 1982, "Mechanical Description of Creep Damage State and Its Experimental Verification," *Journal de Mécanique Théorique et Appliquée*, Vol. 1, pp. 743–761.

Murakami, S., and Ohno, N., 1981, "A Continuum Theory of Creep and Creep Damage," *Creep in Structures*, Ponter, A. R. S., and Hayhurst, D. R., eds., Springer, Berlin, 1981, pp. 422–444.

Murakami, S., and Sanomura, Y., 1986, "Analysis of the Coupled Effect of Plastic Damage and Creep Damage in Nimonic 80A at Finite Deformation," *Engineering Fracture Mechanics*, Vol. 25, pp. 693–704.

Murakami, S., and Sanomura, Y., and Saitoh, K., 1986, "Formulation of Cross-Hardening in Creep and Its Effect on the Creep Damage Process of Copper," *ASME Journal of Engineering Materials and Technology*, Vol. 108, pp. 167–173.

Onat, E. T., and Leckie, F. A., 1988, "Representation of Mechanical Behavior in the Presence of Changing Internal Structure," ASME JOURNAL OF APPLIED MECHANICS, Vol. 55, pp. 1–10.

Stolz, C., 1984, "Étude des Milieux à Configuration Physique et Application," *Comptes Rendus Académie des Sciences Paris*, Série II, Vol. 299, No. 17, pp. 1153–1155.

Rabotnov, Yu. N., 1969, *Creep Problems of Structural Members*, North-Holland, Amsterdam.

Vakulenko, A. A., and Kachanov, M. L., 1971, "Continuum Model of Medium with Cracks," *Mekhanika Tverdogo Tiela*, No. 4, pp. 159–166.

Downloaded 03 May 2010 to 171.66.16.21. Redistribution subject to ASME license or copyright; see http://www.asme.org/terms/Terms_Use.cfm

Nonlocal Continuum Damage, Localization Instability and Convergence

Zdeněk P. Bažant
Professor of Civil Engineering.
Mem. ASME

Gilles Pijaudier-Cabot[1]
Graduate Research Assistant.

Center for Concrete and Geomaterials,
Northwestern University,
Tech-2410,
Evanston, IL 60208

A recent nonlocal damage formulation, in which the spatially averaged quantity was the energy dissipated due to strain-softening, is extended to a more general form in which the strain remains local while any variable that controls strain-softening is nonlocal. In contrast to the original imbricate nonlocal model for strain-softening, the stresses which figure in the constitutive relation satisfy the differential equations of equilibrium and boundary conditions of the usual classical form, and no zero-energy spurious modes of instability are encountered. However, the field operator for the present formulation is in general nonsymmetric, although not for the elastic part of response. It is shown that the energy dissipation and damage cannot localize into regions of vanishing volume. The static strain-localization instability, whose solution is reduced to an integral equation, is found to be controlled by the characteristic length of the material introduced in the averaging rule. The calculated static stability limits are close to those obtained in the previous nonlocal studies, as well as to those obtained by the crack band model in which the continuum is treated as local but the minimum size of the strain-softening region (localization region) is prescribed as a localization limiter. Furthermore, the rate of convergence of static finite-element solutions with nonlocal damage is studied and is found to be of a power type, almost quadratic. A smooth weighting function in the averaging operator is found to lead to a much better convergence than unsmooth functions.

Introduction

Prediction of damage and failure of brittle heterogeneous materials such as concrete or rock requires a mathematically correct and physically realistic description of the strain-softening behavior (Bažant, 1986; Mazars and Pijaudier-Cabot 1986). Although it has been argued that strain-softening does not exist on the continuum level (Read and Hegemier, 1984), the macroscopic result of distributed microcracking or void growth is a behavior whose continuum description must incorporate strain-softening. Numerous attempts to describe this type of behavior by local inelastic continuum theories such as plasticity or continuum damage mechanics have been unsatisfactory because the phenomenon of strain localization caused by strain-softening cannot be captured objectively (Bažant, 1986). The principal fault of the local continuum models is that the energy dissipated at failure is incorrectly predicted to be zero, and the finite-element solutions converge to this incorrect, physically meaningless, solution as the mesh is refined.

To remedy the situation, one must introduce some form of a localization limiter (Bažant and Belytschko, 1987). Its simplest form is obtained by imposing a lower bound on the finite-element size, as is done in the crack band model. As a better localization limiter which permits arbitrary mesh refinement, one may adopt the nonlocal concept. Introduced into continuum mechanics long ago by Kröner (1967); Eringen (1972); Krumhansl (1968) and others, this concept was recently successfully applied to strain-softening (Bažant, et al., 1984). However, the formulation, in which all the state variables were nonlocal, turned out to be quite complicated. It required additional boundary and interface conditions, led to a nonstandard form of the differential equations of equilibrium, and the finite-element implementation required imbrication of the elements.

In the preceding study (Pijaudier-Cabot and Bažant, 1986) to be further expanded here, a new idea which turns out to bring considerable simplification was introduced. It was shown that it suffices to consider as nonlocal only the strain-softening damage, while the elastic behavior (including unloading and reloading) should be treated as local. This formulation was shown to require no element imbrication and no overlay with local continuum, which had to be previously used by Bažant, et al., (1984) in order to suppress certain periodic

[1]On leave from Laboratoire de Mécanique et Technologie, Cachan, France.

Contributed by the Applied Mechanics Division for presentation at the Winter Annual Meeting, Chicago, IL, November 28 to December 2, 1988, of The American Society of Mechanical Engineers.

Discussion on this paper should be addressed to the Editorial Department, ASME, United Engineering Center, 345 East 47th Street, New York, 10017, and will be accepted until two months after final publication of the paper itself in the JOURNAL OF APPLIED MECHANICS. Manuscript received by ASME Applied Mechanics Division, March 9, 1987; final revision, November 13, 1987.

Paper No. 88-WA/APM-18.

Copyright © 1988 by ASME
Downloaded 03 May 2010 to 171.66.16.21. Redistribution subject to ASME license or copyright; see http://www.asme.org/terms/Terms_Use.cfm

zero-energy modes in the imbricate, fully nonlocal solutions. The purpose of the present study is to show that, more generally, the key attribute of the nonlocal formulation for strain-softening is that the strain as a kinematic variable should be defined as local, and to study various aspects yet unexplored, including: (1) Static strain-localization instability; (2) Symmetry of the field operator; (3) Influence of various types of spatial averaging; (4) Convergence at mesh refinement.

Before embarking on our analysis, it should be mentioned that other forms of localization limiters are possible and deserve to be studied. The oldest idea, proposed already by L'Hermite (1952) in a study of concrete cracking due to shrinkage, is to introduce a dependence of the strength or yield limit on the strain gradient. In a general form, which may involve introduction of the strain gradient into the yield function, this idea has recently been developed by Floegl and Mang (1981), Schreyer and Chen (1984) and Mang and Eberhardsteiner (1986). Introduction of higher-order gradients into the differential equations of equilibrium or into the definition of strength was studied by Aifantis (1984) and also by Bažant (1984) and Bažant and Belytschko (1987). As another approach, Sandler (1984) as well as Needleman (1987) showed that the introduction of viscosity, whether real or artificial, may act in certain problems as a localization limiter, although this can be true only for a limited time period of response.

Nonlocal Generalization of Continuum Damage Mechanics

The principal idea for the treatment of softening is that only those variables which cause softening may be considered as nonlocal while the model must reduce to a local one for the special case of elastic response, which also includes unloading and reloading. This condition can be satisfied by a nonlocal formulation in which the strain, when used as a kinematic variable, is local. To implement this condition it is convenient, albeit not necessary, to use continuum damage mechanics because in this theory the strain-softening is characterized by a distinct single variable ω, called damage. For the nonlocal generalization, we adopt the simple, scalar damage formulation, although the same concept could be implemented in a similar manner in the anisotropic damage models, derived, e.g., by Mazars and Pijaudier-Cabot (1986) and Ladevèze (1983), which are more realistic. Various other constitutive theories can also be generalized to such a nonlocal form, particularly those which use fracturing strain or a degrading yield limit. (Bažant, et al. 1987). Unimportant from the viewpoint of the type of localization studied here, plastic strains will be omitted from the formulation; their inclusion, however, would require no conceptual changes.

As usual in continuum damage mechanics, we may introduce the relation between the strains ϵ_{ij} and the stresses σ_{ij} in the form (Lemaitre and Chaboche, 1985)

$$\sigma_{ij} = (1-\Omega) C_{ijkm} \epsilon_{km} \tag{1}$$

in which C_{ijkm} are the elastic constants of the material and Ω is the damage. We assume Ω to be nonlocal, defined by spatial averaging as follows

$$\Omega(\mathbf{x}) = \bar{\omega}(\mathbf{x}) = \frac{1}{V_r(\mathbf{x})} \int_V \alpha(\mathbf{s}-\mathbf{x}) \omega(\mathbf{s}) dV(\mathbf{s}) \tag{2}$$

in which

$$V_r(\mathbf{x}) = \int_V \alpha(\mathbf{s}-\mathbf{x}) \mathrm{dV}(\mathbf{s}). \tag{3}$$

Superimposed bar denotes the spatial averaging operator, $\mathbf{x}$ and $\mathbf{s}$ are the coordinate vectors, V = volume of the body, and α = given weighting function. Initially $\Omega = \omega = 0$, and always $0 \le \Omega \le 1$, $0 \le \omega \le 1$.

As the simplest form of the weighting function, one may consider $\alpha = 1$ within a certain representative volume V_r centered at points $\mathbf{x}$, and $\alpha = 0$ outside of it. As we will see, however, a uniform weighting function over a finite domain does not yield the best convergence. A much better convergence on mesh refinement is obtained when function $\alpha(\mathbf{x}-\mathbf{s})$ decays smoothly with the distance from point $\mathbf{x}$. A suitable form is the Gaussian (normal) distribution function, previously used for nonlocal elasticity by Eringen (1972);

$$\alpha(\mathbf{x}) = \exp[-(k|\mathbf{x}|/l)^2] \tag{4}$$

in which we have, for one, two and three dimensions

$$\begin{aligned} &\text{1D:} \quad |\mathbf{x}| = x && k = \pi^{1/2} \\ &\text{2D:} \quad |\mathbf{x}| = (x^2+y^2)^{1/2} && \mathrm{k} = 2 \\ &\text{3D:} \quad |\mathbf{x}| = (x^2+y^2+z^2)^{1/2} && \mathrm{k} = (6\sqrt{\pi})^{1/3}. \end{aligned} \tag{5}$$

x, y, z are the Cartesian coordinates.

The expressions in equation (5) have been determined from the condition that the integral of $\alpha(\mathbf{x})$ for an infinite body be equal for one dimension to the length l (line segment), for two dimensions to the area of a circle of diameter l, and for three dimensions to the volume of a sphere of diameter l.

The function in equation (4) decays so rapidly that for points $\mathbf{s}$ whose distance from point $\mathbf{x}$ exceeds $2l$ one may set $\alpha = 0$. Calculation of $V_r(\mathbf{x})$ according to equation (3) is needed for the treatment of boundaries. Function α in general extends beyond the boundaries of the body. The domain beyond the boundary is simply deleted from integration, but the weighting function is scaled so that the integral of all effective weights $\alpha'(\mathbf{x}, \mathbf{s}) = \alpha(\mathbf{s}-\mathbf{x})/V_r(\mathbf{x})$ over the body should be exactly 1 for any $\mathbf{x}$. In numerical programming, the integrals in equations (2) and (3) are approximated as finite sums. The values of $\alpha'(\mathbf{x}, \mathbf{s})$ are generated for all combinations of all integration points of all elements in advance of the finite-element analysis. The programming of the averaging integral, which was demonstrated by Bažant, et al. (1987) in a study of cave-in of a tunnel due to compressive strain-softening for a nonlocal finite-element system with up to 3248 unknowns, is easier when the integral in equation (2) extends over the entire body. When a finite averaging domain is used, it is important to closely match by finite elements the precise boundaries of this domain, but this is difficult to implement (Saouridis, et al., 1987).

Length l, called the characteristic length, represents a material property and is of the same order of magnitude as the maximum size of material inhomogeneities. Length l has been determined experimentally (Bažant and Pijaudier-Cabot, 1987*a*) by comparing the responses of specimens in which the damage (e.g., microcracking) remains distributed with the responses of fracture specimens, in which damage localizes. For concrete, such experiments indicated that l is roughly equal to 2.7-times the maximum aggregrate size.

Length l can be determined also by micromechanics analysis. In a parallel study (Bažant, 1987), a local homogeneous elastic continuum, containing an array of growing circular cracks with periodic spacing l and quasi-periodic crack sizes, was analyzed. It was shown that by applying the usual homogenization conditions, one obtains a nonlocal continuum with local strain and a nonlocal cracking strain, for which the weighting function is uniform and the characteristics length is equal to crack spacing. For the case when the crack spacing is not constant but randomly distributed, this indicates that one should superpose at each point a set of uniform weighting functions with various characteristics lengths l. This, however, appears to be approximately equivalent to using a nonuniform weighting function.

For a uniform weighting function, volume V_r has a similar

Downloaded 03 May 2010 to 171.66.16.21. Redistribution subject to ASME license or copyright; see http://www.asme.org/terms/Terms_Use.cfm

meaning as the representative volume in the statistical theory of heterogeneous materials. However, its size l, is smaller than that of the representative volume and is too small to obtain statistical averages of the microstructure. The representative volume in the statistical theory must be several times larger.

The specific free energy $\rho\psi$ per unit volume (with ρ being the material mass density) and the energy dissipation rate ϕ may be expressed as

$$\rho\psi = \tfrac{1}{2}(1-\Omega)C_{ijkm}\epsilon_{ij}\epsilon_{km} \qquad (6)$$

$$\phi = -\partial(\rho\psi/\partial t) = -\dot{\Omega}\partial(\rho\psi)/\partial\Omega = \dot{\Omega}Y$$

in which Y, called the damage energy release rate, is

$$Y = -\partial(\rho\psi)/\partial\Omega = \tfrac{1}{2}C_{ijkm}\epsilon_{ij}\epsilon_{km}. \qquad (7)$$

The damage evolution is characterized in general by an equation of the type $\dot{\omega} = f(\epsilon_{ij},\omega)$. An integrable special form of the damage evolution law has been used in all computations;

$$\omega = g(Y) = 1 - [1 + b(Y - Y_1)]^{-n} \qquad (8)$$

in which b, n = positive material constants, $n > 2$, and Y_1 = local damage threshold.

Damage is assumed to grow only for loading. For unloading or reloading, $\dot{\bar{\omega}} = 0$, which means the response is elastic. The loading criterion and the nonlocal damage Ω are defined as follows

$$\left.\begin{aligned} &\text{If } F(\bar{\omega}) = 0 \text{ and } \dot{F}(\bar{\omega}) = 0, \text{ then } \dot{\Omega} = \dot{\bar{\omega}} \\ &\text{If } F(\bar{\omega}) < 0, \text{ or if } F(\bar{\omega}) = 0 \text{ and } F(\dot{\bar{\omega}}) < 0, \text{ then } \dot{\Omega} = 0. \end{aligned}\right\} \qquad (9)$$

Function $F(\bar{\omega})$ represents the loading function and is defined as $F(\bar{\omega}) = \bar{\omega} - \kappa(\bar{\omega})$, where $\kappa(\bar{\omega})$ is a softening parameter which is set to be equal to the maximum value of $\bar{\omega}$ achieved up to the present. The initial value of $\kappa(\bar{\omega})$ is zero. The damage expression in equation (8) was found to approximate closely the behavior of concrete, provided that different local damage thresholds Y_1 are introduced for tension and compression (Mazars and Pijaudier-Cabot, 1986).

The formulation of the loading function automatically satisfies the dissipation inequality. The density of the energy dissipation rate due to damage is $\phi = \dot{\Omega}Y$, and since $\dot{\Omega} \geq 0$, we have $\phi \geq 0$.

In view of the use of a loading function, it might be more appealing to introduce some potential function, similar to plasticity. However, a formulation with a potential function has not yet been developed in the literature on continuum damage mechanics of concrete or geomaterials.

The fact that equation (1) uses nonlocal rather than local damage, and that the unloading condition is stated in terms of the nonlocal damage, represents all that is different from the classical local damage theory.

The original formulation of the nonlocal damage theory in the previous study by Pijaudier-Cabot and Bažant (1986) used a somewhat different definition of nonlocal damage. The averaged quantity was the damage energy release rate Y rather than the local damage, and so the nonlocal damage was determined as $\Omega = g(\bar{Y})$. This original formulation can be regarded as a simplified approximation of the present formulation. The numerical results for these two different definitions of nonlocal damage appear to be quite close.

The strains as well as ω have at least a C_0-continuity (i.e., they could consist of Dirac delta functions). According to equations (9) and (2) and the fact that $\phi = Y\dot{\Omega}$, the dissipation rate density is given by a spatial averaging integral over ω. Consequently, ϕ must have at least a C_1-continuity. This simple argument proves that the energy dissipation cannot localize into a zone of zero volume, and numerical solutions confirm it.

In general, one could show that by introducing any variable which causes the dissipation rate to be nonlocal (e.g., nonlocal plastic-strain path in plasticity with softening yield limit Bažant, et al., 1987), the energy dissipation is prevented to localize into a vanishing volume.

Differential Equation of Equilibrium and Boundary Conditions

In the original formulation of the nonlocal continuum for strain-softening in which nonlocal strains $\bar{\epsilon}_{ij}$ are used (Bažant, et al., 1984), the virtual work expression for a body of volume V_b and surface S_b must involve $\delta\bar{\epsilon}_{ij}$ rather than $\delta\epsilon_{ij}$

$$\delta W = \int_{V_b} (\sigma_{ij}\delta\bar{\epsilon}_{ij} - f_i\delta u_i)dV - \int_{S_b} p_i\delta u_i dS \qquad (10)$$

in which u_i = displacement components in Cartesian coordinates x_i ($i = 1,2,3$), and f_i, p_i = distributed volume and surface forces. The fact that $\delta\bar{\epsilon}_{ij}$ involves the spatial averaging operator defined by equation (2) complicates the derivation of the differential equation of equilibrium and boundary conditions and yields a nonstandard form of these equations (Bažant, 1984).

For the present nonlocal theory, ϵ_{ij} is local and so $\delta\bar{\epsilon}_{ij}$ in equation (10) must be replaced by $\delta\epsilon_{ij}$. But then the variational derivation of the differential equation of equilibrium and the boundary conditions is the same as usual (Bažant and Pijaudier-Cabot, 1987). This shows that, as long as the strains are defined as local, the differential equations of equilibrium, as well as the boundary conditions or the interface conditions, will have the standard form. This further means that the finite-element discretization can be of the same type as for the usual, local continuum. Therefore we may conclude that the key simplifying feature of a continuum model for damage is the use of a nonlocal continuum in which the strains are local. In other words, the continuum should not be fully, but only partially nonlocal. It is also clear that if the strain is local then the elastic behavior, including the behavior at unloading and reloading, will be local.

One-Dimensional Strain-Localization Instability

Consider for the sake of simplicity the one-dimensional problem of a bar loaded through two springs of spring constant C (Fig. 1). This problem was used by Bažant (1976) to demonstrate the localization instability due to strain-softening and was recently solved exactly with a fully nonlocal theory (Bažant and Zubelewicz, 1986). The length coordinate is x, the

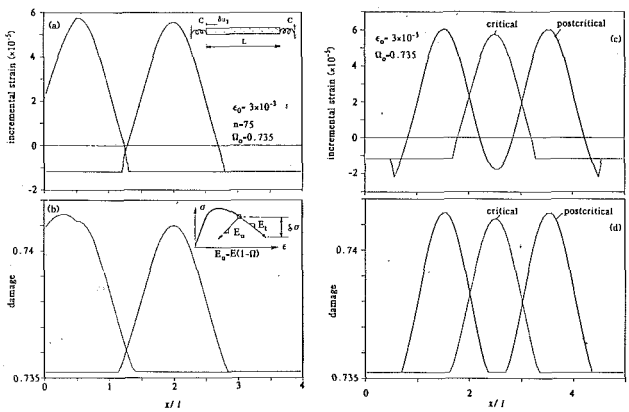


Fig. 1 Strain (*a*) and damage (*b*) localization profiles in the bar center and at the boundary, calculated for a one-dimensional bar; critical and postcritical strain and damage localization profiles (*c*, *d*)

Downloaded 03 May 2010 to 171.66.16.21. Redistribution subject to ASME license or copyright; see http://www.asme.org/terms/Terms_Use.cfm

bar length is L, and the bar ends are $x=0$ and $x=L$. The bar is initially in a state of uniform strain ϵ_0 and stress σ_0, with uniform damage $\Omega_0=\omega_0$. The initial state is in the strain-softening range and satisfies the relation $\sigma_0=(1-\Omega_0)E\epsilon_0$. If the constitutive relation for damage is given in the form of equation (8), we have $\omega_0=1-[1+b(\frac{1}{2}E\epsilon_0^2-Y_1)]^{-n}$.

We now consider a small deviation from the initial state caused by incremental variation of the load at the bar ends. Let $\delta\epsilon(x)=\eta(x)=$ incremental strain and $\delta\sigma=\tau=$ incremental stress. To maintain equilibrium, it is necessary that $\tau=$ constant along the bar. The compatibility condition for fixed supports requires that

$$\int_0^L \eta(x)dx+\frac{2\tau}{C}=0. \tag{11}$$

Taking the one-dimensional form of the constitutive law in equation (1) with the averaging according to equation (2) and the loading criterion according to equation (9), we find

For $\int_0^L \alpha(s-x)\eta(s)ds>0$: $\sigma_0+\tau$

$$=\left[1-\frac{1}{l'(x)}\int_0^L \alpha(s-x)\omega(s)ds\right]E(\epsilon_0+\eta(x)); \tag{12}$$

Otherwise: $\tau=(1-\omega_0)E\eta(x)$

in which $l'(x)=\int_0^L\alpha(s-x)dx=$ effective averaging length for point x. For infinitely small increments $\eta(x)$, the equations can be simplified by incremental linearization. To this end, we may introduce the linear approximation $\omega(x)=\omega_0+\omega_\epsilon\eta(x)$, with $\omega_\epsilon=\partial\omega/\partial\epsilon$ for $\omega=\omega_0$. Substituting into equation (12), neglecting the quadratic term $\eta(x)\eta(s)$, and subtracting the equation $\sigma_0=E(1-\Omega_0)\epsilon_0$, we can reduce equation (12) to the form

$$\tau=(1-\omega_0)E\eta(x)-\frac{k}{l'(x)}<\int_0^L\alpha(s-x)\eta(s)ds> \tag{13}$$

with $k=E\epsilon_0\omega_\epsilon$. The symbol $<\ >$, which introduces the loading criterion, is defined as $<x>=x$ if $x>0$ and otherwise $<x>=0$. For the special damage constitutive law in equation (8), we may evaluate $\omega_\epsilon=E\epsilon_0\omega_Y$, with $\omega_Y=bn[\frac{1}{2}E\epsilon_0^2-Y_1]^{n-1}[1+b(Y-Y_1)]^{-2n}$.

Equation (13) has the form of a linear integral equation of the second kind. However, the problem is not simply that of solving an integral equation, because equation (13) is an integral equation only for those x for which loading takes place. Outside the loading region, equation (12) reduces to the usual linear elastic differential equation for displacements and the behavior is then local, elastic, and unaffected by the strain-localization in another segment of the bar. If we find one solution such that there exist elastic segments of finite length at both ends of the bar, then we can obtain another solution simply by shifting the softening segment along with the softening solution profile as a rigid body. This shift is arbitrary provided the entire original length of the softening region, along with a small neighborhood of points located just outside the softening zone, remains within the bar. Due to this fact, we can calculate the length of the softening region and the solution profile through it by analyzing any bar of a shorter length, provided the bar length exceeds the length of the softening region. The actual boundary conditions and the compatibility condition may be disregarded in such analysis and satisfied afterward. Obviously, one can have infinitely many solutions. Arbitrary shifts of the softening region, however, do not affect the overall response of the bar. The length of the softening region and the solution profile through it is nevertheless unique. The localization profiles terminating at the boundary points are different from the interior one and require a special analysis. For real materials, the actual location of the strain-softening segment that does not reach the boundary is decided by inevitable random fluctuations of material strength along the bar.

Now consider the alternative formulation previously proposed by Pijaudier-Cabot and Bažant (1986), in which the averaged variable is Y rather than ω. For small strain increments, equation (2) can be approximated as $\Omega(x)=\omega_0+\Omega_Y[Y(x)-Y_0]$, with $\Omega_Y=[\partial\Omega/\partial Y]_{\epsilon 0}=\omega_Y$ in which Y_0, Ω_0 and ϵ_0 are the values of Y, Ω and ϵ in the initial state. Linearization for small increments is then accomplished by writing

$$Y(x)=\frac{1}{l'(x)}\int_0^L\alpha(s-x)\frac{E}{2}(\epsilon_0^2+2\eta(s))\epsilon_0 ds. \tag{14}$$

Substituting this into the basic relation $\tau=(1-\Omega)E\eta(x)$, one obtains for $\eta(x)$ an equation identical to equation (13), in which $k=2Y_1\Omega_Y$. An equation of the same form would be obtained for various other possible types of averaging. For problems with nonuniform initial strain, however, different types of averaging do not yield the same field equations.

Equation (13) can be easily solved numerically. If we subdivide the bar length into N equal elements of length $\Delta x=L/N$, use for integration the trapezoidal rule, express τ from equation (11) and substitute it into equation (13), we may approximate the resulting equation as follows

$$\sum_{j=1}^N K_{ij}\eta_j=0 \quad \text{with}$$

$$K_{ij}=(1-\omega_0)E\delta_{ij}-\frac{k\Delta x}{l_i'}I_i\alpha(x_j-x_i)+\frac{C}{2}. \tag{15}$$

Subscripts i, j refer to centroids of elements number i or j, and $I_i=1$ if $\int_0^L\alpha(x_i-s)\eta(s)ds\simeq\Sigma_i\alpha(x_j-x_i)\eta_j\Delta x\geq 0$; otherwise $I_i=0$. Equation (15) represents a system of homogeneous linear algebraic equations for η_j. The critical state occurs at such ϵ_0 for which $\det(K_{ij})=0$. The loading segment, characterized by $I_i=1$, is of course unknown in advance, and so it must be determined iteratively. To search for the critical state with the smallest ϵ_0, the values of ϵ_0 were incremented in small loading steps and, for each ϵ_0, the following algorithm was used:

1 In the first iteration, we assume that only one element i undergoes loading (the central element). In the subsequent iterations, we increase the number of elements that undergo loading by one (either on the left or on the right), unless the number of loading elements already equals N, in which case we start a new loading step with a larger ϵ_0.

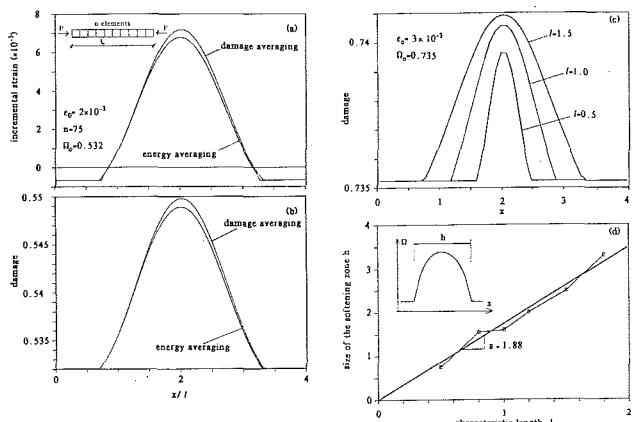


Fig. 2(*a*, *b*) Comparison of localization profiles of strain and damage for the damage and energy release rate averaging; (*c*, *d*) influence of the characteristic length *l* on the damage localization profiles, and the size of the softening zone

Downloaded 03 May 2010 to 171.66.16.21. Redistribution subject to ASME license or copyright; see http://www.asme.org/terms/Terms_Use.cfm

2 For each assumed set of elements with loading, we calculate the lowest eigenvalue λ_1 of K_{ij} and the corresponding eigenvector $\eta_i^{(1)}$. If the positive values of $\eta_i^{(1)}$ in this eigenvector do not agree with the assumed set of loading elements, we return to 1 and repeat the calculation for the same ϵ_0 and a larger number of softening elements. If they agree but $\lambda_1 > 0$, we also return to 1 (after storing the λ_1-value) and commence the next load step with increased ϵ_0; otherwise ($\lambda_1 \leq 0$) the critical state $\epsilon_0 = \epsilon_0^{cr}$ has just been passed. In that case, we interpolate with regard to the λ_1-value in the preceding loading step, in order to estimate more closely the value of ϵ_0 for which $\lambda_1 = 0$. Then we print this ϵ_1-value, calculate the corresponding eigenvector $\eta_i^{(1)}$ and stop.

Lack of Symmetry. As we can see from equation (15), the tangential stiffness matrix K_{ij} is nonsymmetric ($K_{ij} \neq K_{ji}$). The nonsymmetry is inevitable for the present formulation and is due to the loading condition, brought in through parameter I_i, as well as to the variability of l_i'. If I_i as well as l_i' have the same values for all elements, K_{ij} would be symmetric. Similarly, the part of matrix K_{ij} for which I_i and l_i' are constant is symmetric. Matrix K_{ij} also becomes symmetric for $\epsilon_0 \to 0$ (elastic behavior). For small ϵ_0 it is weakly nonsymmmetric. The fact that K_{ij} is nonsymmetric implies that the integral operator in equation (13) is nonsymmetric, too, which means it is not self-adjoint. This further implies that a minimizing functional associated with equation (15) does not exist.

By contrast, the operators and stiffness matrices for the previously formulated imbricate nonlocal continuum (Bažant, et al., 1987) are symmetric. In fact, the requirement of symmetry was shown to inevitably lead to the imbricate nonlocal model (Bažant, 1984). Convenient though the symmetry is for numerical solutions, this advantage is nevertheless more than offset by other disadvantages of the imbricate model, as already mentioned.

Numerical Studies. Typical results of numerical solutions of the strain-localization are plotted in Figs. 1-3. It is assumed that $E = 32000$ MPa, $b = 20.5$, $Y_0 = 8540 \times 10^{-6}$; these values are based on certain measurements (Nazars and Pijaudier-Cabot, 1986), $l = 0.25\ L$. The solutions are calculated for the averaging of ω as well as for the averaging of Y, and also for the uniform weighting function. The loading increment is $\tau = -0.1$ MPa. The number of elements along the bar is $N = 75$.

The profile $\eta(x)$ depends only on the critical state ϵ_0, Ω_0 and the boundary conditions. The strain-localization profile is symmetric if the localization region does not touch the boundary points of the bar. One also can obtain solutions with several waves as shown in Fig. 1(*c*, *d*); these solutions, however, could be reached only if the bar were prevented to fail at smaller strains. Figure 2(*a*, *b*) shows that the present damage averaging formulation and the original energy averaging formulation gives very close results. Note from the solutions that the damage is continuous but the slope of the damage profile may be discontinuous at the boundary of the localization region. Also note that the values of the strain increment can be negative within the loading (i.e., softening) zone. This is not objectionable since the unloading is defined on the basis of the increments of Ω rather than ϵ. This property, which is inevitable if the strains should be continuous and is the physical reason for the lack of symmetry and self-adjointness of equation (13), is revealed by equation (15).

The characteristic length controls the width of the softening zone. It also has a great effect on the smallest strain value ϵ_0 at which instability is possible. Figure 2(*c*) shows the damage profiles for various values of l. The relationship between the length of the softening zone and the characteristic length l is shown in Fig. 2(*d*), and we see that the length h of the softening zone is approximately $h = 1.88$ (at constant strain ϵ_0). This result, which is close to that obtained before for wave propagation problems (Pijaudier-Cabot and Bažant, 1986) has been exploited for measurement of the characteristic length (Bažant and Pijaudier-Cabot, 1987*a*). It also lends simple physical interpretation to the charactristic length, l.

Figure 3(*a*) shows the dependence of the critical value of the tangent modulus E_t on L/l for various values of C; E_t is understood as the effective tangential modulus for further loading (softening) and is evaluated on the basis of local damage (for nonlocal damage the value of E_t cannot be defined uniquely). Figure 3(*b*) shows the numerical results for dependence of the ductility ratio ϵ_0/ϵ_p on the ratio of the bar length L to the characteristic length l, for various values of the spring constant C (A = bar cross section = 1 in the calculation, ϵ_p = strain at peak stress).

Comparison with the previously given local solution (Bažant, 1976) is shown in Fig. 3(*c*). In a local formulation, however, the ratio h/L needs to be fixed in advance, as is done in the crack band theory. In a nonlocal formulation, h is a solution obtained on the basis of nonlocal damage theory; $h = \beta(\epsilon_0)l$ where β is a coefficient, mildly depending on the critical strain; for $\epsilon_0 = 3 \times 10^{-3}$ we find $\beta = 1.88$, as shown in Fig. 2(*d*). We also see that the local and nonlocal solutions are very close to each other. However, such close agreement need not extend to general three-dimensional situations with irregular damage zones.

Figure 3(*c*) compares the nonlocal solutions obtained for the present damage averaging and the previously used energy release rate averaging. The comparisons of solutions for various choices of the weighting function $\alpha(x)$ are presented in Fig. 3(*d*). Both types of averaging and different weight functions yield rather close results.

Energy Analysis of Localization Instability

Although a minimizing functional does not exist for the present nonlocal theory, stability can be checked by calculating the incremental work ΔW that needs to be done on the bar to produce small strain variations $\delta\epsilon(x) = \eta(x)$. Thus the stability condition is $\Delta W > 0$ for all $\eta(x)$ where $\Delta W = \delta W + \delta^2 W$. Since $\delta W = 0$ if the initial state is an equilibrium state, the stability condition is $\delta^2 W > 0$. We have $\delta^2 W = \frac{1}{2}\int \eta(x)\delta\tau dx + \frac{1}{2} C \delta u_2^2$. Upon substituting for $\delta\tau$ according to equation (13), we get the stability condition in the form

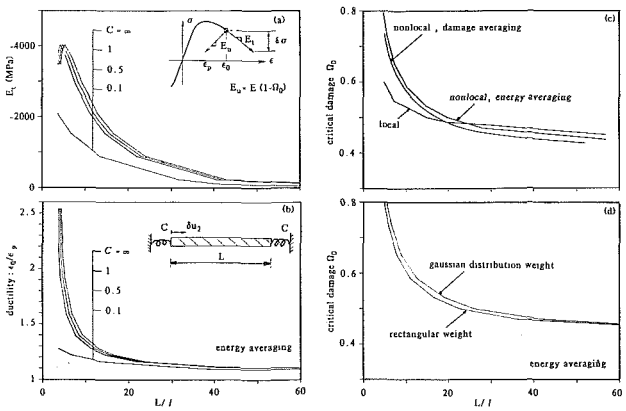


Fig. 3 Stability limits in terms of critical tangential modulus (*a*; ductility (*b*); critical damage obtained from the damage and energy averaging formulations as function of the length of the bar (*c*); influence of the weighting function (*d*)

Downloaded 03 May 2010 to 171.66.16.21. Redistribution subject to ASME license or copyright; see http://www.asme.org/terms/Terms_Use.cfm

$$\delta^2 W = \tfrac{1}{2}\int_0^L \eta(x)[(1-\omega_0)E\eta(x)$$

$$-\frac{E\epsilon_0\omega_0}{l'(x)} < \int_0^L \alpha(s-x)\eta(s)ds >]dx + \frac{C}{2}\delta u_2^2 > 0 \qquad (16)$$

subject to the compatibility condition $\int \delta\eta(x)dx + 2\delta\tau/C = 0$. As expected, $\delta^2 W$ vanishes for the critical state, as indicated by equation (13). From this, it follows that for $\epsilon_0 < \epsilon_0^{cr}$, $\delta^2 W > 0$, and for $\epsilon_0 > \epsilon_0^{cr}$, $\delta^2 W < 0$. Numerical evaluations of equation (16) confirm it. Thus the bar is stable for $\epsilon_0 < \epsilon_0^{cr}$, and unstable for $\epsilon_0 > \epsilon_0^{cr}$.

Note again that the quadratic functional in equation (16) is not symmetric. This is due to the presence of operator $< >$ as well as the variability of $l'(x)$.

Convergence at Mesh Refinement

The chief problem with the local solutions for strain-softening has been their convergence to physically incorrect solutions with zero-energy dissipation and the consequent spurious mesh sensitivity. For dynamic response, a rapid convergence has already been numerically demonstrated by Pijaudier-Cabot and Bažant (1986) but it still remains to examine convergence and determine how it is affected by the choice of the weighting function and other factors. Rapid and correct convergence is particularly important for strain-localization problems since strain-localization may often necessitate a very fine discretization in the damage zones. It is therefore important to capture strain-localization with the smallest possible number of elements per representative length of the material.

We now consider the formulations with the averaging of both the local damage ω and the damage energy release rate Y.

In numerical calculations, we compare the results for a uniform weight ($\alpha = 1$ over the length l), used in the initial work, with various nonuniform weights, such as the Gaussian distribution and the triangular function defined as $\alpha(s) = (2/l)(1-(2/l)|s|)$ for $|s| < l/2$ and $\alpha(s) = 0$ for $|s| \geq l/2$. In contrast to the original, fully nonlocal model (Bažant, et al., 1984), the weighting function, used for the strain-softening only, need not satisfy specific stability conditions stated in terms of the Fourier transform by Bažant and Chang (1984).

For each weighting function, the strain and damage localization profiles for various times were calculated, for the same bar as before, using different numbers, N, of constant-length, two-node finite elements. The number of elements per characteristic length l ranged from 3 to 25. Figure 4(*a–c*) shows the convergence of the strain profiles for a bar initially uniformly strained up to $\epsilon_0 = 3\times 10^{-3}$. We see that, for the uniform weight function, the convergence is relatively slow but improves drastically for the continuous weight functions, especially for the smooth Gaussian distribution function. For this function, only a few elements (3 to 6) over the characteristic length are required in order to determine with a practically sufficient accuracy the failure due to unstable strain-softening. This is also corroborated by Fig. 4(*c*) which shows the dependence of the size of the softening zone on the number of finite elements. Evidently, a relatively crude mesh suffices for good failure prediction if the Gaussian distribution function is used.

Let us now explore numerically the rate of convergence of the energy W dissipated due to damage. The finite-element solutions usually exhibit power-type convergence. This means that for a large enough number, N, of elements the error decreases as a certain power of the finite-element size h. Therefore the values of W calculated for various meshes should (in the asymptotic sense for $h \to 0$) vary as

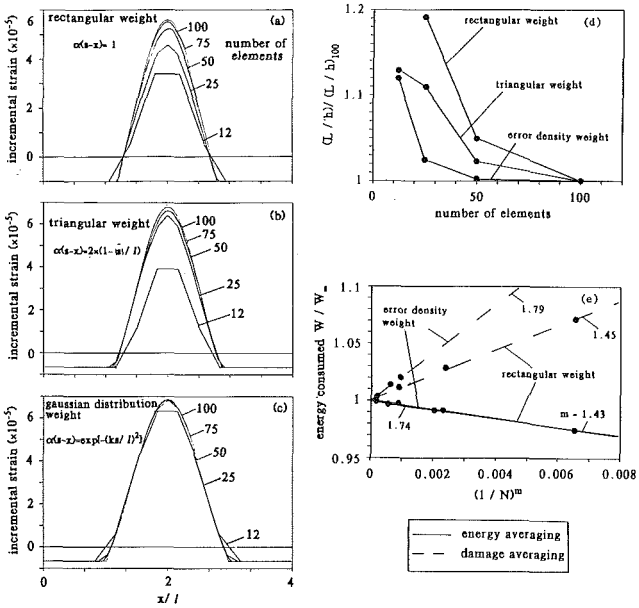


Fig. 4(*a–c*) Convergence of the strain localization profiles for various weighting functions; (*d*) convergence of the size of the softening zone; (*e*) convergence of the energy dissipated

$W = AN^{-m} + W_\infty$, in which A, W_∞ and m are certain constants. For problems of linear elasticity, the convergence is quadratic, i.e., $m = 2$. The value W_∞ represents the limiting solution for $N \to \infty$, which may be considered as the exact solution. For nonlinear problems, the convergence is generally slower than quadratic; i.e., $m < 2$.

The values of W_∞, A and M have been identified by fitting with the formula for W the results on at least three different meshes using Levenberg-Marquardt nonlinear optimization subroutine.

Instead of the static localization problem studied here so far, the dynamic localization problem studied previously by Pijaudier-Cabot and Bažant (1986) has been analyzed numerically. An initially stress-free bar is subjected for times $t > 0$ to constant outward velocities at both ends, which are such that the inward waves are elastic but reach strain-softening when they meet at the middle. Prior to softening, the inward waves are step functions but after softening a complex localization profile develops. For the local case, this problem has been solved exactly (cf. Bažant, 1986), but for the nonlocal case, a numerical solution is necessary. The results are plotted in Fig. 4(*e*) which shows that the convergence rate, as indicated by exponent m, ranges from $m = 1.43$ for the uniform weight function to 1.79 for the Gaussian weight function ($W_\infty = 0.0003925$). Moreover, the magnitude of error is by far the smallest for the Gaussian weight function. We therefore may conclude that this function should be preferred in practical applications.

Comparisons have also been made between the two types of averaging used in this paper. The convergence was found to be distinctly better for the averaging of the local damage ω than of the local damage energy release rate Y.

Conclusions

1 The key feature of a simple nonlocal theory of strain-softening is that the strain should be local. This implies that the elastic behavior, including unloading after strain-softening as well as reloading, must be local. Nonlocal must be the variables that determine damage, the phenomenon responsible for strain-softening.

2 Owing to the continuity properties introduced by the nonlocal concept, the energy dissipation due to damage can-

Downloaded 03 May 2010 to 171.66.16.21. Redistribution subject to ASME license or copyright; see http://www.asme.org/terms/Terms_Use.cfm

not localize into a region of vanishing volume. The present solutions of static strain-localization confirm this result, and so do the previous wave propagation solutions.

3 The field operator in the equilibrium for the present theory is nonsymmetric, except for the elastic part of response, and discretization yields a nonsymmetric tangential stiffness matrix. The lack of symmetry is caused by applying the spatial averaging operator only to damage. A symmetric operator can be achieved with the previously proposed imbricate nonlocal formulation, but that formulation has other more serious disadvantages.

4 Analysis of the strain-localization instability in a bar that is initially under uniform strain leads to an eigenvalue problem for an integral equation. This equation can be accurately solved numerically. The solution yields the size h of the localization zone. This size is found to be approximately proportional to the characteristic length l of the nonlocal continuum ($h = 1.88\ l$).

5 The magnitude of the critical strain for static localization instability in a strain-softening bar decreases as the bar length increases or as the support stiffness decreases. This agrees with previous solutions in which the size of the strain-softening region was considered to be a material property. In the present theory, this size is calculated and depends mainly on the characteristic length of the nonlocal continuum.

6 Finite-element analysis for the presently proposed nonlocal damage formulation appears to exhibit power-type convergence which is almost quadratic in energy, even if the entire bar is initially in the strain-softening state. A smooth weighting function, such as the Gaussian distribution function (normal distribution), yields a subtantially better convergence than unsmooth weighting functions.

Acknowledgment

Financial support under U. S. Air Force Office of Scientific Research Grant No. F49620-87-C-0030DEF to Northwestern University, monitored by Dr. Spencer T. Wu, is gratefully acknowledged.

References

Aifantis, E. C., 1986, "On the Microstructural Origin of Certain Inelastic Models," *J. Eng. Mat. Tech.*, No. 106, pp. 326–330.

Bažant, Z. P., 1976, "Instability, Ductility and Size Effect in Strain-Softening Concrete," *Journal of the Engineering Mechanics Division, ASCE*, Vol. 102, No. EM2, pp. 331–344; discussions Vol. 103, pp. 357–358, 775–777, Vol. 104, pp. 501–502 (based on Struct. Eng. Report No. 74-8/640, Northwestern University, Aug. 1974).

Bažant, Z. P., 1984, "Imbricate Continuum and its Variational Derivation," *Journal of the Engineering Mechanics Division, ASCE*, Vol. 110, No. 12, pp. 1693–1712.

Bažant, Z. P., 1986, "Mechanics of Distributed Cracking," ASME *Applied Mechanics Reviews*, Vol. 39, No. 5, May, pp. 675–705.

Bažant, Z. P., 1987, "Why Continuum Damage is Nonlocal: Justification by Quasiperiodic Crack Array," Concrete and Geomaterials Report No. 87-8/498W, Northwestern University, Evanston, IL (August); also *Mechanics Research Communications*, Vol. 14, 1987, pp. 407–419.

Bažant, Z. P., and Belystschko, T. B., 1987, "Strain-Softening Continuum Damage: Localization and Size Effect," Preprints, International Conference on Constitutive Laws for Engineering Materials, Vol. 1, eds. Desai, C. S, et al., held in Tucson, AZ., Jan., Elsevier, NY, pp. 11–33.

Bažant, Z. P., Belytschko, T. B., and Chang, T. P., 1984, "Continuum Theory for Strain-Softening," *Journal of the Engineering Mechanics Division, ASCE*, Vol. 110, No. 12, pp. 1666–1692.

Bažant, Z. P., and Chang, T. P., 1984, "Instability of Nonlocal Continuum and Strain Averaging," *Journal of Engineering Mechanics, ASCE*, Vol. 110, No. 10, pp. 1441–1450.

Bažant, Z. P., Lin, F. B., and Pijaudier-Cabot, G., 1987, "Yield Limit Degradation: Nonlocal Continuum with Local Strains," Preprints, *International Conference on Computational Plasticity*, held in Barcelona, Eds., Oñate, E., Owen, R., and Hinton. E., University of Wales, Swansea, pp. 1757–1779.

Bažant, Z. P., and Pijaudier-Cabot, G., 1987, "Modeling of Distributed Damage by Nonlocal Continuum with Local Strain," *Proceedings 4th International Conference on Numerical Methods in Fracture Mechanics*, held in San Antonio, TX, Mar., Eds., Luxmore, A. R., et al., Pineridge Press, Swansea, U.K., pp. 411–432.

Bažant, Z. P., and Pijaudier-Cabot, G., 1987a, "Measurement of Characteristic Length of Nonlocal Continuum," Report 87-12/498 m, Center for Concrete and Geomaterials, Northwestern University, November. Also *Journal of Engineering Mechanics*, ASCE, in press.

Bažant, Z. P., and Zubelewicz, A., 1986, "Strain-Softening Bar and Beam: Exact Nonlocal Solution," *Report*, Center for Concrete and Geomaterials, Northwestern University, Evanston, IL; also *International Journal of Solids and Structures*, in press.

Eringen, A. C., 1972, "Linear Theory of Nonlocal Elasticity and Dispersion of Plane Waves," *International Journal of Engineering Science*, No. 10, pp. 425–435.

Floegl, H., and Mang, H. A., 1981, "On Tension-Stiffening in Cracked Reinforced Concrete Slabs and Shells Considering Geometric and Physical Nonlinearity," *Ingenieurm Archiv*, Vol. 51, No. 314, pp. 215–242.

Kröner, E., 1967, "Elasticity Theory of Materials with Long-range Cohesive Forces," *International Journal of Solids and Structures*, No. 3, pp. 731–742.

Krumhansl, J. A., 1968, "Some Considerations of the Relations Between Solid State Physics and Generalized Continuum Mechanics," *Mechanics of Generalized Continua*, Eds., Kröner, E., Springer-Verlag, W. Berlin, W. Germany, pp. 298–331.

L'Hermite, R., and Grieu, J. J., 1952, "Etude expérimentales récentes sur le retrait des ciments et des bétons," *Annales I.T.B.T.P.* (Paris), Vol. 5, No. 52–53, pp. 494–51.

Ladevèze, P., "On an Anisotropic Damage Theory," (in French), *Internal Report*, No. 34, Laboratoire de Mécanique et Technologie, Cachan, France.

Lemaitre, J., Chaboche, J. L., "Mêcanique des matériaux solides," Dunod-Bordas, Paris.

Mang, H., and Eberhardsteiner, J., 1986, "Collapse Analysis of Thin R. C. Shells on the Basis of a New Fracture Criterion," *Finite Element Analysis of Reinforced Concrete* (*Proceedings of the U.S.-Japan Seminar Held in Tokyo*, May 1985). Eds., Meyer, C., and Okamura, H., ASCE, New York, pp. 579–601.

Mazars, J., and Pijaudier-Cabot, G., 1986, "Continuum Damage Theory: Application to Concrete," *Internal Report*, Laboratorie de Mêcanique et Technologie, Cachan, France, also *Journal of Engineering Mechanics*, ASCE, in press.

Needleman, A., 1987, "Material Rate Dependence and Mesh Sensitivity in Localization Problems," *Report*, Division of Engineering, Brown University, Providence, RI, January.

Pijaudier-Cabot, G., and Bažant, Z. P., 1986, "Nonlocal Damage Theory," *Journal of Engineering Mechanics, ASCE*, Vol. 113, No. 10, Oct., pp. 1512–1533, see also, Report No. 86-8/428n, Northwestern University, Evanston, IL.

Read, H. E., and Hegemier, G. P., 1984, "Strain-softening of Rock, Soil and Concrete—A Review Article," *Mech. Mat.*, Vol. 3, No. 4, pp. 271–294.

Sandler, I. S., 1986, "Strain-Softening for Static and Dynamic Problems," *Proceedings, Symposium on Constitutive Equations: Micro, Macro and Computational Aspects*, ASME Winter Annual Meeting, New Orleans, Dec., Eds., William, K. J., ASME, New York, pp. 217–231.

Saouridis, C., Mazars, J., and Billardon, R., 1987, "Evolution nonlocale de l'endommagement et limiteurs de localisation en êlêments finis," *Proceedings 8th Congress of the Association Universitaire de Mecanique*, held in Nantes, Sept. A.U.M., Ed., pp. 147–148.

Schreyer, H. I., and Chen, Z., 1984, "The Effect of Localization on the Softening Behavior of Structural Members," *Proceedings, Symposium on Constitutive Equations: Micro, Macro, and Computational Aspects*, ASME Winter Annual Meeting, New Orleans, Ed., William, K., ASME, New York, December, pp. 193–203; also ASME JOURNAL OF APPLIED MECHANICS, Vol. 53, December 1986, pp. 791–797.

Downloaded 03 May 2010 to 171.66.16.21. Redistribution subject to ASME license or copyright; see http://www.asme.org/terms/Terms_Use.cfm

Alan C. F. Cocks
Engineering Department,
The University of Leicester,
Leicester, England

Frederick A. Leckie
Department of Mechanical Engineering,
The University of California,
Santa Barbara, CA 95106
Mem. ASME

Creep Rupture of Shell Structures Subjected to Cyclic Loading

A bounding theorem is obtained for the time of creep rupture of shell structures subjected to cyclic loading. It is found that the shakedown concepts can be used in which a reference rupture stress replaces the yield stress.

1 Introduction

When metals are subjected to stress at temperatures in excess of $T_m/3$, where T_m is the melting temperatures in °K, the metal suffers time-dependent creep deformations. In addition, internal damage increases with time so that the metal ultimately ruptures. Consequently, when designing shell structures which operate at such elevated temperatures, consideration must be made to ensure that creep deformations do not exceed operational requirements during the life of the component. Common allowable deformations are 1 percent average and 5 percent maximum strain. In addition, the rupture conditions are that no part of the component may separate nor that local leakage can occur.

By establishing suitable constitutive equations which give the strain rates and the rate of increase of internal damage of the material, it is possible in principle to establish by numeric means the strain, stress, and damage history at all points in the shell. Such procedures tend to be very complex and it is difficult on the basis of the calculations to draw conclusions of the type which can help to reach a deeper understanding of the shell behavior.

In a companion study [1], it was shown how bounds could be obtained on the creep deformations which occur when shells are subjected to cyclic loading. It was shown how the role of the shakedown concept, so strongly associated with plasticity theory can be extended by replacing the yield stress with the uniaxial stress σ_0 which causes the steady-state strain rate $\dot{\epsilon}_0$, which, in turn, is a design parameter given by the relationship

$$\dot{\epsilon}_0 t_L = \epsilon_D$$

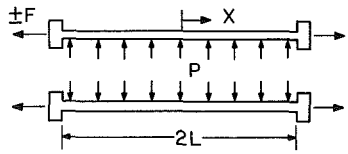
where t_L is the life of the component and ϵ_D is the allowable design strain.

This paper is concerned with the determination of the creep rupture life of shell components subjected to cyclic loading. It shall be shown that the shakedown concept can again be extended to give estimates of the creep rupture life. The role of the yield surface in plasticity is replaced by the so-called isochronous surface which is a surface in stress space for which the rupture time is constant. It proves convenient to let this time correspond to the design life of the component.

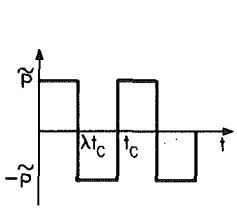
For the purpose of illustration, the creep rupture behavior of a cylindrical shell shall be studied. The loading case to be considered is that of a constant internal pressure p and a cyclic end load $\pm F$ (Fig. 1).

2 Material Behavior

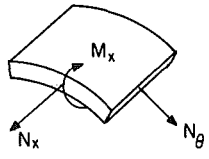
The high temperature strain/time response of a metal subjected to constant stress has the form shown in Fig. 2. After the initial time-independent response, the strain rate decreases with time during the so-called transient period I when the hardening processes which occur within the material exceed the effects of thermal softening. In Region II, referred to as the steady state, the hardening and softening rate are equal and opposite so that the strain rate is constant. In the tertiary Region III, the effects of internal damage become evident so



Cyclic End Load



Form of Cyclic Loading



Sign Convention

Fig. 1 Cylindrical shell subjected to cyclic load

Contributed by the Applied Mechanics Division for presentation at the Winter Annual Meeting, Chicago, IL, November 28 to December 2, 1988, of The American Society of Mechanical Engineers.

Discussion on this paper should be addressed to the Editorial Department, ASME, United Engineering Center, 345 East 47th Street, New York, N.Y. 10017, and will be accepted until two months after final publication of the paper itself in the JOURNAL OF APPLIED MECHANICS. Manuscript received by ASME Applied Mechanics Division June 5, 1987; final revision, January 18, 1988.

Paper No. 88-WA/APM-30.

Copyright © 1988 by ASME
Downloaded 03 May 2010 to 171.66.16.21. Redistribution subject to ASME license or copyright; see http://www.asme.org/terms/Terms_Use.cfm

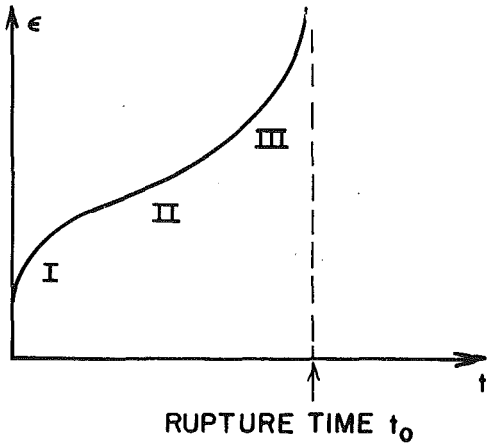


Fig. 2 Uniaxial creep curve showing the three stages of creep

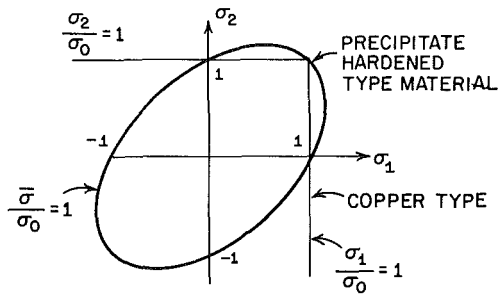


Fig. 3 Isochronous surfaces for $\bar{\sigma}$ and σ_1 materials in plane stress space

that the strain rate increases until rupture eventually occurs. In a previous paper [1], constitutive equations were developed which describe the deformations in portions I and II of the creep curve. For rupture life predictions, equations are necessary which describe the internal damage occurring within the metal and the increasing strain-rate characteristic of the tertiary behavior. It is these equations which shall be used in the present investigation.

2.1 Creep Rupture Constitutive Equations. The constitutive equations which describe the tertiary portion of the creep curve are given by

$$\frac{\dot{\epsilon}_{ij}}{\dot{\epsilon}_0}=\phi^n\left(\frac{\sigma_{ij}}{\sigma_0}\right)\frac{\partial\phi}{\partial\sigma_{ij}}\,g_1(\omega) \tag{2.1a}$$

$$\dot{\omega}=A\Delta^{\nu}\left(\frac{\sigma_{ij}}{\sigma_0}\right)g_2(\omega) \tag{2.1b}$$

where $\dot{\epsilon}_0$, σ_0, n, ν and A are material constants and $\phi(\sigma_{ij})$ is a homogeneous function of degree one in stress and is proportional to the effective stress $\bar{\sigma}$. The quantity ω is a measure of the internal damage in the material. The physical nature of the damage depends upon the material and its operating conditions. It is possible to identify ω rather precisely with specific forms of damage, and special forms of $g_1(\omega)$ and $g_2(\omega)$ in equation (2.1) can indeed be used to describe the range of mechanisms which have been identified [2, 3]. In the case when grain-boundary diffusion is responsible for the growth of voids, it is found that $\omega=(r/l)^2$ where r is the radius of the void and $2l$ is the spacing between voids. In other situations, especially those associated with precipitate hardened materials, the damage is in fact a softening mechanism associated with dislocation loops left behind on the precipitate particles by dislocations which account for creep deformation. The presence of the dislocation loops increases the climb rate [3]. In those circumstances, it is the density of the dislocation loops which provides the measure of the damage. The function of stress $\Delta(\sigma_{ij}/\sigma_0)$ describes the so-called isochronous surface which is the locus of multiaxial stress states for which the rupture time is constant (Fig. 3). The constant A is selected to give the rupture time t_0 observed for an applied stress σ_0. For the uniaxial loading with $\sigma=\sigma_0$, equation (2.1b) becomes

$$\dot{\omega}=A\,g_2(\omega)$$

which on integration gives the rupture time t_0

$$t_0=\int_{\omega_i}^{\omega_f}\frac{1}{A}\,\frac{d\omega}{g_2(\omega)}$$

where ω_i is the initial damage and ω_f the critical value that results in failure.

Two specific forms of Δ are discussed which represent the extremes of material behavior. For some materials strengthened by precipitate $\Delta(\sigma_{ij}/\sigma_0)=\bar{\sigma}/\sigma_0$ where $\bar{\sigma}$ is the effective stress, and equation (2.1b) then has the form

$$\dot{\omega}=A\left(\frac{\bar{\sigma}}{\sigma_0}\right)^{\nu}g_2(\omega). \tag{2.1c}$$

A material within this class shall be referred to as a $\bar{\sigma}$ material. For the situation, when the damage is in the form of voids, which grow by grain boundary diffusion, the maximum principal stress σ_1 detemines the growth rate. Then $\Delta(\sigma_{ij}/\sigma_0)=\sigma_1/\sigma_0$ and the damage growth equation becomes

$$\dot{\omega}=A\left(\frac{\sigma_1}{\sigma_0}\right)^{\nu}g_2(\omega). \tag{2.1d}$$

Materials satisfying this relationship are referred to as σ_1 materials. These extreme forms of the isochronous surface for plane-stress conditions are shown in Fig. 3, and both forms shall be used in this study. Nonproportional loading tests [8] on a precipitate hardened aluminum alloy which is a $\bar{\sigma}$ material indicate that the damage is isotropic and that the rate of damage is dependent only on the magnitude of $\bar{\sigma}$ and not on the direction of stress. Similar tests on copper, for which the damage is in the form of intergranular cavities, indicate, however, that damage grows on planes independent of each other. Consequently, if the stress field is rotated, the life of the material is dictated by the rupture of the plane which suffers longest exposure to maximum stress, and the failure time is independent of the damage in other directions. Consequently, the concept of independent damage directions becomes useful and this property shall be used in the next section.

3 Generalized Forces and Moments

When analyzing shell problems, it often proves advantageous to express the constitutive behavior on terms of generalized forces. The generalized forces to be considered in this problem are the hoop stress resultant N_θ the moment resultant M_x, and the axial stress resultant N_x (Fig. 1). The corresponding strain rates are $\dot{\epsilon}_\theta$, $\dot{\kappa}$ and $\dot{\epsilon}_x$, where $\dot{\epsilon}_\theta$ and $\dot{\epsilon}_x$ are strain rates in the θ and x-direction and $\dot{\kappa}$ is the curvature rate in the x-direction.

Appropriate forms of the constant energy dissipation rate surfaces for steady-state creep are given in [1]. For the shell geometry under consideration, the rate of energy dissipation becomes

$$\dot{D}(N_i)=N_0\dot{\epsilon}_0\phi^{n+1}(n_i) \tag{3.1}$$

where the potential function $\phi(n_i)$ is defined by the following intersecting planes

Downloaded 03 May 2010 to 171.66.16.21. Redistribution subject to ASME license or copyright; see http://www.asme.org/terms/Terms_Use.cfm

$$
\begin{aligned}
&n_\theta = \pm 1\\
&n_\theta - n_x = \pm 1\\
&n_x + m_x = \pm 1\\
&n_x - m_x = \pm 1\\
&n_\theta - n_x - \frac{m_x}{2} = \pm 1\\
&n_\theta - n_x + \frac{m_x}{2} = \pm 1
\end{aligned}
\tag{3.2}
$$

and

$$
n_x = \frac{N_x}{N_0}\ ,\quad n_\theta = \frac{N_\theta}{N_0}\ ,\quad m_x = \frac{M_x}{M_0}
$$

where M_0 and N_0 are the normalizing factors

$$
M_0 = \frac{\sigma_0 t^2}{4} \quad \text{and} \quad N_0 = \sigma_0 t. \tag{3.3}
$$

These expressions are recognized as those used in Hodge's [5] expressions with σ_0 replacing the yield stress σ_y when $n_x = 0$. In forming this surface, the same through thicknes stress fields as exist in plasticity are assumed to exist also in creep. This procedure gives an upper bound on energy dissipation rates [6], which is nevertheless close to the exact value. It also is convenient for shell rupture calculations to express the isochronous surface in terms of stress resultants. For materials whose rate of creep damage is governed by the effective stress $\bar{\sigma}$, damage occurs irrespective of the sign of the stress. Experiments by Hayhurst [7] on precipitates hardened aluminum beams in bending verify the validity of the assertion. He also demonstrates that when the applied moment is

$$
M_0 = \sigma_0 t^2/4 \tag{3.3}
$$

the rupture time of the beam is t_0. From this behavior, it can be deduced that the isochronous surface for rupture time t_0 has the same form as the constant energy dissipation rate surface. The resulting isochronous surface for a $\bar{\sigma}$ material and for the given shell is then defined by equations (3.2).

When materials suffer the type of creep damage which is dependent on the value of the maximum stress, it is implied that the stress is tensile. Damage does not grow when the stress is compressive. This means, in the case of a beam in bending, for example, that damage only occurs in those portions where stress is tensile. Hayhurst [7] has shown in this case that the moment which gives a rupture time t_0 is given by

$$
M_0 = \frac{\sigma_0 t^2}{4.2^{1/\nu}}\ . \tag{3.4}
$$

Since the beam is symmetric, a moment of opposite sign shall give the same rupture time except that it is the opposite face that shall suffer damage.

Finally, it was noted from previous experiments on nonproportional loading [8] that faces in different directions do not interact. Hence, M_x and N_x do not interact with N_θ, and the isochronous surface is defined by equations (3.5). Since no damage is caused by compressive stress, the surface extends infinitely far to the left so that the so-called noninteracting isochronous surface is defined by

$$
\begin{aligned}
&n_\theta = 1\\
&n_x + m_x = 1\\
&n_x - m_x = 1
\end{aligned}
\tag{3.5}
$$

The damage growth-rate equation in terms of generalized forces then becomes

$$
\dot{\omega} = A\Delta^\nu(n_i) g_2(m) \tag{3.6}
$$

where $\Delta(n_i)$ is given by equations (3.2) for an effective stress material and equations (3.5) for a maximum principal stress material.

4 Upper Bound on Rupture Time

We follow Ponter [9] in deriving a bound on the time for initiation of rupture in a structure subjected to cyclic loading of the type shown in Fig. 1, where one extreme of loading is maintained for $0 \le \tau < \lambda$ and the other extreme for $\lambda \le \tau \le 1$, where $0 \le \lambda \le 0.5$ and $\tau = t/t_c$, t_c being the cycle time. From equation (2.1*b*), we note that prior to failure for a material element which experiences a stress σ_{ij} that

$$
\int_0^t \Delta^\nu(n_i)\,dt = \int_{\omega_i}^{\bar{\omega}} \frac{1}{A}\,\frac{d\omega}{g_2(\omega)} \le t_0 \tag{4.1}
$$

where $\bar{\omega} \le \omega_f$. For conditions of rapid cycling, the stress at each end of the cycle remains approximately constant and the convexity condition for Δ^ν at any instant is given by

$$
\Delta^\nu(n_i) - \Delta^\nu(n_i^s) - \frac{\partial \Delta^\nu}{\partial n_i^s}\,(n_i - n_i^s) \ge 0 \tag{4.2}
$$

We identify n_i with the actual solution and n_i^s with the shakedown solution for a perfectly plastic material of yield strength N_0, where

$$
\Delta^\nu(n_i) = 1;\ d\epsilon_i^p = d\mu\,\frac{\partial \Delta^\nu}{\partial n_i}\ ,\ d\mu \ge 0 \tag{4.3}
$$

represent the yield surface and associated flow rule. The plastic strain measure $d\epsilon_i^p$ represents axial curvature as well as axial and hoop strain. When the generalized strain is represented in this form, the dimensionless measure of curvature is $d\epsilon_\kappa^p = d\kappa_x^p\, M_0/N_0$ where $d\kappa_x^p$ is the increment of axial curvature. Applying equation (4.2) at each extreme of the cycle

$$
\begin{aligned}
&d\mu_1 \Delta^\nu(n_i^1) - d\mu_1 \Delta^\nu(n_i^{1s}) - d\mu_1\,\frac{\partial \Delta^\nu}{\partial n_i^{1s}}\,(n_i^1 - n_i^{1s}) \ge 0\\
&d\mu_2 \Delta^\nu(n_i^2) - d\mu_2 \Delta^\nu(n_i^{2s}) - d\mu_2\,\frac{\partial \Delta^\nu}{\partial n_i^{2s}}\,(n_i^2 - n_i^{2s}) \ge 0
\end{aligned}
\tag{4.4}
$$

where the first of equations (4.3) applies when $0 \le \tau < \lambda$ and the second when $\lambda \le \tau \le 1$. Combining equations (4.4), and noting that plastic straining can only occur when $\Delta^\nu(n_i^s) = 1$, for the perfectly plastic material, we obtain

$$
\begin{aligned}
&\frac{d\mu_1}{\lambda}\,\lambda\Delta^\nu(n_i^1) + \frac{d\mu_2}{(1-\lambda)}\,(1-\lambda)\Delta^\nu(n_i^2)\\
&\qquad - (d\mu_1 + d\mu_2) - d\epsilon_i^p \rho_i \ge 0
\end{aligned}
\tag{4.5}
$$

where $d\epsilon_i^p$ is the plastic strain experienced by the element over the cycle at shakedown and $\rho_i = n_i^1 - n_i^{1s} = n_i^2 - n_i^{2s}$ is a residual stress field. The equality arises from the fact that n_i^1 and n_i^2, and n_i^{1s} and n_i^{2s} differ by the same elastic generalized force field. The inequality of equation (4.5) is still retained if $d\mu_1/\lambda$ and $d\mu_2/(1-\lambda)$ are replaced by $d\bar{\mu}$, where $d\bar{\mu}$ is the maximum of $d\mu_1/\lambda$ and $d\mu_2/(1-\lambda)$. Integrating equation (4.5) over the volume then gives

$$
\int_V d\bar{\mu}\{\lambda\Delta^\nu(n_i^1) + (1-\lambda)\Delta^\nu(n_i^2)\}dV \le \int_V (d\mu_1 + d\mu_2)dV \tag{4.6}
$$

Integrating equation (4.6) from $t = 0$ to $t = t_i$, the initiation time for rupture, and making use of the inequality of equation (4.1) yields

$$
t_i \le t_0\,\frac{\int_V^d \bar{\mu}\,dV}{\int_V (d\mu_1 + d\mu_2)dV} \le \frac{t_0}{\lambda} \tag{4.7}
$$

Downloaded 03 May 2010 to 171.66.16.21. Redistribution subject to ASME license or copyright; see http://www.asme.org/terms/Terms_Use.cfm

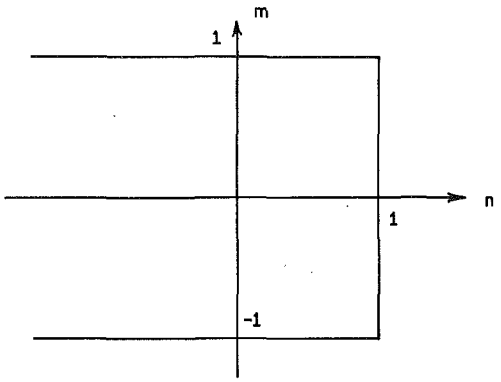


Fig. 4 Limited interaction isochronous surface

where t_0 is the time to failure in a uniaxial test under a stress σ_0.

As discussed by Ponter [9], this bound can drastically overestimate the time to rupture if λ is small. In the present paper, we limit our attention to situations where $\lambda = 1/2$ and equation (4.7) becomes

$$t_i \leq 2t_0 \tag{4.8}$$

The bounding technique therefore reduces the problem to the determination of the shakedown load for the shell structure when the yield stress is σ_0 and the yield condition is $\Delta(n_i) = 1$.

5 Shakedown Solutions for Shell Problem

For the present class of problems for which a structure is subjected to a constant load and a cyclic load, the shakedown boundary is best obtained using the method due to Gokhfeld and Cherniavsky [10]. The method involves the construction of a modified yield surface which is used in a limit load calculation for the structure subjected only to the constant load. The problem to be considered is that of the cylindrical shell subjected to a constant internal pressure and a cyclic end load $\pm F$ (Fig. 1). Since the solution for this problem was solved previously in connection with creep deformation [1], it means that the current problem is solved for materials whose isochronous surface is defined by $\Delta = \bar{\sigma}$ defined by the equalities (3.2). In this section, therefore, the shakedown boundary shall be determined for the case when the shell consists of a σ_1 material whose isochronous surface is defined by the limited interaction surface defined by the equalities (3.5). First, the limit load is obtained for the constant internal pressure p (Fig. 1) and $F = 0$. The equilibrium equation is

$$\frac{\partial^2 M_x}{\partial x^2} + \frac{N_\theta}{R} - p = 0 \tag{5.1}$$

With

$$m_x = \frac{M_x}{M_0}, \quad n_\theta = \frac{N_\theta}{N_0}, \quad \bar{p} = \frac{pR}{N_0} \quad \text{and} \quad \bar{x} = \sqrt{R\bar{M}_0/\bar{N}_0}$$

equation (5.1) becomes

$$\frac{\partial^2 \bar{m}}{\partial \bar{x}^2} + 4(\bar{n} - \bar{p}) = 0 \tag{5.2}$$

The yield condition for noninteracting surfaces, equation (3.5), when $n_x = 0$ has the form shown in Fig. 4.

We assume that a solution exists for which $n_\theta = 1$, together with the boundary conditions,

$$\frac{\partial m_x}{\partial \bar{x}} = 0 \text{ and } m_x = -1 \text{ at } \bar{x} = 0 \tag{5.3a}$$

$$m_x = 1 \text{ at } \bar{x} = \pm L \tag{5.3b}$$

where $\bar{L} = L/\sqrt{R\bar{M}_0/\bar{N}_0}$.

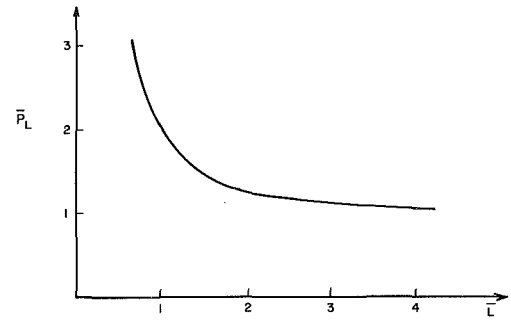


Fig. 5 Variation of limit load with length

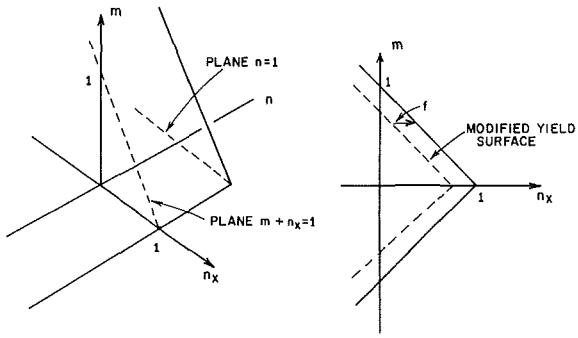


Fig. 6 Isochronous surface and section of n_θ = constant

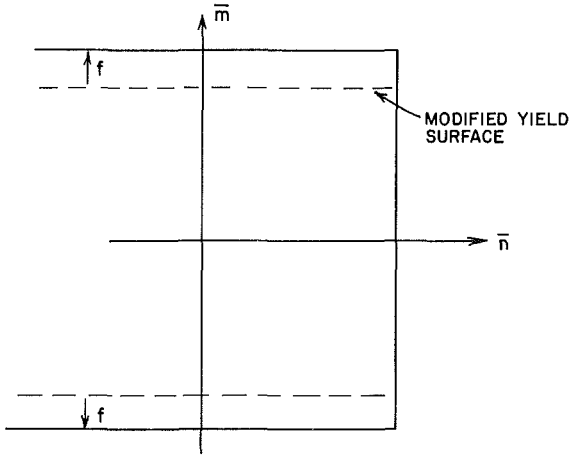


Fig. 7 Modified surface for $n_x = 0$

The limit pressure is then given by

$$\bar{p}_L = \left(1 + \frac{1}{\bar{L}^2}\right) \tag{5.4}$$

Equation (5.4) is plotted in Fig. 5 for a range of values of $\bar{L}$. To determine the shakedown solution, the yield surface in m_x, n_θ, and n_x is required. The portion of this surface for $m_x \geq 0$ and its section through an $\bar{n}_\theta$ = constant plane are shown in Fig. 6. The elastic solution for cyclic loading is given by

$$N_x = \pm \frac{F}{2\pi R}$$

and the limit load for F acting alone is $F_L = N_0 2\pi R$. Defining $n_x = N_x/N_0 = \pm F/F_L = \pm f$ the yield surface modified by the elastic solution is shown in Fig. 6 for constant n_θ, and in Fig. 7 for $n_x = 0$. The limit load for the pressure loading for the modified yield surface is determined using the governing equation (5.4) solved subject to the boundary conditions

Downloaded 03 May 2010 to 171.66.16.21. Redistribution subject to ASME license or copyright; see http://www.asme.org/terms/Terms_Use.cfm

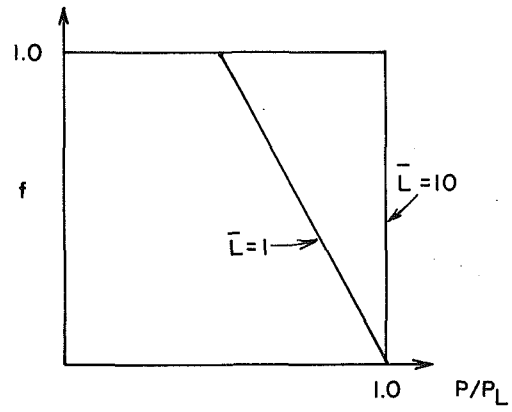


Fig. 8 Shakedown boundaries

$$\partial m_x/\partial \bar{x}=0 \text{ and } m_x=-(1-f) \text{ at } \bar{x}=0$$
$$m_x=(1-f) \text{ at } \bar{x}=\pm\bar{L}$$

The resulting solution is

$$\bar{P}=1+\frac{1-f}{\bar{L}^2} \text{ or } P/P_L=\frac{\bar{L}^2+1-f}{\bar{L}^2+1} \tag{5.5}$$

When $f=1$, the yield surface disappears and $\bar{p}=0$. The shakedown boundary formed by equation (5.5) is plotted in Fig. 8 for $\bar{L}=1$ and $\bar{L}=10$. This solution can be compared with the shakedown boundary given in [1] for an effective stress material

$$P/P_L=(1-f) \tag{5.6}$$

For each type of material the time to failure can be obtained by selecting the value of N_0 such that the applied loads lie on the shakedown boundary of Fig. 8 or equation (5.6). The time to failure is then given by equation (4.8) where t_0 is the time to failure in a uniaxial test conducted at a constant stress $\sigma_0=N_0/t$.

6 Conclusions

It has been demonstrated how shakedown solution can be used to obtain bounds on the life of a creeping structure subjected to cyclic loading histories. The shakedown analysis is performed using a yield surface which has the same shape as the isochronous surface for the material. When analyzing shell structures, the isochronous surface can be presented directly in terms of generalized forces, and the analysis performed in terms of these quantities. In situations where one load applied to a structure is kept constant while another is cycled, the method of Gokhfeld and Cherniavsky [10] can be used to obtain the shakedown solution.

Acknowledgment

The authors acknowledge the support of the National Science Foundation through Grant No. MSM 82-10620.

References

1 Cock, A. C. F., and Leckie, F. A., 1986, "Deformation Bounds for Cyclically Loaded Shell Structures Operating Under Creep Conditions," Department of Theoretical and Applied Mechanics Report, University of Illinois, Urbana, IL, to appear in the JOURNAL OF APPLIED MECHANICS.

2 Ashby, M. F., and Dyson, B. F., 1984, "Creep Damage Mechanics and Micromechanisms," National Physical Laboratory, Report DMA/1A/77.

3 Cocks, A. C. F., and Leckie, F. A., 1986, "Creep Constitutive Equations for Damaged Materials," Theoretical and Applied Mechanics, Department Report 480.

4 Leckie, F. A., and Hayhurst, D. L., 1974, "Creep Rupture of Structures," *Proceedings of the Royal Society, London*, Series A, Vol. 340, pp. 323-347.

5 Hodge, P. G., 1963, *Limit Analysis of Rotationally Symmetric Plates and Shells*, Prentice-Hall, Englewood Cliffs, NJ.

6 Ponter, A. R. S., and Leckie, F. A., 1970, "The Application of Energy Theorems to Bodies Which Creep in the Plastic Range," ASME JOURNAL OF APPLIED MECHANICS, Vol. 37, pp. 753-758.

7 Hayhurst, D. R., 1976, "Estimates of the Creep Rupture Lives of Structures Subjected to Cyclic Loading," *International Journal of Mechanical Sciences*, Vol. 18, pp. 75-83.

8 Trampczynski, W. A., Hayhurst, D. R., and Leckie, F. A., 1981, "Creep Rupture of Copper and Aluminum under Non-proportional Loading," *Journal of the Mechanics and Physics of Solids*, Vol. 29, pp. 353-374.

9 Ponter, A. R. S., 1977, "Upper Bounds on the Creep Rupture Life of Structures Subjected to Variable Load and Temperature," *International Journal of Mechanical Sciences*, Vol. 19, pp. 79-92.

10 Gokhfeld, D. A., and Cherniavsky, O. R., 1989, *Limit Analysis of Structures at Thermal Cycles*, Sijthoff and Noordhoof, Amsterdam.

Downloaded 03 May 2010 to 171.66.16.21. Redistribution subject to ASME license or copyright; see http://www.asme.org/terms/Terms_Use.cfm

Elastic-Plastic Analysis of Cracks on Bimaterial Interfaces: Part I—Small Scale Yielding

C. F. Shih
Mem. ASME

R. J. Asaro

Division of Engineering,
Brown University,
Providence, RI 02912

Full-field numerical solutions for a crack which lies along the interface of an elastic-plastic medium and a rigid substrate are presented. The solutions are obtained using a small strain version of the J_2-deformation theory with power-law strain hardening. In the present article, results for loading causing only small scale yielding *at the crack tip are described; in subsequent articles the mathematical structure of the crack-tip fields under small scale yielding and results for contained yielding and fully plastic behavior will be presented. We find that although the near-tip fields do not appear to have a separable singular form, of the HRR-type fields as in homogeneous media, they do, however, bear interesting similarities to certain mixed-mode HRR fields. Under small scale yielding, where the remote elastic fields are specified by a complex stress-concentration vector $\mathbf{Q} = |\mathbf{Q}|e^{i\phi}$ with ϕ being the phase angle between the two in-plane stress modes, we find that the plastic fields are members of a family parameterized by a new phase angle ξ, $\equiv \phi + \epsilon \ln(\mathbf{Q}\bar{\mathbf{Q}}/\sigma_0^2\mathbf{L})$, and the fields nearly scale with the well-defined energy release rate as evaluated by the J-integral. Here σ_0 is the reference yield stress and* L *is the total crack length (or a relevant length of the crack geometry). Numerical procedures appropriate for solving a general class of interface crack problems are also presented. A description of a numerical method for extracting the mixed mode stress intensities for cracks at interfaces and in homogeneous isotropic or anisotropic media, is included.*

1 Introduction

Fracture, whether it occurs by fibrous or cleavage modes, invariably begins at interfaces. In structural alloys, precipitation or segregation of impurities at grain boundaries can lead to transitions from ductile to cleavage fracture and to concomitant losses in ductility and toughness. In so-called *advanced materials* such as structural ceramics, composites, and polycrystalline intermetallic alloys, interfacial and intergranular fractures are common and may, in large part, determine the material's overall mechanical response. At present, however, what exists is only a relatively small group of solutions for the crack-tip fields at the interfaces of isotropic linear elastic media (e.g., Williams, 1959; Erdogan, 1963, 1965; Sih and Rice, 1964; Rice and Sih, 1965; England, 1965). A formal solution for the field of an isolated crack lying along the interface of linear anisotropic media has been given by Willis (1971) which, while perhaps not lending itself to a ready evaluation of the nature of the field, does allow for a computation of the energy release rate for crack extension along the interface. Another analysis of a crack between dissimilar media has been given by Clements (1971). To our knowledge, there are no solutions for the fields of interface cracks in elastic-plastic materials and this makes it difficult to analyze the legion of interface fraction phenomena previously mentioned. One purpose of this study is to provide such solutions within a framework consistent with what exists for nonlinear fracture mechanics in homogeneous materials (see, e.g., Hutchinson, 1983). Another is to develop numerical procedures capable of accurately resolving the complex fields which develop at interfaces. One presentation is to be given in three parts: In the present paper, the near-tip fields under small scale yielding conditions as obtained from the solution of a full boundary-value problem are discussed; in Part II the structure of the asymptotic fields for cracks on interfaces separating general elastic-plastic media is derived; the fields that develop under contained yielding and fully plastic conditions are presented in Part III. Implications of the characteristic stress and deformation fields that form at and near interfaces for fracture mechanics will be detailed in the latter.

Specifically, the plane-strain boundary-value problem for a center cracked plate loaded with uniform remote stresses is solved and discussed here. This is illustrated along with a version of the finite-element mesh used for the numerical solution

Contributed by the Applied Mechanics Division for publication in the JOURNAL OF APPLIED MECHANICS.

Discussion on this paper should be addressed to the Editorial Department, ASME, United Engineering Center, 345 East 47th Street, New York, N.Y. 10017, and will be accepted until two months after final publication of the paper itself in the JOURNAL OF APPLIED MECHANICS. Manuscript received by ASME Applied Mechanics Division, March 6, 1987; final revision, December 4, 1987.

Copyright © 1988 by ASME
Downloaded 03 May 2010 to 171.66.16.21. Redistribution subject to ASME license or copyright; see http://www.asme.org/terms/Terms_Use.cfm

in Fig. 3. The crack lies on the interface between a rigid substrate and a nonlinear elastic-plastic material characterized by a J_2-deformation theory. This problem serves as a prototype for a wide class of physically interesting phenomena involving microcracking and macroscopic fracture, while, at the same time, allowing for an unambiguous and definitive study of the structure of the fields of interface cracks within the context of a complete boundary-value problem. Crack-tip fields have been evaluated numerically for linear elastic materials and nonlinear elastic-plastic materials (characterized by a small strain J_2-deformation theory) under small scale yielding, contained yielding, and fully plastic conditions. In the present paper, attention is focused on elastic behavior and elastic-plastic behavior under small scale yielding. For this analysis, a domain formulation of an interaction energy release rate is employed to extract the complex stress-intensity factors from the numerical fields. Some discussion of results for contained yielding is provided, but as previously noted, a full treatment of these cases along with the fields for cracks under loading conditions that cause fully yielded behavior will be given in a subsequent article.

In the context of interface cracks, small scale yielding is meant to pertain to loading conditions for which the plastic zone emanating from the crack tip is surrounded by elastic fields which are well approximated by the elastic singular fields for the interface crack. We do not suggest that the plastic zones develop in a self-similar manner as they do for cracks in homogeneous media. Indeed the change in plastic zone size and shape with increasing remote stress is detailed in Sections 4.3, and this should be kept in mind in interpreting the results presented in Sections 4.3 and 5.

As mentioned, the calculations are performed for a material described by a small strain, isotropic J_2-deformation theory. This was done in order to facilitate the connection between the interface crack solutions, the existing framework of nonlinear fracture mechanics, and specific solutions for crack-tip fields in homogeneous media. Both qualitative and quantitative similarities between the fields are highlighted in the results we present. It is found, for example, that the near-tip stress and strain fields are inherently mixed mode regardless of the far-field loading. Although the fields for the interface crack are not of the usual separate form, there are nontheless strong similarities between them and the mixed-mode fields for cracks in homogeneous media. (Thus far, our attempts to find fields near the tip of an interface crack which are of a separable form have not been successful.) These features have important implications for the mathematical characterization of the fields as well as for failure processes that may be induced at or near the interface.

The stress histories that develop near the tip of the interface crack cannot be described as proportional stressing in the boundary-value problem we studied. At low remote stress levels, for example, the fields that develop near the tip are of a strongly mixed-mode nature, reflecting the mixed-mode character of the linear elastic field. At higher remote stresses, our results show that the crack-tip fields are more nearly like those corresponding to pure Mode I fields of cracks in homogeneous media. The transition from strongly mixed-mode fields to nearly Mode I fields certainly involves nonproportional stressing. Thus interface crack-tip behavior is more complex than is found for cracks in homogeneous media for which proportional remote loading induces proportional stressing near the crack tip. The link between the fields calculated here for a J_2-deformation theory material and those appropriate to path-dependent incremental elastic-plastic theories is the subject of the current investigation.

The plan of the paper is as follows. In the next section, we present a summary of available results for crack-tip stress and displacement fields in linear isotropic media. This introduces the notion of a *stress-concentration vector*, or stress-intensity factors, for interface cracks and provides the requisite background to analyze the elastic-plastic results. A complete description of the boundary-value problem to be solved is also given. Numerical methods are then described, followed by the presentation of the full-field solutions. A short discussion on the nature of the computed fields concludes this paper.

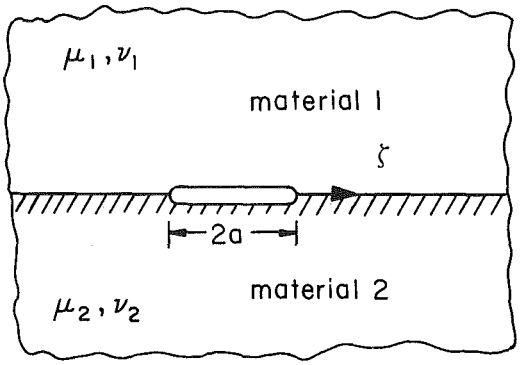


Fig. 1 Interface crack between two bonded dissimilar materials

2 Perspectives on Cracks at Bimaterial Interfaces

2.1 Overview of Results for Linear Elastic Media. A number of solutions for the stress and displacement fields for cracks lying along bimaterial interfaces have been obtained for isotropic materials by, for example, Williams (1959), England (1965), Erdogan (1963, 1965), Sih and Rice (1964), and Rice and Sih (1965). For anisotropic materials, Willis (1971) has provided a formal solution which allows the energy release rate to be evaluated. Our concern in this section is to illustrate the nature of the tractions and the displacement discontinuities on the crack line at the crack tip, identify stress-intensity factors and relate them to energy release rates. The discussion is confined to isotropic elastic media where the results are easily represented in a concise structure.

We refer to Fig. 1 which shows a crack lying along an interface separating media 1 and 2. The shear moduli and Poisson's ratios are μ_1, μ_2 and ν_1, ν_2. ζ is the distance measured along the bond line from the crack tip such that $\zeta = r$, the polar coordinate, when $\theta = 0$ and $\theta = \pi$. In what follows, it is to be understood that ζ is directed along the bond line in the expressions for tractions, whereas it is directed back along the crack faces in the expressions given next for the displacement jumps across the crack face. Existing solutions show that the tractions on the bond line can be expressed in the form

$$\sigma_{22} = \frac{Q_1 \cos[\epsilon \ln (\zeta/2a)]}{\sqrt{2\pi\zeta}} - \frac{Q_2 \sin[\epsilon \ln (\zeta/2a)]}{\sqrt{2\pi\zeta}} \tag{2.1a}$$

and

$$\sigma_{12} = \frac{Q_1 \sin[\epsilon \ln (\zeta/2a)]}{\sqrt{2\pi\zeta}} + \frac{Q_2 \cos[\epsilon \ln (\zeta/2a)]}{\sqrt{2\pi\zeta}} \tag{2.1b}$$

where ϵ is the bimaterial constant introduced by Williams (1959), Erdogan (1963), Sih and Rice (1964), and England (1965), defined as

$$\epsilon \equiv \frac{1}{2\pi} \ln \left\{ \frac{\dfrac{3-4\nu_1}{\mu_1} + \dfrac{1}{\mu_2}}{\dfrac{1}{\mu_1} + \dfrac{3-4\nu_2}{\mu_2}} \right\}. \tag{2.2}$$

Downloaded 03 May 2010 to 171.66.16.21. Redistribution subject to ASME license or copyright; see http://www.asme.org/terms/Terms_Use.cfm

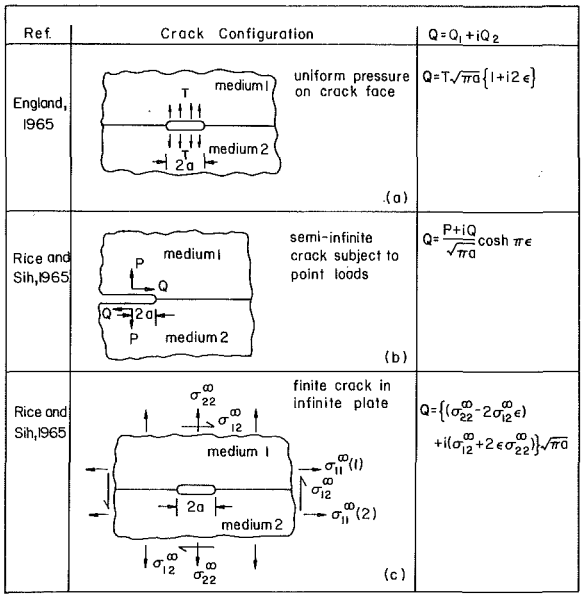


Fig. 2 Stress-intensity for three crack geometries

Q_1 and Q_2 define two *stress-intensity factors* which, we note, have units of stress-(length)$^{1/2}$ in analogy with the definition of stress-intensity factors in homogeneous media. It is convenient to introduce a *complex stress-intensity factor* defined by $\mathbf{Q}=Q_1+iQ_2$. This definition is related in a simple way to others available in the literature and, for example, is related to the complex stress-intensity factor of Sih and Rice (1964), $\mathbf{k}=k_1+ik_2$, by $\mathbf{Q}=\sqrt{\pi}\cosh(\pi\epsilon)(2a)^{i\epsilon}\mathbf{k}$.

Combining (2.1) as in the original solutions just cited [see also, Willis (1971), equation (4.4)], the tractions on the bonding surface can also be expressed as the complex vector

$$\mathbf{t}=\sigma_{22}+i\sigma_{12}=\frac{\mathbf{Q}}{\sqrt{2\pi\zeta}}\,e^{i\epsilon\ln(\zeta/2a)}=\frac{\mathbf{Q}}{\sqrt{2\pi\zeta}}\,(\zeta/2a)^{i\epsilon}. \tag{2.3}$$

Explicit examples of $\mathbf{Q}$ for three crack geometries and loading configurations, taken from the foregoing references, are given in Fig. 2. We note that, in general, the two stress modes defined by Q_1 and Q_2 each involve mixed tension and shear on the bonding surface and, in isotropic media, represent orthogonal modes. That is, if

$$\mathbf{t}_1\equiv\frac{Q_1}{\sqrt{2\pi\zeta}}e^{i\epsilon\ln(\zeta/2a)}, \tag{2.4a}$$

then

$$\mathbf{t}_2=\frac{Q_2}{\sqrt{2\pi\zeta}}\,e^{i\{\epsilon\ln(\zeta/2a)+\pi/2\}} \tag{2.4b}$$

which is oriented at a right angle to $\mathbf{t}_1$ when plotted on a graph with σ_{22} on the real axis and σ_{12} on the imaginary axis. When the two media are identical, $\epsilon=0$ and Q_1 and Q_2 reduce to the usual Mode I and II stress-intensity factors, K_I and K_{II}.

Displacement jumps across the crack face also have been given (explicitly by England, 1965) and, at the crack tip, take the form

$$\Delta\mathbf{U}=\Delta u_2+i\Delta u_1=\frac{2\left\{\dfrac{1-\nu_1}{\mu_1}+\dfrac{1-\nu_2}{\mu_2}\right\}}{(1+2i\epsilon)\cosh\pi\epsilon}\,\mathbf{Q}\sqrt{\zeta/2\pi}\;e^{i\epsilon\ln(\zeta/2a)}. \tag{2.5}$$

This can also be written as

$$\Delta\mathbf{U}=\frac{2\left\{\dfrac{1-\nu_1}{\mu_1}+\dfrac{1-\nu_2}{\mu_2}\right\}}{(1+4\epsilon^2)^{1/2}\cosh\pi\epsilon}\,\mathbf{Q}\sqrt{\zeta/2\pi}\;(\zeta/2a)^{i\epsilon}e^{-i\beta} \tag{2.6}$$

where $\beta=\tan^{-1}2\epsilon$. Thus the contributions to $\Delta\mathbf{U}$ associated with the stress modes Q_1 and Q_2 (call them $\Delta\mathbf{U}_1$ and $\Delta\mathbf{U}_2$) are also orthogonal but are not precisely aligned with $\mathbf{t}_1$ and $\mathbf{t}_2$. In fact, if $\mathbf{t}_1$ and $\mathbf{t}_2$ are placed on a graph whose axes are σ_{22} and σ_{12} then the orthogonal pair $\Delta\mathbf{U}_1$, $\Delta\mathbf{U}_2$, when graphed with respect to axes Δu_2 and Δu_1, would appear to be rigidly rotated with respect to the orthogonal pair $\mathbf{t}_1$, $\mathbf{t}_2$ by the angle β.

As noted by Williams (1959) and, in subsequent works, a characteristic of the linear elastic fields of interface cracks is that they violate compatibility at distances very close to the tip; the stresses and displacement fields on the crack line oscillate with unbounded amplitude and vanishing wavelength. Looking ahead to the problem of the center cracked panel under far-field tension that we investigate numerically, we note that Rice and Sih's (1965) results yield the stress intensity vector $\mathbf{Q}=\sigma_{22}^{\infty}\sqrt{\pi a}\,(1+2i\epsilon)$. This means, for example, that the normal tractions on the bond line become compressive as soon as

$$\mathrm{Re}\,\{(1+2i\epsilon)e^{i\epsilon\ln(\zeta/2a)}\}<0, \tag{2.7}$$

or using the definition for β introduced earlier, when

$$\mathrm{Re}\,\{e^{i[\epsilon\ln(\zeta/2a)+\beta]}\}<0. \tag{2.8}$$

Since $(\zeta/2a)<1$, this first occurs as soon as

$$\epsilon\ln(\zeta/2a)+\beta<-\pi/2. \tag{2.9}$$

Thus $\sigma_{\theta\theta}$ first becomes compressive at

$$(\zeta/2a)=e^{-[\pi/2+\beta]/\epsilon}. \tag{2.10}$$

For the case of a crack on a rigid substrate, where in the deformable half-space $\nu=0.3$, $\epsilon\cong0.0935$, and this leads to a value of $\zeta/2a\cong7\times10^{-9}$. Our numerical results reproduced this (albeit *nonphysical*) feature of the linear elastic field. In fact, looking ahead to Fig. 8, where the numerical solution for the interface crack in a linear elastic medium is presented, it may be noted that along a ray at an angle of 7.5° with the bond line (i.e., essentially on the bond line) $\sigma_{\theta\theta}$ becomes compressive at $r/a\cong1\times10^{-9}$ which is completely consistent with this stress component first becoming compressive at $\zeta/a\cong14\times10^{-9}$ at $\theta=0^0$ at $\theta=0°$. However, we note that when the loading is a combined remote tension and shear, $\mathbf{Q}=[(\sigma_{22}^{\infty}-2\sigma_{22}^{\infty}\epsilon)+i(\sigma_{12}^{\infty}+2\epsilon\sigma_{22}^{\infty})]\sqrt{\pi a}$ and a similar analysis shows that $\sigma_{\theta\theta}$ first becomes compressive on the bond line when

$$(\zeta/2a)=e^{-[\pi/2+\lambda]/\epsilon} \tag{2.11}$$

where

$$\phi=\tan^{-1}\{(\sigma_{12}^{\infty}+2\epsilon\sigma_{22}^{\infty})/(\sigma_{22}^{\infty}-2\epsilon\sigma_{12}^{\infty})\}. \tag{2.12}$$

Now suppose $\sigma_{22}^{\infty}>0$ but $\sigma_{12}^{\infty}=-2\sigma_{22}^{\infty}$; then $\phi\cong-58.7°$ and $\zeta/2a\cong1\times10^{-3}$! If $\sigma_{12}^{\infty}=-\sigma_{22}^{\infty}$, $\phi\cong-38.2°$ and $\zeta/2a\cong3\times10^{-5}$. Thus the regions where the stresses (based on small strain linear elasticity assumptions) oscillate are not always confined to vanishingly small regions near the crack tip and their extents are quite sensitive to the nature of the remote loading and the value of ϵ. In Section 5, full-field results are presented for the interface crack in nonlinear materials subjected to remote *mixed* loadings. For the load combinations considered, the stresses are nonoscillatory at distances as small as $\zeta/2a=1\times10^{-15}$ when the remote stresses are small fractions of the material's yield stress. This also is shown in detail in Section 4 for the case of pure remote tensile loading. It may be noted that when $\nu=1/2$, $\epsilon=0$ and the near-tip displacements vanish identically on the bond line for the plane-strain problem. For this case, the fields in the upper and lower slabs are nonoscillatory and are identical to the fields for the corresponding homogeneous media. This fact has been noticed by Knowles and Sternberg (1983).

Downloaded 03 May 2010 to 171.66.16.21. Redistribution subject to ASME license or copyright; see http://www.asme.org/terms/Terms_Use.cfm

When written out in full the asymptotic crack-tip stress field is given by

$$\sigma_{ij} = \sum_{\alpha=1}^{2} \frac{Q_\alpha}{(2\pi r)^{1/2}} g_{ij}^{(\alpha)}[\theta, \epsilon \ln (r/2a); \epsilon] \tag{2.13}$$

and, for completeness, the functions $g_{ij}^{(\alpha)}$ are given in Appendix I in a form consistent with our definition of the complex stress-intensity vector $\mathbf{Q}$. It should be noted that the fields (2.13) are not of a separable form. In contrast, the singular fields of cracks in homogeneous media are separable. It should also be noted that with our definition of the complex stress-concentration factor, crack geometry appears in the angular functions as well as in the stress-concentration factors.

The energy release rate is readily computed from the given expressions for the traction and displacement fields as the *virtual work integral*

$$G = \lim_{\Delta a \to 0} \frac{1}{2\Delta a} \int_0^{\Delta a} \mathbf{t}(\zeta;0) \cdot \Delta \bar{\mathbf{U}}(\zeta; 0+\Delta a) d\zeta \tag{2.14}$$

where $\mathbf{t}(\zeta;0)$ is the complex traction vector at the crack tip, given by (2.3), when the crack is at $x=0$, and $\Delta\bar{\mathbf{U}}(\zeta; 0+\Delta a)$ is the complex conjugate to the displacement jump vector when the crack has advanced to the position $0+\Delta a$. The integral is easily reduced to the form

$$\frac{|\mathbf{Q}|^2 \left\{ \frac{1-\nu_1}{\mu_1} + \frac{1-\nu_2}{\mu_2} \right\}}{2\pi \cosh \pi\epsilon} \times \frac{1}{(1-2i\epsilon)} \int_0^1 \left(\frac{1-t}{t} \right)^{1/2 - i\epsilon} dt \tag{2.15}$$

where the last integral is recognizable as the complex Beta function $B(1/2+i\epsilon, 3/2-i\epsilon)$. Upon evaluation of B,

$$G = \frac{(Q_1^2 + Q_2^2) \left\{ \frac{1-\nu_1}{\mu_1} + \frac{1-\nu_2}{\mu_2} \right\}}{4\cosh^2 \pi\epsilon}. \tag{2.16}$$

Orthogonality of the stress modes guarantees that they decouple such that there are no terms of the form $Q_1 Q_2$. Note also that the integral in (2.14) has no imaginary part, a fact noticed in the general anisotropic case by Willis (1971).

List of Stress-Intensity Factors. We complete this section with the short list of stress-intensity factors tabulated in Fig. 2. Included in this list is the center cracked panel we have studied numerically. It may be noted in these examples that, with $\mathbf{Q}$ defined by (2.3), the ratio of Q_1 to Q_2 does not depend on the characteristic dimension $2a$. However, a specification of the crack-tip fields requires the value of $\mathbf{Q}$ and a characteristic crack dimension (which is the total crack length $2a$ for the boundary-value problem considered here). On the other hand, the Sih and Rice (1964) complex stress-intensity factor $\mathbf{k}$ alone uniquely specifies the crack-tip fields.

2.2 Structure of Fields Under Small Scale Yielding. For the purpose of developing the structure of the fields under small scale yielding, it is helpful to write the complex stress-concentration vector introduced in (2.1) as a magnitude and a phase, i.e.,

$$\mathbf{Q} = Q_1 + iQ_2 = |\mathbf{Q}| e^{i\phi} \tag{2.17}$$

Thus tractions on the bonding surface near the tip (2.3) can be written as

$$\mathbf{t} = \sigma_{22} + i\sigma_{12} = \frac{\mathbf{Q}}{\sqrt{2\pi r}} \left(\frac{r}{L} \right)^{i\epsilon} = \frac{|\mathbf{Q}|}{\sqrt{2\pi r}} e^{i(\phi + \epsilon \ln r/L)} \tag{2.18}$$

In this general development, the relevant length of the crack geometry denoted by L may be associated with the length $2a$ indicated in Fig. 2. The variation of the near-tip stresses along any radial line has the form of (2.18). In the small scale yielding problem, the actual crack problem is replaced by a semi-infinite crack in an infinite medium with asymptotic boundary condition that at large r the field approaches that of the form given by (2.18). If one or both of the bonded solids deforms plastically, the plastic zone size and shape will depend on the elastic and plastic properties of the two solids and the stress-concentration vector $\mathbf{Q}$. Furthermore, if the material behavior is assumed to be governed by a deformation theory of plasticity, there is a one-to-one correspondence between the crack-tip fields and the plastic zone. In this section, a dimensional analysis leading to the description of the plastic zone is outlined. A detailed discussion is given in Part II.

Let σ_{01} and σ_{02} be the yield strengths of the upper and lower solids. It is convenient to denote the yield strength of the weaker solid by σ_0, its strain-hardening characteristics by n, and its Young's modulus and Poisson's ratio by E and ν, respectively. Under small scale yielding, the stresses depend on the stress-concentration vector $\mathbf{Q}$ and material properties σ_0, the dimensionless ratios σ_{01}/σ_{02} and E_1/E_2, and Poisson's ratio ν_1 and ν_2 and strain-hardening characteristics parameterized by n_1 and n_2. From dimensional considerations, the linearity of the equilibrium and strain-displacement relations and (2.18), we write

$$\sigma_{ij} = \sigma_0 f_{ij} \left(\frac{r\sigma_0^2}{\mathbf{Q}\bar{\mathbf{Q}}}, \theta, \text{phase} \left\{ \mathbf{Q} \left(\frac{r}{L} \right)^{i\epsilon} \right\}; \right.$$
$$\left. \text{dimensionless material parameters} \right) \tag{2.19a}$$

where it may be noted that $\mathbf{Q}\bar{\mathbf{Q}}$ has dimensions of the square of stress times length.

Directing our attention to the dependence of σ_{ij} on $\mathbf{Q}$ and distance from the crack tip, we write

$$\sigma_{ij} = \sigma_0 f_{ij} \left(\frac{r\sigma_0^2}{\mathbf{Q}\bar{\mathbf{Q}}}, \theta, \phi + \epsilon \ln \frac{r}{L} \right) \tag{2.19b}$$

where it being understood that the dimensionless function f_{ij} depends additionally on dimensionless material properties. It may be noted that the dependence on distance r in the third argument in (2.19*b*) may be eliminated by division with the first argument. Let ξ denote the new phase parameter, then

$$\xi = \phi + \epsilon \ln \left(\frac{r}{L} \times \frac{\mathbf{Q}\bar{\mathbf{Q}}}{r\sigma_0^2} \right) = \phi + \epsilon \ln \left(\frac{\mathbf{Q}\bar{\mathbf{Q}}}{L\sigma_0^2} \right) \tag{2.20}$$

The stress field in small scale yielding has the form

$$\sigma_{ij} = \sigma_0 f_{ij} \left(\frac{r\sigma_0^2}{\mathbf{Q}\bar{\mathbf{Q}}}, \theta; \xi, \text{ dimensionless material parameters} \right), \tag{2.21}$$

where f_{ij} has a periodicity of 2π with respect to the argument ξ. Similarly, the effective stress has the form

$$\sigma_e = \sigma_0 f_e \left(\frac{r\sigma_0^2}{\mathbf{Q}\bar{\mathbf{Q}}}, \theta; \xi, \text{ dimensionless material parameters} \right). \tag{2.22}$$

The elastic-plastic boundary is defined by the contour $\sigma_e = \sigma_0$ and using this in (2.22) with rearrangement, we obtain the length of the plastic zone

$$r_p(\theta) = \frac{\mathbf{Q}\bar{\mathbf{Q}}}{\sigma_0^2} R(\theta; \xi, \text{ dimensionless material parameters}) \tag{2.23}$$

where R is a dimensionless angular function. It further follows from the linearity of the equilibrium and strain-displacement relations that R has the following periodic structure

$$R(\theta;\xi) = R(\theta;\xi + m\pi) \tag{2.24}$$

where m is an integer.

Downloaded 03 May 2010 to 171.66.16.21. Redistribution subject to ASME license or copyright; see http://www.asme.org/terms/Terms_Use.cfm

To arrive at the mathematical structure of the fields (2.19)–(2.23), and in particular (2.24), contact between the crack faces have been disregarded. The structure of the fields in (2.21), (2.23), and (2.24) has been confirmed by full-field finite-element calculations for the small scale yielding problem and the center cracked plate boundary-value problem. These calculations with details of the angular functions $R(\theta)$ for the full range of ξ and contact between crack faces are discussed in Part II. It follows from the one-to-one correspondence between the plastic zone and the stresses within the plastic zone that the plastic fields are members of a family parameterized by the phase angle ξ and the magnitude of the stresses nearly scale with $\mathbf{Q}\bar{\mathbf{Q}}$ or the J-integral since $J = G$ for a deformation theory plasticity solid; see (2.16). A result similar to (2.23) has been obtained by Rice (1987). Using the notation in this paper, his result has the form

$$r_p = \frac{\mathbf{Q}\bar{\mathbf{Q}}}{\sigma_0^2} R(\phi - \epsilon \ln \{L/r_p\}) \tag{2.25}$$

where r_p is a characteristic dimension of the plastic zone. The foregoing implicit equation for r_p can be made explicit by replacing the r_p in the argument by $\mathbf{Q}\bar{\mathbf{Q}}/\sigma_0^2$, whereupon the result (2.23) is recovered.

2.3 The Interface Crack Small Scale Yielding Problem. The specific problem we are concerned with here, illustrated in Fig. 3, is that of a large plate loaded remotely by uniform stresses. Crack length, $2a$, is the characteristic dimension with respect to which the stress-intensity factors listed in Fig. 2, and the asymptotic angular stress functions given in Appendix I, are evaluated. Uniform normal stresses are imposed on the external boundaries with the primary variable being σ_{22}^{∞}. No remote shear is imposed although, as is evident from the elastic solutions, large shear stresses develop on and near the crack line due to the differences in material properties. This is also true for the elastic-plastic cases treated numerically.

As noted by Rice and Sih (1965), continuity of the extensional strain ϵ_{11} across the bond line requires that the normal stress parallel to the bond line be discontinuous. They derived the required jump in σ_{11}^{∞}, viz.

$$\sigma_{11}^{\infty}(2) = \omega \sigma_{11}^{\infty}(1) + \frac{(3+\omega)e^{2\pi\epsilon} - (3\omega+1)}{1+e^{2\pi\epsilon}} \sigma_{22}^{\infty} \tag{2.26}$$

where

$$\omega = \frac{\mu_2(1-\nu_1)}{\mu_1(1-\nu_2)}. \tag{2.27}$$

For the present case of the crack on the rigid substrate, $\omega \to \infty$ and the previous relation takes the form

$$\sigma_{11}^{\infty}(1) = \frac{3 - e^{2\pi\epsilon}}{1+e^{2\pi\epsilon}} \sigma_{22}^{\infty} = \frac{\nu_1}{(1-\nu_i)} \sigma_{22}^{\infty}. \tag{2.28}$$

In the numerical solutions described next, the normal stress given by (2.28), for $\nu_1 = 0.3$, was imposed on the side faces of the deformable medium shown in Fig. 3.

The small scale yielding study is carried out within the context of small strain theory. The deformable medium is taken to be described by J_2-deformation theory for a Ramberg-Osgood stress-strain behavior. In uniaxial tension, the material deforms according to

$$\epsilon/\epsilon_0 = \sigma/\sigma_0 + \alpha(\sigma/\sigma_0)^n \tag{2.29}$$

where σ_0 and ϵ_0 are the reference stress and strain, α is a material constant (taken to be 0.1 in this study) and n is the strain-hardening exponent. Under multiaxial stress states σ_{ij}, the strain is

$$\epsilon_{ij} = \frac{1+\nu}{\mathrm{E}} s_{ij} + \frac{1-2\nu}{3\mathrm{E}} \sigma_{kk}\delta_{ij} + \frac{3}{2}\alpha\left(\frac{\sigma_e}{\sigma_0}\right)^{n-1} \frac{s_{ij}}{\mathrm{E}}. \tag{2.30}$$

Here, s_{ij} is the stress deviator, $\sigma_e = (3s_{ij}s_{ij}/2)^{1/2}$ is the effective stress, and ν and E are the elastic constants. In writing (2.30), we have used the connection $\sigma_0 = \epsilon_0 \mathrm{E}$. Numerical solutions under plane-strain assumptions have been obtained for a range of hardening exponents. However, only results for $n = 3$ (a high hardening material) and $n = 10$ (a moderate to low hardening material) will be presented. In all the calculations, we have used ν equal to 0.3.

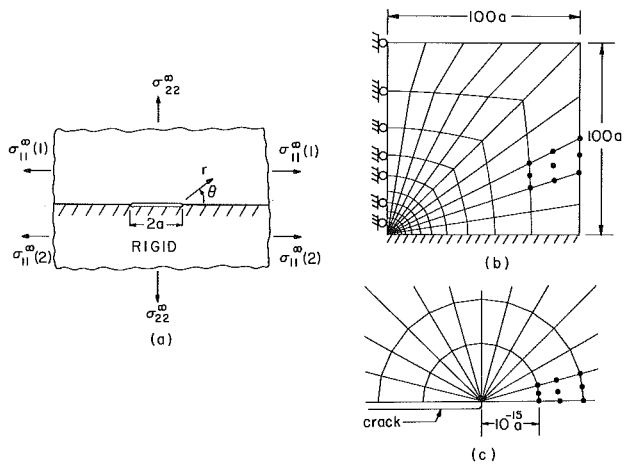


Fig. 3(a) Interface crack between deformable medium and rigid substrate; (b) finite-element mesh of right half of deformable medium; (c) arrangement of elements at crack tip

3 Numerical Procedure

3.1 Selective Integration. The standard displacement-based serendipity and Lagrangian isoparametric quadrilateral elements perform poorly as the deformation progresses into the fully plastic (incompressible) range (Nagtegaal, et al., 1974). These difficulties can be alleviated by selective/reduced integration and one implementation of this is the so-called *B-bar method* (Hughes, 1980). The strain-displacement matrix, referred to as the B-matrix, is assembled in the following manner. The deviatoric components of the B-matrix are evaluated at the regular quadrature points. Volumetric components are evaluated at the reduced quadrature points; the volumetric B-matrix associated with the regular quadrature points is obtained by interpolation/extrapolation using a lower-order shape function. The volumetric and deviatoric components are then combined to give the desired matrix associated with the regular quadrature points. The latter matrix, denoted by $\bar{B}$ (to distinguish it from the usual B-matrix, Zienkiewicz, 1977), is used in the formation of element stiffness matrix and for evaluating strains.

The full Lagrangian shape functions are necessary for approaching the incompressible limit (Malkus and Hughes, 1978). In this regard, it appears that an optimal element for treating nearly incompressible deformation is the 9-node Lagrangian quadrilateral element. For this element, the deviatoric part of B is evaluated at 3×3 Gaussian quadrature points while the volumetric part is evaluated at 2×2 quadrature points. The volumetric B at each of the 3×3 quadrature points is obtained by bilinear interpolation/extrapolation and combined with the deviatoric part to give $\bar{B}$, i.e.,

$$\bar{B} = B^{\mathrm{dev}} + \bar{B}^{\mathrm{vol}}. \tag{3.1}$$

The (tangent) stiffness matrix for an element is given by the sum of the inner products at each Gauss point

$$k^e = \sum_{p=1}^{9} (\bar{B}^T D \bar{B}) w_p. \tag{3.2}$$

Downloaded 03 May 2010 to 171.66.16.21. Redistribution subject to ASME license or copyright; see http://www.asme.org/terms/Terms_Use.cfm

where D is the matrix of material moduli evaluated at the 3×3 quadrature points and w_p is the appropriate weight. It is known that the selective integration method gives rise to a spurious pressure mode in the 4-node quadrilateral element. For this element, $\bar{B}^{vol}$ is evaluated with one-point quadrature. Belytschko and Tsay (1983) have proposed a stabilization procedure to suppress such spurious modes. Spurious pressure modes are avoided by using the 9-node Lagrangian element.

We obtained results that are nearly identical in our numerical experimentations with the B-bar method and selective integration (2×2 quadrature on volumetric stiffness matrix and 3×3 quadrature on deviatoric stiffness matrix) on several boundary-value problems based on the volume preserving plasticity relations (2.20). In this connection, it may be noted that accurate solutions to fully plastic crack problems in homogeneous media have been obtained using the 9-node Lagrangian element in conjunction with selective integration and parameter tracking (e.g., Shih and Needleman, 1984). For the present boundary-value problem based on (2.30), the incompressibility constraint is more directly and efficiently accommodated by the B-bar method. In passing, we point out that the results plotted in the figures of this paper are the actual values computed at the quadrature points – smoothing has not been applied to any data.

3.2 Parameter Tracking. The solution to the nonlinear boundary-value problem is obtained by the Newton-Raphson method. The iterative method is second-order convergent if a close initial estimate of the solution is available. For highly nonlinear problems of the type being investigated here, the initial estimate is generated by parameter tracking. We begin by obtaining the solution to the linear elastic problem at the desired remote stress. The linear elasitc solution is then employed as the initial estimate in the iterations for the mildly nonlinear problem with $n=2$. The convergent solution for the mildly nonlinear problem is then employed as the initial estimate for a more nonlinear problem, say $n=3$. In this manner, solutions for material characteristics ranging from high hardening to nearly nonhardening are obtained. Similar tracking is performed on the remote stress levels; that is once a convergent solution is obtained for a given remote loading and nonlinear material description, it may be used as the initial guess for a new solution at a higher remote load or a slightly different load combination.

3.3 Domain Representation of J. We consider the line integral (Rice, 1968) defined by

$$J=\int_\Gamma \left(W\delta_{1j}-\sigma_{ij}\frac{\partial u_i}{\partial x_1}\right)n_j d\Gamma. \tag{3.3}$$

Here, Γ is a contour beginning at the bottom crack face and ending on the top face and n_j is the outward normal to Γ as shown in Fig. 4 and W is the stress work density. For a nonlinear elastic solid or deformation theory solid, the integrand is divergence-free. With regard to the crack between a deformable medium and a rigid substrate, the contour Γ begins on the bonding plane and ends on the upper crack face. Since there are no contributions to the integral along the traction-free crack face and the interface $x_2=0^+$ (u_i vanishes on the bond line), the value of J does not depend on the contour Γ, i.e., the integral is path-independent. For the general bimaterial problem, the contour Γ begins on the lower crack face and ends on the upper crack face. Path-independence is easily demonstrated for this general case once it is recognized that the contribution from the upper interface, $x_2=0^+$, negates the contribution from the lower interface, $x_2=0^-$. For monotonic loading conditions and proportional stress history at each material point, the aforementioned integral is also path-independent for elastic-plastic solids.

For numerical purposes, it is more advantageous to recast the line-integral (3.3) as an area/domain integral. Such a

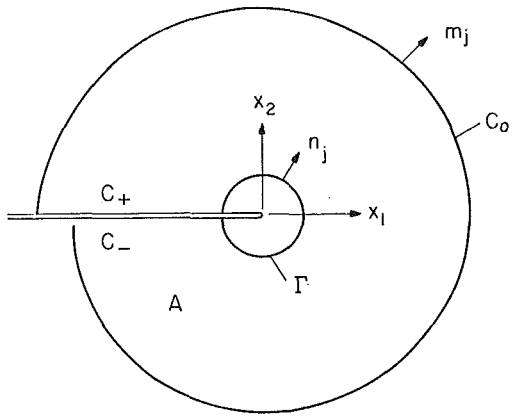


Fig. 4 Conventions for domain J; domain A is enclosed by Γ, C_+, C_- and C_0; unit normal $m_j=n_j$ on C_0 and $m_j=-n_j$ on Γ

representation is naturally suited for the finite-element method and very accurate values for J have been obtained using the domain representation. A domain integral formulation for the crack-tip force (including the J-integral) for general material response and arbitrary crack tip motion has been detailed by Moran and Shih (1986) and has been applied to several crack problems in homogeneous media (e.g., Li, et al., 1985; Shih, et al., 1986). To obtain the desired domain representation for J, weighting functions q_i are introduced. For two-dimensional problems with the crack line oriented in the x_1-direction, q_1 is the only nonzero function and it has the value of unity on the contour Γ and zero on the outer contour C_0 shown in Fig. 4. Within the area enclosed by Γ, C_0 and the crack faces C_+ and C_-, q_1 is an arbitrary smooth function of x_1 and x_2 with values in the range from zero to one. The function $q_1(x_1,x_2)$ may be interpreted as the virtual translation of the material point at (x_1, x_2) due to a unit virtual extension of the crack in the x_1-direction. Development along these latter lines has been given by Parks (1977), Hellen (1975) and deLorenzi (1982).

For a function q_1 that satisfies the foregoing conditions, the integral in (3.3) can be restated as a line integral over the closed contour C which consists of Γ, C_0 and the crack faces given by

$$J=\int_C \left(\sigma_{ij}\frac{\partial u_i}{\partial x_1}-W\delta_{1j}\right)m_j q_1 dC. \tag{3.4}$$

Here m_j are the components of the unit vector normal to C that points away from the enclosed area. On the contour Γ, m_j is equal to the negative of n_j which has been defined earlier. The crack faces are assumed to be traction-free. Applying the divergence theorem to (3.4) and using the equation of equilibrium, the equivalent domain representation of (3.3) is

$$J=\int_A \left[\sigma_{ij}\frac{\partial u_i}{\partial x_1}-W\delta_{1j}\right]\frac{\partial q_1}{\partial x_j}\,dA \tag{3.5}$$

where A is the area enclosed by the closed contour C. In deriving the expression (3.5), W is taken to be a potential function of stress, i.e., $\sigma_{ij}=\partial W/\partial\epsilon_{ij}$.

3.4 Finite-Element Representation of Domain J. The finite-element form of the domain representation (3.5) is briefly discussed. In isoparametric (η_1, η_2) $(-1\le\eta_i\le1,\ i=1,2)$ space, the shape functions are constructed from the basic functions

$$f_1=-\frac{1}{2}\eta(1-\eta),\ f_2=(1-\eta)(1+\eta),\ f_3=\frac{1}{2}\eta(1+\eta) \tag{3.6}$$

via

$$N_{3J+I-3}=f_I(\eta_1)f_J(\eta_2),\ I,J=1,2,3. \tag{3.7}$$

Downloaded 03 May 2010 to 171.66.16.21. Redistribution subject to ASME license or copyright; see http://www.asme.org/terms/Terms_Use.cfm

The coordinates (x_1,x_2) in the physical space and the displacements (u_1,u_2) are given by

$$x_i = \sum_{K=1}^{9} N_K X_{iK},\ u_i = \sum_{K=1}^{9} N_K U_{iK}\ \ i=1,2 \tag{3.8}$$

where X_{iK} are the nodal coordinates and U_{iK} are the nodal displacements.

The discrete form of J based on 3×3 Gaussian quadrature appropriate to the 9-node biquadratic Lagrange element is

$$\mathrm{J} = \sum_{\substack{\text{all elements}\\ \text{in } A}} \sum_{p=1}^{9} \left\{\left[\sigma_{ij}\frac{\partial u_j}{\partial x_1} - W\delta_{1j}\right]\frac{\partial q_1}{\partial x_i}\det\left(\frac{\partial x_k}{\partial \eta_k}\right)\right\}_p w_p. \tag{3.9}$$

The field quantities, including q_1 and its spatial derivatives, are evaluated at the nine quadrature points and weighted by w_p and the determinant of Jacobian matrix, $\det(\partial x_k/\partial\eta_k)$. To be consistent with the isoparametric formulation the values of q_1 and $\partial q_1/\partial x_i$ at the quadrature points are evaluated from

$$q_1 = \sum_{I=1}^{9} N_I Q_{1I},\ \frac{\partial q_1}{\partial x_i} = \sum_{I=1}^{9}\sum_{k=1}^{2}\frac{\partial N_I}{\partial \eta_k}\frac{\partial \eta_k}{\partial x_i}Q_{1I}. \tag{3.10}$$

where N_I is the biquadratic shape function and Q_{1I} is the value of q_1 associated with the Ith node of an element. Nodal values Q_{1I} are assigned in accordance with a smooth function. Numerical experiments have shown that the value of J is insensitive to the type of smooth function. Thus mesh design and convenience are the only considerations in selecting a smooth function. A detailed discussion of several aspects of the implementation of the domain representation of J, including candidate q_i functions, has been given by Shih, et al. (1986).

3.5 Interaction Integral for Extracting Complex Stress-Intensity Factors. Under the assumption of linear elasticity $G=\mathrm{J}$, and therefore G has the line-integral representation

$$G = \int_\Gamma \left(\frac{1}{2}\sigma_{ik}\epsilon_{ik}\delta_{1j} - \sigma_{ij}\frac{\partial u_i}{\partial x_1}\right)n_j d\Gamma. \tag{3.11}$$

The interaction energy release rate [see Appendix II, equation (II-18)] is defined by

$$G_{\text{int}} = G_{\text{tot}} - G - G_{\text{aux}}. \tag{3.12}$$

G_{tot} is the energy release rate of the total field (the actual field plus the auxiliary field) and G_{aux} is the energy release rate of the auxiliary field. It follows from (3.11) and (3.12) that

$$G_{\text{int}} = \int_\Gamma \left[\sigma_{ik}(\epsilon_{ik})_{\text{aux}}\delta_{1j} - \sigma_{ij}\left(\frac{\partial u_i}{\partial x_1}\right)_{\text{aux}} - (\sigma_{ij})_{\text{aux}}\frac{\partial u_i}{\partial x_1}\right]n_j d\Gamma. \tag{3.13}$$

We have used the reciprocity theorem to make the connection

$$\frac{1}{2}\sigma_{ij}(\epsilon_{ij})_{\text{aux}} + \frac{1}{2}(\sigma_{ij})_{\text{aux}}\epsilon_{ij} = \sigma_{ij}(\epsilon_{ij})_{\text{aux}}. \tag{3.14}$$

By virtue of (3.12) and the path-independence of the integral in (3.11), the integral in (3.13) is also path-independent for an elastic homogeneous medium and for the bimaterial problem under consideration.

As mentioned in Section 3.3, it is more advantageous to work with domain representations in finite-element computations. Using the weighting function q_1 discussed in Section 3.3, the domain representation of (3.13) is

$$G_{\text{int}} = \int_A \left\{\left[-\sigma_{ik}(\epsilon_{ik})_{\text{aux}}\delta_{1j} + \sigma_{ij}\left(\frac{\partial u_i}{\partial x_1}\right)_{\text{aux}} + (\sigma_{ij})_{\text{aux}}\frac{\partial u_i}{\partial x_1}\right]\frac{\partial q_1}{\partial x_j}\right\}dA \tag{3.15}$$

where A is any annular domain surrounding the crack tip. Replacing the terms within the brackets [ ] in (3.9) by the terms within the brackets [ ] in (3.15), we have the finite-element representation for G_{int}.

The method of extracting complex stress-intensity factors will be explained using the particular boundary-value problem under study. A more complete discussion is given in Appendix II. Let $(\sigma_{ik})_{\text{aux}}$, $(\epsilon_{ik})_{\text{aux}}$ and $(\partial u_i/\partial x_1)_{\text{aux}}$ be the singular fields for the deformable medium corresponding to unit value of the stress-concentration factor Q_1. The singular stresses are given in Appendix I. The strains can be obtained using Hooke's law and $\partial u_2/\partial x_1$ can be obtained, after some effort, from available solutions (e.g., Sih and Rice, 1964). The integral in (3.15) is evaluated using the actual numerical fields σ_{ij} and $\partial u_i/\partial x_1$ evaluated at the Gauss points, and the auxiliary fields (from Appendix I) also evaluated at the same Gauss points. Let $G_{\text{int}}^{(1)}$ denote the value of the interaction integral. As discussed in Appendix II [see, equations (II-22) and (II-23)], the value of Q_1 of the actual numerically determined fields for the problem at hand is given by

$$Q_1 = \frac{2\cosh^2\pi\epsilon}{(1-\nu)/\mu}G_{\text{int}}^{(1)}. \tag{3.16}$$

Similarly, with the help of auxiliary singular fields appropriate to unit value of Q_2, $G_{\text{int}}^{(2)}$ is evaluated. The value of Q_2 of the actual numerical fields is then given by

$$Q_2 = \frac{2\cosh^2\pi\epsilon}{(1-\nu)/\mu}G_{\text{int}}^{(2)}. \tag{3.17}$$

It may be noted that the method can also be applied to inclined crack and three-dimensional crack problems. In the case of isotropic homogeneous bodies, the usual K_{I}, K_{II} and K_{III} stress-intensity factors are extracted from the numerical fields by using auxiliary fields appropriate to the isotropic homogeneous medium and the well-known relation between the energy release rate and K_{I}, K_{II} and K_{III}. Such an approach, using the line-integral (3.13) to calculate what is in effect G_{int}, has been employed by Yau, et al. (1980), and Stern, et al. (1976) for isotropic homogeneous media. A reciprocal work contour integral method for evaluating stress-intensity/concentration factors in dissimilar materials has also been proposed by Hong and Stern (1978).

3.6 Computational Model. With reference to the geometry depicted in Fig. 3(*a*), only the right half of the deformable medium need be considered in the finite-element analysis since the problem possesses reflective symmetry with respect to the vertical plane bisecting the crack. The half-crack length is a, and the half-width and height of the deformable slab is $100a$. The finite-element model is constructed using 9-node quadrilateral Lagrangian elements; see Fig. 3(*b*). We employ an arrangement of wedge-shaped 9-node elements in the immediate crack-tip region – short of embedding the actual singularity fields into the elements, such an arrangement of elements contains sufficient degrees of freedom to reproduce the qualitative features of crack-tip fields.

The wedge-shaped element has a radial length of $10^{-15}a$. The arrangement of wedge elements is surrounded by semicircular strips of elements as shown in Fig. 3(*c*). Each decade of radial length is spanned by four semicircular strips of elements – thus the domain between $10^{-15}a$ and a is spanned by 60 strips of elements which are generated by a logarithmic scale. Within each strip, the angular distance from 0 to π is spanned by 12 equally sized elements. The mesh for the domain $r\le a$, as laid out in this manner, has 732 elements.

The domain beyond $r>a$, bounded by the remote boundaries and the symmetry plane, is modeled by 140 elements. All in all, there are 872 elements and 3639 nodes in the model. To test the adequacy of the mesh for the problem at hand, we car-

Downloaded 03 May 2010 to 171.66.16.21. Redistribution subject to ASME license or copyright; see http://www.asme.org/terms/Terms_Use.cfm

ried out several elastic and elastic-plastic test calculations using the foregoing mesh and a refined mesh which had twice as many elements. The results differed typically by less than 1 percent and we chose to use the coarser mesh to generate the results to be reported in the next section. The adequacy of the mesh design and the element type in conjunction with selective integration, and the accuracy of the domain representation for calculating J and the interaction integral will become evident in Section 4.

4 Results

4.1 Mixed-Mode Crack-Tip Fields in Homogeneous Media. The plane-strain elastic-plastic fields for the center cracked panel have been computed for the case where the upper and lower half materials are identical and are described by J_2-deformation theory with power-law hardening. In this case, the near-tip fields are essentially of the type originally derived by Hutchinson (1968*a*,*b*) and Rice and Rosengren (1968) for pure Modes I and II and by Shih (1974) for mixed mode. Hereafter, they will be referred to as HRR fields. Application of the J-integral to the mixed-mode small-scale-yielding problem reveals that the dominant singularity governing the asymptotic behavior of the stresses, strains, and displacements near the crack tip has the form

$$\sigma_{ij} = \sigma_0 K^p r^{-1/(n+1)} \tilde{\sigma}_{ij}(\theta;M^p,n),$$

$$\epsilon_{ij} = \frac{\alpha\sigma_0}{E}(K^p)^n r^{-n/(n+1)} \tilde{\epsilon}_{ij}(\theta;M^p,n) \qquad (4.1a,b)$$

$$u_i = \frac{\alpha\sigma_0}{E}(K^p)^n r^{1/(n+1)} \tilde{u}_i(\theta;M^p,n),$$

$$\sigma_e = \sigma_0 K^p r^{-1/(n+1)} \tilde{\sigma}_e(\theta;M^p,n). \qquad (4.1c,d)$$

In the aforementioned expressions the dimensionless angular functions $\tilde{\sigma}_{ij}$, $\tilde{\epsilon}_{ij}$, and $\tilde{u}_i$ depend parametrically on the plastic mixity parameter, M^p, and the hardening exponent, n. The plastic mixity is defined as

$$M^p = \frac{2}{\pi}\tan^{-1}\left|\lim_{r\to 0}\frac{\sigma_{\theta\theta}(r,\theta=0)}{\sigma_{r\theta}(r,\theta=0)}\right| \qquad (4.2)$$

such that $M^p = 1$ for pure Mode I and $M^p = 0$ for pure Mode II. The amplitude of the HRR singularity field, K^p (plastic stress-intensity factor), is defined by Shih (1974) such that the angular distribution, $\tilde{\sigma}_e$, attains a maximum value of unity. With this definition, K^p is related to the value of J by

$$J = \frac{\alpha\sigma_0^2}{E} I_n (K^p)^{n+1}. \qquad (4.3)$$

The factor I_n depends on the degree of mixity, M^p, and n, and has been determined for a wide range of these parameters by Shih (1974). For our present purposes, we find it convenient to rescale K^p by setting $I_n \equiv 1$.

For strictly linear elasticity, the mixity parameter can be reinterpreted as

$$M^p \to M^e \equiv \frac{2}{\pi}\tan^{-1}\left|\frac{K_I}{K_{II}}\right|. \qquad (4.4)$$

For small scale yielding, where the stresses beyond the plastic zone are those of the elastic K-field, M^e is also defined by

$$M^e \equiv \frac{2}{\pi}\tan^{-1}\left|\frac{\sigma_{\theta\theta}(r^*,\theta=0)}{\sigma_{r\theta}(r^*,\theta=0)}\right| \qquad (4.5)$$

where r^* is within the zone of dominance of the elastic field. In this case, J is given by

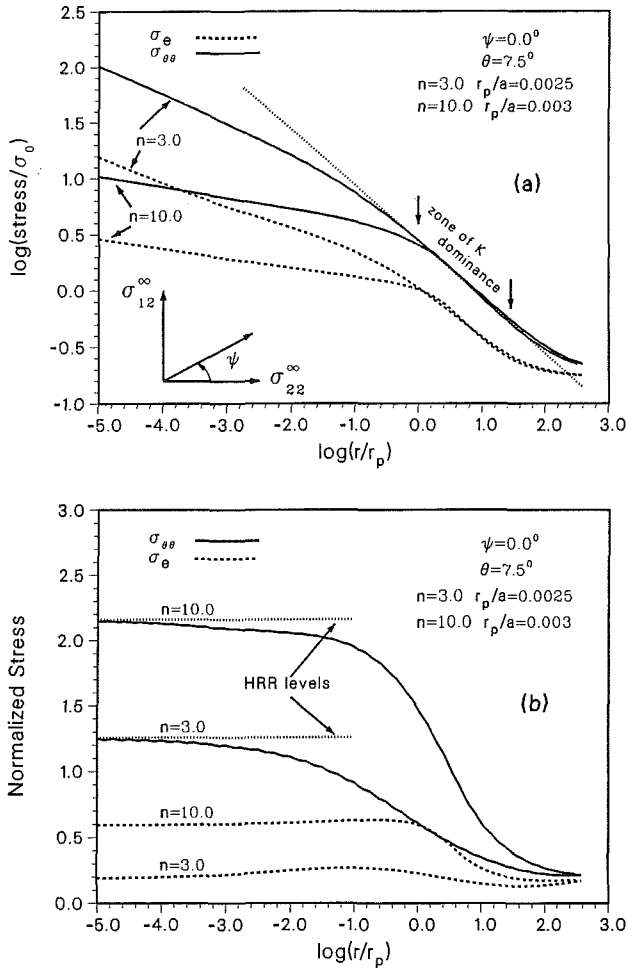


Fig. 5(*a*) Stresses ahead of crack tip in homogeneous medium; the zone of *K* dominance is indicated. (*b*) Normalized stress versus distance normalized by plastic zone size.

$$J = \frac{(1-\nu^2)}{E}(K_I^2 + K_{II}^2). \qquad (4.6)$$

For the case of a finite crack in an infinite homogeneous plate, two types of loading are analyzed, one for which the elastic K-field corresponds to pure Mode I, and the other for which the mode is mixed. We define ψ as

$$\psi \equiv \tan^{-1}\left(\frac{\sigma_{12}^\infty}{\sigma_{22}^\infty}\right) = \tan^{-1}\left(\frac{K_{II}}{K_I}\right) = \frac{\pi}{2}(1-M^e) \qquad (4.7)$$

Thus the two cases correspond to $\psi = 0°$ and $-30°$. We chose to display the results for $\psi = -30°$ because the mixed plastic field that develops under this loading bears noteworthy similarities to the field near the interface crack tip when the remote loading on the bimaterial plate is pure tension.

Figures 5(*a*,*b*) show distributions of stress ahead of the crack tip in a nonlinear homogeneous medium. The hoop stress, $\sigma_{\theta\theta}$, and effective stress, σ_e, along the central row of quadrature points in the first row of elements, $\theta = 7.5°$, are shown for the cases where $n = 3$ and 10. The radial distances are normalized by r_p, the length of the plastic zone along $\theta = 0°$. Note that the stresses plotted are the actual values computed at the Gauss points – we do not apply any smoothing to the data points in this and other figures in this paper.

In Fig. 5(*a*) ln(stress/σ_0) is plotted on the ordinate and the dotted line is the hoop stress according to the K-field. The regions of elastic K-field dominance are indicated. Within the plastic zone the curves indeed take on the slopes $-1/4$ and

Downloaded 03 May 2010 to 171.66.16.21. Redistribution subject to ASME license or copyright; see http://www.asme.org/terms/Terms_Use.cfm

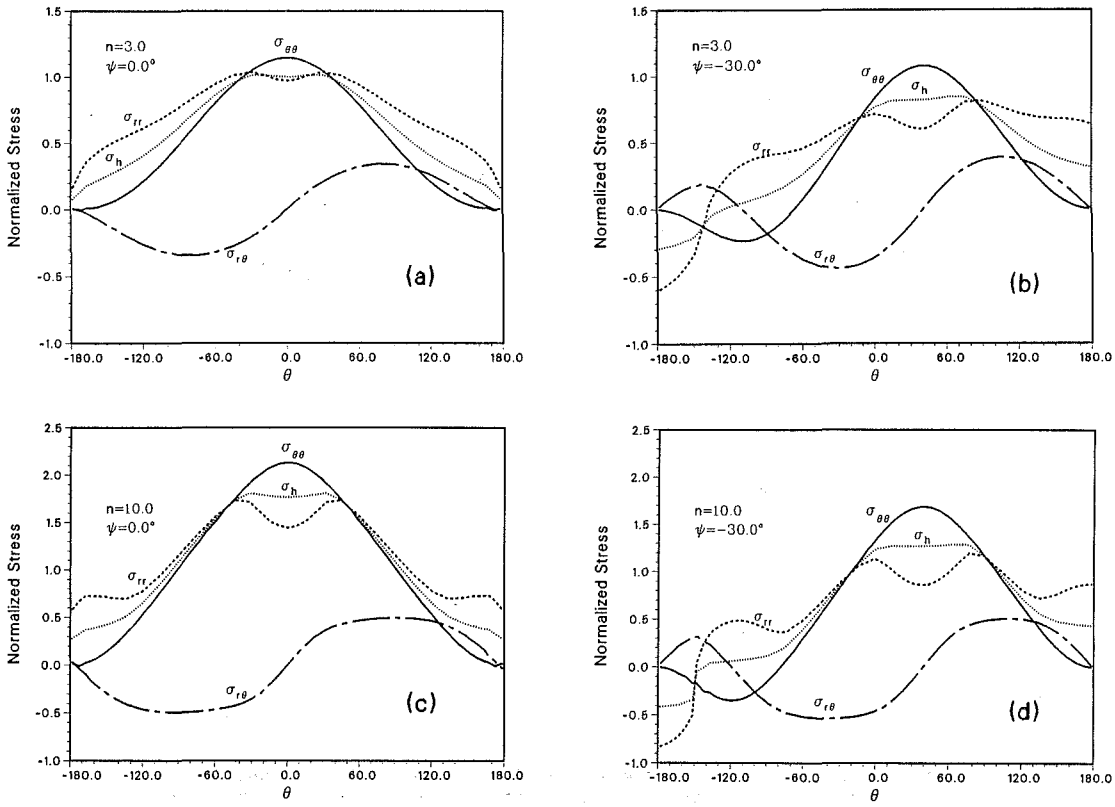


Fig. 6 Angular variations of normalized stresses in homogeneous medium subject to pure Mode I and mixed-mode loadings; (a,b) $n = 3$ material; (c,d) $n = 10$ material

$-1/11$ in accordance with (4.1a). In Fig. 5(b), the normalized stress, stress $/\{\sigma_0[J/(\alpha\sigma_0\epsilon_0 r)]^{1/(n+1)}\}$, is plotted on the ordinate. The stress levels according to the HRR singularity fields (4.1a) for $n=3$ and 10 are indicated. (These levels correspond to values of the dimensionless stress $\tilde{\sigma}_{\theta\theta}$ which are 1.26 and 2.16, respectively.) The normalized stresses are nearly invariant for $r<r_p$ and indicate fields that are entirely of pure Mode I HRR form. Figures 6(a,c) show the angular distribution of normalized stress (defined as in Fig. 5(b) deep inside the plastic zone, for $n=3$ and 10, and $\psi=0°$. Figures 6(b,d) show the angular variations in stress for the mixed-mode field corresponding to $\psi=-30°$. These normalized fields which are obtained from a full-field analysis agree perfectly with the mixed-mode asymptotic fields (Shih, 1974). One noteworthy feature of these fields is that the levels of normal stress, for a given overall value of the J-integral, are reduced for the mixed-mode field. This is not only the case for the normal stress levels directly ahead of the crack, but is also true for the maximum values of stress over the full range of θ. Another interesting feature of the mixed-mode solutions is the large shear stresses ahead of the crack tip.

Plastic zones determined from the analysis of the full boundary-value problem are shown for these same values of n in Figs. 7(a,b) for pure Mode I loading ($\psi=0°$) and mixed-mode loading ($\psi=-30°$). The plastic zones are essentially identical to those obtained by Shih (1974) based on an analysis of the small-scale-yielding boundary-value problem. For the mixed-mode case, the plastic zones are no longer symmetrical above and below the crack line and, for a fixed value of remote loading as measured by the value of J, extend further than for the pure Mode I case (note the difference in the scale of the plots).

Contours of hydrostatic stress are shown in Figs. 7(c,d). Here again, it is noteworthy that with pure Mode I loading the contours are, as expected, symmetric about the crack line but become highly skewed under mixed-mode loading. A feature of the hydrostatic stress field for the $n=10$ material is worth attention: At a fixed overall load level as measured by the value of J, the hydrostatic stress contour, $\sigma_h=\sigma_0$, for the mixed-mode field extends further than the contour for the pure Mode I field; however, the zone of high hydrostatic stress, $\sigma_h \geq 2\sigma_0$, is smaller under mixed-mode field.

4.2 The Interface Crack in Linear Elastic Media. Figure 8 shows results for the near-tip stress fields of the interface crack for $\nu=0.3$. In Figs. 8(a–d), normalized stresses are plotted in the form stress/$(JE/r)^{1/2}$. The analytically obtained asymptotic field (see Appendix I) is shown by the dotted line and the essentially exact correspondence between it and our numerical solution is evident. At distances $r/a<0.05$ from the crack tip, the differences between the numerical fields of the full boundary-value problem of the center cracked plate and the analytic asymptotic fields are less than 5 percent; see Fig. 8(a). This establishes a zone of dominance for the asymptotic linear elastic field.

Figure 8(a), like Fig. 5, shows the radial distribution of stress along a ray connecting the central row of quadrature points in the elements along the bond line. Note that the field is of a strongly mixed nature characterized by large shear stresses. As noted in Section 2.1, the stresses begin to oscillate as the crack tip is approached and, $\sigma_{\theta\theta}$ first becomes compressive at $r/a \cong 10^{-9}$ at $\theta=7.5°$.

Figures 8(b–d) show angular variations of stress at three radial distances from the crack tip. The strong dependence of the angular variations of the fields on the relative radial distance is evident.

To extract the stress-concentration factors Q_1 and Q_2 from the numerical fields, the interaction integral (3.15) was evaluated on several semicircular strips of elements with mean radii ranging from $10^{-14}a$ to a. The values of G_{int} obtained

Downloaded 03 May 2010 to 171.66.16.21. Redistribution subject to ASME license or copyright; see http://www.asme.org/terms/Terms_Use.cfm

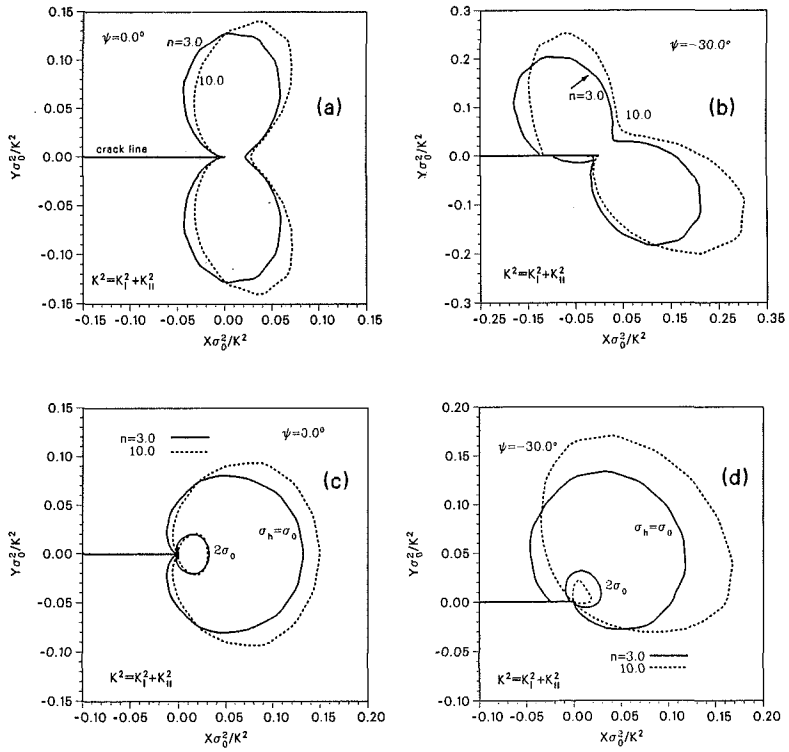


Fig. 7(*a*,*b*) Plastic zones in homogeneous medium subject to Mode I and mixed-mode loadings; (*c*, *d*) hydrostatic stress contours corresponding to Mode I and mixed-mode loadings

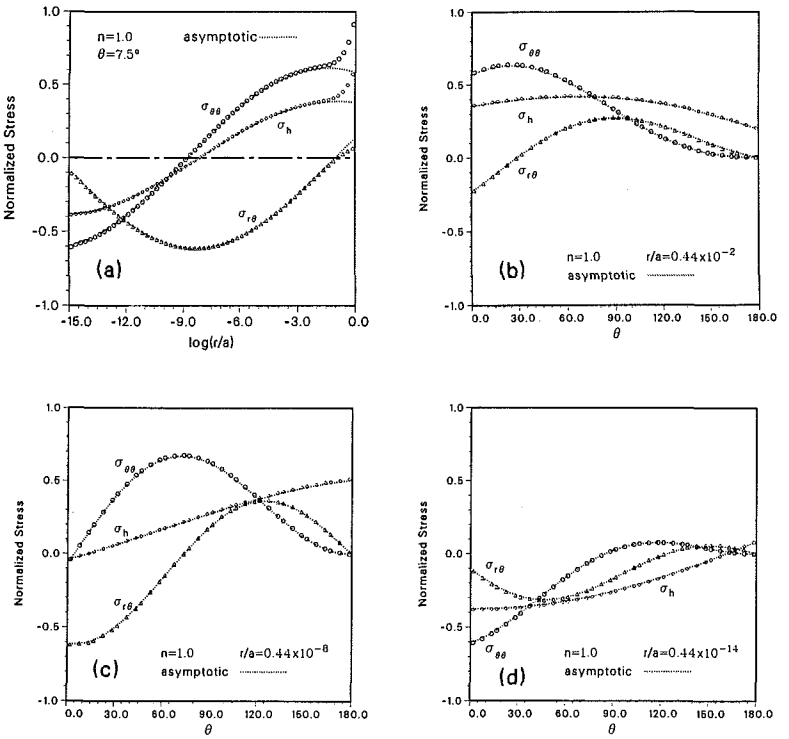


Fig. 8(*a*) Normalized stresses (from linear elastic calculations, $n = 1$) near the bond line versus log distance; the asymptotic stresses are included. (*b*–*d*) Angular variations of normalized stresses at three radial distances.

from the various strips differed only in the third or fourth significant digit. Specifically, for ν ranging from 0.0 to 0.499, the value for Q_1 and Q_2, as determined by (3.16) and (3.17), agreed with the analytical solution given by Rice and Sih (1965) (see Fig. 2) to better than 2 significant digits. The excellent agreement attests to the quality of the numerical fields and the accuracy of the domain interaction integral (3.15) for uncoupling and evaluating stress-intensity factors.

Downloaded 03 May 2010 to 171.66.16.21. Redistribution subject to ASME license or copyright; see http://www.asme.org/terms/Terms_Use.cfm

4.3 Small Scale Yielding for the Interface Crack Subject to Remote Tension. As discussed previously a characteristic feature of the asymptotic linear elastic solution is the increasingly rapid oscillations of the fields as the crack tip is approached. The relative crack-face displacements, given by (2.5), imply wrinkling of the faces and interpenetration near the tip of the crack. The finite-element solutions accurately reproduce the oscillation in the stress field (see Fig. 8) and crack-face penetration into the rigid substrate.

However, using the nonlinear model based on a power-law hardening behavior, we find that at remote load levels which are a fraction of the yield stress, the crack face opens up smoothly. (In Part II, we will show that within the small-scale-yielding zone, contact between crack faces must be phrased in terms of the small-scale-yielding phase parameter ξ as defined in Section 2.2.) The stresses increase monotonically as we probe deeper into the plastic zone and there is no pattern that suggests that the stresses would reach a peak and then decrease as the distance within the plastic zone becomes vanishingly small. For one particular load level, we repeated the entire calculation using a mesh which had twice as many elements. The numerical fields agreed to within two significant digits, strongly suggesting that fields at distances of $10^{-10}a$ to $10^{-15}a$ are accurately resolved by our computations.

At each stress level, the value of J was extracted from the numerical fields using (3.9) and the "plateau" q_1 function. The values of J evaluated on annular domains with mean radii ranging from $10^{-14}a$ to a generally agreed to within 3 significant digits. At stress levels where the maximum plastic zone size is much smaller than the crack length, the value of J agreed precisely with the analytical result of (2.16), viz.,

$$J = G = \frac{(1-\nu)/\mu}{4\cosh^2 \pi\epsilon}(Q_1^2 + Q_2^2). \tag{4.8}$$

The essentially exact path-independence of the numerically evaluated J and the precise agreement with (4.8) under small scale yielding demonstrate the quality of the numerical solution and the accuracy of the domain method. The J-values thus obtained are employed for the purpose of normalizing the fields to be discussed.

We choose to present results for a high hardening material ($n=3$) and a moderate to low hardening material ($n=10$) to reveal the effect of plasticity on the near-tip fields. In particular, the behavior of the hoop stress ahead of the crack is shown in detail since it is rather descriptive of the conditions at the interface and also plays an important role in fracture processes. Also, the variation of the hoop stress with radial distance is representative of the other stress components. In particular, the hoop stress normalized by the remotely applied stress provides a direct indication of the intensification of the stress field. As before, the hoop stress at points on a radial line passing through the central row of Gauss points in the elements bonded to the interface ($\theta = 7.5°$) is chosen for detailed examination. Since the distances under discussion range from $10^{-15}a$ to a, it is necessary to plot log (r/a) on the abscissa. Over distances that differ by 15 orders of magnitude, the normalized hoop stress varies by several orders of magnitude and, in some cases, is compressive. With the exception of a small interval where the hoop stress goes to zero and changes sign, the magnitude of the normalized hoop stress is much larger than unity within the distances under discussion. To grasp an overall picture of the behavior of the fields, we confine our attention to normalized stresses with magnitudes greater than unity. This permits the results to be presented in a rather compact and informative way. Specifically, we take the log of $|\sigma_{\theta\theta}/\sigma^\infty|$ and to preserve the algebraic sign of the stress, the sign is then appended. Accordingly, we plot sign $(\sigma_{\theta\theta})$ log $|\sigma_{\theta\theta}/\sigma^\infty|$.

The normalized stress determined by the finite-element

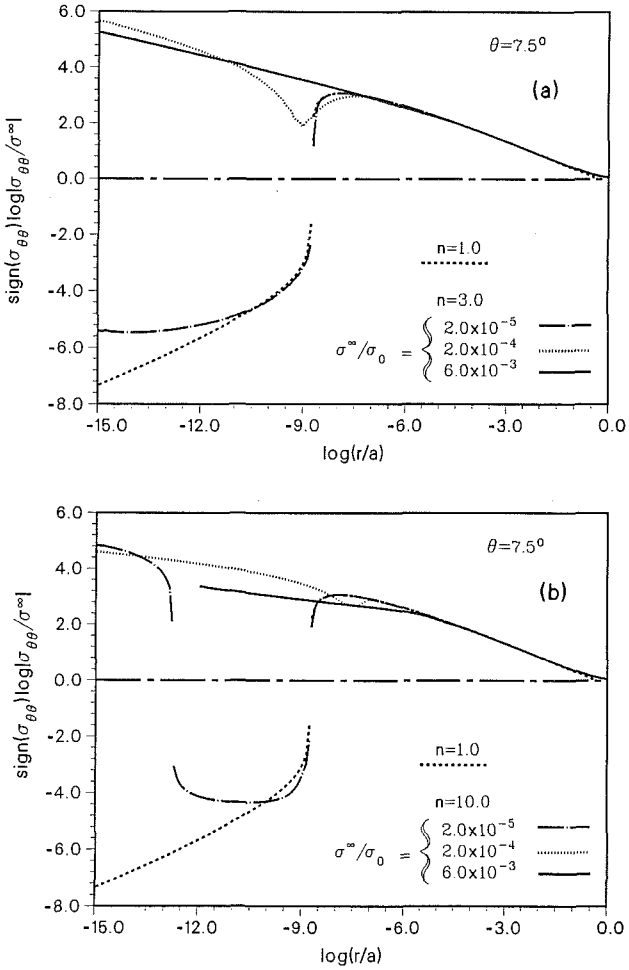


Fig. 9 Plots of log of normalized hoop stress (near the bond line) against log of normalized distance for the interface crack; (a) $n=3$ material, (b) $n=10$ material. The elastic ($n=1$) result is included.

calculations for the strictly elastic material is plotted against normalized distance in Fig. 9(*a*); see dashed-line curve. The break in the dashed-line curve near log $(r/a) = -9.0$ corresponds to the stress changing from tension to compression. It should be noted that the position of the break in the dashed-line curve is independent of the remote tensile stress level. We now examine the behavior of the stress for the strongly hardening ($n=3$) nonlinear material. At the lowest load level considered, $\sigma^\infty/\sigma_0 = 2.0\times10^{-5}$, the plastic zone is confined to a distance of about $10^{-11}a$. While the stress is negative within the plastic zone, the slope of the curve becomes positive for $r/a < 10^{-14}$. At the next load level, $\sigma^\infty/\sigma_0 = 2.0\times10^{-4}$, the stress is positive over the entire distance studied, however, at the outer fringe of the plastic zone, $10^{-9} < r/a < 10^{-8}$, the trend of the surrounding elastic field is felt. At distances well inside the plastic zone, the hoop stress increases monotonically as the crack tip is approached. At a still higher load level, $\sigma^\infty/\sigma_0 = 6\times10^{-3}$, the hoop stress increases monotonically over the entire distance under discussion – there is no trace of an oscillatory field. It is important to note that to reveal the mathematical structure of the crack-tip fields, it is necessary to examine fields within distances which are well below those that are physically relevant. Of course in applying these results to the analysis of interface failure, fields within such distances would be disregarded.

The behavior of the hoop stress for a moderate-to-low hardening material is shown in Fig. 9(*b*). For comparison purposes, the linear elastic result is again included. At the very

Downloaded 03 May 2010 to 171.66.16.21. Redistribution subject to ASME license or copyright; see http://www.asme.org/terms/Terms_Use.cfm

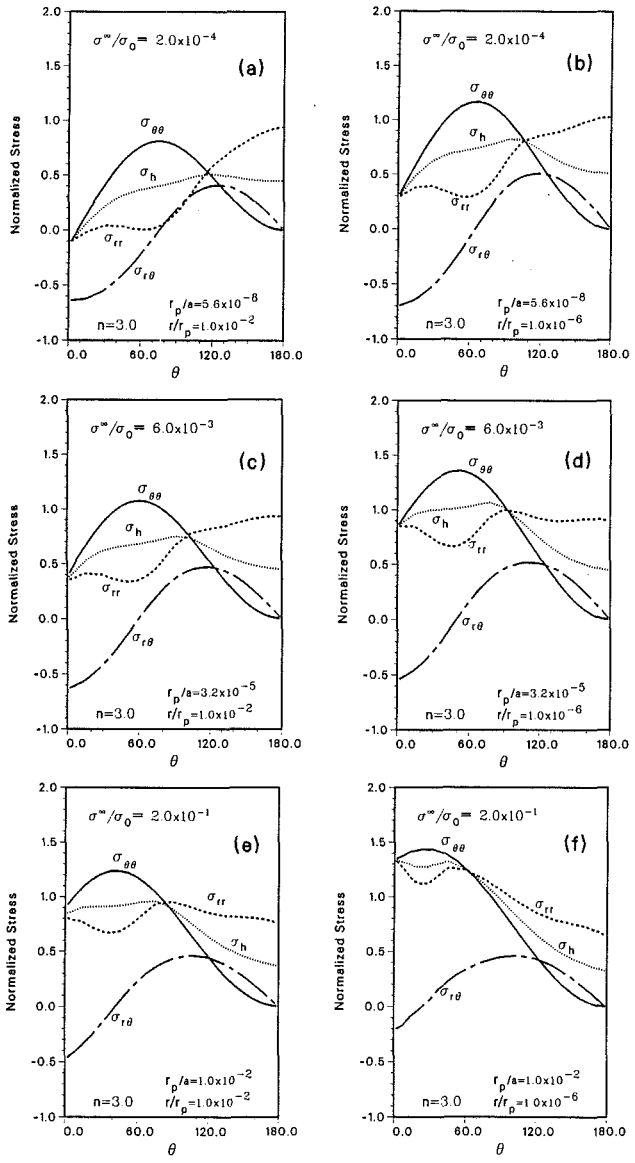


Fig. 10 Plots of angular variations of normalized stresses for the interface crack with $n=3$ at two distances within the plastic zone and for three remote stress levels

low remote stress level $\sigma^\infty/\sigma_0 = 2.0\times10^{-5}$, the stress in the outer plastic zone is compressive in response, we note, to the compressive pressure of the surrounding elastic fields. Well within the plastic zone the stress is tensile. At the next remote stress level, $\sigma^\infty/\sigma_0 = 2.0\times10^{-4}$, the hoop stress in the outermost fringe of the plastic zone is weakly affected by the elastic fields. A short distance into the plastic zone, the hoop stress increases monotonically as the crack tip is approached. At the final load level, $\sigma^\infty/\sigma_0 = 6.0\times10^{-3}$, shown in the plot, there is no trace of any oscillatory field. (The solid line is terminated at log $(r/a) = -12$ because we were unable to complete the calculations for the $n=10$ material at this load level using a mesh which could resolve fields at distances of $10^{-15}a$ from the crack tip.) We also note that, even at the largest remote stress level, the nonlinear crack-tip region is surrounded by an annular zone, $10^{-5} < r/a < 10^{-2}$, in which the stresses are well approximated by the elastic singular fields (2.13).

To develop a better understanding of the plastic fields, we detail their angular distribution at two radial distances within the plastic zone and at three load levels: $\sigma^\infty/\sigma_0 = 2\times10^{-4}$, $\sigma^\infty/\sigma_0 = 6\times10^{-3}$ and $\sigma^\infty/\sigma_0 = 2\times10^{-1}$. We begin with the $n=3$ material. The length of the plastic zone as measured along the interface is denoted by r_p. The relative plastic zone size, r_p/a, corresponding to the three remote loads are 5.6×10^{-8}, 3.2×10^{-5} and 1.0×10^{-2}, respectively. Consider the region whose "remote" boundary conditions are given by the elastic singular fields; see (2.1). As discussed in Section 2.2, the fields within this region are members of a family parameterized by the phase angle ξ and the magnitude of the stresses nearly scales with the J-integral. Guided by these observations and additional considerations discussed in Part II, we normalized the stresses using an HRR structure. The normalized stresses are defined as

$$\hat{\sigma}_{ij} = \frac{\sigma_{ij}/\sigma_0}{(J/\alpha\sigma_0\epsilon_0 r)^{1/(n+1)}} \tag{4.9}$$

The angular distribution of the normalized stresses at a fixed relative distance $r/r_p = 1\times10^{-2}$, are shown in Figs. 10(*a,c,e*) for the three remote load levels corresponding to ξ equal to -1.36, -0.727 and -0.071, respectively. The angular fields deep inside the plastic zone, $r/r_p = 1.0\times10^{-6}$ for the same values of ξ, are shown in Figs. 10(*b,d,e*). It is clear from these plots that the fields are quite similar to the mixed-mode HRR fields, for positive values of θ, shown in Fig. 6(*b*). Specifically, within any given plastic zone, the stress fields shift toward a Mode I HRR-type angular distribution as the distance moves deeper into the plastic zone; e.g., compare Figs. 10(*e,f*). At a fixed distance, relative to the plastic zone size, the angular fields also shift toward a Mode I HRR-type angular distribution as the remote load or the size of the plastic zone increases; e.g., compare Figs. 10(*c,e*). Finally, we point out that within the range of distances and loads examined, the normalized stresses are of order unity; the maximum value of the normalized hoop stress vary between 0.8 and 1.4.

It is instructive to examine the changes in the size and shape of the plastic zone as the remote load increases. To facilitate comparisons with the usual presentation of these plots (e.g., Shih, 1974), the distances are normalized by $JE/\{(1-\nu^2)\sigma_0^2\}$. The plastic zones at the three load levels are plotted in Fig. 11(*a*), using these normalized distances

$$\bar{X} = x(1-\nu^2)\sigma_0^2/JE \text{ and } \bar{Y} = y(1-\nu^2)\sigma_0^2/JE. \tag{4.10}$$

The relative size of the plastic zone decreases (when plotted on these nondimensionalized axes) and changes over to a nearly Mode I pattern as the remote load increases. Hydrostatic stress contours for $\sigma_h = \sigma_0$ and $\sigma_h = 2.0\sigma_0$ are shown in Figs. 11(*b,c,d*). The zone of high hydrostatic stress, $\sigma_h \geq 2\sigma_0$, increases in size as the field shifts toward a Mode I distribution.

We detail the fields for the $n=10$ material at remote stress levels, σ^∞/σ_0 of 2×10^{-4}, 6×10^{-3} and 2×10^{-1} corresponding to ξ equal to -1.36, -0.727, and -0.071, respectively. The respective plastic zone sizes, r_p/a, are 8.2×10^{-8}, 4.2×10^{-5}, and 1.2×10^{-2}. Plots of the angular fields at distances of $r/r_p = 1\times10^{-2}$ and 1×10^{-4} for the three remote stress levels are shown in Fig. 12. It is easily seen that the angular distribution of the plastic fields are nearly those of the mixed-mode HRR type and that the fields deep inside the plastic zone, as in Fig. 12(*f*), shift toward the Mode I HRR distribution as shown in Fig. 6(*c*).

Plastic zones corresponding to the three remote stress levels are shown in Fig. 13(*a*). Again the shift toward a Mode I pattern with increasing remote stress is easily seen. Hydrostatic stress contours are plotted in Figs. 13(*b,c,d*); note the increase in the size of the zone of high hydrostatic stress, $\sigma_h \geq 1.7\sigma_0$, in Fig. 13(*d*).

5 Discussion

Our results suggest that a finite-element method which uses selective integration (Malkus and Hughes, 1978; Hughes, 1980) and 9-node Lagrangian quadrilateral element is well

Downloaded 03 May 2010 to 171.66.16.21. Redistribution subject to ASME license or copyright; see http://www.asme.org/terms/Terms_Use.cfm

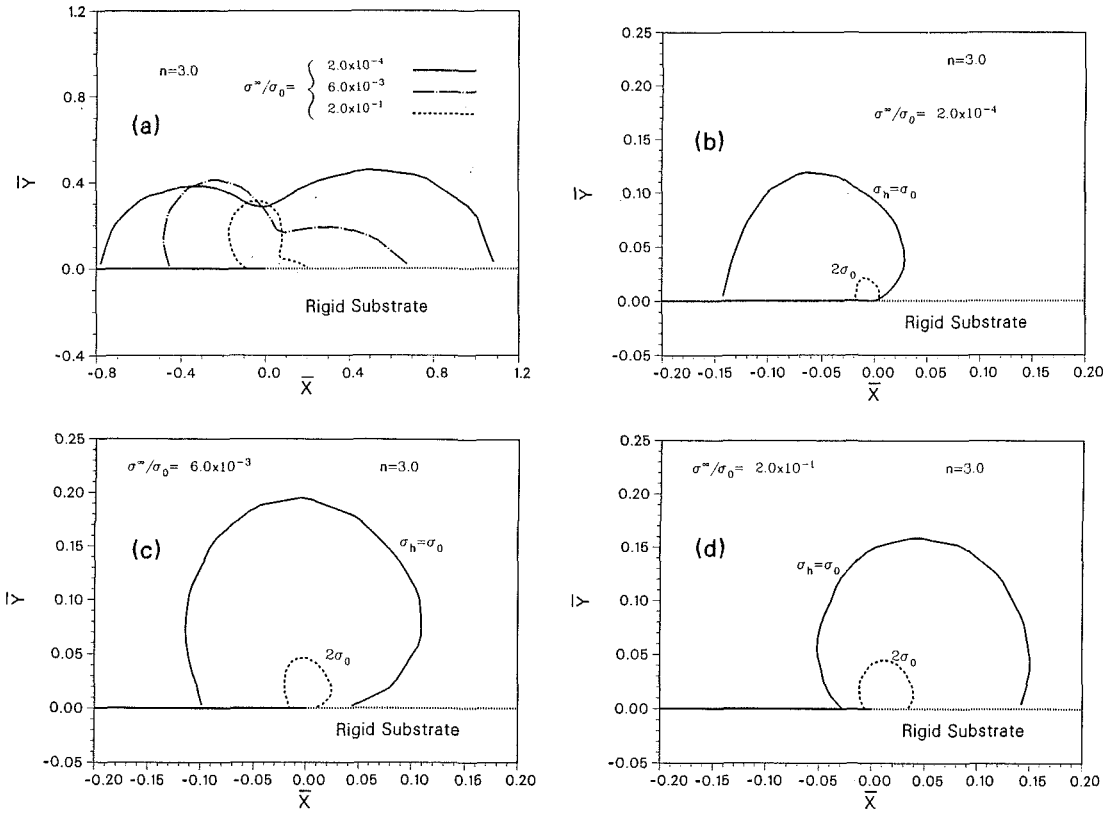


Fig. 11(*a*) Plastic zones for the interface crack with $n = 3$ for three remote stress levels. (*b–d*) Hydrostatic stress contours for three remote stress levels. The normalized distances are defined as $X = x(1-\nu^2)\,\sigma_0^2/JE$ and $Y = y(1-\nu^2)\sigma_0^2/JE$.

suited for studying the complex nonlinear stress-strain fields near the tip of an interface crack. We find the method to be highly stable; the reduced integrations of volumetric fields using 4 quadrature points display no *hourglass* or other spurious modes. The method is easily programmed and, we note, lends itself to coding which is readily vectorized for supercomputers.

The full-field numerical results presented in Section 4.3 indeed suggest that the near-tip fields of the interface crack do not have a separable form of the type given by the HRR singularity (4.1). Nevertheless our small-scale-yielding solutions for the interface crack bear remarkable similarities to the fields for cracks in homogeneous media subject to mixed-mode loading.

For the boundary-value problem at hand, we note that, under small-scale-yielding conditions

$$J = \frac{(\sigma_{22}^{\infty})^2 \pi a (1+4\epsilon^2)}{4\cosh^2 \pi\epsilon}(1-\nu)/\mu. \tag{5.1}$$

If J_0 is the value of J for a similar crack in a homogeneous plate then, for a fixed remote stress σ_{22}^{∞}

$$\frac{J}{J_0} = \frac{(1+4\epsilon^2)}{2\cosh^2 \pi\epsilon}. \tag{5.2}$$

For the case of the crack on a rigid substrate with $\nu = 0.3$ in the deformable medium, $\epsilon \cong 0.0935$ as already noted, and $J/J_0 \cong 0.475$. We now recall the distributions in each of Figs. 6, 10, and 12, where the stresses are normalized by the quantity $q = \sigma_0[J/(\alpha\sigma_0\epsilon_0 r)]^{1/(n+1)}$. With this perspective, it is clear that for a fixed intensity of remote loading, as measured by σ_{22}^{∞}, the stresses near the tip are generally lower for the interface crack than those for the crack in a homogeneous media. However, at a given value of J, the stresses near the tip of the interface crack are generally higher; at larger distances from the crack tip, the stresses are comparable or lower than thoe for the homogeneous media. For example, the maximum value of $(\sigma_{\theta\theta}/q)$ in a homogeneous medium, under mixed-mode loading corresponding to $\psi = -30°$, is $\sigma_{\theta\theta}/q \cong 1.1$ when $n = 3$ and $\sigma_{\theta\theta}/q \cong 1.7$ when $n = 10$. For the interface crack, the maximum stress levels, at each radial distance, depend on distance and remote stress level. At the normalized distance $r/r_p = 1.0 \times 10^{-2}$, $\sigma_{\theta\theta}/q \cong 0.9$, 1.1, and 1.25 for the three remote stress levels plotted in Fig. 10 $n = 3$. At the distance $r/r_p = 1.0 \times 10^{-6}$, $\sigma_{\theta\theta}/q \cong 1.2$, 1.35, and 1.45, which are considerably larger than those for a crack in a homogeneous medium. The same trends hold for $n = 10$. It should be noted that the angular distribution of the stresses for the interface crack can be quite different from those for the crack in a homogeneous medium. An important difference is the large shear stresses and strains that develop near the bond line of an interface crack despite the tensile nature of the remote stresses.

Another intriguing feature of the stress fields of the interface crack is how the degree of mixity of the near-tip fields changes with the extent of plasticity. For example, comparing Figs. 12 and 6(*c,d*) for $n = 10$, it may be seen that as the remote stress level increases, and as the positions examined are closer to the crack tip, the field more nearly resembles that a pure Mode I HRR field. Indeed, near-tip fields for remote stress $\sigma^{\infty}/\sigma_0 > 0.2$ are essentially of pure Mode I distribution. A discussion of these fields is deferred to a later paper. At lower stress levels, and at distances more remote from the crack tip, the field has features similar to the homogeneous mixed mode, for example, that for $\psi = -30°$.

As noted in Sections 2 and 4, the small strain linear elastic asymptotic field for an interface crack is characterized by displacement incompatibilities and oscillatory stresses. In Section 2, it was noted that under combined remote tension and shear, the regions ahead of the crack where the stresses

Downloaded 03 May 2010 to 171.66.16.21. Redistribution subject to ASME license or copyright; see http://www.asme.org/terms/Terms_Use.cfm

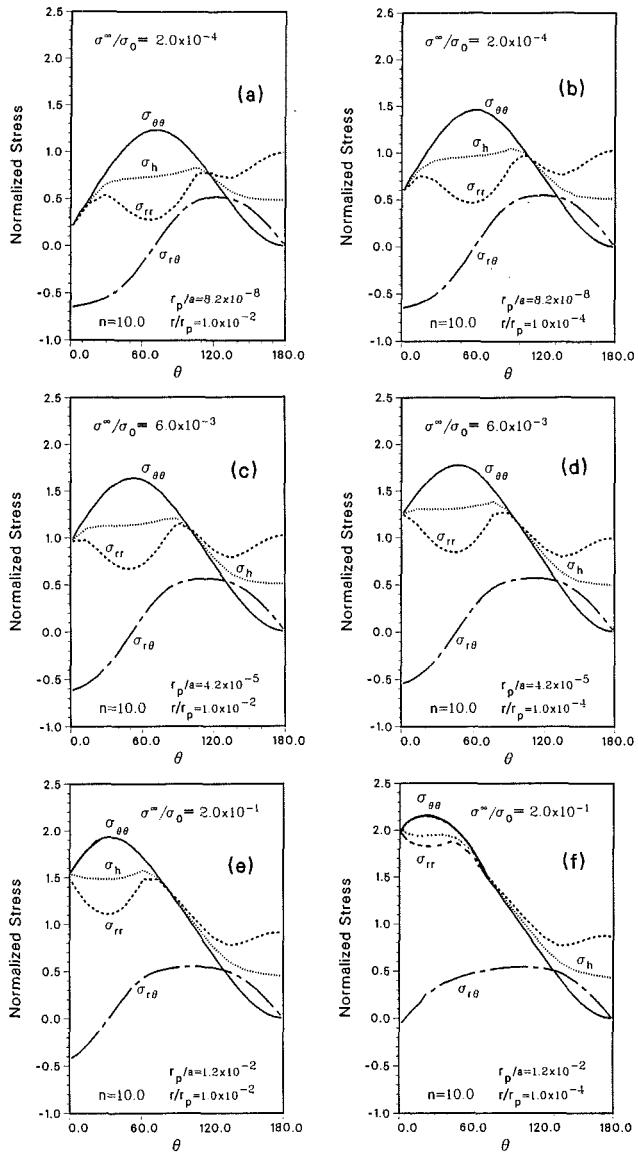


Fig. 12 Plots of angular variations of normalized stresses for the interface crack with $n=10$ at two distances within the plastic zone and for three remote stress levels

oscillate can be significant fractions of the crack length, thus rendering the solutions physically unacceptable. Within the nonlinear theory of plane stress, Knowles and Sternberg (1983) have carried out an elegant asymptotic analysis of an interface crack between two neo-Hookean sheets. Their asymptotic fields, based on nonlinear kinematics and a linear relation between the Cauchy shear stress and shear displacement, are free of oscillatory singularities; they also found that the crack opens smoothly near its ends. Our full-field solutions based on linearized kinematics show that the zone of crack-face contact is strongly affected by nonlinear material behavior. To demonstrate this, we analyzed the case where $\sigma_{22}^{\infty}>0$ and $\sigma_{12}^{\infty}=-2\sigma_{22}^{\infty}$. The results, shown in Figs. 14 and 15, were obtained by performing a *boundary layer*, small-scale-yielding analysis in which the stresses, given by the asymptotic field in Appendix I, were imposed at a distance which is large compared to the plastic zone size. The stress intensities for this case were prescribed as $Q_1=\sigma_{22}^{\infty}\{1+4\epsilon\}\sqrt{\pi a}$ and $Q_2=\sigma_{22}^{\infty}\{-2+2\epsilon\}\sqrt{\pi a}$ with σ_{22}^{∞} taken to be the scaler stress variable; see, Fig. 2(*c*). Thus $|\mathbf{Q}|=4.03\sigma_{22}^{\infty}\sqrt{a}$, $\phi=-52.8°$ $(-0.922$ rad).

Figure 14(*a*) shows the linear elastic results for the stress variations along a radial line at $\theta=7.5°$ for the combined remote tension and shear loading. It may be recalled from Section 2 that, on the bond line, $\sigma_{\theta\theta}$ is compressive at $r/a\cong 2\times 10^{-3}$. At $\theta=7.5°$, $\sigma_{\theta\theta}$ is compressive at $r/a\cong 3\times 10^{-4}$. Figure 14(*b*) shows the radial distributions of stress, again along the central row of quadrature points at $\theta=7.5°$, for a nonlinear material with $n=3$ and for three remote stress levels, σ^{∞}/σ_0, of 2×10^{-4}, 6×10^{-3} and 1×10^{-1} which correspond to ξ of -2.32, -1.68, and -1.16, respectively. In the plot, the hoop stress $\sigma_{\theta\theta}$ is normalized by σ_{22}^{∞} which is labeled as σ^{∞}. Note, that with combined loading of this sort, that is with $\sigma_{12}^{\infty}<0$, larger remote levels of σ_{22}^{∞}, as compared to the cases dominated by remote tension, are required to "open the crack" and produce monotonically increasing stresses as the crack tip is approached. Nevertheless, even at the rather low remote stress level of $\sigma_{22}^{\infty}/\sigma_0=1.0\times 10^{-1}$ oscillatory stresses and overlapping of the crack faces are precluded in a high hardening material. In a moderate-to-low hardening material, the oscillatory fields are precluded at substantially lower remote tensile stresses. Indeed, even at rather low stress levels, the characteristics of the plastic fields (which are totally different from those predicted by linear elasticity) prevail over significant length scales.

Figure 15 shows the angular distribution of stresses at six radial distances within the plastic zone for the remote loading corresponding to $\sigma_{22}^{\infty}/\sigma_0=1.0\times 10^{-1}$ and $\sigma_{12}^{\infty}/\sigma_0=-2.0\times 10^{-1}$ and ξ of -1.16. For this load level, $r_p/a\cong 5.0\times 10^{-2}$ which is also the maximum extent of the plastic zone. A remarkable feature of these fields is the gradual shift toward a Mode I like HRR field as the distance r/r_p becomes vanishingly small despite the relatively large remote shear stresses. Indeed the angular variations of the fields in Fig. 15 bear striking resemblance to the fields in Fig. 10 which are associated with pure remote tension.

Despite the pathological nature of the linear elastic singular fields, we must point out that there is a finite annular region where the elastic singular fields (2.13) is a good approximation of the full-field solution as can be seen in Figs. 9 and 14. It is in this more restricted sense, that we speak of small scale yielding; the term does not imply self-similar growth of the plastic zone. Our analyses have shown that the small scale yielding fields are members of a family parameterized by a new phase angle, ξ, and the fields nearly scale with the value of the J-integral. Furthermore, pathological features of the linear elastic solutions such as near tip oscillations in stresses and displacements are somewhat mitigated by nonlinear material response. These latter aspects are elaborated upon in Part II.

Acknowledgments

We are grateful to Margaret Symington who made many helpful suggestions in the presentation of the material. This investigation is supported by the Office of Naval Research through ONR Grant "Mechanics of Interface Cracks." The computations reported on were performed in the Computational Mechanics Facility at Brown University and at the Supercomputer Facility at the U.S. Naval Research Laboratory. Helpful suggestions by a reviewer are gratefully acknowledged.

References

Barnett, D. M., and Asaro, R. J., 1972, "The Fracture Mechanics of Slit-like Cracks in Anisotropic Elastic Media," *Journal of the Mechanics and Physics of Solids*, Vol. 20, pp. 353–366.

Belytschko, T., and Tsay, C. S., 1983, "A Stabilization Procedure for the Quadrilateral Plate Element with One-Point Quadrature," *International Journal for Numerical Methods in Engineering*, Vol. 19, pp. 405–419.

Clements, D. L., 1971, "A Crack between Dissimilar Anisotropic Media," *International Journal of Engineering Science*, Vol. 9, pp. 257–265.

deLorenzi, H. G., 1982, "On Energy Release Rate and the J-integral for 3-D

Downloaded 03 May 2010 to 171.66.16.21. Redistribution subject to ASME license or copyright; see http://www.asme.org/terms/Terms_Use.cfm

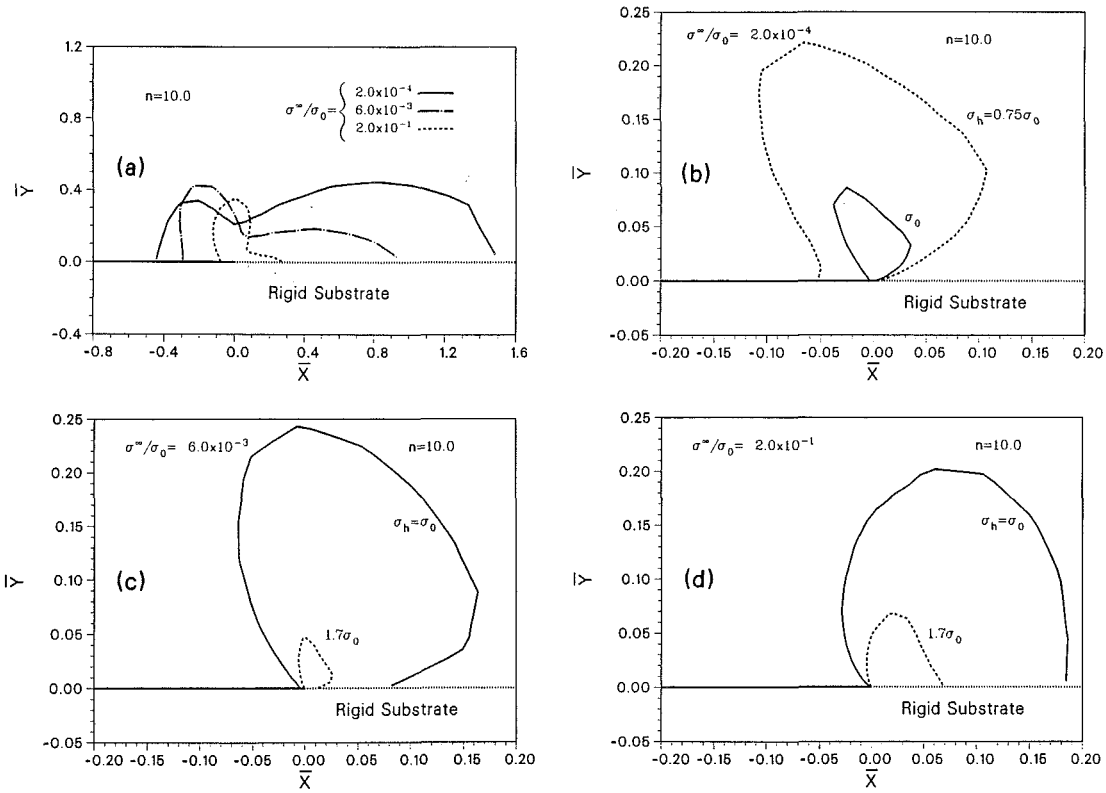


Fig. 13(a) Plastic zones for the interface crack with $n = 10$ for three remote stress levels. (b–d) Hydrostatic stress contours for three remote stress levels. The normalized distances are defined as $X = x(1-\nu^2)\,\sigma_0^2/JE$ and $Y = y(1-\nu^2)\,\sigma_0^2/JE$.

Crack Configurations," *International Journal of Fracture*, Vol. 19, pp. 183–193.

England, A. H., 1965, "A Crack Between Dissimilar Media," ASME JOURNAL OF APPLIED MECHANICS, Vol. 32, pp. 400–402.

Erdogan, F., 1963, "Stress Distribution in a Nonhomogeneous Elastic Plane with Cracks," ASME JOURNAL OF APPLIED MECHANICS, Vol. 30, pp. 232–236.

Erdogan, F., 1965, "Stress Distribution in Bonded Dissimilar Materials With Cracks," ASME JOURNAL OF APPLIED MECHANICS, Vol. 32, pp. 403–410.

Eshelby, J. D., 1956, "The Continuum Theory of Lattice Defects," *Solid State Physics*, Eds., Seitz and Turnbull, Vol. 3, pp. 79–144.

Eshelby, J. D., 1961, "Elastic Inclusions and Inhomogeneities," *Progress in Solid Mechanics*, Eds., Sneddon & Hill, Vol. 2, pp. 87–140.

Hong, C. C., and Stern, M., 1978, "The Computation of Stress Intensity Factors in Dissimilar Materials," *Journal of Elasticity*, Vol. 8, pp. 21–34.

Hellen, T. K., 1975, "On the Method of Virtual Crack Extension," *International Journal for Numerical Methods in Engineering*, Vol. 9, pp. 187–207.

Hughes, T. J. R., 1980, "Generalization of Selective Integration Procedures to Anisotropic and Nonlinear Materials," *International Journal for Numerical Methods in Engineering*, Vol. 15, pp. 1413–1418.

Hutchinson, J. W., 1968a, "Singular Behavior at the End of a Tensile Crack in a Hardening Material," *Journal of the Mechanics and Physics of Solids*, Vol. 16, pp. 13–31.

Hutchinson, J. W., 1968*b*, "Plastic Stress and Strain Fields at a Crack Tip," *Journal of the Mechanics and Physics of Solids*, Vol. 16, pp. 337–347.

Hutchinson, J. W., 1983, "Fundamentals of the Phenomenological Theory of Nonlinear Fracture Mechanics," ASME JOURNAL OF APPLIED MECHANICS, Vol. 50, pp. 1042–1051.

Knowles, J. K., and Sternberg, E., 1983, "Large Deformations Near a Tip of an Interface-Crack Between Two Neo-Hookean Sheets," *Journal of Elasticity*, Vol. 13, pp. 257–293.

Li, F. Z., Shih, C. F., and Needleman, A., 1985, "A Comparison of Methods for Calculating Energy Research Rates," *Engineering Fracture Mechanics*, Vol. 21, pp. 405–421.

Malkus, D. S., and Hughes, T. J. R., 1978, "Mixed Finite Element Methods – Reduced and Selective Integration Techniques: A Unification of Concepts," *Computer Methods in Applied Mechanics and Engineering*, Vol. 15, pp. 63–81.

Moran, B., and Shih, C. F., 1987, "Crack Tip and Associated Domain Integrals from Momentum and Energy Balance," *Engineering Fracture Mechanics*, Vol. 27, pp. 615–642.

Nagtegaal, J. C., Parks, D. M., and Rice, J. R., 1974, "On Numerically Accurate Finite Element Solutions in the Fully Plastic Range," *Computer Methods in Applied Mechanics and Engineering*, Vol. 4, pp. 153–178.

Parks, D. M., 1977, "The Virtual Crack Extension Method for Nonlinear Material Behavior," *Computer Methods in Applied Mechanics and Engineering*, Vol. 12, pp. 353–365.

Rice, J. R., and Sih, G. C., 1965, "Plane Problems of Cracks in Dissimilar Media," ASME *Journal of Applied Mechanics*, Vol. 32, pp. 418–423.

Rice, J. R., and Rosengren, G. F., 1968, "Plane Strain Deformation Near a Crack Tip in a Power Law Hardening Material," *Journal of the Mechanics and Physics of Solids*, Vol. 16, pp. 1–12.

Rice, J. R., 1968, "A Path-Independent Integral and the Approximate Analysis of Strain Concentration by Notches and Cracks," ASME *Journal of Applied Mechanics*, Vol. 35, pp. 379–386.

Rice, J. R., 1987, "Elastic Fracture Mechanics Concepts for Interfacila Cracks," to appear in the ASME *Journal of Applied Mechanics*.

Shih, C. F., 1974, "Small-Scale Yielding Analysis of Mixed-Mode Plane-Strain Crack Problems," in *Fracture Analysis*, ASTM STP 560, pp. 187–210.

Shih, C. F., and Needleman, A., 1984, "Fully Plastic Crack Problems," Parts I and II, ASME JOURNAL OF APPLIED MECHANICS, Vol. 51, pp. 48–56, pp. 57–64.

Shih, C. F., Moran, B., and Nakamura, T., 1986, "Energy Release Rate Along a Three-Dimensional Crack Front in a Thermally Stressed Body," *International Journal of Fracture*, Vol. 30, pp. 79–102.

Sih, G. C., and Rice, J. R., 1964, "The Bending of Plates of Dissimilar Materials With Cracks," ASME JOURNAL OF APPLIED MECHANICS, Vol. 31, pp. 477–482.

Stern, M., Becker, E. B., and Dunham, R. S., 1976, "A Contour Integral Computation of Mixed Mode Stress Intensity Factors," *International Journal of Fracture*, Vol. 12, pp. 359–368.

Williams, M. L., 1959, "The Stresses Around a Fault or Crack in Dissimilar Media," *Bulletin of the Seismological Society of America*, Vol. 49, pp. 199–204.

Willis, J. R., 1971, "Fracture Mechanics of Interfacial Cracks," *Journal of the Mechanics and Physics of Solids*, Vol. 19, pp. 353–368.

Yau, J. F., Wang, S. S., and Corten, H. T., 1980, "A Mixed-Mode Crack Analysis of Isotropic Solids Using Conservation Laws of Elasticity," ASME JOURNAL OF APPLIED MECHANICS, Vol. 47, pp. 335–341.

Zienkiewicz, O. C., 1977, *The Finite Element Method*, 3rd Ed., McGraw-Hill, London.

APPENDIX I

Singular Fields Near the Tip of an Interface Crack. As noted in the text, the asymptotic crack-tip fields for the case of linear isotropic media take the form

$$\sigma_{ij} = \sum_{\alpha=1}^{2} \frac{Q_\alpha}{\sqrt{2\pi r}}\, g_{ij}^{(\alpha)}[\theta, \epsilon \ln (r/2a); \epsilon]. \tag{I-1}$$

The stress-intensity factors, Q_α, in (I-1) were defined in (2.1)

Downloaded 03 May 2010 to 171.66.16.21. Redistribution subject to ASME license or copyright; see http://www.asme.org/terms/Terms_Use.cfm

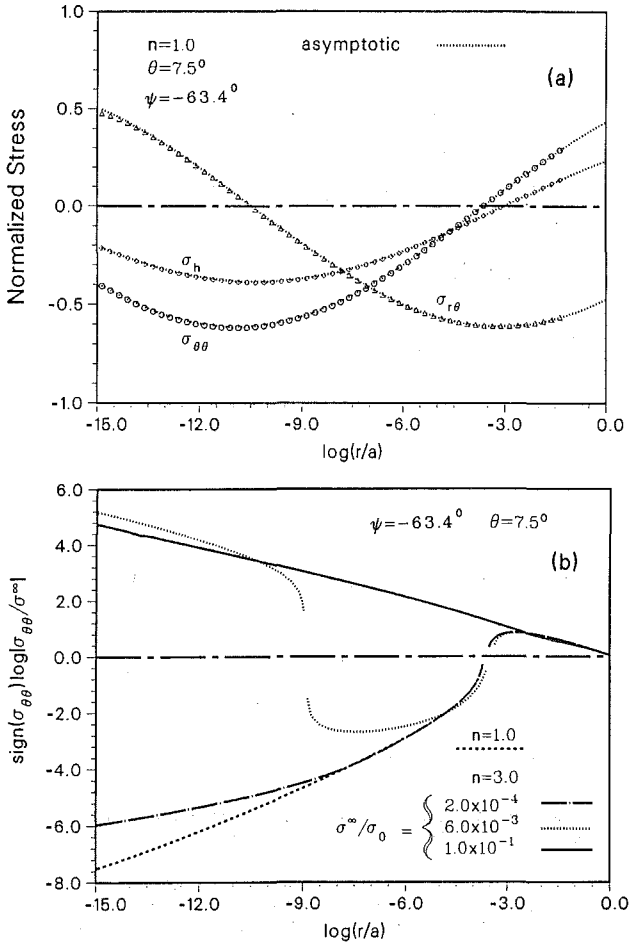


Fig. 14 Hoop stress near the bond line due to combined remote tension and shear. (*a*) Normalized stresses from linear elastic calculations ($n = 1$); the asymptotic stresses are included. (*b*) Normalized hoop stress for nonlinear material behavior with $n = 3$. The elastic ($n = 1$) result is included.

with examples given in Fig. 2. For the bimaterial geometries, shown in Fig. 2, the full form of the singular field in region 1 is given by (I-1) with the $g_{ij}^{(\alpha)}$ defined as follows. Let (ij) denote the polar indices $(r\theta)$ and define A as

$$A = \frac{1}{2\cosh(\pi\epsilon)}. \tag{I-2}$$

Then the $g_{ij}^{(\alpha)}$'s for the upper half-plane are

$$g_{rr}^{(1)} = A\Big\{e^{-\epsilon(\pi-\theta)}\Big\{3\cos[\theta/2+\epsilon\ln(r/2a)] + 2\epsilon\sin\theta\cos[\theta/2-\epsilon\ln(r/2a)] - \sin\theta\sin[\theta/2-\epsilon\ln(r/2a)]\Big\} - e^{\epsilon(\pi-\theta)}\cos[3\theta/2+\epsilon\ln(r/2a)]\Big\}, \tag{I-3}$$

$$g_{rr}^{(2)} = A\Big\{e^{-\epsilon(\pi-\theta)}\Big\{-3\sin[\theta/2+\epsilon\ln(r/2a)] + 2\epsilon\sin\theta\sin[\theta/2-\epsilon\ln(r/2a)] + \sin\theta\cos[\theta/2-\epsilon\ln(r/2a)]\Big\} + e^{\epsilon(\pi-\theta)}\sin[3\theta/2+\epsilon\ln(r/2a)]\Big\}, \tag{I-4}$$

$$g_{\theta\theta}^{(1)} = A\Big[e^{-\epsilon(\pi-\theta)}\Big\{\cos[\theta/2+\epsilon\ln(r/2a)] - 2\epsilon\sin\theta\cos[\theta/2-\epsilon\ln(r/2a)] + \sin\theta\sin[\theta/2-\epsilon\ln(r/2a)]\Big\} + e^{\epsilon(\pi-\theta)}\cos[3\theta/2+\epsilon\ln(r/2a)]\Big\}, \tag{I-5}$$

$$g_{\theta\theta}^{(2)} = A\Big\{e^{-\epsilon(\pi-\theta)}\Big\{-\sin[\theta/2+\epsilon\ln(r/2a)] - 2\epsilon\sin\theta\sin[\theta/2-\epsilon\ln(r/2a)] - \sin\theta\cos[\theta/2-\epsilon\ln(r/2a)]\Big\} - e^{\epsilon(\pi-\theta)}\sin[3\theta/2+\epsilon\ln(r/2a)]\Big\}, \tag{I-6}$$

$$g_{r\theta}^{(1)} = A\Big\{e^{-\epsilon(\pi-\theta)}\Big\{\sin[\theta/2+\epsilon\ln(r/2a)] - 2\epsilon\sin\theta\sin[\theta/2-\epsilon\ln(r/2a)] - \sin\theta\cos[\theta/2-\epsilon\ln(r/2a)]\Big\}$$

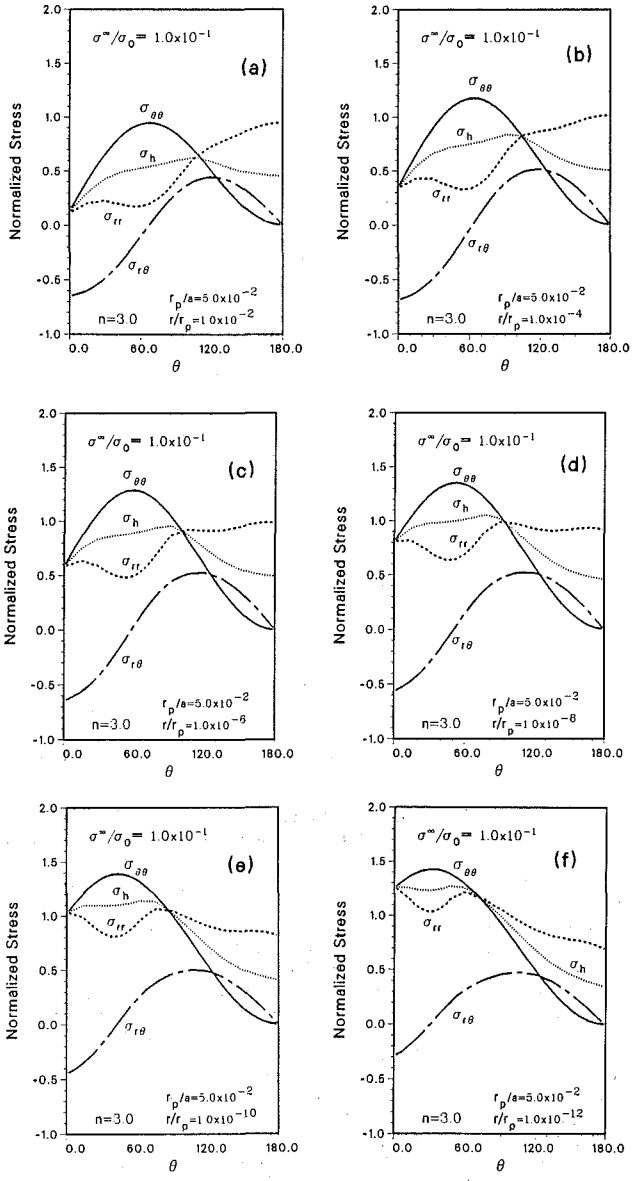


Fig. 15 Plots of angular variations of normalized stresses for the interface crack with $n = 3$ at six distances within the plastic zone for remote stresses given by $\sigma_{22}^{\infty}/\sigma_0 = 0.1$ and $\sigma_{12}^{\infty}/\sigma_0 = -0.2$.

Downloaded 03 May 2010 to 171.66.16.21. Redistribution subject to ASME license or copyright; see http://www.asme.org/terms/Terms_Use.cfm

$$+ e^{\epsilon(\pi-\theta)}\sin[3\theta/2+\epsilon\ \ln\ (r/2a)]\Big\}, \tag{I-7}$$

$$g^{(2)}_{r\theta}=A\Big\{e^{-\epsilon(\pi-\theta)}\Big\{\cos[\theta/2+\epsilon\ \ln\ (r/2a)] + 2\epsilon\ \sin\theta\ \cos[\theta/2-\epsilon\ \ln\ (r/2a)] - \sin\theta\ \sin[\theta/2-\epsilon\ \ln\ (r/2a)]\Big\} + e^{\epsilon(\pi-\theta)}\cos[3\theta/2+\epsilon\ \ln\ (r/2a)]\Big\}. \tag{I-8}$$

With $e^{-\epsilon\pi}$ in (I-3) through (I-8) replaced by $e^{\epsilon\pi}$, and $e^{\epsilon\pi}$ by $e^{-\epsilon\pi}$, the $g^{(\alpha)}_{ij}$ now pertain to the lower half-plane. These asymptotic fields can easily be rearranged into the form given by Sih and Rice (1964) by redefining **Q** as their **k** as described in Section 2.

APPENDIX II

Crack-Field Mode Interaction. In this section, we describe a method of calculating the individual stress modes for a crack subjected to mixed-mode loading. The method is applicable to cracks in isotropic or anisotropic media. Our method is motivated by Eshelby's (1956, 1961) notion of *interaction forces* and, in the present context, this means an *interaction energy release rate*, G_{int}. To begin, consider the field of a finite size crack (such as shown in Fig. 1) in an arbitrary anistropic but homogeneous elastic media. The remote tension loading, σ^{∞}_{22}, is augmented with the remote shear stress σ^{∞}_{12}, as depicted in Fig. 2(*c*). Let x_1, x_2 be the Cartesian coordinates such that the line crack lies along the x_1-axis over the region $-a\le x_1\le a$. Along the crack line

$$\sigma_{i2}=\sigma^{\infty}_{i2}\frac{|x_1|}{(x_1^2-a^2)^{1/2}};\quad |x_1|>a,\ x_2=0,\ i=1,2,3. \tag{II-1}$$

At a vanishingly small distance from the right crack tip and, with ξ defined as in the text (Fig. 1),

$$\sigma_{i2}=\sigma^{\infty}_{i2}\left(\frac{a}{2\zeta}\right)^{1/2},\quad \zeta>a,\ x_2=0. \tag{II-2}$$

Note that on the crack line the tractions are independent of elastic constants and are essentially set by static equilibrium (Barnett and Asaro, 1972).

In homogeneous media, the notion of stress-intensity factors is tied to the symmetry in the stress fields which are expressed in the form (r,θ are polar coordinates centered on the crack tip)

$$\sigma_{ij}=\sum_{\alpha=\text{I}}^{\text{III}}\frac{K_\alpha}{(2\pi r)^{1/2}}f^{(\alpha)}_{ij}(\theta) \tag{II-3}$$

where

$$f^{\text{I}}_{22}(\theta=0)=1,\quad f^{\text{I}}_{12}(0)=0=f^{\text{I}}_{32}(0) \tag{II-4$_1$}$$

$$f^{\text{II}}_{12}(\theta=0)=1,\quad f^{\text{II}}_{22}(0)=0=f^{\text{II}}_{32}(0) \tag{II-4$_2$}$$

and

$$f^{\text{III}}_{32}(\theta=0)=1,\ f^{\text{III}}_{22}(0)=0=f^{\text{III}}_{12}(0) \tag{II-4$_3$}$$

For the problem at hand then,

$$K_{\text{I}}=\sigma^{\infty}_{22}\sqrt{a\pi},\ K_{\text{II}}=\sigma^{\infty}_{12}\sqrt{a\pi},\ K_{\text{III}}=\sigma^{\infty}_{32}\sqrt{a\pi}. \tag{II-5$_{1,2,3}$}$$

The displacement fields will not possess such simple symmetries, and again, for the problem at hand, we note that the jump in displacement across the crack tip is given by Barnett and Asaro (1972) as

$$\Delta u_i=B^{-1}_{ij}\sigma_{j2}\sqrt{a/\pi}\ \sqrt{x/2\pi},\quad |x|\le a \tag{II-6}$$

where $\mathbf{B}^{-1}$ is the inverse of the so-called prelogarithmic energy-factor matrix, **B**.

For plane strain, we can define a *stress-intensity vector* with components

$$\mathbf{K}=\{K_{\text{II}},K_{\text{I}}\} \tag{II-7}$$

such that the crack traction vector and the displacement jumps on the crack line

$$\mathbf{t}=\{\sigma_{12},\sigma_{22}\} \tag{II-8}$$

and

$$\Delta\mathbf{u}=\{\Delta u_1,\Delta u_2\} \tag{II-9}$$

are given by

$$\mathbf{t}=\frac{1}{\sqrt{2\pi x}}\mathbf{K},\quad x>a \tag{II-10}$$

and

$$\Delta\mathbf{u}=\frac{1}{\pi}\mathbf{B}^{-1}\cdot\mathbf{K}\sqrt{x/2\pi},\quad |x|<a. \tag{II-11}$$

The energy release rate can be calculated from the virtual work integral of (2.14) and is given by Barnett and Asaro (1972) as

$$G=\frac{1}{8\pi}K_\alpha B^{-1}_{\alpha\beta}K_\beta \tag{II-12}$$

where the indices α,β can be interpreted such that 1 is identified with II and 2 with I. Note that, for isotropic media, **B** is diagonal, with components

$$B_{11}=B_{22}=\frac{\mu}{4\pi(1-\nu)}\ \text{and}\ B_{33}=\frac{\mu}{4\pi}, \tag{II-13}$$

and the usual expressions for **t**, $\Delta\mathbf{u}$, and G are recovered, i.e.,

$$G=\frac{(1-\nu)}{2\mu}[K_{\text{I}}^2+K_{\text{II}}^2]+\frac{1}{2\mu}K_{\text{III}}^2. \tag{II-14}$$

Stress mode decoupling in a given mixed-mode stress field is accomplished through computation of what might be referred to as an *interaction energy release rate*. To appreciate the procedure, the details of calculating the K_{I} component of a total crack-tip field are illustrated.

We first note that, for the actual (mixed-mode) crack field, the crack extension force is given by

$$G=\frac{1}{8\pi}\Big[K_{\text{I}}B^{-1}_{11}K_{\text{I}}+2K_{\text{I}}B^{-1}_{12}K_{\text{II}}+2K_{\text{I}}B^{-1}_{13}K_{\text{III}} + (\text{terms not involving } K_{\text{I}})\Big]. \tag{II-15}$$

Now suppose that an auxiliary pure Mode I field, of intensity k_{I}, is superimposed on the actual field and the crack extension force again computed; the result is

$$G_{\text{tot}}=\frac{1}{8\pi}\Big[(K_{\text{I}}+k_{\text{I}})B^{-1}_{11}(K_{\text{I}}+k_{\text{I}})+2(K_{\text{I}}+k_{\text{I}})B^{-1}_{12}K_{\text{II}} + 2(K_{\text{I}}+k_{\text{I}})B^{-1}_{13}K_{\text{III}}+(\text{terms not involving } K_{\text{I}} \text{ or } k_{\text{I}})\Big]. \tag{II-16}$$

The auxiliary field itself has the energy release rate

$$G_{\text{aux}}=\frac{1}{8\pi}k_{\text{I}}B^{-1}_{11}k_{\text{I}}. \tag{II-17}$$

From the foregoing relations, we can define an interaction extension force as

$$G_{\text{int}}=G_{\text{tot}}-G-G_{\text{aux}} =\frac{1}{8\pi}\Big[2k_{\text{I}}B^{-1}_{11}K_{\text{I}}+2k_{\text{I}}B^{-1}_{12}K_{\text{II}}+2k_{\text{I}}B^{-1}_{13}K_{\text{III}}\Big]. \tag{II-18}$$

Downloaded 03 May 2010 to 171.66.16.21. Redistribution subject to ASME license or copyright; see http://www.asme.org/terms/Terms_Use.cfm

All three energy release rates, G, G_{tot}, and G_{aux}, including G_{int} itself, are computable from either line or domain integrals as explained in Sections 3.3–3.5. When the previously mentioned calculations are performed for the other two modes a simple linear system of equations of the form

$$G_{int}^{(\alpha)} = \frac{1}{4\pi} k_\alpha B_{\alpha s}^{-1} K_s, \quad \text{(no sum on } \alpha = 1,2,3) \tag{II-19}$$

results which may easily be solved for the K_s; when the k_α are assigned unit values the solution for the Q_s are

$$K_\alpha = 4\pi B_{\alpha s} G_{int}^{(s)}. \tag{II-20}$$

It may be noted that G_{int} is readily evaluated with high precision via the domain integrals described in Section 3.5.

A completely analogous procedure can be applied to evaluate the respective intensities of the two stress modes Q_1 and Q_2 for the present interface crack being investigated. For plane strain, we note by (2.16) that, if G is written in the form

$$G = Q_\alpha B_{\alpha\beta}^{-1} Q_\beta, \tag{II-21}$$

that $\mathbf{B}$ is diagonal with the nonzero components

$$B_{11}^{-1} = B_{22}^{-1} = B^{-1} = \{(1-\nu_1)/\mu_1\}/(4\cosh^2 \pi\epsilon). \tag{II-22}$$

Once the two $G_{int}^{(\alpha)}$ are evaluated, the two stress intensities are determined from

$$Q_\alpha = \frac{1}{2} B G_{int}^{(\alpha)}. \tag{II-23}$$

Downloaded 03 May 2010 to 171.66.16.21. Redistribution subject to ASME license or copyright; see http://www.asme.org/terms/Terms_Use.cfm

On the Mechanical Modeling of the Interfacial Region in Bonded Half-Planes[1]

F. Delale
Associate Professor,
Department of Mechanical Engineering,
The City College of New York,
New York, NY

F. Erdogan
Professor of Mechanics,
Department of Mechanical Engineering
and Mechanics,
Building No. 19,
Lehigh University,
Bethlehem, PA 18015
Fellow ASME

In this paper the crack problem for two bonded dissimilar homogeneous elastic half-planes is considered. It is assumed that the interfacial region can be modeled by a very thin layer of nonhomogeneous material. Even though the formulation given is rather general, in the particular model used the elastic properties of the interfacial layer are assumed to vary continuously between that of the two semi-infinite planes. The layer is assumed to have a series of collinear cracks parallel to the nominal interface. The related mixed boundary problem is formulated for arbitrary crack surface tractions which can be used to accommodate any general external loading condition through a proper superposition. A single crack problem for two different material combinations is solved as examples, and Modes I and II stress-intensity factors, the energy release rate and the direction of a probable crack growth are calculated.

1 Introduction

In studying the mechanics, in general, and fracture mechanics, in particular, of adhesively bonded joints and variety of composite materials, one often needs to model the interface or the interface region between the adjacent constituents. In the simplest model, one assumes that the interface is a smooth surface along which the elastic constants of the medium are discontinuous. If, on the other hand, a very thin layer of a third material is used as adhesive to bond the two primary components, the adhesive layer may be approximated by a pair of generally uncoupled shear and tension springs, neglecting the variation of stresses in the layer in thickness direction. A somewhat more realistic version of this model would be to treat the adhesive layer as a separate homogeneous elastic continuum. Fracture mechanics studies in such piecewise homogeneous materials invariably require the elasticity solution for a crack near or at an interface. These problems have been rather extensively studied and there are a large number of solutions in the technical literature for isotropic, orthotropic, and anisotropic bonded materials containing cracks of various locations and orientations. For typical studies, one may refer to, for example, [1] for a brief review, [2–7] for standard interface crack solutions, [8–12] for an interface crack with contacting crack tip regions, [13–20] for cracks lying in the neighborhood of or intersecting interfaces, [21] for the shear/tension spring model of adhesive layers, and [22–24] for continuum modeling of the adhesive layer.

As indicated in the foregoing studies and elsewhere, as long as the crack tip is embedded in a homogeneous medium, the stress state around the crack tip would have the standard square-root singularity and the conventional methods of fracture mechanics would be applicable. On the other hand, if the crack is located on or intersects the interface, then the linear elasticity solutions predict certain physically disagreeable results. In a piecewise homogeneous composite medium, if the crack intersects the interface perpendicularly, then the power of the stress singularity is real but is not equal to 1/2. Although this result is physically acceptable, it is not readily suitable for conventional fracture mechanics applications. If the crack is located on the interface or generally intersects it at an angle other than 90°, then the power of stress singularity is a complex number implying oscillations in stresses and crack surface displacements. Even though in the important case of interface crack, the size of the zone of displacement interference (or stress oscillations) is shown to be very small (relative to the crack size) and the strain-energy release rate is largely uninfluenced and may readily be evaluated, partly for theoretical reasons, the problem has attracted a great deal of attention. The crack tip contact model (e.g., [8–12]) tries to resolve the problem within the confines of linear elasticity. Our view is that the resolution of this anomalous behavior predicted by the linear elastic theory will have to come almost certainly from the proper modeling of the bonded materials. Furthermore, as one might expect on physical grounds, the oscillatory behavior of stresses and displacements very near the interface crack tips does not seem to disappear even if the materials are assumed to be nonlinear. For example, recent analytical results obtained from the solution of a nonlinear elastic half-space, acted upon by a rigid stamp, predict oscilla-

[1]This work was supported by NSF under the Grant MSM-8613611 and by NASA-Langley under the Grant NAG-1-713.

Contributed by the Applied Mechanics Division for presentation at the Winter Annual Meeting, Chicago, IL, November 28 to December 2, 1988, of The American Society of Mechanical Engineers.

Discussion on this paper should be addressed to the Editorial Department, ASME, United Engineering Center, 345 East 47th Street, New York, N.Y. 10017, and will be accepted until two months after final publication of the paper itself in the JOURNAL OF APPLIED MECHANICS. Manuscript received by ASME Applied Mechanics Division, June 2, 1987.

Paper No. 88-WA/APM-25.

Copyright © 1988 by ASME
Downloaded 03 May 2010 to 171.66.16.21. Redistribution subject to ASME license or copyright; see http://www.asme.org/terms/Terms_Use.cfm

tions similar to the linear theory which disappear only when the Poisson's ratio approaches 1/2 [25]. Even though a highly refined finite-element solution of the same problem as that considered in [25] and given in [26] and the solution of a rigid rectangular stamp on a harmonic elastic half-space [27], both obtained from a small deformation theory, show no stress oscillations, in light of the results found in [25], the reason for this appears to be the assumed material incompressibility rather than the nonlinearity.[2]

Up to now in modeling the crack problems for bonded materials, it has been assumed that the medium is piecewise homogeneous, that is, the interfaces are smooth surfaces across which the material parameters exhibit a jump discontinuity. In studying the micromechanics of the problem, particularly for a crack lying along or intersecting the nominal interface, such an idealized interface model may be too unrealistic. For two dissimilar materials, whatever the actual mechanism of binding at the atomic or the molecular level, in many cases for the sake of thermodynamical consistency, the "interfacial layer" needs to be considered as a distinct phase or a distinct chemical species [28]. The thickness of this layer may vary from that of few atomic layers to microns. There is always some interdiffusion or interpenetration of molecules in the interfacial region that would result in a material which is, from the viewpoint of mechanical properties, structurally different than the adhering base materials.

The justification for assuming the existence of a distinct interfacial layer is perhaps strongest for bonded dissimilar materials in which at least one of the phases is polymeric; see, for instance, the review articles by Stromberg, Huntsberger, Kaelble, and Gardon in [29]. For example, in graphite-epoxy systems, changing the surface properties of fibers is needed for efficient coupling and consequently for improved "interfacial strength." The coupling is generally accomplished by compounds that contain molecular end groups capable of interacting with certain sites on the fiber surface on one hand and with functional groups of the matrix on the other [30]. Improved interfacial strength, on the other hand, results in generally decreased impact resistance. It is, therefore, desirable to treat the surface of fibers in such a way that the interfacial layer would be sufficiently tough for impact resistance as well as having strong adhesion to fiber and to the epoxy matrix. One way of doing this would be to coat the fibers by a polymer interlayer [31]. An electrodeposition method of coating graphite fibers by an interphase polymer is described in [31]. The electron microprobe line scans across the interfacial region, given in [31], suggest the existence of a layer of distinct and steeply varying properties between the fiber and the bulk matrix. Other interfacial processes yielding a different morphology include, for example, crystallization (resulting in a columnar structure as in PEEK-carbon composites) and copolymerization of the matrix with the coupling agent; see [32] and [33] for a review of recent work.

Although quantitative investigations regarding the mechanical characterization is still lacking, the foregoing studies indicate that the interfacial region often constitutes not a single phase but rather a thin layer that may exhibit a steep gradient of composition, morphology, and consequently, mechanical behavior. Because of the interdiffusion character of the binding process between the interfacial region and the homogeneous adherends, one may assume also that, in many material systems, the spatial variation of the material parameters would be continuous; that is, there would be no jump discontinuity in the distribution of, for example, elastic moduli of the composite medium. The micromechanics problems that need to be studied relating to the fracture initiation and propagation in and near the interfacial regions in composites are, therefore, the continuum (linear or nonlinear) elasticity problems for a crack having certain positions and orientations with respect to the nominal interface.

[2]It should be pointed out that if both adjacent materials are incompressible, the linear elastic theory also predicts no stress oscillations.

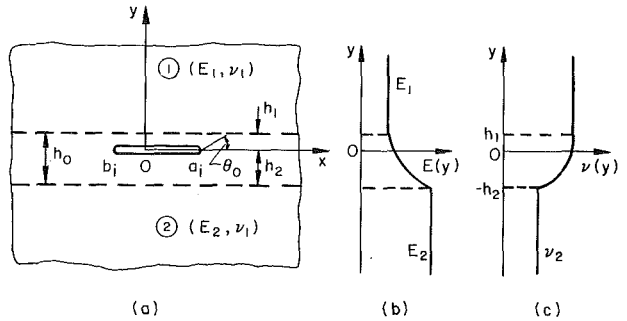


Fig. 1 Notation for two homogeneous elastic half-planes bonded through a nonhomogeneous layer with collinear cracks

The problem considered in this paper is that of two homogeneous isotropic half-planes bonded through a nonhomogeneous layer of constant thickness. It is assumed that the elastic moduli vary continuously throughout the composite medium having, therefore, steep gradients within the interfacial layer. A crack is assumed to be located parallel to the nominal interface and at an arbitrary position in the layer, Fig. 1. Due to the lack of material symmetry with respect to the plane of the crack, the problem is necessarily one of mixed mode. The linear perturbation problem considered is formulated for arbitrary crack surface tractions. Therefore, by using superposition the problem can be solved for any arbitrary external loading. The in-plane elasticity solution for a crack in an infinite nonhomogeneous medium is given in [34] and the antiplane shear problem for two bonded nonhomogeneous planes may be found in [35]. Other solutions include the plane steady-state propagation of a crack [36] and the antiplane shear problem [37] in a nonhomogeneous elastic plane.

2 Basic Equations of Interfacial Region

The plane elasticity problem under consideration is described in Fig. 1, showing basically a nonhomogeneous isotropic medium with a crack. By observing that the elastic moduli are constant for $y > h_1$ and $y < -h_2$, the problem may be formulated by assuming that the medium consists of three different materials perfectly bonded along the planes $y = h_1$ and $y = -h_2$. If $\mathrm{E}(x, y)$ and $\nu(x, y)$ $(-h_2 < y < h_1, -\infty < x < \infty)$, are the elastic moduli of the layer, then in terms of the Airy stress function F defined by

$$\sigma_{xx} = \frac{\partial^2 F}{\partial y^2}, \quad \sigma_{yy} = \frac{\partial^2 F}{\partial x^2}, \quad \sigma_{xy} = -\frac{\partial^2 F}{\partial x \partial y}, \tag{1}$$

The compatibility condition may be expressed as

$$\nabla^4 F - \frac{2}{\mathrm{E}}\left(\frac{\partial \mathrm{E}}{\partial x}\frac{\partial}{\partial x} + \frac{\partial \mathrm{E}}{\partial y}\frac{\partial}{\partial y}\right)\nabla^2 F + \left[\nu\frac{\partial^2 \mathrm{E}}{\partial y^2} - \frac{2\nu}{\mathrm{E}}\left(\frac{\partial \mathrm{E}}{\partial y}\right)^2 - \frac{\partial^2 \mathrm{E}}{\partial x^2} + \frac{2}{\mathrm{E}}\left(\frac{\partial \mathrm{E}}{\partial x}\right)^2 + 2\frac{\partial \mathrm{E}}{\partial y}\frac{\partial \nu}{\partial y} - \mathrm{E}\frac{\partial^2 \nu}{\partial y^2}\right]\frac{1}{\mathrm{E}}\frac{\partial^2 F}{\partial x^2} + \left[\nu\frac{\partial^2 \mathrm{E}}{\partial x^2} - \frac{2\nu}{\mathrm{E}}\left(\frac{\partial \mathrm{E}}{\partial x}\right)^2 - \frac{\partial^2 \mathrm{E}}{\partial y^2} + \frac{2}{\mathrm{E}}\left(\frac{\partial \mathrm{E}}{\partial y}\right)^2 + 2\frac{\partial \mathrm{E}}{\partial x}\frac{\partial \nu}{\partial X}\right.$$

Downloaded 03 May 2010 to 171.66.16.21. Redistribution subject to ASME license or copyright; see http://www.asme.org/terms/Terms_Use.cfm

$$-\mathrm{E}\frac{\partial^2\nu}{\partial x^2}\Big]\frac{1}{\mathrm{E}}\frac{\partial^2 F}{\partial y^2}+\Big[(1+\nu)\Big(\frac{2}{\mathrm{E}}\frac{\partial \mathrm{E}}{\partial x}\frac{\partial \mathrm{E}}{\partial y}-\frac{\partial^2 \mathrm{E}}{\partial x\partial y}\Big)$$

$$+\mathrm{E}\frac{\partial^2\nu}{\partial x\partial y}-\frac{\partial \mathrm{E}}{\partial y}\frac{\partial\nu}{\partial x}-\frac{\partial \mathrm{E}}{\partial x}\frac{\partial\nu}{\partial y}\Big]\frac{2}{\mathrm{E}}\frac{\partial^2 F}{\partial x\partial y}=0. \tag{2}$$

If we further assume that the functions E and ν are independent of x and $\mathrm{E}(y)$ has the form

$$\mathrm{E}(y)=\mathrm{E}_0 e^{\beta y}, \tag{3}$$

equation (2) would reduce to

$$\nabla^4 F-2\beta\frac{\partial}{\partial y}\nabla^2 F+\beta^2\frac{\partial^2 F}{\partial y^2}$$

$$-\Big(\frac{d^2\nu}{dy^2}-2\beta\frac{d\nu}{dy}+\beta^2\nu\Big)\frac{\partial^2 F}{\partial x^2}=0. \tag{4}$$

It was previously shown that the value of the Poisson's ratio does not significantly influence the stress-intensity factors [34]. Thus, in this paper, we will further restrict the study to a special class of materials for which

$$\frac{d^2\nu}{dy^2}-2\beta\frac{d\nu}{dy}+\beta^2\nu=0, \tag{5}$$

giving the following particular variation:

$$\nu(y)=(A_0+B_0 y)e^{\beta y}. \tag{6}$$

The function $\nu(y)$ given by (6) is subject to the restriction that $0\le\nu\le 0.5$ for $-h_2<y<h_1$. The unknown constants E_0, β, A_0 and B_0 in (3) and (6) are determined from the assumed continuity conditions[3] for $\mathrm{E}(y)$ and $\nu(y)$ at $h=h_1$ and $y=-h_2$, namely

$$\mathrm{E}_0 e^{\beta h_1}=\mathrm{E}_1,\quad \mathrm{E}_0 e^{-\beta h_2}=\mathrm{E}_2,$$

$$(A_0+B_0 h_1)e^{\beta h_1}=\nu_1,\quad (A_0-B_0 h_2)e^{-\beta h_2}=\nu_2 \tag{7a-d}$$

From (7), it follows that

$$\beta=\frac{1}{h_0}\log(\mathrm{E}_1/\mathrm{E}_2),\quad \mathrm{E}_0=\mathrm{E}_1 e^{-\beta h_1}$$

$$A_0=\nu_2 e^{\beta h_2}+B_0 h_2,\quad B_0=\frac{1}{h_0}(\nu_1 e^{-\beta h_1}-\nu_2 e^{\beta h_2}), \tag{8}$$

where $h_0=h_1+h_2$ is the thickness of the layer.

With the assumption (5), the governing equation (4) for the interfacial layer becomes

$$\nabla^4 F-2\beta\frac{\partial}{\partial y}\nabla^2 F+\beta^2\frac{\partial^2 F}{\partial y^2}=0. \tag{9}$$

By using standard Fourier transforms, the solution of (9) may be obtained either by considering the two strips $0<y<h_1$ and $-h_2<y<0$ separately or by expressing F as the sum of two functions F_1 and F_2, respectively, associated with an infinite plane containing a crack on the x-axis and with an uncracked strip $-h_2<y<h_1$. Following the latter procedure, for the infinite plane we have[4]

$$F_1(x,y)=\int_{-\infty}^{\infty}G_1(y,\alpha)e^{-i\alpha x}d\alpha. \tag{10}$$

[3]The formulation given in this paper is not dependent on the assumption of continuity of E and ν at $y=h_1$ and $y=-h_2$. If E and ν are discontinuous, then the right-hand sides in (7) must be replaced by $\mathrm{E}(h_1-0)$, $\mathrm{E}(-h_2+0)$, $\nu(h_1-0)$ and $\nu(-h_2+0)$, respectively. Indeed in polymer matrix composites generally the elastic moduli are continuous only along the interfacial region/matrix interface. This is important, because in many cases, this interface is also the weakest cleavage plane in the composite.

[4]The reason for selecting this procedure is to obtain, at the same time, the formulation of an infinite nonhomogeneous plane containing a crack which, for the mixed-mode condition considered, is not available.

By letting $G_1(y,\alpha)=A(\alpha)\exp(my)$, from (9) and (10), the characteristic equation is found to be

$$(m^2-\beta m-\alpha^2)^2=0. \tag{11}$$

The roots of (11) are

$$m_1=m_3=\frac{\beta}{2}-\sqrt{\alpha^2+\beta^2/4},\quad \mathrm{Re}(m_1)<0, \tag{12}$$

$$m_2=m_4=\frac{\beta}{2}+\sqrt{\alpha^2+\beta^2/4},\quad \mathrm{Re}(m_2)>0. \tag{13}$$

Considering the continuity conditions

$$\sigma_{yy}(x,+0)=\sigma_{yy}(x,-0),\quad \sigma_{xy}(x,+0)=\sigma_{xy}(x,-0) \tag{14}$$

and the conditions of regularity at $y=\mp\infty$, we find

$$G_1(y,\alpha)=\begin{cases}(A+By)e^{m_1 y}, & y>0,\\ [A+(B+\lambda_1 A)y]e^{m_2 y}, & y<0,\end{cases} \tag{15}$$

where

$$\lambda_1=m_1-m_2=-2\sqrt{\alpha^2+\beta^2/4}. \tag{16}$$

If we now define the functions

$$f_1(x)=\frac{\partial}{\partial x}[u_y(x,+0)-u_y(x,-0)], \tag{17a}$$

$$f_2(x)=\frac{\partial}{\partial x}[u_x(x,+0)-u_x(x,-0)],\quad (-\infty<x<\infty), \tag{17b}$$

$$g_1(\alpha)=\frac{\mathrm{E}_0}{2\pi}\int_{-\infty}^{\infty}f_1(t)e^{i\alpha t}dt, \tag{18a}$$

$$g_2(\alpha)=\frac{\mathrm{E}_0}{2\pi}\int_{-\infty}^{\infty}f_2(t)e^{i\alpha t}dt, \tag{18b}$$

and let

$$A(\alpha)=\gamma_1(\alpha)g_1(\alpha)+\gamma_2(\alpha)g_2(\alpha), \tag{19a}$$

$$B(\alpha)=\gamma_3(\alpha)g_1(\alpha)+\gamma_4(\alpha)g_2(\alpha), \tag{19b}$$

by using (1), (10), (15), and the Hooke's law, after some lengthy manipulations, we obtain

$$\gamma_1(\alpha)=-\frac{2i\alpha m_1}{\lambda_1^2(2\alpha^2+\beta m_1)},\quad \gamma_2(\alpha)=\frac{\beta m_1}{\lambda_1^2(2\alpha^2+\beta m_1)},$$

$$\gamma_3(\alpha)=\frac{i\alpha m_1}{\lambda_1(2\alpha^2+\beta m_1)},\quad \gamma_4(\alpha)=\frac{\alpha^2}{\lambda_1(2\alpha^2+\beta m_1)}, \tag{20a-d}$$

$$\sigma_{ij}^{(1)}(x,y)=\int_{-\infty}^{\infty}\sum_1^2 K_{ijk}(x,y,t)f_k(t)dt,\quad (i,j=x,y),\quad y>0, \tag{21}$$

$$u_i^{(1)}(x,y)=\int_{-\infty}^{\infty}\sum_1^2 K_{ik}(x,y,t)f_k(t)dt,\quad (i=x,y),\quad y>0, \tag{22}$$

$$\sigma_{ij}^{(1)}(x,y)=\int_{-\infty}^{\infty}\sum_1^2 L_{ijk}(x,y,t)f_k(t)dt,\quad (i,j=x,y),\quad y<0, \tag{23}$$

$$u_i^{(1)}(x,y)=\int_{-\infty}^{\infty}\sum_1^2 L_{ik}(x,y,t)f_k(t)dt,\quad (i=x,y),\quad y<0. \tag{24}$$

where the kernels K and L are known functions. The expressions of these functions and the relatively straightforward

Downloaded 03 May 2010 to 171.66.16.21. Redistribution subject to ASME license or copyright; see http://www.asme.org/terms/Terms_Use.cfm

details of the remaining analysis concerning the derivation of the integral equations of the problem may be found in [38].

We now express the Airy stress function associated with the uncracked nonhomogeneous strip $-h_2 < y < h_1$ as

$$F_2(x,y) = \int_{-\infty}^{\infty} G_2(y,\alpha) e^{-i\alpha x} d\alpha. \tag{25}$$

From (9) and (25), it follows that

$$G_2(y,\alpha) = (C_1 + C_2 y) e^{m_1 y} + (C_3 + C_4 y) e^{m_2 y}, \tag{26}$$

where m_1 and m_2 are again given by (13) and the functions $C_i(\alpha)$, $(i = 1, \ldots, 4)$ are unknown. By using (1) and the Hooke's law and by carrying out the necessary integrations, from (25) and (26), the stresses $\sigma_{ij}^{(2)}$ and the displacements $u_i^{(2)}$, $(i, j = x, y)$ may be obtained in terms of C_k, $(k = 1, \ldots, 4)$ in a straightforward manner.

We now note that the stresses and displacements in the nonhomogeneous strip, $-h_2 < y < h_1$, $-\infty < x < \infty$, containing a system of collinear cracks on the x-axis may be expressed by adding the two sets of solutions as follows:

$$\sigma_{ij}(x,y) = \sigma_{ij}^{(1)}(x,y) + \sigma_{ij}^{(2)}(x,y), \quad (i,j = x,y), \tag{27}$$

$$u_i(x,y) = u_i^{(1)}(x,y) + u_i^{(2)}(x,y), \quad (i = x,y). \tag{28}$$

Up to this point, the formulation of the cracked strip problem is complete. The four unknowns $C_1, \ldots, C_4$ are accounted for by the boundary conditions at $y = h_1$ and $y = -h_2$ and the remaining unknown functions f_1 and f_2 are determined by using the following mixed boundary conditions at $y = 0$:

$$\sigma_{yy}(x,0) = -p(x), \quad \sigma_{xy}(x,0) = -q(x), \quad x \in L, \tag{29}$$

$$u_x(x,+0) - u_x(x,-0) = 0, \quad u_y(x,+0) - u_y(x,-0) = 0, \quad x \in L', \tag{30}$$

where p and q are known functions, L represents a series of cracks (b_i, a_i), $(i = 1, \ldots, n)$ on the x-axis and L' is the complement of L in $(-\infty \le x \le \infty)$. By substituting from (27) into (29), one obtains the integral equations needed to determine f_1 and f_2. One may further note that the solution for the nonhomogeneous infinite plane containing cracks along the x-axis is obtained by letting $h_1 \to \infty$ and $h_2 \to \infty$, in which case the functions $C_1, \ldots, C_4$ are zero.

Similarly, the stresses and displacements $\sigma_{ij}^{(3)}$, $u_i^{(3)}$ and $\sigma_{ij}^{(4)}$, $u_i^{(4)}$, $(i, j = x, y)$ for the elastic homogeneous half-planes $y > 0$ and $y < 0$ may be obtained by expressing the corresponding Airy stress functions as follows:

$$F_3(x,y) = \int_{-\infty}^{\infty} [B_1(\alpha) + yB_2(\alpha)] e^{-|\alpha| y - i\alpha x} d\alpha, \quad (0 < y < \infty), \tag{31}$$

$$F_4(x,y) = \int_{-\infty}^{\infty} [D_1(\alpha) + yD_2(\alpha)] e^{|\alpha| y - i\alpha x} d\alpha, \quad (-\infty < y < 0). \tag{32}$$

3 The Integral Equations

The formulation given in the previous section for the nonhomogeneous strip and the homogeneous half-planes contain eight unknown functions (of α); namely, C_1, C_2, C_3, C_4, B_1, B_2, D_1, and D_2. These functions are determined from the following conditions of continuity of the stress and displacement vectors for $y = h_1$ and $y = -h_2$:

$$\sigma_{yy}^{(1)}(x,h_1) + \sigma_{yy}^{(2)}(x,h_1) = \sigma_{yy}^{(3)}(x,0), \tag{33a}$$

$$\sigma_{xy}^{(1)}(x,h_1) + \sigma_{xy}^{(2)}(x,h_1) = \sigma_{xy}^{(3)}(x,0), \tag{33b}$$

$$u_x^{(1)}(x,h_1) + u_x^{(2)}(x,h_1) = u_x^{(3)}(x,0), \tag{33c}$$

$$u_y^{(1)}(x,h_1) + u_y^{(2)}(x,h_1) = u_y^{(3)}(x,0), \quad (-\infty < x < \infty) \tag{33d}$$

$$\sigma_{yy}^{(1)}(x,-h_2) + \sigma_{yy}^{(2)}(x,-h_2) = \sigma_{yy}^{(4)}(x,0), \tag{34a}$$

$$\sigma_{xy}^{(1)}(x,-h_2) + \sigma_{xy}^{(2)}(x,-h_2) = \sigma_{xy}^{(4)}(x,0), \tag{34b}$$

$$u_x^{(1)}(x,-h_2) + u_x^{(2)}(x,-h_2) = u_x^{(4)}(x,0), \tag{34c}$$

$$u_y^{(1)}(x,-h_2) + u_y^{(2)}(x,-h_2) = u_y^{(4)}(x,0), \quad (-\infty < x < \infty). \tag{34d}$$

The eight unknown functions $C_1, \ldots, C_4, B_1, B_2, D_1$ and D_2 are obtained by substituting from (27) and (28) and similar equations obtained from (31) and (32) into (33) and (34) in the following form (see [38] for details)

$$C_j(\alpha) = C_{j1}(\alpha) \int_{-\infty}^{\infty} f_1(t) e^{i\alpha t} dt + C_{j2}(\alpha) \int_{-\infty}^{\infty} f_2(t) e^{i\alpha t} dt, \quad (j = 1, \ldots, 4), \tag{35}$$

$$B_j(\alpha) = B_{j1}(\alpha) \int_{-\infty}^{\infty} f_1(t) e^{i\alpha t} dt + B_{j2}(\alpha) \int_{-\infty}^{\infty} f_2(t) e^{i\alpha t} dt, \quad (j = 1,2), \tag{36}$$

$$D_j(\alpha) = D_{j1}(\alpha) \int_{-\infty}^{\infty} f_1(t) e^{i\alpha t} dt + D_{j2}(\alpha) \int_{-\infty}^{\infty} f_2(t) e^{i\alpha t} dt, \quad (j = 1,2). \tag{37}$$

The functions C_{ij}, B_{kj} and D_{kj} $(i = 1, \ldots, 4, j = 1, 2, k = 1, 2)$ may be obtained by solving the related algebraic system and identifying the coefficients of g_1 and g_2. This may be done by using one of the symbolic manipulators and it will henceforth be assumed that the functions C_{ij}, B_{kj} and D_{kj} are known.

In the foregoing formulation, at $y = 0$, the mixed boundary conditions (29) and (30) have been replaced by (17), that is, it is assumed that at $y = 0$, in addition to satisfying the continuity of the stress vector, the displacement derivatives are prescribed. Now, let us assume that the nonhomogeneous layer contains a series of cracks on the x-axis along $L = \Sigma_1^n L_i$, $L_i = (b_i, a_i)$, $(-\infty < b_1, a_n < \infty)$. Clearly, f_1 and f_2 will be unknown on L and will be zero elsewhere on the x-axis and the information regarding the crack surface tractions (29) will have to be used to determine f_1 and f_2. Thus, from (17), (29), (30), the integral equations of the problem may be obtained as follows

$$\frac{E_0}{4\pi} \int_L f_1(t) \frac{dt}{t-x} + \int_L \sum_1^2 k_{ij}(x,t) f_j(t) dt = -p(x), \quad x \in L, \tag{38a}$$

$$\frac{E_0}{4\pi} \int_L f_2(t) \frac{dt}{t-x} + \int_L \sum_1^2 k_{2j}(x,t) f_j(t) dt = -q(x), \quad x \in L, \tag{38b}$$

where the Cauchy kernels have been separated through a standard asymptotic analysis [34] and [38].

4 Stress-Intensity Factors

From (27) and (28) and the derivation of the integral equations, it is clear that the left-hand sides in (38) represent the stress components $\sigma_{yy}(x, 0)$ and $\sigma_{xy}(x, 0)$ on the entire x-axis. Thus, by observing that the fundamental function of the singular integral equations (38) is [39]

$$X(z) = \prod_1^n [(z-a_i)(z-b_i)]^{-1/2}, \tag{39}$$

and defining the stress-intensity factors at a crack tip a_i by

$$k_1(a_i) = \lim_{x \to a_i} \sqrt{2(x-a_i)}\, \sigma_{yy}(x,0), \tag{40a}$$

$$k_2(a_i) = \lim_{x \to a_i} \sqrt{2(x-a_i)}\, \sigma_{xy}(x,0), \tag{40b}$$

from (38) it may easily be shown that (see, for example, [35] for the procedure followed)

Downloaded 03 May 2010 to 171.66.16.21. Redistribution subject to ASME license or copyright; see http://www.asme.org/terms/Terms_Use.cfm

Table 1 Stress-intensity factors for the nonhomogeneous medium A; $p(x) = p_0$, $q(x) = 0$

h_1/h_0	a/h_1	$k_1(a)/p_0\sqrt{a}$	$k_2(a)/p_0\sqrt{a}$	$10^6G(a)/p_0^2a$	$\theta_0(a)$
0.25	0.1	1.001	0.001	0.138	
	0.2	1.003	0.004	0.138	
	0.5	1.016	0.026	0.142	
	1.0	1.044	0.051	0.150	
	2.0	1.090	0.088	0.165	
	4.0	1.134	0.131	0.180	
	8.0	1.159	0.164	0.189	
	10.0	1.166	0.168	0.191	
0.50	0.1	1.001	0.004	0.182	0.46
	0.2	1.004	0.023	0.183	2.62
	0.5	1.014	0.058	0.187	6.51
	1.0	1.026	0.092	0.193	10.09
	2.0	1.036	0.127	0.197	13.58
	4.0	1.039	0.151	0.200	15.90
	8.0	1.042	0.165	0.202	17.17
	10.0	1.046	0.169	0.204	17.50
0.75	0.1	0.998	0.011	0.238	
	0.2	0.993	0.031	0.235	
	0.5	0.970	0.067	0.226	
	1.0	0.950	0.098	0.218	
	2.0	0.935	0.129	0.213	
	4.0	0.923	0.148	0.209	
	8.0	0.915	0.158	0.206	
	10.0	0.913	0.160	0.205	

Table 2 Stress-intensity factors for the nonhomogeneous medium A; $p(x) = 0$, $q(x) = q_0$

	$h_1/h_0 = 0.25$		$h_1/h_0 = 0.50$			$h_1/h_0 = 0.75$	
a/h_1	$\frac{k_1(a)}{q_0\sqrt{a}}$	$\frac{k_2(a)}{q_0\sqrt{a}}$	$\frac{k_1(a)}{q_0\sqrt{a}}$	$\frac{k_2(a)}{q_0\sqrt{a}}$	$\theta_0(-a)$	$\frac{k_1(a)}{q_0\sqrt{a}}$	$\frac{k_2(a)}{q_0\sqrt{a}}$
0.1	-0.001	1.000	-0.004	1.000	70.61	-0.011	0.998
0.2	-0.004	1.001	-0.023	1.000	70.97	-0.031	0.994
0.5	-0.026	1.004	-0.057	1.000	71.61	-0.068	0.984
1.0	-0.060	1.011	-0.089	1.002	72.24	-0.101	0.973
2.0	-0.082	1.023	-0.124	1.007	72.89	-0.132	0.958
4.0	-0.120	1.042	-0.148	1.014	73.34	-0.150	0.940
8.0	-0.152	1.072	-0.162	1.024	73.57	-0.160	0.926
10.0	-0.156	1.084	-0.166	1.027	73.65	-0.161	0.922

Table 3 Stress-intensity factors for the nonhomogeneous medium B; $p(x) = p_0$, $q(x) = 0$

h_1/h_0	a/h_1	$k_1(a)/p_0\sqrt{a}$	$k_2(a)/p_0\sqrt{a}$	$10^6G(a)/p_0^2a$	$\theta_0(a)$
0.25	0.1	1.000	-0.001	4.883	
	0.2	1.000	-0.006	4.880	
	0.5	0.995	-0.034	4.843	
	1.0	0.981	-0.064	4.716	
	2.0	0.957	-0.100	4.524	
	4.0	0.938	-0.137	4.390	
	8.0	0.923	-0.166	4.299	
	10.0	0.921	-0.171	4.282	
0.5	0.1	1.002	-0.006	3.431	0.69
	0.2	1.007	-0.026	3.469	2.96
	0.5	1.025	-0.071	3.605	7.85
	1.0	1.047	-0.117	3.788	12.45
	2.0	1.064	-0.160	3.952	16.40
	4.0	1.070	-0.192	4.035	19.20
	8.0	1.077	-0.197	4.095	19.53
	10.0	1.079	-0.198	4.114	19.58
0.75	0.1	1.010	-0.015	2.437	
	0.2	1.031	-0.040	2.546	
	0.5	1.103	-0.092	2.927	
	1.0	1.176	-0.145	3.355	
	2.0	1.228	-0.196	3.697	
	4.0	1.259	-0.200	3.886	
	8.0	1.293	-0.183	4.076	
	10.0	1.307	-0.173	4.154	

Table 4 Stress-intensity factors for the nonhomogeneous medium B; $p(x) = 0$, $q(x) = q_0$

	$h_1/h_0 = 0.25$		$h_1/h_0 = 0.50$			$h_1/h_0 = 0.75$	
a/h_1	$\frac{k_1(a)}{q_0\sqrt{a}}$	$\frac{k_2(a)}{q_0\sqrt{a}}$	$\frac{k_1(a)}{q_0\sqrt{a}}$	$\frac{k_2(a)}{q_0\sqrt{a}}$	$\theta_0(a)$	$\frac{k_1(a)}{q_0\sqrt{a}}$	$\frac{k_2(a)}{q_0\sqrt{a}}$
0.1	0.001	1.000	0.006	1.000	-70.41	0.015	1.002
0.2	0.006	0.999	0.026	1.000	-70.03	0.039	1.007
0.5	0.034	0.995	0.069	1.000	-69.22	0.085	1.024
1.0	0.064	0.986	0.113	1.005	-68.40	0.129	1.046
2.0	0.102	0.976	0.152	1.015	-67.70	0.173	1.083
4.0	0.140	0.965	0.184	1.028	-67.15	0.180	1.136
8.0	0.170	0.946	0.192	1.046	-67.07	0.168	1.200
10.0	0.175	0.941	0.193	10.52	-67.07	0.161	1.223

$$k_1(a_i) = -\lim_{x\to a_i} \frac{2\mu_0}{1+\kappa_0}\sqrt{2(a_i-x)}f_1(x), \tag{41a}$$

$$k_1(b_i) = \lim_{x\to b_i} \frac{2\mu_0}{1+\kappa_0}\sqrt{2(x-b_i)}f_1(x), \tag{41b}$$

$$k_2(a_i) = -\lim_{x\to a_i} \frac{2\mu_0}{1+\kappa_0}\sqrt{2(a_i-x)}f_2(x), \tag{41c}$$

$$k_2(b_i) = \lim_{x\to b_i} \frac{2\mu_0}{1+\kappa_0}\sqrt{2(x-b_i)}f_2(x), \tag{41d}$$

where $\kappa(y)$ and $\mu(y)$ are the standard elastic constants and $\kappa(0) = \kappa_0$ and $\mu(0) = \mu_0$. For the problem under consideration, we have

$$\frac{2\mu_0}{1+\kappa_0} = \frac{E_0}{4}, \quad \mu_0 = \frac{E_0}{2(1+A_0)},$$

$$\kappa_0 = \frac{3-A_0}{1+A_0}, \quad A_0 = \nu(0). \tag{42}$$

One may also note that (40) and (41) describe the asymptotic behavior of the (cleavage) stresses and crack surface displacements near the crack tips. By using the crack closure concept, the strain-energy release rate for a crack growing in its own plane (at the crack tip $x = a_i$) may be obtained as

$$G(a_i) = \frac{\pi(1+\kappa_0)}{8\mu_0}[k_1^2(a_i) + k_2^2(a_i)]. \tag{43}$$

Referring to (8), for the generalized plane-stress problem under consideration described in Fig. 1, equation (43) may be rewritten as

$$G(a_i) = \frac{\pi}{E_1}[k_1^2(a_i) + k_2^2(a_i)](E_1/E_2)^{h_1/h_0}. \tag{44}$$

5 Examples and Discussion

The integral equations (38) are solved and the stress-intensity factors are calculated for the following material combinations:

Combination A:

$$E_1 = 3\times10^7(\text{psi}) = 20.685\times10^{10}(\text{N/m}^2), \quad \nu_1 = 0.3,$$
$$E_2 = 10^7(\text{psi}) = 6.895\times10^{10}(\text{N/m}^2), \quad \nu_2 = 0.3. \tag{45}$$

Combination B:

$$E_1 = 0.45\times10^6\text{psi} = 3.1\times10^9\text{N/m}^2, \quad \nu_1 = 0.35,$$
$$E_2 = 1.88\times10^6\text{psi} = 12.96\times10^9\text{N/m}^2, \quad \nu_2 = 0.25. \tag{46}$$

The elastic constants of the nonhomogeneous layer defined by equations (3) and (6) are obtained from (8) once the dimensions h_0 and h_1 are specified. The examples are given for a single crack ($n = 1$, $a_1 = a$, $b_1 = -a$) of length $2a$ that is subjected to uniform tractions

Downloaded 03 May 2010 to 171.66.16.21. Redistribution subject to ASME license or copyright; see http://www.asme.org/terms/Terms_Use.cfm

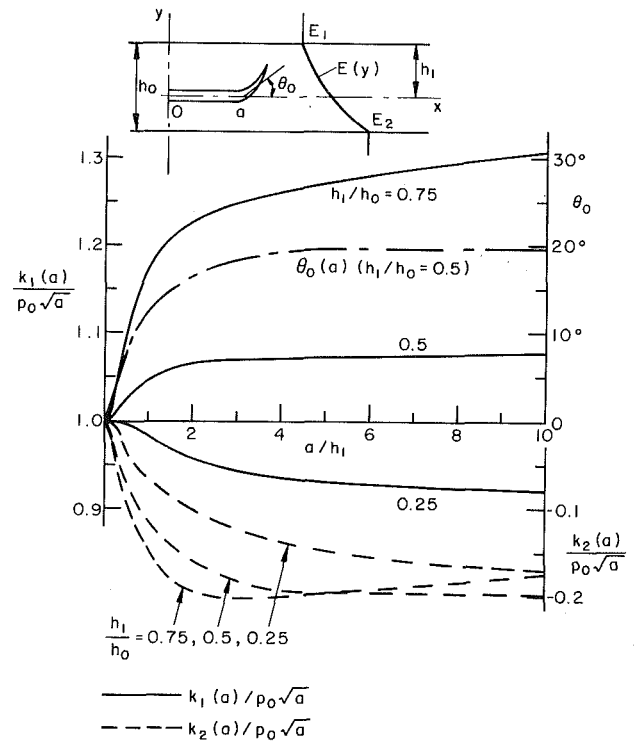


Fig. 2 Stress-intensity factors for the nonhomogeneous medium *B* containing a pressurized single crack (see equation (46) for material parameters)

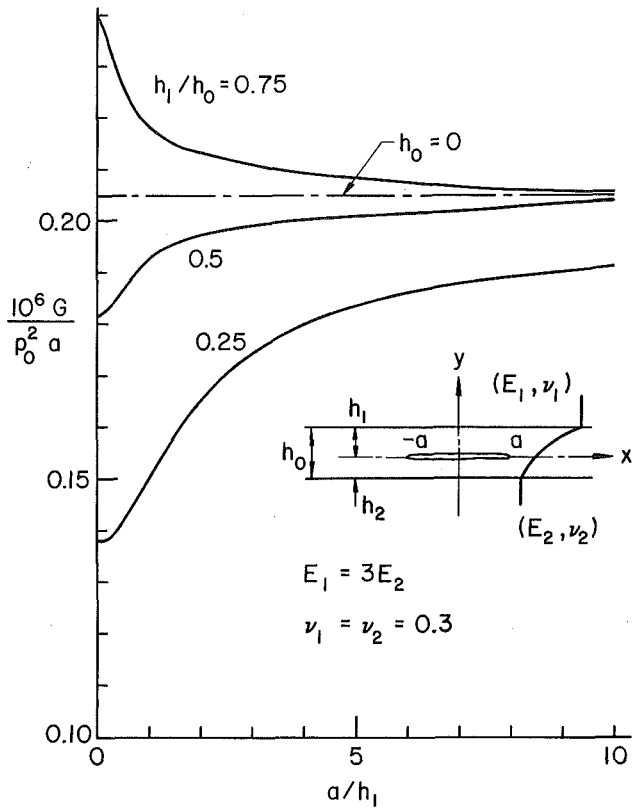


Fig. 3 Strain-energy release rate for the nonhomogeneous medium *A* containing a pressurized single crack (see equation (45) for material parameters)

$$p(x)=p_0, \quad q(x)=q_0. \tag{47}$$

The calculated results are shown in Tables 1–4. Some limited results are also displayed in Figs. 2 and 3. In order to discuss the results it may be worthwhile to recall some general qualitative arguments from the linear elastic fracture mechanics. The stress-intensity-factor ratios in a uniformly loaded infinite homogeneous plane are known to be unity (that is, $k_1/p_0\sqrt{a}=1$, $k_2/q_0\sqrt{a}=1$). If the crack approaches a free boundary or an interface with a less stiff medium, these ratios tend to increase, and if the boundary is fixed or the adjacent medium has higher stiffness, they tend to decrease. From equation (43) (which is also valid for homogeneous materials), it may be observed that for given stress-intensity factors (meaning that for given loading and geometry) the strain-energy release rate is inversely proportional to the stiffness of the medium. If the material, loading, and geometry lack symmetry, the problem is one of mixed-mode, meaning that generally k_1 and k_2 are both nonzero regardless of the loading conditions. For a pressurized crack under mixed-mode conditions, the sign of k_2 and the resulting orientation of the maximum cleavage plane are such that the crack would tend to propagate toward the free boundary or the interface with the medium that has a lower stiffness and away from the fixed boundary or the interface with stiffer adjacent medium.

A close examination of the results given in the tables would show that these general observations are also valid for the nonhomogeneous medium considered. For example, as the crack location approaches the less stiff material, the strain-energy release rate increases (Tables 1 and 3). The overall stiffness of material combination *A* is also greater than that of *B*; consequently, the strain-energy release rate for *B* is greater than for *A* (Tables 1 and 3). As in the infinite nonhomogeneous medium considered in [34], when the crack length $2a$ approaches zero, the primary stress-intensity ratio tends to unity and the secondary one tends to zero. For cracks under mixed mode loading conditions, the direction of the probable crack propagation may be estimated by determining the plane of the maximum cleavage stress $\sigma_{\theta\theta}(r,\theta)$ around the crack tip (that is, by calculating the value of $\theta=\theta_0$ for which $\sigma_{\theta\theta}$ is maximum and tensile, where r and θ are the polar coordinates at the crack tip). By assuming that locally the homogeneous asymptotic results are valid, this angle can be calculated from [1]

$$\tan^2\frac{\theta_0}{2}-\frac{k_1}{2k_2}\tan\frac{\theta_0}{2}-\frac{1}{2}=0 \quad \text{for} \quad k_1\geq 0, \tag{48}$$

and

$$\tan^2\frac{\theta_0}{2}=\frac{1}{2} \quad \text{for} \quad k_1\leq 0. \tag{49}$$

Equation (49) is valid under the additional assumption that the friction on the crack surfaces is negligible. The particular choice of the root in (48) or (49) is dictated by the condition $\sigma_{\theta\theta}(r,\theta_0)>0$.

For the crack location $h_1/h_0=0.5$, the calculated values of θ_0 are shown in Tables 1 and 3 (see also, Fig. 2 for material *B*). In these examples, the external load is crack surface pressure. Consequently, k_1 is the primary stress-intensity factor and k_2 arises from the lack of material symmetry with respect to the plane of the crack. The angles given in the tables are the particular roots of (48) for which $\sigma_{\theta\theta}(r,\theta)$ has a positive extremum. The sign of these angles, that is, $\theta_0<0$ for material *A* (Table 1) and $\theta_0>0$ for *B* (Table 3 and Fig. 2), indicate that the crack would tend to grow in a direction of decreasing material stiffness, Fig. 2. This is also the physically expected result provided the medium is isotropic with respect to its fracture resistance and its toughness does not increase with decreasing stiffness—which may not always be the case. It

Downloaded 03 May 2010 to 171.66.16.21. Redistribution subject to ASME license or copyright; see http://www.asme.org/terms/Terms_Use.cfm

should be noted that in the examples considered $x = 0$ is a plane of symmetry with respect to the external loads as well as the material properties. Therefore, the stress-intensity factors are calculated at $x = a$ only and following symmetry conditions are valid

$$k_1(-a) = k_1(a), \quad k_2(-a) = -k_2(a), \tag{50}$$

for $p(x) = p_0$, $q(x) = 0$ (Tables 1 and 3), and

$$k_1(-a) = -k_1(a), \quad k_2(-a) = k_2(a), \tag{51}$$

for $p(x) = 0$, $q(x) = q_0$ (Tables 2 and 4).

From the results given in [34] for the nonhomogeneous infinite plane, it can be shown that, for practical ranges of the nonhomogeneity constant β—see equations (3) and (8)—under Mode I loading conditions, the strain-energy release rate at the crack tip embedded in the portion of the medium with lower stiffness is greater than that corresponding to the crack tip in the stiffer side of the material. The importance of this observation may be apparent in crack problems under pure shear. For example, Table 2 shows that (for $h_1/h_0 = 0.5$) $\theta_0(-a) > 0$ and $\theta_0(a) < 0$. Since $k_1(a) < 0$, from (49), it follows that $\theta_0(a) = -70.5°$. In this case, it may be concluded that when the loading reaches a critical level, since $\theta_0(a)$ is in the decreasing and $\theta_0(-a)$ in the increasing stiffness direction, the crack would start growing at the tip $x = a$ and the tip $x = -a$ would remain dormant. Similarly, in the nonhomogeneous medium B under pure shear $q_0 > 0$ (Table 4), $k_1(-a) < 0$ and the crack growth would start at $x = -a$ in the direction $\theta_0 = 70.5°$, which is the direction of decreasing material stiffness.

As h_0/a goes to zero, physically one would expect the strain-energy release rate approach that obtained for two bonded half-planes containing an interface crack of length $2a$. This trend may be observed from Fig. 3 where G is given for the material combination A [see equation (45)] under the external loading p_0. In this figure, the value of G corresponding to $h_0 = 0$ is obtained from (see, for example, [23])

$$G = \frac{\pi}{4} \frac{1+\kappa_1}{c\mu_1} p_0^2 a(1+4\omega^2), \tag{52a}$$

$$c = 2 - \frac{\kappa_2\mu_1 - \kappa_1\mu_2}{\mu_2 + \kappa_2\mu_1} - \frac{\mu_2 - \mu_1}{\mu_1 + \kappa_1\mu_2}, \tag{52b}$$

$$\omega = \frac{1}{2\pi} \log \left(\frac{1+\gamma}{1-\gamma}\right), \tag{52c}$$

$$\gamma = \frac{(\kappa_1\mu_2 + \mu_1) - (\kappa_2\mu_1 + \mu_2)}{(\kappa_1\mu_2 + \mu_1) + (\kappa_2\mu_1 + \mu_2)}, \tag{52d}$$

where μ_i is the shear modulus and $\kappa_i = 3 - 4\nu_i$ for plane strain and $\kappa_i = (3 - \nu_i)/(1 + \nu_i)$ for plane stress, $(i = 1, 2)$. The figure also shows another physically expected result; namely, the strain-energy release rate decreases as the crack approaches the stiffer side of the interfacial layer.

It should be emphasized that the problem is linear and the results given, for example, in Tables 1 and 2, and Tables 3 and 4 can be superimposed for any values of p_0 and q_0. For the final result to be valid, the Mode I stress-intensity factor k_1 also must be positive at both crack tips. The foregoing discussion regarding the mixed mode stress state at the crack tips and the resulting considerations of crack growth would, therefore, be quite useful in studying the problem under more general loading conditions.

Finally, it should be observed that the important special case of the problem in which $h_1 = 0$ or $h_2 = 0$ has not been considered in this paper. The necessary asymptotic analysis to determine the nature of the stress singularities for this "interface" crack has been carried out on a much simpler problem of two bonded half-planes and is given in reference [40]. The results presented in [40] show that, in such nonhomogeneous materials the stress and displacement oscillations around the interface crack tips disappear as long as there are no discontinuities in the elastic properties of the medium.

References

1 Erdogan, F., "Fracture Problems in Composite Materials," *Journal of Engng. Fracture Mechanics*, Vol. 4, 1972, pp. 811–840.

2 Erdogan, F., "Stress Distribution in Bonded Dissimilar Materials With Cracks," ASME JOURNAL OF APPLIED MECHANICS, Vol. 32, 1965, pp. 403–410.

3 England, A. H., "A Crack Between Dissimilar Media," ASME JOURNAL OF APPLIED MECHANICS, Vol. 32, 1965, pp. 400–402.

4 Rice, J. R., and Sih, G. C., "Plane Problems of Cracks in Dissimilar Media," ASME *Journal of Applied Mechanics*, Vol. 32, 1965, pp. 418–423.

5 Erdogan, F., "Stress Distribution in a Nonhomogeneous Plane With Cracks," ASME JOURNAL OF APPLIED MECHANICS, Vol. 30, 1963, pp. 232–236.

6 Erdogan, F., and Ozbek, T., "Stresses in Fiber-Reinforced Composites With Imperfect Bonding," ASME JOURNAL OF APPLIED MECHANICS, Vol. 36, 1969, pp. 865–869.

7 Delale, F., "Stress Singularities in Bonded Anisotropic Materials," *International Journal of Solids and Structures*, Vol. 20, 1984, pp. 31–40.

8 Comninou, M., "The Interface Crack," ASME JOURNAL OF APPLIED MECHANICS, Vol. 44, 1977, pp. 631–636.

9 Comninou, M., "The Interface Crack in a Shear Field," ASME JOURNAL OF APPLIED MECHANICS, Vol. 45, 1978, pp. 287–290.

10 Atkinson, C., "On Stress Singularities and Interfaces in Linear Elastic Fracture Mechanics," *International Journal of Fracture*, Vol. 13, 1977, pp. 807–820.

11 Wang, S. S., and Choi, I., "The Interface Crack Behavior in Dissimilar Anisotropic Composites Under Mixed-Mode Loading," ASME JOURNAL OF APPLIED MECHANICS, Vol. 50, 1983, pp. 169–178.

12 Wang, S. S., and Choi, I., "The Interface Crack Behavior in Dissimilar Anisotropic Composites Under Mixed-Mode Loading," ASME JOURNAL OF APPLIED MECHANICS, Vol. 50, 1983, pp. 179–183.

13 Cook, T. S., and Erdogan, F., "Stresses in Bonded Materials With a Crack Perpendicular to the Interface," *International Journal of Engineering Science*, Vol. 10, 1972, pp. 667–696.

14 Erdogan, F., and Bircikoglu, V., "Two Bonded Half Planes With a Crack Going Through the Interface," *International Journal of Engineering Science*, Vol. 11, 1973, pp. 745–766.

15 Erdogan, F., and Gupta, G. D., "The Inclusion Problem With a Crack Crossing the Boundary," *International Journal of Fracture*, Vol. 11, 1975, pp. 13–27.

16 Erdogan, F., and Aksogan, O., "Bonded Half Planes Containing an Arbitrarily Oriented Crack," *International Journal of Solids and Structures*, Vol. 10, 1974, pp. 569–589.

17 Ratwani, M., and Gupta, G. D., "Interaction Between Parallel Cracks in Layered Composites," *International Journal of Solids and Structures*, Vol. 10, 1974, pp. 701–708.

18 Erdogan, F., Gupta, G. D., and Ratwani, M., "Interaction Between a Circular Inclusion and an Arbitrarily Oriented Crack," ASME JOURNAL OF APPLIED MECHANICS, Vol. 41, 1974, pp. 1007–1013.

19 Erdogan, F., "The Interaction Between Inclusions and Cracks," *Fracture Mechanics of Ceramics*, Brandt, R. C., Hasselman, D. P. H., Lange, F. F., Eds., Plenum Press, 1974, pp. 245–267.

20 Bassani, J. L., and Erdogan, F., "Stress Intensity Factors in Bonded Half Planes Containing Inclined Cracks and Subjected to Antiplane Shear Loading," *International Journal of Fracture*, Vol. 15, 1979, pp. 145–158.

21 Gecit, M. R., and Erdogan, F., "The Effect of Adhesive Layers on the Fracture of Laminated Structures," ASME *Journal of Engineering Materials and Technology*, Vol. 100, 1978, pp. 3–9.

22 Erdogan, F., and Gupta, G. D., "The Stress Analysis of Multi-Layered Composites With a Flaw," *International Journal of Solids and Structures*, Vol. 7, 1971, p. 39.

23 Erdogan, F., and Gupta, G. D., "Layered Composites With an Interface Flaw," *International Journal of Solids and Structures*, Vol. 7, 1971, p. 1089.

24 Gupta, G. D., "A Layered Composite With a Broken Laminate," *International Journal of Solids and Structures*, Vol. 9, 1973, pp. 1141–1154.

25 Varley, E., private communication on certain unpublished nonlinear elasticity solutions.

26 Shih, C. F., and Asaro, R. J., "Elastic-Plastic Analysis of Cracks on Bimaterial Interfaces, Part I: Small Scale Yielding," Brown University Report ONR-N00014-86-K-0235/2, Mar. 1987.

Downloaded 03 May 2010 to 171.66.16.21. Redistribution subject to ASME license or copyright; see http://www.asme.org/terms/Terms_Use.cfm

27 Knowles, J. K., and Sternberg, E., "On the Singularity Induced by Certain Mixed Boundary Conditions in Linearized and Nonlinear Elastostatics," *International Journal of Solids and Structures*, Vol. 11, 1975, pp. 1173–1201.

28 Good, R. J., "Intermolecular and Interactomic Forces," *Treatise on Adhesion and Adhesives*, Ed., Patrick, R. L., Marcel Dekker, New York, 1967, pp. 9–68.

29 Patrick, R. L., Ed., *Treatise on Adhesion and Adhesives*, Marcel Dekker, New York, 1967.

30 Gutfreund, K., "Interfacial Relationships in Fiber-Reinforced Plastic Composites," *Modern Composite Materials*, Ed., Brautman, L. J., Addison-Wesley, 1967, pp. 177–194.

31 Subramanian, R. V., and Crasto, A. S., "Electrodeposition of a Polymer Interphase in Carbon-Fiber Composites," *Polymer Composites*, Vol. 7, 1986, pp. 201–218.

32 Ishida, H., "A Review of Recent Progress in the Studies of Coupling Agents," *Polymer Composites*, Vol. 5, 1984, p. 101.

33 Manson, J. A., "Interfacial Effects in Composites," *Pure and Applied Chemistry*, Vol. 57, 1985, p. 1667.

34 Delale, F., and Erdogan, F., "The Crack Problem for a Nonhomogeneous Plane," ASME JOURNAL OF APPLIED MECHANICS, Vol. 50, 1983, pp. 609–614.

35 Erdogan, F., "The Crack Problem for Bonded Nonhomogeneous Materials Under Antiplane Shear Loading," ASME JOURNAL OF APPLIED MECHANICS, Vol. 52, 1985, pp. 823–828.

36 Atkinson, C., and List, R. D., "Steady State Crack Propagation into Media with Spatially Varying Elastic Properties," *International Journal of Engineering Science*, Vol. 16, 1978, pp. 717–730.

37 Atkinson, C., "On Stress Singularities and Interfaces in Linear Elastic Fracture Mechanics," *International Journal of Fracture*, Vol. 13, 1977, pp. 807–820.

38 Delale, F., and Erdogan, F., "On the Mechanical Modelling of the Interfacial Region in Bonded Half-Planes," NASA Project Report, Grant NAG-1-713, Langley Research Center, June 1987.

39 Muskhelishvili, N. I., *Singular Integral Equations*, P. Noordhoff, Groningen, 1953.

40 Delale, F., and Erdogan, F., "Interface Crack in a Nonhomogeneous Elastic Medium," to appear in *International Journal of Engineering Science*, 1988.

Downloaded 03 May 2010 to 171.66.16.21. Redistribution subject to ASME license or copyright; see http://www.asme.org/terms/Terms_Use.cfm

A Crystallographic Model for Nickel Base Single Crystal Alloys[1]

L. T. Dame
International TechneGroup Incorporated,
Milford, OH 45150

D. C. Stouffer
Professor,
Department of Aerospace Engineering
and Engineering Mechanics,
University of Cincinnati,
Cincinnati, OH 45221-0070
Mem. ASME

The purpose of this research is to develop a tool for the mechanical analysis of nickel-base single-crystal superalloys, specifically Rene N4, used in gas turbine engine components. This objective is achieved by developing a rate-dependent anisotropic constitutive model and implementing it in a nonlinear three-dimensional finite-element code. The constitutive model is developed from metallurgical concepts utilizing a crystallographic approach. An extension of Schmid's law is combined with the Bodner-Partom equations to model the inelastic tension/compression asymmetry and orientation-dependence in octahedral slip. Schmid's law is used to approximate the inelastic response of the material in cube slip. The constitutive equations model the tensile behavior, creep response and strain-rate sensitivity of the single-crystal superalloys. Methods for deriving the material constants from standard tests are also discussed. The model is implemented in a finite-element code, and the computed and experimental results are compared for several orientations and loading conditions.

I Introduction

Nickel-base single-crystal superalloys have attracted considerable interest for use in gas turbine engines because of their superior high temperature properties. However, to use these alloys, it is necessary to develop better analysis methods for the design of single-crystal engine components. This study contains a constitutive model for single-crystal superalloy Rene N4 at 760°C and the implementation of the model in a nonlinear three-dimensional finite-element code.

Rene N4 was developed by the General Electric Company specifically for use as a turbine blade and vane alloy. The nominal chemical composition of Rene N4 as given by Miner, et al. (1986), does not contain the elements C, B, and Zr which are typically included in polycrystalline high temperature nickel-base superalloys for the purpose of strengthening the grain boundaries. Modern single-crystal materials are two-phase alloys with a large volume fraction of γ' phase. The γ' precipitates have L_{12}-type crystal structure and are interspersed in a coherent face center cubic γ solid solution. Experimentally, it has been determined by Pope and Ezz (1984), and Shah and Duhl (1984) that the peak creep strength is achieved with a volume fraction of γ' of about 60 percent and deformation occurs by shearing of the precipitates.

Elastic strains are associated with crystal lattice distortions and are fully recoverable, and the effects of inelastic strains on the elastic properties are assumed to be negligible. Further, Yang (1984) has shown single-crystal alloys exhibit cubic symmetry in the elastic range. There are three independent material parameters (for example, elastic modulus, shear modulus and Poisson ratio).

The inelastic response of single-crystal materials is quite different from the behavior of polycrystalline nickel-base superalloys. The yield stress of single-crystal alloys is a function of the material orientation relative to the direction of the applied stress. Shah and Duhl (1984) also have shown they exhibit a significant tension/compression asymmetry in yielding except near the [111] orientation. Further, the orientation-dependence and tension/compression asymmetry decrease as a function of increasing temperature above a critical temperature of about 750°C. In creep, at lower strains rates, single-crystal alloys also exhibit orientation-dependence even though the deformation mechanisms are different. Other observed behavior is similar to that seen in isotropic nickel-base superalloys. The materials exhibit both strain-rate sensitivity and cyclic hardening.

The crystallographic approach to modeling crystal behavior is based on identifying the active slip planes and slip directions in the crystal. The shear stresses are computed on each of the slip planes from the applied stress. The slip deformation is computed on each slip system and the macroscopic inelastic strain rates or strain increments are then the sum of the contributions of the individual slip systems. Early developments in the crystallographic approach are attributed to Taylor (1938), Bishop and Hill (1951) and Bishop (1952). The application of the crystallographic approach to single-crystal nickel-base superalloys began with the work of Paslay, Wells, Leverant and Burck (1970 and 1971), and more recently by Shah (1983) to the γ' phase of these alloys. The classical constitutive assumption is Schmid's law, in which the slip on a

[1]The University of Cincinnati is grateful for the support of this research from the National Aeronautics and Space Administration, Lewis Research Center, Cleveland, OH, under Grant NAG3-511.

Contributed by the Applied Mechanics Division for publication in the JOURNAL OF APPLIED MECHANICS.

Discussion on this paper should be addressed to the Editorial Department, ASME, United Engineering Center, 345 East 47th Street, New York, NY 10017, and will be accepted until two months after final publication of the paper itself in the JOURNAL OF APPLIED MECHANICS. Manuscript received by ASME Applied Mechanics Division, January 22, 1986; final revision, January 20, 1988.

Copyright © 1988 by ASME
Downloaded 03 May 2010 to 171.66.16.21. Redistribution subject to ASME license or copyright; see http://www.asme.org/terms/Terms_Use.cfm

particular system is a function of the resolved shear stress on the slip plane in the direction of slip. This assumption, however, does not apply for L_{12} crystals, or for single-crystal nickel-base superalloys. More recently, Pope (1984), Shah and Duhl (1984), Shah (1983), Umakoshi, et al. (1984), Takeuchi (1973), Lall, et al., (1979), Ezz, et al. (1982), Wee, et al. (1984), and Pope and Heredia (1984), have proposed an extension to Schmid's law that appears to be successful in correlating the deformation mechanism with several of the macroscopic anisotropic effects. The principal advantage of this approach is that a significant portion of the model is based on the physics of the deformation mechanisms.

II Physical Basis of the Crystallographic Approach

Slip trace studies of single-crystal alloys indicate that one or more types of slip may occur under different temperature, orientation and strain-rate conditions. These include octahedral slip on the four octahedral planes in the three directions similar to the [$\bar{1}$ 0 1] direction (Fig. 1); octahedral slip on the octahedral planes in the three directions similar to the [$\bar{1}$ 2 $\bar{1}$] direction; and cube slip on the three cube planes in the two directions similar to the [$\bar{1}$ 0 1] direction. The slip mechanisms occurring during tensile and creep tests are reviewed for use in development of the model.

Recent metallurgical research by Pope and Ezz (1984), Shah and Duhl (1984), and Pope and Heredia (1984) in the tensile behavior of nickel-base single-crystal superalloys indicates that the response is controlled to a large extent by the behavior of the γ' phase alone, thus the response of L_{12} ordered alloys and γ/γ' single crystals are similar. In uniaxial tests the critical resolved shear stress (CRSS), or component of stress on the slip plane in the direction of slip required for yielding, is approximately constant or increases slightly up to a critical temperature and is a function of orientation. Below this critical temperature, slip occurs primarily on the octahedral systems and significant orientation-dependence and tension/compression asymmetry is observed. Above the critical temperature, Pope and Heredia (1984) demonstrated there is a sharp drop in the CRSS, cube slip becomes more prominent and the tension/compression asymmetry is reduced. There are two exceptions to this behavior. First, test specimens near the [111] orientation exhibit cube slip at all temperatures. Second, loading near the [0 0 1] orientation produces only octahedral slip at all temperatures since the resolved shear stress on the cube planes is zero.

The knowledge of the creep properties and the active slip systems during creep in γ/γ' alloys is much less complete than the tensile response and only a few observations can be included in this review. Unlike the tensile yield response, Davies and Johnston (1970) have shown that the creep properties of ordered L_{12} crystals are much different than the creep response of the γ/γ' alloys. The creep rate of γ' is significantly higher than that of γ/γ' alloys under identical conditions. Some nickel-base superalloy single crystals exhibit an incubation period prior to the usual primary, secondary and tertiary creep. The incubation period and primary creep are attributed to (111) [$\bar{1}$ 2 $\bar{1}$] slip. In single-crystal Rene N4 at temperatures from 760°F to 1150°C, the response did not include an incubation. In secondary creep at temperatures above the critical temperature, Shah (1983) has shown that slip is inferred to occur by (111) [$\bar{1}$ 0 1] slip. However, Giamei (1979) demonstrated cube slip is present near the [111] orientation and absent near the [0 0 1] orientation similar to the tensile response. In this study, a tension/compression asymmetry was observed and typical response showed a creep rate that is higher in tension than compression for creep in the [1 1 0]-direction. This response is similar to the tension/compression asymmetry observed in the yield stress.

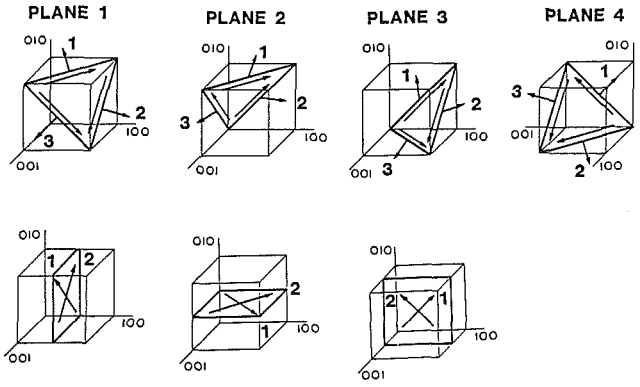


Fig. 1 Direction of the local shear stress and slip rates in the octahedral and cube slip systems are shown in the positive direction. The [101]-directions are shown normal to the triangular region whereas the [121]-direction are parallel to the triangular region in the octahedral slip system.

III Metallurgical Models

A major step in understanding orientation-dependence was made by Takeuchi and Kuramoto (1973) in their study of Ni_3Ga single crystals. They proposed that the increase in CRSS up to the critical temperature and non-Schmid's law behavior is a result of cross slip of screw dislocation segments from the octahedral to cube planes. The cross slipped segments pin the dislocations and therefore increase the flow stress. They further proposed that the cross slip mechanism is thermally activated and is driven by the resolved shear stress in the (010) [$\bar{1}$ 0 1] system. However, their model did not fully explain the tension/compression asymmetry or the orientation-dependence observed in other L_{12} alloys.

An improvement in the Takeuchi-Kuramoto model was proposed by Lall, Chin, and Pope (1979). In their theory, the octahedral $(a/2)$ [$\bar{1}$ 0 1] dislocation is an extended dislocation consisting of two Shockley partial dislocation pairs, $(a/6)$ [$\bar{2}$ 1 1] + $(a/6)$ [$\bar{1}$ $\bar{1}$ 2] . In order to cross slip, the pair must constrict into a single $(a/2)$ [$\bar{1}$ 0 1] dislocation. The constriction is aided by a shear stress on the (111) plane in the [1 $\bar{2}$ 1]-direction. It is important to note that a shear stress in the opposite direction extends the dislocation pair and thus inhibits cross slip. This effect is generally referred to as the "core width effect" and gives rise to the tension/compression asymmetry observed in these alloys. Lall, Chin, and Pope also proposed that the change in flow stress $\Delta\tau_{(111)}$ on the octahedral plane in the [$\bar{1}$ 0 $\bar{1}$]-direction, for example, from a reference state of 0°K is given by

$$\Delta\tau_{(111)} = A \exp\left(-\frac{H}{kT}\right), \tag{1}$$

where A is a constant, T is temperature, and k is Boltzmann's constant. The parameter H is a function of the resolved shear stress on the (111) plane in the [$\bar{1}$ 2 $\bar{1}$]-direction, τ_1, and the resolved shear stress on the (010) plane in the [$\bar{1}$ 0 1]-direction, τ_2. The stress components τ_1 and τ_2 are shown in Fig. 1. By expanding H in a Taylor series about the reference condition H_0, equation (1) becomes

$$\Delta\tau_{(111)} = A \exp\frac{-H_0 + V_1\tau_1 + V_2\tau_2 + \ldots}{kT} \tag{2}$$

where V_1 and V_2 are constants.

In the orientations and at temperatures where cube slip is dominant, the orientation-dependence and tension/compression asymmetry is reduced considerably. Therefore, it is believed that Schmid's law can be used to relate the slip rate to the resolved shear stress on the cube planes.

A major effort in this work is to recast the previous results,

Downloaded 03 May 2010 to 171.66.16.21. Redistribution subject to ASME license or copyright; see http://www.asme.org/terms/Terms_Use.cfm

both experimental and theoretical, into the form of a constitutive equation involving state variables that characterize the change in material properties due to the deformation history. These results are valuable for determining the appropriate independent variables and functional forms.

IV Inelastic Constitutive Equations

The constitutive model is based on separating the total global strain at a point in a body into elastic and inelastic components. Inelastic strains are obtained by integrating the inelastic strain rate with time. The inelastic strain rate is calculated by summing the slip contributions from each of the crystallographic slip systems. The inelastic shear strain rate on each of the slip systems is computed from the inelastic constitutive equations which are developed in the remainder of this paper. In addition, the inelastic shear strain rates on the active slip systems are a function of the local shear stresses.

To begin, it is necessary to have the kinematic equations that relate the shear stresses on the crystallographic planes and in the directions of interest to the stress tensor relative to the principal material axes. The constitutive equations are applied at the crystallographic level and it is therefore necessary to also know the relationship between the crystallographic shear strain rates and the macroscopic inelastic strain-rate tensor. The required stress and infinitesimal strain relations were derived by Bishop (1952) and are used in this study.

There are at least two separate flow equations required to describe the tensile response of single crystals, i.e., cube slip and octahedral slip so that

$$\dot{\epsilon}^I_{ij} = \left(\dot{\epsilon}^I_{ij}\right)_{\mathrm{OCT}} + \left(\dot{\epsilon}^I_{ij}\right)_{\mathrm{CUBE}}. \tag{3}$$

In addition, there appears to be at least two deformation mechanisms present; i.e., at high and low strain rates. At the higher strain rates, such as in tensile tests, deformation occurs by dislocations cutting the γ' precipitate. The deformation rate depends on the size and volume fraction of γ'. The orientation-dependence of the CRSS at temperatures below the critical temperature depends on the core width effect and the cross slip mechanism. The creep strength of γ/γ' alloys appears to be controlled by the γ/γ' interfaces in the material. This explains the difference in creep behavior of γ' and γ/γ' alloys. The activation energy during creep is much higher than expected from a vacancy diffusion process. Tien, et al. (1972), proposed that, during steady-state creep, the presence of γ' particles leads to a dislocation network that exhausts the vacancy concentration. Deformation occurs by the less favorable process of emitting and diffusing interstitials, which is consistent with the higher activation energies. This model has been supported by many observations as summarized by Pope and Ezz (1984). Thus the flow equation for each system should have terms to account for each of the foregoing deformation mechanisms.

Next, it is desirable to use a state variable constitutive equation to relate the local stress and slip-rate components. Most current state variable models have a drag stress and back stress as proposed by Walker (1981), Robinson (1978), and Robinson and Swindeman (1982) or a drag stress alone as proposed by Bodner, et al. (1975, 1979), and Stouffer and Bodner (1982). In selecting a formulation to use with single crystals, it is useful to review the mechanisms related to drag stress and back stress. The drag stress is usually associated with the resistance to dislocation motion provided by local obstacles such as precipitates. The dislocations shear or loop the precipitates during the deformation of the material. Thus the local obstacle retards the dislocation motions. The back stress is associated with the increase in dislocation resistance to motion attributed to pileups at global obstacles such as grain boundaries that cannot be sheared or looped. In this case, the obstacle is a permanent barrier. The dislocation resistance is a function of the distance from the obstacle and the dislocation density increases as the distance to the obstacle decreases. Polycrystalline materials exhibit both drag stress and back stress due to dislocation interaction with precipitates and grain boundaries. However, in single crystal materials, it is expected that drag stress (precipitate shear and looping mechanisms) should control the deformation due to the absence of grain boundaries and the reduced potential for a back stress. Thus it appears appropriate to construct a constitutive model for single-crystal materials with only a drag stress; however, if back stress does appear to be important it can be added at a later time.

V Octahedral Flow Equation

The octahedral slip system is active for both tensile and creep deformation, but the deformation mechanisms are different as previously discussed. The inelastic shear strain rate $\dot{\gamma}^{\alpha\beta}_{\mathrm{OCT}}$, on an α octahedral plane in the β-direction is proposed as the sum of two components, i.e.,

$$\dot{\gamma}^{\alpha\beta}_{\mathrm{OCT}} = \dot{\gamma}^{\alpha\beta}_{\mathrm{OCT}_1}, + \dot{\gamma}^{\alpha\beta}_{\mathrm{OCT}_2}, \tag{4}$$

The first component is used to characterize dislocation shearing and looping of the γ' particles and the second is motivated by the interstitial emission and diffusion mechanism. The two terms must be coupled to characterize the effect of the dislocation network on both mechanisms. Equation (4) is typical of classical models involving the use of both plastic and creep strain components. The origin of this approach is clearly based on the physical motivation of two or more deformation mechanisms. The thrust of the unified strain measure is to eliminate the need to identify the coupling between the two mechanisms. Unfortunately, many unified models are reasonable for modeling plasticity or creep but are not completely adequate for both. In the present study, coupling is proposed in combination with the flow laws for $\dot{\gamma}^{\beta}_{\mathrm{OCT}_1}$ and $\dot{\gamma}^{\alpha\beta}_{\mathrm{OCT}_2}$ that appears to be an improvement.

The functional form of the octahedral flow equations for

Table 1 Material constants for Rene N4 at 760°C

CONSTANT	VF317	GABB, GAYDA, MINER VOIGT DATA
D_1	10000 SEC^{-1}	10000 SEC^{-1}
n_1	2.02	2.02
D_2	1 SEC^{-1}	----
n_2	.708	----
Φ_1	959.1 MPA	1109 MPA
V_{11}	3.7454	.5752
V_{12}	3.5799	-.5799
M_1	5.656 MPA^{-1}	8.194 MPA^{-1}
W_1	177.9 Mpa	437.5 MPA
a	52.52	----
Φ_2	5626 MPa	----
V_2	20070 MPa	----
V_{22}	18690 MPa	----
D_3	----	10000 sec^{-1}
n_3	----	2.02
D_4	----	----
n_4	----	----
Φ_3	----	1198 MPA
M_3	----	8.194 MPa^{-1}
W_3	----	437.5 MPa
b	----	----
Φ_4	----	----

The elastic constants at 760°C are E = 100.0 GPa, G = 96.5 GPa and ν = .38.

Downloaded 03 May 2010 to 171.66.16.21. Redistribution subject to ASME license or copyright; see http://www.asme.org/terms/Terms_Use.cfm

$\dot{\gamma}^{\alpha\beta}_{\mathrm{OCT}_1}$ is assumed similar to the exponential form with only drag stress developed by Bodner, et al. This form has been used with reasonable success by Bodner, et al. (1975, 1978) and Bodner and Stouffer (1982) for a number of materials including isotropic nickel-base superalloys at high temperatures. The Bodner flow equation was taken from an expression for mobile dislocation velocity and is expected to capture the essential features of the response for Rene N4 at the higher strain rates below the critical temperature. The form of the equation used in this study is

$$\dot{\gamma}^{\alpha\beta}_{\mathrm{OCT}_1} = D_1 \exp\left[-\left(\frac{Z_1^{\alpha\beta}}{|\tau^{\alpha\beta}|}\right)^{n_1}\right]\frac{\tau^{\alpha\beta}}{|\tau^{\alpha\beta}|} \tag{5}$$

where $Z_1^{\alpha\beta}$ is a state variable introduced to characterize the γ' resistance to inelastic flow. The parameters D_1 and n_1 are used to characterize the limiting strain rate and the strain-rate sensitivity. The octahedral flow equation and state variable $Z_1^{\alpha\beta}$ must also characterize the orientation and tension/compression asymmetry properties. Since the form of the flow equation is similar to the Lall, Chin, and Pope model their results can easily be incorporated into equation (5).

The functional form of the octahedral flow equation for creep is taken in a form similar to equation (5). This form is selected because it is consistent with representations used to characterize thermally driven diffusion processes as welll as mobile dislocation velocities. Further, maintaining a similar structure allows for the same interpretation of the state variables $Z_1^{\alpha\beta}$ and $Z_2^{\alpha\beta}$, which should aid in establishing coupling between the two terms.

The total octahedral flow equation is given by

$$\dot{\gamma}^{\alpha\beta}_{\mathrm{OCT}} = \left\{D_1 \exp\left[-\left(\frac{Z_1^{\alpha\beta}}{|\tau^{\alpha\beta}|}\right)^{n_1}\right] + D_2 \exp\left[-\left(\frac{Z_2^{\alpha\beta}}{|\tau^{\alpha\beta}|}\right)^{n_2}\right]\right\}\frac{\tau^{\alpha\beta}}{|\tau^{\alpha\beta}|} \tag{6}$$

The constants D_1 and D_2 are chosen to be 10^4 sec^{-1} and 1 sec^{-1} to allow uncoupling at high and low strain rates. The first term is negligible during creep and the second term is negligible during high rate tensile tests. Both terms are active at intermediate values of stress or strain rate. The constants n_1 and n_2 characterize the strain-rate sensitivity and are determined independently. This is consistent with the response observed by Pope and Ezz (1984) for single-crystal alloys. The state variables $Z_1^{\alpha\beta}$ and $Z_2^{\alpha\beta}$ include work hardening arising from the development of a dislocation microstructure and include core width and cross slip effects.

The drag stress at high strain rates, $Z_1^{\alpha\beta}$, is assumed to be similar to the Lall, Chin, and Pope result, equation (2), and is given by

$$Z_1^{\alpha\beta} = Z^{\alpha\beta} + \phi_1 - V_{11}\,\tau_1^{\alpha\beta} + V_{12}\,|\tau_2^{\alpha\beta}| \tag{7}$$

where ϕ_1 is the initial value of $Z_1^{\alpha\beta}$, $Z^{\alpha\beta}$ (0) = 0 and V_{11} and V_{12} are constants. The parameter $Z^{\alpha\beta}$ is a measure of work hardening and $\tau_1^{\alpha\beta}$ and $\tau_2^{\alpha\beta}$ are the shear stress components associated with the core width effect and the cross slip mechanism previously discussed. The shear stress $\tau_1^{\alpha\beta}$ is on the same octahedral plane and is perpendicular to $\tau^{\alpha\beta}$. The shear stress $|\tau^{\alpha\beta}|$ is the magnitude of the resolved shear stress on the cube plane in the same direction as $\tau^{\alpha\beta}$. The increase in flow resistance due to work hardening, $Z^{\alpha\beta}$, is given by the evolution equation

$$\dot{Z}^{\alpha\beta} = M_1(W_1 - Z^{\alpha\beta})\tau^{\alpha\beta}\dot{\gamma}^{\alpha\beta} \tag{8}$$

where M_1 and W_1 are material constants. The functional form of the evolution equation involving inelastic work rate $\tau^{\alpha\beta}\dot{\gamma}^{\alpha\beta}$ rather than $\dot{\gamma}^{\alpha\beta}$ alone is very similar to the form used in the Bodner model for isotropic materials. A major difference is that there is no recovery term included in equation (8). Also absent is an explicit function to model the effect of hardening due to intersecting slip systems.

The expression for the state variable $Z_2^{\alpha\beta}$ at low strain rates is similar in form to equation (7) and is given by

$$Z_2^{\alpha\beta} = aZ^{\alpha\beta} + \phi_2 - \frac{V_{21}\tau_1^{\alpha\beta}}{\sqrt{3J_2}} + \frac{V_{22}|\tau_2^{\alpha\beta}|}{\sqrt{3J_2}} \tag{9}$$

where V_{21}, and V_{22} are material parameters associated with the shear stress components $\tau_1^{\alpha\beta}$ and $\tau_2^{\alpha\beta}$ and J_2 is the second invariant of the deviatoric stress tensor. Equations (7) and (9) are coupled since the same work-hardening term $Z^{\alpha\beta}$ appears in both equations. The parameters a and ϕ_2 define the development of the dislocation structure (hardening) at the stress-strain rate levels associated with creep. Equation (9) is valid for primary and secondary creep only. A thermal recovery term may also be necessary at higher temperatures. Tertiary creep is beyond the range of interest in this study.

VI Cube Flow Equation

Cube slip occurs in specimens where the loading is near the [111] material direction and becomes increasingly important at high temperature. Furthermore, Schmid's law is a good approximation for cube slip. The inelastic shear strain rate, $\dot{\gamma}^{\alpha\beta}_{\mathrm{CUBE}}$, on an α cube plane in the β-direction is formulated with two terms similar to equation (6) for octahedral slip and is given by

$$\dot{\gamma}^{\alpha\beta} = \left\{D_3 \exp\left|-\left(\frac{Z_3^{\alpha\beta}}{|\tau^{\alpha\beta}|}\right)^{n_3}\right| + D_4 \exp\left|-\left(\frac{Z_4^{\alpha\beta}}{|\tau^{\alpha\beta}|}\right)^{n_4}\right|\right\}\frac{\tau^{\alpha\beta}}{|\tau^{\alpha\beta}|}. \tag{10}$$

Once again the constants D_3 and D_4 are the limiting strain rates and are chosen to be 10^4 sec^{-1} and 1 sec^{-1} to allow separation of the two terms. The constants n_3 and n_4 reflect the strain-rate sensitivity of the material in cube slip; and, $Z_3^{\alpha\beta}$ and $Z_4^{\alpha\beta}$ are the state variables that include work hardening.

Table 2 Comparison of montonic yield stresses and calculated saturation stresses with octahedral and cube slip constitutive models active

ORIENTATION	TENSION OR COMPRESSION	.02% YIELD STRESS (REF [37]) (MPa)	CALCULATED SATURATION STRESS (MPa)	|ERROR| (%)
[001]*	T	956	956	0
[001]*	C	-818	-819	.1
[011]*	T	748	752	.5
[011]	C	-905	-865	4.4
[$\bar{1}$11]*	T	817	827	1.3
[$\bar{1}$11]	C	-842	-828	1.7
[023]	T	695	705	1.5
[023]	C	-747	-741	.9
[$\bar{2}$36]	T	716	725	1.2
[$\bar{2}$36]	C	-714	-752	5.3
[$\bar{1}$45]	T	656	692	5.5
[$\bar{1}$45]	C	-792	-763	3.6

* CONSTANTS WERE DERIVED USING THIS DATA

Downloaded 03 May 2010 to 171.66.16.21. Redistribution subject to ASME license or copyright; see http://www.asme.org/terms/Terms_Use.cfm

The evolution equations that account for the work hardening are similar to that for octahedral slip except that the orientation factors are excluded. These can be summarized as

$$Z_3^{\alpha\beta} = \phi_3 + Z^{\alpha\beta} \tag{11}$$

and

$$Z_4^{\alpha\beta} = \phi_4 + bZ^{\alpha\beta} \tag{12}$$

where the evolution of $Z^{\alpha\beta}$ is given by

$$\dot{Z}^{\alpha\beta} = M_3(W_3 - Z^{\alpha\beta})\tau^{\alpha\beta}\dot{\gamma}^{\alpha\beta}, \tag{13}$$

where $Z^{\alpha\beta}$ (0) = 0 and W_3 and M_3 are determined from the high rate data. The parameters ϕ_4 and b relate the hardening in the high rate and low rate response for the cube slip.

VII Derivation of the Material Parameters

Material parameters were determined for Rene N4 from data published in the literature to provide a means to test the constitutive model. In this study, the temperature is limited to 760° because the orientation dependence and tension/compression asymmetry are more predominant and the repeatability of the data is better.

At 760°C, the stress-strain response for several orientations in both tension and compression, and fatigue response was determined by Gabb, Gayda, Miner, and Voigt (1986, 1988). Also available at 760°C are tensile stress-strain and creep data of Wukusick (1980) at three orientations for an earlier version of Rene N4, designated as VF317. The slightly different chemistry for VF317 may be the source of difference in the observed response. The yield stress reported by Gabb, Gayda, Miner, and Voigt for specimens oriented in the [0 0 1] was about 30 percent less than VF317 in tension. Since the response characteristics are significantly different for the two data sets, it was not possible to develop a single set of material constants for the constitutive model. The Gabb, Gayda, Miner, and Voigt data were used to develop the constants and test the model for octahedral and cube slip at high strain rates in tension and compression. The VF317 data were used to develop the constants for octahedral slip at high strain rates in tension and were used to develop the constants for octahedral slip at high strain rates in tension and low stress levels in creep.

The octahedral slip constants are derived from tests where cube slip is not present, for example, the [0 0 1] and [0 1 1] orientations. Conversely, the cube slip constants are derived from tests where octahedral slip is not present, i.e., [1 1 1] orientation. In addition, the first term in the octahedral or cube flow equation is negligible in creep and the second term is negligible at high strain rates. When a choice of orientations is available for developing constants, the data from the [0 0 1] orientation is used since it is the primary loading direction in turbine blade applications.

For the purpose of developing material constants, it is important to choose test orientations where the local stress and strain rate on each of the slip planes can be determined. For example, a load in the [0 0 1]-direction will produce equal stresses on eight of the (111) [$\bar{1}$ 0 1] slip systems and no stress on the other (111) [$\bar{1}$ 0 1] systems or the cube systems. It is expected that slip on all eight systems will be the same. By comparison, a load on a [930] specimen will have shear stresses in all of the (111) [$\bar{1}$ 0 1] slip directions. Further, it is expected that these shear stresses will produce slip on more than one system and the slip rates are not expected to be equal. Thus the tests in the [0 0 1], [0 1 1] and [1 1 1] are preferred for evaluating constants due to the uniformity of stress and strain rate in the octahedral and cube systems. Furthermore, only octahedral slip is found near the [0 0 1] orientation (no stress on the cube planes) and only cube slip is found near the [1 1 1]-direction (dominant stress on the cube planes).

Details of the methods of determining the constants are reported by Dame (1985). The constants used in the calculations in the study are given in Table 1 for each data set.

VIII Comparison of the Calculated and Experimental Results

All numerical calculations were performed using a nonlinear finite-element code. A modified Newton-Raphson procedure was used because it is an efficient technique for incorporating time-dependent constitutive models. This technique is economical because the stiffness matrix is recalculated only for temperature changes. A 20-noded isoparametric solid element was chosen to allow for any orientation of the material principal axes. Order two Gaussian integration was used for both stiffness generation and calculation of the body forces. The ability to model piecewise linear load histories was also included.

An important aspect of the constitutive equation subroutine was an automatic time-stepping system. The time increment used for the calculation is chosen as the minimum from three different control criteria based on a maximum stress increment, maximum strain increment, and maximum strain-rate increment. The maximum stress increment is used to control the time step primarily during elastic loading. The inelastic strain increment criterion controls the time step when the stress and inelastic strain rate are not changing significantly. The rate of change of the inelastic strain rate is used to control the time step when the inelastic strain rate is changing rapidly.

Since all of the calculations were for uniaxial tests, it was not necessary to model the actual specimen geometry and a model with two 20-noded bricks was used to simulate the specimen response. The calculations were performed to compare with test results and also to exercise the constitutive model and computer code under conditions for which no data are available.

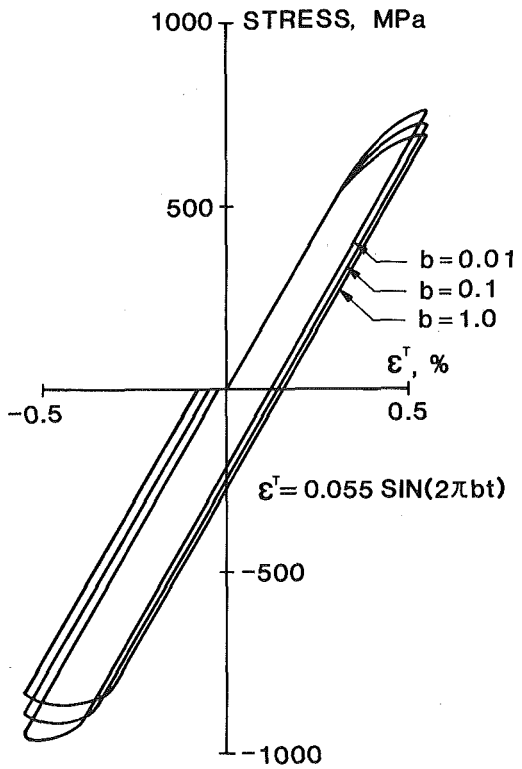


Fig. 2 Predicted strain-rate sensitivity of Rene N4 at 760°C for a specimen in the [011]-direction

Downloaded 03 May 2010 to 171.66.16.21. Redistribution subject to ASME license or copyright; see http://www.asme.org/terms/Terms_Use.cfm

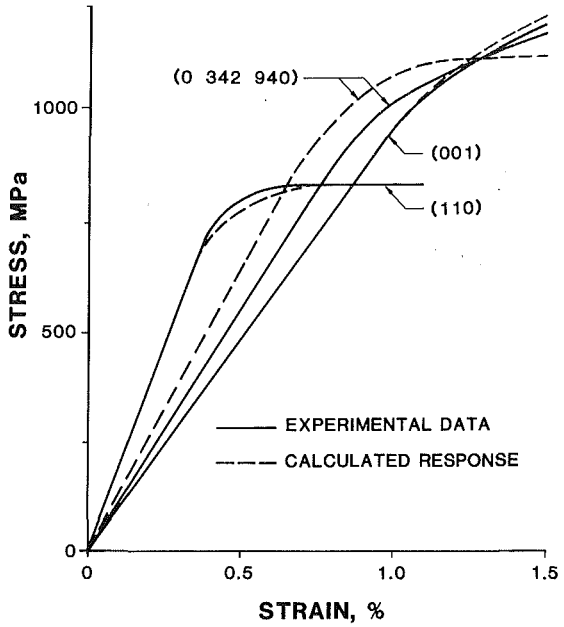


Fig. 3 Predicted and experimental tensile response for Rene N4 VF317 at 760°C; (data taken by Wukusick, 1980)

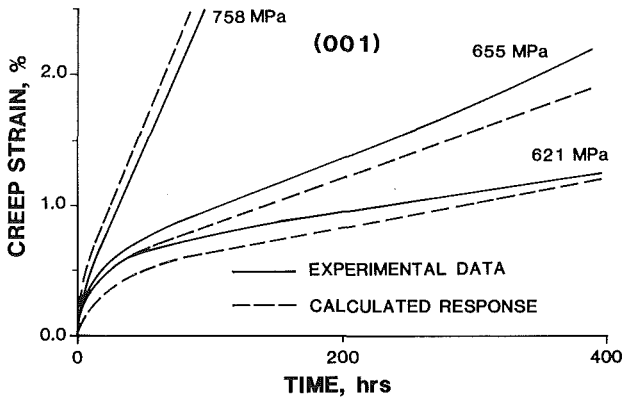


Fig. 4 Creep response of Rene N4 VF317 in the [001]-direction at 760°C; (data taken by Wukusick, 1980)

(*a*) Comparison for the Gabb, Gayda, Minor and Voigt Data. The calculations were performed using the constants derived from the data presented by Gabb, Gayda, Miner, and Voigt (1986, 1988). The constants are for octahedral and cube slip at high strain rate (Table 1). The model was exercised to evaluate the orientation dependence, tension/compression asymmetry, strain rate dependence and cyclic response. Because of the assumptions required in the derivation of the material constants due to the limited data base, most of the exercises for this data set are intended to demonstrate features of the constitutive model rather than correlation with experimental data.

The constants were derived by hypothesizing that the .02 percent yield stress for the first quarter cycle of sinusoidal loading was representative of the orientation dependence and tension/compression asymmetry for constant strain rate tests. The octahedral constants were derived using the [001] tension and compression tests and the [011] tension data. The cube slip constants were derived using the [111] tension data. The stress response was calculated for these tests and for the tests at other orientations. The calculated results are compared to the experimental results in Table 2. All of the predicted results are within 6 percent of the experimental values and within the confidence level for the experiments. It can be concluded that the constitutive model successfully predicts the orientation dependence and tension/compression asymmetry in octahedral slip. It can also be seen that the octahedral and cube flow equations produce good results when simultaneously activated.

In order to demonstrate the strain-rate sensitivity of the constitutive model, first cycle fatigue loops were calculated for two different orientations and three different rates using the sinusoidal total strain history. The results of this exercise are shown in Fig. 2. Qualitatively, it can be stated that the observed trend is as expected. Since no data are available, quantitative comparisons are not possible.

(*b*) Comparison for the Wukusick Data. The calculations were performed using the constants derived from the experiments by Wukusick (1980) for Rene N4 VF317. The constants are for octahedral slip at high strain rate and creep. The features of the model that are exercised are orientation-dependent stress-strain curves and orientation-dependent creep response.

The stress-strain response was calculated for a constant strain rate of 8.333×10^{-5} sec^{-1} for three orientations. The calculated response compared to the experimental data is shown in Fig. 3. The orientation constants were determined using all three curves so the variation in the yield stress levels is reproduced well. The hardening parameters were calculated from the [001] curve only.

Notice that there is a significant mismatch in the elastic modulus for the predicted and experimental response for the [0 342 940] orientation. The difference in the experimental and calculated elastic modulus suggests that the specimens in this data set designated as being in the [039]-direction are probably much closer to the [001]-direction. This inconsistency is further verified through an example compression calculation. The predicted saturation stress response for a [001] specimen in compression was less than a third of the corresponding tensile [001] response. This is not realistic; especially since the model worked very well for the previous tension/compression exercises. This would further explain the large differences in the constants V_{11} and V_{12} for the two data sets.

The tensile creep curves for seven specimens at three orientations were calculated and are compared with experimental data in Figs. 4–6. The experimental data are from creep rupture tests which usually do not yield reliable data at the beginning of a test. Usually this type of test produces significant variation from test-to-test due to poor alignment and strain measuring systems as well as inherent differences from specimen-to-specimen. The correlation between the predicted and actual response for this type of test must be considered to be excellent.

IX Conclusion

The constitutive model developed in this study successfully predicts an important part of the observed material behavior although a great deal remains to be done. A method has been developed for the derivation of material constants and no special or difficult tests are required.

The implementation of the constitutive model in a nonlinear finite-element code has been accomplished. It is computationally more intensive than comparable rate-dependent isotropic models or rate-independent anisotropic models, but it is not significantly more expensive.

References

Bishop, J., 1952, "A Theoretical Examination of the Plastic Deformation of Crystals by Glide," *Philosophical Magazine*, p. 51.

Bishop, J., and Hill, R., 1951, "A Theoretical Derivaton of the Plastic Pro-

Downloaded 03 May 2010 to 171.66.16.21. Redistribution subject to ASME license or copyright; see http://www.asme.org/terms/Terms_Use.cfm

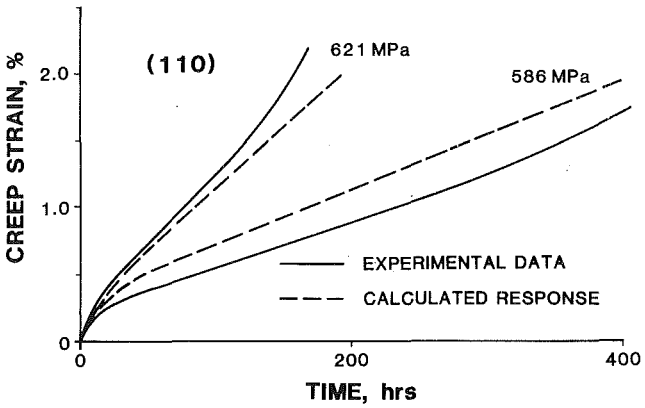


Fig. 5 Creep response of Rene N4 VF317 in the [110]-direction at 760°C; (data taken by Wukusick, 1980)

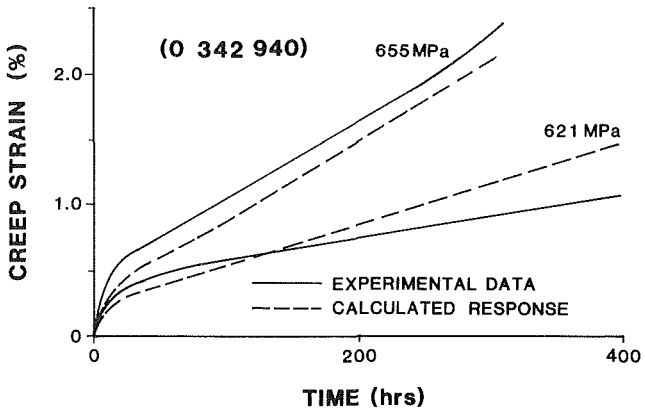


Fig. 6 Creep response of Rene N4 VF317 in the [0 342 960] direction at 760°C; (data taken by Wukusick, 1980)

perties of a Polycrystalline Face-Centered Metal," *Philosophical Magazine*, Vol. 42, 1298.

Bishop, J., and Hill, R., 1951, "A Theory of the Plastic Distortion of a Polycrystalline Aggregate Under Combined Stresses," *Philosophical Magazine*, p. 414.

Bodner, S., and Partom, Y., 1975, "Constitutive Equations for Elastic-Viscoplastic Strain-Hardening Materials," ASME JOURNAL OF APPLIED MECHANICS, Vol. 42, p. 385.

Bodner, S., Partom, I., and Partom, Y., 1979, "Uniaxial Cyclic Loading of Elastic-Viscoplastic Materials," ASME JOURNAL OF APPLIED MECHANICS, Vol. 46, p. 805.

Dame, L., Stouffer, D, and Abuelfoutouh, N., 1984, "Finite Element Analysis of Notch Behavior Using a State Variable Constitutive Equation," *Proceedings of 2nd Symposium on Nonlinear Constitutive Relations for High Temperature Applications*, NASA Lewis.

Dame, L. T., 1985, "Anisotropic Constitutive Model for Nickel Base Single Crystal Alloys: Development and Finite Element Implementation," PhD Dissertation, University of Cincinnati, 1985.

Davies, R., and Johnston, T., 1970, *Ordered Alloys*, Eds. B. Kear, et al., p. 447, Baton Rouge, LA, Claitor's Publishing Division.

Ezz, S., Pope, D., and Paidar, V., 1982, "The Tension/Compression Flow Stress Asymmetry in Ni_3 (Al,Nb) Single Crystals," *Acta Metallurgica*, Vol. 30, p. 921.

Gabb, T., Gayda, J., and Miner, R., 1986, "Orientation and Temperature Dependence of Some Mechanical Properties of the Single-Crystal Nickel-Base Superalloy RENE N4: Part II. Low Cycle Fatigue," *Metallurgical Transactions A*, Vol. 17, pp. 497–505.

Giamei, A., 1979, "Deformation and Fracture of Advanced Anisotropic Superalloys," Final Technical Report, Contract No. F44620-76-C-0028, Air Force Office of Scientific Research.

Lall, C., Chin, S., and Pope, D., 1979, "The Orientation and Temperature Dependence of the Yield Stress of Ni_3 (Al,Nb) Single Crystals," *Metallurgical Transactions A*, Vol. 10A, p. 1323.

Miner, R., Voigt, R., Gayda, J., and Gabb, T., 1986, "Orientation and Temperature Dependence of Some Mechanical Properties of the Single-Crystal Nickel-Base Superalloy Rene N4: Part I. Tensile Behavior," *Metallurgical Transaction A*, Vol. 17, pp. 491–496.

Paslay, P., Wells, C., and Leverant, G., 1970, "An Analysis of Primary Creep of Nickel-Base Superalloy Single Crystals," ASME JOURNAL OF APPLIED MECHANICS, p. 759.

Paslay, P., Wells, C., Leverant, G., and Burck, L., 1971, "Creep of Single Crystal Nickel-Base Superalloy Tubes Under Biaxial Tension," ASME JOURNAL OF APPLIED MECHANICS, Vol. 38, p. 623.

Pope, D., and Ezz, S., 1984, "Mechanical Properties of Ni_3Al and Nickel-Base Alloys with High Volume Fraction of γ' ," *International Metals Reviews*, Vol. 29, No. 3, p. 136.

Pope, D., and Heredia, F., 1984, "The Tension/Compression Asymmery in High γ' Volume Fraction Nickel Base Alloy Single Crystals," Fifth International Symposium on Superalloys, ASM, Metals Park, OH.

Robinson, D. N., 1978, "A Unified Creep Plasticity Model for Structural Metals at High Temperature," ORNL TM-5969.

Robinson, D.N., and Swindeman, R. W., 1982, "Unified Creep-Plasticity Constitutive Equations for 2¼ CR-1 M_0 Steel at Elevated Temperature," ORNL TM-8444.

Shah, D., and Duhl, D., 1984, "The Effect of Orientation, Temperature and Gamma Prime Size on the Yield Strength of a Single Crystal Nickel Base Superalloy," *Proceedings of the Fifth International Symposium on Superalloys*, ASM, Metals Park, OH.

Shah, D., 1983, "Orientation Dependence of Creep Behavior of Single Crystal γ' (Ni_3Al)," *Scripta Metallurgica*, Vol. 17, p. 997.

Stouffer, D., and Bodner, S., 1982, "A Relationship Between Theory and Experiment for a State Variable Mechanical Testing for Deformation Model Development," ASTM STP 765, American Society for Testing and Materials, p. 239, 1982.

Takeuchi, S., and Kuramoto, E., 1973, "Temperature and Orientation Dependence of the Yield Stress in Ni_3Ga Single Crystals," *Acta Metallurgica*, Vol. 21, p. 415.

Taylor, G., 1938, "Plastic Strains in Metals," *Journal Inst. Metals*, Vol. 62, p. 307.

Tien, J., Kear, B., and Leverant, G., 1972, "On the High Activation Energy for Steady State Creep of Particle Strengthened Systems," *Scripta Metallurgica*, Vol. 6, p. 135.

Umakoshi, Y., Pope, D., and Vitek, V., 1984, "The Asymmetry of The Flow Stress in Ni_3(Al,Ta) Single Crystals," *Acta Metallurgica*, Vol. 32, No. 3, p. 449.

Walker, K. P., 1981, "Research and Development Program for Nonlinear Structural Modeling and Advanced Time-Temperature Dependent Constitutive Relationships," NASA CR165533.

Wee, D., Pope, D., and Vitek, V., 1984, "Plastic Flow of Pt_3Al Single Crystals," *Acta Metallurgica*, Vol. 32, No. 6, p. 829.

Wukusick, C., 1980, "Directional Solidification Alloy Development," NADC-78136-60, Naval Air Systems Command.

Yang, S., 1984, "Elastic Constants of a Monocrystalline Nickel-Base Superalloy," *Metallurgical Transactions A.*, Vol. 16A-No. 4, p. 661.

Downloaded 03 May 2010 to 171.66.16.21. Redistribution subject to ASME license or copyright; see http://www.asme.org/terms/Terms_Use.cfm

Finite Axisymmetric Deformation of Rubber-Like Shells of Revolution

W. J. Keppel
National Optical Astronomy Observatories,
950 N. Cherry Avenue,
P.O. Box 26732,
Tucson, AZ 85726-6732

D. A. DaDeppo
The University of Arizona,
Tucson, AZ

The finite axisymmetric deformation of a thin shell of revolution is treated in this analysis. The governing differential equations are given for a hyperelastic shell material with the Mooney-Rivlin strain-energy-density function. These equations are solved numerically using a 4th-order Runge-Kutta integration method. A generalized Newton-Raphson iteration procedure is used to systematically improve trial solutions of the differential equations. The governing differential equations are differentiated with respect to a set of generalized coordinates to derive associated rate equations. The rate equations are solved numerically to generate the tangent stiffness matrix which is used to determine the load deformation history of the shell with incremental loading. Numerical examples are presented to illustrate the major characteristics of nonlinear shell behavior.

Introduction

The subject of this paper is the nonlinear analysis of a thin shell of revolution which has bending rigidity and is in a state of axisymmetric deformation for which the displacements, rotations, and strains may be arbitrarily large. The analysis, therefore, will be applicable to a shell of revolution which is thin and made of a material that permits large elastic strains. A precise description of this problem requires use of exact nonlinear equations of equilibrium and constitutive relations that are suitable for a material undergoing large elastic strains. Thus the problem has both geometric and material nonlinearity.

Until recently, most analyses of nonlinear shell problems have been based primarily on equations for large deflection and rotation with the assumption of small strain. The assumption of small strain in some cases permits the use of linear constitutive relations. In particular, the Reissner equations (1949) for shells of revolution have been used widely. Examples can be found in the papers of Archer (1962), Kalnins (1964, 1967), Mescal (1965), Wilson and Spier (1965) and Lehner and Batterman (1974). Interest in large material deformation of shells is growing, especially in the field of biomechanics, where shell structures such as the heart, bladder, and red blood cells often undergo large elastic strains. Although theories for arbitrarily large bending and membrane strain have been available for years, Naghdi (1972), the full nonlinear equations are not readily solvable even by numerical methods. Thus recent papers by Reissner (1972), Libai and Simmonds (1981, 1983), Simmonds (1985), and Taber (1985) treat portions of the general problem with an emphasis on application.

Contributed by the Applied Mechanics Division for publication in the JOURNAL OF APPLIED MECHANICS.

Discussion on this paper should be addressed to the Editorial Department, ASME, United Engineering Center, 345 East 47th Street, New York, N.Y. 10017, and will be accepted until two months after final publication of the paper itself in the JOURNAL OF APPLIED MECHANICS. Manuscript received by ASME Applied Mechanics Division, June 26, 1986; final revision, December 11, 1987.

The theory of large elastic deformation or rubber-like shells obtained through integration of a three-dimensional strain-energy-density function W was first developed by Biricikoglu and Kalnins (1971) who took W to be of the Mooney-Rivlin form. However, the analysis of Biricikoglu and Kalnins (1971) contains two major deficiencies. First, the kinematic model employed allows the incompressibility condition to be satisfied only at the reference surface of the shell. The resulting equations are applicable when stretching dominates bending. Second, the method used to obtain the constitutive relations for the shell does not enable the stress resultants and couples to be expressed as partial derivatives of a strain-energy-density function. Thus the property of hyperelasticity for the shell is not preserved and, as a consequence, the tangent stiffness matrix of the shell derived from this constitutive law may not be symmetric. Recent work by DaDeppo and Keppel (1986) has shown that the tangent stiffness matrix must be symmetric if the material is hyperelastic and the applied loading is conservative.

A method of obtaining an approximate two-dimensional strain-energy-density function, Φ, valid for large extensional strain has been presented by Simmonds (1985). The function Φ is determined using intrinsic, two-dimensional arguments in which the difference between the metric and curvature tensors of the deformed and undeformed shell are taken as measures of extensional and bending strain, respectively. In addition, Φ was derived from a three-dimensional strain-energy density function W.

For the case of axisymmetric deformation of a thin shell of revolution undergoing large stretching and bending, Taber (1985) has obtained approximate constitutive relations for the stress resultants and couples and derived a form for Φ for a hyperelastic and incompressible material with strain-energy-density function W. The effects of various simplifications on the constitutive relations were also investigated and numerical

Copyright © 1988 by ASME
Downloaded 03 May 2010 to 171.66.16.21. Redistribution subject to ASME license or copyright; see http://www.asme.org/terms/Terms_Use.cfm

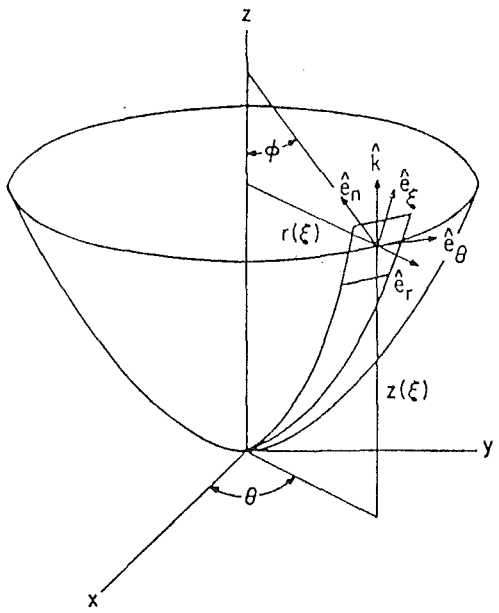


Fig. 1 Middle surface of shell, showing coordinates ξ, θ on middle surface and unit vectors associated with middle surface

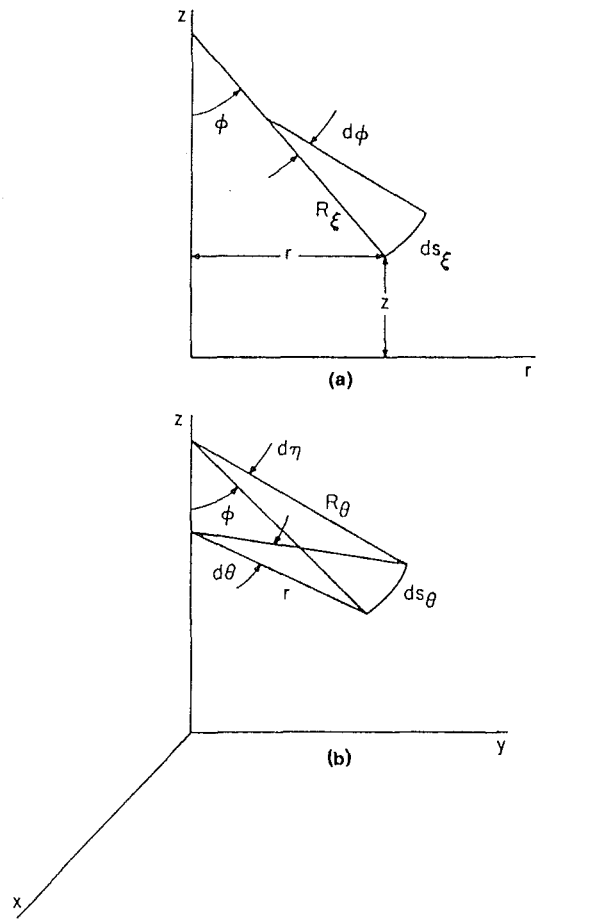


Fig. 2 Meridional and circumferential radii of curvature of middle surface

results were presented for clamped edges of cylindrical and spherical shells.

The primary objective of this paper is to obtain highly accurate results which could serve as a guide in the development of, and as a standard of comparison for, approximate methods of analysis. The method of solution used in this work is numerical integration of the exact nonlinear differential equations which govern the finite axisymmetric deformation of a thin shell of revolution. This method of analysis consists of solving a two-point boundary-value problem associated with a typical segment of the shell with the aid of a forward integration method and the Newton-Raphson method. The Newton-Raphson method is also used to solve the problem of determining nodal positions such that the nodal equations of equilibrium are satisfied. Incremental loading is prescribed to obtain the load-deformation behavior of the shell. All of the required derivatives for the Newton-Raphson method are obtained by integration of differential equations derived from the governing differential equations for the shell.

The pre- and post-buckling behavior of hemispherical shells with the Mooney-Rivlin strain-energy-density function is investigated under the action of nodal and distributed loads. Numerical results are presented in the form of load-deflection curves and deformed geometry plots.

Formulation of Shell Equations

An exact formulation of the basic governing shell equations is made within the limitations of the following assumptions:

1 The shell is thin.
2 The material is incompressible.
3 The effects of transverse normal stress and shear deformation are negligible.
4 Line elements, normal to the undeformed reference surface, remain normal to the deformed reference surface but undergo change in length during deformation.
5 The deformation and applied loading are axisymmetric.

The resulting equations are exact in the sense that no restrictions are placed on the magnitude of the deformation of the reference surface.

Geometric Relations. The basic geometric variables used to describe a surface of revolution are illustrated in Fig. 1. The equation of the middle surface of the shell is written in parametric form

$$r = r(\xi) \tag{1}$$

$$z = z(\xi) \tag{2}$$

so that ξ, which locates position on a meridian, and the polar angle θ in the x-y plane are the coordinates of the middle surface.

Let $\hat{\mathbf{i}}$, $\hat{\mathbf{j}}$, and $\hat{\mathbf{k}}$ be unit vectors in the x, y, and z-directions, respectively. The radial and circumferential unit vectors $\hat{\mathbf{e}}_r$ and $\hat{\mathbf{e}}_\theta$ are then defined by

$$\hat{\mathbf{e}}_r = \cos\theta\,\hat{\mathbf{i}} + \sin\theta\,\hat{\mathbf{j}} \tag{3}$$

$$\hat{\mathbf{e}}_\theta = -\sin\theta\,\hat{\mathbf{i}} + \cos\theta\hat{\mathbf{j}} \tag{4}$$

and the tangential and normal unit vectors $\hat{\mathbf{e}}_\xi$ and $\hat{\mathbf{e}}_n$ by

$$\hat{\mathbf{e}}_\xi = \cos\phi\,\hat{\mathbf{e}}_r + \sin\phi\,\hat{\mathbf{k}} \tag{5}$$

$$\hat{\mathbf{e}}_n = -\sin\phi\,\hat{\mathbf{e}}_r + \cos\phi\,\hat{\mathbf{k}} \tag{6}$$

A meridional element of arc length ds_ξ and its radius of curvature R_ξ are shown in Fig. 2(a) and the corresponding circumferential element of arc length ds_θ and its radius of curvature R_θ are shown in Fig. 2(b). For a shell of revolution, R_ξ and R_θ are the principal radii of curvature of the middle surface.

Using Figs. 2 (a, b), it can be established that

$$\frac{dr}{ds_\xi} = \cos\phi, \tag{7}$$

Downloaded 03 May 2010 to 171.66.16.21. Redistribution subject to ASME license or copyright; see http://www.asme.org/terms/Terms_Use.cfm

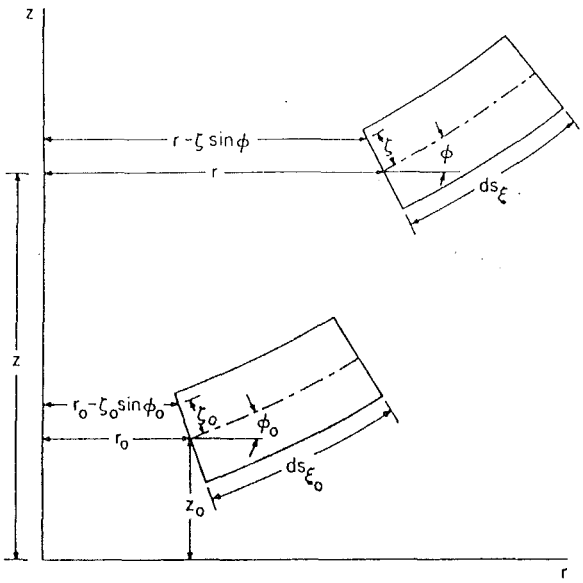


Fig. 3 Side view of element of shell in undeformed and in deformed state

$$\frac{dz}{ds_\xi} = \sin\phi, \tag{8}$$

$$\frac{d\phi}{ds_\xi} = \frac{1}{R_\xi} \tag{9}$$

$$\frac{d\eta}{ds_\theta} = \frac{1}{R_\theta} = \frac{\sin\phi}{r} \tag{10}$$

With reference to the geometry of Fig. 3, at a point in the deformed shell whose position in the undeformed shell is (ξ_0, θ_0, ζ_0), the principal stretch ratios as given by Taber (1985) are

$$\Lambda_\xi = \frac{dS_\xi}{dS_{\xi_0}} = \frac{\lambda_\xi\,(1-\zeta\kappa_\xi)}{(1-\zeta_0\kappa_{\xi_0})} \tag{11}$$

$$\Lambda_\theta = \frac{dS_\theta}{dS_{\theta_0}} = \frac{\lambda_\theta(1-\zeta\kappa_\theta)}{(1-\zeta_0\kappa_{\theta_0})} \tag{12}$$

$$\Lambda_\zeta = \frac{d\zeta}{d\zeta_0} = \frac{1}{\Lambda_\xi\Lambda_\theta} \tag{13}$$

where the subscript "0" indicates values for the undeformed geometry and ζ represents the distance from the middle surface of the shell. Equation (13) expresses the condition of material incompressibility $\Lambda_\xi\Lambda_\theta\Lambda_\zeta = 1$. The stretch ratios at the middle surface are

$$\lambda_\xi = \Lambda_\xi\ \ (\zeta=\zeta_0=0) = \frac{ds_\xi}{ds_{\xi_0}} \tag{14}$$

$$\lambda_\theta = \Lambda_\theta\,(\zeta=\zeta_0=0) = \frac{ds_\theta}{ds_{\theta_0}} = \frac{r}{r_0} \tag{15}$$

$$\lambda_\zeta = \frac{1}{\lambda_\xi\lambda_\theta} \tag{16}$$

and the curvatures are

$$\kappa_\xi = \frac{1}{R_\xi} = \frac{c_\xi}{\lambda_\xi}, \quad \kappa_\theta = \frac{1}{R_\theta} = \frac{c_\theta}{\lambda_\theta}$$
$$\kappa_{\xi_0} = \frac{1}{R_{\xi_0}} = c_{\xi_0}, \quad \kappa_{\theta_0} = \frac{1}{R_{\theta_0}} = c_{\theta_0} \tag{17}$$

where

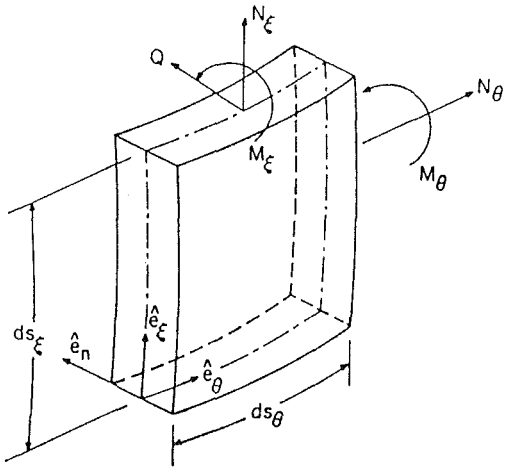


Fig. 4 Element of shell showing stress resultants and stress couples

$$c_\xi = \frac{d\phi}{ds_{\xi_0}}, \quad c_\theta = \frac{d\eta}{ds_{\theta_0}} \tag{18}$$

are curvature type terms for the deformed shell.

The state of strain at a location ζ is completely determined once the midsurface stretch ratios are specified. The explicit dependence on the deformed coordinate ζ is eliminated by enforcing the condition of incompressibility through the deformed thickness of the shell.

Following the method outlined in Simmonds (1985), the deformed transverse coordinate ζ is taken as a third-order power series

$$\zeta = \lambda_\zeta\left(\zeta_0 + g_1\frac{\zeta_0^2}{2} + g_2\frac{\zeta_0^3}{3}\right) \tag{19}$$

where g_1 and g_2 are independent of ζ_0. Differentiating equation (19) with respect to ζ_0 gives

$$\Lambda_\zeta = \frac{d\zeta}{d\zeta_0} = \lambda_\zeta\,(1 + g_1\zeta_0 + g_2\zeta_0^2) \tag{20}$$

which reduces to $\Lambda_\zeta = \lambda_\zeta$ at the reference surface ($\zeta_0 = 0$). Substitution of equations (11)–(13), (19), and (20) into the incompressibility condition $\Lambda_\xi\Lambda_\theta\Lambda_\zeta = 1$ and equating coefficients of the first two powers of ζ_0 yields

$$g_1 = \bar\kappa_\xi + \bar\kappa_\theta$$
$$g_2 = \frac{1}{2}\left[3\bar\kappa_\xi^2 + 4\bar\kappa_\xi\bar\kappa_\theta + 3\bar\kappa_\theta^2 + \bar\kappa_\xi(3\kappa_{\xi_0} + \kappa_{\theta_0}) + \bar\kappa_\theta\,(\kappa_{\xi_0} + 3\kappa_{\theta_0})\right] \tag{21}$$

where

$$\bar\kappa_\xi = \lambda_\zeta\kappa_\xi - \kappa_{\xi_0} = \frac{c_\xi}{\lambda_\xi^2\lambda_\theta} - c_{\xi_0}$$
$$\bar\kappa_\theta = \lambda_\zeta\kappa_\theta - \kappa_{\theta_0} = \frac{c_\theta}{\lambda_\xi\lambda_\theta^2} - c_{\theta_0} \tag{22}$$

represent measures of change in curvature for the shell.

Equilibrium Equations. The stress resultants and stress couples which act on an element of the reference surface of the shell are shown in Fig. 4. Illustrated in Fig. 5 is a deformed meridional segment in an equilibrium position under the action of stress resultants and stress couples as well as the components of the distributed load, which are measured per unit of deformed circumferential arc length and per unit of deformed area of the reference surface, respectively. The horizontal stress resultant H and the vertical stress resultant V are related to the tangential stress resultant N_ξ and the shear stress resultant Q through the relations

Downloaded 03 May 2010 to 171.66.16.21. Redistribution subject to ASME license or copyright; see http://www.asme.org/terms/Terms_Use.cfm

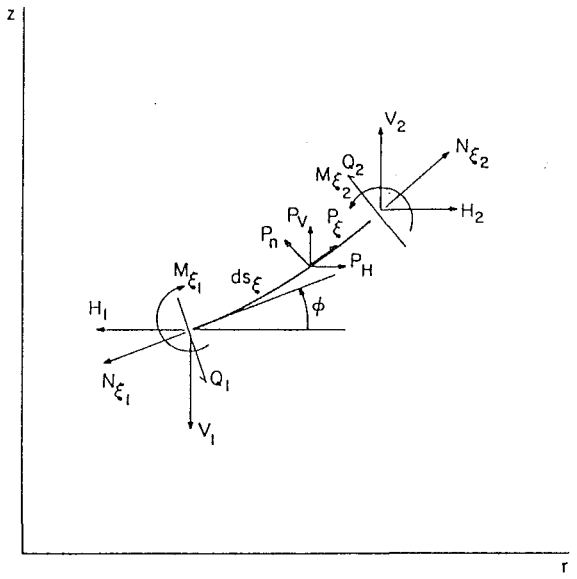


Fig. 5 Side view of element of shell in the deformed state showing visible stress resultants and couples and distributed load components

$$N_\xi = H\cos\phi + V\sin\phi \quad Q = -H\sin\phi + V\cos\phi \tag{23}$$

Governing Differential Equations. Combining the geometric relations of equations (7)–(9) with the equilibrium equations of Reissner (1949) provides the governing differential equations for axisymmetric deformation of a shell of revolution. Written in terms of s_{ξ_0} and λ_ξ they are

$$\begin{aligned}
\frac{dr}{ds_{\xi_0}} &= \lambda_\xi \cos\phi \\
\frac{dz}{ds_{\xi_0}} &= \lambda_\xi \sin\phi \\
\frac{d\phi}{ds_{\xi_0}} &= c_\xi \\
\frac{d}{ds_{\xi_0}}(rH) &= \lambda_\xi N_\theta - \lambda_\xi\, r\, P_H \\
\frac{d}{ds_{\xi_0}}(rV) &= -\lambda_\xi\, r\, P_v \\
\frac{d}{ds_{\xi_0}}(r\,M_\xi) &= \lambda_\xi\, M_\theta \cos\phi - \lambda_\xi\, rQ
\end{aligned} \tag{24}$$

In equation (24), in general

$$\begin{aligned}
P_H &= P_H\,(s_{\xi_0};\, r,\, z,\, \phi,\, \lambda_\xi,\, \lambda_\theta,\, \lambda_d) \\
P_V &= P_V\,(s_{\xi_0};\, r,\, z,\, \phi,\, \lambda_\xi,\, \lambda_\theta,\, \lambda_d)
\end{aligned} \tag{25}$$

where λ_d represents a distributed load intensity parameter. Equations (24) must be supplemented with appropriate constitutive relations for the shell to obtain a set of equations sufficient for solution.

Virtual Work. In the development of the governing differential equations (24), both force and deformation variables have been introduced. The principle of virtual work provides the connecting relation between these two sets of variables and, for a hyperelastic material, defines the appropriate deformation variables to be used in the strain-energy-density function and the way in which the stress resultants and couples are to be measured.

The virtual work done by the pairs of stress resultants and stress couples and by the components of distributed load, shown in Fig. 5, during an arbitrary virtual displacement (δr, δz, $\delta\phi$) from the deformed configuration, is

$$\begin{aligned}
d\delta W_e &= [d(rH\delta r) + d(rV\delta z) + d(rM_\xi\delta\phi)]d\theta \\
&\quad + P_H r d\theta ds_\xi \delta r + P_V r d\theta ds_\xi \delta z = \delta\hat{\mathbf{W}}_e\, ds_{\theta_0} ds_{\xi_0}
\end{aligned} \tag{26}$$

Following several algebraic manipulations which make use of equations (23) and (24), equation (26) may be written as

$$\delta\hat{W}_e = \hat{N}_\xi\delta\lambda_\xi + \hat{N}_\theta\delta\lambda_\theta + \hat{M}_\xi\delta c_\xi + \hat{M}_\theta\delta c_\theta \tag{27}$$

where

$$\begin{aligned}
\hat{N}_\xi &= \lambda_\theta N_\xi, \quad \hat{N}_\theta = \lambda_\xi N_\theta \\
\hat{M}_\xi &= \lambda_\theta M_\xi, \quad \hat{M}_\theta = \lambda_\xi M_\theta
\end{aligned} \tag{28}$$

are stress resultants and stress couples measured per unit undeformed arc length.

Constitutive Relations. A hyperelastic material is characterized by a strain-energy density W per unit of undeformed volume. For an isotropic material which satisfies the condition of incompressibility $\Lambda_\xi\Lambda_\theta\Lambda_\zeta = 1$, W is a function of the strain invariants

$$\begin{aligned}
I_1 &= \Lambda_\xi^2 + \Lambda_\theta^2 + \Lambda_\zeta^2 = \Lambda_\xi^2 + \Lambda_\theta^2 + \frac{1}{\Lambda_\xi^2\Lambda_\theta^2} \\
I_2 &= \Lambda_\xi^2\Lambda_\theta^2 + \Lambda_\theta^2\Lambda_\zeta^2 + \Lambda_\xi^2\Lambda_\zeta^2 \\
&= \Lambda_\xi^2\Lambda_\theta^2 + \frac{1}{\Lambda_\xi^2} + \frac{1}{\Lambda_\theta^2}
\end{aligned} \tag{29}$$

Since the shell is thin the differential element of volume in the undeformed shell is given by

$$dV_0 = ds_{\theta_0}\, ds_{\xi_0}\, d\zeta_0 \tag{30}$$

and the strain-energy density per unit undeformed area of the reference surface of the shell is

$$U = \int_{-t_0/2}^{t_0/2} W(I_1, I_2)\, d\zeta_0 \tag{31}$$

where t_0 is the thickness of the undeformed shell.

Approximate constitutive relations for the shell may be obtained through the technique outlined by Simmonds (1985). Let W have a power series expansion about $\zeta_0 = 0$, the first three terms of which are

$$W(\zeta_0) = W + \frac{\partial W}{\partial\zeta_0}\zeta_0 + \frac{1}{2}\frac{\partial^2 W}{\partial\zeta_0^2}\zeta_0^2 \tag{32}$$

where the coefficients in equations (32) are evaluated at $\zeta_0 = 0$. Substitution of equation (32) into equation (31) provides the approximation

$$\Phi(\lambda_\xi, \lambda_\theta, c_\xi, c_\theta) = t_0\left[W + \frac{t_0^2}{24}\frac{\partial^2 W}{\partial\zeta_0^2}\right]_{\zeta_0=0} \tag{33}$$

for the strain-energy density per unit undeformed area of the reference surface of the shell.

By definition of a hyperelastic material

$$\delta\hat{W}_e = \delta\Phi \tag{34}$$

since

$$\delta\Phi = \frac{\partial\Phi}{\partial\lambda_\xi}\delta\lambda_\xi + \frac{\partial\Phi}{\partial\lambda_\theta}\delta\lambda_\theta + \frac{\partial\Phi}{\partial c_\xi}\delta c_\xi + \frac{\partial\Phi}{\partial c_\theta}\delta c_\theta \tag{35}$$

the constitutive relations for the shell are

$$\hat{N}_\xi = \frac{\partial\Phi}{\partial\lambda_\xi}, \quad \hat{N}_\theta = \frac{\partial\Phi}{\partial\lambda_\theta}, \quad \hat{M}_\xi = \frac{\partial\Phi}{\partial c_\xi}, \quad \hat{M}_\theta = \frac{\partial\Phi}{\partial c_\theta} \tag{36}$$

Constitutive Model for Rubber. The Mooney-Rivlin model for the strain-energy density has the form

$$W = C_1(I_1 - 3) + C_2(I_2 - 3) \tag{37}$$

Downloaded 03 May 2010 to 171.66.16.21. Redistribution subject to ASME license or copyright; see http://www.asme.org/terms/Terms_Use.cfm

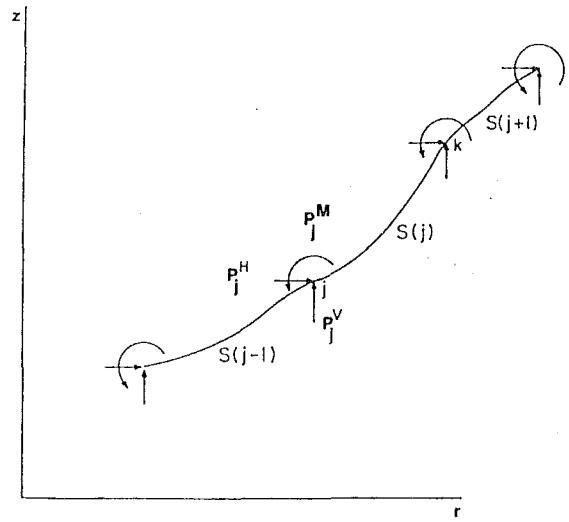


Fig. 6 Shell composed of three segments

where I_1 and I_2 are defined in equations (29) and C_1 and C_2 are material constants. The Mooney-Rivlin model for rubber is employed in this work. The derivatives of W and Φ in equations (33) and (36) are presented in Appendix A.

Solution of Shell Equations

Shell Structures. Nonlinear first-order differential and algebraic equations govern the finite deformation of a shell of revolution. These equations must be solved numerically because it is not yet possible to obtain analytical solutions. The numerical procedures employed in this work are based on a rate formulation of the problem of quasi-static deformation. The governing equations valid for quasi-static deformation may be differentiated with respect to a set of generalized coordinates for a shell segment to obtain rate equations which are linear with respect to the rates.

The rate equations may be integrated numerically over arc length to calculate the tangent stiffness matrix, which plays a central role in a stability analysis, and to evaluate related rates which are used to obtain the load-deformation behavior of the shell under prescribed loading.

Consider a shell composed of several segments rigidly connected to nodal points such that the tangent to the meridian is continuous as shown in Fig. 6. The nodes occur at natural points of discontinuity in the governing differential equations, e.g., at a point corresponding to a line load along a parallel circle. With reference to Fig. 6, let r_j, z_j, and ϕ_j be generalized coordinates of node j; let P_j^H, P_j^V, and P_j^M be the prescribed forces at node j and let P_{jk} be a distributed load applied to segment jk. For simplicity in the subsequent discussion, proportional loading with independent load intensity parameters for nodal and segment loads is assumed; i.e, it is assumed that

$$P_j^H = \lambda P_j^{H0},\ P_j^V = \lambda P_j^{V0},\ P_j^M = \lambda P_j^{M0},\ P_{jk} = \lambda_d\, P_{jk}^0$$

where λ and λ_d are the load intensity parameters.

In terms of the nodal forces and generalized coordinates, the structural analysis problem consists in determining the coordinates r_j, z_j, and ϕ_j for all nodes j and the deformed geometries of all segments such that the shell is in equilibrium under the prescribed loads defined by λ and λ_d. The analytical solution to this problem may be accomplished through the following steps: (1) regard r_j, z_j, and ϕ_j for all nodes and λ_d for the distributed loads as independent parameters; (2) integrate the governing differential equations (24) for each segment jk and evaluate the horizontal force, vertical force, and meridional bending moment at the ends of the segment jk in terms of the load parameter λ_d and the nodal position coordinates r_j, z_j, ϕ_j, r_k, z_k, and ϕ_k; (3) use the conditions of force and moment equilibrium of the nodes to determine the components R_j^H, R_j^V, and R_j^M of the nodal forces required to maintain the shell structure in the equilibrium configuration defined by the coordinates r_j, z_j, and ϕ_j and distributed loads P_{jk}. Application of this procedure furnishes the holding forces R_j^H, R_j^V, and R_j^M as functions of λ_d and r_j, z_j, and ϕ_j for all nodes j. For the shell to be in an equilibrium configuration consistent with the prescribed nodal loads

$$\begin{aligned} P_j^H &= \lambda P_j^{H0} = R_j^H(r_i,\, z_i,\, \phi_i,\, \lambda_d) \\ P_j^V &= \lambda P_j^{V0} = R_j^V(r_i,\, z_i,\, \phi_i,\, \lambda_d) \\ P_j^M &= \lambda P_j^{M0} = R_j^M(r_i,\, z_i,\, \phi_i,\, \lambda_d) \quad i, j = 1,2,\ldots N \end{aligned} \tag{38}$$

The analysis is then reduced to the solution of the nonlinear equations (38) for the nodal coordinates as functions of the load parameters λ and λ_d. In practice, the functions R_j^H, R_j^H, and R_j^M cannot be produced in analytical form; however, since the functions and their derivatives can be evaluated, the analysis can be performed numerically. Only an abbreviated outline of the procedure employed is given herein. Details are contained in Qashu and DaDeppo (1983). Let the prescribed force components P_j^H, P_j^V, and P_j^M, the holding force components R_j^H, R_j^V, and R_j^M, and the position coordinates r_j, z_j, and ϕ_j be arranged as ordered variables P_i, R_i, and X_i, respectively. In this arrangement, it is understood that if $P_i = P_j^H$, then $R_i = R_j^H$ and $X_i = r_j$, etc. In terms of these variables, the problem of solving equations (38) becomes that of finding the roots of the equations

$$f_i = \lambda P_i^0 - R_i\,(X_1, X_2, \ldots, X_N, \lambda_d) \tag{39}$$

If for given λ and λ_d, $X_i^{(a)}$, $i = 1,2\ldots,N$ represents a close approximation to the solution of equations (39), then by the Newton-Raphson method an improved solution is

$$X_i^{(a+1)} = X_i^{(a)} + \delta X_i$$

where the corrections δX_i are solutions of the linear equations

$$f_i^{(a)} = -\sum_{j=1}^{N} R_{ij}^{(a)}\, \delta X_j \quad i = 1,2,\ldots N \tag{40}$$

where

$$R_{ij} = \frac{\partial R_i}{\partial X_j}$$

and

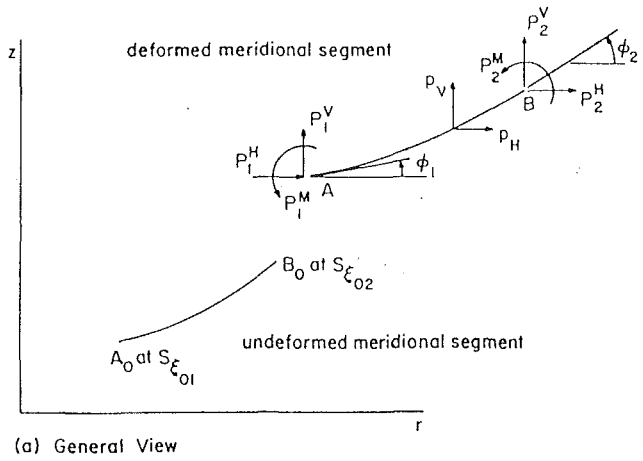
$$\begin{aligned} f_i^{(a)} &= f_i\,(X_1^{(a)}, X_2^{(a)}, \ldots, X_N^{(a)}, \lambda_d) \\ R_{ij}^{(a)} &= R_{ij}\,(X_1^{(a)}, X_2^{(a)}, \ldots, X_N^{(a)}, \lambda_d) \end{aligned}$$

The coefficients $R_{ij}^{(a)}$ are the elements of the tangent stiffness matrix of the shell in the configuration X_i under the distributed loads $P_{jk} = \lambda_d\, P_{jk}^0$. Repeated applications of the Newton-Raphson method can be made to obtain the solution values within a prescribed tolerance.

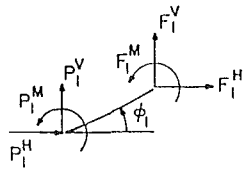
For sufficiently small changes in λ and λ_d, the corresponding variation of the equilibrium configuration of the shell may be evaluated numerically using the Newton-Raphson method. Let $\Delta\lambda$ and $\Delta\lambda_d$ be load increments and let ΔX_i be the corresponding position increments such that the structure is in equilibrium in the configuration $X_i + \Delta X_i$. Then equations to calculate the first-order approximations δX_i to the increments ΔX_i are derived by expanding equations (39) with $f_i = 0$ in a Taylor's series about the point $(X_1, X_2, \ldots, X_N, \lambda, \lambda_d)$ and retaining only the linear terms in the position coordinate increments. This gives

$$\sum_{j=1}^{N} R_{ij}\, \delta X_j = \Delta\lambda P_j^0 + R_{i\lambda_d}\, \Delta\lambda_d \tag{41}$$

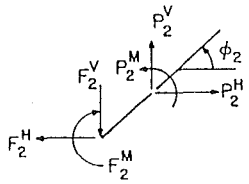
Downloaded 03 May 2010 to 171.66.16.21. Redistribution subject to ASME license or copyright; see http://www.asme.org/terms/Terms_Use.cfm



(a) General View



(b) End A



(c) End B

Fig. 7 Forces (*a*) general view; (*b*) end A; (*c*) end B

in which the differential coefficients

$$R_{ij} = \frac{\partial R_i}{\partial X_j} \text{ and } R_{i\lambda d} = \frac{\partial R_i}{\partial \lambda_d}$$

are evaluated in the current equilibrium configuration.

If R_{ij} is nonsingular, equation (41) may be solved for δX_i and an improved approximation, $X_i + \delta X_i$, to the equilibrium configuration may be obtained. This procedure may be repeated to calculate the nodal coordinates X_i to a specified degree of accuracy.

If the shell material is hyperelastic and the applied loads are conservative, the elements, R_{ij}, of the tangent stiffness matrix form a symmetric array. As the shell passes through a succession of equilibrium configurations going from stable-to-unstable equilibrium, the tangent stiffness matrix changes from being positive-definite to being positive-semidefinite to being indefinite. At the transition from stable-to-unstable equilibrium the stiffness matrix is positive semi-definite. Therefore, a critical equilibrium configuration from which buckling may occur is characterized by the change in sign of the determinant of the tangent stiffness matrix; i.e., when the derminant is zero, the equilibrium configuration is critical. The corresponding load is the critical or buckling load.

Numerical Examples. A general purpose computer program was written to implement the numerical methods outlined in the preceding sections. The numerical solutions to the following example problems were generated through application of the computer program. In the program, the Newton-Raphson method is considered to have converged when $\max_i |\delta x_i/x_i| < 0.001$.

The inversion of a hemispherical shell ($R_0/t_0 = 10$) is studied under three different types of applied loading: (1) ring load; (2) edge couple; (3) uniform vertical load. For each of these cases, the shell is made of the Mooney-Rivlin material ($\gamma = C_2/C_1 = 0.3$) with unrestrained edges such that vertical but not horizontal edge displacement is prevented. The shell is modeled using three equal 30-deg segments.

In each of the examples, the tangential stiffness matrix was found to be nonsingular at all but the turning points on the loading path. Therefore, there are no branching points along the loading paths and buckling is of the snap-through type as discussed in Thompson (1963).

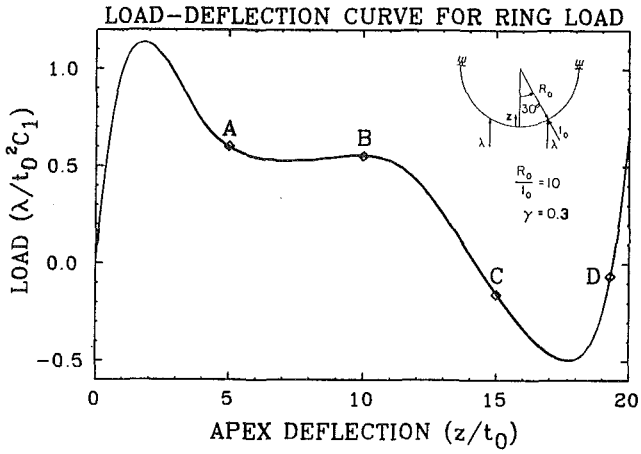


Fig. 8 Load-deflection curve for ring load

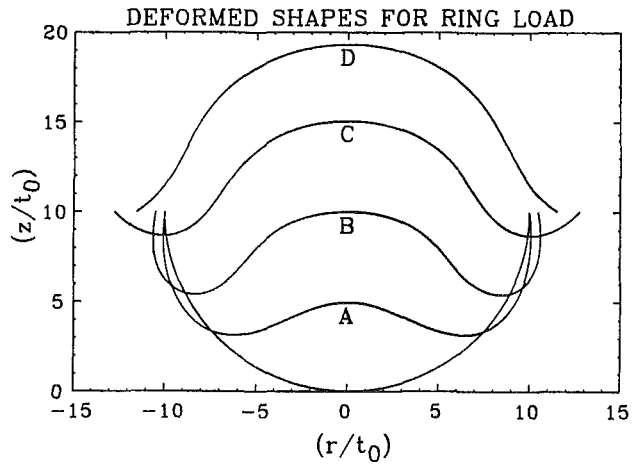


Fig. 9 Deformed shapes for ring load

(*1*) *Hemispherical Shell With Ring Load.* Figure 8 illustrates a nondimensional load-deflection curve for a hemisphere with a ring load applied as shown. A sharp primary turning point is evidenced with a nondimensional snap-buckling load of 1.128. Three additional turning points, where the determinant of the tangent stiffness matrix changes sign, occur during inversion of the shell; a second between points A and B, a third between points B and C, and a fourth between points C and D of the nondimensional load deflection curve. The deformed shapes, corresponding to four different equilibrium configurations, are shown in Fig. 9. For configurations A and B, most of the deformation occurs in the interior part of the shell. There is virtually no edge displacement for configuration A and only a small amount for configuration B. However, as the shell deforms from configuration B to configuration C, there is an appreciable edge displacement resulting in a maximum circumferential stretch ratio of 1.288 at the free edge. Point D represents the closest equilibrium configuration generated by the numerical solution algorithm to the unloaded and inverted configuration. The inverted shell has a region of reversed curvature near the unrestrained edge. The nondimensional radius at the apex (9.396) is smaller than that of the undeformed shell (10).

(*2*) *Hemipsherical Shell With Edge Couple.* Figure 10 shows a generalized nondimensional load-deflection curve for a hemisphere subject to edge couples. A snap-buckling condition with a smooth turning point is exhibited with a nondimen-

Downloaded 03 May 2010 to 171.66.16.21. Redistribution subject to ASME license or copyright; see http://www.asme.org/terms/Terms_Use.cfm

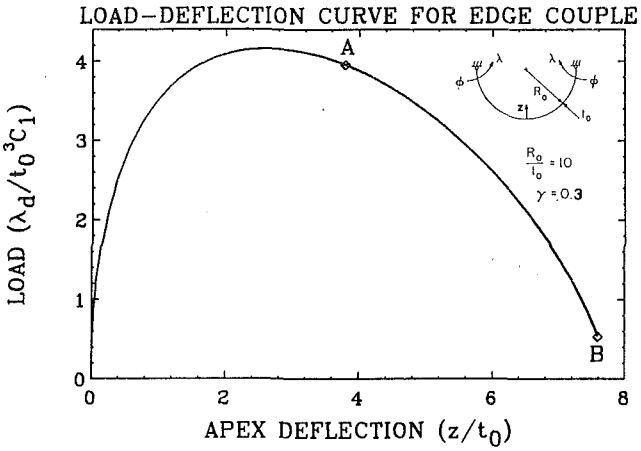


Fig. 10 Load-deflection curve for edge couple

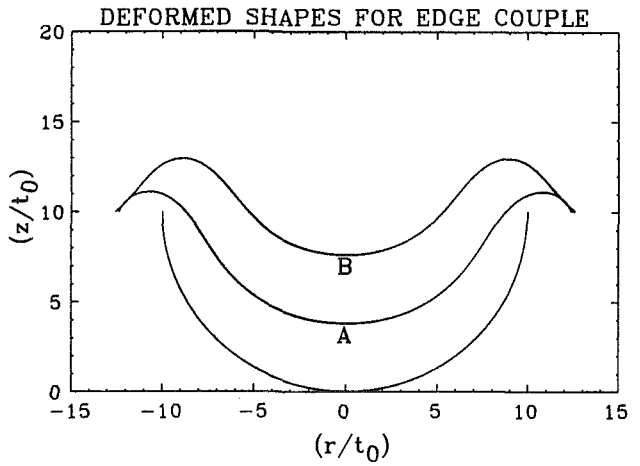


Fig. 11 Deformed shapes for edge couple

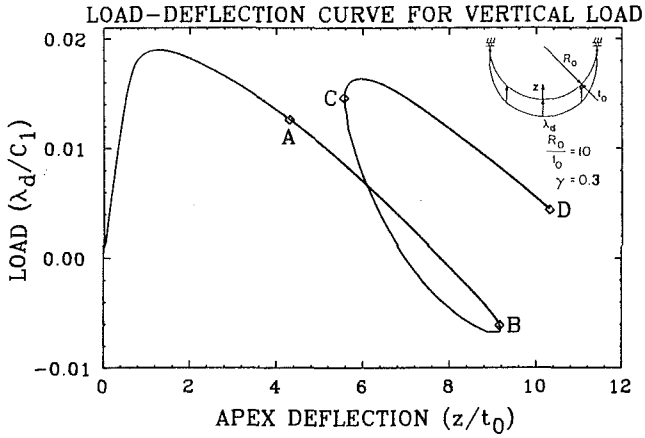


Fig. 12 Load-deflection curve for vertical load

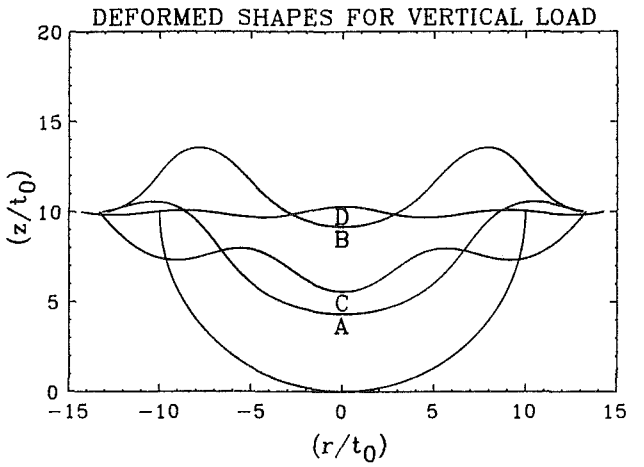


Fig. 13 Deformed shapes for vertical load

sional buckling load of 4.417. The maximum rotation ϕ at the roller supports during the deformation is 2.920 rad. The deformed shapes corresponding to two different equilibrium configurations are shown in Fig. 11. For both configurations A and B, nearly all of the deformation occurs in the segment adjacent to the supports. The maximum circumferential stretch ratio at the free edge experienced during the deformation is 1.256. It was not possible to invert the shell with edge couples. Discussion of the difficulties encountered is deferred until after the presentation of the third example problem.

(3) Hemispherical Shell With Uniform Vertical Load. A nondimensional load-deflection curve for a hemisphere loaded by a uniform vertical load is given in Fig. 12. A fairly smooth primary turning point is evidenced with a nondimensional snap-buckling load of 0.0185. There are two additional turning points depicted on the curve of Fig. 12. The second point is near point B and is quite sharp. The third point is near point C and has a degree of sharpness somewhere between those of the other two turning points. The deformed shapes corresponding to four different equilibrium configurations are shown in Fig. 13. In contrast to the ring load case, there is significant edge displacement during the initial portion of the deformation between the undeformed configuration and configuration A. The circumferential stretch ratio at the free edge in configuration A is 1.315. As the deformation progresses from configuration A to configuration B nearly all of the deformation occurs in the interior of the shell with the curvature reversed over a substantial portion of the shell. Between configurations B and C, the load increases from a negative level at B to a positive level at C. During this part of the deformation, the shell relaxes and exhibits some wrinkling with the apex position decreasing to the position shown in configuration C. Between configurations C and D, the shell undergoes significant stretching and is nearly a flat sheet in configuration D. The circumferential stretch ratio at the free edge in configuration D is 1.4304. It was also not possible to invert the shell with a uniform vertical load.

The principal difficulty encountered in attempting to invert the shell under the loadings of cases (2) and (3) was the inability to solve the constitutive relations, equations (36), under certain conditions. The numerical algorithm employed in this work requires that, at each integration point, the first and third of equations (36) be solved for λ_ξ and c_ξ. To accomplish this the matrix

$$\begin{bmatrix} \dfrac{\partial^2\Phi}{\partial\lambda_\xi^2} & \dfrac{\partial^2\Phi}{\partial c_\xi \partial\lambda_\xi} \\ \dfrac{\partial^2\Phi}{\partial c_\xi \partial\lambda_\xi} & \dfrac{\partial^2\Phi}{\partial c_\xi^2} \end{bmatrix} \tag{42}$$

must be nonsingular. However, numerical experiments performed as part of this work with cylindrical and spherical shells made of the Mooney-Rivlin material and having clamped edges show that, for large bending (nondimensional curvature $|t_0 c_\xi| = 0.5$ to 0.6), the matrix (42) becomes singular. In this case, the Newton-Raphson method fails to converge and the numerical solution algorithm breaks down.

Downloaded 03 May 2010 to 171.66.16.21. Redistribution subject to ASME license or copyright; see http://www.asme.org/terms/Terms_Use.cfm

Even though the constitutive relations become noninvertible for large bending, the strain-energy-density function Φ remains positive-definite. The paper of Rivlin (1980) contains a discussion of some of the problems which arise in attempting to find suitable conditions on the strain-energy-density function for a material undergoing finite deformation.

The location along the meridian of the deformed shell at which the constitutive relations become noninvertible occurs at the unrestrained edge (the point of application of the applied load) for case (2) and near the apex for case (3). This difficulty also occurred in other load cases which were not included in the present discussion.

Additional work is necessary to determine the reason for noninvertibility of the constitutive relations for large bending and also to investigate what modifications could be made to the constitutive relations to increase the range of bending deformation over which they are invertible.

References

Archer, R. R., 1962, "On the Numerical Solution of the Nonlinear Equations for Shells of Revolution," *Journal of Mathematics and Physics*, Vol. 41, September, pp. 165–178.

Biricikoglu, V., and Kalnins, A., 1971, "Large Elastic Deformations of Shells with the Inclusion of Transverse Normal Strain," *International Journal of Solids and Structures*, Vol. 7, May, pp. 431–444.

DaDeppo, D. A., and Keppel, W. J., "Betti's Theorem for Rotationally Symmetric Infinitesmal Deformations Superimposed on the Finite Deformation of a Thin Shell of Revolution," to appear in *Industrial Mathematics*.

Kalnins, A., 1964, "Analysis of Shells of Revolution Subjected to Symmetrical and Nonsymmetrical Loads," ASME JOURNAL OF APPLIED MECHANICS, Vol. 31, Series E., September, pp. 467–476.

Kalnins, A., and Lestingi, J. F., 1967, "On Nonlinear Analysis of Elastic Shells of Revolution," ASME JOURNAL OF APPLIED MECHANICS, Vol. 34, Series E, March, pp. 59–64.

Lehner, J. R., and Batterman, S. C., 1974, "Nonlinear Static and Dynamic Deformations of Shells of Revolution," *International Journal of Nonlinear Mechanics*, Vol. 9, December, pp. 501–519.

Libai, A., and Simmonds, J. G., 1981, "Large-Strain Constitutive Laws for the Cylindrical Deformation of Shells," *International Journal of Nonlinear Mechanics*, Vol. 16, No. 2, pp. 91–103.

Libai, A., and Simmonds, J. G., 1983, "Highly Non-Linear Cylindrical Deformations of Rings and Shells," *International Journal of Nonlinear Mechanics*, Vol. 18, No. 3, pp. 181–197.

Mescall, J. F., 1965, "Large Deflections of Spherical Shells Under Concentrated Loads," ASME JOURNAL OF APPLIED MECHANICS, Vol. 32, Series E, December, pp. 936–938.

Naghdi, P. M., 1972, "The Theory of Shells and Plates," *S. Flugge's Handbuch der Physik*, Vol. VIa/2, Truesdell, C., ed., Springer-Verlag, NY, pp. 425–640.

Qashu, R. K., DaDeppo, D. A., 1983, "Large Deflection and Stability of Rigid Frames," *Journal of Engineering Mechanics*, ASCE, Vol. 109, No. 3, June, pp. 765–779.

Reissner, E., 1949, "On the Theory of Thin Elastic Shells," *H. Reissner Anniverary Volume, Contribution to Applied Mechanics*, Edwards, J. W., Ann Arbor, MI, pp. 231–247.

Reissner, E., 1972, "On Finite Symmetrical Deflections of Thin Shells of Revolution," ASME JOURNAL OF APPLIED MECHANICS, Vol. 39, Series E, December, pp. 1137–1138.

Rivlin, R. S., 1980, "Some Thoughts on Material Stability," *Proceedings of I.U.T.A.M. Symposium of Finite Elasticity*, Lehigh University, Bethlehem, PA, August 10–15, Carlson, D. E., and Shield, R. T., eds., Martinus Nyhoff, The Hague, The Netherlands, 1982, pp. 105–122.

Simmonds, J. G., 1985, "The Strain-Energy Density of Rubber-Like Shells," *International Journal of Solids and Structures*, Vol. 21, No. 1, pp. 67–77.

Taber, L. A., 1985, "On Approximate Large Strain Relations for a Shell of Revolution," *International Journal of Nonlinear Mechanics*, Vol. 20, No. 1, pp. 27–39.

Thompson, J. M. T., 1963, "Basic Principles in the General Theory of Elastic Stability," *Journal of the Mechanics of Physics of Solids*, Vol. 11, January-February, pp. 13–20.

Wilson, P. E., and Spier, E. E., 1965, "Numerical Analysis of Large Axisymmetric Deformations of Thin Spherical Shells," *AIAA Journal*, Vol. 3, September, pp. 1716–1725.

APPENDIX A

Strain-Energy Function Derivatives

The purpose of this Appendix is to present expressions for the derivatives of W in equation (33) and also for the derivatives of Φ in equations (36).

Applying the chain rule twice to W yields

$$\ddot{W}_0 = \left[\frac{\partial W}{\partial I_1}\ddot{I}_1 + \frac{\partial W}{\partial I_2}\ddot{I}_2 + \frac{\partial^2 W}{\partial I_1^2}\dot{I}_1^2 + \frac{\partial^2 W}{\partial I_2^2}\dot{I}_2^2 + 2\frac{\partial^2 W}{\partial I_1 \partial I_2}\dot{I}_1\dot{I}_2\right]_0 \tag{A-1}$$

where dot denotes partial differentiation with respect to ζ_0 and the subscript "0" indicates $\zeta_0 = 0$, and

$$\dot{I}_{10} = -2(\lambda_\xi^2\kappa_\xi + \lambda_\theta^2\kappa_\theta - \lambda_\zeta^2 g_1) \tag{A-2}$$

$$\dot{I}_{20} = 2\left(\frac{\kappa_\xi}{\lambda_\xi^2} + \frac{\kappa_\theta}{\lambda_\theta^2} - \frac{g_1}{\lambda_\zeta^2}\right) \tag{A-3}$$

$$\begin{aligned}\ddot{I}_{10} = -2\{&\lambda_\xi^2(3\kappa_{\xi_0}\kappa_\xi + \kappa_\xi\kappa_\theta + \kappa_{\xi_0}\kappa_\theta) + \lambda_\theta^2(3\kappa_{\theta_0}\kappa_\theta + \kappa_\xi\kappa_\theta \\ &+ \kappa_{\theta_0}\kappa_\xi) - \lambda_\zeta^2[4\kappa^2{}_\xi + 6\kappa_\xi\kappa_\theta + 4\kappa_\theta^2 + \kappa_{\xi_0}(3\kappa_\xi + \kappa_\theta) \\ &+ \kappa_{\theta_0}(\kappa_\xi + 3\kappa_\theta)]\}\end{aligned} \tag{A-4}$$

$$\begin{aligned}\ddot{I}_{20} = 2\Bigg\{&\frac{4\kappa_\xi^2 + \kappa_\xi\kappa_\theta + \kappa_{\xi_0}(3\kappa_\xi + \kappa_\theta)}{\lambda_\xi^2} \\ &+ \frac{4\kappa_\theta^2 + \kappa_\xi\kappa_\theta + \kappa_{\theta_0}(\kappa_\xi + 3\kappa_\theta)}{\lambda_\theta^2} \\ &+ \frac{2\kappa_\xi\kappa_\theta - \kappa_{\xi_0}(3\kappa_\xi + \kappa_\theta) - \kappa_{\theta_0}(\kappa_\xi + 3\kappa_\theta)}{\lambda_\zeta^2}\Bigg\}\end{aligned} \tag{A-5}$$

Mooney Rivlin Model. Since for the Mooney-Rivlin material

$$\frac{\partial W}{\partial I_1} = 1,\ \frac{\partial W}{\partial I_2} = \gamma = C_2/C_1,\ \frac{\partial^2 W}{\partial I_1^2} = 0,\ \frac{\partial^2 W}{\partial I_2^2} = 0,\ \frac{\partial^2 W}{\partial I_1 \partial I_2} = 0 \tag{A-6}$$

only the derivatives of W_0 in equations (33) and of $\ddot{I}_{10}$ and $\ddot{I}_{20}$ in equation (A-1) need to be considered in the evaluation of the derivatives which appear in equation (36). Therefore

$$\frac{\partial W_0}{\partial \lambda_\xi} = \frac{2}{\lambda_\xi^3\lambda_\theta^2}(\lambda_\xi^4\lambda_\theta^2 - 1)(1 + \gamma\lambda_\theta^2) \tag{A-7}$$

$$\frac{\partial W_0}{\partial \lambda_\theta} = \frac{2}{\lambda_\xi^2\lambda_\theta^3}(\lambda_\xi^2\lambda_\theta^4 - 1)(1 + \gamma\lambda_\xi^2) \tag{A-8}$$

$$\frac{\partial^2 W_0}{\partial \lambda_\xi^2} = \frac{2}{\lambda_\xi^4\lambda_\theta^2}(\lambda_\xi^4\lambda_\theta^2 + 3)(1 + \gamma\lambda_\theta^2) \tag{A-9}$$

$$\frac{\partial^2 W_0}{\partial \lambda_\theta^2} = \frac{2}{\lambda_\xi^2\lambda_\theta^4}(\lambda_\xi^2\lambda_\theta^4 + 3)(1 + \gamma\lambda_\xi^2) \tag{A-10}$$

$$\frac{\partial^2 W_0}{\partial \lambda_\theta \partial \lambda_\xi} = \frac{4(1 + \gamma\lambda_\xi^4\lambda_\theta^4)}{\lambda_\xi^3\lambda_\theta^3} = \frac{\partial^2 W_0}{\partial \lambda_\xi \partial \lambda_\theta} \tag{A-11}$$

$$\begin{aligned}\frac{\partial \ddot{I}_{10}}{\partial \lambda_\xi} = -2\Bigg\{&2\lambda_\xi(3\kappa_{\xi_0}\kappa_\xi + \kappa_\xi\kappa_\theta + \kappa_{\xi_0}\kappa_\theta) \\ &+ \lambda_\xi^2\left(3\frac{\partial \kappa_\xi}{\partial \lambda_\xi} + \frac{\partial \kappa_\theta}{\partial \lambda_\xi}\right)\kappa_{\xi_0} + \lambda_\theta^2\left(3\frac{\partial \kappa_\theta}{\partial \lambda_\xi} + \frac{\partial \kappa_\xi}{\partial \lambda_\xi}\right)\kappa_{\theta_0} \\ &+ \left(\lambda_\xi^2 + \lambda_\theta^2\right)\left(\frac{\partial \kappa_\xi}{\partial \lambda_\xi}\kappa_\theta + \kappa_\xi\frac{\partial \kappa_\theta}{\partial \lambda_\xi}\right) \\ &+ \frac{2\lambda_\zeta^2}{\lambda_\xi}[4\kappa_\xi^2 + 6\kappa_\xi\kappa_\theta + 4\kappa_\theta^2 + \kappa_{\xi_0}(3\kappa_\xi + \kappa_\theta) \\ &+ \kappa_{\theta_0}(\kappa_\xi + 3\kappa_\theta)] - \lambda_\zeta^2\left[8\kappa_\xi\frac{\partial \kappa_\xi}{\partial \lambda_\xi}\right.\end{aligned}$$

Downloaded 03 May 2010 to 171.66.16.21. Redistribution subject to ASME license or copyright; see http://www.asme.org/terms/Terms_Use.cfm

$$+6\left(\frac{\partial\kappa_\xi}{\partial\lambda_\xi}\kappa_\theta+\kappa_\xi\frac{\partial\kappa_\theta}{\partial\lambda_\xi}\right)+8\kappa_\theta\frac{\partial\kappa_\theta}{\partial\lambda_\xi}+\left(3\frac{\partial\kappa_\xi}{\partial\lambda_\xi}+\frac{\partial\kappa_\theta}{\partial\lambda_\xi}\right)\kappa_{\xi_0}+\left(\frac{\partial\kappa_\xi}{\partial\lambda_\xi}+3\frac{\partial\kappa_\theta}{\partial\lambda_\xi}\right)\kappa_{\theta_0}\Big]\Big\} \tag{A-12}$$

$$\frac{\partial\ddot{I}_{20}}{\partial\lambda_\xi}=2\Bigg\{\frac{(8\kappa_\xi+\kappa_\theta)\frac{\partial\kappa_\xi}{\partial\lambda_\xi}+\kappa_\xi\frac{\partial\kappa_\theta}{\partial\lambda_\xi}+\kappa_{\xi_0}\left(3\frac{\partial\kappa_\xi}{\partial\lambda_\xi}+\frac{\partial\kappa_\theta}{\partial\lambda_\xi}\right)}{\lambda_\xi^2}-\frac{2}{\lambda_\xi^3}[4\kappa_\xi^2+\kappa_\xi\kappa_\theta+\kappa_{\xi_0}(3\kappa_\xi+\kappa_\theta)]$$

$$+\frac{8\kappa_\theta\frac{\partial\kappa_\theta}{\partial\lambda_\xi}+\frac{\partial\kappa_\xi}{\partial\lambda_\xi}\kappa_\theta+\kappa_\xi\frac{\partial\kappa_\theta}{\partial\lambda_\xi}+\kappa_{\theta_0}\left(\frac{\partial\kappa_\xi}{\partial\lambda_\xi}+3\frac{\partial\kappa_\theta}{\partial\lambda_\xi}\right)}{\lambda_\theta^2}$$

$$+\frac{2\frac{\partial\kappa_\xi}{\partial\lambda_\xi}\kappa_\theta+2\kappa_\xi\frac{\partial\kappa_\theta}{\partial\lambda_\xi}-\left(3\frac{\partial\kappa_\xi}{\partial\lambda_\xi}+\frac{\partial\kappa_\theta}{\partial\lambda_\xi}\right)\kappa_{\xi_0}-\left(\frac{\partial\kappa_\xi}{\partial\lambda_\xi}+3\frac{\partial\kappa_\theta}{\partial\lambda_\xi}\right)\kappa_{\theta_0}}{\lambda_\zeta^2}+2\lambda_\xi\lambda_\theta^2\left[2\kappa_\xi\kappa_\theta-\kappa_{\xi_0}(3\kappa_\xi+\kappa_\theta)-\kappa_{\theta_0}(\kappa_\xi+3\kappa_\theta)\right]\Bigg\} \tag{A-13}$$

$$\frac{\partial\ddot{I}_{10}}{\partial\lambda_\theta}=-2\{2\lambda_\theta(3\kappa_{\theta_0}\kappa_\theta+\kappa_\theta\kappa_\xi+\kappa_{\theta_0}\kappa_\xi)+\lambda_\theta^2\left(3\frac{\partial\kappa_\theta}{\partial\lambda_\theta}+\frac{\partial\kappa_\xi}{\partial\lambda_\theta}\right)\kappa_{\theta_0}$$

$$+\lambda_\xi^2\left(3\frac{\partial\kappa_\xi}{\partial\lambda_\theta}+\frac{\partial\kappa_\theta}{\partial\lambda_\theta}\right)\kappa_{\xi_0}+\left(\lambda_\xi^2+\lambda_\theta^2\right)\left(\frac{\partial\kappa_\theta}{\partial\lambda_\theta}\kappa_\xi+\kappa_\theta\frac{\partial\kappa_\xi}{\partial\lambda_\theta}\right)$$

$$+2\frac{\lambda_\zeta^2}{\lambda_\theta}\left[4\kappa_\theta^2+6\kappa_\theta\kappa_\xi+4\kappa_\xi^2+\kappa_{\xi_0}(3\kappa_\xi+\kappa_\theta)+\kappa_{\theta_0}(\kappa_\xi+3\kappa_\theta)\right]$$

$$-\lambda_\zeta^2[8\kappa_\theta\frac{\partial\kappa_\theta}{\partial\lambda_\theta}+6\left(\frac{\partial\kappa_\theta}{\partial\lambda_\theta}\kappa_\xi+\kappa_\theta\frac{\partial\kappa_\xi}{\partial\lambda_\theta}\right)+8\kappa_\xi\frac{\partial\kappa_\xi}{\partial\lambda_\theta}+\left(3\frac{\partial\kappa_\theta}{\partial\lambda_\theta}+\frac{\partial\kappa_\xi}{\partial\lambda_\theta}\right)\kappa_{\theta_0}+\left(\frac{\partial\kappa_\theta}{\partial\lambda_\theta}+3\frac{\partial\kappa_\xi}{\partial\lambda_\theta}\right)\kappa_{\xi_0}\Big]\Big\} \tag{A-14}$$

$$\frac{\partial\ddot{I}_{20}}{\partial\lambda_\theta}=2\Bigg\{\frac{(8\kappa_\theta+\kappa_\xi)\frac{\partial\kappa_\theta}{\partial\lambda_\theta}+\kappa_\theta\frac{\partial\kappa_\xi}{\partial\lambda_\theta}+\kappa_{\theta_0}\left(3\frac{\partial\kappa_\theta}{\partial\lambda_\theta}+\frac{\partial\kappa_\xi}{\partial\lambda_\theta}\right)}{\lambda_\theta^2}-\frac{2}{\lambda_\theta^3}[4\kappa_\theta^2+\kappa_\theta\kappa_\xi+\kappa_{\theta_0}(3\kappa_\theta+\kappa_\xi)]$$

$$+\frac{8\kappa_\xi\frac{\partial\kappa_\xi}{\partial\lambda_\theta}+\frac{\partial\kappa_\theta}{\partial\lambda_\theta}\kappa_\xi+\kappa_\theta\frac{\partial\kappa_\xi}{\partial\lambda_\theta}+\kappa_{\xi_0}\left(\frac{\partial\kappa_\theta}{\partial\lambda_\theta}+3\frac{\partial\kappa_\xi}{\partial\lambda_\theta}\right)}{\lambda_\xi^2}$$

$$+\frac{2\frac{\partial\kappa_\theta}{\partial\lambda_\theta}\kappa_\xi+2\kappa_\theta\frac{\partial\kappa_\xi}{\partial\lambda_\theta}-\left(3\frac{\partial\kappa_\xi}{\partial\lambda_\theta}+\frac{\partial\kappa_\theta}{\partial\lambda_\theta}\right)\kappa_{\xi_0}-\left(\frac{\partial\kappa_\xi}{\partial\lambda_\theta}+3\frac{\partial\kappa_\theta}{\partial\lambda_\theta}\right)\kappa_{\theta_0}}{\lambda_\zeta^2}+2\lambda_\theta\lambda_\xi^2[2\kappa_\theta\kappa_\xi-\kappa_{\theta_0}(3\kappa_\theta+\kappa_\xi)-\kappa_{\xi_0}(\kappa_\theta+3\kappa_\xi)]\Bigg\}$$

(A-15)

$$\frac{\partial\ddot{I}_{10}}{\partial c_\xi}=-2\{\lambda_\xi^2(3\kappa_{\xi_0}+\kappa_\theta)+\lambda_\theta^2(\kappa_\theta+\kappa_{\theta_0})-\lambda_\zeta^2[8\kappa_\xi+6\kappa_\theta+3\kappa_{\xi_0}+\kappa_{\theta_0}]\}\frac{\partial\kappa_\xi}{\partial c_\xi} \tag{A-16}$$

$$\frac{\partial\ddot{I}_{20}}{\partial c_\xi}=2\left[\frac{8\kappa_\xi+\kappa_\theta+3\kappa_{\xi_0}}{\lambda_\xi^2}+\frac{\kappa_\theta+\kappa_{\theta_0}}{\lambda_\theta^2}+\frac{2\kappa_\theta-3\kappa_{\xi_0}-\kappa_{\theta_0}}{\lambda_\zeta^2}\right]\frac{\partial\kappa_\xi}{\partial c_\xi} \tag{A-17}$$

$$\frac{\partial\ddot{I}_{10}}{\partial c_\theta}=-2\{\lambda_\theta^2(3\kappa_{\theta_0}+\kappa_\xi)+\lambda_\xi^2(\kappa_\xi+\kappa_{\xi_0})-\lambda_\zeta^2[8\kappa_\theta+6\kappa_\xi+3\kappa_{\theta_0}+\kappa_{\xi_0}]\frac{\partial\kappa_\theta}{\partial c_\theta} \tag{A-18}$$

$$\frac{\partial\ddot{I}_{20}}{\partial c_\theta}=2\left[\frac{8\kappa_\theta+\kappa_\xi+3\kappa_{\theta_0}}{\lambda_\theta^2}+\frac{\kappa_\xi+\kappa_{\xi_0}}{\lambda_\xi^2}+\frac{2\kappa_\xi-3\kappa_{\theta_0}-\kappa_{\xi_0}}{\lambda_\zeta^2}\right]\frac{\partial\kappa_\theta}{\partial c_\theta} \tag{A-19}$$

where the derivatives of κ_ξ and κ_θ are given by

$$\frac{\partial\kappa_\xi}{\partial\lambda_\xi}=-\frac{2c_\xi}{\lambda_\xi^3\lambda_\theta},\quad\frac{\partial\kappa_\xi}{\partial\lambda_\theta}=-\frac{c_\xi}{\lambda_\xi^2\lambda_\theta^2},\quad\frac{\partial\kappa_\xi}{\partial c_\xi}=\frac{1}{\lambda_\xi^2\lambda_\theta} \tag{A-20}$$

$$\frac{\partial\kappa_\theta}{\partial\lambda_\xi}=-\frac{c_\theta}{\lambda_\xi^2\lambda_\theta^2},\quad\frac{\partial\kappa_\theta}{\partial\lambda_\theta}=-\frac{2c_\theta}{\lambda_\xi\lambda_\theta^3},\quad\frac{\partial\kappa_\theta}{\partial c_\theta}=\frac{1}{\lambda_\theta\lambda_\xi^2} \tag{A-21}$$

Downloaded 03 May 2010 to 171.66.16.21. Redistribution subject to ASME license or copyright; see http://www.asme.org/terms/Terms_Use.cfm

The Linear Elastic Properties of Open-Cell Foams[1]

W. E. Warren
Mem. ASME

A. M. Kraynik

Sandia National Laboratories,
Albuquerque, NM 87185

A theoretical model for the linear elastic properties of three-dimensional open-cell foams is developed. We consider a tetrahedral unit cell, which contains four identical half-struts that join at equal angles, to represent the essential microstructural features of a foam. The effective continuum stress is obtained for an individual tetrahedral element arbitrarily oriented with respect to the principal directions of strain. The effective elastic constants for a foam are determined under the assumption that all possible orientations of the unit cell are equally probable in a representative volume element. The elastic constants are expressed as functions of compliances for bending and stretching of a strut, whose cross section is permitted to vary with distance from the joint, so the effect of strut morphology on effective elastic properties can be determined. Strut bending is the primary distortional mechanism for low-density foams with tetrahedral microstructure. For uniform strut cross section, the effective Young's modulus is proportional to the volume fraction of solid material squared, and the coefficient of proportionality depends upon the specific strut shape. A similar analysis for cellular materials with cubic microstructure indicates that strut extension is the dominant distortional mechanism and that the effective Young's modulus is linear in volume fraction. Our results emphasize the essential role of microstructure in determining the linear elastic properties of cellular materials and provide a theoretical framework for investigating nonlinear behavior.

Introduction

In part, the prevalence of cellular solids can be attributed to their mechanical properties. Cellular materials, which we will refer to as foams, encompass biomaterials like bone and lung parenchyma as well as polymeric and other synthetic foams. Here, we address the linear elastic properties of open-cell foams and develop a theoretical framework that can be extended to analyze their large-strain response and ultimate failure.

This represents an extension to three-dimensional materials of our previous work on two-dimensional foams (Warren and Kraynik, 1987) in which we analyzed the linear elastic properties of honeycombs with nonuniform film thickness. An important conclusion of that analysis had been reported by Gibson, et al. (1982): Film bending is the primary film-level deformation mechanism for small distortions of low-density foams. The theories of foam mechanics that originate with the work of Gent and Thomas (1959, 1963) assume that the displacement of junctions within the microstructure is affine; this disregards requirements of mechanical equilibrium at the junctions. In addition, this suppresses bending and only incorporates effects associated with stretching of the microstructure. The influence of film-level deformation mechanisms on the elastic properties of a two-dimensional foam is well illustrated for the case of uniform film thickness: When bending dominates, the effective Young's modulus E_f is proportional to the cube of the solid volume fraction ϕ; when film stretching dominates, E_f varies linearly with ϕ. These conclusions do not depend upon the orientation of the principal axes of strain relative to the cell structure since the hexagonal symmetry of a honeycomb insures isotropy in the plane (Lekhnitskii, 1963). In summary, the honeycomb is a relatively soft, transversely isotropic material in the linear deformation regime. By contrast, a foam with square network structure is highly anisotropic in the plane and the primary film-level deformation mechanism varies with cell orientation.

The work of Ko (1965) suggests that the strong relationship between foam network connectivity, deformation mechanisms, and stiffness, which is observed in two dimensions, carries over to three-dimensional materials. Ko relates the network structure of an idealized foam to that of uniform close-packed spheres. He considers two open-cell structures, chooses a particular direction of uniaxial strain, and calculates an effective Young's modulus for each structure using beam theory. His results are consistent with the following: When connecting struts are aligned throughout the material and must stretch to accommodate macroscopic deformation, $E_f \sim \phi$. However, when struts are not aligned and bending at the cell level accommodates macroscopic deformation, $E_f \sim \phi^2$.

[1]This work was performed at Sandia National Laboratories and supported by the U.S. Department of Energy under Contract #DE-AC04-76DP00789.

Contributed by the Applied Mechanics Division for presentation at the Winter Annual Meeting, Chicago, IL, November 28 to December 2, 1988, of The American Society of Mechanical Engineers.

Discussion on this paper should be addressed to the Editorial Department, ASME, United Engineering Center, 345 East 47th Street, New York, N.Y. 10017, and will be accepted until two months after final publication of the paper itself in the JOURNAL OF APPLIED MECHANICS. Manuscript received by ASME Applied Mechanics Division, May 27, 1987; final revision, December 7, 1987.

Paper No. 88-WA/APM-20.

Copyright © 1988 by ASME
Downloaded 03 May 2010 to 171.66.16.21. Redistribution subject to ASME license or copyright; see http://www.asme.org/terms/Terms_Use.cfm

Menges and Knipschild (1975, 1982) studied a mechanically loaded, rigid polyurethane foam under a microscope and observed strut bending. Even though their foams are closed-cell, the films are very thin compared to the struts (Plateau borders), so the response of an open-cell foam is expected. They argue that elastic response is determined by bending and stretching effects and provide a simple analysis for which $E_f \sim \phi^2$ when ϕ is small. The choice of microstructural element – four identical struts meeting at a tetrahedral junction – is a noteworthy feature of their model. Gibson and Ashby (1982) accept bending as the essential small-distortion mechanism for three-dimensional foams, and illustrate their point of view with "cubic" microstructural models for which adjacent struts or films do not align.

The microstructure of foams reflects their method of preparation, which usually involves a continuous liquid phase that eventually solidifies; therefore, surface tension and related interfacial effects often control foam structure. Two elementary features of liquid foam structure that are required to minimize surface energy are well known (Bikerman, 1973): Three films always meet at equal angles of 120° to form a film junction region called a Plateau border, and four Plateau borders always join at the tetrahedral angle of $\cos^{-1}(-1/3) \approx 109.47°$. In two dimensions, the hexagonal network structure of a honeycomb satisfies the film-angle constraint for a monodisperse foam and represents a logical model for investigating foam mechanics (Warren and Kraynik, 1987). When considering arbitrary homogeneous deformations of this spatially periodic structure, one can exploit the symmetry involved and reduce the structural element under consideration to a unit cell containing three half-films and their junction. The displacement of the film midpoints is affine – the displacement of the junction is not. A crucial feature of affine film-midpoint displacement is compatibility with both film-level deformation mechanisms, bending and stretching. We note that strict affine film-midpoint displacement is a consequence of perfectly ordered structure and cannot be expected for foams that are polydisperse or possess other attributes of disorder.

In this work, we assume that essential features of mechanical response for three-dimensional open-cell foams are captured by analyzing the deformation of a representative microstructural element under the assumption that the displacement of strut midpoints is affine. By contrast with our previous analysis for two-dimensional foams, justification of the basic assumptions is more intuitive. The representative element under consideration consists of four identical half-struts that meet at equal tetrahedral angles. The struts can be identified with Plateau borders in a precursor liquid foam. While the films in a completely open-cell foam are absent, we only require them to be very thin relative to the transverse dimension of the strut so that they do not affect strut deformation. Our choice of microstructural element is consistent with the two topological features of liquid foam structure discussed previously. One should recognize, however, that no cell in a three-dimensional foam is a simple polyhedron with planar faces and straight edges, because a planar polygon cannot have all angles equal to the tetrahedral angle. We neglect curvature along the strut axis, which derives from this. The relative orientation of adjacent tetrahedral elements that possess a common strut is assumed to be random. The boundaries of our unit cell consist of four planes that are perpendicular to each strut at its midpoint and form a regular tetrahedron. The corners of the tetrahedral volume element correspond to the centers of adjacent foam cells. It is important to recognize that the following analysis explicitly accounts for both the connectivity of struts and mechanical equilibrium at the junctions. Strut deformation due to bending and stretching is also incorporated in a natural way.

Analysis

We choose a single tetrahedral unit cell with four half-struts of length L to represent the important microstructural features in an open-cell foam and consider the displacement of and the force acting upon each strut midpoint. The strut geometry and coordinate system for this problem are shown in Fig. 1. We assume that homogeneous deformations of this structure are completely determined by the affine displacement of strut midpoints. The strut-midpoint configuration can be represented by three position vectors, $\mathbf{b}_1$, $\mathbf{b}_2$, $\mathbf{b}_3$, whose common origin coincides with the fourth strut midpoint. Small displacements of each midpoint from its equilibrium position are considered.

Isolating the tetrahedral element with four identical half-struts as a free body in equilibrium, the displacements of the four strut midpoints with respect to the joint itself are considered first. The force $\mathbf{F}_i$ at the ith midpoint is represented in terms of components parallel to and normal to the strut centerline in the form

$$\mathbf{F}_i = (\mathbf{F}_i \cdot \mathbf{e}_i)\mathbf{e}_i + (\mathbf{e}_i \times \mathbf{F}_i) \times \mathbf{e}_i, \quad i = 1\text{-}4 \tag{1}$$

where $\mathbf{e}_i$ is a unit vector parallel to the ith strut and directed away from the joint. The displacement of the ith midpoint with respect to the joint, Δ_i, is represented by

$$\Delta_i = M(\mathbf{F}_i \cdot \mathbf{e}_i)\mathbf{e}_i + N(\mathbf{e}_i \times \mathbf{F}_i) \times \mathbf{e}_i + L\psi \times \mathbf{e}_i, \tag{2}$$

where M is the axial elastic compliance of the strut, N is the transverse or bending compliance of the strut which is assumed to be the same in all directions, and ψ is a rigid-body rotation of the entire unit. The three strut-midpoint position vectors $\mathbf{b}_i$ can be represented by

$$\mathbf{b}_i = \mathbf{b}_i^0 + \delta_i, \quad i = 1, 2, 3 \tag{3}$$

where $\mathbf{b}_i^0$ is the undeformed position vector and $\delta_i = \Delta_i - \Delta_4$. For a given homogeneous deformation, the affine displacements of the $\mathbf{b}_i$ determine the δ_i and this provides three vector equations in the four unknown forces and rigid-body rotation. The remaining two vector relations necessary to determine the unknown forces and rotation are obtained from equilibrium considerations which provide

$$\sum_{i=1}^{4} \mathbf{F}_i = \mathbf{0},$$

and (4)

$$\sum_{i=1}^{4} \mathbf{e}_i \times \mathbf{F}_i = \mathbf{0}.$$

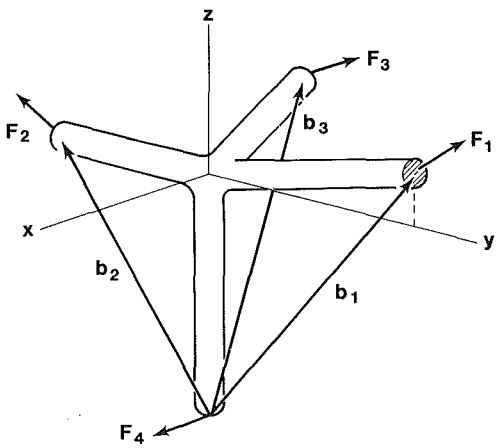


Fig. 1 Schematic of a tetrahedral element, which is considered to be the primary microstructural feature in low-density open-cell foams. Four identical half-struts meet at equal angles. The vectors $\mathbf{b}_i$ represent the relative positions of the strut midpoints and the $\mathbf{F}_i$ represent the forces at a strut midpoint.

Downloaded 03 May 2010 to 171.66.16.21. Redistribution subject to ASME license or copyright; see http://www.asme.org/terms/Terms_Use.cfm

When the forces at the strut midpoints are known, the effective continuum stress for the tetrahedral unit cell shown in Fig. 2 can be determined. Cutting this volume element on the plane $x=0$ and considering the effective stress that must act upon the exposed face to maintain equilibrium with the forces on the remaining volume gives

$$12\sqrt{2}L^2(\sigma_{xx}\mathbf{i}+\sigma_{xy}\mathbf{j}+\sigma_{xz}\mathbf{k})=\mathbf{F}_2-\mathbf{F}_3. \tag{5}$$

Similarly, cutting the volume element on the plane $y=0$ gives

$$12\sqrt{6}L^2(\sigma_{xy}\mathbf{i}+\sigma_{yy}\mathbf{j}+\sigma_{yz}\mathbf{k})=-3(\mathbf{F}_2+\mathbf{F}_3)-2\mathbf{F}_4, \tag{6}$$

and on the bottom triangular face in the plane $z=-L$,

$$6\sqrt{3}L^2(\sigma_{xz}\mathbf{i}+\sigma_{yz}\mathbf{j}+\sigma_{zz}\mathbf{k})=-\mathbf{F}_4, \tag{7}$$

where **i**, **j**, **k** are unit vectors associated with an (x, y, z) coordinate system that is fixed with respect to the unit cell. The system of equations (5)–(7) for determining the six independent components of the stress tensor can be shown to be consistent through the equilibrium relations of equation (4). We now consider two specific homogeneous deformations of the unit cell.

Pure Shear. Consider pure shear with respect to an (x', y', z') coordinate system oriented from the (x, y, z) coordinate system through the Euler angles ϕ, θ, and ψ (Goldstein, 1950). The transformation taking (x, y, z) into (x', y', z') is

$$\begin{aligned}
x' &= (\cos\psi\cos\phi-\cos\theta\sin\phi\sin\psi)x \\
&\quad+(\cos\psi\sin\phi+\cos\theta\cos\phi\sin\psi)y+\sin\psi\sin\theta\, z, \\
y' &= -(\sin\psi\cos\phi+\cos\theta\sin\phi\cos\psi)x \\
&\quad-(\sin\psi\sin\phi-\cos\theta\cos\phi\cos\psi)y+\cos\psi\sin\theta\, z, \\
z' &= \sin\theta\sin\phi\, x-\sin\theta\cos\phi\, y+\cos\theta\, z.
\end{aligned} \tag{8}$$

The unit vectors $\mathbf{i}'$, $\mathbf{j}'$, $\mathbf{k}'$ of (x', y', z') are given in terms of the unit vectors **i**, **j**, **k** of (x, y, z) by

$$\begin{aligned}
\mathbf{i}' &= (\cos\psi\cos\phi-\cos\theta\sin\phi\sin\psi)\mathbf{i} \\
&\quad+(\cos\psi\sin\phi+\cos\theta\cos\phi\sin\psi)\mathbf{j}+\sin\psi\sin\theta\,\mathbf{k}, \\
\mathbf{j}' &= -(\sin\psi\cos\phi+\cos\theta\sin\phi\cos\psi)\mathbf{i} \\
&\quad-(\sin\psi\sin\phi-\cos\theta\cos\phi\cos\psi)\mathbf{j}+\cos\psi\sin\theta\,\mathbf{k}, \\
\mathbf{k}' &= \sin\theta\sin\phi\,\mathbf{i}-\sin\theta\cos\phi\,\mathbf{j}+\cos\theta\,\mathbf{k}.
\end{aligned} \tag{9}$$

The affine displacements associated with this condition of pure shear are

$$\delta_i=\gamma(\mathbf{b}_i^0\cdot\mathbf{k}')\mathbf{j}', \quad i=1, 2, 3 \tag{10}$$

where γ is the magnitude of the shearing strain. Evaluating the stresses in (x, y, z) and transforming to (x', y', z') provides

$$\sigma_{x'x'}=-\frac{\gamma M}{2D}(N-M)[f_3^*+f_4^*],$$

$$\sigma_{y'y'}=-\frac{\gamma M}{2D}(N-M)[3f_3^*-f_4^*],$$

$$\sigma_{z'z'}=\frac{2\gamma M}{D}(N-M)f_3^*,$$

$$\sigma_{x'y'}=-\frac{\gamma M}{2D}(N-M)[f_3-f_4],$$

$$\sigma_{x'z'}=-\frac{\gamma M}{D}(N-M)f_2^*,$$

$$\sigma_{y'z'}=\frac{\gamma M}{D}[3(17N+7M)+(N-M)(f_1+f_2)], \tag{11}$$

where

$$D=288\sqrt{3}LMN(2M+N).$$

The functions $f_1(\theta, \phi)$, $f_2(\theta, \phi, \psi)$, $f_3(\theta, \phi, \psi)$, and $f_4(\theta, \phi, \psi)$ are given by

$$\begin{aligned}
f_1(\theta, \phi) &= 4\sqrt{2}(2\sin2\theta-\sin4\theta)\cos3\phi \\
&\quad-(4\cos2\theta+7\cos4\theta), \\
f_2(\theta, \phi, \psi) &= (3+4\cos2\theta-7\cos4\theta)\cos2\psi \\
&\quad+4\sqrt{2}(3\sin3\theta-\sin\theta)\sin3\phi\sin2\psi \\
&\quad-4\sqrt{2}(2\sin2\theta+\sin4\theta)\cos3\phi\cos2\psi, \\
f_3(\theta, \phi, \psi) &= (2\sin2\theta+7\sin4\theta)\sin\psi \\
&\quad+4\sqrt{2}(\cos2\theta-\cos4\theta)\cos3\phi\sin\psi \\
&\quad+6\sqrt{2}(\cos\theta-\cos3\theta)\sin3\phi\cos\psi, \\
f_4(\theta, \phi, \psi) &= 7(2\sin2\theta-\sin4\theta)\sin3\psi \\
&\quad+4\sqrt{2}(7\cos2\theta+\cos4\theta)\cos3\phi\sin3\psi \\
&\quad+2\sqrt{2}(7\cos\theta+9\cos3\theta)\sin3\phi\cos3\psi.
\end{aligned} \tag{12}$$

The $f_i^*(\theta, \phi, \psi)$ are obtained from the $f_i(\theta, \phi, \psi)$ by replacing terms of the form $(\sin p\psi, \cos p\psi)$ by $(\cos p\psi, -\sin p\psi)$, respectively.

Uniaxial Extension. For uniaxial extension in the z'-direction, the strut-midpoint displacements are given by

$$\delta_i=\epsilon(\mathbf{b}_i^0\cdot\mathbf{k}')\mathbf{k}', \quad i=1, 2, 3 \tag{13}$$

where ϵ is the magnitude of the uniaxial strain. Evaluating the stresses in (x, y, z) and transforming to (x', y', z') provides

$$\sigma_{x'x'}=\frac{\epsilon(N-M)}{D}[(16N+11M)+M(f_1-f_2)],$$

$$\sigma_{y'y'}=\frac{\epsilon(N-M)}{D}[(16N+11M)+M(f_1+f_2)],$$

$$\sigma_{z'z'}=\frac{2\epsilon}{D}[(8N^2+53MN+11M^2)-M(N-M)f_1], \tag{14}$$

$$\sigma_{x'y'}=-\frac{\epsilon}{D}M(N-M)f_2^*,$$

$$\sigma_{x'z'}=\frac{2\epsilon}{D}M(N-M)f_3,$$

$$\sigma_{y'z'}=\frac{2\epsilon}{D}M(N-M)f_3^*,$$

where the functions f_i and f_i^* are the same as those for simple shear. By contrast with our previous two-dimensional analysis (Warren and Kraynik, 1987) the stress fields associated with the affine strut-midpoint displacements corresponding to pure shear and uniaxial strain are dependent upon the orientation of the microstructural element with respect to the principal directions of strain.

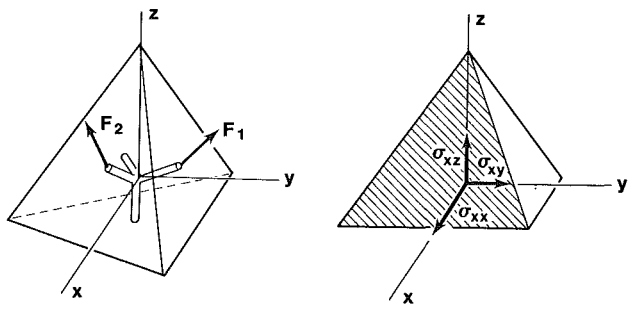


Fig. 2 Schematic of the volume element that contains each tetrahedral element showing the coordinate system used to determine the effective stress. In the undeformed state, the volume element is a regular tetrahedron.

Downloaded 03 May 2010 to 171.66.16.21. Redistribution subject to ASME license or copyright; see http://www.asme.org/terms/Terms_Use.cfm

Effective Elastic Constants

At this point, we enlarge the size scale of our analysis and consider a representative volume of cellular material to contain tetrahedral elements of all possible orientations with equal probability. Under these conditions, the effective stress of the representative volume element is the volume average of the stress associated with the individual tetrahedral elements, the average being taken over all possible orientations. The volume-averaged stress $\bar{\underline{\sigma}}$ is given by

$$\bar{\underline{\sigma}} = \frac{1}{V}\int_V \underline{\sigma}(\phi, \theta, \psi)\, dv, \tag{15}$$

where $\underline{\sigma}(\phi, \theta, \psi)$ represents the stress associated with an individual element of particular orientation. It is clear that the elastic properties of this representative volume element must be isotropic since we have averaged over all possible orientations and there can be no preferred direction within the material which exhibits a different elastic response from any other direction.

The volume average implied by equation (15) becomes an average over all possible values of the Euler angles and takes the explicit form

$$\bar{\underline{\sigma}} = \frac{1}{V}\int_0^{2\pi}\int_0^{\pi}\int_0^{2\pi} \underline{\sigma}(\phi,\theta,\psi)\, \sin\theta\, d\phi\, d\theta\, d\psi, \tag{16}$$

where

$$V = \int_0^{2\pi}\int_0^{\pi}\int_0^{2\pi} \sin\theta\, d\phi\, d\theta\, d\psi = 8\pi^2.$$

Considering the stress components given in equations (11) and (14) for simple shear and uniaxial extension, respectively, the only volume averages required are those of the functions f_1, $f_2, f_2^*, f_3, f_3^*, f_4$, and f_4^*, since all other terms in these expressions are independent of the Euler angles. One finds

$$\bar{f}_1 = 9/5 \quad \text{and} \quad \bar{f}_2 = \bar{f}_2^* = \bar{f}_3 = \bar{f}_3^* = \bar{f}_4 = \bar{f}_4^* = 0. \tag{17}$$

For an isotropic material the components of stress and strain are related in the usual form

$$\bar{\sigma}_{ij} = \lambda_f \bar{\epsilon}_{kk}\delta_{ij} + 2\mu_f \bar{\epsilon}_{ij}, \tag{18}$$

where λ_f and μ_f are the effective Lamé constants. For our condition of pure shear, the only nonzero component of strain is $\bar{\epsilon}_{y'z'} = \frac{1}{2}\gamma$, and from equation (18) the only nonzero stress is given by

$$\bar{\sigma}_{y'z'} = \mu_f \gamma. \tag{19}$$

For our condition of uniaxial extension, the only nonzero component of strain is $\bar{\epsilon}_{z'z'} = \epsilon$, and from equation (18) the nonzero components of stress are

$$\begin{aligned} \bar{\sigma}_{x'x'} &= \bar{\sigma}_{y'y'} = \lambda_f \epsilon, \\ \bar{\sigma}_{z'z'} &= (\lambda_f + 2\mu_f)\epsilon. \end{aligned} \tag{20}$$

Equations (19) and (20) provide a redundant but consistent set of relations for determining the effective Lamé constants. The stress expressions of equations (11) and (14), together with equation (17), provide the result

$$\lambda_f = \frac{(N-M)(5N+4M)}{90\sqrt{3}LMN(2M+N)},$$

and

$$\mu_f = \frac{(11N+4M)}{60\sqrt{3}LN(2M+N)}, \tag{21}$$

where μ_f is the effective shear modulus. The more usual elastic constants, Young's modulus E_f, Poisson's ratio ν_f, and bulk modulus κ_f, are given by

$$E_f = \frac{(11N+4M)}{2\sqrt{3}L(10N^2+31NM+4M^2)},$$

$$\nu_f = \frac{(N-M)(5N+4M)}{(10N^2+31NM+4M^2)}, \tag{22}$$

and

$$\kappa_f = \frac{1}{18\sqrt{3}LM}.$$

We note that the effective Poisson's ratio satisfies $-1 < \nu_f < 1/2$, which insures that the material strain-energy function is positive-definite. Also, the bulk modulus κ_f is independent of the bending compliance N. For low-density foams, the bending compliance is much greater than the axial compliance M and our results indicate that the effective Young's modulus E_f and shear modulus μ_f will be dominated by strut bending. We now show how the effective elastic constants depend upon the volume fraction of solid and the strut shape.

Examples for Specific Strut Morphology

Consider the case where the struts have a uniform cross section of area A and isotropic moment of inertia Aq^2, where q is the radius of gyration of the section. The volume fraction of solid material ϕ is assumed to be sufficiently small that the effective elastic length of the strut is equal to the total strut length $2L$ and ϕ is given by

$$\phi = \frac{A}{2\sqrt{3}L^2}. \tag{23}$$

The axial compliance M and bending compliance N are

$$M = \frac{L}{EA} \quad \text{and} \quad N = \frac{L^3}{3EAq^2}, \tag{24}$$

where E is the elastic modulus of the strut material. The compliances of equation (24) written in terms of the volume fraction of solid are

$$\frac{1}{M} = 2\sqrt{3}EL\phi \quad \text{and} \quad \frac{1}{N} = \frac{36Eq^2L\phi^2}{A}. \tag{25}$$

For low-density foams, where $\phi \ll 1$, equations (22) and (25) provide

$$\frac{E_f}{E} = \frac{33\sqrt{3}q^2\phi^2}{5A}. \tag{26}$$

Considering specific strut cross sections, the parameter q^2/A and the effective Young's moduli are given by

Circular:

$$q^2/A = 1/4\pi = 0.080, \qquad E_f/E = 0.91\ \phi^2,$$

Triangular:

$$q^2/A = \frac{1}{6\sqrt{3}} = 0.096, \qquad E_f/E = 1.10\ \phi^2, \tag{27}$$

Plateau Border:

$$q^2/A = \frac{(20\sqrt{3}-11\pi)}{6(2\sqrt{3}-\pi)^2} = 0.134, \qquad E_f/E = 1.53\ \phi^2,$$

which indicates the effect of strut shape on the stiffness of low-density foams. The Plateau border cross section referred to in equation (27) corresponds to the space between three identical, mutually tangent circles and represents the typical shape of a Plateau border in liquid foams when the films are very thin; this shape is representative of liquid foams that solidify with films intact. Film rupture prior to solidification would favor reduction in strut surface area with circular cross section representing the extreme. Table 1 shows the dependence of effective elastic constants on volume fraction

Downloaded 03 May 2010 to 171.66.16.21. Redistribution subject to ASME license or copyright; see http://www.asme.org/terms/Terms_Use.cfm

for equilateral triangular strut sections. We observe that for low-density foams the effective elastic constants E_f and μ_f vary as ϕ^2, which indicates the dominance of strut bending. On the other hand, the bulk modulus κ_f varies as ϕ, which indicates the absence of strut bending. Thus any deformations of the foam that are pure dilatation will suppress the effect of strut bending, while those deformations that involve distortion will be dominated by strut bending.

We illustrate the effect of nonuniform strut cross section for the case where the transverse strut dimension $t(\xi)$ varies as

$$t(\xi) = t_0(1+\eta\xi/L)^{-1/4}, \tag{28}$$

where t_0 is the value at the joint, ξ is a coordinate directed along the strut centerline with its origin at the joint, and η is a parameter. The compliances M and N are given by

$$M = \frac{2L}{3EA_0\eta}\,[(1+\eta)^{3/2}-1],$$

and $$N = \frac{L^3(4-\eta)}{12EA_0q_0^2}\,, \tag{29}$$

where the strut has area A_0 and moment of inertia $A_0q_0^2$ at the joint, $\xi = 0$. The volume fraction of solid material is given by

$$\phi = \frac{A_0}{\sqrt{3}L^2\eta}\,[(1+\eta)^{1/2}-1]. \tag{30}$$

The compliances expressed in terms of the volume fraction ϕ are

$$\frac{1}{M} = \frac{3\sqrt{3}EL\phi\eta^2}{2[(1+\eta)^{3/2}-1][(1+\eta)^{1/2}-1]}\,,$$

and $$\frac{1}{N} = 36EL\phi^2\left(\frac{q_0^2}{A_0}\right)\frac{[(1+\eta)^{1/2}+1]^2}{(4+\eta)}\,. \tag{31}$$

Equations (22) and (31) provide the effective Young's modulus for low-density foams

$$\frac{E_f}{E} = \frac{33\sqrt{3}\phi^2}{5}\left(\frac{q_0^2}{A_0}\right)\frac{(\rho^2+1)^2}{(\rho^4+3)}\,, \tag{32}$$

where we have introduced the parameter $\rho = t_0/t(L) \geqq 1$ as a measure of strut tapering; ρ is the ratio of thickness at the joint to that at the midpoint. The case $\rho = 1$ corresponds to a strut of uniform thickness as considered previously. The effective Young's modulus of equation (32) is a maximum when $\rho = \sqrt{3}$ for all cross-sectional shapes and is

$$\left(\frac{E_f}{E}\right)_{\max} = \frac{44\sqrt{3}}{5}\left(\frac{q_0^2}{A_0}\right)\phi^2, \tag{33}$$

which is 4/3 the value for a uniform strut with the same volume fraction of material.

Foam With Cubic Network Structure

In this section, we present results for an open-cell foam presumed to have cubic network structure in which six identical struts meet at right angles. The analysis parallels that for tetrahedral structure. We first isolate an individual cubic element as a free body in equilibrium and determine the forces at the strut midpoints resulting from their affine displacements. The effective stress associated with an individual element depends strongly upon the orientation of the joint with respect to the principal strain directions. The effective elastic constants for a cellular material composed of cubic joints are obtained as before by averaging over all possible orientations, and found to be

Table 1 Effective elastic constants for uniform struts with triangular cross section

Tetrahedral Structure	Cubic Structure
$\frac{E_f}{E} = \frac{\phi^2(11+4\phi)}{(10+31\phi+4\phi^2)}$	$\frac{E_f}{E} = \frac{\phi(1+\phi/\sqrt{3})}{(6+\phi/\sqrt{3})}$
$\nu_f = \frac{(1-\phi)(5+4\phi)}{(10+31\phi+4\phi^2)}$	$\nu_f = \frac{(1-\frac{2}{3\sqrt{3}}\phi)}{(4+\frac{2}{3\sqrt{3}}\phi)}$
$\frac{\mu_f}{E} = \frac{\phi^2(11+4\phi)}{30(1+2\phi)}$	$\frac{\mu_f}{E} = \frac{\phi}{15}(1+\phi/\sqrt{3})$
$\frac{\kappa_f}{E} = \frac{\phi}{9}$	$\frac{\kappa_f}{E} = \frac{\phi}{9}$

$$\mu_f = \frac{2N+3M}{40LMN}\,,$$

$$E_f = \frac{2N+3M}{4LM(4N+M)}\,,$$

$$\nu_f = \frac{N-M}{4N+M}\,, \tag{34}$$

and

$$\kappa_f = \frac{1}{12LM}\,.$$

Poisson's ratio satisfies $-1 < \nu_f < 1/4$, which insures that the material strain-energy function is positive-definite. The results in equation (34) are in sharp contrast with their counterparts in equation (22) for the tetrahedral element. For low-density foams, where $N \gg M$, the Young's modulus E_f and shear modulus μ_f are now determined by strut extension rather than bending.

For cubic structure, struts of uniform cross section, and small ϕ

$$\phi = 3A/4L^2. \tag{35}$$

The compliances M and N are again given by equation (24), which provides the following for struts of uniform triangular cross section

$$\frac{1}{M} = \frac{4}{3}EL\phi \quad \text{and} \quad \frac{1}{N} = \frac{8}{9\sqrt{3}}EL\phi^2. \tag{36}$$

Table 1 shows the variation of effective elastic constants with volume fraction for cubic structure with struts of triangular cross section. We note the linear dependence of Young's modulus E_f and shear modulus ν_f on ϕ, which is indicative of the dominance of strut extension and the suppression of strut-bending effects. For small ϕ, $E_f/E \to \phi/6$ and $\nu_f \to 1/4$, as obtained from the theory of Gent and Thomas (1959) which does not incorporate bending.

When the struts taper according to equation (28), the effective Young's modulus is given by

$$\frac{E_f}{E} = \frac{\phi(\rho^2+1)^2}{8(\rho^4+\rho^2+1)}\,. \tag{37}$$

Downloaded 03 May 2010 to 171.66.16.21. Redistribution subject to ASME license or copyright; see http://www.asme.org/terms/Terms_Use.cfm

This result is independent of the strut cross-sectional shape and attains a maximum value of $(E_f/E)_{max} = \phi/6$ for the uniform section when $\rho = 1$.

Concluding Remarks

These results illustrate and reinforce the strong connection between elastic properties of foams and their microstructure. The analysis indicates which strut deformation mechanism – bending or stretching – determines the various effective elastic constants for particular foam network structures. When network structure is tetrahedral, strut bending provides a square dependence of the distortional moduli upon volume fraction of solid material. This microstructure is favored when surface tension forces are prevalent during foam formation from liquids. For cubic microstructure, which is not consistent with a liquid foam precursor, strut extension results in a linear variation of the moduli with volume fraction. Such linear variation is also predicted by theories that do not incorporate strut bending. Previous assertions regarding the importance of a strut bending mechanism depend upon network structure and, therefore, are not universal.

References

Bikerman, J. J., 1973, *Foams*, Springer-Verlag, New York, pp. 33–64.

Gent, A. N., and Thomas, A. G., 1959, "The Deformation of Foamed Elastic Materials," *Journal of Applied Polymer Science*, Vol. 1, pp. 107–113.

Gent, A. N., and Thomas, A. G., 1963, "Mechanics of Foamed Elastic Materials," *Rubber Chem. Tech.*, Vol. 36, pp. 597–610.

Gibson, L. J., Ashby, M. F., Schajer, G. S., and Robertson, C. I., 1982, "The Mechanics of Two-Dimensional Cellular Materials," *Proceedings of the Royal Society of London Series A*, Vol. 382, pp. 25–42.

Gibson, L. J., and Ashby, M. F., 1982, "The Mechanics of Three-Dimensional Cellular Materials," *Proceedings of the Royal Society of London Series A*, Vol. 382, pp. 43–59.

Goldstein, H., 1950, *Classical Mechanics*, Addison-Wesley, Cambridge, MA, pp. 107–109.

Ko, W. L., 1965, "Deformations of Foamed Elastomers," *Journal of Cellular Plastics*, Vol. 1, pp. 45–50.

Lekhnitskii, S. G., 1963, *Theory of Elasticity of an Anisotropic Elastic Body*, Holden-Day, San Francisco, pp. 21–25.

Menges, G., and Knipschild, F., 1975, "Estimation of Mechanical Properties for Rigid Polyurethane Foams," *Polymer Eng. Sci.*, Vol. 15, pp. 623–627.

Menges, G., and Knipschild, F., 1982, "Stiffness and Strength – Rigid Plastic Foams," in *Mechanics of Cellular Plastics*, ed., Hilyard, N. C., Macmillan, New York, pp. 27–72.

Warren, W. E., and Kraynik, A. M., 1987, "Foam Mechanics: The Linear Elastic Response of Two-Dimensional Spatially Periodic Cellular Materials," *Mechanics of Materials*, Vol. 6, pp. 27–37.

Downloaded 03 May 2010 to 171.66.16.21. Redistribution subject to ASME license or copyright; see http://www.asme.org/terms/Terms_Use.cfm

Bounds on the Effective Transport and Elastic Properties of a Random Array of Cylindrical Fibers in a Matrix

S. Torquato
Associate Professor.
Department of Mechanical and Aerospace Engineering and Department of Chemical Engineering,
Box 7910.
Mem. ASME

F. Lado
Professor.
Department of Physics,
Box 8202.

North Carolina State University,
Raleigh, NC 27695

This paper studies the determination of rigorous upper and lower bounds on the effective transport and elastic moduli of a transversely isotropic fiber-reinforced composite derived by Silnutzer and by Milton. The third-order Silnutzer bounds on the transverse conductivity σ_e, the transverse bulk modulus k_e, and the axial shear modulus μ_e, depend upon the microstructure through a three-point correlation function of the medium. The fourth-order Milton bounds on σ_e and μ_e depend not only upon three-point information but upon the next level of information, i.e., a four-point correlation function. The aforementioned microstructure-sensitive bounds are computed, using methods and results of statistical mechanics, for the model of aligned, infinitely long, equisized, circular cylinders which are randomly distributed throughout a matrix, for fiber volume fractions up to 65 percent. For a wide range of volume fractions and phase property values, the Silnutzer bounds significantly improve upon corresponding second-order bounds due to Hill and to Hashin; the Milton bounds, moreover, are narrower than the third-order Silnutzer bounds. When the cylinders are perfectly conducting or perfectly rigid, it is shown that Milton's lower bound on σ_e or μ_e provides an excellent estimate of these effective parameters for the wide range of volume fractions studied here. This conclusion is supported by computer-simulation results for σ_e and by experimental data for a graphite-plastic composite.

1 Introduction

The problem of predicting the effective transport and elastic properties of composite materials is an outstanding one in science and engineering, and has received considerable attention in recent years (see Christensen, 1979; Chou and Kelly, 1980; Hashin, 1983; Torquato, 1987; and references therein). From a fundamental as well as design standpoint, it is desirable to calculate the effective properties from a knowledge of the microstructure of the composite medium; one can then relate changes in the microstructure quantitatively to changes in the macroscopic variables. Unfortunately, in order to exactly predict the effective property, an infinite set of correlation functions, which statistically characterize the microstructure, must be known (Milton, 1981; Torquato, 1985). Except in a few special cases (e.g., idealized periodic arrays—see Perrins, McKenzie, and McPhedran, 1979), the infinite set of correlation functions is never known and, hence, an exact determination of the effective property, for all phase property values and volume fractions, is generally out of the question, even for simple random materials (e.g., random array of impenetrable cylinders).

Rigorous bounding methods, however, provide a means of estimating the effective property given a *limited* amount of microstructural information on the composite material. Rigorous upper and lower bounds on the effective properties are useful because: (*i*) They enable one to test the merits of a theory; (*ii*) As successively more microstructural information is included, the bounds become progressively tighter; (*iii*) One of the bounds can typically provide a relatively accurate estimate of the property even when the reciprocal bound diverges from it (Torquato, 1987).

We shall be concerned with the evaluation of bounds on the effective transverse thermal (electrical) conductivity σ_e, effective transverse bulk modulus k_e, and effective axial shear modulus μ_e of transversely isotropic fiber-reinforced materials composed of two different materials (phases). By "fiber-reinforced" material we mean any material whose phase boundaries are cylindrical surfaces, with generators parallel to one axis (Hill, 1964; Hashin, 1965). Continuous glass, carbon, or graphite fibers in an epoxy matrix are examples of composites that fall within this category (Hashin, 1983).

Given only the phase volume fractions, conductivities, bulk

Contributed by the Applied Mechanics Division for publication in the JOURNAL OF APPLIED MECHANICS.

Discussion on this paper should be addressed to the Editorial Department, ASME, United Engineering Center, 345 East 47th Street, New York, N.Y. 10017, and will be accepted until two months after final publication of the paper itself in the JOURNAL OF APPLIED MECHANICS. Manuscript received by ASME Applied Mechanics Division, September 21, 1987; final revision, January 22, 1988.

Copyright © 1988 by ASME
Downloaded 03 May 2010 to 171.66.16.21. Redistribution subject to ASME license or copyright; see http://www.asme.org/terms/Terms_Use.cfm

moduli, and shear moduli, denoted respectively by ϕ_1 and ϕ_2, σ_1 and σ_2, K_1 and K_2, and G_1 and G_2, the best possible rigorous bounds on σ_e, k_e, and μ_e have been derived by Hill (1964) and by Hashin (1965, 1970). More restrictive bounds on these effective properties which include additional microstructural information on the transversely isotropic fiber-reinforced material have been obtained by Silnutzer (1972) and by Milton (1981, 1982). The Silnutzer bounds on σ_e, k_e, and μ_e incorporate the three-point probability function S_3. The quantity $S_n(\mathbf{r}_1, \ldots, \mathbf{r}_n)$ gives the probability of finding n points at positions $\mathbf{r}_1, \ldots, \mathbf{r}_n$ all in one of the phases, say phase 2. Milton's bounds on σ_e depend not only upon S_3 but upon S_4. Application of the Silnutzer and Milton bounds for disordered composites has been virtually nonexistent because of the difficulty involved in determining S_3 and S_4, either experimentally or theoretically. Substantial progress in the quantitative characterization of the microstructure of disordered heterogeneous media has been made in the past several years, including experimental (Berryman and Blair, 1986), computer-simulation (Haile, Massobrio, and Torquato, 1985; Seaton and Glandt, 1986; Smith and Torquato, 1988) and theoretical (Torquato and Stell, 1982; Torquato and Stell, 1985; Torquato, 1986) advances.

In this article, we shall compute the Silnutzer and Milton bounds on the aforementioned effective properties for the practically useful model of impenetrable, parallel, infinitely long, equisized, circular cylinders (or circular disks in two dimensions) distributed randomly throughout a matrix. To our knowledge, such calculations have heretofore not been carried out. This is accomplished here, for a wide range of cylinder or fiber volume fractions, employing the recent theoretical formalism developed by Torquato and Stell (1982) to represent the n-point probability functions in terms of the n-particle distribution functions, and using methods and results of statistical mechanics.

The remaining part of the paper is organized as follows. In Section 2, we present and discuss the Silnutzer and Milton bounds on the effective properties. These bounds depend upon a multidimensional integral ζ_2 involving lower-order n-point probability functions. In Section 3, we greatly simplify ζ_2 for the aforementioned model of randomly distributed impenetrable, parallel cylinders and evaluate it for this microstructure as a function of fiber volume fraction up to a value of 65 percent. The analysis described here is general in that it may be applied to composites consisting of inclusions of arbitrary shape, size, and penetrability (e.g., circular cylinders with particle-size distributions, elliptical cylinders, partially penetrable cylinders, etc.) In Section 4, we compute the Silnutzer and Milton bounds on the effective properties for our model, for a wide range of phase property values and volume fractions. Comparison of Milton's lower bound with computer-simulation results for σ_e and experimental data of a graphite-plastic composite are presented.

2 Third and Fourth-Order Bounds on σ_e, k_e, and μ_e

For any transversely isotropic fiber-reinforced material, Silnutzer (1972) derived bounds on σ_e and k_e which depend upon the phase volume fractions and properties, and two integrals involving certain three-point correlation functions. Milton (1982) demonstrated that both integrals may be expressed in terms of a single integral ζ_2 (defined below) which depends upon the three-point probability function described in the Introduction. The simplified form of the Silnutzer bounds (Milton, 1982) for the transverse conductivity and bulk modulus are, respectively, given by

$$\sigma_L^{(3)} \le \sigma_e \le \sigma_U^{(3)}, \tag{1}$$

where

$$\sigma_U^{(3)} = \left[<\sigma> - \frac{\phi_1\phi_2(\sigma_2-\sigma_1)^2}{<\tilde{\sigma}> + <\sigma>_\zeta} \right], \tag{2}$$

$$\sigma_L^{(3)} = \left[<1/\tilde{\sigma}> - \frac{\phi_1\phi_2(1/\sigma_2-1/\sigma_1)^2}{<1/\tilde{\sigma}> + <1/\sigma>_\zeta} \right]^{-1}; \tag{3}$$

and

$$k_L^{(3)} \le k_e \le k_U^{(3)}, \tag{4}$$

where

$$k_U^{(3)} = \left[<k> - \frac{\phi_1\phi_2(k_2-k_1)^2}{<\tilde{k}> + <G>_\zeta} \right], \tag{5}$$

$$k_L^{(3)} = \left[<1/k> - \frac{\phi_1\phi_2(1/k_2-1/k_1)^2}{<1/\tilde{k}> + <1/G>_\zeta} \right]^{-1}. \tag{6}$$

Here we define $<b> = b_1\phi_1 + b_2\phi_2$, $<\tilde{b}> = b_1\phi_2 + b_2\phi_1$, and $<b>_\zeta = b_1\zeta_1 + b_2\zeta_2$, where b represents any property. The quantities k_1 and k_2 are the transverse bulk moduli of the phases for transverse compression without axial extension and may be expressed in terms of the isotropic phase moduli as $k_i = K_i + G_i/3$ $(i = 1, 2)$. The microstructural parameter $\zeta_2 = 1 - \zeta_1$, which must lie in the closed internal [0, 1], is defined by

$$\zeta_2 = \frac{2}{\pi\phi_1\phi_2}\int_0^\infty \frac{dr}{r}\int_0^\infty \frac{ds}{s}\int_0^{2\pi} d\theta \left[S_3(r,s,t) - \frac{S_2(r)S_2(s)}{\phi_2} \right]\cos 2\theta. \tag{7}$$

The quantities $S_2(r)$ and $S_3(r, s, t)$ are, respectively, the probabilities of finding in phase 2 the end points of a line segment of length r and the vertices of a triangle with sides of length r, s, and t; θ is the angle opposite the side of length t. One can drop the factor S_2S_2/ϕ_2 appearing in equation (7), since it makes no contribution to the integral. Its presence, however, ensures the absolute convergence of the integral (Torquato, 1985).

It should be noted that the simplified version of the Silnutzer bounds on σ_e is not entirely new. Schulgasser (1976) simplified Silnutzer's upper bound on σ_e, by rewriting it in terms of a single microstructural parameter, and using a certain two-dimensional symmetry property, derived a lower bound on σ_e (in terms of the same parameter) which, as noted by Milton (1981), is equavalent to Silnutzer's lower bound.

As noted by Hashin (1970), the problem of determining the effective transverse conductivity σ_e (given σ_1 and σ_2) has the same underlying mathematics as the problem of determining the effective *axial* shear modulus μ_e (given G_1 and G_2) and, hence, results for the former translate immediately into results for the latter and vice versa. Replacement of σ_i with G_i $(i = 1, 2)$ in relation (1), therefore, gives the corresponding bounds on μ_e.

The expressions (1) and (4) are referred to as third-order bounds since they are exact through third order in the difference $(\sigma_2 - \sigma_1)$ and $(k_2 - k_1)$, respectively. At the extreme values of the three-point parameter ζ_2, $\zeta_2 = 0$ and $\zeta_2 = 1$, the Silnutzer bounds on σ_e and k_e coincide and equal one of the corresponding second-order bounds obtained by Hill (1964) and by Hashin (1965). For all possible values of $\zeta_2 (0 \le \zeta_2 \le 1)$, the third-order bounds are alwaysmore restrictive than the corresponding second-order bounds. It should be noted that Silnutzer (1972) also derived analogous third-order bounds for the effective *transverse* shear modulus that were shown (Milton 1982) to depend on not only ζ_2 but another three-point parameter η_2. In practice, η_2 is more difficult to obtain than ζ_2. The evaluation of η_2 and, hence, third-order bounds on the effective transverse shear modulus for the model composite considered here, shall be the subject of a future investigation.

Downloaded 03 May 2010 to 171.66.16.21. Redistribution subject to ASME license or copyright; see http://www.asme.org/terms/Terms_Use.cfm

Milton (1981) obtained fourth-order bounds on σ_e for transversely isotropic fiber-reinforced materials which depend not only upon σ_1, σ_2, ϕ_2, and ζ_2, but upon a multidimensional integral that involves the four-point probability function S_4. Utilizing a phase-interchange theorem for fiber-reinforced materials, Milton showed that the integral involving S_4 can be expressed in terms of ϕ_2 and ζ_2 only. The fourth-order bounds derived by Milton are, for the case $\sigma_2 \geq \sigma_1$, given by

$$\sigma_L^{(4)} \leq \sigma_e \leq \sigma_U^{(4)}, \tag{8}$$

$$\sigma_U^{(4)} = \sigma_2\left[\frac{(\sigma_1+\sigma_2)(\sigma_1+<\sigma>)-\phi_2\zeta_1(\sigma_2-\sigma_1)^2}{(\sigma_1+\sigma_2)(\sigma_2+<\tilde{\sigma}>-\phi_2\zeta_1(\sigma_2-\sigma_1)^2}\right], \tag{9}$$

$$\sigma_L^{(4)} = \sigma_1\left[\frac{(\sigma_1+\sigma_2)(\sigma_2+<\sigma>)-\phi_1\zeta_2(\sigma_2-\sigma_1)^2}{(\sigma_1+\sigma_2)(\sigma_1+<\tilde{\sigma}>-\phi_1\zeta_2(\sigma_2-\sigma_1)^2}\right]. \tag{10}$$

Thus the three-point parameter ζ_2 determines third-order bounds on σ_e (or μ_e) and k_e, and fourth-order bounds on σ_e or μ_e. To date, ζ_2 has been computed only for two models of disordered fiber-reinforced materials, namely, symmetric-cell materials (Beran and Silnutzer, 1971) and fully penetrable cylinders (Torquato and Beasley, 1986; Joslin and Stell, 1986). Symmetric-cell materials (Miller, 1969) are constructed by partitioning space into cells of possibly varying shapes and sizes, with cells randomly designated as phase 1 or phase 2 with probabilities ϕ_1 and ϕ_2, respectively. Although a useful mathematical construct, a symmetric-cell material could not be employed as a model of the more realistic microstructure of a distribution of equisized impenetrable cylinders in a matrix, since the space could not be completely filled by such cells. By "fully penetrable" cylinders, we mean a distribution of randomly centered, and thus spatially uncorrelated, cylinders. As the fiber volume fraction is increased for such a model, the fibers tend to form clusters (because the fibers may overlap each other), and eventually, at the percolation threshold $\phi_2^c \cong 0.68$ (Gawlinski and Stanley, 1981), the fiber phase changes from a discontinuous phase to a continuous one. The space ultimately can be entirely filled with cylinders. Fully penetrable-cylinder distributions, therefore, are not good models (at high fiber volume fractions) of a large class of fiber-reinforced materials which are characterized by impenetrable fibers.

3 Simplification and Calculation of the Parameter ζ_2 for Rigid Cylinders

The general n-point probability function for the ith phase of a two-phase system of arbitrary dimensionality consisting of inclusions distributed throughout a matrix phase has been shown by Torquato and Stell (1982) to be an infinite series. For the specific instance of an isotropic distribution of identical, impenetrable disks (infinitely long, parallel cylinders) of radius R at an area (volume) fraction ϕ_2, the infinite series for the probability function associated with the included phase (phase 2) terminates with the nth term (Torquato and Stell 1985); in the case $n = 3$, it is given by

$$S_3(r_{12},r_{13},r_{23}) = S_3^{(1)}(r_{12},r_{13},r_{23}) + S_3^{(2)}(r_{12},r_{13},r_{23}) + S_3^{(3)}(r_{12},r_{13},r_{23}), \tag{11}$$

where

$$S_3^{(1)} = \rho\int m(r_{14})m(r_{24})m(r_{34})d\mathbf{r}_4, \tag{12}$$

$$S_3^{(2)} = \rho^2\int\int m(r_{14})m(r_{24})m(r_{35})g_2(r_{45})d\mathbf{r}_4 d\mathbf{r}_5 + \rho^2\int\int m(r_{14})m(r_{25})m(r_{34})g_2(r_{45})d\mathbf{r}_4 d\mathbf{r}_5 + \rho^2\int\int m(r_{15})m(r_{24})m(r_{34})g_2(r_{45})d\mathbf{r}_4 d\mathbf{r}_5, \tag{13}$$

and

$$S_3^{(3)} = \rho^3\int\int\int m(r_{14})m(r_{25})m(r_{36})g_3(r_{45},r_{46},r_{56})d\mathbf{r}_4 d\mathbf{r}_5 d\mathbf{r}_6. \tag{14}$$

Here ρ is the number density of disks (cylinders), $m(r)$ is the particle indicator function which, for the simple case of a disk or a sphere, is equal to one for $r < R$ and zero otherwise, g_2 is the pair (radial) distribution function, g_3 is the triplet distribution function, and $r_{ij} \equiv |\mathbf{r}_j - \mathbf{r}_i|$. In general, the quantity $\rho^n g_n$ is the probability density associated with finding a particular configuration of n inclusions. Note that the disk area fraction (or cylinder volume fraction) is simply related to the number density, i.e., $\phi_2 = \rho\pi R^2$. The domain of integration in each of the integrals in (12)–(14) is the infinite area of the macroscopic sample. When points 2 and 3 coincide (i.e., when $r_{13} = r_{23} = 0$), $S_3(r_{12}, r_{13}, r_{23}) \to S_2(r_{12})$ and, hence, $S_2(r_{ij})$ can be obtained from equation (11) whenever points j and k coincide, under all permutations of i, j, and k.

Each term of equation (11) has a simple interpretation. Recall that $S_3(r_{12}, r_{13}, r_{23})$ gives the probability of finding all three points $\mathbf{r}_1$, $\mathbf{r}_2$ and $\mathbf{r}_3$ in the included phase. $S_3^{(1)}$ (a two-fold integral) gives the contribution of S_3 when all three points lie in the same disk (cylinder)—a quantity trivially related to the intersection area (volume) of three disks (cylinders) with centers separated by the distances r_{12}, r_{13}, and r_{23} (Torquato and Stell, 1982; Torquato and Stell 1985; Torquato and Beasley, 1986). $S_3^{(2)}$ (a four-fold integral) gives the contribution to S_3 when one point is in one disk (cylinder) and the two other points are in another disk (cylinder); this quantity must obviously involve the pair distribution function g_2 [cf. equation (13)]. Finally, $S_3^{(3)}$ (a six-fold integral) gives the contribution to S_3 when all three points lie in different disks (cylinders) and, hence, depends upon the triplet distribution function g_3 [cf. equation (14)]. Note that S_n in the paper by Torquato and Stell, unlike the present work, denotes the probability function associated with the matrix phase; the latter quantity is simply related to the included-phase analog (Torquato and Stell, 1982).

It is important to note that the three-point probability function for dispersions containing particles of arbitrary shape and size has the same functional form as equations (11)–(14). For the case of identical inclusions of arbitrary shape, one simply lets $\mathbf{r}_i$ ($i = 4, 5, 6$) denote not only the center-of-mass coordinate but the orientation of the particle and, hence, in general, g_2 and g_3 depend upon absolute coordinates, i.e., $g_2(\mathbf{r}_4, \mathbf{r}_5)$ and $g_3(\mathbf{r}_4, \mathbf{r}_5, \mathbf{r}_6)$. The particle indicator function m is retained in the equations but now, of course, its argument is a position vector $\mathbf{r}$ measured with respect to the centroid of the inclusion; it still is unity when $\mathbf{r}$ is inside the particle and zero otherwise. This simple generalization of equations (11)–(14) enables one to determine S_3 for anisotropic as well as inhomogeneous suspensions of identical inclusions of arbitrary shape (e.g., oriented, finite cylinders or ellipsoids); the probabilistic interpretations of the integrals $S_3^{(i)}$ given previously for disks or spheres hold for these more general suspensions as well. The generalization of equation (11) to particles with size distributions is formally straightforward; such a formalism is provided by Torquato and Stell (1983).

Substitution of equations (11)–(14) into the key integral ζ_2, equation (7), reveals that one must perform five-fold, seven-fold, and nine-fold integrations. These complicated "cluster" integrals are reminiscent of those that arise in the study of the statistical mechanics of the liquid state. The cluster integrals can be greatly simplified by employing a technique analogous to the one used by Lado and Torquato (1986) in the three-dimensional problem. For isotropic three-dimensional two-

Downloaded 03 May 2010 to 171.66.16.21. Redistribution subject to ASME license or copyright; see http://www.asme.org/terms/Terms_Use.cfm

phase media, the three-point parameter (which determines third-order bounds) is similar to (7) but involves the Legendre polynomial of degree 2 instead of $\cos 2\theta$. For isotropic distributions of impenetrable spheres, Lado and Torquato (1986) greatly simplified the cluster integrals (associated with the three-point parameter) by expanding angle-dependent terms in the integrands in spherical harmonics and employing the orthogonality properties of this basis set. For the problem at hand, the analogous procedure involves expanding angle-dependent terms in circular harmonics (i.e., Chebyshev polynomials) and using the orthogonality properties of this basis set. Application of this technique leads to the following substantially simplified expression for the three-point parameter for impenetrable disks of unit diameter

$$\zeta_2 = \frac{2}{\pi\phi_1}\left[c_2\phi_2 + c_3\phi_2^2\right], \tag{15}$$

where

$$c_2 = \frac{\pi}{4}\int_1^\infty dr\,\frac{r\,g_2(r)}{(r^2-1/4)^2} \tag{16}$$

and

$$c_3 = \sum_{n=2}^{\infty}\frac{n-1}{4^{n-3}}\int_1^\infty\frac{dr}{r^{n-1}}\int_1^r\frac{ds}{s^{n-1}}\int_0^\pi d\theta\Big[g_3(r,s,t) - g_2(r)g_2(t)\Big]T_n(\cos\theta). \tag{17}$$

The details leading to equations (15)–(17) are somewhat complicated and lengthy and, hence, will not be given here; they are described, however, in another article (Torquato and Lado, 1988). Note that the original five, seven, and nine-fold cluster integrals have been reduced to a one and three-fold integral; cf., equations (16) and (17). In equation (17), $T_n(\cos\theta) = \cos n\theta$ is the Chebyshev polynomials of the first kind. As noted in the Introduction, the analysis which leads to equations (15)–(17) can be applied to composites consisting of particles of arbitrary shape, size, and penetrability.

In order to compute the two and three-body integrals of equation (15), we need to know the density-dependent pair g_2 and triplet g_3 distribution functions for the model. Determination of g_2 and g_3 for general random distributions is at best a highly formidable task. We shall assume an equilibrium distribution of impenetrable, parallel cylinders since: (*i*) The structure of this model has been extensively studied in the study of the liquid state (Lado, 1968); (*ii*) Such a model may be viewed as the most random distribution of cylinders subject to the constraint of impenetrability and thus a reasonable model of a real fiber-reinforced material. Specifically, we employ the accurate Percus-Yevick approximation to g_2 for impenetrable disks obtained numerically by Lado (1968).

The calculation of the triplet distribution function, as is well known in liquid-state theory, is more problematical. Lacking any more fundamental alternative, we have resorted to the familiar Kirkwood Superposition Approximation (KSA) (Hansen and McDonald, 1976),

$$g_3(r_{12},r_{13},r_{23}) \approx g_2(r_{12})g_2(r_{13})g_2(r_{23}) \tag{18}$$

to evaluate this quantity. The KSA (18) is exact in the zero-density limit for all particle configurations and for cases in which one particle is distant from the other two, regardless of the density. For equilateral-triangle configurations, the KSA is accurate, especially at high densities; the approximation is not as accurate at low densities and for less symmetric triplet configurations. Beasley and Torquato (1986) showed that the use of the KSA in computing the three-dimensional analog of ζ_2 for dispersions of spheres slightly underestimates ζ_2; the error increases with increasing density. It must be emphasized that incorporation of a value of ζ_2 smaller than the exact value (at some fixed volume fraction) in two or three-dimensional conductivity bounds still results in rigorous bounds on σ_e, albeit weaker bounds than ones employing the exact ζ_2. Since the integral (7) bears a strong similarity to its three-dimensional counterpart, it is expected that the use of the KSA in equation (17) should not lead to significantly large errors in ζ_2 (see also, discussion of Section 4).

Table 1 Three-point parameter ζ_2 for three models of disordered fiber-reinforced materials: (*i*) symmetric-cell material with cylindrical cells (Beran and Silnutzer, 1971; Milton, 1982); (*ii*) fully penetrable cylinders (Torquato and Beasley, 1986) (*iii*) equilibrium distribution of impenetrable cylinders calculated in the present study

ϕ_2	ζ_2		
	Symmetric-Cell Material	Fully Penetrable Cylinders	Random Impenetrable Cylinders
0.0	0.0	0.0	0.0
0.1	0.1	0.061	0.032
0.2	0.2	0.123	0.063
0.3	0.3	0.186	0.092
0.4	0.4	0.249	0.121
0.5	0.5	0.312	0.165
0.55	0.55	---	0.194
0.60	0.60	0.377	0.251
0.65	0.65	---	0.372
0.70	0.70	0.444	
0.80	0.80	0.514	
0.90	0.90	0.590	

Given the Percus-Yevick $g_2(r)$ (Lado, 1968), the two-body integral c_2 of equation (16) can be evaluated employing any standard numerical quadrature technique. To compute the three-fold integral c_3, equation (17), we use a Gaussian-Chebyshev quadrature technique (*Handbook of Mathematical Functions*, 1964). Such numerical integration methods have been utilized to accurately evaluate related multifold integrals (Torquato and Beasley, 1986). The integration domain for (17) was subdivided so that 24 Gaussian points in each dimension gave convergence to four significant figures. In principle, the expansion (17) in Chebyshev polynomials is infinite but, in practice, only the first seven to nine terms are needed to give convergence to four significant figures. To compute c_3 at large cylinder volume fractions (the most time intensive cases), the Gaussian quadrature scheme required about 48 min of CPU time on a VAX 785. The one-fold integral c_2, equation (16), was also evaluated using the same Gaussian method; here we used 64 Gaussian points.

In Table 1, the three-point parameter ζ_2 for our model of a random array of impenetrable cylinders is given at selected values of the cylinder volume fraction ϕ_2. Since the Percus-Yevick approximation, for the pair distribution function, appears to break down as the random close-packing volume fraction $\phi_2 \cong 0.81$ (Stillinger, DiMarzio and Kornegay, 1964) is approached, the highest volume fraction reported here is $\phi_2 = 0.65$, at which the Percus-Yevick results are still in relatively good agreement with Monte Carlo simulations. The percolation threshold ϕ_2^c for an equilibrium distribution of impenetrable disks has been conjectured to be the random-packing limit.

The microstructural parameter ζ_2 can be evaluated exactly through second order in ϕ_2. We find

$$\zeta_2 = \frac{1}{3}\,\phi_2 - 0.05707\,\phi_2^2 + 0\left(\phi_2^3\right). \tag{19}$$

Downloaded 03 May 2010 to 171.66.16.21. Redistribution subject to ASME license or copyright; see http://www.asme.org/terms/Terms_Use.cfm

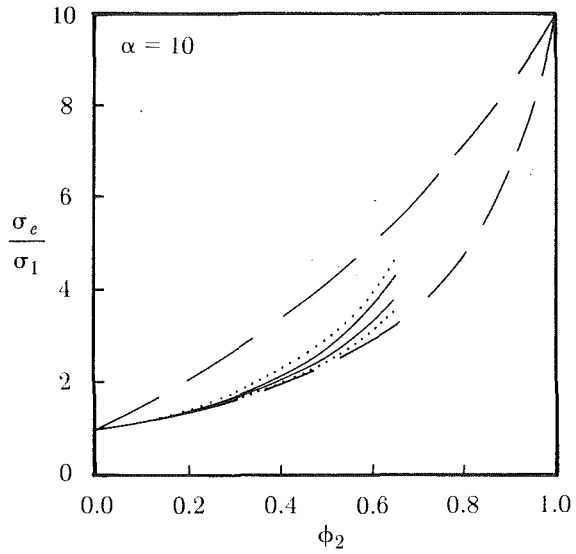


Fig. 1 Bounds on the scaled effective transverse conductivity σ_e/σ_1 versus the fiber volume fraction ϕ_2 at $\alpha = \sigma_2/\sigma_1 = 10$; — — — — second-order Hashin (1965, 1970) bounds; .... third-order Silnutzer (1970) bounds; and ——— fourth-order Milton (1981) bounds, for a random distribution of impenetrable cylinders

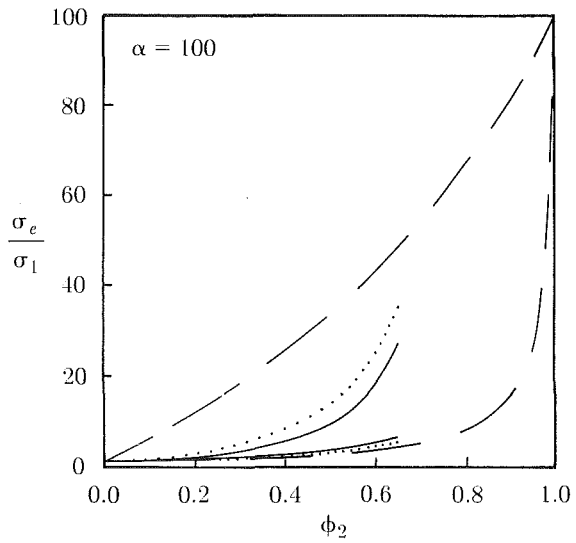


Fig. 2 As in Fig. 1, with $\alpha = 100$

The details of this calculation are given by Torquato and Lado (1988). The first-order coefficient depends upon the zero-density limit of g_2. The second-order coefficient depends upon g_2 through order ρ and the zero-density limit of the triplet distribution functions g_3 in which case the superposition approximation (18) is exact. Therefore, equation (19) is an exact result. Note that the low-density expansion (19) provides a relatively good approximation of our calculations of ζ_2 through all orders in ϕ_2 (Table 1) for the range $0 \leq \phi_2 \leq 0.4$.

For purposes of comparison, we include in Table 1 the parameter ζ_2 for the symmetric-cell material with cylindrical cells (Beran and Stilnutzer, 1971; Milton, 1982) for which $\zeta_2 = \phi_2$ and for fully penetrable cylinders (Torquato and Beasley, 1986). As noted earlier, these latter two geometries represent the only other random-media models for which ζ_2 has been computed. The physical significance of ζ_2 for general microstructures is described by Torquato and Lado (1988). It suffices here to make the following observations. The parameter ζ_2 for the random-impenetrable case is always below the corresponding values of ζ_2 for the other two models for the values of ϕ_2 calculated here (i.e., $\phi_2 \leq 0.65$). For the model examined in the present study, ζ_2 is approximately linear for the range $0 \leq \phi_2 \leq 0.4$ and significantly increases with ϕ_2 as the maximum random-close-packing volume fraction ($\phi_2^c \cong 0.81$) is approached. This is to be contrasted with the symmetric-cell material, for which ζ_2 is exactly linear in ϕ_2, and the fully penetrable-cylinder model, for which ζ_2 is approximately linear for all ϕ_2; in both cases ϕ_2 can take on all possible values, i.e., $0 \leq \phi_2 \leq 1$.

4 Evaluation of Bounds on σ_e, k_e, and μ_e for Rigid Cylinders

Before presenting third and fourth-order bounds for the effective properties for our model, it is useful to first comment on the general utility of bounds when the phase property values widely differ. For the case of conduction, all nth-order lower bounds (for finite n) tend to zero as $\alpha \to 0$ and all nth-order upper bounds tend to infinity as $\alpha \to 0$, where $\alpha = \sigma_2/\sigma_1$. Similarly, for the elasticity problem, all nth-order lower bounds tend to zero as $\beta = G_2/G_1 \to 0$ (i.e., when phase 2 is a void phase) and all nth-order upper bounds tend to infinity as $\beta \to \infty$ (i.e., when phase 2 is infinitely more rigid than phase 1). This does not mean that bounds cannot be employed to estimate effective properties, however, since the reciprocal bounds in the aforementioned instances remain finite and can provide a useful estimate of them. Specifically, Torquato (1985) has observed that lower-order lower bounds (such as second, third, and fourth-order bounds) should yield good estimates of σ_e/σ_1 for $\alpha \gg 1$, provided that ϕ_2 is not only below its percolation-threshold value ϕ_2^c but that the mean cluster size of phase 2, Λ_2, is much smaller than the macroscopic length of the sample L. (A cluster of phase i is defined as that part of phase i which can be reached from a point in phase i without touching any part of phase j, $i \neq j$). Of course, the accuracy of the lower-order lower bounds increases as the order increases. Note that since the mean cluster size Λ_2 at the percolation point ϕ_2^c becomes infinitely large, the foregoing condition $\Lambda_2 \ll L$ implies that the system is below the percolation threshold (i.e., $\phi_2 < \phi_2^c$). For periodic arrays of disks and for an equilibrium distribution of rigid disks, the condition $\Lambda_2 \ll L$ is satisfied for all ϕ_2, except at the close-packing or percolation-threshold value. Similarly, lower-order upper bounds should provide a useful estimate of σ_e/σ_1 for $\alpha \gg 1$, provided that $\phi_2 > \phi_2^c$ and $\Lambda_1 \ll L$, where Λ_1 is the mean cluster size of phase 1. The accuracy of the lower-order upper bounds of course will improve as n increases. Analogous statements apply as well to bounds on k_e and μ_e.

Using the tabulation of ζ_2 for a random array of impenetrable cylinders obtained in the previous section, we evaluate third and fourth-order bounds on σ_e (or μ_e) and k_e described in Section 2. In Fig. 1, we plot third and fourth-order bounds on the scaled effective conductivity σ_e/σ_1 [equations (1) and (8)] as a function of cylinder volume fraction ϕ_2 for the case $\alpha = 10$. Included in this figure is the corresponding second-order bounds derived by Hashin. The third-order Silnutzer bounds substantially improve upon the second-order bounds; the fourth-order Milton bounds, in turn, are more restrictive than the third-order bounds. At $\phi_2 = 0.5$, the third-order bounds are about 3.7 times narrower than the second-order bounds, whereas the fourth-order bounds are about 2.1 times more restrictive than the third-order bounds and, hence, almost 8 times narrower than the Hashin bounds. Note that most of the improvement provided by the third and fourth-order bounds is provided by the upper bounds rather than the lower bounds. For the case $\alpha = 0.1$ (not shown here), the Silnutzer and Milton bounds provide similar improvement over the Hashin bounds, except that

Downloaded 03 May 2010 to 171.66.16.21. Redistribution subject to ASME license or copyright; see http://www.asme.org/terms/Terms_Use.cfm

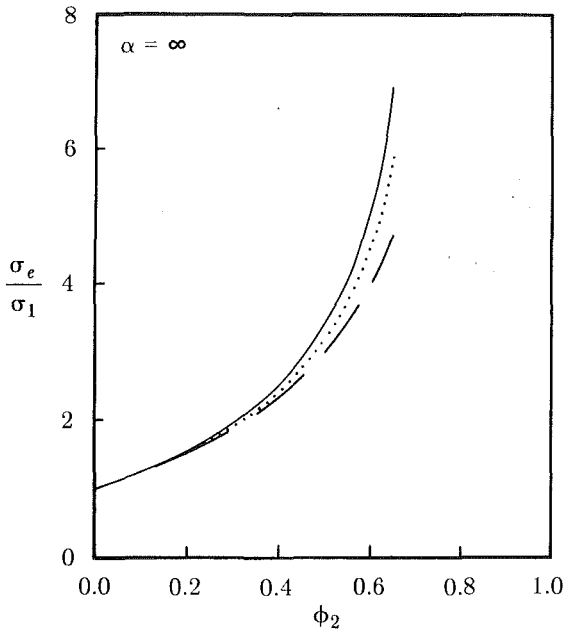


Fig. 3 As in Fig. 1, with $\alpha = \infty$; upper bounds are not shown since they diverge to infinity in this limit

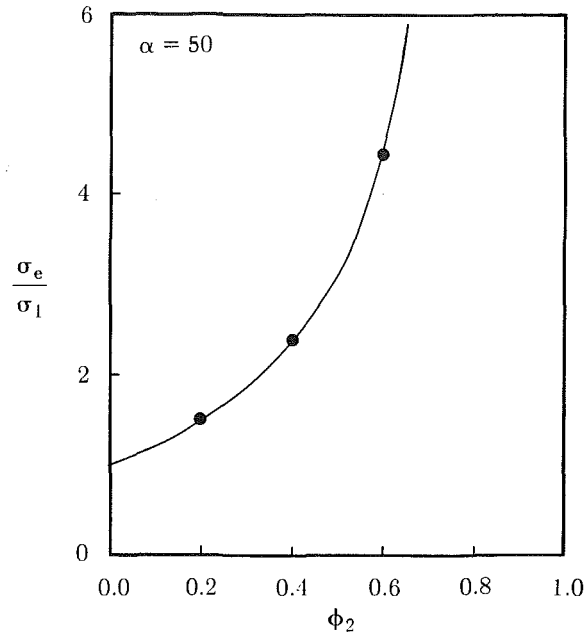


Fig. 4 Comparison of the fourth-order lower bound on the scaled effective transverse conductivity to simulation results (solid circles) for the same equilibrium model of cylinders examined here (Durand and Ungar, 1988) for $\alpha = 50$

most of the improvement is in the lower bound. To summarize, for the range $0.1 \leq \alpha \leq 10$, the fourth-order Milton bounds are sharp enough to give a good estimate of σ_e/σ_1 for the entire range of volume fractions.

In Fig. 2, we plot all three bounds on the reduced conductivity σ_e/σ_1 versus ϕ_2 for inclusions which are 100 times more conducting than the matrix phase, i.e., $\alpha = 100$. As expected, all the bounds widen. At $\phi_2 = 0.5$, the third-order bounds are about 2.8 times narrower than the second-order bounds; the fourth-order bounds are about 1.7 times narrower than the third-order bounds and, therefore, are almost 5 times more restrictive than the second-order bounds. For the range $0.01 \leq \alpha \leq 100$, the fourth-order Milton bounds are restrictive enough to give good estimates of the effective conductivity for the volume fraction range $0 \leq \phi_2 \leq 0.4$.

As noted above, the fact that the bounds diverge as α is made large does not imply that they cannot be utilized to estimate the effective conductivity. Since ϕ_2 is below the percolation threshold ($\phi_2^c \cong 0.81$) for randomly distributed cylinders and because there are no particle contacts ($\Lambda_2 \ll L$), the lower bound is expected to yield a relatively good estimate of σ_e for $\alpha \gg 1$. In Fig. 3, we plot all three lower bounds on σ_e/σ_1 for the most difficult and extreme instance of $\alpha = \infty$, i.e., perfectly conducting cylinders—the case in which all upper bounds diverge to infinity. Milton's fourth-order lower bound should yield a good estimate of σ_e, with the maximum error occurring at the maximum volume fraction reported here, i.e., at $\phi_2 = 0.65$ or equivalently, at 80 percent of the closing-packing volume fraction ($\phi_2/\phi_2^c \cong 0.80$). We can estimate the maximum error by comparing the Milton lower bound (10) for square and hexagonal arrays (McPhedran and Milton, 1981) at $\phi_2/\phi_2^c = 0.8$ and $\alpha = \infty$ to the exact results of Perrins, McKenzie, and McPhedran (1979) for these idealized periodic arrays. (For periodic arrays, the symmetry associated with the periodicity enables one to obtain σ_e exactly numerically. Such geometries share an important property with equilibrium distributions of cylinders, namely, there are no particle contacts ($\Lambda_2 \ll L$) until the respective close-packing volume fraction is attained.) For square arrays at $\phi_2/\phi_2^c = 0.80$ and $\alpha = \infty$, $\sigma_L^{(4)}/\sigma_1 = 4.89$, whereas the exact result for $\sigma_e/\sigma_1 = 4.93$. For hexagonal arrays under the same conditions, $\sigma_L^{(4)}/\sigma_1 = 6.51$, whereas the exact result for $\sigma_e/\sigma_1 = 6.53$. Therefore, the maximum error in using Milton's lower bound to estimate σ_e for a random array of perfectly conducting cylinders is about 1 percent for the range $0 \leq \phi_2 \leq 0.65$. For values of α in the range $1 \leq \alpha < \infty$, the deviation of Milton's lower bound from exact results is even less than it is for $\alpha = \infty$. In short, Milton's lower bound provides an excellent estimate of the actual effective conductivity of our model system for all α and for $0 \leq \phi_2 \leq 0.65$.

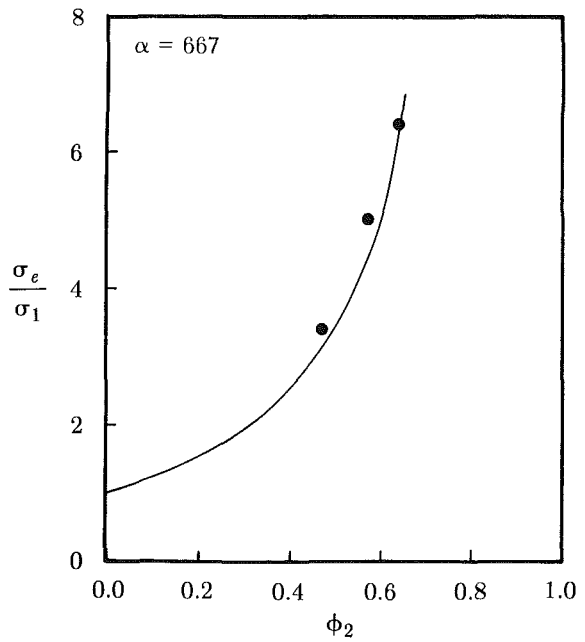


Fig. 5 Comparison of the fourth-order lower bound on the scaled effective transverse conductivity to experimental data (solid circles) for a graphite-plastic composite (Thornburgh and Pears, 1965) with $\alpha = 667$

In Fig. 4, we compare the fourth-order lower bound on σ_e/σ_1 for $\alpha = 50$ to exact simulation results (for the equilibrium model studied here) very recently obtained by Durand and Ungar (1988) using the Boundary Element Method (BEM). The fourth-order lower bound, not surpris-

Downloaded 03 May 2010 to 171.66.16.21. Redistribution subject to ASME license or copyright; see http://www.asme.org/terms/Terms_Use.cfm

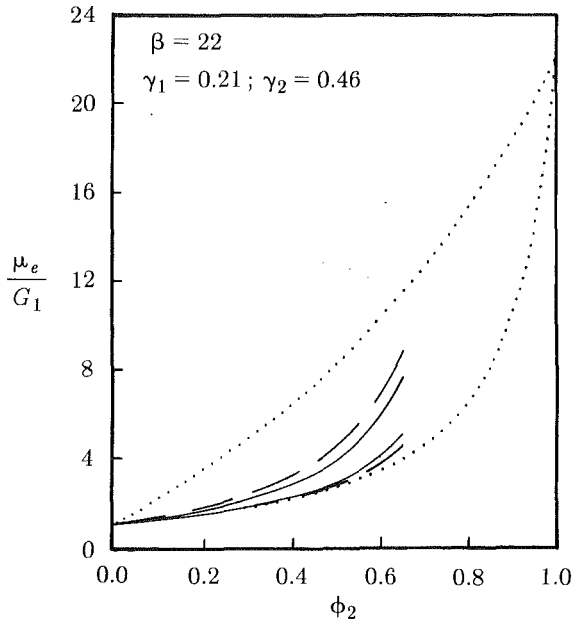


Fig. 6 Bounds on the scaled effective axial shear modulus μ_e/G_1 versus ϕ_2 for a glass-epoxy composite for which $\beta = G_2/G_1 = 22$; legend is the same as in the previous figures

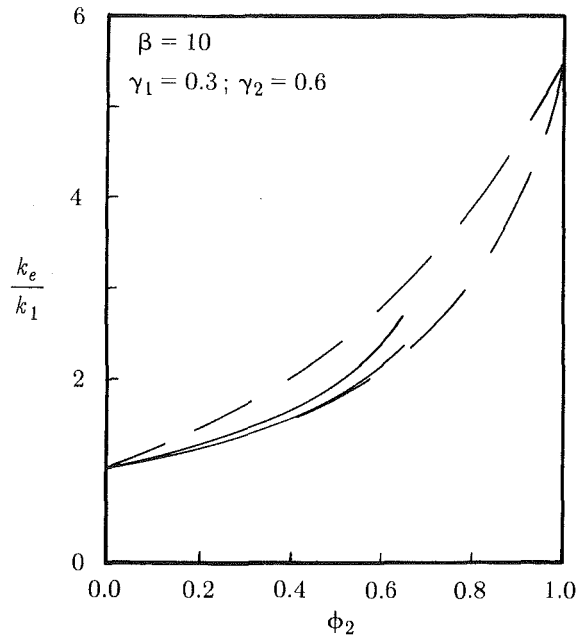


Fig. 7 Bounds on the scaled effective transverse bulk modulus k_e/k_1 versus ϕ_2 for $\beta = 10$, $\gamma_1 = 0.3$, $\gamma_2 = G_2/K_2 = 0.6$; ———— second-order bounds (Hill, 1964; Hashin, 1965); ——— third-order Silnutzer (1972) bounds for a random distribution of impenetrable cylinders

ingly, is seen to predict the effective conductivity extremely accurately. This supports our assertion that bounds, which incorporate nontrivial microstructural information on the medium, can be used to accurately estimate effective properties, even when the phase properties are widely different.

In Fig. 5, we compare the fourth-order lower bound on σ_e/σ_1 to the experimental data of Thornburgh and Pears (1965) for a composite composed of highly conducting graphite fibers in a plastic matrix for which $\alpha = 667$. As expected, the fourth-order lower bound provides an excellent estimate of the experimental data. This further supports our claims about the utility of bounds.

Before discussing evaluation of the bounds for the elastic moduli, it is useful to remark on the suitability of the KSA, equation (18), to compute the integral ζ_2 [cf., equations (15) and (17)]. The fact that the fourth-order lower bound on σ_e for our model provides an excellent estimate of the conductivity indicates that the use of the KSA in equation (17) does not lead to significantly large errors in ζ_2.

As noted in Section 2, results obtained for σ_e/σ_1 given α translate immediately into equivalent results for the scaled axial shear modulus μ_e/G_1 given $\beta = G_2/G_1$. Therefore, the general conclusions made about third and fourth-order bounds on the effective conductivity previously described apply as well to μ_e. For example, when the cylindrical fibers are perfectly rigid ($\beta = \infty$), the fourth-order lower bound should provide an excellent estimate of μ_e/G_1. It is useful, nonetheless, to show the bounds on μ_e/G_1 using elastic moduli property values for a real composite material. This is done in Fig. 6 for a typical glass-epoxy composite of which $\beta = 22$, $\gamma_1 = G_1/K_1 = 0.21$ and $\gamma_2 = G_2/K_2 = 0.46$ (Chou and Kelly, 1980). The ratio $\gamma = (3 - 6\nu)/(2\nu + 2)$, where ν is Poisson's ratio and $0 \le \nu \le 0.5$, then $0 \le \gamma \le 1.5$. The bounds given in Fig. 6 are of course independent of the γ_i; the γ_i are required in general, however.

Figure 7 shows the third-order Silnutzer bounds on the scaled effective transverse bulk modulus k_e/k_1 [cf., equation (4)], for our model, as a function of ϕ_2 for $\beta = 10$, $\gamma_1 = 0.3$ and $\gamma_2 = 0.6$. Included in the figure are the corresponding second-order bounds (Hill, 1964; Hashin, 1965). The third-order bounds provide significant improvement over the second-order bounds. In Fig. 8, we plot the same bounds for a glass-epoxy composite for which $\beta = 22$, $\gamma_1 = 0.21$, and $\gamma_2 = 0.46$.

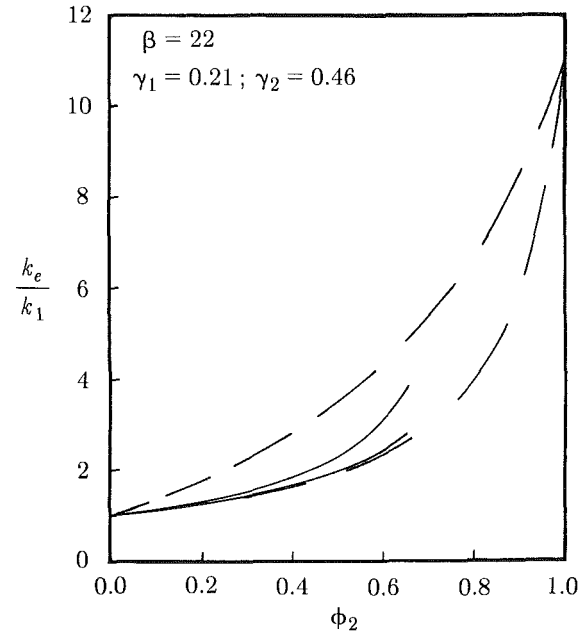


Fig. 8 As in Fig. 7, for a glass-epoxy composite, for which $\beta = 22$, $\gamma_1 = 0.21$, and $\gamma_2 = 0.46$

Acknowledgments

S. Torquato gratefully acknowledges the support of the Office of Basic Energy Services, U. S. Department of Energy, under Grant No. DEFG05-86ER13482. F. Lado acknowledges the support of the National Science Foundation under Grant Number CHE-8402144.

Downloaded 03 May 2010 to 171.66.16.21. Redistribution subject to ASME license or copyright; see http://www.asme.org/terms/Terms_Use.cfm

References

Beasley, J. E., and Torquato, S., 1986, "Bounds on the Conductivity of Suspensions of Impenetrable Spheres," *Journal of Applied Physics*, Vol. 60, pp. 3576–3581.

Beran, M. J., and Silnutzer, N., 1971, "Effective Electrical, Thermal and Magnetic Properties of Fiber-Reinforced Materials," *Journal of Composite Materials*, Vol. 5, pp. 246–249.

Berryman, J. G., and Blair, S. C., 1986, "Use of Digital Image Analysis to Estimate Fluid Permeability of Porous Materials: Application of Two-Point Correlation Functions," *Journal of Applied Physics*, Vol. 60, pp. 1930–1938.

Chou, T.-W., and Kelly, A., 1980, "Mechanical Properties of Composites," *Annual Review of Materials Science*, Vol. 10, pp. 229–259.

Christensen, R. M., 1979, *Mechanics of Composite Materials*, Wiley-Interscience, New York, 1979.

Durand, P. P., and Ungar, L. H., 1988, "Application of the Boundary Element Method to Dense Dispersions," *International Journal of Numerical Methods in Engineering*, in press.

Gawlinski, E. T., and Stanley, H. E., 1981, "Continuum Percolation in Two Dimensions: Monte Carlo Tests of Scaling and Universality for Noninteracting Disks," *Journal of Physics A: Mathematics and General*, Vol. 14, pp. L291–L299.

Haile, J. M., Massobrio, C., and Torquato, S., 1985, "Two-Point Matrix Probability Function for Two-Phase Random Media: Computer Simulation Results for Impenetrable Spheres," *Journal of Chemical Physics*, Vol. 83, pp. 4075–4078.

Handbook of Mathematical Functions, 1965, Abramowitz, M., and Stegun, I. A., Eds., Dover.

Hansen, J. P., and McDonald, I. R., 1976, *Theory of Simple Liquids*, Academic Press, NY, 1976.

Hashin, Z., 1965, "On Elastic Behavior of Fibre Reinforced Materials of Arbitrary Transverse Phase Geometry," *Journal of the Mechanics and Physics of Solids*, Vol. 13, pp. 119–134.

Hashin, Z., 1970, "Theory of Composite Materials," *Mechanics of Composite Materials*, Wendt, F. W., Liebowitz, H., and Perrone, N., Eds., Pergamon Press, NY, pp. 201–242.

Hashin, Z., 1983, "Analysis of Composite Materials," ASME JOURNAL OF APPLIED MECHANICS, Vol. 50, pp. 481–505.

Hill, R., 1964, "Theory of Mechanical Properties of Fibre-Strengthened Materials—I. Elastic Behavior," *Journal of the Mechanics and Physics of Solids*, Vol. 12, pp. 199–212.

Joslin, C. G., and Stell, G., 1986, "Bounds on the Properties of Fiber-Reinforced Composites," *Journal of Applied Physics*, Vol. 60, pp. 1607–1610.

Lado, F., 1968, "Equation of State of the Hard-Disk Fluid from Approximate Integral Equations," *Journal of Chemical Physics*, Vol. 49, pp. 3092–3096.

Lado, F, and Torquato, S., 1986, "Effective Properties of Two-Phase Disordered Composite Media. I. Simplification of Bounds on the Conductivity and Bulk Modulus of Dispersions of Impenetrable Spheres," *Physical Review B*, Vol. 33, pp. 3370–3378.

McPhedran, R. C., and Milton, G. W., 1981, "Bounds and Exact Theories for the Transport Properties and Inhomogeneous Media," *Applied Physics*, Vol. A26, pp. 207–220.

Miller, M. N., 1969, "Bounds for Effective Electrical, Thermal, and Magnetic Properties of Heterogeneous Materials," *Journal of Mathematical Physics*, Vol. 10, pp. 1988–2004.

Milton, G. W., 1981, "Bounds on the Transport and Optical Properties of a Two-Component Composite Material," *Journal of Applied Physics*, Vol. 52, pp. 5294–5304.

Milton, G. W., 1982, "Bounds on the Elastic and Transport Properties of Two-Component Composites," *Journal of the Mechanics and Physics of Solids*, Vol. 30, pp. 177–191.

Perrins, W. T., McKenzie, D. R., and McPhedran, R. C., 1979, "Transport Properties of Regular Arrays of Cylinders," *Proceedings of the Royal Society of London A*, Vol. 369, pp. 207–225.

Schulgasser, K., 1976, "On the Conductivity of Fiber-Reinforced Materials," *Journal of Mathematical Physics*, Vol. 17, pp. 382–387.

Seaton, N. A., and Glandt, E. D., 1986, "Spatial Correlation Functions from Computer Simulations," *Journal of Chemical Physics*, Vol. 85, pp. 5262–5268.

Silnutzer, N., 1972, "Effective Constants of Statistically Homogeneous Materials," PhD thesis, University of Pennsylvania, Philadelphia, PA.

Smith, P. A., and Torquato, S., 1988, "Computer Simulation Results for the Two-Point Probability Function of Composite Media," *Journal of Computational Physics*, Vol. 76, pp. 176–190.

Stillinger, F. H, DiMarzio, E. A., and Kornegay, R. L., 1964, "Systematic Approach to Explanation of the Rigid Disk Phase Transition," *Journal of Chemical Physics*, Vol. 40, pp. 1564–1576.

Thornburgh, J. D., and Pears, C. D., 1965, "Prediction of the Thermal Conductivity of Filled and Reinforced Plastics," *ASME Paper* 65-WA/HT-4.

Torquato, S., and Stell, G., 1982, "Microstructure of Two-Phase Random Media. I. The *n*-Point Probability Functions," *Journal of Chemical Physics*, Vol. 77, pp. 2071–2077.

Torquato, S., and Stell, G., 1983, "Microstructure of Two-Phase Random Media. II. The Mayer-Montroll and Kirkwood-Salisburg Hierarchies," *Journal of Chemical Physics*, Vol. 78, pp. 3262–3272.

Torquato, S., 1985, "Effective Electrical Conductivity of Two-Phase Disordered Composite Media," *Journal of Applied Physics*, Vol. 58, pp. 3790–3797.

Torquato, S., and Stell, G., 1985, "Microstructure of Two-Phase Random Media. V. The *n*-Point Matrix Probability Functions for Impenetrable Spheres," *Journal of Chemical Physics*, Vol. 82, pp. 980–987.

Torquato, S., 1986, "Microstructure Characterization and Bulk Properties of Disordered Two-Phase Media," *Journal of Statistical Physics*, Vol. 45, pp. 843–873.

Torquato, S., and Beasley, J. D., 1986, "Effective Properties of Fiber-Reinforced Materials: I. Bounds on the Effective Thermal Conductivity of Dispersions of Fully Penetrable Cylinders," *International Journal of Engineering Science*, Vol. 24, pp. 415–433.

Torquato, S., 1987, "Thermal Conductivity of Disordered Heterogeneous Media from the Microstructure," *Reviews in Chemical Engineering*, Vol. 4, pp. 151–204.

Torquato, S., and Lado, F., 1988, "Bounds on the Conductivity of a Random Array of Cylinders," *Proceedings of the Royal Society of London A*, Vol. 417, pp. 59–80.

Downloaded 03 May 2010 to 171.66.16.21. Redistribution subject to ASME license or copyright; see http://www.asme.org/terms/Terms_Use.cfm

Inclusion and Misfit Effects in Hydrostatic Tension

Benjamin Wilner
Assistant Professor,
Engineering Science and Mechanics Program,
School of Civil Engineering,
Georgia Institute of Technology,
Atlanta, GA 30332

A study of the effect of an elastic spherical particle embedded in an infinite elastic-plastic matrix subject to hydrostatic tension is presented. Two types of particles will be considered: (1) a perfectly fitting inclusion, (2) a misfitting one. A numerical solution is developed to solve the governing equations. Various combinations of elastic constants and power hardening coefficients are studied for different load levels. The analysis is concentrated on the interfacial normal stresses and its dependence on the different parameters.

Introduction

Second-phase particles and inclusions are often embedded inside a material to improve its mechanical characteristics. On the other hand, hard particles tend to raise the stresses in their vicinity, in particular the ones along the particle-matrix interface, which may result in the enhancement of local damage. It is well established that at moderate temperatures cracks and voids nucleate in and around inclusions. Experiments show that for equiaxed inclusions, voids and cracks initiate by decohesion of the particle-matrix interface. Such voids and cracks could then grow and coalesce with neighboring ones, and eventually cause total failure. More detailed reviews on the nucleation of microcracks and voids can be found in Goods and Brown (1979), and in Wilner (1986). Analytical studies (see Budiansky, Hutchinson, and Slutsky (1982)) show that a high triaxial stress state enhances void growth which, in turn, promotes fracture.

The metal and the particle may have different thermal expansion coefficients. If, as the temperature changes, the inclusion tends to expand less than the surrounding matrix (hence the term "misfit"), the interfacial stresses will rise and aid void nucleation.

A different type of misfitting inclusions is found in the design of "ductile" ceramics, where particles are placed inside the ceramic. These particles, when subject to high stresses, expand mainly in a hydrostatic manner. Hopefully, this expansion will make the ceramic more fracture-resistant by closing the crack, and hence, eliminate, temporarily, its damaging effects (Budiansky (1983)). Such expansions are also found in phase transformations, where part of the material undergoes a crystallographic change, (see Lee et al., (1980); Earmme et al., (1981)).

It is the purpose of this paper to study the stresses in the vicinity of a perfectly fitting and a misfitting inclusion embedded in an elastic-plastic infinite matrix subject to a far-field load. The analysis will focus only on a hydrostatic load which is known to extensively accelerate void growth, and which, to first approximation, could model the triaxial stress field ahead of a crack tip where cavitation is known to occur as found by Rice and Johnson (1970) and also by McMeeking (1977).

The solution to the spherical symmetric problem, where both the matrix and the inclusion are elastic, can be found analytically or can be derived from Eshelby (1957). Lee, et al. (1980) and Earmme, et al. (1981) have studied the effect of a misfitting inclusion on an elastoplastic matrix but have not included interaction with any loadings.

Formulation

Consider an isolated elastic inclusion of radius $r=a$, embedded in an infinite elastic-plastic matrix. The matrix is subject at infinity to a hydrostatic load S. Due to the spherical symmetry of the problem, a spherical coordinates system is employed throughout the paper. In the following text the superscripts I and M will be used to denote the inclusion and the matrix, respectively.

Governing Equations. Within both the matrix and the inclusion, the following equations must be satisfied:

(1) Equilibrium

$$\frac{d\sigma_{rr}}{dr}+\frac{2}{r}(\sigma_{rr}-\sigma_{\phi\phi})=0, \tag{1}$$

(2) Compatibility

$$\epsilon_{rr}=\frac{d}{dr}(r\epsilon_{\phi\phi}), \tag{2}$$

and the constitutive laws described in the next section. Note that due to the spherical symmetry $\sigma_{\phi\phi}=\sigma_{\theta\theta}$, $\epsilon_{\phi\phi}=\epsilon_{\theta\theta}$, and all shear stresses and strain are zero.

The various boundary conditions will be stated separately.

Constitutive Equations. Let E^I and ν^I be the Young's modulus and the Poisson's ratio of the inclusion, respectively. The matrix is considered to be elastic-plastic and to obey, in

Contributed by the Applied Mechanics Division for presentation at the Winter Annual Meeting, Chicago, IL, November 28 to December 2, 1988, of The American Society of Mechanical Engineers.

Discussion on this paper should be addressed to the Editorial Department, ASME, 345 East 47th Street, New York, NY 10017, and will be accepted until two months after final publication of the paper itself in the JOURNAL OF APPLIED MECHANICS. Manuscript received by ASME Applied Mechanics Division, July 14, 1987; final revision, December 7, 1987.

Paper No. 88-WA/APM-38.

Copyright © 1988 by ASME
Downloaded 03 May 2010 to 171.66.16.21. Redistribution subject to ASME license or copyright; see http://www.asme.org/terms/Terms_Use.cfm

pure tension, the Ramberg-Osgood (1943) stress-strain relation

$$\epsilon = \frac{\sigma}{E^M}\left[1 + \frac{3}{7}\left(\frac{\sigma}{\sigma_I}\right)^{n-1}\right]. \quad (3)$$

Here ϵ and σ are the uniaxial strain and stress, respectively. E^M is the Young's modulus of the matrix, and n is the power hardening coefficient which varies from one to infinity. The stress σ_I is a material characteristic which provides best curve fitting with experimental results. It is important to note that equation (3) reduces to the linear stress-strain relation $\epsilon = \sigma/E^M$ for $\sigma << \sigma_I$, and to the pure power-hardening relation $\epsilon = c\sigma^n$ for $\sigma >> \sigma_I$.

Generalization of the Ramberg-Osgood relations (3) to a multiaxial stress state, σ_{ij}, by the J_2 deformation theory of plasticity is given by

$$\epsilon_{ij} = \frac{1}{E^M}\{(1+\nu^M)\sigma_{ij} - \nu^M \sigma_{pp}\delta_{ij}\} + \frac{9}{14}\left(\frac{\sigma_e}{\sigma_I}\right)^{n-1}\frac{s_{ij}}{E^M}, \quad (4)$$

where ν^M is the matrix Poisson's ratio, and s_{ij} is the deviatoric stress defined as

$$s_{ij} = \sigma_{ij} - \frac{1}{3}\sigma_{pp}\delta_{ij}.$$

δ_{ij} is the Kronecker delta given by

$$\delta_{ij} = \begin{cases} 0 & \text{if } i \neq j; \\ 1 & \text{if } i = j. \end{cases}$$

The effective stress σ_e is defined as

$$\sigma_e = \sqrt{\frac{3}{2}s_{ij}s_{ij}}. \quad (5)$$

A 0.2 percent offset strain criterion will be employed to define nominal yield in the matrix. For many metals, this criterion is closely satisfied by $\sigma = \sigma_I$ or, in the multiaxial stress state, by $\sigma_e/\sigma_I = 1$.

In light of the symmetry of the problem, the stress state is always in the form of an hydrostatic stress (which by plastic incompressibility does not produce plastic deformation) superimposed on a uniaxial stress. Thus a state of proportional loading is obtained for which deformation theory and incremental theory are known to yield identical results. No unloading is considered.

The Perfectly Fitting Inclusion

This section consists of two main parts: (*a*) the elastic-perfectly plastic matrix, (*b*) the power-hardening matrix. Analytic solutions are available only for the elastic matrix, and numerical techniques must therefore be developed to analyze the plastically deforming situation.

The Elastic-Perfectly Plastic Matrix. In the case of an elastic-ideally plastic material, the uniaxial stress strain curve is given by

$$\sigma = \begin{cases} \epsilon E^M & \text{if } \epsilon \leq \epsilon_I; \\ \sigma_I & \text{if } \epsilon > \epsilon_I. \end{cases}$$

Here ϵ_I is a characteristic strain given by $\epsilon_I = \sigma_I/E^M$.

The analysis must be considered in two stages: (1) At first, the matrix remains fully elastic until plastic deformation develops along the particle-matrix interface; (2) After yielding has occurred, the matrix consists of a plastic shell surrounding the inclusion, and an elastic region outside.

Stage One – The Elastic Matrix. Let the Stress Concentration Factor (SCF) be defined as the interfacial normal stress normalized by the far-field load, i.e.,

$$\text{SCF} = \frac{\sigma_{rr}(r=a)}{S}.$$

This stress concentration factor can be calculated analytically

$$\text{SCF} = \frac{3(1-\nu^M)}{1+\nu^M + 2(1-2\nu^M)\dfrac{K^M}{K^I}},$$

where K^M and K^I are the bulk moduli of the matrix and the inclusion, respectively.

Note that the SCF increases as K^I/K^M is raised, and that

$$\text{SCF} > 1 \quad \text{for} \quad K^I/K^M > 1$$
$$\text{SCF} = 1 \quad \text{for} \quad K^I/K^M = 1$$
$$\text{SCF} < 1 \quad \text{for} \quad K^I/K^M < 1.$$

Plastic deformation first develops along the interface when the effective stress σ_e reaches the yield stress σ_I. The load S_Y, at which yield first occurs, is

$$S_Y = \frac{\sigma_I\left\{2(1-2\nu^M) + (1+\nu^M)\dfrac{K^I}{K}\right\}}{3(1-2\nu^M)\left(\dfrac{K^I}{K} - 1\right)}.$$

Stage Two – The Plastically Deforming Matrix. As the load is increased, i.e., $S > S_Y$, three regions must be considered: the elastic inclusion, the portion of the matrix surrounding the inclusion and undergoing plastic deformation, and the remaining elastic matrix. Let $r = d$ denotes the interface between the elastic portion of the matrix and its plastic section.

The general stress distribution in the elastic inclusion ($r < a$) is given by

$$\sigma^I_{rr} = \frac{A}{r^3} + B,$$

$$\sigma^I_{\phi\phi} = \sigma^I_{\theta\theta} = -\frac{A}{2r^3} + B.$$

The stresses in the elastic portion of the matrix ($r > d$) are given by

$$\sigma^{ME}_{rr} = \frac{\alpha}{r^3} + \beta,$$

$$\sigma^{ME}_{\phi\phi} = \sigma^{ME}_{\theta\theta} = -\frac{\alpha}{2r^3} + \beta.$$

A, B, α, and β are constants which must be determined from the boundary conditions.

Let the stresses in the plastic region be σ^{MP}_{rr}, and $\sigma^{MP}_{\phi\phi} = \sigma^{MP}_{\theta\theta}$. It is assumed that the inclusion is more rigid than the matrix ($K^I > K^M$), so that $\sigma^{MP}_{rr} > \sigma^{MP}_{\phi\phi}$.

The stress state within the plastic region is given by (see Hill (1950))

$$\sigma^{MP}_{rr} = -2\sigma_I \ln r + C,$$

and

$$\sigma^{MP}_{\phi\phi} = \sigma^{MP}_{\theta\theta} = -\sigma_I(2\ln r + 1) + C.$$

Here C is a constant and must be determined.

Applying the boundary conditions:

1 At $r \to \infty$; $\sigma^{ME}_{rr} = S$,

2 At $r = 0$; $u^I_i = 0$,

3 Traction continuity at $r = a$ and $r = d$,

4 Yield condition at $r = d^+$,

Downloaded 03 May 2010 to 171.66.16.21. Redistribution subject to ASME license or copyright; see http://www.asme.org/terms/Terms_Use.cfm

results in $\beta = S$, $A = 0$, $\alpha = \frac{2}{3}\sigma_I d^3$, $C = B + 2\sigma_I \ln a$, and

$$d = ae^{\left[\frac{1}{2}\left(\frac{B}{\sigma_I} - \frac{S}{\sigma_I}\right) - \frac{1}{3}\right]}. \tag{6}$$

The undetermined constant B is found by satisfying the compatibility equation (2), and by imposing displacement continuity at $r = a$ and at $r = d$. This yields a nonlinear algebraic equation for B/S

$$\frac{B}{S} = \frac{(1-\nu^M)\frac{\sigma_I}{S}}{(1-2\nu^M)\left(1-\frac{K^M}{K^I}\right)} e^{\left[\frac{3}{2}\frac{S}{\sigma_I}\left(\frac{B}{S}-1\right)-1\right]},$$

which, for a given load S/σ_I, can be solved numerically for SCF = B/S. The elastic-plastic interface within the matrix, $r = d$, is found from (6).

The Power-Hardening Matrix. In this section, we consider a matrix that obeys the power-hardening constitutive relations presented earlier. We will only consider the hard inclusion ($K^I > K^M$) where the stress concentration factor along the particle-matrix interface is expected to be larger than unity.

The equilibrium equation (1) can be rewritten as

$$\sigma^M_{\phi\phi} = \sigma^M_{rr} + \frac{r}{2}\frac{d\sigma^M_{rr}}{dr}. \tag{7}$$

Inserting these stresses into the constitutive relations (4) results in the following strains

$$\tilde{\epsilon}^M_{rr} = (1-2\nu^M)\tilde{\sigma}^M_{rr} - \nu^M r\frac{d\tilde{\sigma}^M_{rr}}{dr} + \frac{3}{7}\left(-\frac{r}{2}\frac{d\tilde{\sigma}^M_{rr}}{dr}\right)^n$$

$$\tilde{\epsilon}^M_{\phi\phi} = (1-2\nu^M)\tilde{\sigma}^M_{rr} + \frac{1-\nu^M}{2} r\frac{d\tilde{\sigma}^M_{rr}}{dr} - \frac{3}{14}\left(-\frac{r}{2}\frac{d\tilde{\sigma}^M_{rr}}{dr}\right)^n,$$

where $\tilde{\epsilon}^M_{ij}$ and $\tilde{\sigma}^M_{ij}$ are nondimensional strains and stresses defined as $\tilde{\epsilon}^M_{ij} = \epsilon^M_{ij}/\epsilon_I$ and $\tilde{\sigma}^M_{ij} = \sigma^M_{ij}/\sigma_I$. In the foregoing we have used

$$\tilde{\sigma}^M_e = -\frac{r}{2}\frac{d\tilde{\sigma}^M_{rr}}{dr},$$

which follows directly from (7) and (5). (The negative sign is consistent with a stress concentration factor larger than one, with $\tilde{\sigma}^M_{rr}$ monotonically decreasing with r.)

Substitution of these strains into the compatibility equation (2), results in a nonlinear differential equation

$$\frac{3}{14}n\rho\phi^{n-1}\frac{d\phi}{d\rho} + \frac{9}{14}\phi^n + (1-\nu^M)\rho\frac{d\phi}{d\rho} + 3(1-\nu^M)\phi = 0, \tag{8}$$

where

$$\phi(\rho) = -\frac{\rho}{2}\frac{d\tilde{\sigma}^M_{rr}}{d\rho}, \tag{9}$$

and ρ is a dimensionless radius $\rho = r/a$.

Introducing a new variable

$$Z(\rho) = (1-\nu^M)\phi + \frac{3}{14}\phi^n,$$

and substituting into equation (8) reduces the nonlinear differential equation to a first-order one,

$$3Z + \rho\frac{dZ}{d\rho} = 0,$$

for which the general solution is

$$(1-\nu^M)\phi + \frac{3}{14}\phi^n = Z(\rho) = \frac{C}{\rho^3}, \tag{10}$$

C is a constant of integration which must be determined from the boundary conditions.

To satisfy the boundary conditions, equation (9) will be rewritten as

$$\frac{d\tilde{\sigma}^M_{rr}}{d\rho} = -\frac{2}{\rho}\phi. \tag{11}$$

Integration of the aforementioned, yields

$$\tilde{\sigma}^M_{rr}(\rho) - \tilde{\sigma}^M_{rr}(\rho_0) = -2\int_{\rho_0}^{\rho}\frac{\phi}{\rho}d\rho,$$

which, by taking $\rho_0 = \infty$ such that σ^M_{rr} $(\rho_0 = \infty) = S$, reduces to

$$\tilde{\sigma}^M_{rr}(\rho) = \frac{S}{\sigma_I} + 2\int_{\rho}^{\infty}\frac{\phi}{\rho}d\rho. \tag{12}$$

The continuity of the radial stresses and displacements along the inclusion-matrix interface together with equations (10)–(12) result in

$$C = (1-2\nu^M)\left(1-\frac{K^M}{K^I}\right)\left\{\frac{S}{\sigma_I} + 2\int_1^{\infty}\frac{\phi}{\rho}d\rho\right\}, \tag{13}$$

where C is the constant of integration found in (10).

The problem is now reduced to solving equations (10) and (13) simultaneously. The radial stress at each point is calculated from (12).

The numerical technique implemented in this paper is based on trying to find a zero for the function $F(C)$ defined as

$$F(C) = (1-2\nu^M)\left(1-\frac{K^M}{K^I}\right)\left\{\frac{S}{\sigma_I} + 2\int_1^{\infty}\frac{\phi}{\rho}d\rho\right\} - C. \tag{14}$$

Let C_i be an estimate of the unknown constant, an improved Newton-Raphson estimate is given by

$$C_{i+1} = C_i - \frac{F(C_i)}{F'(C_i)},$$

where

$$F'(C) = \frac{dF(C)}{dC}.$$

For each value of C_i, $F(C_i)$ is evaluated by numerical integration, where the value of ϕ at each integration point is found numerically from (10). To evaluate $F'(C)$, the derivative of $F(C)$ must be taken

$$\frac{dF}{dC} = (1-2\nu^M)\left(1-\frac{K^M}{K^I}\right)2\int_1^{\infty}\frac{\phi'}{\rho}d\rho - 1,$$

where from (10)

$$\phi' = \frac{d\phi}{dC} = \frac{1}{\rho^3\left[(1-\nu^M) + \frac{3}{14}n\phi^{n-1}\right]}.$$

This procedure is repeated until convergence is reached.

Checks on the numerical accuracy and convergence were made by comparison to the analytic elastic solution (by applying small loads), and to the perfectly plastic solution (by taking large power-hardening coefficients). The results were also compared to particular cases of an axisymmetrical analysis by the author (1987), and to those of Lee, et al. (1980), and Earmme, et al. (1981). All the values were within less than 0.1 percent of each other. Convergence occurred very rapidly with no more than three iterations. Once C was found, the stress σ^M_{rr} was calculated from equation (12) by numerical integration.

Results and Discussion. Various combinations of ν^M and K^I/K^M were used with the different power-hardening coefficients $n = 3, 5, 9, 19$.

In Fig. 1, the stress concentration factor is shown against a large load range, $0 < S/\sigma_I < 1000$, for $K^I/K^M = 2$, $\nu^M = 0.25$,

Downloaded 03 May 2010 to 171.66.16.21. Redistribution subject to ASME license or copyright; see http://www.asme.org/terms/Terms_Use.cfm

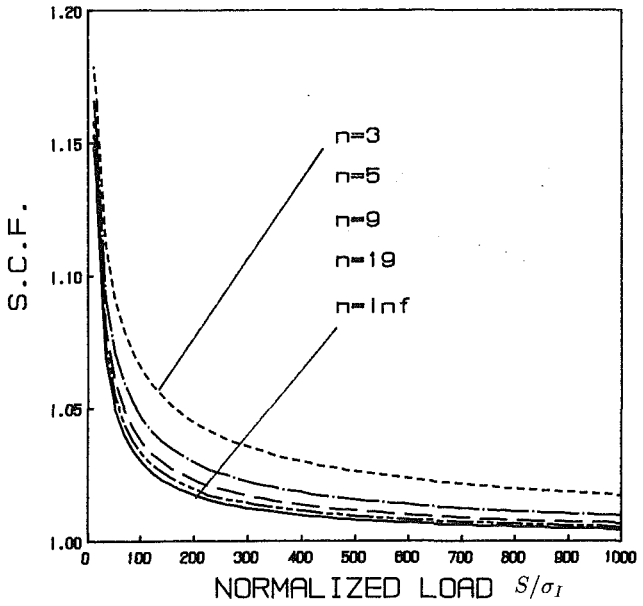


Fig. 1 SCF versus normalized load (S/σ_I) for $\nu^M = 0.25$, $K^I/K^M = 2$ (wide range)

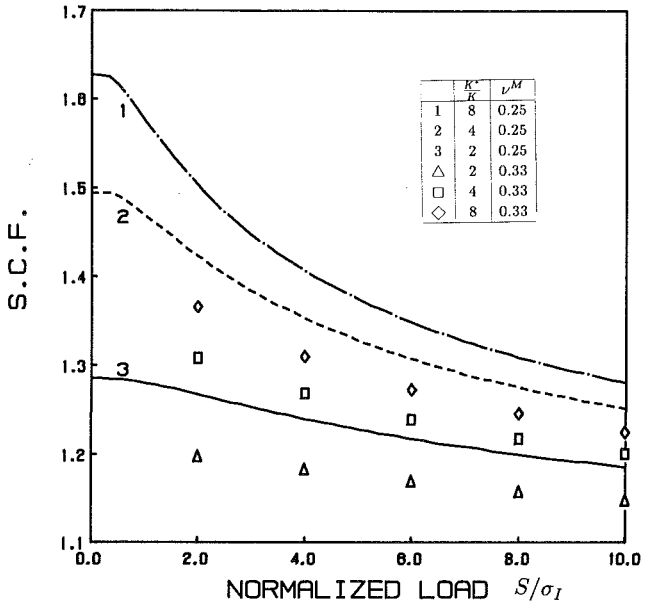


Fig. 3 SCF versus normalized load (S/σ_I) for $n = 3$ and various elastic constants

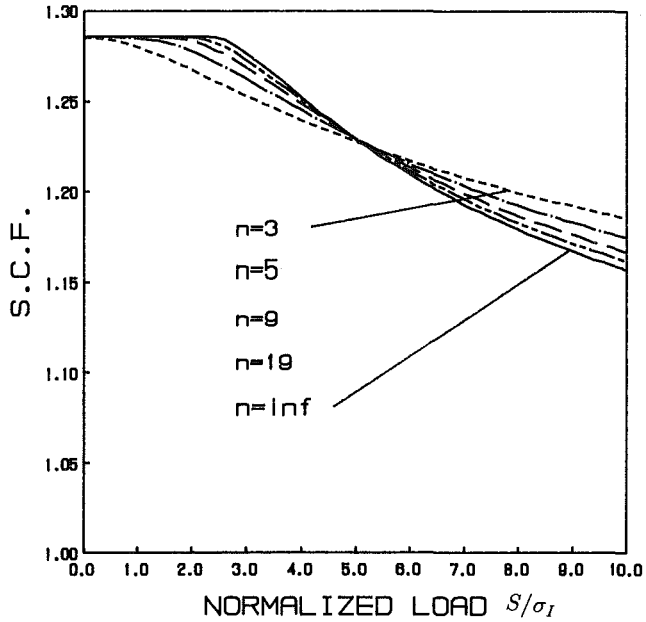


Fig. 2 SCF versus normalized load (S/σ_I) for $\nu^M = 0.25$, $K^I/K^M = 2$ and $0 < S < 10\ \sigma_I$

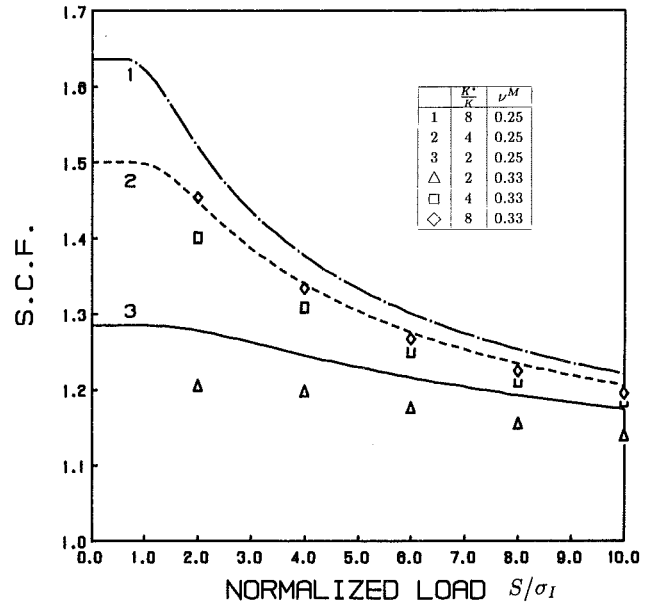


Fig. 4 SCF versus normalized load (S/σ_I) for $n = 9$ and various elastic constants

and various power-hardening coefficients. The SCF asymptotes to unity as the load S is raised. These results are consistent with the asymptotic analysis of Wilner (1986), where it is shown that the stresses must asymptote to those of a rigid inclusion embedded in a pure power-hardening incompressible matrix. Very large loads were required for the SCF to approach this asymptote. This could be explained from the nature of a spherical symmetric problem, where the effective stress grows very slowly as the load S is increased.

A more practical loading range, $0 < S/\sigma_I < 10$, is shown in Fig. 2. As expected, smaller power-hardening coefficients require smaller loads to initiate yielding. The fact that all curves cross at about $S/\sigma_I \simeq 4.5$, can be attributed to the nature of the Ramberg-Osgood relations, which possess a similar characteristics feature.

It is also clear from Figs. 1 and 2 that $n = 19$ can successfully be used to model an elastic-perfectly plastic material (at least in the spherically symmetric configuration).

The elastic constants K^I/K^M and ν^M have a moderately small effect on the SCF as displayed in Figs. 3–5 for power-hardening coefficients $n = 3$, $n = 9$ and $n = \infty$, respectively. The ratio of the bulk moduli has a moderate effect on the interfacial stresses, in particular for small loads, while the influence of the Poisson's ratio is much smaller. For large loads the effect of the elastic constants is negligible.

Note that, for $K^I/K^M = 1$, the matrix never yields and the stress concentration factor equals unity. This holds for both types of materials: power-hardening and elastic-perfectly plastic.

Plots of the growth of the nominal plastic zone ($r = d$ at $\sigma_e = \sigma_I$) versus the applied load are shown in Fig. 6. The power-hardening coefficient has almost no effect on the position of the elastic-plastic interface, which depends primarily on the load S. Loads of 800 times the yield stress were required to bring the elastic-plastic interface, $r = d$, to about seven times the inclusion size.

Downloaded 03 May 2010 to 171.66.16.21. Redistribution subject to ASME license or copyright; see http://www.asme.org/terms/Terms_Use.cfm

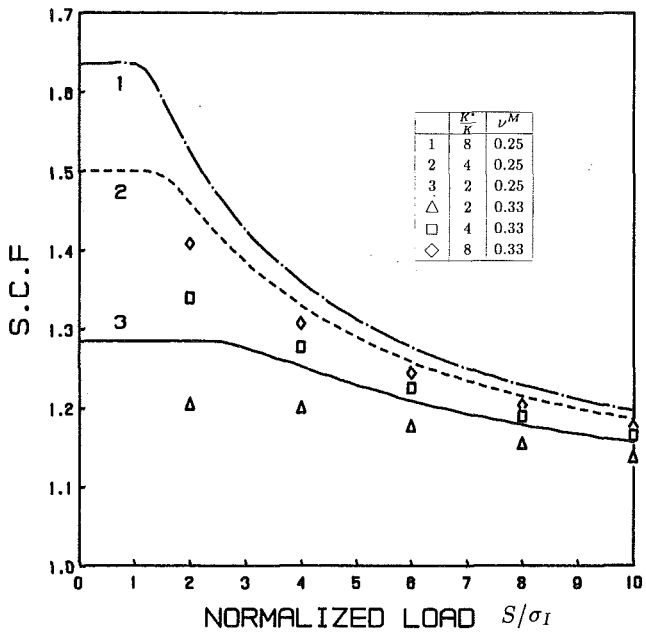


Fig. 5 SCF versus normalized load (S/σ_I) for $n = \infty$ and various elastic constants

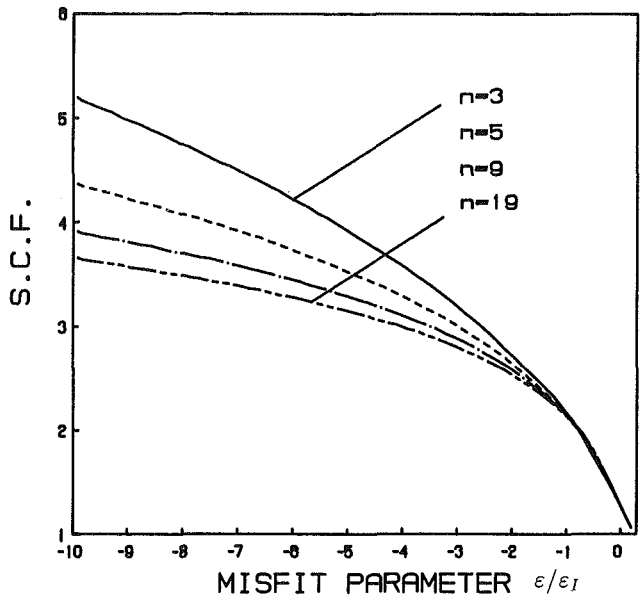


Fig. 7 Misfitting effects for $S/\sigma_I = 1$ and various n's ($\nu^M = 0.25$, $K^I/K^M = 2$)

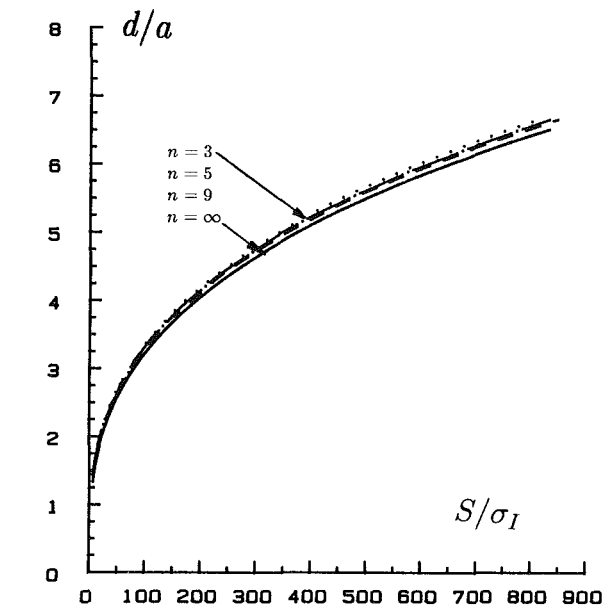


Fig. 6 Elastic-plastic interface inside the matrix for various n's ($\nu^M = 0.25$, $K^I/K^M = 2$)

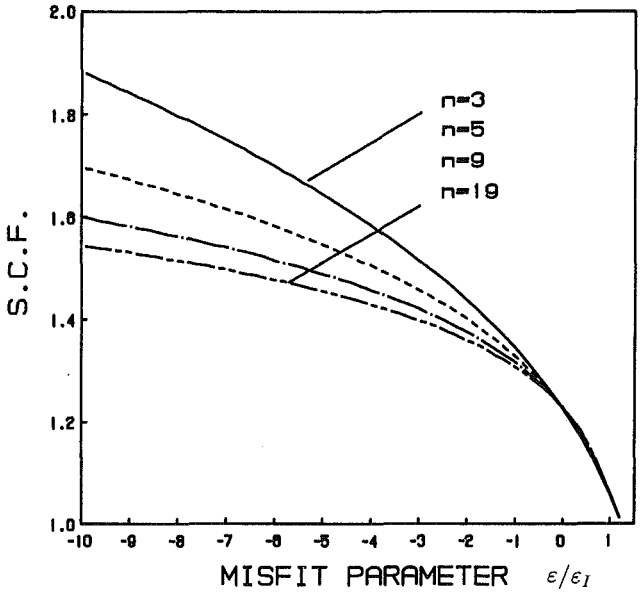


Fig. 8 Misfitting effects for $S/\sigma_I = 5$ and various n's ($\nu^M = 0.25$, $K^I/K^M = 2$)

The Misfitting Inclusion. In this section, the case of a misfitting inclusion will be considered. It is assumed that an elastic particle of radius $r = a(1 + \hat{\epsilon})$ is inserted into a spherical void of radius $r = a$ inside an infinite elastic-plastic matrix. The matrix is subjected at infinity to a hydrostatic tensile load S.

Both materials obey the constitutive equations presented earlier, with one exception: The misfit will be modeled by initial strains within the inclusion

$$[\hat{\epsilon}_{ij}] = \begin{vmatrix} \hat{\epsilon} & 0 & 0 \\ 0 & \hat{\epsilon} & 0 \\ 0 & 0 & \hat{\epsilon} \end{vmatrix}.$$

Inserting these initial strains into the constitutive equations and following the procedure outlined in the Section, "The Power-Hardening Matrix," results in a modification to equation (13)

$$C = (1 - 2\nu^M)\left(1 - \frac{K^M}{K^I}\right)\left\{\frac{S}{\sigma_I} + 2\int_1^\infty \frac{\phi}{\rho} d\rho\right\} - \frac{\hat{\epsilon}}{\epsilon_I}. \quad (15)$$

The problem is now reduced to solving equation (10) and equation (15) simultaneously. As before a zero of a function $\mathcal{F}$ is sought, where

$$\mathcal{F}(C) = (1 - 2\nu^M)\left(1 - \frac{K^M}{K^I}\right)\left\{\frac{S}{\sigma_I} + 2\int_1^\infty \frac{\phi}{\rho} d\rho\right\} - \frac{\hat{\epsilon}}{\epsilon_I} - C.$$

A similar Newton-Raphson technique is employed to find C.

Figures 7–9 display the stress concentration factor against $\hat{\epsilon}/\epsilon_I$, for different load levels. It is demonstrated that a misfitting inclusion could cause the stresses along the interface to significantly increase, especially at small loads. This effect is decreasing as the loads become larger. The elastic constants have a minor effect on the SCF as demonstrated in Fig. 10.

The misfitting parameter $\hat{\epsilon}/\epsilon_I$ depends on the problem configuration, the phase transformation characteristics, and

Downloaded 03 May 2010 to 171.66.16.21. Redistribution subject to ASME license or copyright; see http://www.asme.org/terms/Terms_Use.cfm

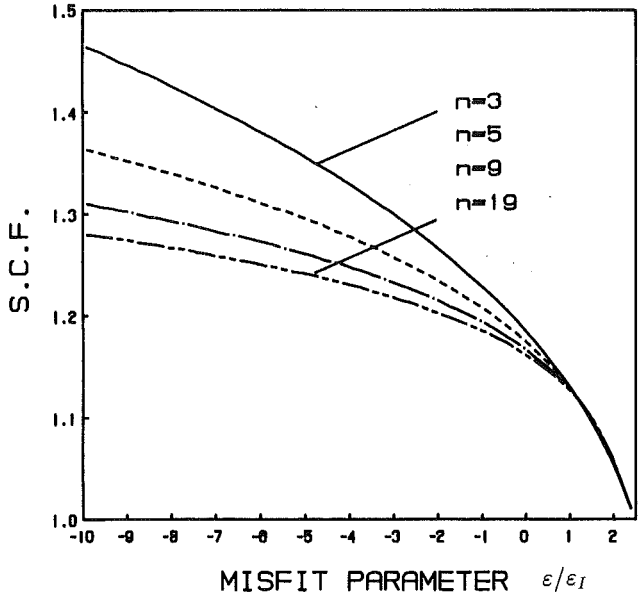


Fig. 9 Misfitting effects for $S/\sigma_I = 10$ and various n's ($\nu^M = 0.25$, $K^I/K^M = 2$)

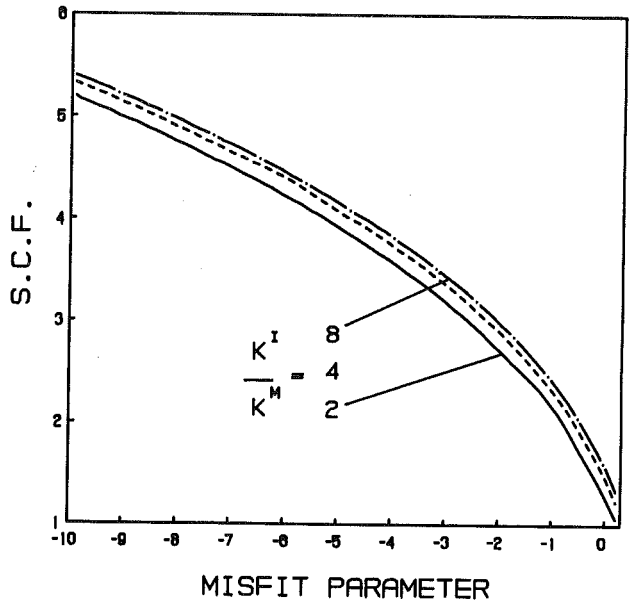


Fig. 10 Misfitting effects for $S/\sigma_I = 1$, $n = 3$, $\nu^M = 0.25$, and $K^I/K^M = 2$, 4, 8

temperature. For example, one can consider $\hat{\epsilon}$ to be determined by the difference in the temperature expansion

$$\hat{\epsilon} = (\alpha^I - \alpha^M)\Delta T,$$

where α^I and α^M are the thermal expansion coefficients of the inclusion and the matrix, respectively, and ΔT is the temperature difference between the actual operating temperature and the one at which a perfect fit is obtained.

Conclusions

Numerical techniques were developed to solve the problem of a spherical elastic inclusion embedded in an infinite elastic-plastic matrix subject to a hydrostatic tensile load. Two types of particles were considered: (1) a perfectly fitting inclusion, (2) a misfitting one.

In the case of a perfectly fitting inclusion, the elastic constants have a moderately small effect on the interfacial normal stress. This effect is restricted to moderate loads. For large loads, the normal stress on the particle-matrix interface asymptotes to the load, independent of the material properties of the constituents. The size of the plastic zone in the matrix seems to depend primarily on the applied load.

For a misfitting inclusion, it was observed that the normal interfacial stress strongly depends on the extent of the misfit. This effect is much more obvious at small loads and diminishes as the load increases. As expected, negative misfits $\hat{\epsilon} < 0$ raise the normal stress, while positive ones lower it. For practical metals and inclusions, the stresses can rise up to more than 100 percent of the perfectly fitting configuration. This phenomenon can be used in the design of metals, to reduce the stresses that cause cracks and voids to initiate at particles.

Acknowledgment

The author is thankful to his student Brett Stockdale of the School of Engineering Science and Mechanics, Georgia Institute of Technology, for his assistance in formulating the misfitting inclusion.

References

Budiansky, B., Hutchinson, J. W., and Slutsky, S., (1982), "Void Growth and Collapse in Viscous Solids," *Mechanics of Solids*, Eds., Hopkins, H. G., and Sewell, M. J., Pergamon Press.

Budiansky, B., (1983), "Micromechanics," *Computers and Structures*, Vol. 16, No. 1-4, p. 3-12.

Earmme, Y. Y., Johnson, W. C., and Lee, J. K., (1981), "Plastic Relaxation of the Transformation Strain Energy of a Misfitting Spherical Precipitate: Linear and Power-Law Strain Hardening," *Met. Trans.* A, Vol. 12A, p. 1521.

Eshelby, J. D., (1957), "The Determination of the Elastic Field of an Ellipsoidal Inclusion and Related Problems," *Proceedings of the Royal Society*, A241, p. 376.

Goods, S. H., and Brown, L. M., (1979), "The Nucleation of Cavities by Plastic Deformation," *Acta Metallurgia*, Vol. 27, p. 1.

Hill, R., (1950), *The Mathematical Theory of Plasticity*, Oxford University Press.

Lee, J. K., Earmme, Y. Y., Aaronson, H. I., and Russel, K. C., (1980), "Plastic Relaxation of the Transformation Strain Energy of a Misfitting Spherical Precipitate: Ideal Plastic Behavior," *Met. Trans. A*, Vol. 11A, p. 1837.

McMeeking, R. M., (1977), "Finite Deformation Analysis of a Crack-Tip Opening in Elastic-Plastic Materials and Implications for Fracture," *Journal of the Mechanics and Physics of Solids*, Vol. 25, p. 357.

Ramberg, W., and Osgood, W. R., (1943), "Description of Stress-Strain Curves by Three Parameters," NACA TN 902.

Rice, J. R., and Johnson, M. A., (1970), "The Role of Large Crack Tip Geometry Changes in Plane Strain Fracture," *Inelastic Behavior of Solids*, Eds., Kanninen, M. F., Adler, W. F., Rosefield, A. R., and Jaffee, R. I., McGraw Hill, New York, p. 641.

Wilner, B., (1986), PhD thesis, Harvard University, Cambridge, MA.

Wilner, B., (1988), "Stress Analysis of Particles in Metals," *Journal of the Mechanics and Physics of Solids*, to be published.

Downloaded 03 May 2010 to 171.66.16.21. Redistribution subject to ASME license or copyright; see http://www.asme.org/terms/Terms_Use.cfm

J. M. Duva
Department of Applied Mathematics,
University of Virginia,
Charlottesville, VA 22903
Assoc. Mem. ASME

The Singularity at the Apex of a Rigid Wedge Embedded in a Nonlinear Material

The singular behavior of the stress and strain fields at the apex of a square rigid wedge embedded in a nonlinear material under plane-strain conditions is described. Both a power law and a bilinear law for the nonlinear material are considered.

1 Introduction

The problem considered herein arises in the study of metal-matrix short-fiber-reinforced composites. Such composites can be much less tough and ductile than the unreinforced matrix in part because of the stress concentrations at the fiber ends (Nutt and Duva, 1986). We employ an idealized model of a fiber end consisting of a right rigid wedge embedded in a nonlinear material subject to plane strain to investigate the singular behavior of the stress and strain fields at the corner of a fiber. The model problem is constructed as follows.

Consider a single rigid right circular cylinder embedded in a matrix that is subjected to loads symmetric with respect to the fiber axis. We restrict our attention to the immediate vicinity of a corner of the fiber; see Fig. 1. If distances from the fiber corner are small compared to the fiber radius, the curvature of the corner of the fiber can be ignored and plane-strain conditions hold (Atkinson, et al., 1982). Nonlinearity is explicitly introduced through the constitutive relation for the material surrounding the fiber. This nonlinearity is essential in the accurate portrayal of the plastic deformation of the material near a fiber end.

Two nonlinear constitutive relations will be used in the following calculations, a power-law relation and a bilinear relation. Each material will be regarded as a nonlinear elastic material but where loads are large, nondecreasing, and nearly proportional, each material behaves as a corresponding deformation theory plastic material would. We will assume that the conditions required to establish this connection to deformation theory plasticity are approximately satisfied; no attempt will be made to prove that departures from proportionality are small or that unloading does not occur, although in principle our approximate solutions could be checked for consistency with these assumptions.

The governing equations applicable to both material cases are the equilibrium equations

$$(r\sigma_{rr})_{,r} + \sigma_{r\theta,\theta} - \sigma_{\theta\theta} = 0 \tag{1a}$$

$$(r\sigma_{r\theta})_{,r} + \sigma_{\theta\theta,\theta} + \sigma_{r\theta} = 0 \tag{1b}$$

and the strain-displacement equations

$$\epsilon_{rr} = \frac{\partial u}{\partial r} \tag{2b}$$

$$\epsilon_{\theta\theta} = \frac{1}{r}\frac{\partial v}{\partial \theta} + \frac{u}{r} \tag{2b}$$

$$\epsilon_{r\theta} = \frac{1}{2}\left(\frac{1}{r}\frac{\partial u}{\partial \theta} + \frac{\partial v}{\partial r} - \frac{v}{r}\right). \tag{2c}$$

Here u and v are the radial and polar components of displacement as illustrated in Fig. 1. Linear strain-displacement relations are used for simplicity even though large strains are anticipated at the corner of the wedge.

Our approach mimics that suggested by Williams (1952) and adopted by Hutchinson (1968) among others in that we assume the solution to the governing equations has a separated asymptotic solution for small values of r given by r^s times a function of θ. Recently, Rice (1987) has shown that, in

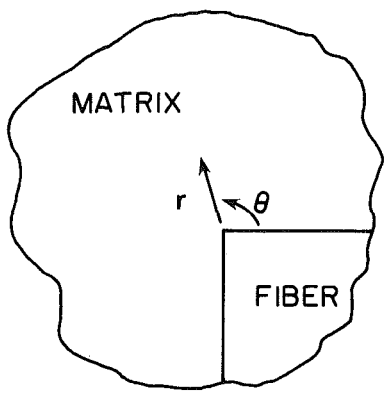


Fig. 1 Fiber corner geometry with local polar coordinates

Contributed by the Applied Mechanics Division for presentation at the Winter Annual Meeting, Chicago, IL, November 28 to December 2, 1988, of The American Society of Mechanical Engineers.

Discussion of this paper should be addressed to the Editorial Department, ASME, United Engineering Center, 345 East 47th Street, New York, N.Y. 10017, and will be accepted until two months after final publication of the paper itself in the JOURNAL OF APPLIED MECHANICS. Manuscript received by ASME Applied Mechanics Division, April 27, 1987; final revision, December 3, 1987. Paper No. 88-WA/APM-21.

Copyright © 1988 by ASME
Downloaded 03 May 2010 to 171.66.16.21. Redistribution subject to ASME license or copyright; see http://www.asme.org/terms/Terms_Use.cfm

general, solutions of this form do not exist at the tip interfacial crack. When one of the materials is taken to be rigid, the interfacial crack configuration differs from the configuration considered here only in the boundary conditions and the extent of the deforming material. Calculations performed by Shih and Asaro (1987) support Rice's conclusion. However, when the nonrigid material is incompressible, Rice's analysis shows that a separated solution may exist. It is this possibility that we pursue.

The equations will be solved for s, leaving the magnitude of the function of θ undetermined. Values of s between zero and one give rise to bounded displacements and singular stresses and strains. Admissible values of s also give rise to integrable strain-energy densities; other values of s will be ignored. In the subsequent sections, the two material cases will be considered in turn. In the final section, the results will be discussed.

2 Analysis for a Power-Law Material

We assume the strain in the matrix is given by

$$\epsilon = \epsilon_0 (\sigma/\sigma_0)^n \tag{3}$$

in uniaxial tension. Here ϵ_0, σ_0, and n are material parameters. The extension of (3) to multiaxial stress states is

$$\epsilon_{ij} = \frac{3}{2}\,\epsilon_0 \left(\frac{\sigma_e}{\sigma_0}\right)^{n-1} \frac{s_{ij}}{\sigma_0} \tag{4}$$

where s_{ij} is the stress deviator and $\sigma_e = (3/2\, s_{kl} s_{kl})^{1/2}$ is the effective stress. As just mentioned, it is convenient to regard (4) as the plastic strain for a power-law deformation theory material when the effective stress is in excess of σ_0. We could include a strain contribution linear in the stress but for sufficiently large stresses this contribution is negligible compared to the contribution from (4). Anticipating large stresses at the vertex of the wedge, we ignore the linear strains. In this idealization the matrix is incompressible.

We assume that the displacements have the form

$$u = r^s f'(\theta) \quad v = -(1+s) r^s f(\theta) \tag{5}$$

where s and $f(\theta)$ are unknown. Incompressibility is automatically satisfied by this displacement field. Equations (1) can be combined to give

$$2s_{rr,r\theta} + \frac{2}{r}\, s_{rr,\theta} + \frac{1}{r}\, s_{r\theta,\theta\theta} - 3s_{r\theta,r} - r s_{r\theta,rr} = 0. \tag{6}$$

Use of (2) and (4) allows the recasting of the foregoing equation as a fourth-order ordinary differential equation in f involving s and n as parameters; this equation is given in the Appendix. Note that the equilibrium equation is homogeneous of degree $1/n$ in f; thus if f is a solution, so is any multiple of f. The boundary conditions

$$f = f' = 0 \quad \theta = 0, 3\pi/2 \tag{7}$$

follow from (5) and the assumption that the fiber is perfectly bonded to the surrounding material. In imposing these boundary conditions, no particular symmetry is assumed. Equations (6) and (7) together comprise a generalized eigenvalue problem for s. For $0 < s < 1$ displacements are bounded and stresses vary as r^{s-1}. This problem was solved (for some values of n) via the shooting method. The eigenvalue s and $f^{iv}(0)$ were regarded as unknowns and $f'''(0)$ was set equal to 1. An explicit damped fourth-order Runge-Kutta scheme was used to integrate the differential equation, and Newton's method was used to improve the estimates of s and $f^{iv}(0)$ at each stage. The procedure was halted when the boundary conditions at $\theta = 3\pi/2$ were satisfied to 1 part in 10^4. For $n = 1$, the eigenvalue $s = 0.54$, in agreement with the known result for a linear material (Dempsey and Sinclair, 1981).

The shooting method broke down at values of $n \approx 6$.

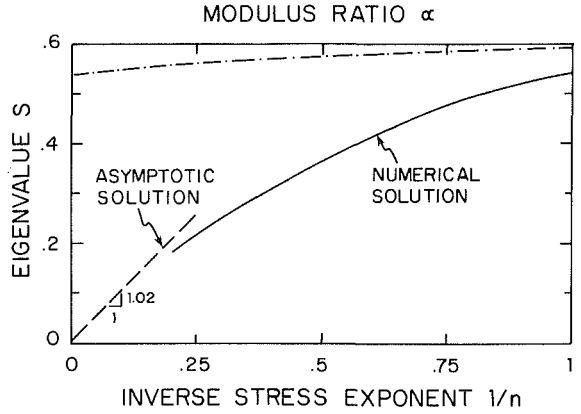


Fig. 2 Eigenvalue s versus inverse stress exponent $1/n$ for a power-law material (solid and dashed lines) and eigenvalues s versus modulus ratio $E_T/E = \alpha$ for a bilinear material with $\nu = 0.34$ (dashed-dot line)

Newton's method for correcting the "shot" fails to converge as the Jacobian matrix involved becomes increasingly singular. An implicit integration scheme was tried with no greater success. The results obtained with the shooting method are displayed in Fig. 2 with a solid line.

To obtain an approximation to the remainder of the curve, an asymptotic analysis was performed for small $t = 1/n$ with

$$f = f_0 + t f_1 + Q(t^2) \quad s = s_0 + t s_1 + O(t^2). \tag{8}$$

Retaining only $O(1)$ terms in the equilibrium equation shows $s_0 = 0$. Retaining $O(t)$ terms gives a relatively simple fourth-order ordinary differential equation in f_0 where s_1 appears as a parameter. Equations of both orders are discussed in the Appendix. The shooting technique previously described was used to obtain an estimate of s_1 and the results are displayed in Fig. 2 with a dashed line. When $n = 5$, the difference in the approximations is only a few percent.

3 Analysis for a Bilinear Material

We assume the matrix obeys

$$\epsilon = \frac{\sigma}{E} \quad \sigma < \sigma_0$$

$$\epsilon = \epsilon_0 + \frac{\sigma - \sigma_0}{E_I} \quad \sigma > \sigma_0 \tag{9}$$

in uniaxial tension, where E and E_T are the elastic modulus and the tangent modulus of the material, respectively. The multiaxial generalization, for $\sigma_e > \sigma_0$, is

$$\epsilon_{ij} = \frac{1}{E}\left[(1+\nu)\sigma_{ij} - \nu\delta_{ij}\sigma_{kk} + \frac{3}{2}\left(\frac{E_T}{E} - 1\right)\frac{\sigma_e - \sigma_0}{\sigma_e}\, s_{ij}\right]. \tag{10}$$

Here ν is Poisson's ratio. We will assume that in the vicinity of the corner of the fiber stresses are sufficiently high that (10) holds. If we regard the material as a deformation theory material we still must retain the elastic portion of the strain. As discussed below, the elastic component of strain does not become negligible compared to the plastic strain for large stresses. Note that only the plastic component of strain is necessarily incompressible.

Following Ponte (1987), we assume

$$u = r^s f_1 \quad v = r^s f_2$$

$$\sigma_{\theta\theta} = r^{s-1} f_3 \quad \sigma_{r\theta} = r^{s-1} f_4 \quad \sigma_{rr} = r^{s-1} f_5 \quad \sigma_{zz} = r^{s-1} f_6 \tag{11}$$

where the f_i are functions of θ. The 2 equilibrium equations and 4 stress-strain equations can be expressed as 4 coupled first-order ordinary differential equations and 2 algebraic equations in the unknown f_i, where the ratio $E_T/E \equiv \alpha$ ap-

Downloaded 03 May 2010 to 171.66.16.21. Redistribution subject to ASME license or copyright; see http://www.asme.org/terms/Terms_Use.cfm

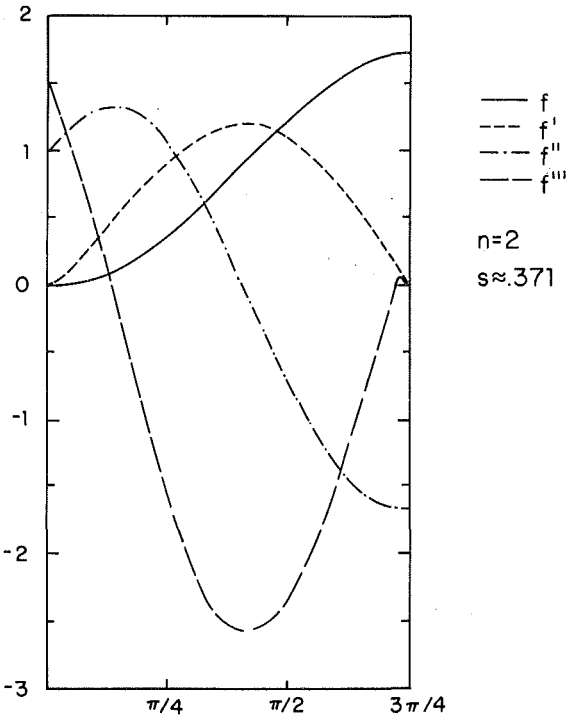


Fig. 3 Eigenfunction shape for a power-law material with $n = 2$; the function f is even about $3\pi/4$

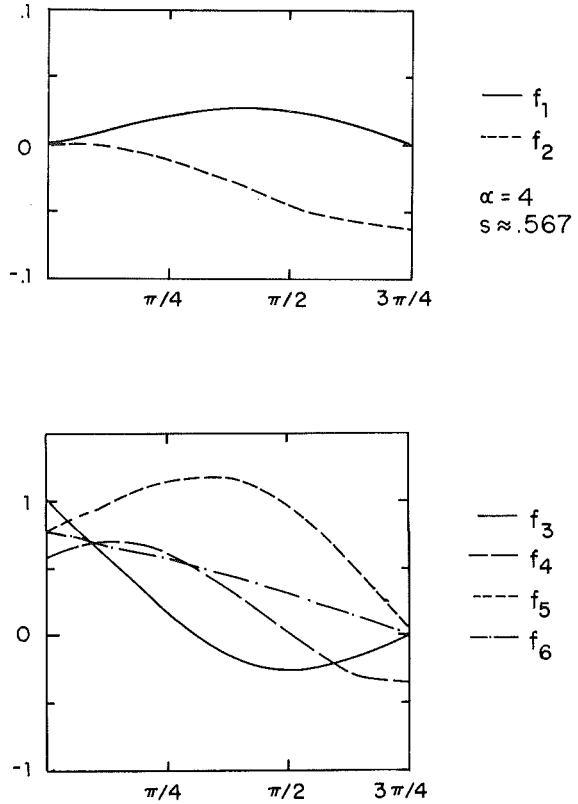


Fig. 4 Eigenfunction shapes for a bilinear material with $\alpha = 4$; the functions f_1, f_3, f_5, and f_6 are odd about $3\pi/4$ while f_2 and f_4 are even about $3\pi/4$

pears as a parameter as reported in the Appendix. These equations, along with the same homogeneous boundary conditions described in the previous section, comprise a generalized eigenvalue problem for s. The shooting method was used on the system of differential equations, with the requirement that the algebraic equations were solved at each integration step. When stresses are large, as anticipated, the algebraic equations are simple enough to solve explicitly. Results for s are shown in Fig. 2 for the case that $\nu = 0.34$ for a full range of α-values. Note that as α approaches zero, s approaches 0.54 and, for $\alpha = 1$, the eigenvalue $s = 0.60$, in agreement with the results of Dempsey and Sinclair (1981).

4 Discussion

When regarded as deformation theory materials, the materials just considered each approximate perfect plastic behavior for small values of $1/n$ for the power-law material and for small values of α for the bilinear material. Yet, the calculated values of s do not agree in this limit. The disperity can be explained as follows. For a power-law material model, elastic strains were neglected because, as stresses grow large for any value of $n > 1$, the ratio of elastic strain to plastic strain approaches zero. However, for a bilinear material, elastic strains increase along with the plastic strains as the stress increases and the ratio of the strains approaches $\alpha/(1 - \alpha)$. As α decreases, the elastic strains become negligible and the bilinear material behaves like an incompressible linear material as long as E_T is not identically zero.

In treating the singularity problem for a linear material with the separated solution used previously, one hopes that the eigenfunctions obtained form a sufficiently general set so that the solution, due to a particular loading, can be constructed. For the nonlinear problem treated here, superpositioning is not permissible; thus solutions corresponding to other eigenvalues (which exist but have not been reported here) must be regarded as distinct solutions that may or may not result from a particular applied load. The eigenfunction f and its first three derivatives for the power-law material with $n = 2$ are displayed in Fig. 3, normalized so that the maximum value of f is 1. The six eigenfunctions for the bilinear material case with $\alpha = 4$ are displayed in Fig. 4. In each material case, the functions corresponding to the radial displacement are odd about $\theta = 3\pi/4$ and the functions corresponding to the angular displacement are even about $\theta = 3\pi/4$. Although it was not stated explicitly in the foregoing, the assumption that stresses are large in the vicinity of the corner of the wedge requires that the θ-dependent part of σ_e is never zero. That this condition is satisfied is easily verified from the sort of information presented in Fig. 3 and 4. It remains to determine the amplitude of the deformation as a function of applied load.

Another desirable extension of this work involves accounting for the curvature of the corner of the fiber as Zak (1972) has done in the linear material case. Without superpositioning, the correction term that accounts for the curvature of the corner of the fiber would *not* be simply a higher-order eigensolution of the type derived here.

Because the assumptions made in formulating this problem are restrictive, the practical applicability of the results is also limited. Nevertheless, the results, as they stand, can be used to construct singular elements to be used at the corner of a fiber in a finite-element analysis of the larger characteristics of the deformation field in the vicinity of a fiber end (Carey and Oden, 1983).

References

Atkinson, C., Avila, J., Betz, E., and Smelser, R. E., 1982, "The Rod Pull-Out Problem, Theory and Experiment," *J. Mech. Phys. Sol.*, Vol. 30, No. 3, pp. 97–120.

Carey, G. T., and Oden, J. T., 1983, *Finite Elements, A Second Course*, Prentice-Hall Inc.

Dempsey, J. P., and Sinclair, G. B., 1981, "On the Singular Behavior at the Vertices of a Bi-Material Wedge," *J. of Elas.*, Vol. 11, No. 3, pp. 317–327.

Hutchinson, J. W., 1968, "Singular Behavior at the End of a Tensile Crack in a Hardening Material," *J. Mech. Phys. Sol.*, Vol. 16, pp. 13–31.

Downloaded 03 May 2010 to 171.66.16.21. Redistribution subject to ASME license or copyright; see http://www.asme.org/terms/Terms_Use.cfm

Nutt, S. R., and Duva, J. M., 1986, "A Failure Mechanism in Al-SiC Composites," *Scripta Met*, Vol. 20, pp. 1055–1058.

Ponte Casteneda, P., 1987, "Asymptotic Fields in Steady Crack Growth with Linear Strain Hardening," *J. Mech. Phys. Sol.*, Vol. 35, p. 227.

Rice, J. R., 1987, "Elastic Fracture Mechanics Concepts for Interfacial Cracks," *Harvard University Report*, Mech-101.

Shih, C. F., and Asaro, R. J., 1987, "Elastic-Plastic Analysis of Cracks on Bimaterial Interfaces," *Brown University Report*.

Williams, M. L., 1952, "Stress Singularities Resulting From Various Boundary Conditions in Angular Corners of Plates in Extension," ASME JOURNAL OF APPLIED MECHANICS, Vol. 19, pp. 526–528.

Zak, A. R., 1972, "Elastic Analysis of Cylindrical Configurations With Stress Singularities," ASME JOURNAL OF APPLIED MECHANICS, pp. 501–506.

APPENDIX

The fourth-order nonlinear ordinary differential equation for f obtained in the power-law matrix model is

$$f^{iv} = -(1-s^2)f'' + \frac{6}{4Ng^2+3h^2}\Big((N+1)(s-1)(s+1 + Ns-N)gh^2 - 2(Ns^2-Ns+s^2)(hh'f'N+f''h^2)$$

$$-N(N-1)gh'^2 - 2Ng'hh' + Ngh'^2 - \frac{4}{3}Ng(s^2(f'f''' + f''^2) + g'^2)\Big).$$

In the above

$$N = -1 + 1/n$$

$$g = \frac{1}{2}(f'' + (1-s^2)f)$$

$$h = \left(\frac{4}{3}(s^2f'^2 + g^2)\right)^{1/2}.$$

The functions g and h arise naturally in expressing the equilibrium equation in terms of f; g is the θ-dependent part of the shear strain $\epsilon_{r\theta}$ and h is the θ-dependent part of the effective strain $\epsilon_e = (2/3\epsilon_{kl}\epsilon_{kl})^{1/2}$. Although the equilibrium equation is homogeneous of degree $1/n$ in f and its derivatives, the form previously given is obtained by factoring out $h^{(1/n)-3}$.

In the asymptotic analysis for small t the functions g and h expand to $O(1)$ as

$$g_0 = \frac{1}{2}(f_0'' + f_0) \quad h_0 = \frac{2}{\sqrt{3}}(s_0^2f_0'^2 + g_0^2)^{1/2}.$$

When the aforementioned equilibrium equation is rewritten retaining only $O(1)$ terms, s_0 appears in each term. Thus $s_0 = 0$ is an eigenvalue of the $O(1)$ equation. This very much simplifies the $O(t)$ equation

$$f_0^{iv} = -f_0'' + 4\left(-g_0 + s_1\left(\frac{g_0'}{g_0}f_0' - f_0''\right) + \frac{g_0'^2}{g_0}\right).$$

For the bilinear material, the two algebraic equations are

$$\frac{E}{\sigma_0}sf_1 = f_5 - \nu(f_3+f_6) + \frac{A}{3}(2f_5 - f_3 - f_6)$$

$$0 = f_6 - \nu(f_5+f_3) + \frac{A}{3}(2f_6 - f_5 - f_6)$$

where

$$A = \frac{3}{2}(\alpha - 1).$$

The four differential equations are

$$sf_5 + f_4' - f_3 = 0$$

$$(s-1)f_4 + f_3' = 0$$

$$\frac{E}{\sigma_0}(f_2' + f_1) = f_3 - \nu(f_5+f_6) + \frac{A}{3}(2f_3 - f_5 - f_6)$$

$$\frac{E}{2\sigma_0}(f_1' + (s-1)f_2) = f_4(1+\nu+A).$$

Downloaded 03 May 2010 to 171.66.16.21. Redistribution subject to ASME license or copyright; see http://www.asme.org/terms/Terms_Use.cfm

M. S. Willett
Assoc. Mem. ASME

W. L. Poesch
MRJ, Inc.,
10455 White Granite Drive,
Suite 200,
Oakton, VA 22124

Determining the Stress Distributions in Wound Reels of Magnetic Tape Using a Nonlinear Finite-Difference Approach

A new method of calculating the internal stress distributions in wound reels of magnetic tape using a finite-difference approach is presented. A functional representation of the nonlinear radial elastic modulus is used to model reel behavior more accurately. Procedures are described to measure the radial elastic modulus and radial Poisson's ratio. It is shown, by comparison to experimental data, that the method accurately predicts in-roll stress distributions.

I Introduction

Modern analytical work pertaining to stress distributions in wound reels of magnetic tape has its roots in the late 1950s when the use of this information storage media was becoming widespread. There was a deep concern then, as now, about insuring tape reel integrity through the use of proper winding tension profiles and correct temperature and humidity conditioning. The measures of the integrity of a certain tape reel when exposed to its particular operating conditions are its in-roll stress distributions.

An early study by Gutterman (1959) analyzed the stress distributions in wound reels as a type of accretion process. The reel was treated as a series of concentric disks, each of which had an individual "contribution" to the total interlayer pressure distribution through the winding tension at that particular radius. Altmann (1968) expanded on this theme in what has since become, perhaps, the most widely used analysis in the field. Assuming that the tape reel could be characterized as linearly elastic, he was able to derive a set of integral equations which would predict interlayer pressures and in-roll tensions. The analysis became quite popular because the governing equations were easily derived (second-order Euler differential equations) and relatively straightforward to solve. (Although not quite closed form, simple numerical integration was all that was required.) The assumption that the tape reel is linearly elastic in the radial direction (constant modulus) has since been questioned because of the effect of entrapped air. Altmann himself recognized this and stated in his paper that the radial modulus "was taken to be constant throughout the roll, an assumption necessary to make the mathematics reasonably simple."

Contributed by the Applied Mechanics Division for publication in the JOURNAL OF APPLIED MECHANICS.

Discussion on this paper should be addressed to the Editorial Department, ASME, United Engineering Center, 345 East 47th Street, New York, NY 10017, and will be accepted until two months after final publication of the paper itself in the JOURNAL OF APPLIED MECHANICS. Manuscript received by ASME Applied Mechanics Division, October 2, 1987; final revision, November 5, 1987.

In two extensive articles, Tramposch (1965, 1967) addresses the problem of relaxation of internal forces in wound reels, approaching the analysis using viscoelasticity theory. The tape was represented by an isotropic four-parameter Maxwell-Kelvin model. A second-order, time-dependent governing equation was derived, the solution of which was obtained through the use of Laplace transformations. In the transformed state, the viscoelastic problem becomes an elastic problem. Tramposch also analyzed the effects of high-temperature storage and concluded that given sufficient time, a reel could approach stress-free conditions. While more comprehensive than Altmann's work, Tramposch's analysis has not gained widespread use, perhaps, because it is not as straightforward. The effects of entrapped air on the stress-strain curve also were not included.

After Tramposch, there seemed to be a lull in work published in the field. Monk et al. (1975), reproduced Altmann's analysis and examined the effect of various winding tension profiles (constant tension or torque, tapered tension) on the stress distributions. Crimping or buckling of the tape in the reel due to lengthwise compression was highlighted.

Bertram and Eshel (1980) examined the long-term storage effects on magnetic tape. Theoretical and experimental analyses were presented for the primary magnetic, chemical, and mechanical considerations. In particular, Altmann's work was recalled and applied. Additionally, they present a simple derivation which predicts the effects of temperature changes on winding stress. Again, however, the assumption that a reel is linearly elastic in the radial direction is made. The reel is treated also as orthotropic in elastic modulus, but not in Poisson's ratio. For a true orthotropic material, this is not true. (For further discussion of this topic, see Section VI.) Recommendations are made as to the proper winding tensions and temperature/humidity conditions which produce optimum reel integrity.

The influence of hub compliance on in-roll stress distribu-

Copyright © 1988 by ASME
Downloaded 03 May 2010 to 171.66.16.21. Redistribution subject to ASME license or copyright; see http://www.asme.org/terms/Terms_Use.cfm

tions was examined by Yagoda (1980, 1981). Based largely on Altmann's research, Yagoda focuses on the boundary condition at the hub/reel interface. Further, a "closed-form" solution is presented in the form of an infinite series expansion. Whether this solution is more efficient than numerical integration depends largely on the geometry of the reel and the winding tension profile.

Bhushan et al., (1984), examine the creep and relaxation behavior of polymer film using viscoelasticity. In particular, the relationship between elastic moduli and Poisson's ratio for orthotropic materials is developed and used. The analysis clearly shows how the assumption of isotropy in Poisson's ratio is incorrect.

This development is included in research by Connoly and Winarski (1984). Again, Altmann's analysis is used; however, Poisson's ratio is adjusted to represent, more realistically, an orthotropic material. It is shown that by adjusting moduli and Poisson's ratio according to Bhushan, a better correlation to experimental data can be produced.

Eshel (1984) examines the effect of entrapped air in reels undergoing winding accelerations. It is shown how the use of inadequate winding equipment can produce reels with a greater percentage of entrapped interlayer air. This is usually an undesirable situation because reels with large amounts of entrapped air are generally less stable.

Besides analytical derivations, there are several papers examining stress distributions in tape reels from an experimental point of view. Representative samples are Frye (1967), Rand (1973), and Wheeler (1983). Frye summarizes winding variables and their effect on reel integrity. Rand compares experimental measurements of interlayer pressures with results of Altmann's analysis. Wheeler makes further recommendations as to the winding and care of tape reels to insure integrity.

Most of the experimental work in the literature used Altmann's linear analysis for corroboration of measured data. Experimental data was "fit," after the fact, using Altmann's technique by adjusting the radial elastic modulus and Poisson's ratio. This is the major drawback to this approach: The analytical calculations for the stress-distributions depend directly on experimental measurements of the stress-distributions!

II Theoretical Background

The purpose of this analysis is to develop a method to calculate the stress distributions in wound reels of magnetic tape from first principles; that is, by using realistic governing equations and experimentally measured *material* properties. This approach is an extension of previous work in that the nonlinear character of the tape's stress-strain curve is included.

A stack of magnetic tape, or more specifically, tape wound on a reel, will exhibit nonlinear behavior in the stress-strain relationship for two reasons. The first is that the tape may have some initial curvature through the cross section due to differential thermal expansion of the base material and coatings. The second reason, and the more dominant effect, is entrapped air between layers of tape. As the applied pressure is increased, more air is "squeezed out," effectively stiffening the material. Eventually, most of the air is removed. At this point, the stress-strain curve will start to exhibit a more linear character; see Fig. 1.

If the stack of tape is uniaxially loaded, the stress in the radial direction σ_r is a function of strain in the radial direction ϵ_r only, that is

$$\sigma_r = f(\epsilon_r) \tag{1}$$

Conversely, ϵ_r can be expressed as a function of σ_r as

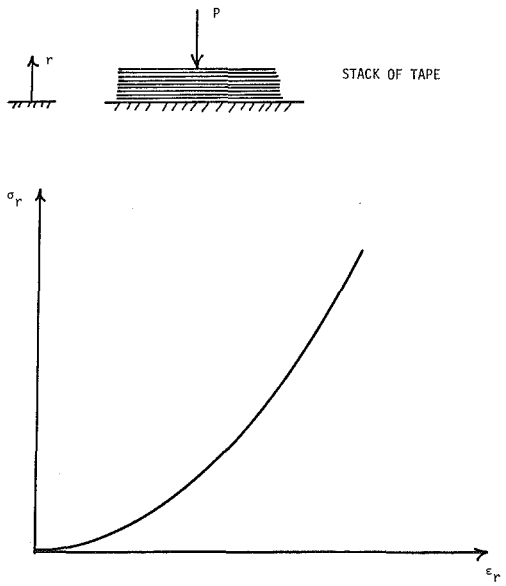


Fig. 1 Nonlinear stress-strain curve for a stack of magnetic tape

$$\epsilon_r = g(\sigma_r) \tag{2}$$

where g will be determined from experimental data. A convenient expression for g is a polynomial. In this case

$$\epsilon_r = \sum_{i=0}^{n} b_n \sigma_r{}^n = b_0 + b_1\sigma_r + b_2\sigma_r{}^2 + b_3\sigma_r{}^3 + \ldots + b_n\sigma_r{}^n \tag{3}$$

Note, that for a simple, linearly elastic material, $b_1 = 1/E_r$, where E_r is the radial modulus, while the other terms drop out, leaving the normal Hooke's law in one dimension. For a biaxially loaded material, Hooke's law in two dimensions is then

$$\epsilon_r = \sum_{i=0}^{n} b_n \sigma_r{}^n - \frac{\nu_t \sigma_t}{E_t} + \alpha_r \Delta T = \frac{du}{dr} \tag{4a}$$

$$\epsilon_t = \frac{\sigma_t}{E_t} - \nu_r \sum_{i=0}^{n} b_n \sigma_r{}^n + \alpha_t \Delta T = \frac{u}{r} \tag{4b}$$

where u is radial displacement, α's are coefficients of thermal expansion, and the t-subscript refers to that quantity in the tangential direction. Again, these equations simplify to the normal Hooke's law for a linear material.

Any governing equation must satisfy equilibrium, which is the same for a nonlinear material

$$\sigma_t - \sigma_r - r\frac{d\sigma_r}{dr} = 0 \tag{5}$$

Use equations (4*a*, *b*) and (5) to get a governing equation in σ_r. Differentiate (4*b*) w.r.t. "*r*" and solve for du/dr

$$\frac{du}{dr} = \frac{\sigma_t}{E_t} + \frac{r}{E_t}\frac{d\sigma_t}{dr} - \nu_r \sum_{i=0}^{n} b_n \sigma_r{}^n$$

$$- r\nu_r \sum_{i=0}^{n} n b_n \sigma_r{}^{n-1} \frac{d\sigma_r}{dr} + \alpha_t \Delta T \tag{6}$$

Eliminate du/dr between (6) and (4*a*) to get

$$(1+\nu_r)\sum_{i=0}^{n} b_n \sigma_r{}^n - \frac{\sigma_t}{E_t}(1+\nu_t) + r\nu_r \sum_{i=0}^{n} n b_n \sigma_r{}^{n-1}\frac{d\sigma_r}{dr}$$

$$- \frac{r}{E_t}\frac{d\sigma_t}{dr} + (\alpha_r - \alpha_t)\Delta T = 0 \tag{7}$$

Differentiate (5) w.r.t. "*r*," and solve for $d\sigma_t/dr$ as

Downloaded 03 May 2010 to 171.66.16.21. Redistribution subject to ASME license or copyright; see http://www.asme.org/terms/Terms_Use.cfm

$$\frac{d\sigma_t}{dr} = r\frac{d^2\sigma_r}{dr^2} + 2\frac{d\sigma_r}{dr} \tag{8}$$

Substitute (8) into (7) and simplify as

$$r^2\frac{d^2\sigma_r}{dr^2} - r\frac{d\sigma_r}{dr}\underline{\left[E_t\nu_r\sum_{i=0}^{n} nb_n\sigma_r^{n-1} - (3+\nu_t)\right]}$$

$$+(1+\nu_t)\sigma_r - \underline{E_t(1+\nu_r)\sum_{i=0}^{n} b_n\sigma_r^{n}} - E_t(\alpha_r-\alpha_t)\Delta T = 0 \tag{9}$$

This is the governing equation for a material with nonlinear radial stress-strain behavior. The terms that are *underlined* are those that account for the nonlinearity of the material. The first represents the nonlinear stiffness of the reel, or in other words, the fact that the radial modulus of the reel is a function of interlayer pressure. The second term expresses the nonlinear stress-strain behavior in the radial direction. If $b_1 = 1/E_r$ while the other terms of the polynomial are zero, (9) simplifies to

$$r^2\frac{d^2\sigma_r}{dr^2} - r\frac{d\sigma_r}{dr}\left[\frac{\nu_r E_t - E_r(3+\nu_t)}{E_r}\right]$$

$$-\sigma_r\left[\frac{E_t(1+\nu_r) - E_r(1+\nu_t)}{E_r}\right] - E_t(\alpha_r-\alpha_t)\Delta T = 0 \tag{10}$$

which is the normal, second-order Euler-type governing equation for a linear material.

Note that the governing equation (9) is nonlinear. As will be shown in the following sections, this fact makes it necessary to use iterative solution techniques. To accomplish this, equation (9) must be linearized by using a set of known values, σ_r', from an initial estimate or the previous iteration. Substituting σ_r' in (9) gives the desired form

$$r^2\frac{d^2\sigma_r}{dr^2} - r\frac{d\sigma_r}{dr}\left[E_t\nu_r\frac{dg(\sigma_r')}{d\sigma_r'} - (3+\nu_t)\right]$$

$$+(1+\nu_t)\sigma_r = E_t(1+\nu_r)g(\sigma_r') + E_t(\alpha_r-\alpha_t)\Delta T \tag{11}$$

or, more simply

$$r^2\frac{d^2\sigma_r}{dr^2} + Br\frac{d\sigma_r}{dr} + C\sigma_r = R \tag{12}$$

III Method of Numerical Analysis: Finite-Difference Technique

The finite-difference technique is well suited to solving Euler-type equations. This is especially true if central-difference approximations are used for the derivatives because a set of simultaneous equations is produced which is tridiagonal. This fact makes for a more efficient computer solution routine.

The differentials in (12) are replaced by central-difference derivative approximations as

$$\left.\frac{d\sigma_r}{dr}\right|_{r=r_n} = \frac{\sigma_{r_{n+1}} - \sigma_{r_{n-1}}}{2h} \tag{13}$$

$$\left.\frac{d^2\sigma_r}{dr^2}\right|_{r=r_n} = \frac{\sigma_{r_{n+1}} - 2\sigma_{r_n} + \sigma_{r_{n-1}}}{h^2} \tag{14}$$

Substituting (13) and (14) into (12) results in

$$\left(\frac{r_n^2}{h^2} - \frac{Br_n}{2h}\right)\sigma_{r_{n-1}} + \left(C - \frac{2r_n^2}{h^2}\right)\sigma_{r_n}$$

$$+\left(\frac{r_n^2}{h^2} + \frac{B_{r_n}}{2h}\right)\sigma_{r_{n+1}} = R \tag{15}$$

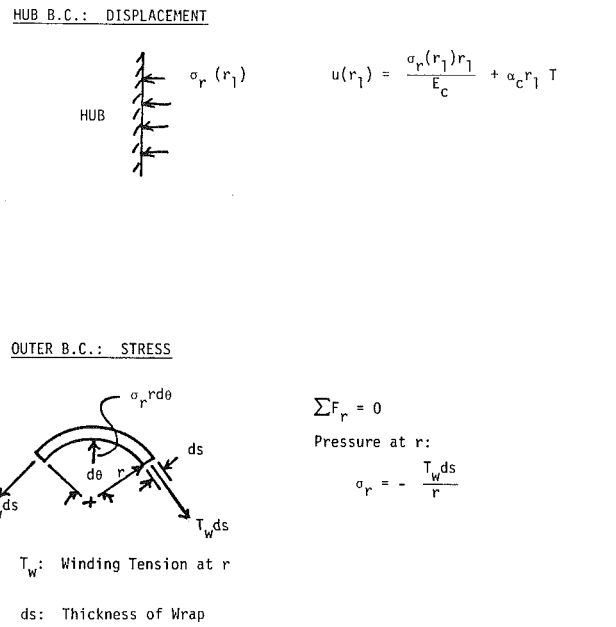


Fig. 2 Boundary conditions for use in finite-difference analysis

Keeping in mind that an iterative solution technique is to be used for the solution of this equation, it is desirable to place all the terms that depend on σ_r'-values from the previous iteration on the "right-hand side." This improves the stability and convergence of iterative schemes. Equation (15) can be rewritten using values of σ_r' from the previous iteration as

$$\frac{r_n^2}{h^2}\sigma_{r_{n-1}} + \left(C - \frac{2r_n^2}{h^2}\right)\sigma_{r_n} + \frac{r_n^2}{h^2}\sigma_{r_{n+1}}$$

$$= R + \frac{Br_n}{2h}\left(\sigma'_{r_{n-1}} - \sigma'_{r_{n+1}}\right) \tag{16}$$

or

$$a_1\sigma_{r_{n-1}} + a_2\sigma_{r_n} + a_3\sigma_{r_{n+1}} = Q \tag{17}$$

where a_1, a_2, a_3, and Q are introduced for convenience.

IV Boundary Conditions

The governing equation for this problem is second-order. It is, therefore, required that the two boundary conditions be specified. The boundary conditions used are shown in Fig. 2. At a certain radial position "r" in the reel, both of these b.c.'s are used.

The inner b.c. (boundary condition) must be converted from a displacement to a stress b.c. (since the governing equation is expressed in terms of σ_r). From Fig. 2

$$u(r_1) = \frac{\sigma_r(r_1)r_1}{E_c} + \alpha_c r_1\Delta T \tag{18}$$

where E_c is the modulus of the core, α_c is the coefficient of thermal expansion. From (4*b*)

$$u = \frac{r\sigma_t}{E_t} - r\nu_r\sum_{i=0}^{n} b_n\sigma_r^{n} + r\alpha_t\Delta T \tag{19}$$

From (5)

$$\sigma_t = r\frac{d\sigma_r}{dr} + \sigma_r \tag{20}$$

Substitute (20) into (19)

$$u = \frac{r^2}{E_t}\frac{d\sigma_r}{dr} + r\frac{\sigma_r}{E_t} - r\nu_r\sum_{i=0}^{n} b_n\sigma_r'^{n} + r\alpha_t\Delta T \tag{21}$$

Downloaded 03 May 2010 to 171.66.16.21. Redistribution subject to ASME license or copyright; see http://www.asme.org/terms/Terms_Use.cfm

Substitute (13) into (21) and evaluate at r_1

$$u(r_1)=\frac{r_1^2}{E_t}(\sigma_2-\sigma_0)+\frac{r_1\sigma_1}{E_t}-r_1\nu_r\sum_{i=0}^{n}b_n\sigma_r'^n+r_1\alpha_t\Delta T$$

$$=\frac{\sigma_1 r_1}{E_c}+\alpha_c r_1\Delta T \tag{22}$$

Note that because central-difference is used at r_1, a fictitious point, σ_0, has to be included in (22). This can be eliminated by using extrapolation from σ_2 to σ_1 as

$$\sigma_0\approx 2\sigma_1-\sigma_2 \tag{23}$$

Substitute this expression into (22) and solve for σ_1 in terms of σ_2. Simplifying yields

$$\sigma_1=\frac{\left[(\alpha_c-\alpha_t)\Delta T+\nu_r\sum_{i=0}^{n}b_n\sigma_r'^n-\frac{r_1}{E_t h}\sigma_2\right]E_tE_ch}{E_ch-E_th-E_cr_1} \tag{24}$$

Referring to Fig. 3, at point 2, the governing equation is, from (16)

$$a_1\sigma_1+a_2\sigma_2+a_3\sigma_3=Q \tag{25}$$

Substitute (24) into (25) to yield

$$\left[a_2-\frac{a_1r_1E_c}{E_ch-E_th-E_cr_1}\right]\sigma_2+a_3\sigma_3=$$

$$Q-\frac{a_1\left[(\alpha_c-\alpha_t)\Delta T+\nu_r\sum_{i=0}^{n}b_n\sigma_r'^n\right]E_tE_ch}{E_ch-E_th-E_cr_1} \tag{26}$$

At point 3, the governing equation is

$$a_1\sigma_2+a_2\sigma_3+a_3\sigma_4=Q \tag{27}$$

For point 4, the governing equation is

$$a_1\sigma_3+a_2\sigma_4+a_3\sigma_5=Q \tag{28}$$

Substitute in $\sigma_5 = -T_w ds/R$ to yield

$$a_1\sigma_3+a_2\sigma_4=Q+\frac{T_w ds}{r}\cdot a_3 \tag{29}$$

The set of equations, then, for the three unknowns, σ_2, σ_3, σ_4, is

$$\begin{bmatrix} a_2-\frac{a_1r_iE_c}{E_ch-E_th-E_cr_i} & a_3 & 0 \\ a_1 & a_2 & a_3 \\ 0 & a_1 & a_2 \end{bmatrix}\begin{Bmatrix}\sigma_2\\ \sigma_3\\ \sigma_4\end{Bmatrix}$$

$$=\begin{bmatrix}\frac{Q-a_1\left[(\alpha_c-\alpha_t)\Delta T+\nu_r\sum_{i=0}^{n}b_n\sigma_r'^n\right]E_tE_ch}{E_ch-E_th-E_cr_i}\\ Q\\ Q+a_3T_w ds/r\end{bmatrix} \tag{30}$$

It is important to note that this system is indeed tridiagonal and is, in fact, symmetric because a_1 equals a_3.

V Computer Implementation: Model of Wound Reels

Winding tape on a reel accumulates stress contributions with each wind, the stress contributions finally summing to the stress distributions in a fully wound reel. These individual contributions can be represented by the finite-difference equations as shown in Fig. 4.

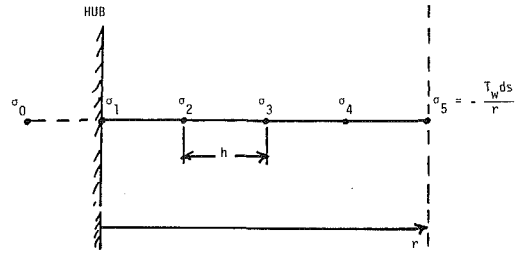


Fig. 3 Finite-difference grid

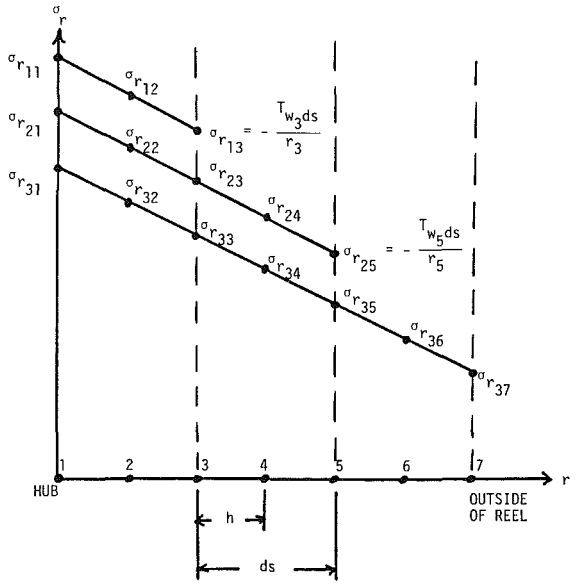


Fig. 4 Schematic of finite-difference routine

The solution procedure starts out at the hub and marches out in increments of *ds*, representing winding on new layers of tape. For example, at point 3 in Fig. 4, a complete Boundary Value Problem (BVP) is set up using the finite-difference equations just discussed. The resulting values of stress due to the winding tension at station 3 alone are taken as $\sigma_{r_{11}}$, $\sigma_{r_{12}}$ and $\sigma_{r_{13}}$. These values are stored. Next, the solution again marches out *ds* to point 5. Another BVP is created and solved. Ultimately, a series of BVP's is solved from the hub to the outside of the reel.

To sum up the individual effects of winding at a certain point, the σ_r-values are added together to get the full interlayer pressure. Thus

$$P_1=\sigma_{r_{11}}+\sigma_{r_{21}}+\sigma_{r_{31}};$$
$$P_3=\sigma_{r_{13}}+\sigma_{r_{23}}+\sigma_{r_{33}};\quad \text{etc.} \tag{31}$$

This represents one iteration assuming that some initial set of σ_r' is known: perhaps from the solution of the problem with $b_1 = 1/E_r$ where E_r is some defined value.

The entire process is repeated until

$$\frac{P-P'}{P}\le\text{Convergence criteria} \tag{32}$$

where P' is the interlayer pressure from the previous iteration.

In-roll tension is easily found from equilibrium as

$$T=P+r\frac{dP}{dr} \tag{33}$$

Downloaded 03 May 2010 to 171.66.16.21. Redistribution subject to ASME license or copyright; see http://www.asme.org/terms/Terms_Use.cfm

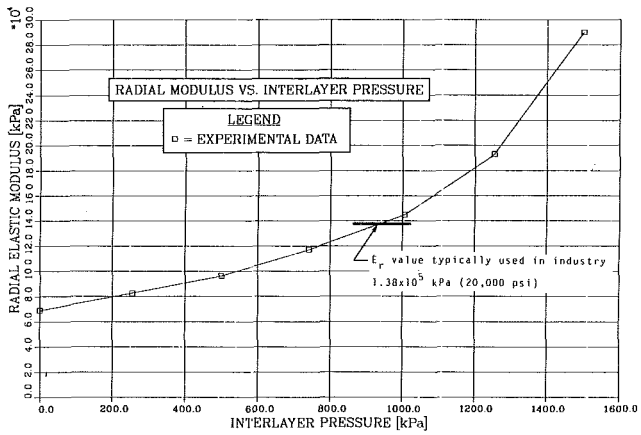


Fig. 5 Experimental radial modulus data

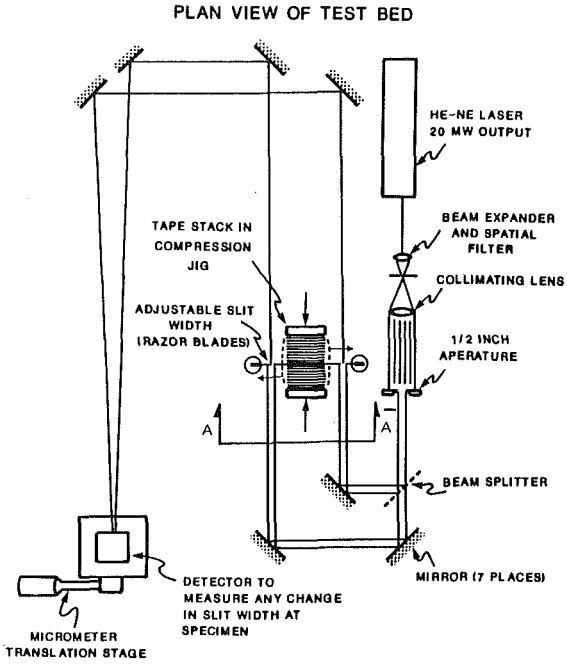


Fig. 6 Poisson's ratio experimental test bed

VI Definition of Material Properties

As shown in the previous sections, several material properties must be specified in the problem solution. This section will focus on two particular properties: nonlinear stress-strain behavior in the radial direction and Poisson's ratio in the radial (thickness) direction.

Besides the actual applied winding tension profile, the moduli and Poisson's ratio determine uniquely the interlayer pressure distribution calculated. The elastic modulus is easily measured in the tangential direction: Simple tension tests of tape samples are sufficient. The corresponding property in the radial direction, however, has a completely different character because of the effect of entrapped interlayer air. Referring back to Fig. 1, it is evident that the tape reel in the radial direction exhibits a "stiffening spring" behavior, in other words, the effective modulus of the reel is increased as the air is removed by increased pressure.

As mentioned, this nonlinear stress-strain behavior can be conveniently represented by a polynomial which fits experimentally determined data. This type of functional representation has been used successively in finite-element analysis [see, for example, Desai (1972), Zienkiewicz (1977), or Joseph (1981)]. Other methods of modeling nonlinear behavior involve using either the local tangent modulus of the stress-strain curve or the secant modulus as the effective stiffness of the material at a particular stress, while adding an incremental strain. This "linearizes" the problem. These methods, however, involve more computational approximations and are less efficient.

To measure the stress-strain characteristics in the radial direction, deformation measurements were made on a stack of tape loaded in compression (Ghorbanpoor, 1985, 1986). A Tinius-Olson machine with 4.45N (1 lb) increment and an accuracy of one-percent was used. A stacking guide was fabricated to allow extremely uniform stacking with side spacing just sufficient to prevent specimen contact during tests. Stack deformations during loading were measured with a tracking microscope capable of resolving deflections as small as 2.5×10^{-3} mm (0.1 mil in.). No appreciable differences were found between flat stacks of tape and those draped over a reel hub.

A seventh-degree polynomial was fit through experimental data using a least-squares routines. This order of polynomial provided the best smooth fit to the experimental data. The curve showing radial modulus as a function of interlayer pressure is shown in Fig. 5.

In addition to assuming that the radial modulus was constant, most tape winding analyses in the literature have assumed that Poisson's ratio in the radial direction was constant and equal to that in the tangential direction. This implies isotropy in Poisson's ratio, but not in modulus.

For an orthotropic material in plane stress, in the absence of shear stresses, Hooke's Law can be expressed as

$$\begin{Bmatrix} \epsilon_r \\ \epsilon_t \end{Bmatrix} = \begin{bmatrix} 1/E_r & -\nu_t/E_t \\ -\nu_r/E_r & 1/E_t \end{bmatrix} \begin{Bmatrix} \sigma_r \\ \sigma_t \end{Bmatrix} \tag{34}$$

Inverting this relationship yields

$$\begin{Bmatrix} \sigma_r \\ \sigma_t \end{Bmatrix} = \frac{E_r E_t}{1-\nu_r\nu_t} \begin{bmatrix} 1/E_t & \nu_t/E_t \\ \nu_r/E_r & 1/E_r \end{bmatrix} \begin{Bmatrix} \epsilon_r \\ \epsilon_t \end{Bmatrix}$$

$$= \begin{bmatrix} C_{11} & C_{12} \\ C_{21} & C_{22} \end{bmatrix} \begin{Bmatrix} \epsilon_r \\ \epsilon_t \end{Bmatrix} \tag{35}$$

The strain-energy-density function, U, represents the potential energy, per unit volume, stored up in the body caused by deformations. The energy function is related to (35) [see, for example, Boresi (1974) or Budynas (1977)].

$$\frac{\delta U}{\delta \epsilon_t} = \sigma_t = C_{21}\epsilon_r + C_{22}\epsilon_t$$

$$\frac{\delta U}{\delta \epsilon_r} = \sigma_r = C_{11}\epsilon_r + C_{12}\epsilon_t \tag{36}$$

Differentiation of (36) yields

$$\frac{\delta^2 U}{\delta\epsilon_r \delta\epsilon_t} = C_{12} = C_{21} \tag{37}$$

or, using (34)

$$\frac{\nu_t}{E_t} = \frac{\nu_r}{E_r} \tag{38}$$

Thus, (38) implies that the coefficient matrix in (36) is symmetric. From a physical point of view, this means that the net potential energy stored in the material due to the strains is independent of the order in which they occur. As can be seen from (38), ν_r can only equal ν_t if E_r equals E_t (the isotropic case).

Downloaded 03 May 2010 to 171.66.16.21. Redistribution subject to ASME license or copyright; see http://www.asme.org/terms/Terms_Use.cfm

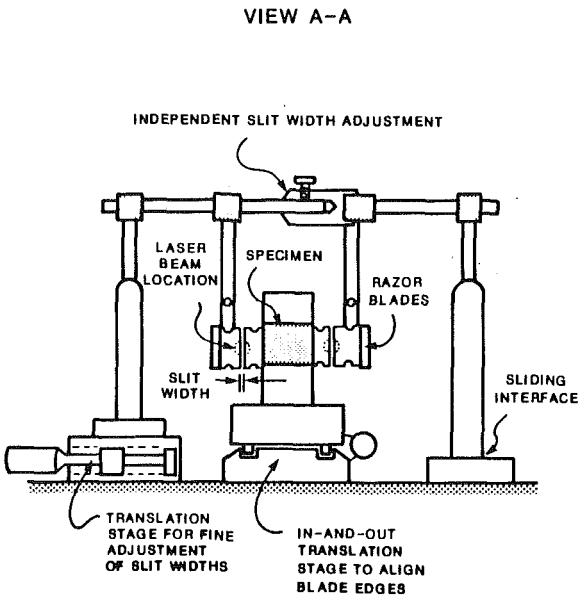


Fig. 7 Closeup view of test fixture

An experimental test program was undertaken to better quantify these effects. The objective of this test was to measure the strain in the tangential direction of a reel of magnetic tape as a fraction of the strain in the radial direction ($\nu_r = \epsilon_r/\epsilon_t$).

It was found in tests that a flat stack of tape had the same compressive properties as layers draped over a reel hub. This made it possible to compress a flat stack of tape normal to the tape layers to observe any unit change in length (ϵ_t) as a function of the unit change in the height of the tape stack (ϵ_r).

The experimental procedure utilized for obtaining the very precise measurements necessary to calculate ϵ_r is outlined as follows:

The experimental test bed is shown in Fig. 6.
The stack of 2.5-cm (1-in.) square magnetic tape was placed in the custom built compression rig.
Two razor blades were implanted within the tape stack (Fig. 7). These blades were positioned such that, as the width of the stack changed while undergoing compression, the separation between the blades equaled the change in width of the tape.
Two additional razor blades were used to create slits with the tape stack blades (Fig. 7). These blades are fixed in position and do not undergo any change during the experiment once initial alignment has been established.
These two slits were illuminated with collimated coherent helium-neon laser light.
The pressure of the stack was set to 445N (100 lb).
The initial slit widths were adjusted such that their diffraction patterns were approximately 1.27 cm (0.5 in.) at the detector. This was accomplished by positioning the two blades that will be fixed in position.
A slit was placed on the front of the detector. The slit was used to narrow the field of view.
The detector was placed on translation stage whose position could be read to 0.013 mm (0.0005 in.).
First, the diffraction pattern of the left slit was measured with the detector; then the diffraction pattern of the right slit was measured.
Each of these patterns was measured three times for each trial.
The pressure applied to the stack was increased to 2200N (500 lb) and the two slit diffraction patterns were measured again.

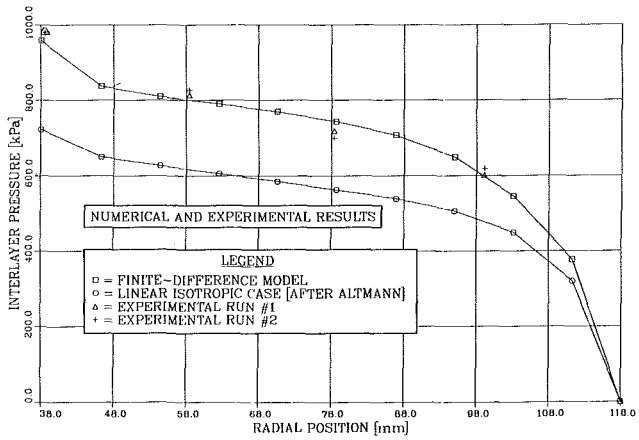


Fig. 8 Computed results—interlayer pressure

From diffraction theory, the slit width was calculated from the following formula: $b = 2Z\lambda/d$

where

b = slit width;
d = diffraction pattern width (first mimimum to first minimum);
λ = wavelength of illumination;
Z = distance between slit and detector (diffraction pattern).

Test results indicated an average value of the radial Poisson's ratio of 0.07. This is much lower than the generally assumed isotropic value of 0.3, but greater than those predicted by orthotropic theory. A satisfactory explanation for this behavior has not yet been developed, but experimental measurements of this kind will provide the necessary values.

VII Computational Example and Experimental Verification

Our test case consisted of the following physical parameters:

Reel inside radius, r_i	= 38.1 mm (1.5 in.)
Reel outside radius, r_0	= 119.4 mm (4.7 in.)
Core modulus, E_c	= 69,000 MPa ($1. \times 10^7$ psi)
Tape radial modulus, E_r	= variable per Fig. 5
Tape tangential modulus, E_t	= 6200 MPa ($9. \times 10^5$ psi)
Tape radial Poisson's ratio, ν_r	= 0.07
Tape tangential Poisson's ratio, ν_t	= 0.3

The winding tension varied linearly from 3.3N (12.0 oz) at the the inside radius to 2.4N (8.5 oz) at the outside.

The numerical simulation was run on a VAX 11/780 computer requiring 70 iterations (successive-over-relaxation was used) and approximately one minute of CPU time. The results of the computations are shown in Fig. 8.

To experimentally verify the simulation, a test rig was fabricated to apply an axial load to a reel of tape at various radii; see Fig. 10. The axial force necessary to telescope or shear the reel is easily calculated as

$$F = 2\pi r w p \mu \tag{39}$$

where w is the width of the tape and μ is the coefficient of friction. Ghorbanpoor (1985) measured μ to be 0.42 for the particular brand of tape used.

The telescoping force is measured at several radii by interchanging different sizes of shear plates. The plates were made of 1.90-cm (0.76-in.) thick aluminum and were considered

Downloaded 03 May 2010 to 171.66.16.21. Redistribution subject to ASME license or copyright; see http://www.asme.org/terms/Terms_Use.cfm

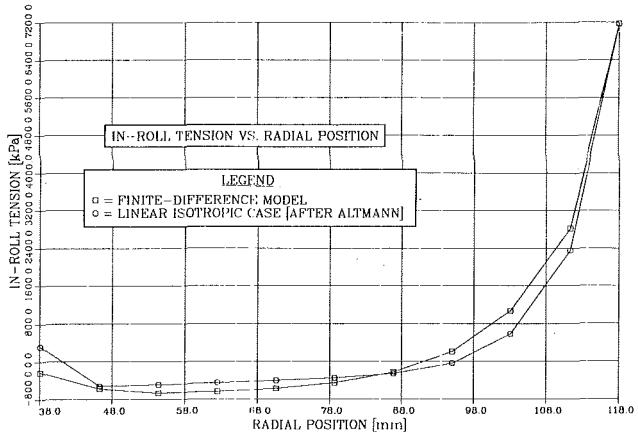


Fig. 9 Computed results—in-roll tension

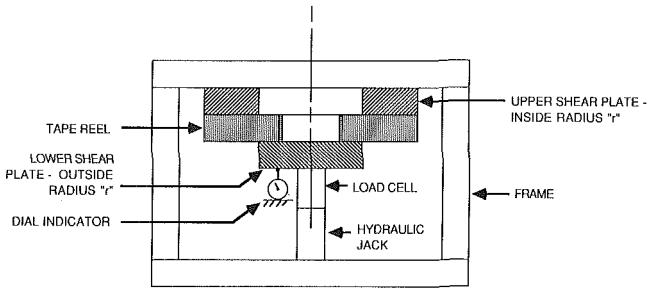


Fig. 10 Schematic of tape reel telescoping rig

rigid in comparison to the tape reel. The clearance between the outside diameter of the lower shear plate and the inside diameter of the upper shear plate was small enough to allow accurate alignment before the tape reel was installed. This was necessary to avoid any interference. A load cell monitors applied load, while three dial indicators measure axial deflection. Telescoping is indicated by a sudden drop in applied load accompanied by a jump in axial deflection as interlayer friction is overcome.

Two separate runs were made on different reels at radial positions of 38.1 mm (1.5 in.); 58.4 mm (2.3 in.); 78.7 mm (3.1 in.); 99.1 mm (3.9 in.). The results for both reels were very similar and are also plotted in Fig. 8. Excellent agreement can be seen between the computational and experimental results. (It should be noted that the creep and relaxation behavior of the tape correlated very well with an analysis similar to that of Tramposch [1967]. This will be the subject of an upcoming paper.)

For comparison, results from Altmann's isotropic analysis for this particular reel assuming a linearly elastic radial modulus are also plotted. (E_r was assumed to be 138 MPa (20,000 psi), a value typically used in industry; see Fig. 5.) Clearly, the linear isotropic case underpredicts interlayer pressure by a substantial amount. This could be important when assessing the stability of a particular reel, because lower interlayer pressures lead to lower magnitudes of lengthwise compression in the tape, implying a decreased probability of crimping or buckling; see Fig. 9.

VIII Summary

A new method of modeling the internal stress distributions in wound reels of magnetic tape using a finite-difference approach was presented. Unique to this analysis was the inclusion of the effects of entrapped interlayer air on the stress-strain curve in the radial direction. Experimental methods were described by which this nonlinear behavior could be measured. A procedure to measure Poisson's ratio in the radial (thickness) direction was presented. Results clearly indicate that the common assumption of isotropy in Poisson's ratio is incorrect.

Results from a computer simulation which incorporated these measured quantities demonstrated excellent agreement with experimental data. These results are to be contrasted with those of earlier analyses. The stress distributions calculated are the results of a more realistic governing equation and experimentally measured material properties, and do not depend on *a priori* knowledge of the stress distributions themselves.

References

Altmann, Heinz C., 1968, "Formulas for Computing the Stresses in Center-Wound Rolls," *Journal of the Technical Association of the Paper and Pulp Industry (TAPPI)*, Vol. 51, No. 4, pp. 176–179.

Bertram, Neal, and Eshel, A., 1980, "Recording Media Archival Attributes," RADC-TR80-123, Griffis Air Force Base, New York.

Bhushan, B., Heinrich, J., and Connolly, D., 1984, "Orthotropic Viscoelastic Behavior of Polyethylene Terephthalate Film Under Plane Stress Conditions," *Tribology and Mechanics of Magnetic Storage Media*, Special Publication 16, American Society of Lubrication Engineers.

Boresi, Arthur, and Lynn, Paul, 1974, *Elasticity in Engineering Mechanics*, Prentice-Hall, NJ, pp. 158–169.

Budynas, Richard, 1977, *Advanced Strength and Applied Stress Analysis*, McGraw-Hill, New York, pp. 313–315.

Connolly, D., and Winarski, J., 1984, "Stress Analysis of Wound Magnetic Tape," *Tribology and Mechanics of Magnetic Storage Media*, Special Publication 16, American Society of Lubrication Engineers.

Desai, Chandrakant, and Abel, John, 1972, *Introduction to the Finite Element Method*, Van Nostrand, New York, pp. 217–238.

Eshel, A., and Baker, S., 1984, "Mechanical Aspects of Archival Storage of Magnetic Tape," *Tribology and Mechanics of Magnetic Storage Media*, Special Publication 16, American Society of Lubrication Engineers.

Frye, Kenneth G., 1967, "Winding Variables and Their Effect on Roll Hardness and Roll Quality," *TAPPI*, Vol. 50, No. 7, pp. 81–86.

Ghorbanpoor, Al, and Mecklenburg, Marion, 1985, "Mechanical Properties of Mylar-Based Magnetic Recording Tape," Department of Civil Engineering Report, University of Maryland.

Ghorbanpoor, Al, and Mecklenburg, Marion, 1986, "Mechanical Properties of Mylar-Based Magnetic Recording Tape," Department of Civil Engineering Report, University of Maryland.

Gutterman, R. P., 1959, "Theoretical and Practical Studies of Magnetic Tape Winding Tensions and of Environmental Roll Stability," Contract No. DA18-119-SC-42, General Kinetics, Inc., Arlington, VA.

Joseph, Jarrad A., Ed., 1981, *MSC/NASTRAN Application Manual*, Section 2.14.

Monk, D. W., Lautner, W. K., and McMullen, J. F., 1975, "Internal Stresses Within Rolls of Cellophane," *TAPPI*, Vol. 58, No. 3, pp. 152–155.

Rand, Thorkild, and Eriksson, Leif G., 1973, "Physical Properties of Newsprint Rolls During Winding," *TAPPI*, Vol. 56, No. 6, pp. 153–156.

Tramposch, H., 1965, "Relaxation of Internal Forces in a Wound Reel of Magnetic Tape," ASME JOURNAL OF APPLIED MECHANICS, Vol. 32, pp. 865–873.

Tramposch, H., 1967, "Anisotropic Relaxation of Internal Forces in a Wound Reel of Magnetic Tape," *TRANS. ASME.*, pp. 888–894.

Wheeler, Jim, 1985, "Long-Term Storage of Videotape," *SMPTE Journal*, pp. 650–654.

Yagoda, H. P., 1980, "Resolution of a Core Problem in Wound Rolls," ASME JOURNAL OF APPLIED MECHANICS, Vol. 47, pp. 847–854.

Yagoda, H. P., 1981, "Generalized Formulas for Stresses in Wound Rolls," *TAPPI*, Vol. 64, No. 2, pp. 91–93.

Zienkiewicz, O. C., 1977, *The Finite Element Method*, McGraw-Hill, New York, pp. 450–485.

Downloaded 03 May 2010 to 171.66.16.21. Redistribution subject to ASME license or copyright; see http://www.asme.org/terms/Terms_Use.cfm

Thermal Stresses Due to a Plane Crack in General Anisotropic Material

F. A. Sturla
J. R. Barber

Department of Mechanical Engineering
and Applied Mechanics,
The University of Michigan,
Ann Arbor, MI 48109

A solution is given for the thermoelastic stress field due to the obstruction of a uniform heat flux by a plane crack in a generally anisotropic body. A Green's function formulation is used to reduce the problem to a set of singular integral equations which are solved in closed form. When the crack is assumed to be traction free, the crack opening displacement is found to be negative over one half of the crack unless a sufficiently large far field tensile stress is superposed. The problem is, therefore, reformulated assuming a contact zone at one crack tip. The extent of this zone and the stress intensity factors in all three modes at each crack tip are obtained as functions of the applied stress and heat flux.

Introduction

When the flow of heat in a solid is disturbed by some discontinuity such as a hole or a crack, the local temperature gradient around the discontinuity is increased. Thermal disturbances of this type can produce material failure through crack propagation. The problem is complicated by the fact that the thermal distortion may cause the crack to open or close, hence changing the thermal boundary conditions. A number of studies dealing with flaw-induced thermal stresses in infinite isotropic regions have been published by Florence and Goodier (1963) and Olesiak and Sneddon (1959). For the plane crack in an infinite isotropic homogeneous body, it can be argued from consideration of symmetry that the crack faces will not separate and there will be only a mode II stress intensity factor, unless heat is generated in the crack.

Anisotropic Materials

The widespread use of composite materials in structural applications has generated renewed interest in anisotropic material behavior. In particular, information on thermal stress concentrations around material discontinuities in anisotropic bodies will have application in high-temperature composite materials. Solutions have been published for the axisymmetric problem of the penny-shaped crack in a transversely isotropic material by Tsai (1983) and for the two-dimensional (plain strain) problem of the Griffith crack in a general anisotropic material by Atkinson and Clements (1977).

Atkinson and Clements (1977) give a solution for the two-dimensional Griffith crack obstructing a uniform heat flux in a general anisotropic medium. They show that modes I, II, and III stress intensity factors are obtained unless the material has certain symmetries, which suggests that a mixed mode of fracture may occur. It also indicates that the crack must close for at least one direction of the heat flow. Closure is also obtained in thermoelastic interface crack problems (Martin-Moran et al., 1983, Barber and Conminou, 1983) where the resulting change in the thermal boundary conditions at the crack faces leads to nonuniqueness of solution in certain cases.

Atkinson and Clements did not consider these questions. Their solution assumes that the crack is always open and hence can only apply for a restricted range of conditions. Furthermore, they did not give explicit expressions for the crack opening displacement from which the physical feasibility of their solution could be checked.

These authors considered the cases of specified temperature on the crack faces and also that of a specified heat flux across the crack. However, the boundary condition taken for this latter problem was $\partial T/\partial X_2 = -Q(X_1)$ across the crack faces and this can only be truly representative of the heat flux for certain symmetries of the thermal conductivity tensor, i.e., $K_{12} = 0$ for a crack lying on the X_1 plane. Furthermore, there are difficulties in adapting the solution method to the more general boundary condition, which will be addressed in a subsequent paper.

In this paper the problem is reconsidered using a Green's function formulation which will allow us to express the solution in terms of physical variables so that it is easier to determine at intermediate stages whether the solution is physically reasonable. The method is then extended to consider the case where the crack is partially closed.

Contributed by the Applied Mechanics Division for presentation at the Winter Annual Meeting, Chicago, IL, November 28 to December 2, 1988, of the American Society of Mechanical Engineers.

Discussion on this paper should be addressed to the Editorial Department, ASME, United Engineering Center, 345 East 47th Street, New York, N.Y. 10017, and will be accepted until two months after final publication of the paper itself in the JOURNAL OF APPLIED MECHANICS. Manuscript received by ASME Applied Mechanics Division, April, 14, 1987; final revision, September 29, 1987.

Paper No. 88-WA/APM-16.

Copyright © 1988 by ASME
Downloaded 03 May 2010 to 171.66.16.21. Redistribution subject to ASME license or copyright; see http://www.asme.org/terms/Terms_Use.cfm

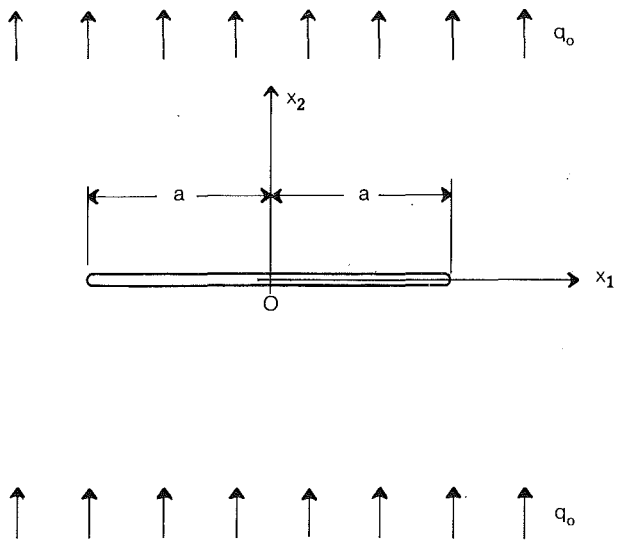


Fig. 1 The thermoelastic plane crack

Statement of the Problem

Let $x_1\ x_2\ x_3$, denote Cartesian coordinates and suppose that a homogeneous generally anistropic material occupies the entire space except for the region $x_2=0,\ |x_1|<a,\ -\infty<x_3<\infty$, where there is a crack. The crack obstructs the heat flow as shown in Fig. 1. The crack is initially assumed to remain open and hence be free of tractions, and to prevent the transfer of heat between its faces. We, therefore, have the boundary conditions

$$q_2=0 \quad ; \quad -a<x_1<a \ ; \ x_2=0 \tag{1}$$

$$\sigma_{i2}=0 \quad ; \quad -a<x_1<a \ ; \ x_2=0 \tag{2}$$

$$q_2\to q_0 \quad ; \quad \sqrt{x_1^2+x_2^2}\to\infty \tag{3}$$

$$\sigma_{ij}\to 0 \quad ; \quad \sqrt{x_1^2+x_2^2}\to\infty \tag{4}$$

The boundary conditions, and hence the displacement, stress, and temperature fields, are independent of the coordinate x_3, but we emphasize that the solution is three-dimensional in the sense that the stress components σ_{i3} and displacement component u_3 are nonzero because of the general anisotropy of the material.

It is convenient to represent the solution as the sum of a uniform heat flux in an unflawed solid (which involves no thermal stress) and a corrective solution, for which the boundary conditions are

$$q_2=-q_0 \quad ; \quad a<x_1<a \ ; \ x_2=0 \tag{5}$$

$$\sigma_{i2}=0 \quad ; \quad -a<x_1<a \ ; \ x_2=0 \tag{6}$$

$$q_2\to 0 \quad ; \quad \sqrt{x_1^2+x_2^2}\to\infty \tag{7}$$

$$\sigma_{ij}\to 0 \quad ; \quad \sqrt{x_1^2+x_2^2}\to\infty \tag{8}$$

Mathematical Formulation

The problem will be formulated in terms of the thermoelastic Green's function derived in a previous paper (Sturla and Barber, 1988), corresponding to a temperature discontinuity of magnitude T_0 on the half-line $x_2=0,\ x_1>0$. The appropriate heat flux and tractions on the surface $x_2=0$ are

$$q_2=-\frac{K_{22}(\tau-\bar{\tau})T_0}{4\pi i x_1} \quad ; \ x_2=0 \tag{9}$$

$$\sigma_{i2}=G_i T_0 \log|x_1| \quad ; \ x_2=0 \tag{10}$$

where τ is the root with positive imaginary part of the equation

$$K_{22}\tau^2+2K_{12}\tau+K_{11}=0, \tag{11}$$

K_{ij} is the thermal conductivity tensor and G_i is a function of the thermoelastic constants for the material, defined by equation (42) of Sturla and Barber (1988).

The thermal boundary conditions (5), (7), can be satisfied by distributing Green's functions of the above form with weight $\Omega(\xi)$ in the interval $-a<x_1<a$. From equations (5) and (9) we then have

$$-K\int_{-a}^{a}\frac{\Omega(\xi)d\xi}{x_1-\xi}=q_2(x_1,0)=-q_0 \ ; \ -a<x_1<a \tag{12}$$

where $K=K_{22}(\tau-\bar{\tau})/4\pi i$ is a real constant.

This distribution will generally produce a discontinuity in temperature in the region $x_2=0,\ x_1>-a$, but temperature continuity outside the crack (i.e., $x_1>a$) can be imposed by enforcing the auxiliary condition

$$\int_{-a}^{a}\Omega(\xi)d\xi=0. \tag{13}$$

Equations (12) and (13) have the well known solution

$$\Omega(\xi)=-\frac{q_0\xi}{\pi K\sqrt{a^2-\xi^2}} \quad -a<\xi<a \tag{14}$$

and the stresses on the plane $x_2=0$ can now be found from equation (10) in the form

$$\sigma_{i2}=G_i\int_{-a}^{a}\Omega(\xi)\log|x_1-\xi|\,d\xi \tag{15}$$

$$=(q_0/K)G_i x_1 \quad ; \quad -a<x_1<a \tag{16}$$

$$=(q_0/K)G_i\{x_1-\sqrt{x_1^2-a^2}\} \ ; \ x_1>a \tag{17}$$

after substituting for $\Omega(\xi)$ from equation (14) and performing the integration.

To satisfy the traction-free boundary condition (6), we must superpose a solution of the corresponding isothermal problem with tractions equal and opposite to those of equation (16) in the range $-a<x_1<a$. This solution is conveniently represented by a distribution of dislocations of strength $B_i(\xi)$ in the same range. The solution for a single dislocation of strength B_i was obtained by Stroh (1958), the corresponding stresses and displacement on $x_2=0$ being

$$\sigma_{i2}=\frac{d_i}{2\pi x_1} \tag{18}$$

$$u_k=\frac{1}{4\pi}\sum_{\alpha}[A_{k\alpha}M_{\alpha j}+\bar{A}_{k\alpha}\bar{M}_{\alpha j}]d_j\log|x_1| \tag{19}$$

in the notation of Stroh (1958). In particular,

$$B_i=b_{ij}d_j, \text{ where } b_{ij}=\frac{i}{2}\sum_{\alpha}[A_{i\alpha}M_{\alpha j}-\bar{A}_{i\alpha}\bar{M}_{\alpha j}],$$

$A_{i\alpha}$ and $M_{\alpha j}$ are functions of the material constants, defined by equations (7) and (38) of Stroh (1958), and the summation on α is over the three roots with positive imaginary part of the equation

$$|c_{i1k1}+p_\alpha(c_{i1k2}+c_{i2k1})+p_\alpha^2 c_{i2k2}|=0 \tag{20}$$

Combining (16) and (18) the boundary condition (6) is satisfied if

$$\frac{1}{2\pi}\int_{-a}^{a}\frac{d_i(\xi)d\xi}{x_1-\xi}+q_0G_i x_1/K=0 \quad -a<x_1<a \tag{21}$$

It is also necessary to impose the closure condition

$$\int_{-a}^{a}d_i(\xi)d\xi=0 \tag{22}$$

Downloaded 03 May 2010 to 171.66.16.21. Redistribution subject to ASME license or copyright; see http://www.asme.org/terms/Terms_Use.cfm

to enforce continuity of displacements in the region $x_2=0$, and $x_1>a$. Solving for $d_i(\xi)$ we have

$$d_i(\xi)=\frac{q_0G_i}{K}\frac{(2\xi^2-a^2)}{\sqrt{a^2-\xi^2}} \tag{23}$$

and hence the stresses σ_{i2} on the plane $x_2=0$, $|x_1|>a$ are given by

$$\sigma_{i2}=\frac{q_0G_i}{K}[x_1\pm\sqrt{x_1^2-a^2}+\frac{q_0G_i}{2\pi K}\int_{-a}^{a}\frac{(2\xi^2-a^2)}{(x_1-\xi)\sqrt{a^2-\xi^2}} \tag{24}$$

$$=\pm\frac{q_0G_i}{2K}\frac{a^2}{\sqrt{x_1^2-a^2}}\quad\begin{matrix}+;\ x_1>a\\ -;\ x_1<-a\end{matrix} \tag{25}$$

from equations (17), (18), and (23). We note that stress intensity factors in all three modes are obtained at $x_1=a+$ of magnitude:

$$K_{\mathrm{I}}=\lim_{x_1\to a}\sqrt{x_1-a}\,\sigma_{22}=\frac{q_0G_2}{K}\left(\frac{a}{2}\right)^{3/2} \tag{26}$$

$$K_{\mathrm{II}}=\lim_{x_1\to a}\sqrt{x_1-a}\,\sigma_{12}=\frac{q_0G_1}{K}\left(\frac{a}{2}\right)^{3/2} \tag{27}$$

$$K_{\mathrm{III}}=\lim_{x_1\to a}\sqrt{x_1-a}\,\sigma_{32}=\frac{q_0G_3}{K}\left(\frac{a}{2}\right)^{3/2} \tag{28}$$

Equal and opposite stress intensity factors are obtained at $x_1=-a$. The displacement in the entire space is given by

$$u_k=2\mathrm{Re}\Big[\frac{E_kq_0}{4\pi i}\int_{-a}^{a}\frac{[\log(z_t-\xi)-1][z_t-\xi]\xi}{\sqrt{a^2-\xi^2}}\,d\xi$$
$$+\sum_\alpha A_{k\alpha}F_\alpha q_0\int_{-a}^{a}\frac{[\log(z_\alpha-\xi)-1][z_\alpha-\xi]\xi}{\sqrt{a^2-\xi^2}}\,d\xi$$
$$+\frac{q_0}{2\pi K}\sum_\alpha A_{k\alpha}M_{\alpha j}G_j\int_{-a}^{a}\frac{(\xi^2-a^2/2)\log(z_\alpha-\xi)}{\sqrt{a^2-\xi^2}}\,d\xi\Big] \tag{29}$$

$$=2\mathrm{Re}\Big[\frac{q_0}{2k}\sum_\alpha A_{k\alpha}M_{\alpha j}G_j\Big\{\frac{z_\alpha}{2}\sqrt{z_\alpha^2-a^2}-\frac{z_\alpha^2}{2}\Big\}$$
$$+\frac{E_kq_0}{4i}\Big\{\frac{a^2}{2}\log(z_t+i\sqrt{a^2-z_t^2})+\frac{iz_t}{2}\sqrt{a^2-z_t^2}-\frac{z_t^2}{2}+a^2\Big\}$$
$$+\sum_\alpha A_{k\alpha}F_\alpha q_0\Big\{\frac{a^2}{2}\log(z_\alpha+i\sqrt{a^2-z_\alpha^2})$$
$$+\frac{iz_\alpha}{2}\sqrt{a^2-z_\alpha^2}-\frac{z_\alpha^2}{2}+a^2\Big\}\Big] \tag{30}$$

where E_k and F_α are functions of the material constants, defined by equations (22) and (38) of Sturla and Barber (1987), also $z_t=x_1+\tau x_2$ and $z_\alpha=x_1+p_\alpha x_2$, where p_α is defined by equation (20). The temperature distribution and hence the strains behave like $1/z_\alpha$ as $|z_\alpha|\to\infty$, therefore the displacement vector $u_k\sim\log|z_\alpha|$ when $|z_\alpha|\to\infty$.

The crack opening displacement is given by

$$\Delta u_2=u_2(x_1,0^+)-u_2(x_1,0^-) \tag{31}$$

$$=(q_0b_{2j}G_j/2K)x_1\sqrt{a^2-x_1^2} \tag{32}$$

using equation (36) of Sturla and Barber (1987).

From equation (32) it can be seen that Δu_2 must be negative in either $-a<x_1<0$ or $0<x_1<a$, depending on the sign of $b_{2j}G_j$ (except in the special case $b_{2j}G_j=0$) and therefore the initial assumption of a fully open crack is invalid for either direction of the heat flow unless the crack has some initial separation between its faces or is opened by an applied tensile stress. If $b_{2j}G_j=0$, $\Delta u_2=0$ for all x_1 within the crack and hence there is no tendency for the crack to open or close. There is, however, a relative *tangential* displacement between the crack faces. This case is obtained if the material is symmetrical about the plane $x_1=0$.

For the latter case, the boundary condition (4) is modified to include

$$\sigma_{22}\to\sigma_0\ ;\ \sqrt{x_1^2+x_2^2}\to\infty \tag{33}$$

and this new problem can be treated by superposing the solution due to Stroh (1958) for the isothermal problem of a Griffith crack in a general anisotropic medium opened by a uniform tensile stress, σ_0.

In particular, we find that the crack opening displacement (equation (32)) is increased to

$$\Delta u_2=\Big(\frac{q_0b_{2j}G_j}{K}x_1+2b_{22}\sigma_0\Big)\sqrt{a^2-x_1^2},\ |x_1|<a \tag{34}$$

and the opening mode stress intensity factor becomes

$$K_{\mathrm{I}}=\pm\frac{q_0G_2}{K}\left(\frac{a}{2}\right)^{3/2}+\sqrt{\frac{a}{2}}\,\sigma_0\quad\begin{matrix}+;\ x_1>a\\ -;\ x_1<-a\end{matrix} \tag{35}$$

The other stress intensity factors, K_{II}, K_{III}, are unaffected by the applied tensile stress.

We can always choose the coordinate system such that $q_0b_{2j}G_j<0$, corresponding to the case where the crack tends to close at the tip $x_1=a$. In this case, equation (34) defines a positive crack opening displacement for all x_1 provided

$$\sigma_0>-q_0b_{2j}G_ja/2b_{22}K \tag{36}$$

Solution With Partial Contact

If the inequality (36) is not satisfied, a negative crack opening displacement is predicted near $x_1=a$ and we anticipate contact between the crack faces, as shown in Fig. 2. The contact is assumed to be frictionless and to afford no resistance to heat flow. There is, therefore, no temperature discontinuity between the faces, except in the open region $-a<x_1<c$. The heat conduction problem is, therefore, identical to that for an insulating crack of extent $-a<x_1<c$ and can be formulated in terms of a distribution $\Omega(\xi)$ of Green's function in this range. Enforcing the condition (5) over this range we obtain

$$K\int_{-a}^{c}\frac{\Omega(\xi)d\xi}{(x_1-\xi)}=q_0\ ;\ -a<x_1<a \tag{37}$$

with the auxiliary condition

$$\int_{-a}^{c}\Omega(\xi)d\xi=0 \tag{38}$$

whose solution is

$$\Omega(\xi)=-\frac{q_0}{\pi K}\frac{\xi+(a-c)/2}{\sqrt{(a+\xi)(c-\xi)}} \tag{39}$$

The mechanical boundary conditions at the crack faces can be stated in the form

$$\sigma_{12}=\sigma_{23}=0\qquad -a<x_1<a \tag{40}$$

$$\sigma_{22}=0\qquad -a<x_1<c \tag{41}$$

$$u_2(x_1,0^+)=u_2(x_1,0^-)\qquad c<x_1<a \tag{42}$$

$$\sigma_{22}\to\sigma_0\ ;\ \sigma_{12},\ \sigma_{23}\to0\qquad \sqrt{x_1^2+x_2^2}\to\infty. \tag{43}$$

We subtract the unperturbed uniform tension solution, $\sigma(x_1,x_2,x_3)=\sigma_0$, thereby modifying the boundary conditions (41), (43) to

$$\sigma_{22}=-\sigma_0\ ;\ -a<x_1<c \tag{44}$$

$$\sigma_{22}\to0\ ;\ \sqrt{x_1^2+x_2^2}\to\infty. \tag{45}$$

Downloaded 03 May 2010 to 171.66.16.21. Redistribution subject to ASME license or copyright; see http://www.asme.org/terms/Terms_Use.cfm

As for the case of a fully opened crack, we solve this boundary value problem by constructing the appropriate stress and displacement fields in terms of a distribution of dislocations $B_i(\xi)$ in the range $-a<x_1<a$. In view of the boundary condition (42), the distribution $B_2(\xi)$ must be nonzero only in the range $-a<x_1<c$, but B_1, B_3 extend over the entire crack length since slip is permitted in the contact region $c<x_1<a$.

The total traction on the crack faces due to the thermoelastic solution and the dislocation distributions can then be written

$$\sigma_{i2}=-\frac{q_0G_i}{\pi K}\int_{-a}^{c}\frac{\xi+(a-c)/2}{\sqrt{(a+\xi)(c-\xi)}}\log|x_1-\xi|\,d\xi + \frac{1}{2\pi}\int_{-a}^{a}\frac{d_i(\xi)d\xi}{(x_1-\xi)} \tag{46}$$

$$= 0\,,\quad i=1,3;\quad -a<x_1<a \tag{47}$$

$$=-\sigma_0,\quad i=2\;;\quad -a<x_1<c \tag{48}$$

The integral in the first term in equation (46) can be evaluated to give

$$\int_{-a}^{c}\frac{\xi+(a-c)/2}{\sqrt{(a+\xi)(c-\xi)}}\log|x_1-\xi|\,d\xi=-\pi\left(x_1-\frac{c-a}{2}\right);\quad -a<x_1<c \tag{49}$$

$$=-\pi\left\{x_1-\frac{c-a}{2}+\sqrt{(x_1+a)(x_1-c)}\right\};\quad x_1>c$$

and hence the boundary conditions (47), (48) are meet if $d_i(\xi)$ $(i=1,2,3)$ satisfies the integral equations

$$\frac{2q_0G_i}{K}\left\{x_1+\frac{a-c}{2}-H(x_1-c)\sqrt{(x_1+a)(x_1-c)}\right\} + \frac{1}{2\pi}\int_{-a}^{a}\frac{d_i(\xi)d\xi}{(x_1-\xi)}=0\;;\; i=1,3\;;\; -a<x_1<a \tag{50}$$

$$\frac{2q_0G_2}{K}\left\{x_1+\frac{a-c}{2}\right\}+\frac{1}{2\pi}\int_{-a}^{a}\frac{d_2(\xi)d\xi}{(x_1-\xi)}=-\sigma_0;\quad -a<x_1<c \tag{51}$$

It is also necessary to impose the conditions

$$\int_{-a}^{a}B_i(\xi)=0;\quad i=1,2,3 \tag{52}$$

$$B_2(\xi)=0\qquad c<x_1<a \tag{53}$$

to ensure that there is continuity of displacement on the plane $x_2=0$, $x_1>a$ and that the crack closes in $c<x_1<a$.

Since $B_i=b_{ij}d_j$ where b_{ij} is a nonsingular matrix, we have

$$\int_{-a}^{a}d_i(\xi)d\xi=0\qquad i=1,3 \tag{54}$$

$$d_2(x_1)=-\frac{b_{21}d_1(x_1)+b_{23}d_3(x_1)}{b_{22}}\qquad c<x_1<a \tag{55}$$

from equations (52), (53) and hence we can solve equations (50), (54) obtaining

$$d_i(\xi)=\frac{q_0G_i}{4K}\left[\frac{(a+c)^2}{\sqrt{a^2-\xi^2}}-8(\xi+a)H(c-\xi)\sqrt{\frac{c-\xi}{\xi+a}}\right];\quad i=1,3 \tag{56}$$

We now write equation (51) and the corresponding closure condition (54) in the form

$$\frac{1}{2\pi}\int_{-a}^{c}\frac{d_2(\xi)d\xi}{(x_1-\xi)}=-\sigma_0-\frac{2q_0G_2}{(a+c)K}\left\{x_1+\frac{(a-c)}{2}\right\} - \frac{1}{2\pi}\int_{c}^{a}\frac{d_2(\xi)d\xi}{(x_1-\xi)}\;;\quad -a<x_1<c \tag{57}$$

$$\int_{-a}^{c}d_2(\xi)d\xi=-\int_{c}^{a}d_2(\xi)d\xi \tag{58}$$

where the expression involving $d_2(\xi)$ in the range $c<\xi<a$ can be evaluated using equations (55), (56).

Equations (55), (56), (57), and (58) have the solution

$$d_2(\xi)=\frac{q_0b_{2j}G_j}{b_{22}K}\frac{\left[2\left\{\xi-\left(\frac{c-a}{2}\right)\right\}^2-\left(\frac{a+c}{2}\right)^2\right]}{\sqrt{(\xi+a)(c-\xi)}} + 2\sigma_0\frac{\left[\xi-\left(\frac{c-a}{2}\right)\right]}{\sqrt{(\xi+a)(c-\xi)}} - \frac{q_0}{4K}\frac{(b_{21}G_1+b_{22}G_2)}{b_{22}}\left[\frac{(a+c)^2}{\sqrt{a^2-\xi^2}} - 8(\xi+a)H(c-\xi)\sqrt{\frac{c-\xi}{\xi+a}}\right] \tag{59}$$

The stresses on $x_2=0$ can now be obtained from equations (46), (56), and (59) in the form

$$\sigma_{i2}=\frac{q_0(a+c)^2}{8K}\frac{\mathrm{sgn}(x_1)}{\sqrt{x_1^2-a^2}}\qquad |x_1|>a\quad i=1,3 \tag{60}$$

$$\sigma_{22}=\left\{\frac{q_0b_{2j}G_j}{b_{22}K}\left(\frac{a+c}{2}\right)^2+\sigma_0(2x_1-c+a)\right\}\frac{\mathrm{sgn}(x_1)}{\sqrt{(x_1+a)(x_1-c)}} + \left(\frac{a+c}{2}\right)^2\frac{(b_{21}G_1+b_{23}G_3)q_0}{2b_{22}K}\frac{[H(x_1-a)-H(-a-x_1)]}{\sqrt{x_1^2-a^2}}\qquad x_1>c;\quad x_1<-a; \tag{61}$$

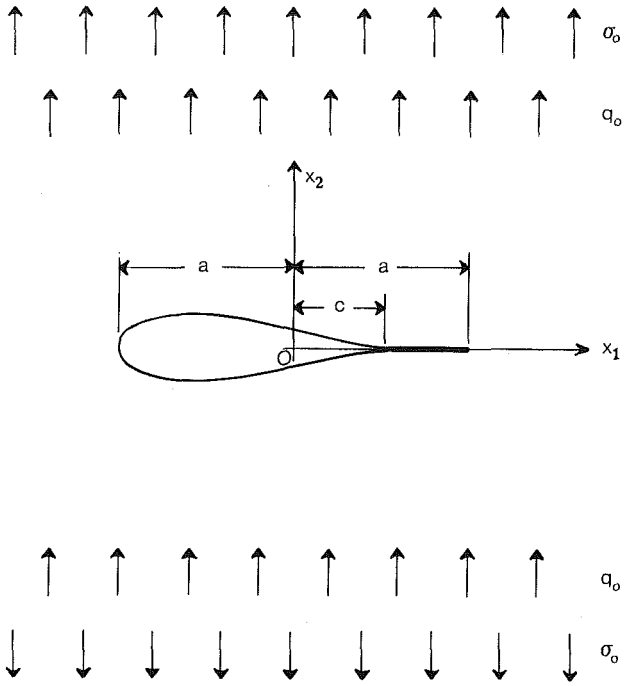


Fig. 2 The plane crack with partial contact

Downloaded 03 May 2010 to 171.66.16.21. Redistribution subject to ASME license or copyright; see http://www.asme.org/terms/Terms_Use.cfm

To complete the solution, we must determine the length of the separation zone from the condition that the stress σ_{22} tend to zero at $x_1 \to c$. Thus, from equation (61) we have

$$c = -\frac{4Kb_{22}\sigma_0}{q_0 b_{2j} G_j} - a \tag{62}$$

Using equation (62), equations (60) and (61) can then be written

$$\sigma_{i2} = 2K \left[\frac{b_{22}}{b_{2j}G_j}\right]^2 G_i \frac{\sigma_0^2}{q_0} \frac{\mathrm{sgn}(x_1)}{\sqrt{x_1^2 - a^2}} \quad |x_1| > a \quad i = 1,3 \tag{63}$$

$$\sigma_{22} = \mp \sigma_0 \sqrt{\frac{x_1 - c}{x_1 + a}} - \frac{2b_{22}K\sigma_0^2(b_{21}G_1 + b_{23}G_3)}{q_0(b_{2j}G_j)^2} \times \frac{[H(x_1 - a) - H(-a - x_1)]}{\sqrt{x_1^2 - a^2}} \qquad \begin{matrix} -;\ x_1 > c \\ +;\ x_1 < -a \end{matrix} \tag{64}$$

Crack Opening Displacement and Stress Intensity Factors. By the definition of a dislocation, we have that the crack opening displacement can be obtained as

$$\Delta u_2 = -\int_{-a}^{x_1} B_2(\xi)d\xi = -b_{2j}\int_{-a}^{x_1} d_j(\xi)d\xi \tag{65}$$

$$= \frac{q_0 b_{2j} G_j}{K} (x_1 - c)\sqrt{(x_1 + a)(c - x_1)} \tag{66}$$

using equations (56), (59), and (62). Thus the crack opening displacement will be positive for $-a < x_1 < c$ if $q_0 b_{2j} G_j < 0$, as assumed. We note that the derivative of Δu_2 is also zero at the transition from contact to separation ($x_1 = c$), as in conventional contact problems.

From equations (63) and (64) it can be seen that all components σ_{i2} ($i = 1, 2, 3$) of the stress tensor are singular at both ends of the crack (i.e., $x_1 \pm a$). The stress intensity factors are given by:

$$K_I = -\frac{2b_{22}(b_{21}G_1 + b_{23}G_3)K}{\sqrt{2a}(b_{2j}G_j)^2} \frac{\sigma_0^2}{q_0} \quad ; \quad x_1 = a+ \tag{67}$$

$$= 2\left[-\frac{b_{22}K\sigma_0^3}{b_{2j}G_j q_0}\right]^{1/2} + \frac{2b_{22}(b_{21}G_1 + b_{23}G_3)K}{\sqrt{2a}(b_{2j}G_j)^2} \frac{\sigma_0^2}{q_0}; \quad x_1 = -a- \tag{68}$$

$$K_{II,III} = \pm K\sqrt{\frac{2}{a}} G_i \left[\frac{b_{22}}{b_{2j}G_j}\right]^2 \frac{\sigma_0^2}{q_0}; \ i = 1,3; \qquad \begin{matrix} +;\ x_1 = a+ \\ -;\ x_1 = -a- \end{matrix} \tag{69}$$

Notice that stress intensity factors in all three modes are obtained at both ends of the crack, including a nonzero K_I at the closed tip, $x_1 = a$. This results from coupling between the tangential displacements (slip) in the contact zone and the stress component σ_{22}, on $x_2 = 0$.

Acknowledgment

The authors are pleased to acknowledge the support of the National Science Foundation under the great number MSM-8419324.

References

Atkinson, C., and Clements, D. L., 1977, "On Some Crack Problems in Anisotropic Thermoelasticity," *Int. J. Solids Structures*, Vol. 13, pp. 855–864.

Barber, J. R., and Comninou, M., 1983, "The Penny-Shaped Interface Crack With Heat Flow: II Imperfect Contact," ASME JOURNAL APPLIED MECHANICS, Vol. 50, pp. 770–776.

Florence, A. L., and Goodier, J. N., 1963, "The Linear Thermoelastic Problem of Uniform Heat Flow Disturbed by a Penny-Shaped Insulated Crack," *Int. J. Eng. Sci.*, Vol. 1, pp. 533–540.

Martin-Moran, C. J., Barber, J. R., and Comninou, M., 1983, "The Penny-Shaped Interface Crack With Heat Flow: I Perfect Contact," ASME JOURNAL APPLIED MECHANICS, Vol. 50, pp. 29–36.

Olesiak, Z., and Sneddon, I. N., 1960, "The Distribution of Thermal Stress in an Infinite Elastic Solid Containing a Penny-Shaped Crack," *Arch. Rational Mech. Anal.*, Vol. 4, pp. 238–254.

Stroh, A. N., 1958, "Dislocations and Cracks in Anistropic Elasticity," *Phil. Mag.*, Vol. 3, pp. 625–646.

Sturla, F. A., and Barber, J. R., 1988, "Thermoelastic Green's Functions for Plane Problems in General Anistropy," ASME JOURNAL OF APPLIED MECHANICS, under review.

Tasi, Y. M., 1983, "Transversely Isotropic Thermoelastic Problem of Uniform Heat Flow Disturbed by a Penny-Shaped Crack," *J. Thermal Stresses*, Vol. 6, pp. 379–389.

Downloaded 03 May 2010 to 171.66.16.21. Redistribution subject to ASME license or copyright; see http://www.asme.org/terms/Terms_Use.cfm

Generalized Coupled Transient Thermoelastic Plane Problems by Laplace Transform/Finite Element Method

Tei-Chen Chen

Cheng-I Weng

Department of Mechanical Engineering,
National Cheng Kung University,
Tainan, Taiwan, R.O.C.

A general finite-element model is proposed to deal with dynamic theromelastic problems especially with longer transient period. The method consists of formulating and solving the problem in the Laplace transform domain by the Finite Element Method (FEM) and then numerically inverting the transformed solution to obtain the time-domain response. Therefore, the transient solutions at any time could be evaluated directly. A number of examples are presented which demonstrate the accuracy, efficiency, and versatility of the proposed method, and show the effects of relaxation times, inertia, and thermoelastic coupling terms.

Introduction

A thermal shock problem arises when thermal stresses are generated by a sudden change in temperature and could be found in many industrial practices. Owing to the mathematical difficulties encountered in coupled thermoelasticity, mainly due to the presence of the inertia and thermoelastic coupling terms in the governing equations, this kind of problem that admits to a closed-form solution is evidently scarce. Most of the investigations, such as Youngdahl and Sternberg (1961), Takeuti and Noda (1973), Ghosn and Sabbaghian (1982), etc., either have been confined to only one-dimensional problems or to the simplification of the problems by disregarding one of the abovementioned factors. However, if both the dynamic effect and thermoelastic coupling term, that may be significant in some applications, are taken into consideration, it will be too complicated to approach analytically. Moreover, if more complex geometries, more sophisticated coupled theories with relaxation times (for instance, generalized coupled thermoelasticity proposed by Lord and Shulman (1967) or by Green and Lindsay (1972), which results in a finite speed of propagation for heat and displacement fields) and multiple substances are involved additionally, numerical techniques, instead of analytical methods, have to be restored. Due to the versatility of the finite-element technique, considerable attention has been focused on this method in many engineering fields. However, to the author's knowledge, within the field of coupled thermoelasticity, the treatment of time gradient in the finite-element equations has been generally discretized by finite-difference algorithm (Prevost and Tao, 1983). Therefore, the solutions, at any time, shall be evaluated step-by-step from initial values, and an optimum difference algorithm (Hughes and Liu, 1978) for time increment is required to achieve both numerical stability and rapid convergence. Due to this severe limitation on the interval of the time-step, an excessive amount of computer time may be required to obtain the long-term transient solutions.

A general and efficient numerical procedure, by combining the Finite Element Method and Laplace transform technique, is proposed in this work to analyze the dynamic problems with generalized coupled thermoelastic theory.

The solid, under consideration, may be composed of composite materials with irregular geometry and subjected to arbitrary time-dependent thermal and/or mechanical loading conditions, under either quasi-static or dynamic cases, thermoelastic coupled or uncoupled conditions, with or without finite wave speeds for thermal disturbances. Therefore, the effects of the foregoing factors on transient response could be easily identified and accurately assessed.

The governing equations are first formulated by the finite-element technique in the Laplace transform domain. Then transformed solutions are obtained. From these transformed solutions, the response in the real domain, at any time, could be evaluated directly.

Mathematical Analysis

1) Basic Equations. Basic equations and corresponding finite-element formulation for both analysis of deformation

Contributed by the Applied Mechanics Division for presentation at the Winter Annual Meeting, Chicago, IL, November 28 to December 2, 1988, of The American Society of Mechanical Engineers.

Discussion on this paper should be addressed to the Editorial Department, ASME, United Engineering Center, 345 East 47th Street, New York, N.Y. 10017, and will be accepted until two months after final publication of the paper itself in the JOURNAL OF APPLIED MECHANICS. Manuscript received by ASME Applied Mechanics Division, September 4, 1987; final revision, November 24, 1987.

Paper No. 88-WA/APM-29.

Copyright © 1988 by ASME

Downloaded 03 May 2010 to 171.66.16.21. Redistribution subject to ASME license or copyright; see http://www.asme.org/terms/Terms_Use.cfm

and heat transfer are derived from the equations of motion and energy balance equation expressed by

$$\sigma_{ij,\,j} + \rho \mathbf{b}_i = \rho_i \ddot{\mathbf{U}}_i \tag{1}$$

$$\rho T \dot{\eta} = -\mathbf{q}_{k,\,k} + Q \tag{2}$$

where σ_{ij} are the components of stress tensor; ρ the density; $\mathbf{b}_i$ the body-force vector; $\mathbf{U}_i$ the components of displacement vector; T the absolute temperature; η the entropy density; $\mathbf{q}_k$ the heat-flux vector; Q the heat source.

A superposed dot ($\dot{}$) is used to denote material time differentiation and a comma ($_{,\,j}$) to denote partial differentiation with respect to coordinate x_j ($j = 1, 2, 3$).

The constitution equations are given by (Prevost and Tao, 1983)

$$\sigma_{ij} = C_{ijkl}\epsilon_{kl} - \beta_{ij} T_m (\theta + t_1 \dot{\theta}) \tag{3a}$$

$$q_i + t_0 \dot{q}_i = -K_{ij} T_m \theta_{,\,j} \tag{3b}$$

$$\eta = \eta_0 + C_E \theta + C_E t_2 \dot{\theta} + \frac{1}{\rho} \beta_{ij} \epsilon_{ij} \tag{3c}$$

where C_{ijkl} is the tensor of elastic moduli; β_{ij} the tensor of thermal moduli; K_{ij} the tensor of thermal conductivity; C_E the specific heat for process with invariant strain tensor; θ the dimensionless temperature ($\theta = (T - T_0)/T_m$); ϵ_{ij} the strain tensor ($\epsilon_{ij} = (U_{i,\,j} + U_{j,\,i})/2$); T_0 the reference temperature chosen such that $(T - T_0)/T_0 \ll 1$; T_m the maximum temperature difference between applied temperature and T_0; t_0 the relaxation time (proposed by Lord and Shulman); t_1, t_2 the relaxation times (proposed by Green and Lindsay).

By substituting equations (3*a–c*) into equations (1) and (2), the resulting generalized field equations, in terms of displacement $\mathbf{U}_i$ and temperature θ, are obtained as follows

$$\rho \ddot{\mathbf{U}}_i + (t_1 \beta_{ij} T_m \dot{\theta})_{,\,j} + (\beta_{ij} T_m \theta - C_{ijkl} U_{k,\,l})_{,\,j} = \rho \mathbf{b}_i \tag{4a}$$

$$\rho C_E (t_2 + t_0)\ddot{\theta} + \rho C_E \dot{\theta} + \beta_{ij} T_0 (\dot{U}_{i,\,j} + t_0 \ddot{U}_{i,\,j})/T_m - (K_{ij}\theta_{,\,j})_{,\,i} = (Q + t_0 \dot{Q})/T_m \tag{4b}$$

In Green and Lindsay's theory, $t_0 = 0$ and two relaxation times t_1 and t_2 are introduced. In Lord and Shulman's theory, $t_1 = t_2 = 0$ and Fourier's law of heat conduction is modified by the introduction of the relaxation time t_0. When t_0, t_1 and t_2 vanish, equations (4*a*, *b*) reduce to the classical coupled theory.

2 Finite-Element Formulation. The formulation associated with this initial-boundary-value problem of coupled thermoelasticity is obtained in a standard way. The solid, under consideration, is divided into nonoverlapping finite-element and nodal points. Two sets of shape functions are introduced to approximate both the displacement and temperature fields on the element level.

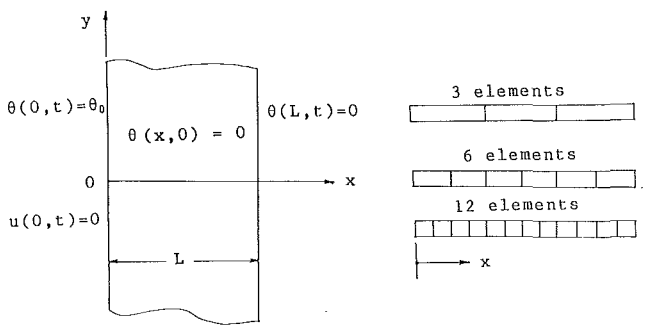


Fig. 1(a) Problem geometry Fig. 1(b) Finite element mesh

Fig. 1 Layer of material subjected to surface heating

$$\{U\} = \begin{Bmatrix} U_x \\ U_y \end{Bmatrix} = [N]\{\mathbf{U}^e\} \tag{5}$$

$$\theta = \sum_{i=1}^{n} N_i \theta_i = [N']\{\theta^e\} \tag{6}$$

Substitution into the integro-differential equations of variational form, which are derived from equations (4*a*, *b*), with equations (5) and (6), the following equations expressed by matrices could be obtained.

$$\sum_{e=1}^{N} \left(\left[\begin{array}{c:c} [M^{(e)}] & 0 \\ \hdashline t_0[H^{(e)}] & (t_0 + t_2)[C^{(e)}] \end{array} \right] \left\{ \begin{array}{c} \{\ddot{\mathbf{U}}^e\} \\ \hdashline \{\ddot{\theta}^e\} \end{array} \right\} + \left[\begin{array}{c:c} 0 & t_1[G^{(e)}] \\ \hdashline [H^{(e)}] & [C^{(e)}] \end{array} \right] \left\{ \begin{array}{c} \{\dot{\mathbf{U}}^e\} \\ \hdashline \{\dot{\theta}^e\} \end{array} \right\} + \left[\begin{array}{c:c} [K_1{}^{(e)}] & [G^{(e)}] \\ \hdashline 0 & [K_2{}^{(e)}] \end{array} \right] \left\{ \begin{array}{c} \{\mathbf{U}^e\} \\ \hdashline \{\theta^e\} \end{array} \right\} = \left\{ \begin{array}{c} \{F_1{}^{(e)}\} \\ \hdashline \{F_2{}^{(e)}\} \end{array} \right\} \right) \tag{7}$$

In equation (7), some matrices involving integrals are defined as

$$\begin{aligned}
[M^{(e)}] &= \int_{V^{(e)}} [N]^T \rho [N] dV, \quad [K_1{}^{(e)}] = \int_{V^{(e)}} B_1]^T [D][B_1] dV, \\
[G^{(e)}] &= \int_{V^{(e)}} [B_1]^T [E][N'] dV, \\
& \quad [C^{(e)}] = \int_{V^{(e)}} C_E \rho [N']^T [N'] dV, \\
[F_1{}^{(e)}] &= \int_{V^{(e)}} [N]^T \rho \{b\} dV + \int_{S^{(e)}} [N]^T \{f\} ds, \\
[K_2{}^{(e)}] &= \int_{V^{(e)}} [K][M]^T [M] dV + \int_{S^{(e)}} h[N']^T [N'] dS, \\
[H^{(e)}] &= \int_{V^{(e)}} [\beta][N']^T [B_2] T_0 dV/T_m, \\
[F_2{}^{(e)}] &= \int_{V^{(e)}} (Q + t_0 \dot{Q})[N'] dV/T_m \\
& \quad + \int_{S_c{}^{(e)}} h\theta_s [N'] dS = \int_{S_0{}^{(e)}} q_n [N'] dS,
\end{aligned} \tag{8a}$$

in which

$$[B_1] = \left[\begin{array}{cc:c:cc} \dfrac{\partial N_1}{\partial x} & 0 & & \dfrac{\partial N_n}{\partial x} & 0 \\ 0 & \dfrac{\partial N_1}{\partial y} & \cdots\cdots & 0 & \dfrac{\partial N_n}{\partial y} \\ \dfrac{\partial N_1}{\partial y} & \dfrac{\partial N_1}{\partial x} & & \dfrac{\partial N_n}{\partial y} & \dfrac{\partial N_n}{\partial x} \end{array} \right] \tag{8b}$$

$$[B_2] = \left\{ \begin{array}{cc:c:cc} \dfrac{\partial N_1}{\partial x} & \dfrac{\partial N_1}{\partial y} & \cdots\cdots & \dfrac{\partial N_n}{\partial x} & \dfrac{\partial N_n}{\partial y} \end{array} \right\} \tag{8c}$$

Downloaded 03 May 2010 to 171.66.16.21. Redistribution subject to ASME license or copyright; see http://www.asme.org/terms/Terms_Use.cfm

$$M_{ij} = N'_{i,j}$$

where $\{\mathbf{U}^e\}$ is the vector of nodal point displacements; $\{\theta^e\}$ the vector of nodal point temperature; $[N]$ the shape function for displacement; $[N']$ the shape function for temperature; e the element number; N the total number of elements; i the node number; n the number of nodes per element; q_n the heat flow along the boundary surface S_0; h the heat transfer coefficient; S_c the boundary surface wherein heat convection is specified; θ_s the environment temperature.

3 Laplace Transform. Making application of the Laplace transform, defined by

$$\bar{f}(s) = \int_0^\infty e^{-st} f(t)\,dt \tag{9}$$

with respect to both sides of equation (7), and supposing all the initial values to be zero, it yields

$$\sum_{e=1}^{N} \left(\left[\begin{array}{c|c} [K_1{}^{(e)}] + s^2[M^{(e)}] & (1+t_1 s)[G^{(e)}] \\ \hline (s+t_0 s^2)[H^{(e)}] & \{s+(t_0+t_2)s^2\}\cdot \\ & [C^{(e)}] + [K_2{}^{(e)}] \end{array} \right] \left\{ \begin{array}{c} \{\bar{\mathbf{U}}^e\} \\ \hline \{\bar{\theta}^e\} \end{array} \right\} = \left\{ \begin{array}{c} \{\bar{F}^{(e)}\} \\ \hline \{\bar{F}_2{}^{(e)}\} \end{array} \right\} \tag{10}$$

where $\{\bar{\mathbf{U}}^e\}$ and $\{\bar{\theta}^e\}$ are the vectors of nodal point displacement and temperature in the transformed domain, respectively; s the Laplace transform parameter ($s = v + iw$).

The solutions of equation (10) for the transformed displacement and temperature vectors are evaluated numerically by "front method," for a sequence of values of "s" that is required by the scheme of numerical inversion of the transformed solutions.

Method of Inversion

In this paper, an accurate and efficient numerical method known as "Korrektur," proposed by Honig and Hirdes (1984), is used to obtain the inversion of the Laplace transform. This inversion method, based upon a Fourier series expansion developed by Durbin (1973), allows a remarkable reduction of the discretization error without increasing the truncation error by the simultaneous application of a method to accelerate the convergence of the Fourier series, and a procedure to calculate approximately the optimal value of the free parameter, v; that is, the real part of the Laplace transform parameter s.

The algorithm of inversion method combines both finite Fourier consine and sine transforms to establish the following Laplace inversion formula for a function $f(t)$ whose transform is $\bar{f}(s)$.

$$f(t) = \frac{e^{vt}}{\tau}\left[-\frac{1}{2}\mathrm{Re}\{\bar{f}(v)\} + \sum_{k=1}^{\infty} \mathrm{Re}\left\{\bar{f}\left(v + \frac{ik\pi}{\tau}\right)\right\}\cos\frac{k\pi t}{\tau} - \sum_{k=0}^{N} \mathrm{Im}\left\{\bar{f}\left(v+\frac{ik\pi}{\tau}\right)\right\}\sin\frac{k\pi t}{\tau}\right]$$

$$-Fl(v, t, \tau) + FA(n, v, t, \tau) \quad \text{for } 0 < t < 2\tau \tag{11}$$

where $Fl(v, t, \tau)$ is the discretization error, given by

$$Fl(v, t, \tau) = \sum_{k=1}^{\infty} e^{-2vk\tau} f(2k\tau + t) \tag{12a}$$

$FA(N, v, t, \tau)$ the truncation error, given by

$$FA(N, v, t, \tau) = \frac{e^{vt}}{\tau}\left[\sum_{k=N+1}^{\infty} \left\{ \mathrm{Re}\left\{\bar{f}\left(v + \frac{ik\Pi}{\tau}\right)\cos\frac{k\Pi t}{\tau}\right\} - \mathrm{Im}\left\{\bar{f}\left(v+\frac{ik\Pi}{\tau}\right)\sin\frac{k\Pi t}{\tau}\right\}\right] \right. \tag{12b}$$

where τ is the half period of $f(t)$.

It is obvious from equation (12a) that the discretization error can be made arbitrarily small if the product $v\tau$, namely, free parameter, is sufficiently large. However, the truncation error shown as equation (12b) may diverge for a large value of $v\tau$ in case "τ" is selected to be equal to "t."

The "Korrektur" method allows a reduction of the discretization error without enlarging the truncation error by an optimal choice of the free parameter $v\tau$. Therefore, in a wide range of application, a high accuracy can be achieved with less terms of the Fourier series.

The present method can efficiently compute the specific nodal displacement or temperature at a specific time by directly using the optimal free parameter at that nodal point. However, this kind of procedure will take an enormous computer time and lose its advantage in case all the nodal solutions at a specific time are completely required. From a viewpoint of engineering applications, we are frequently interested in the stress distributions in the whole domain; therefore, the displacement and temperature at every node in the given domain are fully required from which the stresses at Gaussian sampling points could be hereby evaluated. To meet this actual requirement, an efficient alterate approach, that is capable of evaluating a portion of nodal temperatures and

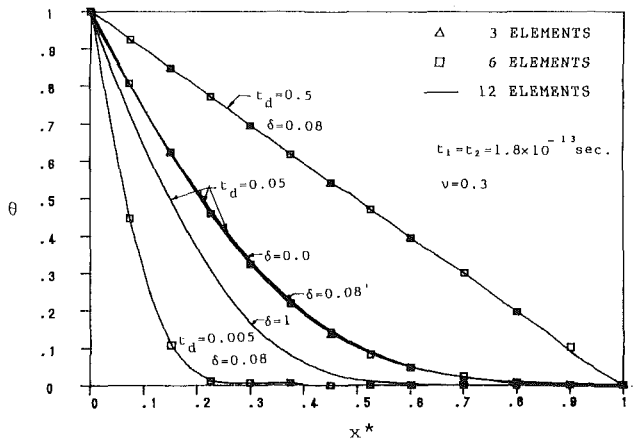


Fig. 2(*a*) Temperature distributions for various time

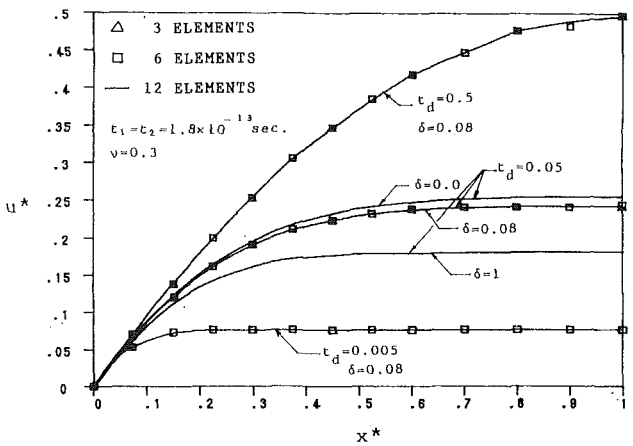


Fig. 2(*b*) Displacement distributions for various time

Downloaded 03 May 2010 to 171.66.16.21. Redistribution subject to ASME license or copyright; see http://www.asme.org/terms/Terms_Use.cfm

Table 1 Optimal free parameters v_T of each nodal variable corresponding to $t_d = 0.05$

node position	3		6		12		18		24	
variables	u	θ	u	θ	u	θ	u	θ	u	θ
40 terms approxi.	6.2	6.3	6.0	6.9	5.9	5.8	6.0	6.3	5.8	6.2
35 terms approxi.	6.2	6.3	6.0	6.7	6.0	5.8	5.8	6.3	5.7	6.4
30 terms approxi.	6.0	6.3	6.1	6.7	6.0	5.8	5.8	6.3	5.8	6.3
25 terms approxi.	6.0	6.3	6.0	6.7	6.0	5.8	5.8	6.3	5.8	6.4
20 terms approxi.	6.3	6.4	6.1	6.7	6.0	5.9	5.8	6.3	5.8	6.3
15 terms approxi.	6.4	6.2	6.1	6.7	6.0	5.6	5.8	6.3	5.8	6.3

displacements simultaneously, is also developed in the present work. First, the optimal values of free parameter v_T at each node are evaluated. Then a number of data zones are classified by collecting a group of free parameters, that are similar in magnitude with a small deviation. Finally, an assigned free parameter, by averaging the lowest and the highest values of each zone, is used as a basis to calculate solutions at that zone in the real time domain. It could be found in the following examples that not only the distribution of optimal free parameter at each node always shows a relatively small range, but also the behavior of Fourier series shows a good convergence. Therefore, generally only one or a few assigned free parameters are required to compute the solutions in the whole domain with excellent convergence. In addition, it is worthwhile to mention that since there exists no time step, it is obvious that the present method takes less computer time if solutions, after a longer time, are required.

Numerical Application

In the following examples, the eight-node isoparametric, quadrilateral element is used for both displacement and temperature calculations, and the material is assumed to be homogeneous and isotropic. Moreover, both the inertia and thermoelastic coupling terms are taken into account without extra remarks.

Example 1. The problem geometry is shown in Fig. 1. A layer of an elastic material, occupying the region $0 \le x \le L$, is subjected to surface heating on its stationary boundary $x = 0$, by sudden exposure to a temperature $T_m + T_0$ (i.e., $\theta = 1$) at time $t = 0$, and keeps original temperature on the traction-free boundary $x = L$. The solutions are conveniently interpreted in terms of the following dimensionless variables

$$x^* = \frac{x}{L}, \quad U^* = \frac{(\lambda + 2\mu)U}{\beta L T_m}, \quad \delta = \frac{\beta^2 T_0}{\rho C_E(\lambda + 2\mu)}, \quad t_d = \frac{\kappa t}{L^2}$$

where λ and μ are the Lamé constants; κ the thermal diffusivity ($\kappa = K/\rho C_E$); α_t the linear thermal expansion coefficient; $\beta = (3\lambda + 2\mu)\alpha_t = E\alpha_t/(1-2\nu)$; δ the thermoelastic coupling coefficient. The material properties are selected as follows:

$$\nu = 0.3; \quad t_1 = t_2 = 1.8 \times 10^{-13}\text{s}; \quad t_0 = 0$$

This problem is basically one-dimensional. Three different sizes of element mesh, consisting of 3, 6 and 12 elements, respectively, are selected to estimate the effect of the element size on the convergence of the solutions. The values of optimal free parameter corresponding to time $t_d = 0.05$ at each nodal displacement and temperature with different terms of the Fourier series are listed in Table 1. It shows that the values of free parameter for each nodal variable are always distributed within a small range, and make the convergence very well even

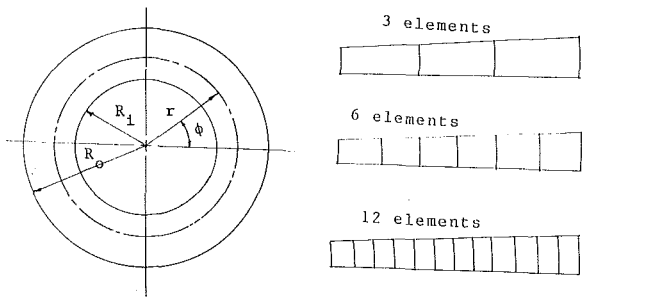


Fig. 3(a) Problem geometry Fig. 3(b) Finite element mesh

Fig. 3 Circular annular cylinder with infinite length

though only 15 terms of Fourier series are used. Solutions evaluated by an assigned optimal free parameter $v_T = 6.4$; that is, the average of the maximum and the minimum values, with different terms of Fourier series, are compared with that evaluated by individual optimal free parameter of each node with 40 terms of the Fourier series. It could be found that only 15-terms approximation are required to evaluate the solutions at the whole domain with excellent convergence by only one assigned free parameter with the maximum error or less than 0.1 percent. Figures 2(*a*, *b*) show the temperature and displacement distributions for various times with different mesh size. It could be found that, from previous results, there is no distinct discrepancy among the aforementioned three different element sizes. Therefore, it could be concluded that the present solutions have already converged to the true solutions with the mesh size used.

In this example, the total consumption in computer time to get the final solutions of each node at a specific time is equivalent to take 60 times in solving equation (10), wherein 45 terms for evaluating optimal free parameter of each node, and 15 times for calculating the solutions of each node with an assigned free parameter.

Example 2. This example considers the problem of an infinitely long annular cylinder, shown in Fig. 3, with inner and outer radii R_i and R_0, respectively, which is subjected to time-dependent or constant surrounding temperature on its traction-free boundary surfaces. The solutions are conveniently interpreted in terms of the following dimensionless variables

$$r^* = \frac{r}{R_i}, \quad U^* = \frac{(\lambda + 2\mu)U}{\beta R_i T_m}, \quad \sigma_{ij}{}^* \frac{\sigma_{ij}}{(3\lambda + 2\mu)\alpha_t T_m}, \quad t_d = \frac{\kappa t}{R_i^2}$$

The dimensions of the geometry and the material properties, in terms of dimensionless quantities, are selected as follows

$$R_0/R_i = 2, \quad \nu = 0.3, \quad H = hR_i/K = 2, \quad t_1 = t_2 = t_0 = 0$$

where h is the heat transfer coefficient; K the thermal conduction coefficient. Thus the boundary conditions, in terms of the dimensionless quantities, are

$$\partial\theta/\partial r^* = H\{\theta - (1.5 + 0.5\sin\omega t)\} \quad \text{at} \quad r = R_i, \quad t > 0$$

$$\partial\theta/\partial r^* = H(1.0 - \theta) \quad \text{at} \quad r = R_0, \quad t > 0$$

Since both geometry and loading conditions are axial symmetric, this problem is essentially one-dimensional and has been solved analytically (Yang, et al., 1986) within the context of classical quasi-static coupled thermoelasticity (i.e., $t_0 = t_1 = t_2 = 0$) by taking the following approximations

$$I_n(rs) = \frac{e^{rs}}{\sqrt{2\pi rs}}, \quad K_n(rs) = \frac{e^{-rs}}{\sqrt{2rs/\pi}}$$

where $I_n(rs)$ and $K_n(rs)$ are the modified Bessel functions of the first kind, and the second kind of order n, respectively. Consequently, it is apparent that these analytical solutions are available for short time only.

Downloaded 03 May 2010 to 171.66.16.21. Redistribution subject to ASME license or copyright; see http://www.asme.org/terms/Terms_Use.cfm

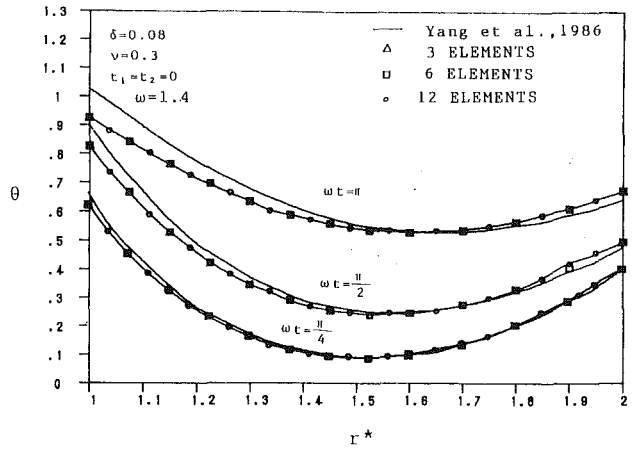


Fig. 4(a) Temperature distributions for various time

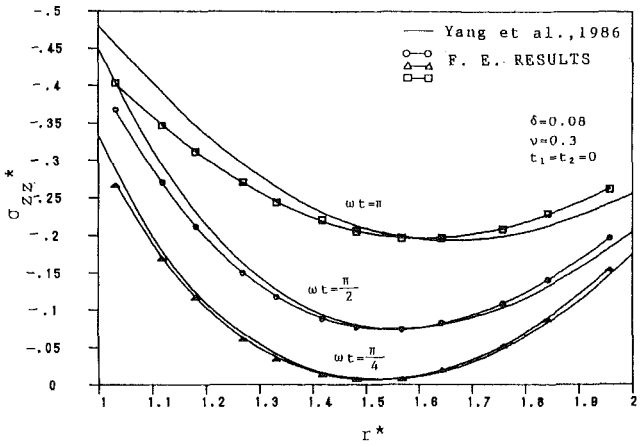


Fig. 4(b) σ_{zz}^* as a function of r^* for various time

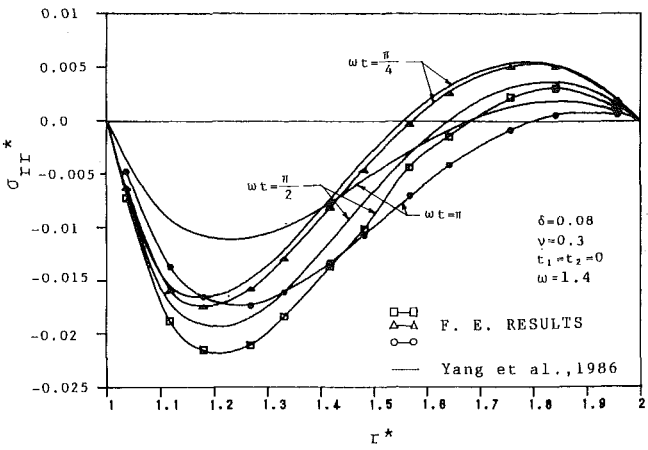


Fig. 4(c) σ_{rr}^* as a function of r^* for various time

The values of optimal-free parameter $v\tau$ for various dimensionless times at each nodal temperature and displacements range from 5.6 to 7.4. In order to accelerate the convergence of the Fourier series evenly in the domain considered, an assigned value of optimal parameter 6.5, by averaging the maximum and the minimum data, is also selected as the basis of the optimal parameter for the whole domain. It could be found that, in comparison with the reference value of which 40 terms of Fourier series and exactly optimal free parameter of each node are considered, there is a maximum error less than 0.1 percent if 15 terms of the Fourier series is selected. Figure 4(a) shows the temperature distributions for various dimensionless times. Figures 4(b, c) show the variations in

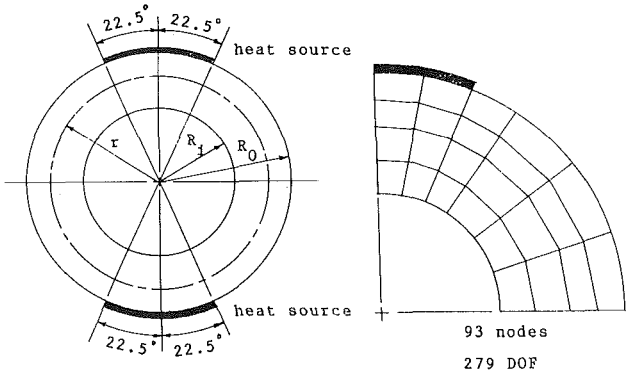


Fig. 5(a) Problem geometry Fig. 5(b) Finite element mesh

Fig. 5 Circular annular cylinder with infinite length subjected to surface heat source

thermal stresses. It also could be found that the effect of inertia term on the values of temperature and displacement at various conditions is slight and could be neglected satisfactorily. The previously mentioned results show good agreement with analytical solutions at condition $\omega t = \Pi/4$. However, considerable discrepancy occurred especially around the inner surface at conditions with higher ωt. In order to test the accuracy of the present solutions, three different sizes of element mesh, consisting of 3, 6 and 12 elements, respectively, are selected to estimate the effect of the element size on the convergence of the solutions. It could be found that there is no distinct discrepancy between these different element sizes. Consequently, it could be concluded that the present solutions have already converged to the true solutions with the mesh size used, and thus the previous analytical solutions are no more available at conditions with higher ωt.

Example 3. The geometry and material properties of this example are the same as that of the second example. However, this infinitely long annular cylinder is loaded by two heat sources acting on the upper and the lower sides of the body, respectively. Suppose the intensity of each heat source divided by T_m is equal to 2.0×10^6 $W/m^2 - °C$, and the remained boundary surfaces are traction-free and subjected to constant surrounding temperature. The Nusselt number H, defined as $H = hR_i/K$, is assumed to be equal to 2.0×10^{-2}. The problem is symmetric about both X and Y-axes; therefore, only a quarter of the cylinder needs to be modeled. Figure 5 shows the geometry and finite-element mesh of the problem. The values of optimal free parameters of each nodal variable at time $t_d = 5.0$ are ranged from 6.2 to 7.8, then only one assigned optimal free parameter 7.0 is sufficiently used to calculate the temperature and displacements of each node in the whole domain. The variations of temperature and stresses at $t_d = 5.0$ are illustrated in Figs. 6(a, b).

Discussion and Conclusions

In this paper, a general finite-element technique/Laplace transform model is proposed to analyze generalized coupled transient thermoelastic plane problems. To illustrate the numerical versatility, accuracy, and efficiency of the present method, three different examples have been analyzed. It could be concluded that all the results are stable and convergent to their true solutions.

Since the present model takes off the time dimension by the Laplace transform, it is easy and it will take similar computer time to calculate a solution of a specific location at a specific time that is either long or short. This kind of approach is quite different from the conventional procedure that treats time do-

Downloaded 03 May 2010 to 171.66.16.21. Redistribution subject to ASME license or copyright; see http://www.asme.org/terms/Terms_Use.cfm

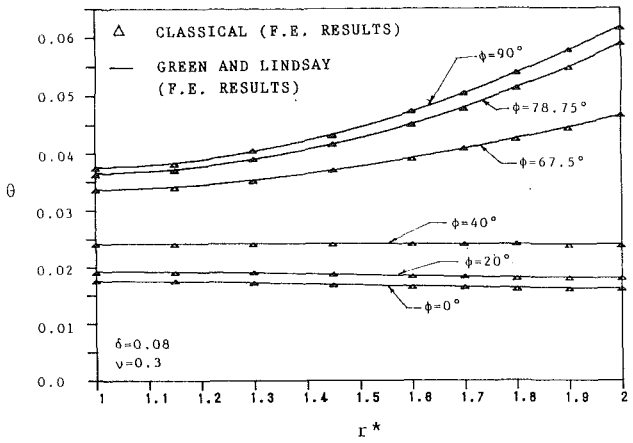


Fig. 6(a) Temperature distributions for $t_d = 5.0$

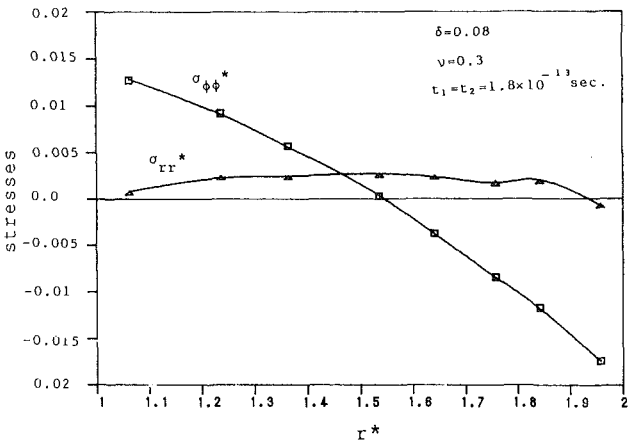


Fig. 6(b) Stress distributions for $t_d = 5.0$ ($\phi = 52.8°$)

main by finite difference or Runge-Kutte method. The latter process will thus lead to a step-by-step or recurrence calculation and is appropriate to evaluate a short-time solution. The only shortcoming of the present method is concerned with the treatment of the numerical Laplace inversion, which, for highly accurate results, requires more computer time [generally, it is equivalent to take 60 times in solving equation (10)] than step-by-step integration schemes. However, it is apparent that the present method is still more economical and better than the classical finite-difference techniques in case a long-time solution is required.

It could be shown from the results of the previous examples that the influence of the relaxation times is very small for a short long-time solution, but this factor is quite important for the solution within a very short-time duration (Prevost and Tao, 1983). Furthermore, the individual effect of inertia and thermoelastic coupling terms, that may be significant in some practical applications, could be easily taken into consideration and accurately assessed.

References

Durbin, F., 1973, "Numerical Inversion of Laplace Transforms: An Effective Improvement of Dubner and Abates's Method," *Comput. Journal*, Vol. 17, pp. 371–376.

Ghosn, A. H., and Sabbaghian, M., 1982, "Quasi-Static Coupled Problem of Thermoelasticity for Cylindrical Regions," *Journal Therm. Stresses*, Vol. 5, pp. 299–311.

Green, A. E., and Lindsay, K. E., 1972, "Thermoelasticity," *Journal of Elasticity*, Vol. 2, pp. 1–7.

Honig, G., and Hirdes, U., 1984, "A Method for the Numerical Inversion of Laplace Transforms," *Journal of Computational and Applied Mathematics*, Vol. 10, pp. 113–132.

Lord, H., and Shulman, Y., 1967, "A Generalized Dynamical Theory of Thermoelasticity," *Journal of the Mechanics and Physics of Solids*, Vol. 15, p. 299.

Prevost, J. H., and Tao, D., 1983, "Finite Element Analysis of Dynamic Coupled Thermoelasticity Problems With Relaxation Times," ASME JOURNAL OF APPLIED MECHANICS, Vol. 50, pp. 817–822.

Takeuti, Y., and Noda, N., 1973, "Transient Thermoelastic Problem in a Polygonal Cylinder With a Circular Hole," ASME JOURNAL OF APPLIED MECHANICS, Vol. 40, pp. 935–940.

Yang, Y. C., Wang, T. S., and Chen, C. K., 1986, "Thermoelastic Transient Response of an Infinitely Long Annular Cylinder," *Journal of Thermal Stresses*, Vol. 9, pp. 19–30.

Youngdahl, C. K., and Sternberg, Eli., 1961, "Transient Thermal Stresses in a Circular Cylinder," ASME JOURNAL OF APPLIED MECHANICS, Vol. 28, pp. 25–34.

Downloaded 03 May 2010 to 171.66.16.21. Redistribution subject to ASME license or copyright; see http://www.asme.org/terms/Terms_Use.cfm

Partial Release and Relocking of a Frictionally Locked Crack Due to Moving Tensile Loads

D. A. Mendelsohn
Department of Engineering Mechanics,
Boyd Laboratory,
The Ohio State University,
Columbus, OH 43210-1181
Assoc. Mem. ASME

K. H. Whang
Korea Institute of Machinery and Metals,
Changwon, Kyungsangnamdo, Korea

A finite length 2D crack is closed by remote compression followed by remote shear, and is sufficiently rough so that it remains locked with zero initial tangential crack-face shift. Then a pair of equal and opposite concentrated line loads acting in tension across the crack plane pass over the crack, causing partial opening and shift and then reclosure with residual (locked-in) shift and associated shear Stress Intensity Factors (SIF). Analytical and numerical solutions of the governing singular integral equations are used in studies of the mixed-mode transient and residual states for various coefficients of friction.

Introduction

Current interest in closed or partially closed cracks or unbonded interfaces is motivated by such diverse applications as mixed-mode fatigue fracture, plasticity induced crack-tip closure, grain boundary cracking or void growth around precipitates in metals, nondestructive evaluation of partially or totally closed flaws, and many geotechnical phenomena, including wave interactions with frictional interfaces. One area of study has been the effect of slowly moving loads (no inertial effects), much of which is on moving compressive contact loading, acting on near-surface flaws; see e.g., Anscombe and Johnson (1974); Comninou, et al. (1983); Keer and Bryant (1983); Chang, et al. (1983); Hearle and Johnson (1985), Sheppard, et al. (1985, 1987), and Kaneta, et al. (1986). While in the previously mentioned work, the moving load causes all the slip on the crack, Dundurs and Gautesen (1983) considered a different situation in which an infinite, locked, rough interface, subjected to remote compression and shear, is pried apart locally by a pair of tensile line loads moving parallel to the interface. All slip is due to the remote shear which is "released" upon application of the tension across the interface. The transient and steady-state phases of this motion were modeled separately, and were found to share the feature that, in contrast to the corresponding static problem and other similar ones (Comninou, et al., 1980), in which the gap has slip zones on either side, there was no trailing slip zone behind the traveling gap. Low and Comninou (1985) considered the steady state of a similar problem with a single line load directed tangent to the interface, which induced moving slip zones only (no separation). The problem solved by Dundurs and Gautesen (1983) will be referred to as the interface problem.

The present paper treats the analogous problem of the motion of a localized gap across an initially frictionally locked, finite length crack. Both the Mode I and the nonincremental history-independent portions of the Mode II problem were treated in Mendelsohn and Whang (to appear), heretofore referred to as MW. In the present paper, the incremental formulation of Sheppard, et al. (1985), is adapted to handle two independently changing active slip boundaries, and used to solve the history-dependent Mode II problem once the shift is locked in, behind the gap. Due to the characteristic lengths in the crack problem, no steady-state solution exists, in contrast to the interface problem.

Problem Description

The crack geometry and loading are shown in Fig. 1 for the general configuration, all others being limiting cases. The crack is subjected first to compressive stress P_∞ and then to shear stress Q_∞ at infinity. The coefficient of friction f is chosen so that no tangential crack-face shift occurs at this time; $Q_\infty < f(P_\infty)$. Next, a pair of local line loads at $(x, y) = (a, \pm L)$, initially located far to the right of the crack ($a >> 1$), move right to left. (In this case, define the right tip, which opens first, as the leading tip and the left tip as the trailing tip.) It is assumed that the velocity of the load movement is sufficiently small that inertia may be neglected.

It will be assumed at the outset that, as in the interface problem, the separation zone does not have a slip zone adjacent to its trailing edge; i.e., $\delta = \beta$ in Fig. 1. The most general scenario of events, as the loads move, is shown in Fig. 2. First, the crack is all closed and sticking, Fig. 2 (*a*). Next, the crack is all closed with a slip zone adjacent to the leading tip, Fig. 2(*b*), and then the crack opens at the leading tip, Fig. 2(*c*). As the

Contributed by the Applied Mechanics Division for presentation at the Winter Annual Meeting, Chicago, IL, November 28 to December 2, 1988, of The American Society of Mechanical Engineers.

Discussion on this paper should be addressed to the Editorial Department, ASME, United Engineering Center, 345 East 47th Street, New York, N.Y. 10017, and will be accepted until two months after final publication of the paper itself in the JOURNAL OF APPLIED MECHANICS. Manuscript received by ASME Applied Mechanics Division, June 24, 1987; final revision, November 6, 1987.
Paper No. 88-WA/APM-27.

Copyright © 1988 by ASME
Downloaded 03 May 2010 to 171.66.16.21. Redistribution subject to ASME license or copyright; see http://www.asme.org/terms/Terms_Use.cfm

crack closes at the leading tip and an isolated separation zone forms, a trailing stick zone also forms, Fig. 2(*d*), which advances into a previous open region with nonzero shift. The transition from Fig. 2(*d*) to 2 (*e*) marks the onset of slip at the trailing tip, while that from Fig. 2(*e*) to 2(*f*) marks the onset of opening at the trailing tip. The final closed state, after one load pass, is shown in Fig. 2(*g*). Note the solution is *history-dependent* only for the configurations in Figs. 2(*d–g*) and that the entire *history-independent* solution is given in MW.

The aforementioned general scenario must be modified in the two limiting scenarios of no separation throughout the load path and separation, but without the isolated separation that occurs in Figs. 2(*d, e*). For a given material, the dimensionless parameters $\bar{P}=(P/l)/P_\infty$ and $\bar{L}=L/l$ determine which of the three scenarios occur. Here l is the half-crack length, which is taken to be unity in the analysis without any loss of generality. By observing the variation in the Mode I solution in MW for varying load position "a" with fixed $\bar{P}$ and $\bar{L}$, it is seen that, in order for separation to occur at all for any value of a, it must occur for $a = 0$. The same is true for the existence of isolated separation. The regions in the $(\bar{P}, \bar{L})$-plane corresponding to "i" – no separation, "ii" – isolated separation, and "iii" – total separation, when $a = 0$, are shown in Fig. 3.

The line

$$\bar{P}_1=\pi\ \bar{L}\ (\kappa+1)/(\kappa+3)$$

is obtained by setting the normal stress on the closed crack, equation (8) in MW, equal to zero, at $x = 0$, thus giving the condition for the onset of separation. The curve

$$\bar{P}_2=\frac{\pi(\kappa+1)(1+\bar{L}^{-2})^{3/2}}{(\kappa-1)(1+\bar{L}^{-2})+2(1+2\bar{L}^{-2})}.$$

is obtained by setting $a = 0$, $\alpha = -1$ and $\beta = 1$ in the closure condition for the isolated opening solution, equation (21) in MW, thus giving the condition for the onset of total separation. Therefore, region "ii" in Fig. 3 corresponds to the general scenario in Fig. 2, which is formulated in the next section, and regions "i" and "iii" correspond to the limiting scenarios.

For the region "i" scenario of no separation throughout the load path, Figs. 2 (*b, c*) coalesce, as do Figs. 2 (*e, f*). Otherwise Fig. 2 and the following formulation still apply. The region "iii" scenario is Fig. 2(*a*) followed by Figs. 2(*b*), (*c*), after which the crack completely opens up, allowing it to unlock completely. The Mode II solution then becomes the well-known one for uniform applied shear and is locked in unchanged, as the loads move further and leave the crack closed and sticking again. This scenario may be treated entirely by the history-independent solution in MW, since a stick zone never advances into a previous slip or open zone.

Since a complete parameter study is prohibitive and a great deal may be learned by observing Fig. 3, the intent is to examine the history-dependent phenomena involved by using a single numerical example of the region "ii" scenario in Fig. 2. A study versus coefficient of friction for the single choice of $\bar{P}$ and $\bar{L}$ is performed and some interesting phenomena observed. While the region "i" scenario of no separation is also history-dependent and soluble by the present formulation, the present focus is on the effects of separation. However, the trends in the no-separation scenario may be inferred from those presented here.

Formulation and Solution

All Mode I formulations and solutions used in the present study may be found in equations (1)–(23) and (26)–(27) of MW, while equations (28)–(47) of the same paper contain the Mode II formulation and solution for the history-independent portion of the load path, Figs. 2(*b,c*). Only the Mode II formulation and solution for the history-dependent portions, Figs. 2(*d–f*), are given here.

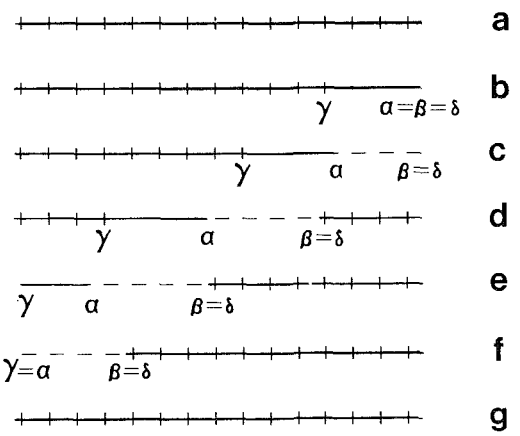


Fig. 2 Schematic of sequence of contact and stick-slip configurations as the loads move right to left; open zones -----; slip zones _____; stick zones ++++

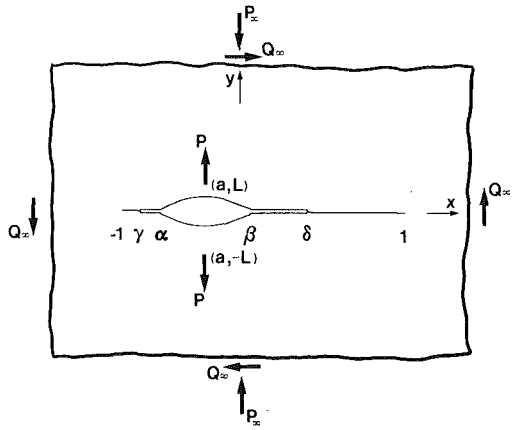


Fig. 1 Crack geometry and loading. The crack is open in $\alpha<x<\beta$, slipping in $\gamma<x<\alpha$ and $\beta<x<\delta$ and sticking elsewhere.

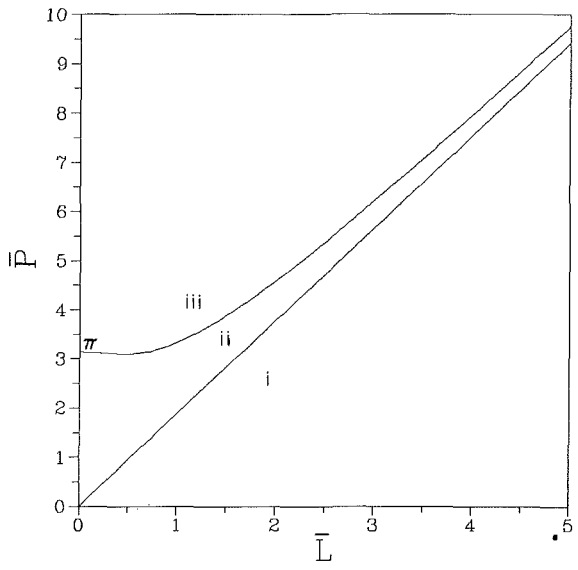


Fig. 3 Regions in the $(\bar{P}, \bar{L})$ plane corresponding to "i"—no separation; "ii"—isolated separation and "iii"—total separation for the loads at a = 0

Downloaded 03 May 2010 to 171.66.16.21. Redistribution subject to ASME license or copyright; see http://www.asme.org/terms/Terms_Use.cfm

Denote the normal and shear tractions on the line $y=0$ as $N(x)$ and $S(x)$, respectively, and define the shift $h(x)$ and the slip velocity $V(x)$ to be

$$h(x)=u_x(x,0+)-u_x(x,0-), \tag{1}$$

$$V(x)=\dot{h}(x). \tag{2}$$

A dot denotes differentiation with respect to time, which is equivalent to differentiation with respect to load position a. The boundary condition in an open or separation zone is

$$S(x)=0, \tag{3}$$

while in a slip zone

$$|S(x)|=f|N(x)|, \tag{4}$$

$$\text{Sgn}\ [V(x)]=\text{Sgn}\ [S(x)], \tag{5}$$

where Sgn ( ) is the signum or sign function. In a stick zone, the conditions are

$$|S(x)|<f|N(x)| \tag{6}$$

$$V(x)=0. \tag{7}$$

Also, define the tangential derivative of the shift, referred to as the shear dislocation density function

$$B_x(x)=-\frac{\partial h}{\partial x}. \tag{8}$$

Solution – Fig. 2(*d*). Consider an incremental formulation and denote two consecutive load positions by A^i and A^{i+1}.Then at each A^{i+1} the boundary conditions (3) and (4) give the integral equation

$$Q_\infty-\frac{C}{\pi}\int_{\gamma^{i+1}}^{1}\frac{B_x(\xi,A^{i+1})}{\xi-x}\,d\xi=-fN(x,A^{i+1}),$$

$$\gamma^{i+1}<x<\delta^{i+1}. \tag{9}$$

Positive slip velocity is assumed throughout. The upper limit is 1 rather than δ^{i+1} because there are locked-in dislocations between δ^{i+1} and 1 which also contribute to the shear stress, and hence, the integral equation, valid only in the active slip zone, is applied over an interval smaller than the range of integration. Even with the condition

$$\int_{\gamma^{i+1}}^{1}B_x(\xi,A^{i+1})d\xi=0, \tag{10}$$

which ensures zero shift at $x=\gamma^{i+1}$ and 1, $B_x(x,A^{i+1})$ still cannot be determined from equation (9). Therefore, following Dundurs and Gautesen (1983) and Sheppard, et al. (1985), a velocity formulation is adopted. Since $\dot{B}_x(x,A^{i+1})=0$ for $\delta^{i+1}<x<1$, differentiating equation (9) with respect to a gives

$$-\frac{C}{\pi}\int_{\gamma^{i+1}}^{\delta^{i+1}}\frac{\dot{B}_x(\xi,A^{i+1})}{\xi-x}\,d\xi=-f\dot{N}(x,A^{i+1}),$$

$$\gamma^{i+1}<x<\delta^{i+1}. \tag{11}$$

The constant $C=2\mu/(\kappa+1)$, where μ is the shear modulus and $\kappa=3-4\nu$ (plane strain), $\kappa=(3-\nu)/(1+\nu)$ (plane stress), and ν is Poisson's ratio. The solution of equation (11) is assumed singular at the endpoints

$$\dot{B}_x(x,A^{i+1})=\frac{\phi^{i+1}(x)}{(x-\gamma^{i+1})^{1/2}\,(\delta^{i+1}-x)^{1/2}}. \tag{12}$$

The right-hand side of equation (11) is approximated by a backward difference. The constraint equation in the active slip zone is

$$\int_{\gamma^{i+1}}^{\delta^{i+1}}\dot{B}_x(\xi,A^{i+1})d\xi=0. \tag{13}$$

The increment in shear traction may be expressed as

$$-\frac{\pi}{C}\Delta S^{i+1}(x)=\int_{A^i}^{A^{i+1}}\int_{\gamma(A)}^{\delta(A)}\frac{\dot{B}_x(\xi,A)}{\xi-x}\,d\xi\,dA. \tag{14}$$

Assuming that ϕ is constant and γ and δ vary linearly in each increment

$$\gamma(A)=\gamma^i+dm(A-A^i), \tag{15a}$$

$$\delta(A)=\delta^i+dn(A-A^i), \tag{15b}$$

$$dm=(\gamma^{i+1}-\gamma^i)/\Delta A=\Delta\gamma/\Delta A \tag{15c}$$

$$dn=(\delta^{i+1}-\delta^i)/\Delta A=\Delta\delta/\Delta A, \tag{15d}$$

Equation (14) becomes

$$-\frac{\pi}{C}\Delta S^{i+1}(x)=\int_{\gamma^{i+1}}^{\delta^i}\frac{\Phi(\xi)F(\xi)d\xi}{\xi-x}, \tag{16}$$

where

$$F(\xi)=\frac{-2}{\sqrt{dmdn}}\tan^{-1}\sqrt{\frac{dn(\xi-\gamma^{i+1})}{dm(\delta^{i+1}-\xi)}},$$

$$\gamma^{i+1}<\xi<\gamma^i,$$

$$=\frac{-2}{\sqrt{dmdn}}\left[\tan^{-1}\sqrt{\frac{dn(\xi-\gamma^{i+1})}{dm(\delta^{i+1}-\xi)}}\right.$$

$$\left.-\tan^{-1}\sqrt{\frac{dn(\xi-\gamma^i)}{dm(\delta^i-\xi)}}\right],\ \gamma^i<\xi<\delta^{i+1},$$

$$=\frac{-2}{\sqrt{dmdn}}\left(\frac{\pi}{2}-\tan^{-1}\sqrt{\frac{dn(\xi-\gamma^i)}{dm(\delta^i-\xi)}}\right),$$

$$\delta^{i+1}<\xi<\delta^i. \tag{17a}$$

$$\Phi(\xi)=\phi^{i+1}(\xi),\ \gamma^{i+1}<\xi<\delta^{i+1},$$

$$=\phi^i(\xi),\ \delta^{i+1}<\xi<\delta^i. \tag{17b}$$

The total shear traction at any time is then given by

$$S(x)=S^\circ(x)+\sum_i\Delta S^{i+1}(x) \tag{18}$$

where $S^\circ(x)$ is the shear at the transition from Figs. 2(*c*) to 2(*d*) (i.e., just before the incremental process begins).

Now, the slip velocity is given by

$$V(x)=-\int_{\gamma(A)}^{x}\dot{B}_x(\xi,A)d\xi,\ \gamma(A)<x<1 \tag{19}$$

which, by a similar procedure as previously shown, leads to

$$-\Delta V_{(x)}^{i+1}=\int_{A^i}^{A^{i+1}}\int_{\gamma(A)}^{x}\dot{B}_x(\xi,A)d\xi\,dA$$

$$=\int_{\gamma^{i+1}}^{x}\Phi(\xi)\,F(\xi)\,d\xi,\quad\gamma^{i+1}<x<\delta^i, \tag{20}$$

where ϕ and F are given in equation (17).

The numerical procedure begins by obtaining the contact points α^{i+1} and β^{i+1} and the normal traction from the Mode I solution. Then δ^{i+1} is set equal to β^{i+1} and equations (11) and (13), subject to the constraint (6), are solved iteratively for B_x and γ^{i+1}, using γ^i as a first guess for γ^{i+1}. To do this, normalize the interval of integration to $(-1,1)$

$$x=\eta r+\omega,\qquad \xi=\eta s+\omega, \tag{21a}$$

$$\eta=(\delta^{i+1}-\gamma^{i+1})/2,\qquad \omega=(\delta^{i+1}+\gamma^{i+1})/2 \tag{21b}$$

Downloaded 03 May 2010 to 171.66.16.21. Redistribution subject to ASME license or copyright; see http://www.asme.org/terms/Terms_Use.cfm

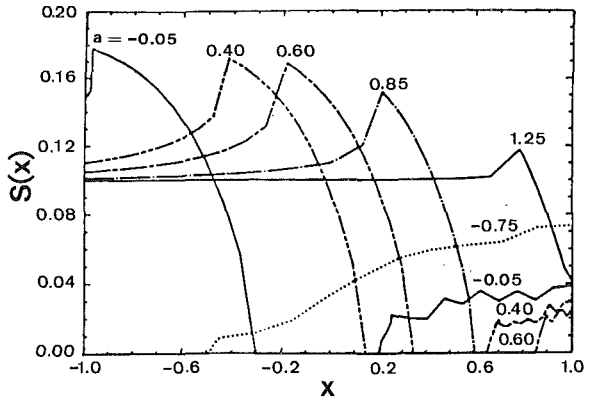


Fig. 4(*a*) Shear stress distribution in the contact; $f = 0.2$

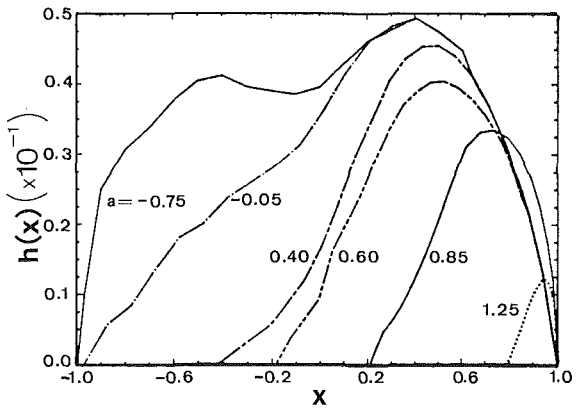


Fig. 4(*b*) Shift distribution for various load positions; $f = 0.2$

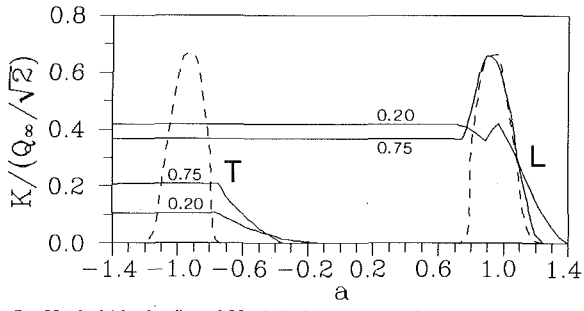


Fig. 5 Mode I (dashed) and Mode II SIF's versus load position; $f = 0.20$, 0.75, *L*-leading tip, *T*-trailing tip

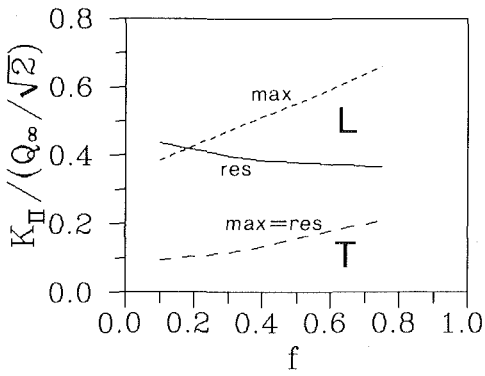


Fig. 6 Maximum (max) and residual (res) Mode II SIF's for one load pass versus *f*; *L*-leading tip, *T*-trailing tip. Total preslip occurs for $f < 0.10$, for which all normalized SIF's would be unity.

Then equation (11) is discretized (Erdogan, Gupta, and Cook, 1973)

$$\frac{1}{K}\sum_{n=1}^{K}\frac{\phi^{i+1}(s_n)}{s_n - r_m} = \frac{\eta f}{C}\dot{N}(r_m, A^{i+1}),$$

$$m = 1, \ldots, K-1 \tag{22a}$$

$$s_n = \cos\left(\pi\frac{2n-1}{2K}\right), \quad r_m = \cos\left(\frac{\pi m}{K}\right) \tag{22b}$$

retaining the same symbols for B_x, ϕ^{i+1} and N in the new variables. The discretized form of equation (13)

$$\sum_{n=1}^{K}\phi^{i+1}(s_n) = 0, \tag{23}$$

and equation (22*a*) provide K equations for the K unknown values of ϕ^{i+1}. After solving, the increment in shear in equation (16) is computed, noting the behavior of F

$$-\frac{\pi}{C}\Delta S^{i+1}(t_m) = \int_{-1}^{1}\frac{\sqrt{1-u^2}}{(u-t)}\left[\frac{\Phi(u)\,F(u)}{\sqrt{1-u^2}}\right]du$$

$$\cong \frac{\pi}{(K+1)}\sum_{n=1}^{K}\frac{\sqrt{1-u_n^2}\Phi(u_n)\,F(u_n)}{(u_n - t_m)} \tag{24a}$$

$$x = \theta t + \psi, \quad \xi = \theta u + \psi, \tag{24b}$$

$$\theta = (\delta^i - \gamma^{i+1})/2, \quad \psi = (\delta^i + \gamma^{i+1})/2 \tag{24c}$$

$$u_n = \cos\left(\frac{n\pi}{K+1}\right), \quad t_m = \cos\left(\frac{\pi}{2}\frac{2m-1}{K+1}\right). \tag{24d}$$

For values of x in (γ^{i+1}, δ^i), the integrand is singular and the quadrature must be used at the collocation points t_m. Otherwise, any value of t may be used. Next, using equation (18), the constraint (6) is checked. This procedure repeats iteratively until the correct γ^{i+1} is found.

Solution – Fig. 2(*e*). Except for equations 24(*a*)-(*d*), the entire formulation for this case may be obtained from that for Fig. 2(*d*) by replacing γ^{i+1} with -1 and the function F with the function G

$$G(\xi) = \frac{2}{dn}\frac{\sqrt{\delta^{i+1}-\xi} - \sqrt{\delta^i - \xi}}{\sqrt{1+\xi}}, \quad -1 < \xi < \delta^{i+1},$$

$$= -\frac{2}{dn}\frac{\sqrt{\delta^i - \xi}}{\sqrt{1+\xi}}, \quad \delta^{i+1} < \xi < \delta^i. \tag{25}$$

Observing the behavior of G, the numerical evalution of the modified equation (16) (G replaced with F) differs from equations (24*a–d*). Instead we get

$$-\frac{\pi}{C}\Delta S^{i+1}(t_m) = \int_{-1}^{1}\sqrt{\frac{1-u}{1+u}}\left(\frac{1}{u-t}\right)\left[\sqrt{\frac{1+u}{1-u}}\,\Phi(u)\,G(u)\right]du$$

$$\cong \frac{2\pi}{(2K+1)}\sum_{n=1}^{K}\frac{\sqrt{1-u_n^2}\Phi(u_n)\,G(u_n)}{(u_n - t_m)} \tag{26a}$$

$$u_n = \cos\left(\frac{2n\pi}{2K+1}\right), \quad t_m = \cos\left(\pi\frac{2n-1}{2K+1}\right). \tag{26b}$$

Solution – Fig. 2(*f*). Because the active shift zone consists only of the gap, $\dot{N}(x, A) = 0$ there; hence, the right-hand side of equation (11) is zero, and the shift and shear traction at the

Downloaded 03 May 2010 to 171.66.16.21. Redistribution subject to ASME license or copyright; see http://www.asme.org/terms/Terms_Use.cfm

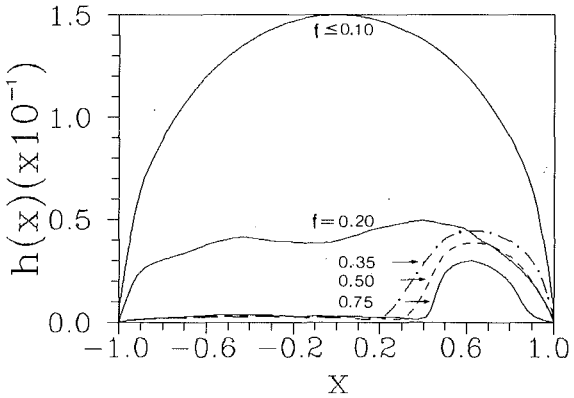


Fig. 7 Residual shift distributions after one load pass for various coefficients of friction, including the preslipped crack, $f<0.1$

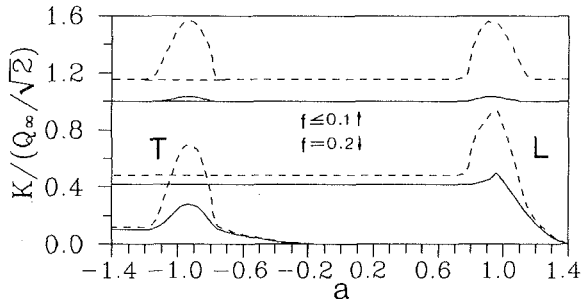


Fig. 8(a) Maximum tensile (dashed) and shear SIF's versus load position for two values of f.

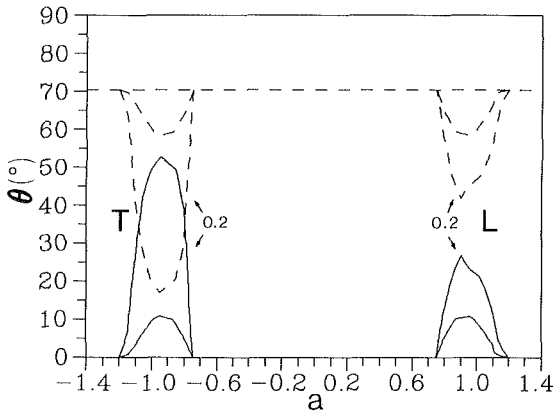


Fig. 8(b) Corresponding angles of the planes emanating from the crack tip on which they occur; $f<0.10$, $f=0.2$. The angle is measured ccw from the x-axis at the leading tip (L) and cw from the negative x-axis at the trailing tip (T), and is plotted negative for tensile planes (dashed).

transition from Figs. 2 (e, f) are the locked-in values after one load pass.

Stress Intensity Factors. The mode I SIF's are given in MW, equations (15) and (18). The Mode II SIF at the leading tip changes only in the history-independent portion of the load path, Figs. 2 (b, c) and is given in MW, equation (47). The Mode II SIF at the trailing tip is found from the previous analysis by summing up SIF increments at the left tip

$$\Delta K_{\mathrm{II}}^{i+1} = -\frac{C}{2}\sqrt{\delta^{i+1}+1}\,\phi^{i+1}(-1) \tag{27a}$$

$$K_{\mathrm{II}} = \sum_i \Delta K_{\mathrm{II}}^{i+1} \tag{27b}$$

Results and Discussion

All calculatons were made in plane strain using $L=0.5$, $\mu=1.00$, $\nu=0.25$, $P_\infty=1.00$, $P=1.15$ and $Q_\infty=0.10$. Figures 4(a,b) illustrate the sequence of events through the changes in the contact shear traction and shift distributions, respectively, for a single value of $f=0.20$. For this f, the load positions at which Figs. 2(b–g) first occur are $a=1.40$, 1.20, 0.75, −0.15, −0.75 and −1.20, respectively. The only transitions which depend on f and Q_∞ are the ones from Figs. 2(a, b), $a=1.40$, and Figs. 2 (d, e), $a=-0.15$, which denote, respectively, the onset of slip at the leading and trailing tips. For the largest f studied, 0.75, these transitions occurred at $a=1.25$ and −0.35. In Fig. 4(a), the shear curves in leading slip and stick zones may be identified by the cusps at the slip-stick boundary and the common asymptote of 0.10 in the stick zone. The remaining curves are in the trailing stick zones. While not shown, the curves for the allowable friction stress in the trailing stick zones lie well above the plotted curves, and indeed, equation (6) is satisfied and there is no trailing slip zone. The gap is identified by vanishing shear. Noting that the increment in load position was fixed at 0.05, the results in the trailing stick zone, for $a=0.60$, 0.40, and −0.05, apparently exhibit some numerical inaccuracies or instabilities. This exhibits itself as well in the progressive accumulation and locking-in of shift beginning at $a=0.75$ illustrated in Fig. 4(b).

The variation of the SIF's is shown in Fig. 5 for the two extremes in f which were studied, 0.20 and 0.75. Figure 6 shows the dependence on f of the maximum and residual Mode II SIF's for a single load pass. The curves have been extrapolated to $f=0.10$, the minimum value to prevent preslip. In contrast to Mode I, the Mode II results show a marked asymmetry between leading and trailing tip and a strong dependence on f. The leading-tip SIF undergoes more severe transients and a larger range of magnitudes than the trailing tip. Also, upon release, the greater f is, the greater the transients and maximum responses at both tips. However, the residual SIF at the leading tip decreases with increasing f, while at the trailing tip it increases.

Figure 7 shows the residual shift for four values of f and for the preslipped crack ($f<0.10$), for which the shift is independent of the moving loads. Note that the gap lies between $x=0.5$ and $x=1.0$ when it breaks away from the leading tip and Fig. 2(d) begins. It was found that, for $f=0.75$, the slip zone sizes were very small compared to the gap size. Therefore, it appears that increasing f further will have little effect.

In order to assess the near-tip stress fields more thoroughly, the maximum tensile and shear SIF's and the angles of the planes at the crack tips on which they occur were calculated using the expressions in Erdogan and Sih (1963). Those results are shown in Figs. 8 (a, b) for the preslipped crack and for $f=0.20$. The trends in Fig. 8(a) are similar to those in Fig. 5. However, Fig. 8(b) shows that, for $f>0.10$, the trailing tip experiences greater transients and excursions in angles of planes of maximum SIF than the leading tip.

Assuming the applied loads are sufficiently large, it appears that, if failure will occur upon release, it will occur at the leading tip. It also appears that failure will be controlled by the Mode I solution in a brittle material, independent of friction, while, for more shear sensitive materials, the rougher the crack, the higher the likelihood of failure. Also, the sensitivity of the transients in the Mode II response to changes in friction should be carefully noted in treating similar dynamic crack problems in the future.

Acknowledgments

The support of The Ohio State University through a Univer-

Downloaded 03 May 2010 to 171.66.16.21. Redistribution subject to ASME license or copyright; see http://www.asme.org/terms/Terms_Use.cfm

sity Seed Grant is gratefully acknowledged. We also appreciate the partial support of the National Science Foundation through Grant CEE-8505274. Thanks are also due to the referees for their helpful comments.

References

Anscombe, H., and Johnson, K. L., 1974, "Slip of a Thin Solid Tyre Press-Fitted on a Wheel," *International Journal of Mechanical Sciences*, Vol. 16, pp. 329–334.

Chang, F. K., Comninou, M., and Barber, J. R., 1983, "Slip Between a Layer and a Substrate Caused by a Normal Force Moving Steadily Over the Surface, *International Journal of Mechanical Sciences*, Vol. 25, pp. 803–809.

Comninou, M., Schmuesser, D., and Dundurs, J., 1980, "Separation and Slip Between a Layer and a Substrate Caused by a Tensile Load," *International Journal of Engineering Science*, Vol. 18, pp. 1149–1155.

Comninou, M., Barber, J. R., and Dundurs, J., 1983, "Interface Slip Caused by a Surface Load Moving at Constant Speed," *International Journal of Mechanical Sciences*, Vol. 25, pp. 41–46.

Dundurs, J., and Gautesen, A. K., 1983, "On the Approach to Steady State for Frictional Contact Under Moving Loads," ASME JOURNAL OF APPLIED MECHANICS, Vol. 50, pp. 783–788.

Erdogan, F., Gupta, G. D., and Cook, T. S., 1973, "Numerical Solution of Singular Integral Equations," in *Methods of Analysis and Solution of Crack Problems*, ed., Sih, G. C., Noordhoff, Leyden, pp. 368–425.

Erdogan, F., and Sih, G. C., 1963, "On the Crack Extension in Plates Under Plane Loading and Transverse Shear," ASME *Journal of Basic Engineering*, Vol. 86, pp. 519–527.

Hearle, A.D., and Johnson, K. L., 1985, "Mode II Stress Intensity Factors for a Crack Parallel to the Surface of an Elastic Half-Space Subjected to a Moving Point Load," *Journal of the Mechanics and Physics of Solids*, Vol. 33, pp. 61–81.

Kaneta, M., Suetsugu, M., and Murakami, Y., 1986, "Mechanism of Surface Crack Growth in Lubricated Rolling/Sliding Spherical Contact," ASME JOURNAL OF APPLIED MECHANICS, Vol. 53, pp. 354–360.

Keer, L. M., and Bryant, M. D., 1983, "A Pitting Model for Rolling Contact Fatigue," *ASME Journal of Lubrication Technology*, Vol. 105, pp. 196–205.

Low, R. D., and Comninou, M., 1985, "Interface Slip Between Two Half-Planes Caused by a Steadily Moving Force," *Journal of Elasticity*, Vol. 15, pp. 109–114.

Mendelsohn, D. A., and Whang, K. H., 1988, "Localized Asymmetric Crack Closure with Stick-Slip in the Contact," *Engineering Fracture Mechanics*, Vol. 29, pp. 365–384.

Sheppard, S., Barber, J. R., and Comninou, M., 1985, "Short Subsurface Cracks Under Conditions of Slip and Stick Caused by a Moving Compressive Load," ASME JOURNAL OF APPLIED MECHANICS, Vol. 52, pp. 811–817.

Sheppard, S., Barber, J. R., and Comninou, M., 1987, "Subsurface Cracks Under Conditions of Slip, Stick and Separation Caused by a Moving Compressive Load," ASME JOURNAL OF APPLIED MECHANICS, Vol. 54, pp. 393–398.

Downloaded 03 May 2010 to 171.66.16.21. Redistribution subject to ASME license or copyright; see http://www.asme.org/terms/Terms_Use.cfm

J. Aboudi[1]

S. W. Lee

C. T. Herakovich[2]

Department of Engineering Science and Mechanics,
Virginia Polytechnic Institute and State University,
Blacksburg, VA 24061

Three-Dimensional Analysis of Laminates With Cross Cracks

An approximate 3-dimensional analysis to study the effects of a system of transverse and longitudinal matrix cracks in cross-ply laminates is given. The method considers a repeating unit cell containing three subcells in every one of which the displacement vector is expanded to second order. The equilibrium equations, in conjunction with continuity conditions of displacements and tractions, together with the appropriate loading and boundary conditions, provide a system of equations for the elastic field variables. The dependence of the effective axial stiffness and Poisson's ratio of the laminate on the cross-cracks density is given. The Poisson's ratio appears to be a good indicator for the state of damage of the laminate. The distribution of the axial displacement and stress in the cracked laminate is shown.

1 Introduction

The use of laminated composites allows engineers to design structural components by adjusting the orientations, thickness, and stacking sequence of the fiber-reinforced laminae to provide a laminate which possesses the desired stiffness and strength. This, of course, has great advantage over the use of conventional unreinforced materials such as metals. Damage development and failure of composite laminates are, however, much more complicated than those occurring in conventional materials. In composite laminates, numerous modes of damage may take place and contribute to eventual failure. Examples are matrix cracking, fiber breakage, fiber-matrix debonding, and delamination. An analysis and predictive capability of the long-term performance of composite materials would be possible if these modes of damage were fully understood.

Consider a composite laminate subjected to quasi-static or cyclic loading. The early stage of damage development is dominated by matrix cracks which appear in the off-axis plies that are not aligned with the principle loading direction. These cracks typically extend in the fiber direction across the entire laminate from edge to edge. The number of cracks increases monotonically with increase of loading or number of cycles, depending on whether the loading is quasi-static or cyclic, until a saturation density is reached. In this state of damage, called the characteristic damage state (CDS), the cracks are uniformly distributed throughout the laminate (Reifsnider, et al., 1983).

The deterioration of the elastic constants of the composite laminate appears to be a good nondestructive testing indicator of its degree of damage. The reduction of longitudinal stiffness of composite laminates due to transverse matrix cracking was measured by Highsmith and Reifsnider (1982) who used the shear lag model for their theoretical predictions. Another theoretical analysis is given by Herakovich, et al. (1988), where an approximate analytical solution and a finite-element procedure were applied and compared to study the effects of transverse cracks in cross-ply composite laminates. This latter study included the degradation of elastic and thermal coefficients as well as stress distributions. In particular, it was shown that transverse cracks cause significant degradation of the Poisson's ratio of the laminates.

The CDS appears to indicate the termination of the development of the first stage of damage by transverse cracking in the off-axis plies. In the next stage, several modes of damage might take place. In particular, longitudinal cracks or splits appear in the 0-deg plies along the fibers. Both transverse cracks in the off-axis plies and longitudinal cracks in the 0-deg plies are considered as matrix cracks. In a cross-ply laminate they form together a system of cross cracks. In this system, there are points at the interface between the two plies where matrix cracks in each of the plies meet. These crossing points are preferred sites of internal delamination development and fiber breakage. The analysis of a composite laminate with a system of cross cracks is a 3-dimensional problem and therefore much more complicated than that of a cross-ply laminate with transverse cracking which is 2-dimensional. Such a 3-dimensional analysis would provide the distribution of stresses and loss of elastic properties due to the cross-cracks system. The understanding of the stress variation in the damaged laminate is of special importance because it is precisely these variations that cause one damage event to induce subsequent damage development.

[1]On leave from Faculty of Engineering, Tel-Aviv University, Ramat-Aviv 69978, Israel.

Contributed by the Applied Mechanics Division for presentation at the Winter Annual Meeting, Chicago, IL, November 28 to December 2, 1988, of The American Society of Mechanical Engineers.

Discussion on this paper should be addressed to the Editorial Department, ASME, United Engineering Center, 345 East 47th Street, New York, NY 10017, and will be accepted until two months after final publication of the paper itself in the JOURNAL OF APPLIED MECHANICS. Manuscript received by ASME Applied Mechanics Division, August 11, 1987.

Paper No. 88-WA/APM-36.

[2]Presently at the University of Virginia, Charlottesville, VA 22903.

Copyright © 1988 by ASME

Downloaded 03 May 2010 to 171.66.16.21. Redistribution subject to ASME license or copyright; see http://www.asme.org/terms/Terms_Use.cfm

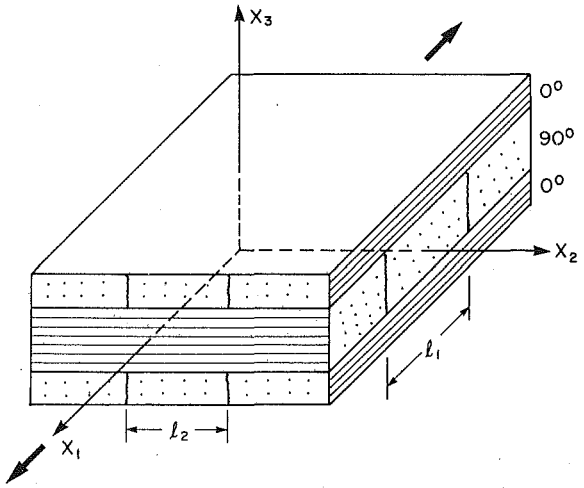


Fig. 1 Cross-ply laminate subjected to a tension load, with longitudinal and transverse cracks

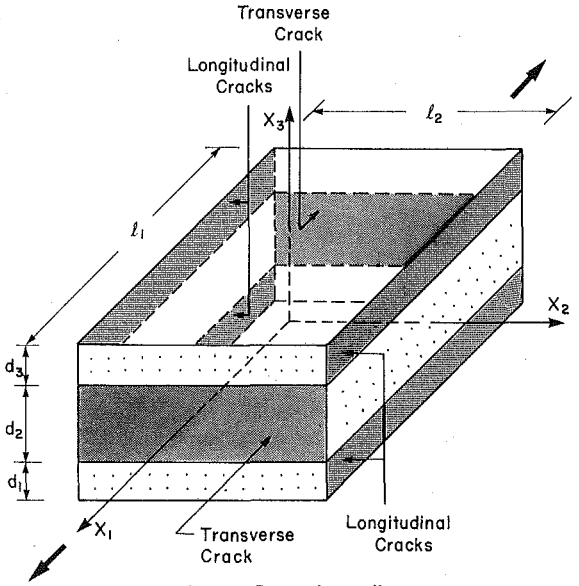


Fig. 2 Repeating cell

An analysis of a cross-ply laminate with cross cracking has been given by Highsmith, et al. (1986). It is based on a structural theory proposed by Pagano (1978) which was developed by assuming that the inplane stresses for a layer of a material vary linearly through the thickness. Equilibrium considerations determine the order of variation through the thickness of the other stress components. Reissner's variational principle yields a system of algebraic and differential equations. An approximate solution in terms of Chebyshev polynomials in conjunction with imposed boundary conditions, provides a system of overdeterminated algebraic equations which is solved by least squares. Details of the method are given by Highsmith (1984).

In the present paper, a different approach is adopted for the 3-dimensional problem of cross-ply laminates with cross cracks. The method relies on the analysis of a repeating unit cell containing 3 subcells. In each subcell the displacement vector is expanded to second order through the thickness and transverse directions. The equilibrium equations in conjunction with the continuity of displacements and tractions provide a system of ordinary differential equations in the unknown field variables. A differencing procedure, together with the appropriate loading and boundary conditions, reduces these equations to a system of linear algebraic equations which can be easily solved by utilizing the band structure

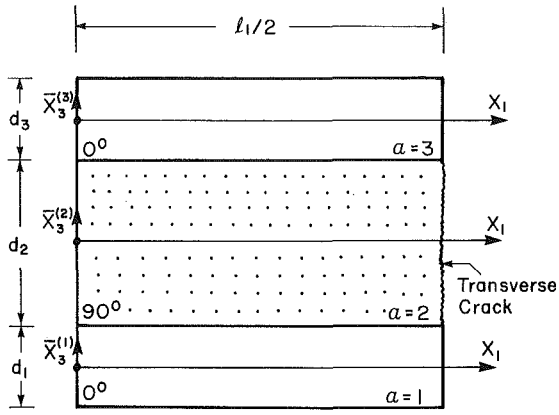


Fig. 3 Modeled region with local coordinates $(x_1, x_2, \bar{x}_3^{(\alpha)})$

of the coefficients matrix. The present method of solution is a generalization of the 2-dimensional analysis employed by Aboudi (1987) for cracked solids and by Herakovich, et al. (1988) for cross-ply laminates with transverse cracks.

It can be seen that the present method differs from that of Highsmith, et al. (1986) in that the axial stress (for example) in the loading direction is second order through the thickness (rather than linear). Consequently, it is more accurate and exhibits higher gradients in the vicinity of the tip of the crack as compared with those predicted by Highsmith, et al. (1986). Exact analysis would of course provide singular behavior. There are however other components (shear stresses) which are obtained less accurately by the present approach. The reduction of axial stiffness of the laminate, as predicted by the present analysis, is closer to the experimental results of Highsmith (1984).

Results for the effective axial stiffness, Poisson's ratio, axial displacement distribution, and axial stress distribution are given for a graphite/epoxy laminate, and compared with those of Highsmith (1984). It appears that the Poisson's ratio exhibits a pronounced dependence on cross-cracks density and it also seems to be a good indicator for the state of damage in the laminate.

2 Formulation and Method of Solution

Consider a cross-ply laminate which consists of three plies and is subjected to unidirectional tension in the x_1-direction; see Fig. 1. The internal 90-deg ply contains uniformly distributed transverse cracks, and uniformly distributed longitudinal cracks exist in the 0-deg plies. Both sets of matrix cracks are assumed to be infinite in length in the fiber direction of their respective plies. The spacing of the transverse cracks is l_1 while that of the longitudinal cracks is l_2.

Due to the periodicity of the structure, it is sufficient to analyze a unit cell of a dimension $l_1/2$, l_2, $(d_1+d_2+d_3)$; see Fig. 2. Let us introduce three local systems of coordinates $(x_1, x_2, \bar{x}_3^{(\alpha)})$, $\alpha=1, 2, 3$ as shown in Fig. 3. Let $u_i^{(\alpha)}$ and $\sigma_{ij}^{(\alpha)}$ denote the displacement and stress components in the αth ply with $i, j=1, 2, 3$. Due to symmetry considerations and the traction-free conditions at the crack surfaces, the following boundary conditions are imposed at the unit cell

$$\sigma_{13}^{(1)}=\sigma_{23}^{(1)}=\sigma_{33}^{(1)}=0, \quad 0\le x_1\le l_1/2, \quad |x_2|\le l_2/2, \quad \bar{x}_3^{(1)}=-d_1/2, \tag{1}$$

$$\sigma_{13}^{(3)}=\sigma_{23}^{(3)}=\sigma_{33}^{(3)}=0, \quad 0\le x_1\le l_1/2, \quad |x_2|\le l_2/2, \quad \bar{x}_3^{(3)}=d_3/2, \tag{2}$$

$$\sigma_{12}^{(1)}=\sigma_{22}^{(1)}=\sigma_{23}^{(1)}=0, \quad 0\le x_1\le l_1/2, \quad x_2=\pm l_2/2, \quad |\bar{x}_3^{(1)}|\le d_1/2, \tag{3}$$

Downloaded 03 May 2010 to 171.66.16.21. Redistribution subject to ASME license or copyright; see http://www.asme.org/terms/Terms_Use.cfm

$$\sigma_{12}^{(2)}=\sigma_{23}^{(2)}=0,\quad 0\le x_1\le l_1/2,\ x_2=\pm l_2/2,\ |\bar{x}_3^{(2)}|\le d_2/2, \tag{4a}$$

$$u_2^{(2)}\Big|_{x_2=l_2/2}=u_2^{(2)}\Big|_{x_2=-l_2/2}\quad 0\le x_1\le l_1/2,\ |\bar{x}_3^{(2)}|\le d_2/2, \tag{4b}$$

$$\sigma_{12}^{(3)}=\sigma_{22}^{(3)}=\sigma_{23}^{(3)}=0,\quad 0\le x_1\le l_1/2,\ x_2=\pm l_2/2,\ |\bar{x}_3^{(3)}|\le d_3/2, \tag{5}$$

$$u_1^{(\alpha)}=0,\ \sigma_{12}^{(\alpha)}=\sigma_{13}^{(\alpha)}=0,\quad x_1=0,\ |x_2|\le l_2/2,\ |\bar{x}_3^{(\alpha)}|\le d_\alpha/2, \tag{6}$$

$$\sigma_{11}^{(2)}=\sigma_{12}^{(2)}=\sigma_{13}^{(2)}=0,\quad x_1=l_1/2,\ |x_2|\le l_2/2,\ |\bar{x}_3^{(2)}|\le d_2/2, \tag{7}$$

$$u_1^{(\alpha)}=1,\ \sigma_{12}^{(\alpha)}=\sigma_{13}^{(\alpha)}=0,\quad x_1=l_1/2,\ |x_2|\le l_2/2,$$

$$|\bar{x}_3^{(\alpha)}|\le d_\alpha/2,\quad \alpha=1 \text{ and } 3 \tag{8}$$

Equations (1) and (2) follow from the traction-free conditions prevailing at the upper and lower surface of the laminate, (3) and (5) follow from the traction-free surfaces of the longitudinal cracks at plies $\alpha=1$ and 3, equations (4) and (6) express the symmetry conditions at the appropriate planes, and (7) represents the traction-free conditions at the surface of the transverse crack. Finally, the tension loading of the laminate is given by equation (8) where a unit displacement is imposed for simplicity.

In addition to the foregoing boundary conditions, the following traction and displacement continuity conditions at the ply interfaces should be fulfilled

$$\sigma_{3j}^{(1)}\Big|_{\bar{x}_3^{(1)}=d_1/2}=\sigma_{3j}^{(2)}\Big|_{\bar{x}_3^{(2)}=-d_2/2},$$

$$\sigma_{3j}^{(2)}\Big|_{\bar{x}_3^{(2)}=d_2/2}=\sigma_{3j}^{(3)}\Big|_{\bar{x}_3^{(3)}=-d_3/2}, \tag{9}$$

$$u_i^{(1)}\Big|_{\bar{x}_3^{(1)}=d_1/2}=u_i^{(2)}\Big|_{\bar{x}_3^{(2)}=-d_2/2},$$

$$u_i^{(2)}\Big|_{\bar{x}_3^{(2)}=d_2/2}=u_i^{(3)}\Big|_{\bar{x}_3^{(3)}=-d_3/2}, \tag{10}$$

Once the elastic field distribution in the unit cell is determined, the effective constants of the composite laminate with crossed cracks can be readily obtained.

An approximate analytical solution to the previous 3-dimensional problem can be obtained by expressing the displacement vector of the αth ply in a second-order Legendre expansion in x_2 and $\bar{x}_3^{(\alpha)}$ as follows

$$\mathbf{u}^{(\alpha)}=\mathbf{\Lambda}_0^{(\alpha)}+\mathbf{\Lambda}_1^{(\alpha)}x_2+\mathbf{\Lambda}_2^{(\alpha)}\bar{x}_3^{(\alpha)}+\mathbf{\Lambda}_3^{(\alpha)}x_2\bar{x}_3^{(\alpha)}$$
$$+\frac{1}{2}\mathbf{\Lambda}_4^{(\alpha)}\left[3(x_2)^2-\frac{l_2^2}{4}\right]$$
$$+\frac{1}{2}\mathbf{\Lambda}_5^{(\alpha)}\left[3(\bar{x}_3^{(\alpha)})^2-\frac{d_\alpha^2}{4}\right], \tag{11}$$

where the coefficients $\mathbf{\Lambda}_k^{(\alpha)}$ $(k=1,\ldots 5)$ are functions of x_1 only. Here and in the sequel repeated α does not imply summation.

Let us confine ourselves to a symmetric laminate ($d_1=d_3$). It follows that ($x_3=0$) is a plane of symmetry, so that

$$u_1^{(\alpha)}(x_1,x_2,\bar{x}_3^{(\alpha)}) = u_1^{(\alpha)}(x_1,-x_2,\bar{x}_3^{(\alpha)}),$$
$$u_2^{(\alpha)}(x_1,x_2,\bar{x}_3^{(\alpha)}) = -u_2^{(\alpha)}(x_1,-x_2,\bar{x}_3^{(\alpha)}),$$
$$u_3^{(\alpha)}(x_1,x_2,\bar{x}_3^{(\alpha)}) = u_3^{(\alpha)}(x_1,-x_2,\bar{x}_3^{(\alpha)}), \tag{12}$$

and

$$u_1^{(2)}(x_1,x_2,\bar{x}_3^{(2)}) = u_1^{(2)}(x_1,x_2,-\bar{x}_3^{(2)}),$$
$$u_2^{(2)}(x_1,x_2,\bar{x}_3^{(2)}) = u_2^{(2)}(x_1,x_2,-\bar{x}_3^{(2)}),$$
$$u_3^{(2)}(x_1,x_2,\bar{x}_3^{(2)}) = -u_3^{(2)}(x_1,x_2,-\bar{x}_3^{(2)}), \tag{13}$$

Furthermore, for any point at $\bar{x}_3^{(3)}=\bar{x}_3^{(3)}$, we have

$$u_1^{(1)}(x_1,x_2,x_3^{(1)}) = u_1^{(3)}(x_1,x_2,-\bar{x}_3^{(3)}),$$
$$u_2^{(1)}(x_1,x_2,\bar{x}_3^{(1)}) = u_2^{(3)}(x_1,x_2,-\bar{x}_3^{(3)}),$$
$$u_3^{(1)}(x_1,x_2,\bar{x}_3^{(1)}) = -u_3^{(3)}(x_1,x_2,-\bar{x}_3^{(3)}), \tag{14}$$

Applying the symmetry conditions (12)–(13), reduce expansion (11) to

$$u_1^{(1)} = \phi_0^{(1)}+\phi_2^{(1)}\bar{x}_3^{(1)}+\frac{1}{2}\phi_4^{(1)}\left[3(x_2)^2-\frac{l_2^2}{4}\right]$$
$$+\frac{1}{2}\phi_5^{(1)}\left[3\left(\bar{x}_3^{(1)}\right)^2-\frac{d_1^2}{4}\right],$$

$$u_2^{(1)} = (\chi_1^{(1)}+\chi_3^{(1)}\bar{x}_3^{(1)})x_2,$$

$$u_3^{(1)} = \psi_0^{(1)}+\psi_2^{(1)}\bar{x}_3^{(1)}+\frac{1}{2}\psi_4^{(1)}\left[3(x_2)^2-\frac{l_2^2}{4}\right]$$
$$+\frac{1}{2}\psi_5^{(1)}\left[3(\bar{x}_3^{(1)})^2-\frac{d_1^2}{4}\right] \tag{15}$$

$$u_1^{(2)} = \phi_0^{(2)}+\frac{1}{2}\phi_4^{(2)}\left[3(x_2)^2-\frac{l_2^2}{4}\right]$$
$$+\frac{1}{2}\phi_5^{(2)}\left[3(\bar{x}_3^{(2)})^2-\frac{d_2^2}{4}\right],$$

$$u_2^{(2)} = \chi_1^{(2)}x_2,$$

$$u_3^{(2)} = \psi_2^{(2)}\bar{x}_3^{(2)} \tag{16}$$

$$u_1^{(3)} = \phi_0^{(3)}+\phi_2^{(3)}\bar{x}_3^{(3)}+\frac{1}{2}\phi_4^{(3)}\left[3(x_2)^2-\frac{l_2^2}{4}\right]$$
$$+\frac{1}{2}\phi_5^{(3)}\left[3(\bar{x}_3^{(3)})^2-\frac{d_3^2}{4}\right],$$

$$u_2^{(3)} = (\chi_1^{(3)}+\chi_3^{(3)}\bar{x}_3^{(3)})x_2,$$

$$u_3^{(3)} = \psi_0^{(3)}+\psi_2^{(3)}\bar{x}_3^{(3)}+\frac{1}{2}\psi_4^{(3)}\left[3(x_2)^2-\frac{l_2^2}{4}\right]$$
$$+\frac{1}{2}\psi_5^{(3)}\left[3(\bar{x}_3^{(3)})^2-\frac{d_3^2}{4}\right] \tag{17}$$

Equation (14) yields the following relationships

$$\phi_0^{(3)}=\phi_0^{(1)},\quad \phi_2^{(3)}=-\phi_2^{(1)},\quad \phi_4^{(3)}=\phi_4^{(1)},\quad \phi_5^{(3)}=\phi_5^{(1)},$$
$$\chi_1^{(3)}=\chi_1^{(1)},\quad \chi_3^{(3)}=-\chi_3^{(1)},\ \psi_0^{(3)}=-\psi_0^{(1)},$$
$$\psi_2^{(3)}=\psi_2^{(1)},\quad \psi_4^{(3)}=-\psi_4^{(1)},\quad \psi_5^{(3)}=-\psi_5^{(1)} \tag{18}$$

As a result of the previous relations, we have altogether the 15 unknown field variables

Downloaded 03 May 2010 to 171.66.16.21. Redistribution subject to ASME license or copyright; see http://www.asme.org/terms/Terms_Use.cfm

$\phi_0^{(1)}$, $\phi_2^{(1)}$, $\phi_4^{(1)}$, $\phi_5^{(1)}$, $\chi_1^{(1)}$, $\chi_3^{(1)}$, $\psi_0^{(1)}$,

$\psi_2^{(1)}$, $\psi_4^{(1)}$, $\psi_5^{(1)}$, $\phi_0^{(2)}$, $\phi_4^{(2)}$, $\phi_5^{(2)}$, $\chi_1^{(2)}$, $\psi_2^{(2)}$

The components of the small strain tensor are given by

$$\epsilon_{ij}^{(\alpha)} = \frac{1}{2}(\partial_i u_j^{(\alpha)} + \partial_j u_i^{(\alpha)}) \tag{19}$$

where $\partial_1 = \partial/\partial x_1$, $\partial_2 = \partial/\partial x_2$, and $\partial_3 = \partial/\partial \bar{x}_3^{(\alpha)}$, from which the ply strains in terms of the previous field variables can be determined.

Let us consider the general case of an orthotropic ply for which the stress-strain relations are given by

$$\boldsymbol{\sigma}^{[\alpha]} = \mathbf{C}^{(\alpha)} \boldsymbol{\epsilon}^{[\alpha]}, \tag{20}$$

where

$$\boldsymbol{\sigma}^{[\alpha]} = [\sigma_{11}^{(\alpha)}, \sigma_{22}^{(\alpha)}, \sigma_{33}^{(\alpha)}, \sigma_{23}^{(\alpha)}, \sigma_{12}^{(\alpha)}, \sigma_{13}^{(\alpha)}],$$

$$\boldsymbol{\epsilon}^{[\alpha]} = [\epsilon_{11}^{(\alpha)}, \epsilon_{22}^{(\alpha)}, \epsilon_{33}^{(\alpha)}, 2\epsilon_{23}^{(\alpha)}, 2\epsilon_{12}^{(\alpha)}, 2\epsilon_{13}^{(\alpha)}],$$

and

$$C^{(\alpha)} = \begin{bmatrix} C_{11}^{(\alpha)} & C_{12}^{(\alpha)} & C_{13}^{(\alpha)} & 0 & 0 & 0 \\ C_{12}^{(\alpha)} & C_{22}^{(\alpha)} & C_{23}^{(\alpha)} & 0 & 0 & 0 \\ C_{13}^{(\alpha)} & C_{23}^{(\alpha)} & C_{33}^{(\alpha)} & 0 & 0 & 0 \\ 0 & 0 & 0 & C_{44}^{(\alpha)} & 0 & 0 \\ 0 & 0 & 0 & 0 & C_{55}^{(\alpha)} & 0 \\ 0 & 0 & 0 & 0 & 0 & C_{66}^{(\alpha)} \end{bmatrix}$$

Using (15)–(18) into (19) and (20), the explicit expressions of the stress components of the αth ply can be determined in terms of unknown field variables of the ply. The resulting explicit expressions are lengthy and can be found in Lee (1987).

The equilibrium equations in each ply are given by

$$\partial_i \sigma_{ij}^{(\alpha)} = 0, \quad |\bar{x}_3^{(\alpha)}| \le \frac{d_\alpha}{2} \tag{21}$$

Multiplying (21) by $(x_2)^m (\bar{x}_3^{(\alpha)})^n$, $(n,\ m = 0,1,2)$ and integrating yields

$$\frac{1}{d_\alpha l_2} \int_{-l_2/2}^{l_2/2} \int_{-d_\alpha/2}^{d_\alpha/2} \left[\partial_1 \sigma_{1j}^{(\alpha)} + \partial_2 \sigma_{2j}^{(\alpha)} + \partial_3 \sigma^{(\alpha)}{}_{3j} \right] (x_2)^m (\bar{x}_3^{(\alpha)})^n dx_2 d\bar{x}_3^{(\alpha)} = 0 \tag{22}$$

Integration by parts provides

$$\begin{aligned} &\partial_1 \overset{(m,n)}{S}{}_{1j}^{(\alpha)} - m \overset{(m-1,n)}{S}{}_{2j}^{(\alpha)} - n \overset{(m,n-1)}{S}{}_{3j}^{(\alpha)} \\ &+ \frac{1}{d_\alpha l_2} \left(\frac{l_2}{2} \right)^m \int_{-d_\alpha/2}^{d_\alpha/2} \left[\sigma_{2j}^{(\alpha)} \Big|_{x_2 = l_2/2} \right. \\ &\left. - (-1)^m \sigma_{2j}^{(\alpha)} \Big|_{x_2 = -l_2/2} \right] (\bar{x}_3^{(\alpha)})^n d\bar{x}_3^{(\alpha)} \\ &+ \frac{1}{d_\alpha l_2} \left(\frac{l_2}{2} \right)^n \int_{-l_2/2}^{l_2/2} \left[\sigma_{3j}^{(\alpha)} \Big|_{\bar{x}_3^{(\alpha)} = d_\alpha/2} \right. \\ &\left. - (-1)^n \sigma_{3j}^{(\alpha)} \Big|_{\bar{x}_3^{(\alpha)} = -d_\alpha/2} \right] x_2^m dx_2 = 0 \end{aligned} \tag{23}$$

where the stress moments $\overset{(m,n)}{S}{}_{ij}^{(\alpha)}$ are given by

$$\overset{(m,n)}{S}{}_{ij}^{(\alpha)} = \frac{1}{d_\alpha l_2} \int_{-l_2/2}^{l_2/2} \int_{-d_\alpha/2}^{d_\alpha/2} \sigma_{ij}^{(\alpha)} (x_2)^m (\bar{x}_3^{(\alpha)})^n dx_2 d\bar{x}_3^{(\alpha)} \tag{24}$$

and $(m,\ n) = (0,0)$, $(0,1)$, $(1,0)$, $(1,1)$, $(0,2)$, $(2,0)$. The explicit expressions of $\overset{(m,n)}{S}{}_{ij}^{(\alpha)}$ can be determined readily from those of $\sigma_{ij}^{(\alpha)}$ but they are not reproduced here; see Lee (1987).

By utilizing the traction-free conditions (1), (3), (4*a*) and the traction continuity conditions (9), the boundary and interfacial stress terms in (23) can be eliminated yielding the following set of nontrivial equations

$$\begin{aligned}
&2d_1 \partial_1 \overset{(0,0)}{S}{}_{11}^{(1)} + d_2 \partial_1 \overset{(0,0)}{S}{}_{11}^{(2)} = 0, \\
&2\partial_1 \overset{(0,1)}{S}{}_{13}^{(1)} - 2 \overset{(0,0)}{S}{}_{33}^{(1)} - \partial_1 \overset{(0,1)}{S}{}_{13}^{(2)} + \overset{(0,0)}{S}{}_{33}^{(2)} = 0, \\
&4\partial_1 \overset{(0,1)}{S}{}_{11}^{(1)} - 4 \overset{(0,0)}{S}{}_{13}^{(1)} + d_2 \partial_1 \overset{(0,0)}{S}{}_{11}^{(2)} = 0, \\
&8\partial_1 \overset{(0,2)}{S}{}_{11}^{(1)} - 16 \overset{(0,1)}{S}{}_{13}^{(1)} + d_1 d_2 \partial_1 \overset{(0,0)}{S}{}_{11}^{(2)} = 0, \\
&d_1 \partial_1 \overset{(0,0)}{S}{}_{13}^{(1)} - \partial_1 \overset{(0,1)}{S}{}_{13}^{(2)} + \overset{(0,0)}{S}{}_{33}^{(2)} = 0, \\
&d_2^2 \partial_1 \overset{(0,0)}{S}{}_{11}^{(2)} - 4\partial_1 \overset{(0,2)}{S}{}_{11}^{(2)} + 8 \overset{(0,1)}{S}{}_{13}^{(2)} = 0, \\
&4\partial_1 \overset{(0,2)}{S}{}_{13}^{(1)} - 8 \overset{(0,1)}{S}{}_{33}^{(1)} - d_1 \partial_1 \overset{(0,1)}{S}{}_{13}^{(2)} + d_1 \overset{(0,0)}{S}{}_{33}^{(2)} = 0, \\
&2d_1 \partial_1 \overset{(1,0)}{S}{}_{12}^{(1)} - 2d_1 \overset{(0,0)}{S}{}_{22}^{(1)} + d_2 \partial_1 \overset{(1,0)}{S}{}_{12}^{(2)} - d_2 \overset{(0,0)}{S}{}_{22}^{(2)} = 0, \\
&4\partial_1 \overset{(1,1)}{S}{}_{12}^{(1)} - 4 \overset{(0,1)}{S}{}_{22}^{(1)} - 4 \overset{(1,0)}{S}{}_{23}^{(1)} + d_2 \partial_1 \overset{(1,0)}{S}{}_{12}^{(2)} - d_2 \overset{(0,0)}{S}{}_{22}^{(2)} = 0, \\
&2d_1 \partial_1 \overset{(2,0)}{S}{}_{11}^{(1)} - 4d_1 \overset{(1,0)}{S}{}_{12}^{(1)} + d_2 \partial_1 \overset{(2,0)}{S}{}_{11}^{(2)} - 2d_2 \overset{(1,0)}{S}{}_{12}^{(2)} = 0
\end{aligned} \tag{25}$$

By substituting the various expressions of $\overset{(m,n)}{S}{}_{ij}^{(\alpha)}$ into (25), the following 10 differential equations in the 15 unknown field variables are obtained

$$\begin{aligned}
&2d_1 C_{11}^{(1)} \partial_1^2 \phi_0^{(1)} + 2d_1 C_{12}^{(1)} \partial_1 \chi_1^{(1)} + 2d_1 C_{13}^{(1)} \partial_1 \psi_2^{(1)} \\
&+ d_2 C_{11}^{(2)} \partial_1^2 \phi_0^{(2)} + d_2 C_{12}^{(2)} \partial_1 \chi_1^{(2)} + d_2 C_{13}^{(2)} \partial_1 \psi_2^{(2)} = 0, \\
&24 C_{13}^{(1)} \partial_1 \phi_0^{(1)} - 6d_1^2 C_{66}^{(1)} \partial_1 \phi_5^{(1)} + 24 C_{23}^{(1)} \chi_1^{(1)} + 24 C_{33}^{(1)} \psi_2^{(1)} \\
&- 2d_1^2 C_{66}^{(1)} \partial_1^2 \psi_2^{(1)} - 12 C_{13}^{(2)} \partial_1 \phi_0^{(2)} + 3d_2^2 C_{66}^{(2)} \partial_1 \phi_5^{(2)} - 12 C_{23}^{(2)} \chi_1^{(2)} \\
&- 12 C_{33}^{(2)} \psi_2^{(2)} + d_2^2 C_{66}^{(2)} \partial_1^2 \psi_2^{(2)} = 0, \\
&d_1^2 C_{11}^{(1)} \partial_1^2 \phi_2^{(1)} - 12 C_{66}^{(1)} \phi_2^{(1)} + d_1^2 C_{12}^{(1)} \partial_1 \chi_3^{(1)} - 12 C_{66}^{(1)} \partial_1 \psi_0^{(1)} \\
&+ 3d_1^2 C_{13}^{(1)} \partial_1 \psi_5^{(1)} + 3d_2 C_{11}^{(2)} \partial_1^2 \phi_0^{(2)} + 3d_2 C_{12}^{(2)} \partial_1 \chi_1^{(2)} \\
&+ 3d_2 C_{13}^{(2)} \partial_1 \psi_2^{(2)} = 0, \\
&10d_1^2 C_{11}^{(1)} \partial_1^2 \phi_0^{(1)} + d_1^4 C_{11}^{(1)} \partial_1^2 \phi_5^{(1)} - 60d_1^2 C_{66}^{(1)} \phi_5^{(1)} + 10d_1^2 (C_{13}^{(1)} \\
&- 2C_{66}^{(1)}) \partial_1 \psi_2^{(1)} + 10d_1^2 C_{12}^{(1)} \partial_1 \chi_1^{(1)} + 15d_1 d_2 C_{11}^{(2)} \partial_1^2 \phi_0^{(2)} \\
&+ 15d_1 d_2 C_{12}^{(2)} \partial_1 \chi_1^{(2)} + 15d_1 d_2 C_{13}^{(2)} \partial_1 \psi_2^{(2)} = 0, \\
&12d_1 C_{66}^{(1)} \partial_1 \phi_2^{(1)} + 12d_1 C_{66}^{(1)} \partial_1^2 \psi_0^{(1)} - 3d_2^2 C_{66}^{(2)} \partial_1 \phi_5^{(2)} - d_2^2 C_{66}^{(2)} \partial_1^2 \psi_2^{(2)} \\
&+ 12 C_{13}^{(2)} \partial_1 \phi_0^{(2)} + 12 C_{23}^{(2)} \chi_1^{(2)} + 12 C_{33}^{(2)} \psi_2^{(2)} = 0,
\end{aligned}$$

Downloaded 03 May 2010 to 171.66.16.21. Redistribution subject to ASME license or copyright; see http://www.asme.org/terms/Terms_Use.cfm

$$20C_{11}^{(2)}\partial_1^{\{2)}\phi_0{}^{(2}+60C_{66}^{(2)}\phi_5^{\{2)}-d_2^2C_{11}^{(2)}\partial_1^2\phi_5^{\{2)}$$

$$+20C_{12}^{(2)}\partial_1\chi_1^{\{2)}+20(C_{13}^{(2)}+C_{66}^{(2)})\partial_1\psi_2^{\{2)}=0,$$

$$20d_1^2(C_{66}^{(1)}-2C_{13}^{(1)})\partial_1\phi_2^{\{1)}-40d_1^2C_{23}^{(1)}\chi_3^{\{1)}+20d_1^2C_{66}^{(1)}\partial_1^2\psi_0^{\{1)}$$

$$+2d_1^4C_{66}^{(1)}\partial_1^2\psi_5^{\{1)}-120d_1^2C_{33}^{(1)}\psi_5^{\{1)}+60d_1C_{13}^{(2)}\partial_1\phi_0^{\{2)}$$

$$-15d_1d_2^2C_{66}^{(2)}\partial_1\phi_5^{\{2)}+60d_1C_{23}^{(2)}\chi_1^{\{2)}+60d_1C_{33}^{(2)}\psi_2^{\{2)}$$

$$-5d_1d_2^2C_{66}^{(2)}\partial_1^2\psi_2^{\{2)}=0,$$

$$24d_1C_{12}^{(1)}\partial_1\phi_0^{\{1)}-6d_1l_2^2C_{55}^{(1)}\partial_1\phi_4^{\{1)}+24d_1C_{22}^{(1)}\chi_1^{\{1)}-2d_1l_2^2C_{55}^{(1)}\partial_1^2\chi_1^{\{1)}$$

$$+24d_1C_{23}^{(1)}\psi_2^{\{1)}+12d_2C_{12}^{(2)}\partial_1\phi_0^{\{2)}-3d_2l_2^2C_{55}^{(2)}\partial_1\phi_4^{\{2)}$$

$$+12d_2C_{22}^{(2)}\chi_1^{\{2)}-d_2l_2^2C_{55}^{(2)}\partial_1^2\chi_1^{\{2)}+12d_2C_{23}^{(2)}\psi_2^{\{2)}=0,$$

$$12d_1^2C_{12}^{(1)}\partial_1\phi_2^{\{1)}+12(d_1^2C_{22}^{(1)}+l_2^2C_{44}^{(1)})\chi_3^{\{1)}-d_1^2l_2^2C_{55}^{(1)}\partial_1^2\chi_3^{\{1)}$$

$$+36l_2^2C_{44}^{(1)}\psi_4^{\{1)}+36d_1^2C_{23}^{(1)}\psi_5^{\{1)}+36d_2C_{12}^{(2)}\partial_1\phi_0^{\{2)}-9d_2l_2^2C_{55}^{(2)}\partial_1\phi_4^{\{2)}$$

$$+36d_2C_{22}^{(2)}\chi_1^{\{2)}-3d_2l_2^2C_{55}^{(2)}\partial_1^2\chi_1^{\{2)}+36d_2C_{23}^{(2)}\psi_2^{\{2)}=0,$$

$$20d_1l_2^2C_{11}^{(1)}\partial_1^2\phi_0^{\{1)}+2d_1l_2^4C_{11}^{(1)}\partial_1^2\phi_4^{\{1)}-120d_1l_2^2C_{55}^{(1)}\phi_4^{\{1)}$$

$$+20d_1l_2^2(C_{12}^{(1)}-2C_{55}^{(1)})\partial_1\chi_1^{\{1)}+20d_1l_2^2C_{13}^{(1)}\partial_1\psi_2^{\{1)}$$

$$+10d_2l_2^2C_{11}^{(2)}\partial_1^2\phi_0^{\{2)}+d_2l_2^4C_{11}^{(2)}\partial_1^2\phi_4^{\{2)}-60d_2l_2^2C_{55}^{(2)}\phi_4^{\{2)}$$

$$+10d_2l_2^2(C_{12}^{(2)}-2C_{55}^{(2)})\partial_1\chi_1^{\{2)}$$

$$+10d_2l_2^2C_{13}^{(2)}\partial_1\psi_2^{\{2)}=0. \tag{26}$$

Five additional equations are provided by the displacement continuity conditions (10). Substituting (15) and (16) into (10) yields the 5 equations

$$4\phi_0^{\{1)}+2d_1\phi_2^{\{1)}+d_1^2\phi_5^{\{1)}-4\phi_0^{\{2)}-d_2^2\phi_5^{\{2)}=0,$$

$$\phi_4^{\{1)}-\phi_4^{\{2)}=0,$$

$$2\chi_1^{\{1)}+d_1\chi_3^{\{1)}-2\chi_1^{\{2)}=0,$$

$$4\psi_0^{\{1)}+2d_1\psi_2^{\{1)}+d_1^2\psi_5^{\{1)}+2d_2\psi_2^{\{2)}=0,$$

$$\psi_4^{\{1)}=0 \tag{27}$$

Equations (26) and (27) form a set of 15 linear equations which govern the variation of the aforementioned 15 field variables at any point along $0\le x_1\le l_1/2$. These equations should be supplemented with the boundary conditions (6)–(8). In terms of our field variables, equations (6)–(8) provide

$$\phi_0^{\{1)}=\phi_2^{\{1)}=\phi_4^{\{1)}=\phi_5^{\{1)}=\phi_0^{\{2)}=\phi_4^{\{2)}=\phi_5^{\{2)}=0,$$

$$\partial_1\chi_1^{\{1)}=\partial_1\chi_3^{\{1)}=\partial_1\chi_1^{\{2)}=0,$$

$$\partial_1\psi_0^{\{1)}=\partial_1\psi_2^{\{1)}=\partial_1\psi_4^{\{1)}=\partial_1\psi_5^{\{1)}=\partial_1\psi_2^{\{2)}=0, \quad \text{at} \quad x_1=0 \tag{28}$$

and

$$\phi_0^{\{1)}=1,\ \phi_2^{\{1)}=\phi_4^{\{1)}=\phi_5^{\{1)}=0,$$

$$\partial_1\chi_1^{\{1)}=\partial_1\chi_3^{\{1)}=0,$$

$$\partial_1\psi_0^{\{1)}=\partial_1\psi_2^{\{1)}=\psi_4^{\{1)}=\partial_1\psi_5^{\{1)}=0,$$

$$C_{11}^{(2)}\partial_1\phi_0^{\{2)}+C_{12}^{(2)}\chi_1^{\{2)}+C_{13}^{(2)}\psi_2^{\{2)}=0,$$

$$\partial_1\phi_4^{\{2)}=\partial_1\phi_5^{\{2)}=0,$$

$$3\phi_4^{\{2)}+\partial_1\chi_1^{\{2)}=0,$$

$$3\phi_5^{\{2)}+\partial_1\psi_2^{\{2)}=0, \quad \text{at} \quad x_1=l_1/2 \tag{29}$$

The solution of the system of equations (26)–(29) is performed by approximating the derivations by difference expressions and solving the resulting system of linear algebraic equations utilizing the band structure of the coefficients matrix. The determination of the field variables at points along $0\le x_1\le l_1/2$ provides the variation of displacements and stresses in the laminate as well as its effective stiffness and Poisson's ratio.

3 Application

The previous method is used herein to study the effect of cross cracks on the mechanical behavior of symmetric graphite/epoxy composite laminates. The material properties of the single unidirectional ply are given in Table 1. The thickness of each ply is 0.127 mm. This type of damaged laminates was analyzed by Highsmith, et al. (1986) and their results are used here for comparison.

In order to verify the veracity of the present method, the special case of $l_1/l_2 << 1$ was analyzed. This implies that only transverse cracks are present. Consequently, the 3-dimensional analysis reduces, in this case, to the 2-dimensional problem of a composite laminate with transverse cracks. This situation was analyzed independently by an approximate analytical solution as well as by a finite-element procedure (Herakovich, et al., 1988). It turns out that the results obtained from the present 3-dimensional analysis coincide with those obtained from the 2-dimensional procedure in this special case. This provides a direct necessary check of the proposed method.

3.1 Axial Stiffness. The average axial stress in the symmetric laminate ($d_1=d_3$) is given by

$$\bar{\sigma}_{11}=[2d_1\overset{(0,0)}{S}{}_{11}^{(1)}+d_2\overset{(0,0)}{S}{}_{11}^{(2)}]/(2d_1+d_2). \tag{30}$$

For the unit applied displacement, see equation (8), the average axial strain given by

$$\bar{\epsilon}_{11}=1/(l_1/2). \tag{31}$$

Thus the effective axial stiffness of the damage laminate is determined from

$$E_{11}^*=\bar{\sigma}_{11}/\bar{\epsilon}_{11}. \tag{32}$$

In Fig. 4, the reduction of the effective axial stiffness E_{11}^* of a $[0/90]_s$ laminate with respect to the density of the transverse cracks (in the x_1-direction) and longitudinal cracks (in the x_2-direction) is shown. The effective stiffness is normalized with respect to the uncracked laminate stiffness $E_{11}^0=69.3$ GPa. It can be readily noted that the effect of the transverse cracks on stiffness reduction of the laminate is dominant, whereas the effect of the longitudinal cracks appears to be of less significance.

The predicted values of E_{11}^* by the present method can be compared with those given by Highsmith (1984) for a $[0/90_2]_s$ laminate with crack densities $1/l_1=1.6\ \text{mm}^{-1}$ and $1/l_2=0.63\ \text{mm}^{-1}$. The predicted values are shown in Table 2 which exhibits excellent agreement between the two different approaches; also shown in the table are the results obtained from the lamination theory in conjunction with the ply-discount method. According to this method, the effect of transverse cracking is modeled by reducing E_{22} of the cracked 90-deg plies to zero. The longitudinal cracks are modeled, on the other hand, by reducing E_{22} of the cracked 0-deg plies to zero. The ply-discount method is seen to predict 13.7 percent stiff-

Downloaded 03 May 2010 to 171.66.16.21. Redistribution subject to ASME license or copyright; see http://www.asme.org/terms/Terms_Use.cfm

Table 1 Elastic constants for a unidirectional graphite-epoxy composite

E_{11}(GPa)	ν_{12}	G_{12}(GPa)	E_{22}(GPa)	ν_{23}
128.2	0.31	5.39	9.72	0.49

The parameters E_{11} and ν_{12} denote the axial Young's modulus and Poisson's ratio, G_{12} denotes the axial shear modulus, and E_{22} and ν_{23} stand for the transverse Young's modulus and Poisson's ratio.

Table 2 Comparison of the effective axial stiffness $E_{11}^{\dagger}$ of a cracked $[0/90_{=1}]_s$ graphite-epoxy laminate; the crack densities are $1/l_1 = 1.6$ mm^{-1}, $1/l_2 = 0.63$ mm^{-1}

Damage condition	Present analysis	Highsmith (1984) analysis	Lamination theory
Undamaged	50.2 GPa		49.5 GPa
Transverse cracking	45.5 GPa	44.8 GPa	43.0 GPa
Cross cracking	45.5 GPa	44.8 GPa	42.7 GPa

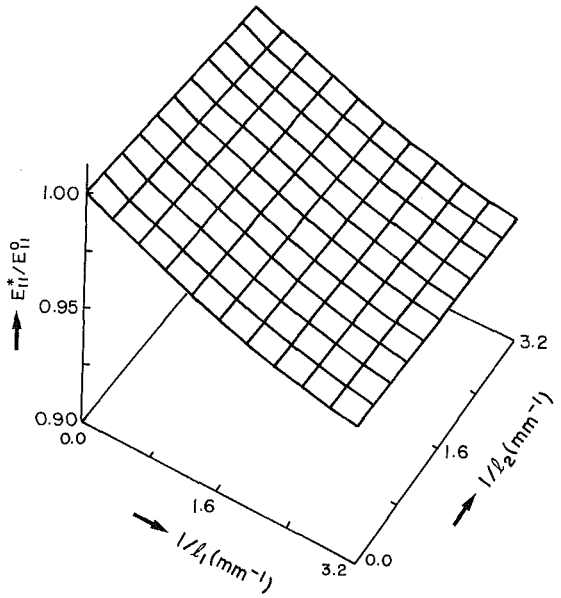


Fig. 4 Degradation of the normalized effective axial stiffness modulus $E_{11}^{\dagger}$ of $[0/90]_s$ laminate with longitudinal and transverse crack densities

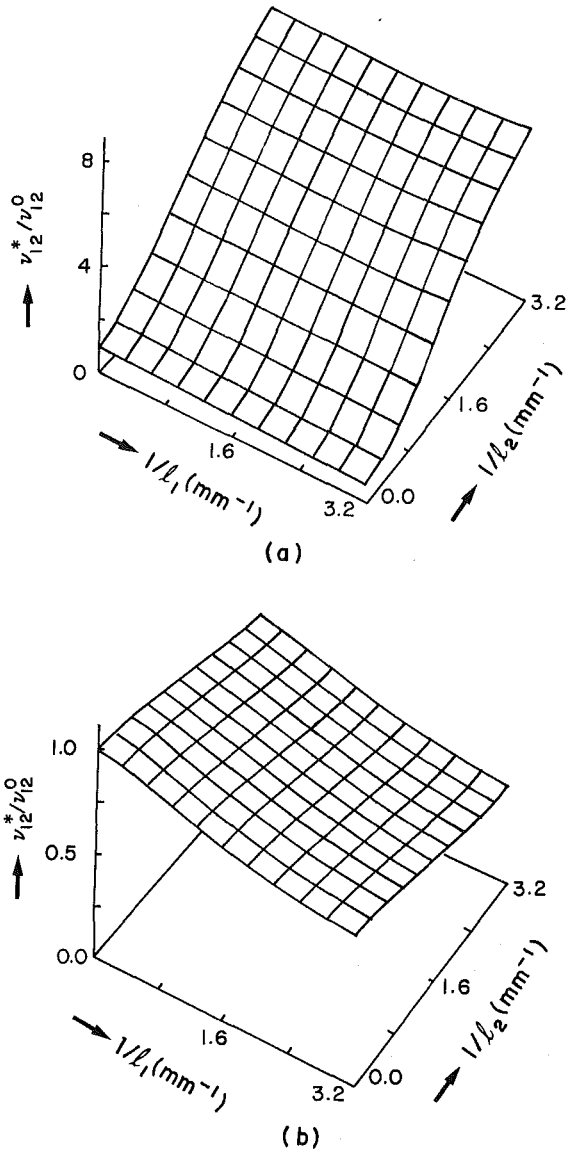


Fig. 5 Degradation of the normalized effective Poisson's ratio $\nu_{12}^{\dagger}$ of $[0/90]_s$ laminate with longitudinal and transverse crack densities; (*a*) $\nu_{12}^{\dagger}$ at the top surface and (*b*) $\nu_{12}^{\dagger}$ at the midplane

ness reduction due to cross cracking as compared with 9 percent and 11 percent according to the present 3-dimensional and Highsmith's analysis, respectively. The experimentally observed stiffness change was 6 percent (Highsmith (1984)).

3.2 Poisson's Ratio. Let us define the lateral strain in the form

$$\hat{\epsilon}_{22} = [u_2|_{x_2 = l_2/2} - u_2|_{x_2 = -l_2/2}]/l_2. \tag{33}$$

By averaging $\hat{\epsilon}_{22}$ from $x_1 = 0$ through $x_1 = l_1/2$, we can define the average lateral strain of the laminate in the form

$$\bar{\epsilon}_{22} = \frac{2}{l_1}\int_0^{l_1/2} \hat{\epsilon}_{22} dx_1. \tag{34}$$

Accordingly, the effective Poisson's ratio of the damaged laminate can be determined from

$$\nu_{12}^* = -\bar{\epsilon}_{22}/\bar{\epsilon}_{11}, \tag{35}$$

with $\bar{\epsilon}_{11}$ given in (31). Note that in general ν_{12}^* is a function of x_3.

In Fig. 5, the Poisson's ratio of a $[0/90]_s$ laminate is shown at two different locations: (*a*) At the top surface (i.e., at $x_3 = d_1 + d_2/2$); (*b*) At the midplane (i.e., at $x_3 = 0$). In both cases the Poisson's ratios are normalized with respect to that of the undamaged laminae: $\nu_{12}^0 = 0.0434$. Both plots of Fig. 5 exhibit clearly the degradation of ν_{12}^* with increase of transverse crack density (i.e., $1/l_1$). The dependence of ν_{12}^* on the longitudinal cracks, however, is significantly different in the two locations. The Poisson's ratio at the top surface rises to several times ν_{12}^0 as the longitudinal crack density ($1/l_2$) increases. This result seems reasonable, since there won't be any constraint for the deformation of the outer layer (0-deg ply) in the x_2-direction. The Poisson's ratio at the midplane, on the other hand, decreases as the longitudinal crack density increases. It may appear that this observation is not plausible, but a simple laminate analysis by the ply-discount method shows also that ν_{12}^* would decrease if there are longitudinal cracks in the outer plies of $[0/90]_s$. This observation can be explained by the mismatch of the Poisson's ratios, $\nu_{12}^{(\alpha)}$, of the 0 and 90-deg layers which are perfectly bonded. Due to the uniaxial loading, there will be a transverse tension in the 0-deg layer (i.e., $\sigma_{22}^{(1)} > 0$) balanced, due to equilibrium, by a transverse compression in the 90-deg layer (i.e., $\sigma_{22}^{(2)} < 0$). Con-

Downloaded 03 May 2010 to 171.66.16.21. Redistribution subject to ASME license or copyright; see http://www.asme.org/terms/Terms_Use.cfm

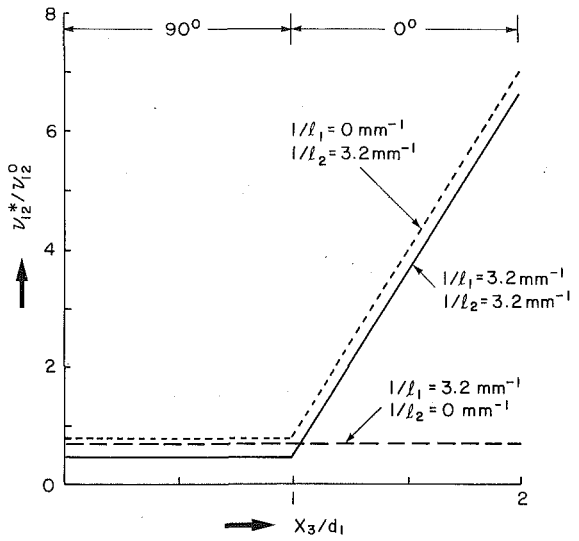


Fig. 6 Variation of the normalized effective Poisson's ratios ν_{12}^* through the thickness of $[0/90]_s$ laminate

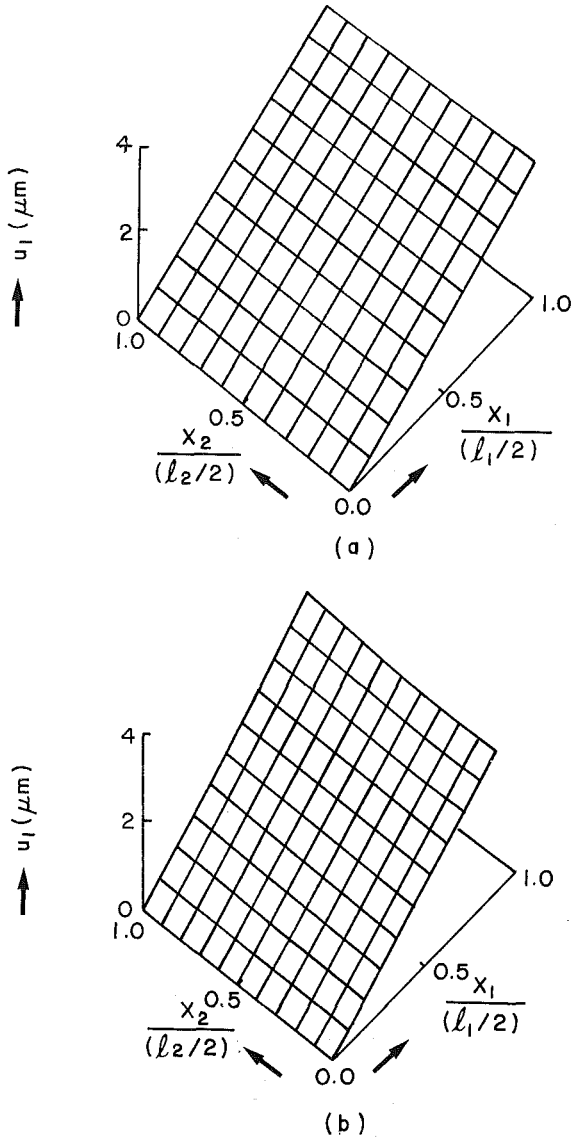


Fig. 7 Variation of the axial displacement u_1 at the top surface of $[0/90_2]_s$ laminate due to an applied axial strain of 1 percent. The crack spacings are $l_1 = 0.636$ mm, $l_2 = 1.588$ mm; (a) present analysis and (b) Highsmith (1984).

sequently, the transverse strain $\epsilon_{22}^{(\alpha)}$ in the ply is not only given by its own Poisson's effect: $-\nu_{12}^{(\alpha)}\sigma_{11}^{(\alpha)}/E_{11}^{(\alpha)}$, but it will be also affected by the corresponding transverse tension or compression $\cdot\sigma_{22}^{(\alpha)}/E_{22}^{(\alpha)}$. Since the longitudinal cracks decrease the transverse tension $\sigma_{22}^{(1)}$ in the 0-deg layer, the transverse compression $\sigma_{22}^{(2)}$ will be reduced as well. As a result, the negative strain $\epsilon_{22}^{(2)}$ in the 90-deg layer will decrease, which implies that ν_{12}^* of this layer becomes smaller. Another support to this result is provided by Highsmith (1984) who indicates that on a global level, the Poisson's ratio should decrease with damage development due to longitudinal cracks.

Figure 6 exhibits the variation of Poisson's ratio ν_{12}^* through the thickness of the $[0/90]_s$ cracked laminate. This variation is shown for several values of crack densities. The figure displays clearly the effect of longitudinal cracks which decrease ν_{12}^* in the 90-deg ply (as just explained) but increase it significantly in the outer layers. It should be noted that if only tranverse cracks exist (i.e., $1/l_2 = 0$), a constant variation is obtained throughout the thickness of the laminate due to the generalized plane-strain state which exists in this 2-dimensional problem. The development of longitudinal cracks decreases ν_{12}^* in the 90-deg ply, but increases it significantly in the 0-deg plies. If the laminate is completely free of transverse cracks in the 90-deg plies (i.e., $1/l_1 = 0$), the two bilinear variations shift by the same amount simultaneously. Thus the transverse cracks reduce the effective Poisson's ratio in both plies by the same amount. Due to the periodicity, the lateral surface of the 90-deg ply (i.e., $|x_2| = l_2/2$) will remain plane after the loading is applied. This implies that ν_{12}^* should be constant through the thickness of the 90-deg ply. This expected behavior is exhibited in the figure by the constant variation along $0 \le x_3/d_1 \le 1$. On the other hand, the variation of ν_{12}^*, through the thickness of the 0-deg ply is seen to be linearly increasing. This steady increase is attributed to the fact that there is no constraint at the traction-free surfaces of the longitudinal cracks. The linear variation of ν_{12}^* through the thickness of the 0-deg ply results from our second-order expansion (11), and a nonlinear increase is expected from a higher-order expansion.

The previous results indicate that the Poisson's ratio of a damaged laminate is a better indicator of the degree of damage by cross cracks than its axial stiffness reduction. The effect of both types of cracks on ν_{12}^* is pronounced in contrast to E_{11}^* on which the effect of longitudinal cracks is small.

For a very high longitudinal crack densities, the measurement of ν_{12}^* on the top surface of the laminate by strain gages or other methods may be misleading. This is because the strain gage may bridge two or more cracks. A more reliable method to measure the effective Poisson's ratio of the damaged laminate may be the use of extensometers.

3.3 Axial Displacement. In Fig. 7, the variation of the axial displacement u_1 computed at the top surface of a $[0/90_2]_s$ cracked laminate by the present and Highsmith, et al. (1986) methods are given. In both cases, the crack spacings are $l_1 = 0.636$ mm, $l_2 = 1.588$ mm and the loading corresponds to an applied axial strain of $\bar{\epsilon}_{11} = 0.01$, which corresponds to an applied displacement of 3.18×10^{-3} mm in (8). Note that the transverse crack is located in the 90-deg ply along the line $x_1/(l_1/2) = 1$, while the longitudinal crack is located in the 0-deg ply along $x_2/(l_2/2) = 1$. The lines $x_1 = 0$ and $x_2 = 0$ are at one half the distance between the successive transverse and longitudinal cracks, respectively. The axial displacement exhibits a linear variation in the x_1-direction which corresponds to the applied state of uniform axial strain loading. The excellent agreement between the two methods, which indicate that neither the longitudinal nor the transverse crack has a significant effect on the axial displacement, can be noticed.

Downloaded 03 May 2010 to 171.66.16.21. Redistribution subject to ASME license or copyright; see http://www.asme.org/terms/Terms_Use.cfm

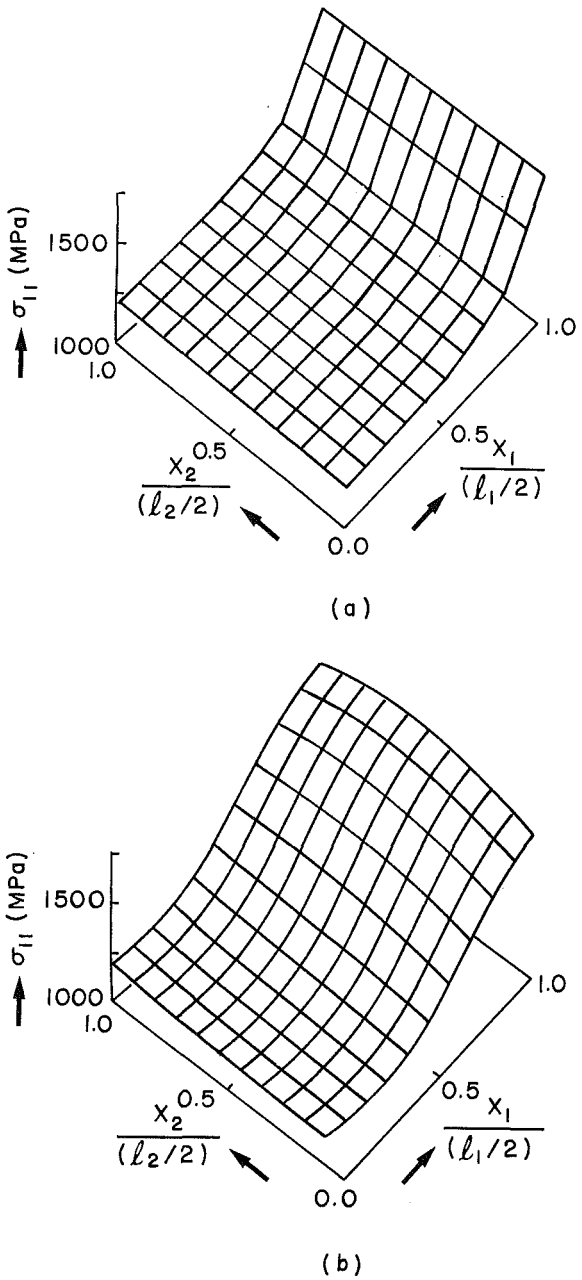


Fig. 8 Variation of the axial stress σ_{11} at the 0-deg at the 0/90 interface of $[0/90_2]_s$ laminate due to an applied axial strain of 1 percent. The crack spacings are $l_1 = 0.636$ mm, $l_2 = 1.588$ mm; (*a*) present analysis and (*b*) Highsmith (1984).

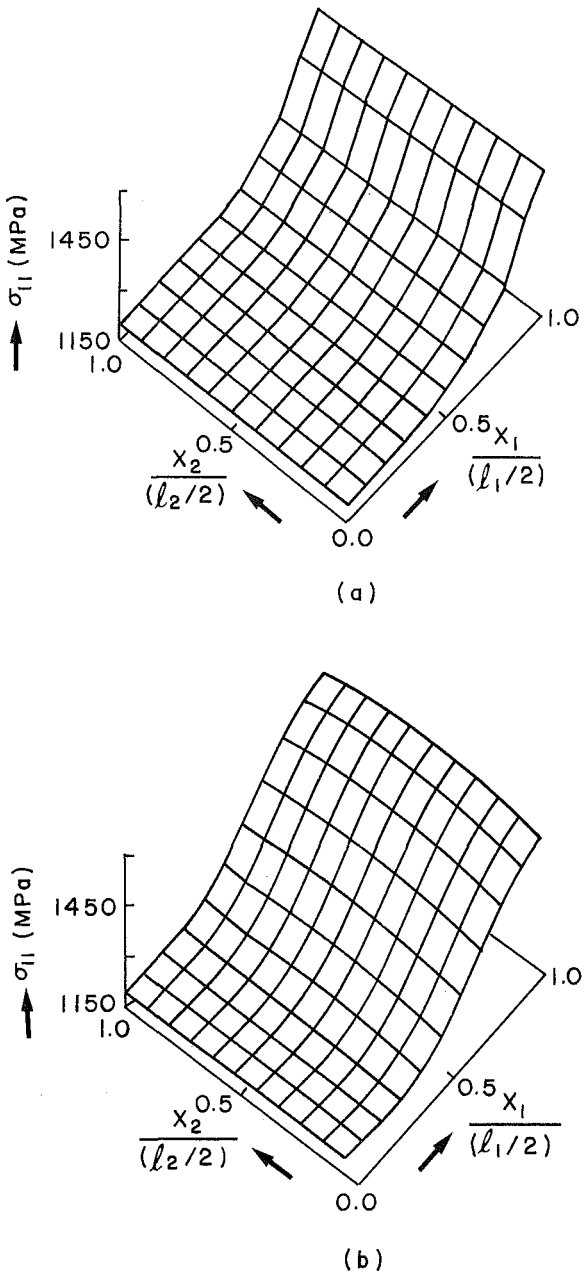


Fig. 9 Variation of the axial stress σ_{11} at the 0/90 interface of $[0/90]_s$ laminate due to an applied axial strain of 1 percent. The crack spacings are $l_1 = 0.482$ mm, $l_2 = 1.588$ mm; (*a*) present analysis and (*b*) Highsmith (1984).

This essentially uniform variation is consistent with the experimental results of Highsmith, et al. (1986).

3.4 Axial Stress. The distribution of the axial stress σ_{11} in the 0-deg ply along the 0/90 interface of the cracked $[0/90_2]_s$ laminate, as predicted by the present analysis and by Highsmith (1984), is shown in Fig. 8. The spacings between the transverse and longitudinal cracks are $l_1 = 0.636$ mm, $l_2 = 1.588$ mm and an applied axial strain of $\bar{\epsilon}_{11} = 1$ percent is assumed.

The present analysis shows that along the line at the midplane between two transverse cracks (i.e., at $x_1 = 0$), the axial stress is: $\sigma_{11} = 1192$ MPa. It increases with the distance from the midplane and reaches a relatively high value of 1743 MPa at $x_1 = l_1/2$. The results of Highsmith (1984) provide an axial stress ranging from 1205 MPa to 1488 MPa. Thus the increase of the axial stress as predicted by the present analysis is 46 percent as compared with the method of Highsmith (1984) which predicts a 23 percent increase. It should be noted that it is this axial stress in the 0-deg plies that is responsible for 0-deg fiber fracture. This is the reason why these fiber fractures occur preferentially along transvere crack lines in the adjacent 90's, and it is in agreement with experimental observations (Highsmith, et al., 1986).

Further comparisons between the interfacial axial stress as predicted by the two methods are given in Fig. 9 for $[0/90]_s$ laminate with $l_1 = 0.482$ mm, $l_2 = 1.588$ mm, and in Fig. 10 for $[0/90_3]_s$ laminate with $l_1 = 0.762$ mm, $l_2 = 1.588$ mm. In all cases the loading corresponds to an applied axial strain of 1 percent.

Downloaded 03 May 2010 to 171.66.16.21. Redistribution subject to ASME license or copyright; see http://www.asme.org/terms/Terms_Use.cfm

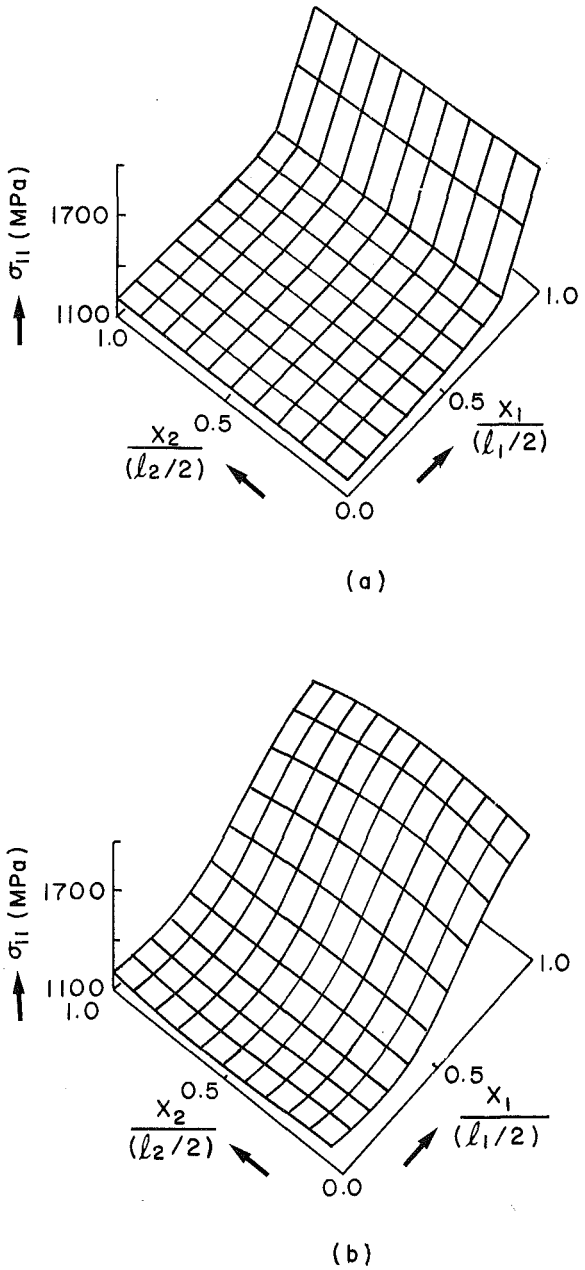


Fig. 10 Variation of the axial stress σ_{11} at the 0/90 interface of $[0/90_3]_s$ laminate due to an applied axial strain of 1 percent. The crack spacings are $l_1 = 0.762$ mm, $l_2 = 1.588$ mm; (a) present analysis and (b) Highsmith (1984).

Generally speaking, the agreement between the two methods is fairly good except at the region near the transverse crack. It appears that the results of Highsmith (1984) are less steep in the vicinity of the transverse cracks as compared to our prediction. It is expected that the present method should provide more accurate axial stresses since σ_{11} involves second-order terms in $\ddot{x}_3^{(\alpha)}$ whereas in the Highsmith, et al. (1986) approach it varies linearly through the thickness of the layer. It should be mentioned that from the elasticity theory point of view, the stresses should be singular at the vicinity of the crack tip. This trend of high gradients is exhibited by our results shown in Figs. 8–10.

4 Conclusions

An approximate analysis is given for the 3-dimensional problem of a cross-ply laminate with cross cracks. The analysis leads to a system of equations in the field variables which can be solved easily. The application of the method to graphite/epoxy damaged laminates reveals the effect of the cracks on the effective constants and axial displacements and stresses. It is shown that the effective Poisson's ratio of the cracked laminate exhibits a peculiar behavior which may be used to determine the extent of damage. This result may give the experimentalist guidelines for the proper measurement of the Poisson's ratio of a laminate with cross cracks and the corresponding state of damage.

Acknowledgment

This research was supported by Hercules Incorporated and the Center for Innovative Technology. The authors gratefully acknowledge this support.

References

Aboudi, J., 1987, "Stiffness Reduction of Cracked Solids," *Engineering Fracture Mechancis*, Vol. 26, pp. 637–650.

Herakovich, C. T., Aboudi, J., Lee, S. W., and Strauss, E. A., "Damage in Composite Laminates: Effects of Transverse Cracks," to appear in *ASME Symposium Volume on Damage*, ASME Applied Mechanics Summer Conference, Berkeley, CA, June, 1988.

Highsmith, A. L., 1984, "Damage Induced Stress Redistribution in Composite Lamimates," PhD dissertation, Virginia Polytechnic Institute and State University.

Highsmith, A. L., Reifsnider, K. L., 1982, "Stiffness-Reduction Mechanisms in Composites Laminates," ASTM STP 775, pp. 103–117.

Highsmith, A. L., and Reifsnider, K. L., 1986, "Internal Load Distribution Effects During Fatigue Loading of Composite Laminates," ASTM STP 907, pp. 233–251.

Lee, S. W., 1987, "Analysis of Composite Laminates with Matrix Cracks," MSc thesis, Virginia Polytechnic Institute and State University.

Pagano, N. J., 1978, "Stress Fields in Composite Laminates," *International Journal of Solids and Structures*, Vol. 14, pp. 385–400.

Reifsnider, K. L., Henneke, E. G., Stinchcomb, W. W., and Duke, J. C., 1983, "Damage Mechanics and NDE of Composite Laminates," in *Mechanics of Composites Materials–Recent Advances*, Eds. Z. Hashin and C. T. Herakovich, Pergamon Press, NY, pp. 399–420.

Downloaded 03 May 2010 to 171.66.16.21. Redistribution subject to ASME license or copyright; see http://www.asme.org/terms/Terms_Use.cfm

The Wavefield Radiated Into an Elastic Half-Space by a Transducer of Large Aperture

John G. Harris
Associate Professor,
Department of Theoretical and
Applied Mechanics,
The University of Illinois,
Urbana, IL 61801
Mem. ASME

The wavefield radiated into an elastic half-space by an ultrasonic transducer, as well as the radiation admittance of the transducer coupled to the half-space, are studied. Two models for the transducer are used. In one an axisymmetric, Gaussian distribution of normal traction is imposed upon the surface, while in the other a uniform distribution of normal traction is imposed upon a circular region of the surface, leaving the remainder free of traction. To calculate the wavefield, each wave emitted by the transducer is expressed as a plane wave multiplied by an asymptotic power series in inverse powers of the aperture's (scaled) radius. This reduces the wave equations satisfied by the compressional and shear potentials to their parabolic approximations. The approximations to the radiated waves are accurate at a depth where the wavefield remains well collimated.

1 Introduction

The purpose of this paper is to examine the wavefield radiated into a homogeneous, isotropic, linearly elastic half-space by an ultrasonic transducer and, moreover, to do so at a depth where the wavefield has not evolved into a spherical wave. A second purpose of this paper is to calculate the radiation admittance detected by the transducer. Miller and Pursey (1954, 1955) carried out a study of this problem, but they restricted their work to calculating the far-field radiation and the radiation admittance for small ka, where k is the compressional wave number and a is the radius of the transducer. The present study is concerned with large values of ka.

Transducers used for active nondestructive testing operate from one to several hundred megahertz. If we assume that the operating frequency is 10 MHz, that the compressional wave speed is 6×10^3 m/s, and that the radius of the transducer a is 0.5 cm, then ka is 52. Further, we can estimate that the wavefield radiated by a transducer remains collimated to approximately a depth $ka^2/2$ (Naze Tjøtta and Tjøtta, 1980). Using the preceding values for k and a, $ka^2/2$ is 13 cm. Therefore, the transducers used for nondestructive testing typically have large apertures and the region of the material that they interrogate may lie at a depth $ka^2/2$ or less. The exact relationship between the voltage applied to or produced by a transducer and the mechanical signal emitted or received by it is not straightforward and most probably not well understood (Bogy and Miu, 1982). Transducers are probably best characterized by an equivalent circuit model (Auld, 1973). Therefore, the complete radiation admittance must be known if the transducer coupled to the half-space is to be treated as a circuit element.

Of equal importance to understanding the transducer, is understanding the wavefield that it radiates. Papadakis (1975) modified the acoustical solution describing the radiation from a baffled piston into an ideal fluid to take account of the elasticity of the solid. He was primarily concerned with estimating the loss caused by beam spreading in pulse-echo measurements. However, his modifications do not capture the coupling of the compressional and shear waves at the surface of the solid. One of the few calculations to do so is that of Miller and Pursey (1954). They considered several distributions of traction over the surface of an elastic half-space and evaluated the far-field radiation in each case. Further, they made a calculation of the radiation impedance in each case for small ka. In a follow-up study Miller and Pursey (1955) calculated the self and mutual radiation admittance for an array of transducers. Each transducer was modeled by a uniform distribution of normal traction acting over a circular area. Again each transducer had a small aperture, though the aperture of the whole array did not need to be small. A more recent study, one that is more intuitive and approximate than that of Miller and Pursey (1954, 1955) and that uses the concepts of geometrical diffraction theory, has been carried out by Weight (1987). He considered the propagation of a short pulse into a solid from a normally coupled compressional wave transducer and took care to include the effects of the waves excited at the edge of the transducer.

Given what we know about the mechanical behavior of transducers, great care in attempting to model their behavior and how they interact with the solid to which they are coupled is not warranted. In this paper, we try to model a compres-

Contributed by the Applied Mechanics Division for publication in the JOURNAL OF APPLIED MECHANICS.
Discussion on this paper should be addressed to the Editorial Department, ASME, United Engineering Center, 345 East 47th Street, New York, N.Y. 10017, and will be accepted until two months after final publication of the paper itself in the JOURNAL OF APPLIED MECHANICS. Manuscript received by ASME Applied Mechanics Division, August 12, 1987; final revision, November 20, 1987.

Copyright © 1988 by ASME
Downloaded 03 May 2010 to 171.66.16.21. Redistribution subject to ASME license or copyright; see http://www.asme.org/terms/Terms_Use.cfm

sional wave transducer that is coupled to a solid with a fluid layer by imposing a known distribution of normal traction. Both an axisymmetric, Gaussian distribution and a circular, uniform one are considered. We call the wavefield radiated by the Gaussian distribution a Gaussian beam and that radiated by the uniform distribution a uniform beam. Pott and this author (Pott and Harris, 1984, Harris and Pott, 1985) have studied, by a different method, the Gaussian beam. Its principal feature is that it remains Gaussian in cross section throughout its propagation. The uniform beam has a structure similar to that of the wavefield diffracted by a circular crack when it is struck by a normally incident compressional plane wave (Achenbach et al., 1982). It consists of a compressional plane wave excited by the central part of the unifrom distribution, and two toroidal waves, one compressional and one shear, excited at the edge of the uniform distribution. An alternative to the present construction is to impose a known displacement upon the surface of the half-space. Robertson (1966) has studied the problem of the forced normal vibration of a rigid circular disk on an elastic half-space and has obtained results for small ka. However, this construction leads to a mixed boundary-value problem, the solution to which entails more work than its end results, within the context of the present study, would seem to warrant.

When a surface traction is imposed upon a half-space, the radiation admittance rather than the radiation impedance is the natural quantity to calculate. However, the surface traction and, most certainly, the particle velocity at the surface, need not be uniform over the region of contact. But a transducer outputs a single voltage that represents, in some unknown way, the integrated effect of everything that it senses throughout its area of contact. Thus there is some ambiguity as to how to define the radiation admittance Y. In the present study, we adopt a definition suggested by Skudrzyk (1971); namely

$$Y^* = 2\Pi_C/[(T_n S)\,(T_n^* S)] \tag{1}$$

where Π_C is the time-averaged complex power and T_n is the normal traction averaged over the area of contact S. The power radiated into the half-space Π is Re (Π_C). The superscript * indicates the complex conjugate. Other definitions of Y are possible. Miller and Pursey (1955), for example, define Y as the normal particle velocity averaged over the area of contact divided by $(T_n S)$.

The present problem is the offspring of two often-studied problems. One is that of a normal point load acting on the surface of an elastic half-space. The solution to this problem is summarized by Achenbach (1973). The second is that of a rigid piston in an infinite, rigid baffle vibrating in and out while in contact, on one side, with an ideal fluid. The solutions to this problem are summarized by Greenspan (1979).

Earlier we indicated that we would calculate the elastodynamic wavefield in a region near a depth $ka^2/2$ where the radiated wavefield still retains its beam-like character. (We call this the intermediate field.) We do this by adapting a method developed by Naze Tjøtta and Tjøtta (1980) for the analogous acoustic problem. Each elastodynamic potential is expressed as a plane wave multiplied by a power series in inverse powers of ka. The wave equations satisfied by the compressional and shear potentials are thereby reduced to a series of parabolic approximations. The solutions to these approximations contain parameters that can only be determined by relating them to the source. For the Gaussian beam, this can be done directly but, for the uniform beam, this must be done by matching these intermediate-field or inner expansions to far-field or outer expansions. The far-field expansions are generated by steepest-descents approximations to the exact integral representations of the radiated potentials.

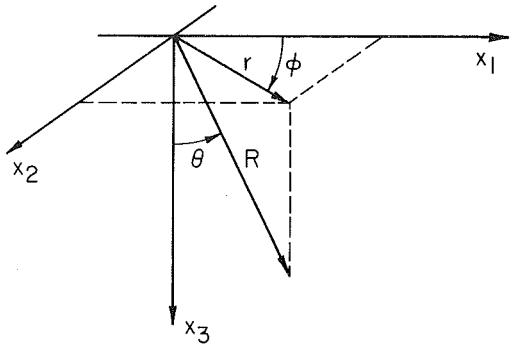


Fig. 1 Coordinate systems used in the problem

2 Transform Solution and the Far-Field Expansion

Imagine that a compressional wave transducer is coupled to a homogeneous, isotropic, linearly elastic half-space by a thin layer of ideal fluid. The half-space occupies the region $x_3 \geq 0$. To model the transducer, and its coupling to the half-space, two distributions of normal traction are imposed upon the surface $x_3 = 0$; namely

$$t_3(r/a) = (\lambda + 2\mu)\,T\,e^{-(r/a)^2} \tag{2}$$

and

$$t_3(r/a) = (\lambda + 2\mu)\,T\,\mathrm{H}(1 - r/a) \tag{3}$$

where T and a are parameters describing the transducer, λ and μ are Lamé's elastic constants, t_3 is the normal traction and equals $-\tau_{33}$, and $\mathrm{H}(x)$ is the Heaviside step function. The tangential tractions are 0. The imposed tractions are assumed to be time-harmonic, but the exp $(-i\omega t)$, where ω is the angular frequency and t is time, has been suppressed. All the waves are assumed to radiate outward from the transducer. The coordinate systems used to describe the radiation into the half-space are shown in Fig. 1.

The equations of elastodynamics are summarized by Achenbach (1973). It suffices to note that, for an axisymmetric problem, the particle displacement $\mathbf{u}$ is given by

$$\mathbf{u} = \nabla\,\Phi + \nabla\,\times\Psi\,\hat{\mathbf{e}}_\phi \tag{4}$$

and that Φ and Ψ satisfy

$$\nabla^2\Phi + k^2\Phi = 0 \tag{5}$$

and

$$\nabla^2\Psi - \frac{1}{r^2}\,\Psi + (k\kappa)^2\Psi = 0. \tag{6}$$

The unit vector $\hat{\mathbf{e}}_\phi$ points in the direction of increasing ϕ (Fig. 1). The parameter k is the compressional wave number and $\kappa = c/c_T$, where c is the compressional wave speed and c_T is the shear wave speed.

Integral representations of the waves excited by a normally directed point load acting on a half-space are constructed in Achenbach (1973). Integral representations for a more general distribution of normal traction are constructed in the same way and are summarized by the following sequence of equations:

$$\Phi = -\kappa^2 Ta^2 \int_H F(ka\xi)P(\xi)J_0(kr\xi)e^{ik\gamma x_3}\xi\,d\xi \tag{7}$$

$$\Psi = \kappa^2 Ta^2 \int_H F(ka\xi)Q(\xi)J_1(kr\xi)e^{ik\gamma_T x_3}\xi\,d\xi \tag{8}$$

$$P(\xi) = (2\xi^2 - \kappa^2)/\mathrm{R}(\xi) \tag{9}$$

$$Q(\xi) = 2i\xi\gamma/\mathrm{R}(\xi) \tag{10}$$

and

Downloaded 03 May 2010 to 171.66.16.21. Redistribution subject to ASME license or copyright; see http://www.asme.org/terms/Terms_Use.cfm

$$F(ka\xi) = a^{-2}\int_0^\infty t_3(r/a)J_0(kr\xi)rdr. \tag{11}$$

The ancillary expressions are the Rayleigh function

$$R(\xi) = (2\xi^2 - \kappa^2)^2 + 4\,\xi^2\gamma\,\gamma_T \tag{12}$$

and the radicals

$$\gamma = (1-\xi^2)^{1/2} \tag{13}$$

and

$$\gamma_T = (\kappa^2 - \xi^2)^{1/2}. \tag{14}$$

The complex ξ-plane is cut so that the imaginary part of each radical is greater than or equal to 0 for all ξ. The contour H in equations (7) and (8) goes from 0 to ∞ and makes a small semicircle below the Rayleigh pole at $\xi = \kappa_R$, where $\kappa_R = c/c_R$ and c_R is the Rayleigh wave velocity. For the Gaussian distribution of normal traction te_3, $F(ka\xi)$ is given by

$$F(ka\xi) = \frac{1}{2}\exp\,[-(ka\xi/2)^2] \tag{15}$$

and, for the uniform distribution, it is given by

$$F(ka\xi) = J_1(ka\xi)/(ka\xi). \tag{16}$$

It should be noted that equations (2)–(16) have been scaled to exhibit explicitly the role of the parameter ka.

We shall need the far-field expressions for the compressional and shear waves; that is, we need to approximate the integrals in equations (7) and (8) for large values of kR, where $R = (x_3^2 + r^2)^{1/2}$ (Fig. 1). The asymptotic approximation, by the method of steepest descents, of integrals very similar to those in equations (7) and (8) is explained at length by Brekhovskikh (1980) so that here we give only the end results. They are

$$\Phi = i\kappa^2 Ta^2 F(ka\,\sin\theta)\,\cos\theta\,P(\sin\theta)e^{ikR}/(kR) + 0(kR)^{-2} \tag{17}$$

and

$$\Psi = -\kappa^4 Ta^2 F(ka\kappa\,\sin\theta)\,\cos\theta\,Q(\kappa\,\sin\theta)e^{ik\kappa R}/(k\kappa R) + 0(kR)^{-2} \tag{18}$$

The angle θ is shown in Fig. 1. To the same order of approximation the R and θ particle displacements are given by $u_R = ik\Phi$ and $u_\theta = -ik\kappa\,\Psi$.

NOTES:

(*i*) By examining the second term of the asymptotic expansions, equations (17) and (18), we find that not only must kR be large but also $(ka)^2/kR$ must be small. This is a consequence of having assumed that, in equations (7) and (8), $F(ka\xi)$ is slowly varying as kR becomes large.

(*ii*) Note that the Gaussian beam initially has a characteristic radius a, but that in the far field that radius has become $(2R/ka)$.

(*iii*) We have omitted giving expressions for the Rayleigh wave because for large ka it carries very little energy. This we shall show when we calculate the radiation admittance.

3 Intermediate Wavefield

Return to the reduced wave equations (5) and (6). Introduce the scaled coordinates $\alpha = r/a$ and $\beta = 2x_3/(ka^2)$. Set

$$\Phi = \exp\,[i(ka)^2\beta/2]k^{-2}C(\alpha,\beta) \tag{19}$$

and

$$\Psi = \exp\,[i\kappa(ka)^2\beta/2]k^{-2}S(\alpha,\beta). \tag{20}$$

The C and S satisfy

$$\frac{1}{\alpha}\frac{\partial}{\partial\alpha}\left(\alpha\frac{\partial C}{\partial\alpha}\right) + 4i\frac{\partial C}{\partial\beta} + \frac{4}{(ka)^2}\frac{\partial^2 C}{\partial\beta^2} = 0 \tag{21}$$

and

$$\frac{1}{\alpha}\frac{\partial}{\partial\alpha}\left(\alpha\frac{\partial S}{\partial\alpha}\right) - \frac{1}{\alpha^2}S + 4i\kappa\frac{\partial S}{\partial\beta} + \frac{4}{(ka)^2}\frac{\partial^2 S}{\partial\beta^2} = 0. \tag{22}$$

By assumption ka is large. If the second derivatives are of order one, then equations (21) and (22) can be simplified by dropping the last term. Equation (21) then becomes the parabolic approximation to the wave equation (Kriegsmann and Larsen, 1978). This observation and a careful study of the work on acoustic beams by Naze Tjøtta and Tjøtta (1980) indicates that the C and S can be expanded as follows:

$$C(\alpha,\beta) = \sum_0^\infty C^n(\alpha,\beta)(ka)^{-2n} \tag{23}$$

and

$$S(\alpha,\beta) = \sum_0^\infty S^n(\alpha,\beta)(ka)^{-2n-1}. \tag{24}$$

Substituting these expressions into equations (21) and (22) leads to the following equations:

$$\frac{1}{\alpha}\frac{\partial}{\partial\alpha}\left(\alpha\frac{\partial C^n}{\partial\alpha}\right) + 4i\frac{\partial C^n}{\partial\beta} = -4\frac{\partial^2 C^{n-1}}{\partial\beta^2} \tag{25}$$

and

$$\frac{1}{\alpha}\frac{\partial}{\partial\alpha}\left(\alpha\frac{\partial S^n}{\partial\alpha}\right) - \frac{1}{\alpha^2}S^n + 4i\kappa\frac{\partial S^n}{\partial\beta} = -4\frac{\partial^2 S^{n-1}}{\partial\beta^2} \tag{26}$$

where C^{-1} and S^{-1} are defined to be zero.

NOTES:

(*i*) Naze Tjøtta and Tjøtta (1980) have used an expansion similar to those in equations (23) and (24) to approximate the pressure field radiated by a baffled piston source. Comparison of their asymptotic approximation with a numerical approximation showed excellent agreement.

(*ii*) We noted earlier that the Gaussian beam retained its Gaussian cross section into the far field. There are no edge waves to distort it. Therefore, the perturbation expansion is a regular one and we can relate the solutions of equations (25) and (26) directly to the boundary condition equation (2).

(*iii*) The uniform beam leads to a singular perturbation problem. In the near field (the near field is a region for which the wavelength $2\pi/k$ and the radius a are, roughly, the governing length scales) the wavefield changes rapidly in both the transverse and x_3-directions because of the presence of the edge-diffracted waves. Therefore, it is not clear that any of the derivatives in the reduced wave equations (5) and (6) can be dropped. This can be seen in part by examining the work of Naze Tjøtta and Tjøtta (1980) and in part by examining the two-dimensional, uniform, compressional beam constructed by Harris (1987). To relate the intermediate-field expansions, equations (23) and (24), to the source distribution, we shall match them to the far-field expansions, equations (17) and (18). But we have only calculated the first terms of the far-field expansions. Therefore, we shall only be able to calculate C^0 and S^0.

3.1 The Gaussian Beam. To proceed with the Gaussian beam calculation, we must express the boundary conditions at $x_3 = 0$ [namely, $\tau_{33} = -t_3$ and $\tau_{r3} = 0$ where t_3 is given by equation (2)] in terms of C^n and S^n. Because we are interested in values of ka on the order of 50, only C^0, S^0 and C^1 will be calculated. Even with this limitation, the boundary conditions, when expressed in terms of C^n and S^n, become complicated. However, the Gaussian beam solutions are sufficiently smooth that equations (25) and (26) are satisfied not only in the region $\beta > 0$, but also in the larger region $\beta \geq 0$. Thus equations (25) and (26) can be used to simplify the boun-

Downloaded 03 May 2010 to 171.66.16.21. Redistribution subject to ASME license or copyright; see http://www.asme.org/terms/Terms_Use.cfm

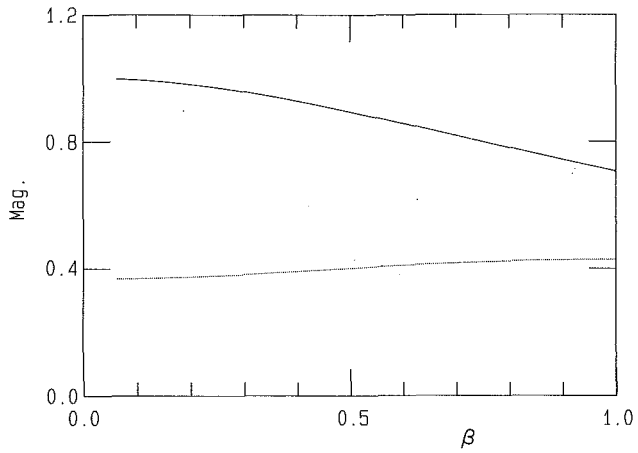


Fig. 2 Gaussian beam—the magnitude of (kU_3/T) is plotted against β; solid line, $\alpha = 0$; dotted line, $\alpha = 1$; terms of $0(ka)^{-2}$ have been dropped.

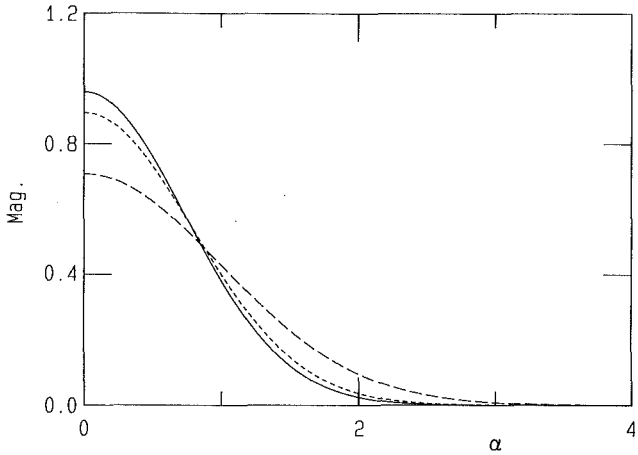


Fig. 3 Gaussian beam—the magnitude of (kU_3/T) is plotted against α; solid line, $\beta = 0.3$; short-dashed line, $\beta = 0.5$; long-dashed line, $\beta = 1$; terms of $0(ka)^{-2}$ have been dropped.

dary conditions. When the algebra is done, we are left with the following boundary conditions at $\beta = 0$:

$$C^0 = Te^{-\alpha^2} \tag{27}$$

$$\kappa^2 S^0 = -2i\,\partial C^0/\partial\alpha \tag{28}$$

and

$$C^1 = (8i)(\kappa-2)\kappa^{-3}\partial C^0/\partial\beta. \tag{29}$$

Solving equation (25) for C^0 and C^1, and equation (26) for S^0, and then imposing the boundary conditions gives

$$C^0 = \frac{-iT}{(\beta-i)}\exp\left(\frac{i\alpha^2}{\beta-i}\right) \tag{30}$$

$$S^0 = \frac{-4iT\alpha}{(\beta-i\kappa)^2}\exp\left(\frac{i\kappa\alpha^2}{\beta-i\kappa}\right) \tag{31}$$

and

$$C^1 = \frac{-C^0}{(\beta-i)}\left[\frac{8i(\kappa-2)}{\kappa^3}C_1 - i\,C_2\right] \tag{32}$$

where

$$C_1 = 1 + \frac{i\,\alpha^2}{(\beta-i)} \tag{33}$$

and

$$C_2 = \frac{\beta}{(\beta-i)}\left[2 + 4\,\frac{i\alpha^2}{(\beta-i)} + \frac{(i\alpha^2)^2}{(\beta-i)^2}\right]. \tag{34}$$

Knowing the potentials, we now calculate the particle displacements. The compressional wave displacement $\mathbf{u}^L$ is given by

$$\mathbf{u}^L = \exp\,[i(ka)^2\beta/2]\mathbf{U}^L \tag{35}$$

where

$$U_r^L = \frac{2i\alpha}{k(ka)(\beta-i)}\,C^0 \tag{36}$$

and

$$U_3^L = \frac{i\,C^0}{k}\left\{1 + \frac{i}{(ka)^2(\beta-i)}\left[\frac{(16-8\kappa+2\kappa^3)}{\kappa^3}C_1 + C_2\right]\right\}. \tag{37}$$

The shear wave displacement $\mathbf{u}^T$ is given by

$$\mathbf{u}^T = \exp\,[i\kappa(ka)^2\beta/2]\mathbf{U}^T \tag{38}$$

where

$$U_r^T = \frac{-i\kappa\,S^0}{k(ka)} \tag{39}$$

and

$$U_3^T = \frac{2S^0}{k(ka)^2}\left[1 + \frac{i\alpha^2}{(\beta-i\kappa)}\right]. \tag{40}$$

NOTE:

The solution of equation (25) for $n = 0$ can be enlivened somewhat by assuming C^0 has the form

$$C^0 = A(\beta)\,\exp\,[i\alpha^2\Gamma(\beta)] \tag{41}$$

rather than by using a Hankel transform. The unknown functions A and Γ satisfying the equations

$$\frac{dA}{d\beta} + A\Gamma = 0 \tag{42}$$

and

$$\frac{d\Gamma}{d\beta} + \Gamma^2 = 0. \tag{43}$$

These equations are easily solved. All the remaining C^n and S^n can be calculated from C^0. This method of solution was suggested by the work of Cerveny et al. (1982).

In Figs. 2 and 3, we have plotted the normalized magnitude of the leading-order displacement term (kU_3/T). In Fig. 2, the magnitude is plotted against β for $\alpha = 0$ and 1 and, in Fig. 3, it is plotted against α for $\beta = 0.3$, 0.5, and 1. These curves are somewhat bland but are of value when compared to the corresponding curves for the uniform beam. The higher-order terms have been ignored because we are interested in values of ka of at least 50.

3.2 The Uniform Beam. By using a Hankel transform general solutions to equations (25) and (26) for $n = 0$ can be written as

$$C^0 = (ka)^2\int_0^\infty C_0(ka\xi)\,\exp\,[-i(ka\xi/2)^2\beta]J_0(ka\alpha\xi)\xi d\xi \tag{44}$$

and

$$S^0 = (k\kappa a)^2 \times \int_0^\infty S_0(k\kappa a\xi)\,\exp\,[-i(k\kappa a\xi/2)^2(\beta/\kappa)]J_1(k\kappa a\alpha\xi)\xi d\xi. \tag{45}$$

The functions C_0 and S_0 are unknown. They are found by matching equations (44) and (45) to equations (17) and (18) using the matching principle explained by Van Dyke (1975). When this is done, we have

$$C^0 = T(ka)^2\int_0^\infty F(ka\xi)\,\exp\,[-i(ka\xi/2)^2\beta]J_0(ka\alpha\xi)\xi d\xi \tag{46}$$

and

Downloaded 03 May 2010 to 171.66.16.21. Redistribution subject to ASME license or copyright; see http://www.asme.org/terms/Terms_Use.cfm

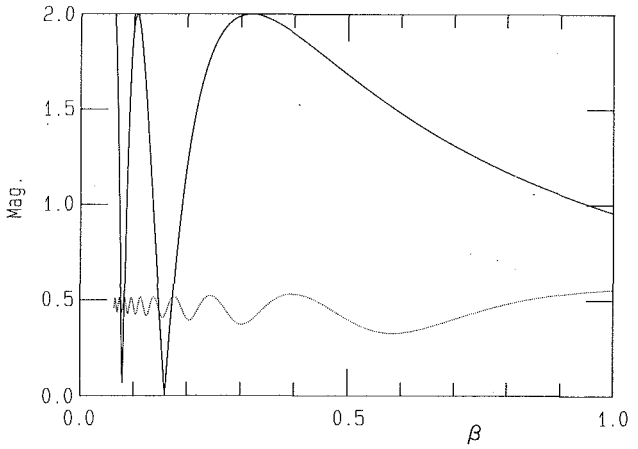


Fig. 4 Uniform beam—the magnitude of (kU_3/T) is plotted against β; solid line, $\alpha = 0$; dotted line $\alpha = 1$

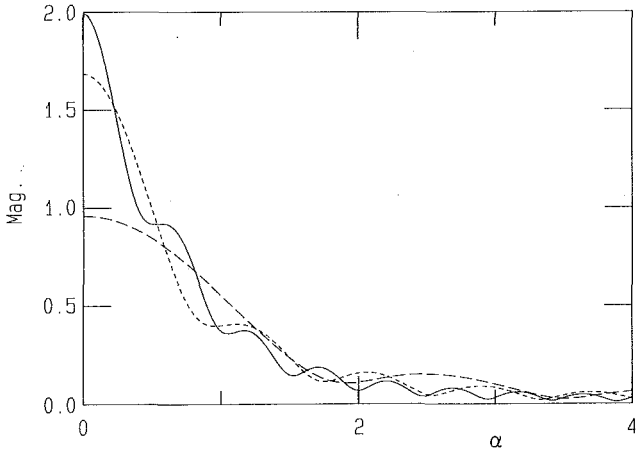


Fig. 5 Uniform beam—the magnitude of (kU_3/T) is plotted against α; solid line, $\beta = 0.3$; short-dashed line, $\beta = 0.5$; long-dashed line, $\beta = 1$

$$S^0 = 2i\kappa T(ka)^3 \times \int_0^\infty F(k\kappa a\xi)\ \exp\ [-i(k\kappa a\xi/2)^2(\beta/\kappa)]J_1(k\kappa a\alpha\xi)\xi^2 d\xi. \quad (47)$$

To complete the calculation we must replace F with the expression in equation (16). The resulting integrals are similar to ones evaluated by Naze Tjøtta and Tjøtta (1980). Adapting the results from that paper, we have

$$C^0 = T\left[1 - e^{i/\beta} + 2e^{i/\beta}\int_0^{\alpha/\beta} e^{i\beta t^2} J_1(2t)\,dt\right] \quad (48)$$

$$= -2T\,e^{i/\beta}\int_{\alpha/\beta}^\infty e^{i\beta t^2} J_1(2t)\,dt \quad (49)$$

and

$$S^0 = \frac{-4iT}{\kappa\beta}\ \exp\ [i\kappa(1+\alpha^2)/\beta]J_1\left(\frac{2\alpha}{\beta}\right). \quad (50)$$

The integrals in equations (48) and (49) can be reduced further [see Note (v) next], but they are easier to evaluate numerically in their present form. Knowing the potentials, we now calculate the particle displacements $\mathbf{u}^L$ and $\mathbf{u}^T$ using equations (35) and (38). The $\mathbf{U}^L$ and $\mathbf{U}^T$ are described by

$$U_r^L = \frac{2T}{k(ka)\beta}\ \exp\ [i(1+\alpha^2)/\beta]J_1\left(\frac{2\alpha}{\beta}\right) \quad (51)$$

$$U_3^L = iC^0/k \quad (52)$$

and

$$U_r^T = -i\kappa\ S^0/[k(ka)]. \quad (53)$$

NOTES:

(i) The matching of equations (44) and (45) to equations (17) and (18) is straightforward because there is little ambiguity about the region of overlap. The intermediate-field expansion remains accurate not only for β of order 1, but also for β large; that is, $(ka)^2/(2kx_3) < 1$. Given that ka is large then kx_3 is very large. The far field near the x_3-axis is defined by exactly the same statements. Further, the intermediate-field expansion demands that α/β be of order 1; that is, r/x_3 is to be of order $(ka)^{-1}$. This defines a cone that cuts out a section of the far field as well as the intermediate field.

(ii) Examine equations (51)–(53). Note that not only have we captured the plane compressional wave radiated by the face of the transducer but also the edge-diffracted waves that are of 0 $(ka)^{-1}$.

(iii) Examine C^0, equation (48), for $\alpha = 0$. As β approaches 0, C^0 oscillates ever more rapidly. This is but an alternate way of discovering that the intermediate-field expansion breaks down within about a wavelength from $\beta = 0$.

(iv) Equations (46) and (47) can be checked by replacing F with the expression for the Gaussian beam, equation (15). When this is done and the two integrations carried out, the end results agree precisely with equations (30) and (31).

(v) Somewhat more progress can be made with the integral in equation (46). It can be written in terms of Lommel functions of two variables (Watson, 1966). Then, using the properties of these functions, we can put C^0 in the forms

$$C^0 = T\ \exp\ [i(1+\alpha^2)/\beta)]\ \sum_0^\infty\ (i\alpha)^{-(m+1)}J_{m+1}\left(\frac{2\alpha}{\beta}\right) \quad (54)$$

and

$$C^0 = T - T\ \exp\ [i(1+\alpha^2)/\beta]\ \sum_0^\infty\ (-i\alpha)^m J_m\left(\frac{2\alpha}{\beta}\right). \quad (55)$$

These expressions agree with similar ones derived by Naze Tjøtta and Tjøtta (1980) by what seems to be a different method. One case is of particular interest; namely

$$C^0 = \frac{T}{2}\left[1 - e^{i2/\beta}J_0\left(\frac{2}{\beta}\right)\right] \quad (56)$$

when $\alpha = 1$.

In Figs. 4 and 5, we have again plotted the normalized magnitude of the leading-order displacement term (kU_3/T). In Fig. 4, the magnitude is plotted against β for $\alpha = 0$ and 1 and, in Fig. 5, it is plotted against α for $\beta = 0.3$, 0.5, and 1. Compare Fig. 4 with Fig. 2. The oscillatory character of the uniform beam must come from the edge waves. The central axis of the uniform beam is a caustic. Rays excited at the edge intersect one another along the central axis. Beyond $\beta = 0.2$, the last oscillation broadens out considerably until, near $\beta = 1$, the amplitude starts to decay toward that characteristic of the far field. Compare Fig. 5 with Fig. 3. The uniform beam starts with considerable structure in its cross section but as it propagates outward, except for the incipient sidelobes, it starts to resemble, in a general way, the Gaussian beam. However, the presence of the side lobes indicate the continued influence of the edge waves.

4 The Radiation Admittance

Using equation (1), the radiation admittance Y can be written as

$$Y = \frac{\int_S t_3^* v_3 dS}{\int_S t_3 dS \int_S t_3^* dS} \quad (57)$$

Downloaded 03 May 2010 to 171.66.16.21. Redistribution subject to ASME license or copyright; see http://www.asme.org/terms/Terms_Use.cfm

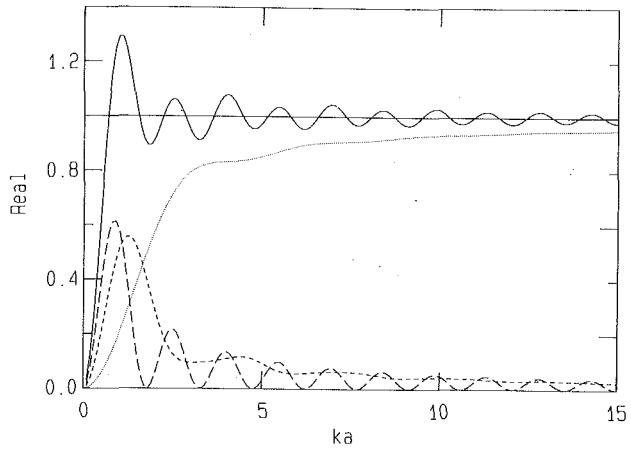


Fig. 6 Real part of the normalized specific admittance ρcy for the uniform beam, and its components, are plotted against ka; the components are identified in the body of the paper

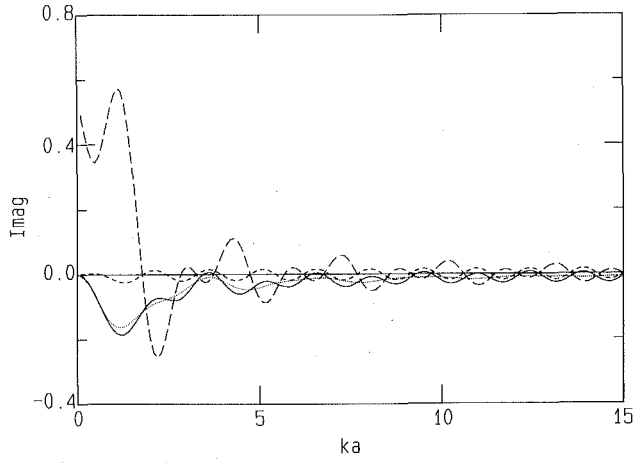


Fig. 7 Imaginary part of the normalized specific admittance ρcy for the uniform beam, and its components, are plotted against ka; the components are identified in the body of the paper

where t_3 is the normal component of traction, and v_3 is the x_3 particle velocity. The integrations are carried out over the area of contact of the transducer S. It is also useful to define the specific admittance y as

$$y = Y S. \tag{58}$$

For the Gaussian beam, the x_3-component of particle velocity v_3 is easily calculated, for large ka, from the corresponding particle displacement, equations (37) and (40). Knowing v_3 and using t_3 from equation (2), the radiation admittance is readily calculated to be

$$Y = \frac{1}{2\pi\rho c}\left\{1 - \frac{1}{\kappa^3 (ka)^2}[4(2-\kappa) + \kappa^3 + (4\kappa - 3)(\pi/2)^{1/2}]\right\}. \tag{59}$$

where ρ is the density of the elastic half-space [recall that $\rho c^2 = (\lambda + 2\mu)$].

For the uniform beam, we do not have an easy way to calculate v_3 because we do not have an approximation to the x_3 particle displacement at $x_3 = 0$. We, therefore, return to the exact transform solution given by the equations for the potentials Φ and Ψ, equations (7) and (8). From these, we calculate the particle velocity v_3 at $x_3 = 0$. Knowing t_3, we can calculate Y or, more conveniently, y. The specific admittance breaks into two parts y_B and y_R, where y_B is associated with the bulk waves and y_R with the Rayleigh wave. The bulk wave specific admittance y_B is given by

$$y_B = \frac{2\kappa^4 (ka)^2}{\rho c} \bar{\int}_0^\infty [F(ka\xi)]^2 \frac{\gamma\xi}{R(\xi)}\, d\xi - i \,\mathrm{Im}\,(y_R) \tag{60}$$

and the surface wave specific admittance y_R is given by

$$y_R = -\frac{2\kappa^4 (ka)^2}{\rho c}\, \pi F(ka\kappa_R) \frac{(\kappa_R^2 - 1)^{1/2}}{DR(\kappa_R)} \kappa_R [F(ka\kappa_R) + iF_R(ka\kappa_R)]. \tag{61}$$

The general expression for F is given by equation (11). For the uniform beam, the specific expression for F is given by equation (16). The Rayleigh function R is given by equation (12) and the radical γ is given by equation (13). The bar indicates that equation (60) is a Cauchy principal-value integral. The derivative of the Rayleigh function evaluated at the Rayleigh pole κ_R is

$$DR(\kappa_R) = 8\kappa_R^3 \left[\left(2 - \frac{\kappa^2}{\kappa_R^2}\right) - \frac{1}{4}\left(2 - \frac{\kappa^2}{\kappa_R^2}\right)^2 - 2\left(2 - \frac{\kappa^2}{\kappa_R^2} - \frac{1}{\kappa_R^2}\right)\left(2 - \frac{\kappa^2}{\kappa_R^2}\right)^{-2}\right]. \tag{62}$$

The function F_R is given by

$$F_R(ka\xi) = a^{-2} \int_0^\infty t_3 (r/a)\, Y_0(kr\xi)\, r dr. \tag{63}$$

For the uniform beam

$$F_R(ka\xi) = [Y_1(ka\xi) + 2/(\pi ka\xi)](ka\xi)^{-1}. \tag{64}$$

NOTES:

(*i*) The expression for the radiation admittance Y for the Gaussian beam is an asymptotic one and is accurate to $0(ka)^{-4}$. There is a Rayleigh wave contribution, but it is of order $\exp(-2\, ka\kappa_R)$.

(*ii*) The expressions for the bulk-wave and Rayleigh-wave specific admittances, y_B and y_R, are quite general. Note that y_B and y_R are complex. The integral giving the first part of y_B is real for ξ between 0 and 1, complex for ξ between 1 and κ, and imaginary for ξ between κ and ∞.

(*iii*) The form taken by y_B may seem odd; however, some thought would show that, despite the term Im (y_R), y_B can be written as an integral around the branch cuts having branch points 1 and κ. Thus y_B can be expressed solely in terms of the bulk waves. The y calculated here, for the uniform beam, agrees with that calculated by Miller and Pursey (1955). However, they do not separate y into its components y_B and y_R.

The integral describing y_B for the uniform beam is not easily approximated for large ka, though it is readily proven that y_B approaches $(\rho c)^{-1}$ as ka goes to infinity. Consequently, we have numerically evaluated y, and the various contributions to y, for all ka, taking $\kappa = 2$. Figures 6 and 7 show the real and imaginary parts, respectively, of ρcy and its components plotted against ka. In Fig. 6, the dotted line indicates the real contribution to ρcy_B of the integration from 0 to 1, the short-dashed line indicates the contribution to the real part of ρcy_B of the integration from 1 to κ, the long-dashed line indicates the real part of ρcy_R and the solid line indicates the real part of ρcy. In Fig. 7, the dotted line indicates the contribution to the imaginary part of ρcy_B of the integration from 1 to κ, the short-dashed line indicates the imaginary contribution to ρcy_B of the integration from κ to ∞, the long-dashed line indicates the imaginary part of ρcy_R and the solid line indicates the imaginary part of ρcy. Looking at both Figs. 6 and 7, we see that for $ka > 10$ the difference between y and $(\rho c)^{-1}$ is negligible. Recall that $(\rho c)^{-1}$ is the specific admittance of a compressional plane wave. Further, only for values of $ka < 5$ is the Rayleigh wave contribution significant.

5 Conclusions

(*i*) An asymptotic technique that can be used to approx-

Downloaded 03 May 2010 to 171.66.16.21. Redistribution subject to ASME license or copyright; see http://www.asme.org/terms/Terms_Use.cfm

imate the wavefield of an ultrasonic transducer of large aperture in a region where the wavefield still retains its highly collimated character has been developed and applied to two model beam profiles, a Gaussian beam and a uniform beam.

(*ii*) Equations (37) and (52) indicate that at approximately a depth of $ka^2/2$ the beams behave somewhat as compressional plane waves do. Moreover, the radiation admittance approaches that of a compressional plane wave. But how closely do the beams approximate a compressional plane wave? Both beams exhibit a good deal of fine structure, especially the uniform beam. It is significantly affected by the waves excited at the edge of the uniform distribution. Equations (35)–(40) and (51)–(53) quantitatively, and quite completely, describe this structure, while Figs. 2–5 partially illustrate it.

(*iii*) The relative simplicity of the expressions describing the two beams, especially those describing the uniform beam, is remarkable. Moreover, note that the asymptotic approximations describing the uniform beam are accurate up to about a wavelength from the transducer.

(*iv*) For large ka, the radiation admittance for both distributions of normal traction is real. This means that almost all the time-averaged power is carried into the far field. Moreover, the Rayleigh wave, for large ka, carries almost no time-averaged power. In contrast, for the uniform beam at small ka, it carries a significant fraction of the time-averaged power.

Acknowledgments

This author wishes to thank Hyung-Chul Choi for carrying out the numerical calculations and plotting the graphs. This work was supported by the National Science Foundation through grant No. MSM 85-13928.

References

Achenbach, J. D., 1973, *Wave Propagation in Elastic Solids*, North-Holland, Amsterdam, pp. 310–321.

Achenbach, J. D., Gautesen, A. K., and McMaken, H., 1982, *Ray Methods for Waves in Elastic Solids*, Pitman, Boston, pp. 165–169.

Auld, B. A., 1973, *Acoustic Fields and Waves in Solids*, Vol. 1, Wiley-Interscience, NY, pp. 324–341.

Bogy, D. B., and Miu, D. K.-K., 1982, "Transient Voltage Across Axisymmetrically Loaded Piezoelectric Disks with Electroded Faces," *Journal of the Acoustical Society of America*, Vol. 72, pp. 487–497.

Brekhovskikh, L. M., 1980, *Waves in Layered Media*, 2nd Ed., Academic Press, NY, pp. 232–246.

Cerveny, V., Popov, M. M., and Psencik, I., 1982, "Computation of Wavefields in Inhomogeneous Media—Gaussian Beam Approach," *Geophys. J. R. Astr. Soc.*, Vol. 70, pp. 109–128.

Greenspan, M., 1979, "Piston Radiator: Some Extensions of the Theory," *Journal of the Acoustical Society of America*, Vol. 65, pp. 608–621.

Harris, J. G., 1987, "Edge Diffraction of a Compressional Beam," *J. Acoustical Soc. Am.*, Vol. 82, pp. 635–646.

Harris, J. G., and Pott, J., 1985, "Further Studies of the Scattering of a Gaussian Beam from a Fluid-Solid Interface," *Journal of the Acoustical Society of America*, Vol. 78, pp. 1072–1080.

Kriegsmann, G. A., and Larsen, E. W., 1978, "On the Parabolic Approximation to the Reduced Wave Equation," *SIAM Journal of Applied Mathematics*, Vol. 34, pp. 200–204.

Miller, G. F., and Pursey, H., 1954, "The Field and Radiation Impedance of Mechanical Radiators on the Free Surface of a Semi-Infinite Isotropic Solid," *Proceedings of the Royal Society of London*, Vol. A223, pp. 521–541.

Miller, G. F., and Pursey, H., 1955, "On the Partition of Energy Between Elastic Waves in a Semi-Infinite Solid," *Proceedings of the Royal Society of London*, Vol. A233, pp. 55–69.

Naze Tjøtta, J., and Tjøtta, S., 1980, "An Analytical Model for the Nearfield of a Baffled Piston Transducer," *Journal of the Acoustical Society of America*, Vol. 68, pp. 334–339.

Papadakis, E. P., 1975, "Ultrasonic Diffraction from Single Apertures with Application to Pulse Measurements and Crystal Physics," *Physical Acoustics*, Vol. 11, Mason, W. P., and Thurston, R. N., Eds., Academic Press, NY, pp. 151–211.

Pott, J., and Harris, J. G., 1984, "Scattering of an Acoustic Gaussian Beam from a Fluid-Solid Interface," *Journal of the Acoustical Society of America*, Vol. 76, pp. 1829–1838.

Robertson, I. A., 1966, "Forced Vertical Vibration of a Rigid Circular Disc on a Semi-Infinite Elastic Solid," *Proceedings of the Cambridge Philosophical Society*, Vol. 62, pp. 547–553.

Skudrzyk, E., 1971, *The Foundations of Acoustics*, Springer-Verlag, Wien, pp. 663–676.

Van Dyke, M., 1975, *Perturbation Methods in Fluid Mechanics*, Parabolic Press, Stanford, CA, pp. 77–97.

Watson, G. N., 1966, *A Treatise on the Theory of Bessel Functions*, 2nd Ed., The University Press, Cambridge, pp. 537–550.

Weight, J. P., 1987, "A Model for the Propagation of Short Pulses of Ultrasound in a Solid," *Journal of the Acoustical Society of America*, Vol. 81, pp. 815–826.

Downloaded 03 May 2010 to 171.66.16.21. Redistribution subject to ASME license or copyright; see http://www.asme.org/terms/Terms_Use.cfm

Scattering From Three-Dimensional Planar Cracks by the Boundary Integral Equation Method

D. E. Budreck
Assistant Professor,
Department of Mathematics,
Iowa State University,
Ames, IA 50011
Mem. ASME

J. D. Achenbach
Professor,
Department of Civil Engineering,
The Technological Institute,
Northwestern University,
Evanston, IL 60208
Fellow ASME

The equations governing three-dimensional elastodynamic scattering from planar cracks are formulated and solved in the frequency domain by Boundary Integral Equation (BIE) methods. The formulation requires a regularization of all nonintegrable kernels in the representation integral for the scattered stress field. The regularization procedure is novel in that it requires an initial discretization of the crack. The resulting discretized system of integral equations can be solved explicitly for the unknown crack-opening displacements. The crack-opening displacements, in conjunction with the appropriate representation integral, have been used to calculate far-field quantities of physical interest. Numerical results are compared with those from earlier papers dealing with a penny-shaped crack under normal incidence of a longitudinal wave field. The code has also been applied to elliptic crack geometries of various aspect ratios under normal longitudinal wave incidence. Numerical results are given for crack-opening displacements, scattered far fields, and scattering cross sections. The numerical results indicate that at sufficiently high frequencies, the scattering process is significantly affected by the extra length parameter of the elliptic crack.

I Introduction

Scattering of elastic waves by an internal planar crack of fairly general shape occurs frequently in quantitative nondestructive evaluation. There is only a limited number of rigorous solutions to such scattering problems, and these have been obtained almost exclusively for the special case of scattering from a penny-shaped crack. Representative examples of such previous works, whose results will be compared to the ones of this paper, are those of Mal (1970), Krenk and Schmidt (1982), Martin and Wickham (1983), and Keogh (1983). Comparison to the more recent works of Niwa and Hirose (1987), and Nishimura and Kobayashi (1988), will also be discussed.

Previous work on scattering from crack geometries other than circular, have been limited to the special case of long-wavelength scattering; see, for example, Visscher (1983), Roy (1984), Lin and Keer (1987). Visscher (1983) has noted that by long-wavelength elastic-wave scattering only very accurate experiments can distinguish a flat crack of general shape from a penny-shaped crack. This is because the characteristic interference patterns of peaks and valleys in the scattered field, which would give information on the crack shape, occur at wavelengths which are comparable to the dimensions of the crack; i.e., in a situation of intermediate and short-wavelength scattering.

In this paper, the problem of intermediate and short-wavelength scattering from penny-shaped and elliptic cracks is solved in the frequency domain by boundary integral equation (BIE) methods. As expected, at sufficiently high frequencies, the elliptic crack radiates a scattered field significantly different from that of the penny-shaped crack.

The utility of the BIE method comes from the divergence theorem, which changes the formulation of the mathematical problem from solving for vector field quantities throughout an elastic domain, V, to solving for the same quantities on the boundary S of V. Hence, only the surface S of V need be discretized. In this way, the computational difficulties that would arise from the entire discretization of V, are replaced by additional analytical work that arises in the derivation of the boundary integral equation. The boundary integral equation yields as its solution the field quantities on S. Then, the appropriate representation integral can be used to calculate the same quantities anywhere in V.

The BIE method was first applied to the formulation and numerical solution of elastostatic problems by Rizzo (1967), and elastodynamic problems by Cruse and Rizzo (1968), and Cruse (1968). Since that time, it has had a rich development; see Beskos (1987) for a detailed review article on the subject.

Contributed by the Applied Mechanics Division for publication in the JOURNAL OF APPLIED MECHANICS.
Discussion on this paper should be addressed to the Editorial Department, ASME, United Engineering Center, 345 East 47th Street, New York, N.Y. 10017, and will be accepted until two months after final publication of the paper itself in the JOURNAL OF APPLIED MECHANICS. Manuscript received by ASME Applied Mechanics Division, August 21, 1987; final revision, December 14, 1987.

Copyright © 1988 by ASME
Downloaded 03 May 2010 to 171.66.16.21. Redistribution subject to ASME license or copyright; see http://www.asme.org/terms/Terms_Use.cfm

However, it was not until recently that the BIE method was used to solve three-dimensional scattering problems; see, for example, Rizzo, et al. (1985), Kitahara and Nakagawa (1985), and Achenbach and Kitahara (1986).

Most recent has been the investigation of the three-dimensional crack-scattering problems by BIE methods; see Nishimura and Kobayashi (1988), and Niwa and Hirose (1987). Geometrically, the crack is simply a special limiting case of a void. However, in this limit, the integral equation for a void gives a degenerate result (see Budreck (1988) for details). Martin (1981) presents a novel way of circumventing this degeneracy, through the use of special penny-shaped crack Green's functions, which are discontinuous across the crack plane. An earlier alternate approach was taken by Budiansky and Rice (1979), who derived instead an integral equation whose unknowns were both the crack-opening displacement and its in-plane derivatives, the dislocation density. The appearance of both terms comes about as a result of the regularization of a nonintegrable kernel in the stress representation integral. This procedure will be outlined in Section III.

In Section IV of this paper yet a different approach is taken. The same nonintegrable kernel is regularized in a procedure that requires the BIE discretization to be carried out simultaneously with the derivation of the integral equation. The result is a discretized integral equation that can be solved explicitly for the crack-opening displacement.

II Integral Form of Problem Statement

Consider a homogeneous, isotropic, linearly elastic, and infinitely extended domain, V, with a bounded internal boundary, $S^+ \; U \; S^-$. Here S^+ and S^- are two coplanar traction-free surfaces that are infinitesimally close, and have outward normals $\mathbf{n}^+ = (0,0,-1)$ and $\mathbf{n}^- = (0,0,+1)$, respectively. In what follows, Latin super/subscripts take on values 1-3, Greek ones take on values 1-2, and the summation convention is assumed throughout. Consider further a time-harmonic ($e^{-i\omega t}$) displacement field with spatial dependence defined by $u_i^{in}(\mathbf{x})$, which is incident upon the crack $S^+ \; U \; S^-$. The crack generates a scattered field, $u_i^{sc}(\mathbf{x})$, such that the total displacement field in V is given by

$$u_i(\mathbf{x}) = u_i^{in}(\mathbf{x}) + u_i^{sc}(\mathbf{x}), \quad \mathbf{x} \epsilon V. \tag{1}$$

An application of the divergence theorem to the Betti-Rayleigh reciprocal relations for the scattered elastodynamic field and the full-space elastodynamic Green's function gives the following well-known representation integral, Achenbach et al. (1982):

$$u_k^{sc}(\mathbf{x}) = I_k(\mathbf{x}), \quad \mathbf{x} \epsilon V, \tag{2a}$$

where

$$I_k(\mathbf{x}) \equiv \int_S D_k^{3m}(\mathbf{x}-\mathbf{y}) \Delta u_m^{sc} dS(\mathbf{y}). \tag{2b}$$

This result is valid provided $u_k^{sc}(\mathbf{x})$ satisfies the usual radiation conditon for $|\mathbf{x}| \to \infty$. In the derivation of equation (2), an integration over the crack $S^+ \; U \; S^-$ has been replaced by integration over the crack-plane S (see Fig. 1), leading to the definition of the crack-opening displacement $\Delta u_m^{sc}(\mathbf{y})$, defined on S and given by

$$\Delta u_m^{sc}(\mathbf{y}) \equiv {}^+u_m^{sc}(\mathbf{y}) - {}^-u_m^{sc}(\mathbf{y}), \tag{3}$$

where ${}^+u_m^{sc}(\mathbf{y})$ and ${}^-u_m^{sc}(\mathbf{y})$ define the scattered displacement field evaluated on the crack faces S^+ and S^-, respectively. The kernel of the integral operator in equation (2b) is the stress Green's function $D_m^{ij}(\mathbf{x}-\mathbf{y})$, which is related to the displacement Green's function $U_m^k(\mathbf{x}-\mathbf{y})$ by the Hookean operator

$$D_m^{ij}(\mathbf{x}-\mathbf{y}) \equiv C_{ijkl} U_m^{k,l}(\mathbf{x}-\mathbf{y}). \tag{4}$$

In equation (4), C_{ijkl} are the isotropic elastic constants given by

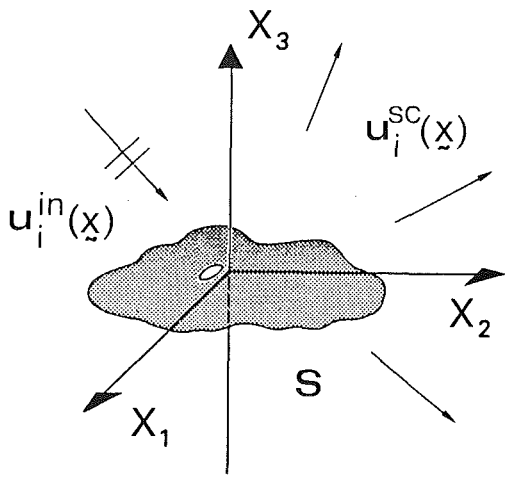


Fig. 1 Scattering geometry of a flat crack

$$C_{ijkl} = \lambda \delta_{ij} \delta_{kl} + \mu(\delta_{il}\delta_{jk} + \delta_{ik}\delta_{jl}), \tag{5}$$

and the notation

$$U_{i,j}^k(\mathbf{x}-\mathbf{y}) \equiv \frac{\partial}{\partial x_j} U_i^k(\mathbf{x}-\mathbf{y}) =$$

$$-\frac{\partial}{\partial y_j} U_i^k(\mathbf{x}-\mathbf{y}) \equiv -U_i^{k,j}(\mathbf{x}-\mathbf{y}) \tag{6}$$

is employed. In this notation, the lower (upper) indices correspond to the field point $\mathbf{x}$ (source point $\mathbf{y}$); physically $U_i^k(\mathbf{x}-\mathbf{y})$ is the displacement at $\mathbf{x}$ in the i-direction due to a unit time harmonic point load applied at $\mathbf{y}$ in the k-direction. The change in sign in equation (6) comes simply from the dependence of U_i^k on its argument $(\mathbf{x}-\mathbf{y})$. Furthermore,

$$D_{k,l}^{ij}(\mathbf{x}-\mathbf{y}) \equiv \frac{\partial}{\partial x_l} D_k^{ij}(\mathbf{x}-\mathbf{y}) =$$

$$-\frac{\partial}{\partial y_l} D_k^{ij}(\mathbf{x}-\mathbf{y}) \equiv -D_k^{ij,l}(\mathbf{x}-\mathbf{y}). \tag{7}$$

The explicit functional forms of D_m^{ij} and U_m^k, as well as their Taylor series expansions in $|\mathbf{x}-\mathbf{y}|$, are given in the Appendix. Together they satisfy the equation of motion

$$-D_{k,l}^{lm}(\mathbf{x}-\mathbf{y}) + \rho\omega^2 U_k^m(\mathbf{x}-\mathbf{y}) = -\delta_{km}\delta(\mathbf{x}-\mathbf{y}), \quad \mathbf{x},\mathbf{y} \epsilon V, \tag{8}$$

where ρ is the mass density of V, δ_{km} is the Kronecker delta, and $\delta(\mathbf{x}-\mathbf{y})$ is the Dirac delta function.

The problem statement is as follows: Given a crack-plane S and an incident field $u_i^{in}(\mathbf{x})$, the resulting scattered field $u_i^{sc}(\mathbf{x})$ is desired. By virtue of equation (2), the problem can be reduced to finding the crack-opening displacement $\Delta u_m^{sc}(\mathbf{y})$ caused by the incident field $u_i^{in}(\mathbf{x})$. The two quantities are connected by the traction-free boundary condition

$$\sigma_{3j}^{sc}(\mathbf{x}) = -\sigma_{3j}^{in}(\mathbf{x}), \quad \mathbf{x} \epsilon S. \tag{9}$$

Thus the crack-opening displacment can be thought of as that displacement that results through the application of tractions $-\sigma_{3j}^{in} n_3^+ = \sigma_{3j}^{in}$ to S^+, and $-\sigma_{3j}^{in} n_3^- = -\sigma_{3j}^{in}$ to S^-.

III Displacement and Traction Boundary Integral Equations

For scattering from a void, one can easily derive an integral equation for the unknown displacement of the void's traction-free surface by considering the limit $\mathbf{x} \to S$ of the appropriate displacement representation integral. In an analogous manner the limit $\mathbf{x} \to S$ of equation (2) may be considered. Unless $\Delta u_m^{sc}(\mathbf{y})$ is zero, such a limit is obviously discontinuous

Downloaded 03 May 2010 to 171.66.16.21. Redistribution subject to ASME license or copyright; see http://www.asme.org/terms/Terms_Use.cfm

through S; note equation (3) and the left-hand side of equation (2a). Provided that $\Delta u_m^{sc}(\mathbf{y})$ satisfies a Hölder condition on S, a careful evaluation of this limit, Budreck (1988), gives

$$^{\pm}u_k^{sc}(\mathbf{x}) = \pm\frac{1}{2}\Delta u_k^{sc}(\mathbf{x}) + [I_k(\mathbf{x})]_{\text{CPV}}, \quad \mathbf{x}\epsilon S, \tag{10}$$

where CPV indicates a Cauchy Principle Value integral.

Subtraction of the two equations in (10) gives equation (3), while addition gives

$$\frac{1}{2}[^{+}u_k^{sc}(\mathbf{x}) + {}^{-}u_k^{sc}(\mathbf{x})] = [I_k(\mathbf{x})]_{\text{CPV}}, \quad \mathbf{x}\epsilon S. \tag{11}$$

Equation (11) is a degenerate displacement integral equation. This is due to the absence of the incident field from the left-hand side of (11).

The degeneracy of equation (11) was circumvented by Budiansky and Rice (1979), who started their analysis by operating on both sides of equation (2) with $C_{3jkl}\partial/\partial x_l$. This gives the scattered-stress representation integral

$$\sigma_{3j}^{sc}(\mathbf{x}) = J_{3j}(\mathbf{x}), \quad \mathbf{x}\epsilon V, \tag{12a}$$

where

$$J_{3j}(\mathbf{x}) \equiv C_{3jkl}\int_S D_{k,l}^{3m}(\mathbf{x}-\mathbf{y})\Delta u_m(\mathbf{y})dS(\mathbf{y}). \tag{12b}$$

The continuity of the incident displacement field through S allows the substitution of $\Delta u_m(\mathbf{y})$ for $\Delta u_m^{sc}(\mathbf{y})$; see equations (1) and (3). However, since $D_{k,l}^{3m} = 0(|\mathbf{x}-\mathbf{y}|^{-3})$ (see Appendix), equation (12b) becomes nonintegrable for $\mathbf{x}\to S$.

Following the methods of Budiansky and Rice (1979), an application of dynamic equilibrium and the divergence therom casts equation (12b) in the alternate form

$$J_{3j}(\mathbf{x}) = C_{3jk\beta}\int_S D_k^{3m}(\mathbf{x}-\mathbf{y})\Delta u_{m,\beta}(\mathbf{y})dS(\mathbf{y})$$

$$- C_{3jk3}\int_S D_k^{\alpha m}(\mathbf{x}-\mathbf{y})\Delta u_{m,\alpha}(\mathbf{y})dS(\mathbf{y})$$

$$+ \rho\omega^2 C_{3jk3}\int_S U_k^m(\mathbf{x}-\mathbf{y})\Delta u_m(\mathbf{y})dS(\mathbf{y}). \tag{13}$$

When $\Delta u_{m,\alpha}(\mathbf{y})$ satisfies a Hölder condition on S, equation (13) gives for $\mathbf{x}\to S$ the integrable limits [see Budreck (1988)]

$$^{\pm}\sigma_{3j}^{sc}(\mathbf{x}) = \pm\frac{1}{2}C_{3jkl}\Delta u_{k,l}(\mathbf{x}) + [J_{3j}(\mathbf{x})]_{\text{CPV}}, \quad \mathbf{x}\epsilon S. \tag{14}$$

Substraction of the two equations in equation (14) gives an identity, and addition gives the integral equation

$$-\sigma_{3j}^{in}(\mathbf{x}) = [J_{3j}(\mathbf{x})]_{\text{CPV}}, \quad \mathbf{x}\epsilon S, \tag{15}$$

where the continuity condition

$$^{+}\sigma_{3j}^{sc}(\mathbf{x}) = {}^{-}\sigma_{3j}^{sc}(\mathbf{x}) \tag{16}$$

has been employed, and the boundary condition (9) has been enforced. It has been verified by explicit substitution of equations (A-4) and (A-10) into equation (13) that the integral equations (15) are equivalent to those of Budiansky and Rice (1979).

The process of converting equation (12b) to (13) is referred to as a regularization of the integrals. Note that this leads to an integral equation (15) involving both the crack-opening displacement $\Delta u_m(\mathbf{y})$ and the dislocation density $\Delta u_{m,\alpha}(\mathbf{y})$. The numerical solution of equation (15) involves conversion to a matrix equation through discretization of S, and is particularly appropriate for *a priori* assumed functional forms of $\Delta u_m(\mathbf{y})$, so that its diffentiation can be carried out explicitly. This methodology was essentially applied by Nishimura and Kobayashi (1988), using cubic spline functions over a circular crack.

IV Discretized Boundary Integral Equation

In this section, an alternate regularization of the representation integral (12) is presented. This regularization is based on an initial discretization of the crack, and gives rise to a discretized boundary integral equation, which can be solved explicity for the crack-opening displacement.

As a first step, the crack-plane S is discretized into N elements

$$S \to \sum_{q=1}^{N} S_q, \tag{17}$$

where the crack-opening displacement over any element S_q is taken as

$$\Delta u_m(\mathbf{y}) = f(\mathbf{y})\Delta u_m(\mathbf{y}_q). \tag{18}$$

Here $\mathbf{y}_q$ denotes the geometrical centroid of the element S_q, and $f(\mathbf{y})$ is a shape function which satisfies

$$f(\mathbf{y}_q) = 1. \tag{19}$$

Two examples of a shape function $f(\mathbf{y})$ are

$$f(\mathbf{y}) \equiv 1, \tag{20a}$$

and

$$f(\mathbf{y}) = [\{1-(y_1/a_1)^2-(y_2/a_2)^2\}/ \{1-[(y_1)_q/a_1]^2-[(y_2)_q/a_2]^2\}]^{1/2}. \tag{20b}$$

Here the uniform shape function (20a) corresponds to a constant approximation of the unknown crack-opening displacement over an element. This shape function will be used over all elements except those sharing a border with the crack edge. Over these edge elements the nonuniform shape function (20b) will be employed, which will cause the element to emulate the crack-opening displacement of an internally pressurized elliptic crack with semi-major and minor axes a_1 and a_2. In problems of scattering from an elliptic crack, these edge shape functions reduce the need for a fine discretization near the crack edge.

Incorporation of equations (17) and (18) into equation (12) gives the discretized stress representation integral in the form

$$\sigma_{3j}^{sc}(\mathbf{x}) = \sum_q H_{jm}^q(\mathbf{x})\Delta u_m(\mathbf{y}_q), \quad \mathbf{x}\epsilon V, \tag{21}$$

where

$$H_{jm}^q(x) \equiv C_{3jkl}\int_{S_q} D_{k,l}^{3m}(\mathbf{x}-\mathbf{y})f(\mathbf{y})dS(\mathbf{y}), \quad \mathbf{x}\epsilon V. \tag{22}$$

The H-matrix is then split up into four parts

$$H_{jm}^q(\mathbf{x}) = {}^{A}H_{jm}^q(\mathbf{x}) + {}^{B}H_{jm}^q(\mathbf{x}) + {}^{C}H_{jm}^q(\mathbf{x}) + {}^{D}H_{jm}^q(\mathbf{x}), \quad \mathbf{x}\epsilon V, \tag{23}$$

where

$${}^{A}H_{jm}^q(\mathbf{x}) = C_{3jkl}\int_{S_q}\left[D_{k,l}^{3m}(\mathbf{x}-\mathbf{y}) - \sum_{n=0}^{N-1} D_{k,l}^{n_3 m}(\mathbf{x}-\mathbf{y})\right]f(\mathbf{y})dS(\mathbf{y}), \tag{24a}$$

$${}^{B}H_{jm}^q(\mathbf{x}) = C_{3jkl}\int_{S_q}\sum_{n=0}^{N-1} D_{k,l}^{n_3 m}(\mathbf{x}-\mathbf{y})[f(\mathbf{y})-1]dS(\mathbf{y}), \tag{24b}$$

$${}^{C}H_{jm}^q(\mathbf{x}) = \sum_{n=0}^{N-1} C_{3jk\alpha}\int_{S_q} D_{k,\alpha}^{n_3 m}(\mathbf{x}-\mathbf{y})dS(\mathbf{y}), \tag{24c}$$

and

Downloaded 03 May 2010 to 171.66.16.21. Redistribution subject to ASME license or copyright; see http://www.asme.org/terms/Terms_Use.cfm

$$^{D}H^{q}_{jm}(\mathbf{x}) = \sum_{n=0}^{N-1} C_{3jk3} \int_{S_q} D^{n3m}_{k,3}(\mathbf{x}-\mathbf{y})\,dS(\mathbf{y}). \tag{24d}$$

In equations (24), the terms of the Taylor series

$$D^{ij}_{k}(\mathbf{x}-\mathbf{y}) = \sum_{n=0}^{\infty} D^{nij}_{k}(\mathbf{x}-\mathbf{y}) \tag{25}$$

have been used, where from the Appendix:

$$D^{nij}_{k,l}(\mathbf{x}-\mathbf{y}) = 0(|\mathbf{x}-\mathbf{y}|^{n-m}), \quad \begin{matrix} n=0: & m=3 \\ n\geq 1: & m=2 \end{matrix} \tag{26}$$

Also, in equations (24) N in some positive finite integer, $N \geq 1$, which is chosen to maximize the efficiency of the subsequent numerical computation. For $N=1$, the terms (24) make distinct contributions to the system H-matrix: $^{A}\mathbf{H}^{q}(\mathbf{x})$ contains the dynamic effect, $^{B}\mathbf{H}^{q}(\mathbf{x})$ contains the static effect of a nonuniform shape function, and $[^{C}\mathbf{H}^{q}(\mathbf{x}) + {}^{D}\mathbf{H}^{q}(\mathbf{x})]$ contains the static effect of a uniform shape function.

The limit $\mathbf{x} \to \mathbf{x}_p$ (the centroid of the element S_p) of the integrals (24) over S_p must be considered carefully. It is convenient to deal with this limit by first considering integration over a small circular patch $\Sigma(\epsilon)\epsilon S_p$ with center $\mathbf{x}_p$ and radius ϵ, so that $dS(\mathbf{y}) = 0(\epsilon^2)$. Consider further the field point $\mathbf{x} \notin S_p$ but near $\mathbf{x}_p$ such that $|\mathbf{x}-\mathbf{x}_p| = 0(\epsilon)$, which then implies that $|\mathbf{x}-\mathbf{y}| = 0(\epsilon)$. Using equation (26), the behavior of the integrals (24) over $\Sigma(\epsilon)$ for $\epsilon \to 0$ $(\mathbf{x} \to \mathbf{x}_p)$ is $0(\epsilon^a)$, where the integral is found to be either regular, CPV, or nonintegrable based on the value of a:

$a > 0$: Regular
$a = 0$: CPV
$a < 0$: Nonintegrable.

Inspection of the integrals (24) reveal the following results. In the limit $\mathbf{x} \to \mathbf{x}_p$ the integral $^{A}\mathbf{H}^{p}(\mathbf{x}_p)$ remains regular, and the integral $^{B}\mathbf{H}^{p}(\mathbf{x}_p)$ becomes at worst CPV, provided

$$f(\mathbf{y}_q + \epsilon) = 1 + 0(|\epsilon|^n), \quad n \geq 1. \tag{27}$$

The static shape function (20b) satisfies condition (27). Note that $^{B}\mathbf{H}^{q}(\mathbf{x}_p) \equiv 0$ if a constant approximation is assumed over S_q. The integrals of $^{C}\mathbf{H}^{p}(\mathbf{x}_p)$ and $^{D}\mathbf{H}^{p}(\mathbf{x}_p)$ with $n \neq 0$ are also seen to remain regular, but the $n=0$ terms are nonintegrable for $\mathbf{x} \to \mathbf{x}_p$. Accordingly, these terms must be regularized before taking the limit $\mathbf{x} \to \mathbf{x}_p$.

An application of static equilibrium

$$D^{olm}_{k,l}(\mathbf{x}-\mathbf{y}) = 0, \quad \mathbf{x} \epsilon V, \tag{28}$$

gives

$$\int_{S_q} D^{o3m}_{k,3}(\mathbf{x}-\mathbf{y})\,dS(\mathbf{y}) = -\int_{S_q} D^{o\alpha m}_{k,\alpha}(\mathbf{x}-\mathbf{y})\,dS(\mathbf{y}), \tag{29}$$

so that equations (24c, d) and (29), together with equation (7) and an application of the divergence theorem, gives

$$^{C}H^{q}_{jm}(\mathbf{x}) = -\sum_{n=0}^{N-1} C_{3jk\alpha} \int_{\Gamma_q} D^{n3m}_{k}(\mathbf{x}-\mathbf{y}) n_\alpha(\mathbf{y})\,d\Gamma(\mathbf{y}), \tag{30a}$$

and

$$^{D}H^{q}_{jm}(\mathbf{x}) = C_{3jk3} \int_{\Gamma_q} D^{o\alpha m}_{k}(\mathbf{x}-\mathbf{y}) n_\alpha(\mathbf{y})\,d\Gamma(\mathbf{y}) + \sum_{n=1}^{N-1} C_{3jk3} \int_{S_q} D^{n3m}_{k,3}(\mathbf{x}-\mathbf{y})\,dS(\mathbf{y}), \tag{30b}$$

where Γ_q denotes the edges of the element S_q, with outward normal n_α.

The integrals of (30) with $n=0$ will remain regular for $\mathbf{x} \to \mathbf{x}_p$ provided $\mathbf{x} \not\to \Gamma_p$, which will of course always be the case, since $x_p \epsilon \Gamma_p$ would imply an element of zero area. In practice, these integrals with $n=0$ are evaluated analytically, so that a static problem with uniform shape functions can be solved without doing any numerical integration whatsoever.

The regularization procedure being complete, taking equation (21) in the limit $\mathbf{x} \to \mathbf{x}_p$ yields the discretized boundary integral equation

$$-\sigma^{in}_{3j}(\mathbf{x}_p) = \sum_{q} H^{q}_{jm}(\mathbf{x}_p) \Delta u_m(\mathbf{y}_q), \quad \mathbf{x}_p \epsilon S_p, \tag{31}$$

where the four terms of $H^{q}_{jm}(\mathbf{x}_p)$ are given, in the order of the right-hand side of equation (23), by equations (24a, b) and (30a, b). Here the boundary condition (9) has been enforced.

Since the medium V is isotropic, it can be shown that the system of equations (31) decouples in such a way that a crack under normal loading gives rise to only a normal crack-opening displacement, which is governed by

$$-\sigma^{in}_{33}(\mathbf{x}_p) = \sum_{q} H^{pq}_{33} \Delta u_3(\mathbf{y}_q), \quad \mathbf{x}_p \epsilon S_p, \tag{32}$$

where again

$$H^{pq}_{33} = {}^{A}H^{pq}_{33} + {}^{B}H^{pq}_{33} + {}^{C}H^{pq}_{33} + {}^{D}H^{pq}_{33}. \tag{33}$$

After substitution of equation (5) into equations (24a, b) and (30a, b), and subsequent simplification, we have

$$^{A}H^{pq}_{33} = \int_{S_q} \left\{ \lambda \left[D^{33}_{\alpha,\alpha}(\mathbf{x}_p - \mathbf{y}) - \sum_{n=0}^{N-1} D^{n33}_{\alpha,\alpha}(\mathbf{x}_p - \mathbf{y}) \right] + (\lambda + 2\mu) \left[D^{33}_{3,3}(\mathbf{x}_p - \mathbf{y}) - \sum_{n=0}^{N-1} D^{n33}_{3,3}(\mathbf{x}_p - \mathbf{y}) \right] \right\} f(\mathbf{y})\,dS(\mathbf{y}), \tag{34a}$$

$$^{B}H^{pq}_{33} = \int_{S_q} \sum_{n=0}^{N-1} \left\{ \lambda D^{n33}_{\alpha,\alpha}(\mathbf{x}_p - \mathbf{y}) + (\lambda + 2\mu) D^{n33}_{3,3}(\mathbf{x}_p - \mathbf{y}) \right\} [f(\mathbf{y}) - 1]\,dS(\mathbf{y}), \tag{34b}$$

$$^{C}H^{pq}_{33} = -\lambda \sum_{n=0}^{N-1} \int_{\Gamma_q} D^{n33}_{\alpha}(\mathbf{x}_p - \mathbf{y}) n_\alpha(\mathbf{y})\,d\Gamma(\mathbf{y}), \tag{34c}$$

and

$$^{D}H^{pq}_{33} = (\lambda + 2\mu) \left\{ \int_{\Gamma_q} D^{o\alpha 3}_{3}(\mathbf{x}_p - \mathbf{y}) n_\alpha(\mathbf{y})\,d\Gamma(\mathbf{y}) + \sum_{n=1}^{N-1} \int_{S_q} D^{n33}_{3,3}(\mathbf{x}_p - \mathbf{y})\,dS(\mathbf{y}) \right\}. \tag{34d}$$

In the next section, various results are presented from the numerical solution of equation (32).

V Numerical Results

The results of this section are for a Poisson's ratio of $\nu = 1/4$. The mesh sizes were selected such that no element has a length in excess of one-tenth the wavelength of a transverse wave. The formulation of Section IV is valid for cracks of arbitrary shape. Here, we present results for penny-shaped and elliptic cracks.

Penny-Shaped Crack. To compare with previous results, a circular crack geometry is first considered. A penny-shaped crack of radius "a" is subjected to a normally incident plane L-wave. For a crack located in the (x_1, x_2)-plane, and centered at the origin (Fig. 1), the incident field may be written as

$$u^{in}_{i}(\mathbf{x}) = d_i A_L e^{ik_L \mathbf{x}\cdot\mathbf{p}}, \tag{35a}$$

Downloaded 03 May 2010 to 171.66.16.21. Redistribution subject to ASME license or copyright; see http://www.asme.org/terms/Terms_Use.cfm

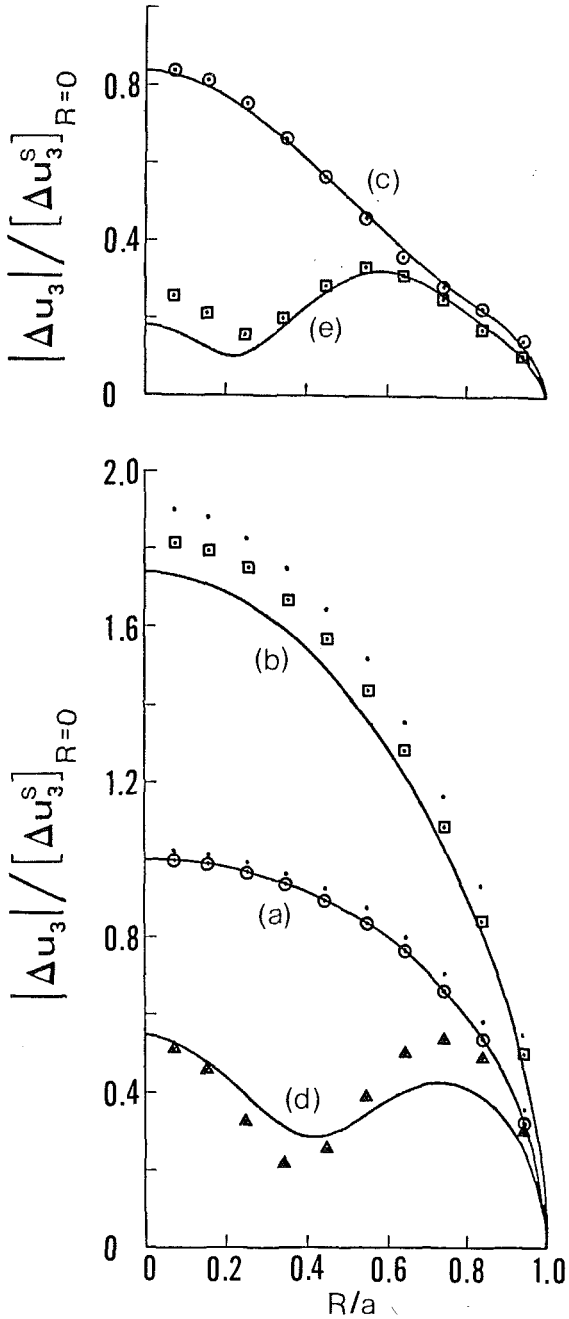


Fig.2 BIEM (points) and Mal (lines) crack-opening displacement for $k_T a$ equal to (a) 0.0; (b) 1.4; (c) 3.2; (d) 4.4; (e) 6.0

where the displacement and propagation vectors are simply

$$d_i = p_i = -\delta_{3i}. \tag{35b}$$

The corresponding input to equation (32) is

$$\sigma_{33}^{in}(\mathbf{x}_p) = ik_L(\lambda + 2\mu)A_L. \tag{36}$$

Figure 2 shows the ratio of the norm of the complex crack-opening displacement and the corresponding (i.e., due to the same stress amplitude) static crack-opening displacement evaluated at the crack's center. The exact solution of the static problem has been given by Sneddon (1951).

The dimensionless crack-opening displacements computed by the BIEM are compared to those presented by Mal (1970). The BIEM results in the top graph of Fig. 2 are almost identical to those presented by Niwa and Hirose (1987). The discretized integral equation solved by these authors is similar to equation (32), but somewhat more complicated, due to their different method of regularization; Hirose (1987). Their formulation also uses the uniform shape function exclusively; Hirose (1987).

The enclosed (by circles, squares, etc) points in Fig. 2 are the BIEM code's best results at the indicated frequencies. Running the code at a finer mesh changed these points an insignificant amount.

The discrepancies between the BEIM points and Mal's curves at the frequencies $k_T a = 1.4$ and 4.4 are slightly larger, but qualitatively the same as those indicated by Nishimura and Kobayashi (1988). One might recognize that these two frequencies are close to those ($k_T a = 1.44, 4.33, 7.22, \ldots$) at which the Rayleigh wavelength is $\lambda_R = 4a/n$; $n = 1, 3, 5, \ldots$. The latter frequencies correspond to the resonant excitation of the crack's axisymmetric drumhead modes. However, since the crack-opening displacement is comprised only in part of Rayleigh wave motion, no matrix singularities were enountered in the BIEM computations.

The enclosed points of Fig. 2 for the higher frequencies ($k_T a = 3.2, 4.4, 6.0$) were run with the basic mesh, i.e., the nonuniform shape function (20*b*) was applied to *only* the *edge* elements. The enclosed points for the lower frequencies ($k_T a = 0.0, 1.4$) were run with a special mesh, for which the nonuniform shape function (20*b*) was applied to *all* elements. The points above those run with the special mesh were run with the basic mesh, and were found to approach their enclosed counterparts when run with finer meshes.

The nonuniform shape function (20*b*) should not be used on elements other than those bordering the crack edge, except when it may be assumed that the crack-opening displacement does not deviate much from the quasi-static elliptic shape. Therefore, unless explicitly stated otherwise, all subsequent numerical results have been obtained with the nonuniform shape function (20*b*) applied only to those elements for which it was originally intended: the elements sharing a border with the crack edge.

The crack-opening displacement, in conjunction with the representation integral (2), allows the calculation of the scattered displacement field throughout the elastic domain. The normal displacement of the far-field scattered L-wave reduces to

$$u_3^{sc}(\mathbf{x}) \sim U_3^L(\psi)\frac{e^{ik_L|\mathbf{x}|}}{4\pi|\mathbf{x}|}, \quad |\mathbf{x}| \to \infty, \tag{37}$$

where ψ is the angle of observation in the (x_α, x_3)-plane as measured from the x_3-axis, and

$$U_3^L(\psi) = -ik_L[2\kappa^{-2}\cos^2\psi + (1 - 2\kappa^{-2})]$$
$$\cos\psi \int_S e^{-ik_L y_\alpha \sin\psi}\Delta u_3(\mathbf{y})dS(\mathbf{y}). \tag{38}$$

Here $\kappa = k_T/k_L$. Equation (37) comes from substituting the far-field representation of the stress Green's function [Achenbach, et al. (1982)] into equation (12). We also define

$$\tilde{U}_3^L \equiv U_3^L(\psi = 0) = -ik_L\int_S \Delta u_3(\mathbf{y})dS(\mathbf{y}). \tag{39}$$

A related quantity is the scattering cross section of the crack; Barratt and Collins (1965). Physically, the scattering cross section, which is frequency and geometry-dependent, is a measure of an obstacle's ability to scatter the incoming field. Under the incident field (35) with $A_L = 1/ik_L$, so that $|\sigma_{33}^{in}| = \lambda + 2\mu$, the scattering cross section of the crack is

$$\Sigma_p = \mathrm{Re}(\tilde{U}_3^L). \tag{40}$$

Table 1 lists the dimensionless scattering cross sections, Σ_p/A, for an L-wave normally incident on a penny-shaped crack, as computed by Krenk and Schmidt (1982), Keogh (1983), Mar-

Downloaded 03 May 2010 to 171.66.16.21. Redistribution subject to ASME license or copyright; see http://www.asme.org/terms/Terms_Use.cfm

Table 1 Dimensionless scattering cross section, Σ_p/A, for normal incidence of an L-wave on a penny-shaped crack as computed by Krenk and Schmidt (1982); Keogh (1983); Martin and Wickham (1983); and the present BIE method. Parentheses ( ) indicate BIE runs with the nonuniform shape function (20*b*) used on *all* crack elements.

$k_T a$	Krenk & Schmidt	Keogh	Martin & Wickham	BIEM
1.0	0.214	____	0.214	.0262 (0.218)
2.0	2.894	3.066	2.895	3.066 (2.911)
3.0	1.910	1.836	1.910	1.904
4.0	1.655	1.617	1.600	1.649
5.0	2.106	2.364	2.314	2.342
6.0	1.801	1.851	1.877	1.890
7.0	1.987	1.770	1.831	1.920
8.0	1.941	2.212	2.208	2.207

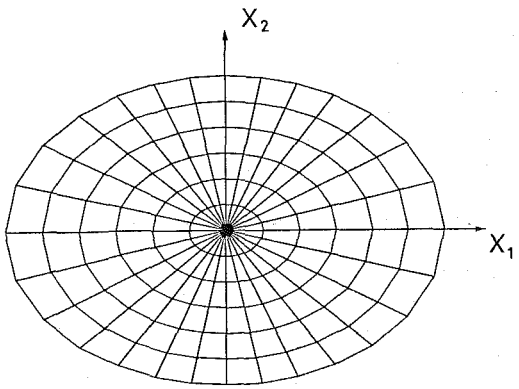


Fig. 3 Elliptic crack with aspect ratio 1:1/√2

tin and Wickham (1983), and the present BIE method. Here "A" is the surface area of the crack.

It is of interest to note that under the same incident field, the Kirchhoff approximation [Achenbach, et al. (1982)] predicts a crack-opening displacement of

$$\Delta u_3(\mathbf{y}) = 2i/k_L, \tag{41}$$

which together with equation (40) gives $\Sigma_p/A = 2$. Note that, for the higher frequencies, the results of Table 1 appear to oscillate about this value.

Elliptic Crack. Consider an elliptic crack lying in the (x_1, x_2)-plane and centered at the origin (Fig. 1), with aspect ratio $1:1/\sqrt{2}$ (Fig. 3). The aspect ratio $a_1:a_2$ denotes the ratio of the x_1 and x_2-axes of the ellipse; as a matter of convention, max $\{a_1, a_2\} \equiv 1$. The crack is subjected to the normally incident L-wave field given by equation (35).

For four distinct frequencies, Fig. 4 shows the resulting dimensionless crack-opening displacements versus the dimensionless radial distance, where the latter is defined as the distance from the crack center divided by the total distance from the crack center to the crack edge. As in Fig. 2, the norm of the complex crack-opening displacement has been divided by the corresponding static solution [see Mura (1982)] evaluated at the center of the crack.

Since the crack-opening displacements are in this case symmetric with respect to the x_1 and x_2-axis, only data from one quarter of the crack is presented. The lines marked a_α correspond to data from elements with an edge lying on the x_α-axis; see Fig. 3. The plots of Fig. 4 were drawn by connecting the values computed at the centroid of each element.

The results of Fig. 4 indicate a strong geometrical

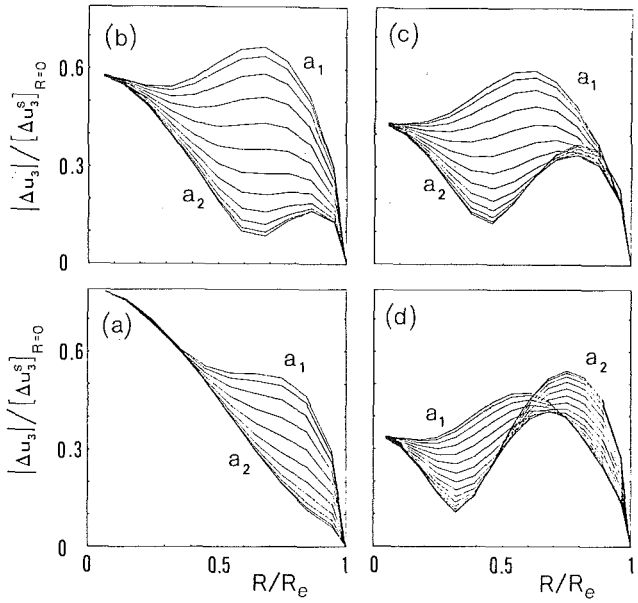


Fig. 4 Crack-opening displacement of an $1:1/\sqrt{2}$ elliptic crack under normal incidence of an L-wave with $k_T \max\{a_1, a_2\}$ equal to (*a*) 4.0; (*b*) 4.5; (*c*) 5.0; (*d*) 5.5

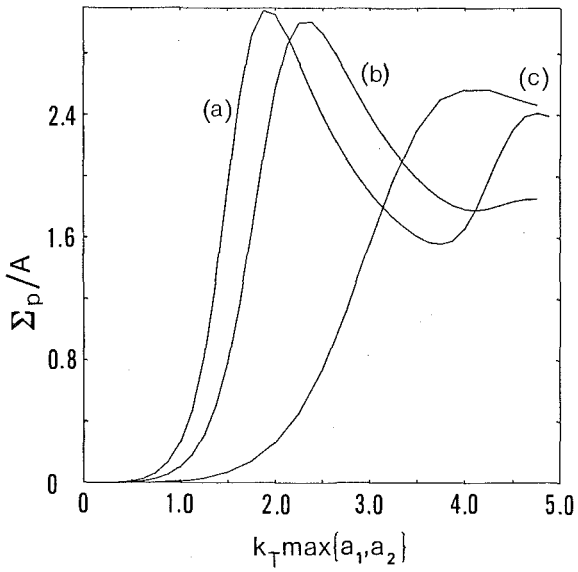


Fig. 5 Scattering cross section of (*a*) 1:1; (*b*) $1:1/\sqrt{2}$, and (*c*) 1:1/3 elliptic cracks under normal incidence of an L-wave

dependence of the crack-opening displacement on the shape of the crack: even with the moderate aspect ratio of $1:1/\sqrt{2}$, the crack-opening displacement is markedly different from the axisymmetric solution of a penny-shaped crack. This is because the elliptic crack has an additional length parameter, which affects the motion of the crack faces, including the propagation of Rayleigh waves traversing the traction-free surfaces of the crack.

In Fig. 5, the scattering cross section (40) is plotted, and Fig. 6 shows the norm of the back-scattered L-wave field, equation (39). Both quantities were nondimensionalized through division by the surface area of the crack, and they are plotted as functions of the dimensionless wave number. The Kirchhoff approximation results are as follows: The crack-opening displacement (41) gives $\Sigma_p/A = 2$ and $|\bar{U}_3^L/A| = 2$, which would appear to be asymptotic values as the dimensionless wave number increases.

The peaks of Figs. 5 and 6 are related to resonant wave mo-

Downloaded 03 May 2010 to 171.66.16.21. Redistribution subject to ASME license or copyright; see http://www.asme.org/terms/Terms_Use.cfm

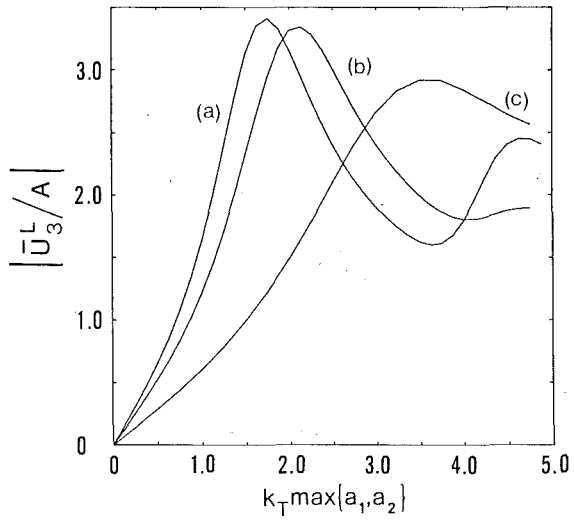


Fig .6 Back-scattered displacement amplitudes of (*a*) 1:1; (*b*) 1:1/√2, and (*c*) 1:1/3 elliptic cracks under normal incidence of an *L*-wave

tion on the faces of the crack. They occur in the exact solution but not in the Kirchhoff approximation. In the Kirchhoff approximation, the crack-face motion is constained; no free motion is permitted. Hence, no resonant condition can be achieved. For oblique incidence peaks in the back-scatter also occur due to optimal constructive interference between scattered signals emanating from different locations on the crack, for both the exact solution and the Kirchhoff approximation.

The spacing of the peaks for case (*a*) of Fig. 6 is approximately $\Delta(k_T a) = 2.88$. This agrees with the predicted increment of $\Delta(k_T a) \approx 2.89$ at which successive axisymmetic Rayleigh modes of the crack are excited in a resonant condition. Since the Rayleigh modes of an elliptic crack are not axisymmetric, the excitation of successive modes do not occur at regular intervals in frequency. Another interesting result seen in Figs. 5 and 6 are the relative locations between the first peak of each of the three cracks. These peaks suggest the following trend: The higher the frequency at which the first peak occurs, the more oblong the elliptic crack, assuming $\max\{a_1, a_2\}$ is held constant.

Finally, Fig. 7 shows the scattered *L*-wave displacement amplitude as a function of the observation angle. The points $\psi = 0$ correspond to the back-scattered displacement amplitudes of Fig. 6.

The plots of Fig. 7 compare the field radiated from a penny-shaped crack and an $1{:}1/\sqrt{2}$ elliptic crack (Fig. 3) at two separate frequencies. The lines corresponding to the $1{:}1/\sqrt{2}$ elliptic crack are marked with an a_α, which indicates that the observation angle is located in the plane spanned by the x_3 and x_α-axis. The a_α lines were constructed by evaluating equation (38) with the appropriate values of y_α.

Notice the difference in amplitude between calculations of the $1{:}1/\sqrt{2}$ elliptic crack in the two orthogonal planes at the same angle ψ. This amplitude difference is not as pronounced in the lower frequency plot, since the crack-opening displacement at this frequency has a simple shape similar to the static result.

Acknowledgment

This work was carried out in the course of research sponsored by the Army Research Office, Project DAAG29-84-K-0163. A grant from Cray Research Inc. for access to the Pittsburgh Supercomputer Center is also gratefully acknowledged.

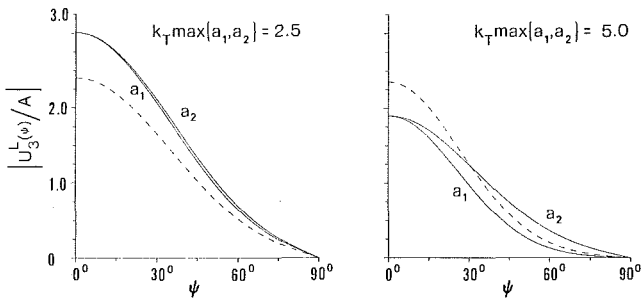


Fig. 7 Scattered *L*-wave displacement amplitudes for $1{:}1/\sqrt{2}$ (solid) and 1:1 (dotted) elliptic cracks under normal incidence of an *L*-wave

References

Achenbach, J. D., Gautesen, A. K., and McMaken, H., 1982, *Ray Methods for Waves in Elastic Solids*, Pitman Publication Inc.

Achenbach, J. D., and Kitahara, M., 1986, "Reflection and Transmission of an Obliquely Incident Wave by an Array of Spherical Cavities," *Journal of the Acoustical Society of America*, Vol. 80 (4), pp. 1209–1214.

Barratt, P. J., and Collins, W. D., 1965, "The Scattering Cross-Section of an Obstacle in an Elastic Solid for Plane-Harmonic Waves," *Proceedings of the Cambridge Philosophical Society*, Vol. 61, pp. 969–981.

Beskos, D. E., 1987, "Boundary Element Methods in Dynamic Analysis," *Applied Mechanics Reviews*, Vol. 40, No. 1, pp. 1–23.

Budiansky, B., and Rice, J. R., 1979, "An Integral Equation for Dynamic Elastic Response of an Isolated 3-D Crack," *WAVE MOTION*, Vol. 1, pp. 187–192.

Budreck, D. E., 1988, PhD thesis, Northwestern University.

Cruse, T. A., and Rizzo, F. J., 1968, "A Direct Formulation and Numerical Solution of the General Transient Elastodynamic Problem I," *J. Math. Anal. Appl.*, Vol. 22, pp. 244–259.

Cruse, T. A., 1968, "A Direct Formulation and Numerical Solution of the General Transient Elastodynamic Problem II," *J. Math. Anal. Appl.*, Vol. 22, pp. 341–355.

Hirose, S., 1987, personal conversation.

Keogh, P. S., 1983, PhD thesis, University of Manchester.

Kitahara, M., and Nakagawa, K., 1985, "Boundary Integral Equation Methods in Three Dimensional Elastodynamics," *Boundary Elements VII*, Springer-Verlag.

Krenk, S., and Schmidt, H., 1982, "Elastic Wave Scattering by a Circular Crack," *Philosophical Transactions of the Royal Society, London*, Vol. A308, pp. 167–198.

Lin, W., and Keer, L. M., 1987, "Scattering by a Planar Three-Dimensional Crack," *Journal of the Acoustical Society of America*, Vol. 82, No. 4, pp. 1442–1448.

Mal, A. K., 1970, "Interaction of Elastic Waves With a Penny-Shaped Crack," *International Journal of Engineering Science*, Vol. 8, pp. 381–388.

Martin, P. A., 1981, "Diffraction of Elastic Waves by a Penny-Shaped Crack," *Proceedings of the Royal Society, London*, Vol. A378, pp. 263–285.

Martin, P. A., and Wickham, G. R., 1983, "Diffraction of Elastic Waves by a Penny-Shaped Crack: Analytical and Numerical Results," *Proceedings of the Royal Society, London*, Vol. A390, pp. 91–129.

Mura, T., 1982, *Micromechanics of Defects in Solids*, The Hague: Martinus Nijhoff Publishing.

Nishimura, N., and Kobayashi, S., 1988, "An Improved Boundary Integral Equation Method for Crack Problems," *IUTAM Symposium on Boundary Elements*, Springer-Verlag, in press.

Niwa, Y., Hirose, S., 1987, "Application of the BEM to Elastodynamics in a Three Dimensional Half-Space," *Recent Applications in Computational Mechanics*, ASCE.

Rizzo, F. J., 1967, "An Integral Equation Approach to Boundary Value Problems of Classical Elastostatics," *Quarterly of Applied Mathematics*, Vol. 25, No. 1, pp. 83–95.

Rizzo, F. J., Shippy, D. J., and Rezayat, M., 1985, "A Boundary Integral Equation Method for Radiation and Scattering of Elastic Waves in Three Dimensions," *International Journal for Numerical Methods in Engineering*, Vol. 21, pp. 115–129.

Roy, A., 1984, "Diffraction of Elastic Waves by an Elliptic Crack," *Internation Journal of Engineering Science*, Vol. 22, No. 6, pp. 729–739.

Sneddon, I. N., 1951, *Fourier Transforms*, McGraw-Hill Inc.

Visscher, W. M., 1983, "Theory of Scattering of Elastic Waves from Flat Cracks of Arbitrary Shape," *WAVE MOTION*, Vol. 5, pp. 15–32.

APPENDIX A

Green's Functions

Let **x** and **y** be two distinct points in a three-dimensional, in-

Downloaded 03 May 2010 to 171.66.16.21. Redistribution subject to ASME license or copyright; see http://www.asme.org/terms/Terms_Use.cfm

finitely extended, linearly elastic, homogeneous and isotropic solid V. The longitudinal and transvere wavenumbers in V are k_L and k_T, respectively. Also, by definition

$$\kappa \equiv k_T/k_L, \tag{A-1}$$

$$r_i \equiv x_i - y_i, \quad r \equiv \sqrt{r_i r_i}, \tag{A-2a,b}$$

and

$$\alpha_L \equiv k_L r, \quad \alpha_T \equiv k_T r. \tag{A-3 a,b}$$

The displacement Green's function $U_i^j(\mathbf{x}-\mathbf{y})$ satisfying the Navier-Cauchy equation for time-harmonic motion, equation (8), is

$$U_i^j(\mathbf{x}-\mathbf{y}) = \frac{k_T}{4\pi\mu}\left[\delta_{ij}A_1 - \frac{r_i r_j}{r^2}A_2\right], \tag{A-4}$$

where

$$A_1 = e^{i\alpha_T}(\alpha_T^{-1} + i\alpha_T^{-2} - \alpha_T^{-3}) - e^{i\alpha_L}(i\alpha_L^{-2} - \alpha_L^{-3})\kappa^{-3}, \tag{A-5a}$$

and

$$A_2 = e^{i\alpha_T}(\alpha_T^{-1} + 3i\alpha_T^{-2} - 3\alpha_T^{-3}) - e^{i\alpha_L}(\alpha_L^{-1} + 3i\alpha_L^{-2} - 3\alpha_L^{-3})\kappa^{-3}. \tag{A-5b}$$

The Taylor series expansion of $U_i^j(\mathbf{x}-\mathbf{y})$, which is defined by

$$U_i^j(\mathbf{x}-\mathbf{y}) = \sum_{n=0}^{\infty} U_i^{nj}(\mathbf{x}-\mathbf{y}), \tag{A-6}$$

has the terms, for $n \geq 1$,

$$U_i^{nj}(\mathbf{x}-\mathbf{y}) = \frac{1}{4\pi\mu}[\delta_{ij}\{a_n + k_T^{-2}b_{n+2}(n+1)\}r^{n-1} + k_T^{-2}\frac{r_i r_j}{r^2}b_{n+3}(n+2)(n)r^n], \tag{A-7}$$

where

$$a_n = \frac{(ik_T)^n}{n!}, \quad b_n = \frac{(ik_T)^n - (ik_L)^n}{n!}. \tag{A-8a,b}$$

The first term ($n=0$) of the series (A-6) is simply the static displacement Green's function

$$U_i^{oj}(\mathbf{x}-\mathbf{y}) = \frac{1}{8\pi\mu}\left[\delta_{ij}(1+\kappa^{-2}) + \frac{r_i r_j}{r^2}(1-\kappa^{-2})\right]r^{-1}. \tag{A-9}$$

The stress Green's function $D_m^{ij}(\mathbf{x}-\mathbf{y})$ is related to $U_i^j(\mathbf{x}-\mathbf{y})$ by equation (4), and is given by

$$D_m^{ij}(\mathbf{x}-\mathbf{y}) = \frac{k_T^2}{4\pi}\left[\delta_{ij}\frac{r_m}{r}B_1 + \left(\delta_{mi}\frac{r_j}{r} + \delta_{mj}\frac{r_i}{r}\right)B_2 - 2\frac{r_i r_j r_m}{r^3}B_3\right], \tag{A-10}$$

where

$$B_1 = (\lambda/\mu)[-e^{i\alpha_L}(i\alpha_L^{-1} - \alpha_L^{-2})\kappa^{-4}] + 2[e^{i\alpha_T}(\alpha_T^{-2} + 3i\alpha_T^{-3} - 3\alpha_T^{-4}) - e^{i\alpha_L}(\alpha_L^{-2} + 3i\alpha_L^{-3} - 3\alpha_L^{-4})\kappa^{-4}], \tag{A-11a}$$

$$B_2 = e^{i\alpha_T}(-i\alpha_T^{-1} + \alpha_T^{-2}) + 2[e^{i\alpha_T}(\alpha_T^{-2} + 3i\alpha_T^{-3} - 3\alpha_T^{-4}) - e^{i\alpha_L}(\alpha_L^{-2} + 3i\alpha_L^{-3} - 3\alpha_L^{-4})\kappa^{-4}], \tag{A11-b}$$

and

$$B_3 = e^{i\alpha_T}(-i\alpha_T^{-1} + 6\alpha_T^{-2} + 15i\alpha_T^{-3} - 15\alpha_T^{-4}) - e^{i\alpha_L}(-i\alpha_L^{-1} + 6\alpha_L^{-2} + 15i\alpha_L^{-3} - 15\alpha_L^{-4})\kappa^{-4}. \tag{A-11c}$$

The Taylor series expansion of $D_m^{ij}(\mathbf{x}-\mathbf{y})$, given by

$$D_m^{ij}(\mathbf{x}-\mathbf{y}) = \sum_{n=0}^{\infty} D_m^{nij}(\mathbf{x}-\mathbf{y}), \tag{A-12}$$

has the following terms, for $n \geq 1$,

$$D_m^{nij}(\mathbf{x}-\mathbf{y}) = -\frac{1}{4\pi\mu}\left[\left\{\lambda\delta_{ij}\frac{r_m}{r} + \mu\left(\delta_{mi}\frac{r_j}{r} + \delta_{mj}\frac{r_i}{r}\right)\right\}a_{n+1}(n) + k_T^{-2}\left[\left\{\lambda\delta_{ij}\frac{r_m}{r} + 2\mu\frac{r_m r_i r_j}{r^3}\right\}b_{n+3}(n+2)(n)(n-2) + \left\{(5\lambda+2\mu)\delta_{ij}\frac{r_m}{r} + 2\mu\left(\delta_{mi}\frac{r_j}{r} + \delta_{mj}\frac{r_i}{r}\right)\right\}b_{n+3}(n+2)(n)\right]\right]r^{n-1}, \tag{A-13}$$

where a_n and b_n were given previously by equation (A-8). The first term ($n=0$) of the series (A-12) is simply the static stress Green's function

$$D_m^{oij}(\mathbf{x}-\mathbf{y}) = \frac{1}{4\pi(\lambda+2\mu)}\left[\mu\left(\delta_{mi}\frac{r_j}{r} + \delta_{mj}\frac{r_i}{r} - \delta_{ij}\frac{r_m}{r}\right) + 3(\lambda+\mu)\frac{r_i r_j r_m}{r^3}\right]r^{-2}, \tag{A-14}$$

which is related to the static displacement Green's function by

$$D_m^{oij}(\mathbf{x}-\mathbf{y}) = C_{ijkl}U_m^{ok,l}(\mathbf{x}-\mathbf{y}). \tag{A-15}$$

Downloaded 03 May 2010 to 171.66.16.21. Redistribution subject to ASME license or copyright; see http://www.asme.org/terms/Terms_Use.cfm

P. Ladevèze
Professor.
Mem. ASME

F. Pécastaings
Assistant Professor.

Laboratoire de Mécanique et Technologie,
E.N.S. de CACHAN/C.N.R.S./
Université Paris 6,
94230 Cachan, France

The Optimal Version of Reissner's Theory

An improved version of Reissner's theory, called Optimal version, is proposed in the case of homogeneous and isotropic plates with any edge boundary conditions. It differs from the classical theory by the value of the transverse shear deformability factor and by the boundary conditions. Three-dimensional displacement and stress distributions expressed in terms of the Optimal version are given for any point of the plate, whether within the plate itself or in the neighborhood of its edge. It is proved that these distributions are second-order approximations of the exact three-dimensional solution—relative error $O(h^2/L^2)$. Consequently, Optimal version is a second-order theory; therefore it is better than Kirchhoff-Love's theory.

1 Introduction

Reissner's theory [see Reissner, 1985] is asymptotically equivalent to the classical theory of Kirchhoff-Love. It has been proved that, by taking the exact edge conditions into account, the error is $O(h/L)$, where h and L are, respectively, of the order of magnitude of the thickness and of the diameter [Ladevèze, 1980]. The errors $O(h^2/L^2)$ that one can find in the literature, in particular in Danielson [1970], Koiter and Simmonds [1972], Ladevèze [1976], must be regarded as interior errors: They are defined through a kinematically admissible displacement field and a "statically" admissible stress field related to the plate solution which does not satisfy the prescribed edge conditions (in particular, in the case of a free edge).

Yet, it has been noted often that Reissner's theory yielded more accurate results. Therefore, in the example of the infinite plate with a circular hole, bent at infinity, various calculations [Shun Cheng, 1979], [Van der Heijden, 1976] have pointed out that the three-dimensional stress distributions suggested by Reissner [1975] were in very good agreement with the exact solution [Alblas, 1957] on the edge of the hole, for a thin plate as well as for a moderately thick plate. The results established by Ladevèze [1980] gives a first explanation of this paradox. Indeed, it is proved in this paper that, for the case of a free edge and for a fixed value B^* of the transverse shear deformability factor, Reissner's theory is a second-order theory; that is, it leads to a relative error for the solution of order h^2/L^2. However, this value B^* is very close to the usual one; this is why Reissner's theory is better than that of Kirchhoff-Love in the case of a free edge. This paper complements this result.

First, we give a version of Reissner's theory, called Optimal version, in the case of isotropic homogeneous plates with loads prescribed on their upper and lower faces and on their lateral surface. Volumic loads have not been taken into account for the purpose of clarity. Optimal version differs from the classical one, on two points:

1 The value of the transverse shear deformability factor: Optimal value is the B^*-value already introduced in [Ladevèze, 1980];
2 The boundary conditions: They differ from the classical ones by a term which is expressed by means of the twisting edge loading.

To introduce such modifications in a calculation does not imply special difficulty. This theory always leads to a problem mathematically well posed, which is not always the case of Kirchhoff-Love's theory with modified boundary conditions [Van der Heijden, 1976], which introduces energy modifications.

Then, we estimate the quality of Optimal version by the method described in [Ladevèze, 1976]: We only consider the case of a regular boundary, weakly curved, that is, locally similar to a straight edge. Contrary to Kirchhoff-Love's theory, Reissner's theory leads to a solution which contains terms with wavelength $O(h)$; therefore its wavelength is not of the order of the plate diameter. Taking this property into account, we prove that it is a second-order theory.

Since the classical version and Optimal version are very close to one another in many practical cases, this result completes the explanation according to which, for any stress data, Reissner's theory is more performing than that of Kirchhoff-Love. Therefore, the main interest of Optimal version lies in the fact that it allows the calculation of thick plates.

Finally, we give a three-dimensional stress and displacement distribution which is, for any point of the plate, whether within the plate itself or in the neighborhood of its edge, a second-order approximation of the exact solution.

The approach that allowed the construction of Optimal version in the case of stress data [Pécastaings, 1985], may be ap-

Contributed by the Applied Mechanics Division for publication in the JOURNAL OF APPLIED MECHANICS.
Discussion on this paper should be addressed to the Editorial Department, ASME, United Engineering Center, 345 East 47th Street, New York, NY 10017, and will be accepted until two months after final publication of the paper itself in the JOURNAL OF APPLIED MECHANICS. Manuscript received by ASME Applied Mechanics Division, March 24, 1987; final revision, October 24, 1987.

Copyright © 1988 by ASME
Downloaded 03 May 2010 to 171.66.16.21. Redistribution subject to ASME license or copyright; see http://www.asme.org/terms/Terms_Use.cfm

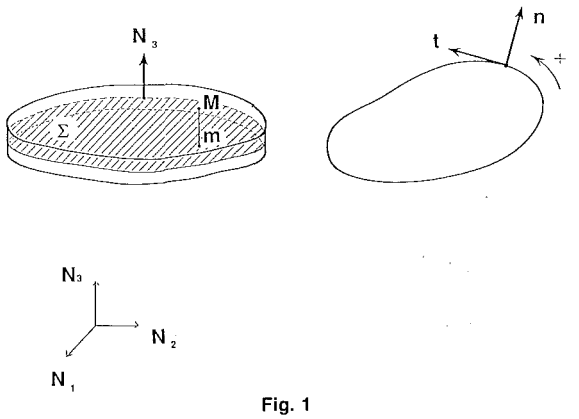


Fig. 1

plied too when dealing with displacement data. The study of these problems will be undertaken in a later paper.

2 Three-Dimensional Boundary-Value Problem

Let us consider a plate Ω, of arbitrary shape, which is homogeneous, isotropic and linearly elastic. Σ is the midplane, $\partial\Sigma$ the edge of Σ, and $2h$ is the thickness (Fig. 1). Cartesian coordinates are taken so that Σ is the plane $z = 0$ and we denote:

$(x_1, x_2, x_3 = z)$ the coordinate of a point M

$U = U_1 N_1 + U_2 N_2 + U_3 N_3$ the displacement

$\epsilon(U) = (\epsilon_{ij})$ with

$$\epsilon_{ij} = \frac{1}{2}(U_{i,j} + U_{j,i}) \text{ the strain related to } U$$

$$\sigma = \begin{bmatrix} \sigma_1 & \tau_{12} & \tau_{13} \\ \tau_{12} & \sigma_2 & \tau_{23} \\ \tau_{13} & \tau_{23} & \sigma_3 \end{bmatrix} \text{ the stress}$$

Only surface loads are supplied to the plate:

F^+ on the upper face Σ^+
F^- on the lower face Σ^-
ϕ on the lateral surface Σ_L

Then the three-dimensional elasticity problem can be written as follows:

(*i*) *Conditions of Equilibrium*

div $\sigma = 0$, that is,

$$\left.\begin{aligned} \sigma_{1,1} + \tau_{12,2} + \tau_{13,3} = 0 \\ \tau_{12,1} + \sigma_{2,2} + \tau_{23,3} = 0 \\ \tau_{13,1} + \tau_{23,2} + \sigma_{3,3} = 0 \end{aligned}\right\} \tag{1}$$

(*ii*) *Conditions of Prescribed Surface Stress*

$$\left.\begin{aligned} \sigma N_3|_{\Sigma^+} = F^+ \\ \sigma N_3|_{\Sigma^-} = -F^- \\ \sigma n|_{\Sigma_L} = \Phi \end{aligned}\right\} \tag{2}$$

(*iii*) *Hooke's Law*

$$\epsilon(U) = \frac{1+\nu}{E}\sigma - \frac{\nu}{E}\,\text{tr}\,\sigma I_3 \tag{3}$$

where E is Young's modulus; ν is Poisson's ratio; tr $\sigma = \sigma_1 + \sigma_2 + \sigma_3$; I_3 is the unity (3,3) matrix.

Those equations define the model that we consider the reference model and which is obviously three-dimensional.

3 Optimal Version of Reissner's Theory

Accuracy of the three-dimensional distributions of stress, strain and displacement, related to a plate theory is mainly connected with the quality of the considered plate theory. Next, we propose the Optimal version which is more performing than the classical one, as we shall see. Optimal version is similar to Reissner's theory under the condition that one modifies:

1 The transverse shear deformability factor;
2 The boundary conditions.

Classically, we introduce the deflexion w, the stretching displacement $u = u_1 N_1 + u_2 N_2$, the mean rotation $v = v_1 N_1 + v_2 N_2$, the resultant N and the moment M of the in-plane stress, the transverse shear stress resultant Q.

Then, the equations of the Optimal version are the following ones:

(*i*) *Bidimensional Conditions of Equilibrium*

$$\text{div } N + \Pi F^+ \Pi F^- = 0$$

$$\text{div } Q + F_3^+ + F_3^- = 0$$

$$\text{div } M - Q + h(\Pi F^+ - \Pi F^-) = 0$$

where ΠF is the in-plane load component: $\Pi F = F_1 N_1 + F_2 N_2$

(*ii*) *Conditions of Prescribed Surface Stress*

$$\left.\begin{aligned} Nn|_{\partial\Sigma} = \bar{N} \\ Mn|_{\partial\Sigma} = \bar{M} + M^* \\ Qn|_{\partial\Sigma} = \bar{Q} \end{aligned}\right\} \tag{5}$$

where $\bar{N}$, $\bar{M}$, $\bar{Q}$ are the classical values

$$\bar{N} = \int_{-h}^{h} \Pi\Phi\, dz, \quad \bar{M} = \int_{-h}^{h} z\Pi\Phi\, dz, \quad \bar{Q} = \int_{-h}^{h} \Phi_3\, dz \tag{6}$$

M^* is the specific modification of the Optimal version

$$M = n\int_{-h}^{h} \Psi(z)\frac{\partial}{\partial s}(t.\underline{\Pi\Phi})\, dz \tag{7}$$

with

$$\Psi(z) = \frac{32h^2}{\pi^3}\sum_{0}^{\infty}(-1)^n \frac{1}{(2n+1)^3}\sin(2n+1)\frac{\pi z}{2h} \tag{8}$$

$$\underline{\Pi\Phi} = \Pi\Phi - \frac{3z}{2h^3}\int_{-h}^{h} z\Pi\Phi\, dz \tag{9}$$

s being the curvilinear abscissa on $\partial\Sigma$.

(*iii*) *Constitutive Law*

$$\left.\begin{aligned} M = D[(1-\nu)\epsilon(v) + \nu\,\text{tr}\,\epsilon(v) I_2] \\ N = A[(1-\nu(\epsilon(u) + \nu\,\text{tr}\,\epsilon(u) I_2] \\ Q = \frac{1}{B^*}[\text{grad } w + v] \end{aligned}\right\} \tag{10}$$

with

D: bending stiffness factor: $D = (2/3)(Eh^3/1-\nu^2)$
A: stretching stiffness factor: $A = 2hE/1-\nu^2$
B^*: transverse shear deformability factor:

$$B^* = \frac{3}{8\dot{G}h}p^2 \text{ where } p = \frac{384}{\pi^5}\sum_{k=0}^{\infty}\frac{1}{(2k+1)^5}$$

$$\text{grad } w = w_{,1}N_1 + w_{,2}N_2 \tag{11}$$

Remarks

1 $B^* = B \times 1{,}0072$ where B is the value proposed by Reissner.

Downloaded 03 May 2010 to 171.66.16.21. Redistribution subject to ASME license or copyright; see http://www.asme.org/terms/Terms_Use.cfm

2 The correction M^* is equal to zero when the twisting load $t.\Phi$ is z-linear.

4 Error Evaluation Method

The quality of the optimal version is evaluated by the method described in Ladevèze [1976]. Using the bidimensional solution of the theory, this method needs the construction of:

1 A three-dimensional displacement U which is kinematically admissible;
2 A three-dimensional stress σ which is statically admissible.

The construction will be detailed later.

The only reference model property displacement U and stress σ that do not satisfy, is Hooke's law. Precisely, we introduce the local quadratic error.

$$\epsilon = \left[\frac{\sup_{\Omega} W(\hat{\sigma} - \sigma(\hat{U}))}{\sup_{\Omega} W(\hat{\sigma})} \right]^{1/2}$$

where $W(\sigma)$ denotes the volumic complementary energy density related to the field σ and $\sigma(U)$ is the stress connected to U by Hooke's law.

$W(\hat{\sigma} - \sigma(\hat{U}))$ and $W(\hat{\sigma})$ are explicit in terms of the data and plate solution. The fields $\hat{U}$ and $\hat{\sigma}$, given in Section 5, lead to an error $O(h^2/L^2)$, as we shall see. This means that the optimal version is a second-order theory, whereas the classical theory is a first-order theory. Hence, three-dimensional distributions $\hat{U}$ and $\hat{\sigma}$ are second-order approximations too.

5 Construction of $(\hat{U}, \hat{\sigma})$

The construction of $\hat{U}$ and $\hat{\sigma}$ is the main difficulty. These fields are taken as the sum of two terms:

$$(\hat{U},\hat{\sigma}) = (\bar{U},\bar{\sigma}) + (\bar{\bar{U}},\bar{\bar{\sigma}})$$

$(\bar{U}, \bar{\sigma})$ is the inner effect; its wavelength is $O(L)$. $(\bar{\bar{U}}, \bar{\bar{\sigma}})$ is the edge effect; its wavelength is $O(h)$. This decomposition comes from the fact that the exact solution verifies such a property [Ladevèze, 1983], [Pécastaings, 1985].

5.1 Construction of the Inner Effect. Before constructing fields $\bar{U}$ and $\bar{\sigma}$, let us examine the equations satisfied by the deflection w, the twist $\omega = \text{div}\,(N_3 \wedge v)$ and the in-plane displacement u

$$\frac{2}{1-\nu}\Delta\Delta w = -\frac{2B^*}{1-\nu}\Delta(F_3^+ + F_3^-) + \frac{3}{2Gh^2}\text{div}\,(\Pi F^+ - \Pi F^-) + \frac{3}{2Gh^3}(F_3^+ + F_3^-) \tag{12}$$

$$\Delta\omega - \frac{4}{(hp)^2}\omega = \frac{3}{2Gh^2}\text{div}\,[N_3 \wedge (F^- - F^+)] \tag{13}$$

$$\text{div}\,N(u) + \Pi F^+ + \Pi F^- = 0 \tag{14}$$

$N(u)$ being defined by (10). It appears that the wavelengths of w and u are $O(L)$.

On the contrary, the wavelength of ω is $O(h)$. Consequently, the wavelength of N is $O(L)$ and Q and M are the sum of two terms:

$$(Q,M) = (\bar{Q},\bar{M}) + (\bar{\bar{Q}},\bar{\bar{M}})$$

where $(\bar{Q}, \bar{M})$ has a wavelength $O(L)$ and $(\bar{\bar{Q}}, \bar{\bar{M}})$ has a wavelength $O(h)$.

The stress $\bar{\sigma}$ is defined by

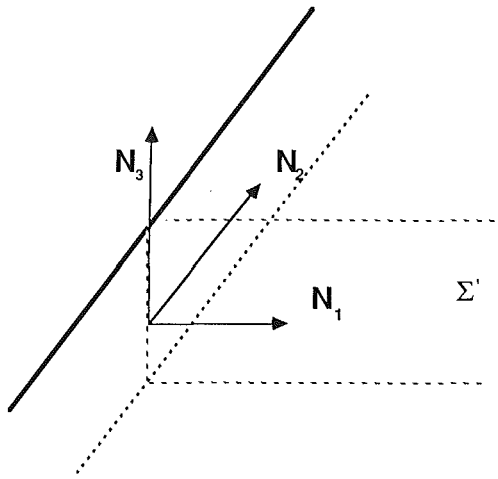


Fig. 2

$$\begin{bmatrix} \bar{\sigma}_1 & \bar{\tau}_{12} \\ \bar{\tau}_{12} & \bar{\sigma}_2 \end{bmatrix} = \frac{1}{2h}N + \frac{3z}{2h^3}\bar{M}$$

$$\begin{bmatrix} \bar{\tau}_{13} \\ \bar{\tau}_{23} \end{bmatrix} = \frac{z+h}{2h}\begin{bmatrix} F_1^+ \\ F_2^+ \end{bmatrix} + \frac{z-h}{2h}\begin{bmatrix} F_1^- \\ F_2^- \end{bmatrix} + \frac{3}{4h^3}(h^2 - z^2)\text{div}\,\bar{M} \tag{15}$$

$$\bar{\sigma}_3 = \frac{h^2 - z^2}{4h^2}\{(h+z)\ \text{div}\,\Pi F^+ + (h-z)\ \text{div}\,\Pi F^-\} - \frac{1}{4h^3}\{(h+z)^2(z-2h)F_3^+ + (z-h)^2(z+2h)F_3^-\}$$

One may remark that σ satisfies equilibrium conditions and stress prescribed conditions on the upper and lower faces.

The displacement U is defined by

$$\begin{pmatrix} \bar{U}_1 \\ \bar{U}_2 \end{pmatrix} = u - z\left(\text{grad}\ w + \frac{1}{2G}[\Pi F^- - \Pi F^+]\right) + \frac{z^2}{2}\left[-\frac{1}{2Gh}\text{div}\,N + \frac{\nu}{1-\nu}\text{grad}\,(\text{div}\,u)\right] + \frac{2-\nu}{6(1-\nu)}z^3\,\text{grad}\,\Delta w \tag{16}$$

$$\bar{U}_3 = w - \frac{\nu z}{1-\nu}\text{div}\,u + \frac{1}{2(1-\nu)}[\nu z^2 - 2h^2]\Delta w$$

The distribution $\bar{\sigma} - \sigma(\bar{U})$ can be expressed by means of the plate solution and data. One can verify that the local error related to $(\bar{U}, \bar{\sigma})$ is $O(h^2/L^2)$.

5.2 Construction of the Edge Effect. Usually, the stress σ and the displacement U do not fulfill the boundary conditions prescribed on the edge Σ_L. The edge effect $(\bar{\bar{U}}, \bar{\bar{\sigma}})$ is connected with the corrections; it is necessary to make it so that the distributions $\hat{U} = \bar{U} + \bar{\bar{U}}$ and $\sigma = \bar{\sigma} + \bar{\bar{\sigma}}$ are, respectively,

1 Kinematically admissible;
2 Statically admissible.

We only investigated the case of a stress-data problem and

Downloaded 03 May 2010 to 171.66.16.21. Redistribution subject to ASME license or copyright; see http://www.asme.org/terms/Terms_Use.cfm

we assumed that the thickness was so weak in respect to the edge curvature radius that we considered the edge Σ_L as a straight one (Fig. 2).

Then, the boundary conditions that the stress $\bar{\bar{\sigma}}$ has to satisfy on the edge Σ_L are as follows:

$$\bar{\bar{\sigma}}_{1|x_1=0} = \underline{\Phi}_1 + z\left[\frac{Gh^2p^2}{2}\,\omega_{,12|x=0} - \frac{3}{2h^3}\,M\right] + c_1^*$$

$$\bar{\bar{\tau}}_{13|x_1=0} = \underline{\Phi}_3 + \frac{1}{2h^2}[F_1^+ - F_1^-][3z^2 - h^2]$$

$$-\frac{z}{2h}(F_1^+ + F_1^-) + \frac{G}{2}(h^2 - z^2)\omega_{,2|x_1=0} \qquad (17)$$

$$\bar{\bar{\tau}}_{12|x_1=0} = \underline{\Phi}_2 - z\,G\,\omega_{|x_1=0} + \tau_{12}^*$$

where

$$\underline{\Phi}_3 = \Phi_3 - \frac{3}{4h^3}(z^2 - h^2)\int_{-h}^{h} \Phi_3 dz \qquad (18)$$

C_1^* and τ_{12}^* are second-order fields explicit in terms of the plate solution. Moreover, $\bar{\bar{\sigma}}$ must fulfill;

$$\operatorname{div} \bar{\bar{\sigma}} = 0$$

$$\bar{\bar{\sigma}} N_{3|_{\Sigma^+}} = 0$$

$$\bar{\bar{\sigma}} N_{3|_{\Sigma^-}} = 0$$

The fields $\bar{\bar{U}}$ and $\bar{\bar{\sigma}}$ are the sum of several fields systematically built from solutions of the following boundary problems in the semi-infinite strip $\Sigma' = \{(x_1, z), x_1 > 0, |z| < h\}$ orthogonal to the edge Σ_L.

Problems of Edge Torsion. Find a function f defined on Σ' which satisfies

$$f_{,11} + f_{,33} = 0$$

$$f_{,3}|_{z=\pm h} = 0 \qquad (19)$$

$$f_{,1}|_{x_1=0} = \int_0^z \left(\int_{-h}^{t} F_2(u)du\right)dt$$

$$\lim_{x_1 \to +\infty} f = 0$$

where F_2 is a given function of z alone defined on $]-h, h[$

Problems of Plane Strain. Find a field $U = \alpha N_1 + uN_3$ defined on Σ' which satisfies $-\operatorname{div} \sigma'(U) = 0$ where

$$\sigma'(U) = \frac{E}{1+\nu}\left[\frac{\nu}{1-2\nu}\operatorname{tr}[\epsilon'(U)]I_2 + \epsilon'(U)\right]$$

with

$$\epsilon'(U) = \frac{1}{2}[U_{\alpha,\beta} + U_{\beta,\alpha}] \quad \text{and} \quad \alpha,\beta = 1,2$$

$$\sigma'(U)N_{3|_{z=\pm h}} = 0 \qquad (20)$$

$$\sigma'(U)N_{1|_{x_1=0}} = F_1 N_1 + F_3 N_3$$

$$\lim_{x_1 \to +\infty} U = 0$$

where F_1 and F_3 are two given functions of z alone defined on $]-h, h[$.

These problems have a solution if the data F_2 and (F_1, F_3) fulfill

$$\int_{-h}^{h} F_2 dz = 0; \quad \int_{-h}^{h} F_1 dz = \int_{-h}^{h} zF_1 dz = 0;$$

$$\int_{-h}^{h} F_3 dz = 0 \qquad (21)$$

and then, the solutions decay from the edge $x_1 = 0$ with a decaying length $O(h)$ [Ladevèze, 1985]. The stress and the displacement that we connect to F_2 on one hand and to (F_1, F_3) on the other hand, are, respectively, denoted

$$\sigma(F_2), U(F_2); \quad \sigma(F_1, F_3), U(F_1, F_3).$$

These fields are localized in a neighborhood of the edge; their expressions are given in the Appendix.

In every case, the stress satisfies

$$\operatorname{div} \sigma = 0$$

$$\sigma N_{3|_{z=\pm h}} = 0$$

The construction of the edge effect is made in two steps:

$$(\bar{\bar{U}}, \bar{\bar{\sigma}}) = (\bar{\bar{U}}_1, \bar{\bar{\sigma}}_1) + (\bar{\bar{U}}_2, \bar{\bar{\sigma}}_2).$$

The distribution $(\bar{\bar{U}}_1, \bar{\bar{\sigma}}_1)$ is defined as follows:

$$\begin{cases} \bar{\bar{U}}_1 = U(F_2^1) + U(F_1^1, 0) \\ \bar{\bar{\sigma}}_1 = \sigma(F_2^1) + \sigma(F_1^1, 0) \end{cases} \qquad (22)$$

with

$$F_2^1 = \frac{1}{G}\,\Phi_{,2} - z\omega_{|x_1=0}$$

$$F_1^1 = \Phi_1 \qquad (23)$$

F_2^1 and F_1^1 fulfill the conditions (21) so that the distribution $(\bar{\bar{U}}_1, \bar{\bar{\sigma}}_1)$ is localized.

The boundary values of the stress σ_1 are a first-order approximation of the conditions (17). In order that these conditions be approximated to the second order, one corrects by a field σ_2 which satisfies on the edge $x_1 = 0$.

$$\bar{\bar{\tau}}_{12}^2|_{x_1=0} = F_2^2 \text{ with } F_2^2 = -N_2.\sigma(F_1^1, 0)N_1$$

$$\bar{\bar{\sigma}}_1^2|_{x_1=0} = F_1^2 \qquad (24)$$

$$\bar{\bar{\tau}}_{13}^2|_{x_1=0} = F_3^2$$

with

$$F_1^2 = z\left[G\,\frac{h^2p^2}{2}\,\omega_{,12}|_{x_1=0} - \frac{3}{3h^3}\,M^*\right] - N_1.\sigma(F_2^1)N_1 \qquad (25)$$

$$F_3^2 = \Phi_3 + \frac{1}{2h^2}(F_1^+ - F_1^-)(3z^2 - h^2)$$

$$+\frac{G}{2}(h^2 - z^2)\omega_{,2}|_{x_1=0} - N_3.\sigma(F_2^1)N_1$$

Since the function ω is solution of the equation (13), we have

$$\omega_{,12}|_{x_1=0} = \frac{2}{hp}\,\omega_{,2}|_{x_1=0}[1 + 0(h/L)]$$

so that, given the choices of B^* and the correction M^*, the moment of the second-order approximation of F_1^2 is zero. Consequently, the distributions defined next are localized in a neighborhood of the plate

$$\bar{\bar{U}}_2 = U(F_2^2) + U(F_1^2, F_3^2)$$

$$\bar{\bar{\sigma}}_2 = \sigma(F_2^2) + \sigma(F_1^2, F_3^2) \qquad (26)$$

Downloaded 03 May 2010 to 171.66.16.21. Redistribution subject to ASME license or copyright; see http://www.asme.org/terms/Terms_Use.cfm

5.3 Evaluation of the Error. The stress $\hat{\sigma}$, thus defined, quite fulfills:

1 The equilibrium conditions: div $\hat{\sigma} = 0$;
2 The boundary conditions on Σ^+ and Σ^-:
$\hat{\sigma}N_3 |_{z=\pm h} = 0$ and its value on Σ_L such that $\hat{\sigma}N_3 |_{\Sigma_L} = \Phi + \bar{\Phi}$ where $\bar{\Phi}$ is a field which satisfies

$$\bar{\Phi} = 0\left(\frac{h^2}{L^2}\Phi\right)$$

$$\int_{-h}^{h} z\bar{\Phi}_3 dz = 0$$

Therefore to satisfy exactly the boundary conditions on Σ_L, a new correction (U_c, σ_c) would be necessary, but we do not make it. Indeed it is easy to prove that this correction, which is global, is such that

$$U_c = 0\left(\hat{U}\frac{h^2}{L^2}\right);\ \sigma_c = 0\left(\hat{\sigma}\frac{h^2}{L^2}\right).$$

The difference $\hat{\sigma} - \sigma(\hat{U})$ can be expressed by means of x_2-derivatives of the load Φ and bending moment $\bar{M}$ of order two at least. Therefore, the local error e related to $(\hat{U}, \hat{\sigma})$ is $O(h^2/L^2)$.

6 Stress and Displacement Connected to the Optimal Version

The displacement $\hat{U}$ and the stress $\hat{\sigma}$ are second-order approximations of the exact three-dimensional solution. One notes that these field may be written as follows

$$\hat{U} = V + 0\left(\frac{h^2}{L^2}V\right)$$

$$\hat{\sigma} = C + 0\left(\frac{h^2}{L^2}C\right) \tag{27}$$

where V and C are the fields that one gets by disregarding second-order contributions in the expression of $\hat{U}$ and $\hat{\sigma}$. Therefore, (V, C) is a second-order approximation of the exact solution.

(V, C) is the sum of two terms: $(\bar{V}, \bar{C}) + (\bar{\bar{V}}, \bar{\bar{C}})$.
$(\bar{V}, \bar{C})$ is the inner effect; $(\bar{\bar{V}}, \bar{\bar{C}})$ is the edge effect.

These fields are defined by means of the solution of the Optimal version as follows:

$$\begin{bmatrix} \bar{c}_1 & \bar{c}_{12} \\ \bar{c}_{12} & \bar{c}_2 \end{bmatrix} = \frac{1}{2h}N + \frac{3z}{2h^3}\bar{M}$$

$$\begin{bmatrix} \bar{c}_{13} \\ \bar{c}_{23} \end{bmatrix} = \frac{z+h}{2h}\begin{bmatrix} F_1^+ \\ F_2^+ \end{bmatrix} + \frac{z-h}{2h}\begin{bmatrix} F_1^- \\ F_2^- \end{bmatrix}$$

$$+ \frac{3}{4h^3}(h^2 - z^2)\ \text{div}\ \bar{M} \tag{28}$$

$$\bar{c}_{33} = 0$$

$$\bullet\ \Pi\bar{V} = u - \frac{z^2}{4Gh}\ \text{div}\ N - z\left[\text{grad}\ w + \frac{1}{2G}(\Pi F^- - \Pi F^+)\right]$$

$$\bar{V}_3 = w - \frac{\nu z}{1-\nu}\ \text{div}\ u \tag{29}$$

$$\bullet\ \bar{\bar{V}} = N\wedge\ \text{grad}\ f + \text{grad}\ \beta + uN_3$$

where f is the solution of the problem of edge torsion related to the load $F_2 = F_2^1 + F_2^2$, $\beta = \int_{\pm\infty}^{x_1} \alpha dx$, $\alpha N_1 + uN_3$ being the solution of the problem of plane strain related to the load $(F_1, F_3) = (F_1^1, F_3^1) + (F_1^2, F_3^2)$. The fields F_i^k $(k = 1, 2; i = 1, 2, 3)$ are defined by (23) and (25).

$$\bullet\ \bar{\bar{C}} = \bar{\bar{C}}_1 + \bar{\bar{C}}_2$$

where

$$\bar{\bar{C}}_1 = G\begin{bmatrix} -2f_{,12} & f_{,1} & -f_{,23} \\ f_{,11} & 2f_{,12} & f_{,13} \\ -f_{,23} & f_{,13} & 0 \end{bmatrix}$$

$$\bar{\bar{C}}_2 =$$

$$\begin{bmatrix} (\lambda+2G)\epsilon_{11} + \lambda\epsilon_{33} & 2G\epsilon_{12} & 2G\epsilon_{13} \\ 2G\epsilon_{12} & \lambda(\epsilon_{11}+\epsilon_{33}) & 2G\epsilon_{23} \\ 2G\epsilon_{13} & 2G\epsilon_{23} & (\lambda+2G)\epsilon_{33} + \lambda\epsilon_{11} \end{bmatrix}$$

with

$$\lambda = \frac{\nu E}{(1-2\nu)(1+\nu)},\quad G = \frac{E}{2(1+\nu)}.$$

(ϵ_{ij}): strain related to the displacement grad $\beta + uN_3$.

7 Conclusion

We would like to point out two facts:

1 Stress and displacement three-dimensional distributions given by Reissner [1985] are in the best cases, a second-order approximation of the exact solution, only in the interior of the plate;

2 The edge effect contained in the solution of Reissner's theory allows one to fulfill the boundary conditions satisfactorily on the edge but does not allow under any circumstances one to describe the true edge effect in the whole neighborhood of the edge.

References

Alblas, J. B., 1957, "Theorie van de driedimensionale spannings toes tand in een doorboorde plaat," Thesis Delft.

Danielson, D. A., 1970, "Improved Error Estimates in the Linear Theory of Thin Elastic Shells," *Proceedings Kon Ned. Ak. Wet. B74*, pp. 294-300.

Koiter, W. T., and Simmonds, J. G., 1972, "Foundations of Shell Theory," Report No. 473, Laboratory of Engineering Mechanics, Melkelveg 2, Delft.

Ladevèze, P., 1976, "Justification de la théorie linéaire des coques élastiques," *Journal de Mécanique*, Vol. 15, pp. 813-856.

Ladevèze, P., 1980, "On the Validity of Linear Shell Theories," *Theory of Shells*, Koiter, W. T. and Mikhailov, G. K., Eds., North-Holland, pp. 367-391.

Ladevèze, P., 1983, "Sur le Principe de Saint-Venant en élasticité," *Journal de Mécanique Théorique et Appliquée*, Vol. 1, pp. 161-184.

Ladevèze, P., 1985, "On Saint-Venant's Principle in Elasticity," *Local Effects in the Anlaysis of Structures*, Ladevèze, P., Ed., Elsevier, pp. 3-34.

Pécastaings, F., 1985, "Sur le principe de Saint-Venant pour les plaques," Thesis, Paris.

Reissner, E., 1975, "On Transverse Bending of Plates, Including the Effect of Transverse Shear Deformation," *International Journal of Solids and Structures*, Vol. 12, pp. 545-554.

Reissner, E., 1985, "Reflections on the Theory of Elastic Plates," *Applied Mechanics Reviews*, Vol. 38, No. 11, pp. 1453-1463.

Shun, Cheng, 1979, "Elasticity Theory of Plates and a Refined Theory," ASME JOURNAL OF APPLIED MECHANICS, Vol. 46, pp. 644-650.

Van der Heijden, A. M. A., 1978, "Thick Plate Theories: Fiction and Fact," Report No. 609, Laboratory Engineering Mechanics, University of Technology, Delft.

Van der Heijden, A. M. A., 1976, "On Modified Boundary Conditions for the Free Edge of a Shell," Thesis, Technische Hogeschool Delft, Delft University Press.

Downloaded 03 May 2010 to 171.66.16.21. Redistribution subject to ASME license or copyright; see http://www.asme.org/terms/Terms_Use.cfm

APPENDIX

1 $U(F_2) = N\wedge \text{grad } f$

$\sigma(F_2)$ is such that

$$\sigma_1 = -2Gf_{,12} + 2G\int_{+\infty}^{x_1} f_{,222}dx_1,\ \tau_{12} = G[f_{,11} - 2f_{,22}]$$

$$\sigma_2 = 2Gf_{,12},\ \tau_{13} = -Gf_{,23}$$

$$\sigma_3 = 0,\ \tau_{23} = -Gf_{,13}.$$

2 $U(F_1, F_3) = \text{grad } \beta + uN$ with $\beta = \int_{+\infty}^{x_1} \alpha dx$

$\sigma(F_1, F_3)$ is such that

$$\sigma_1 = (\lambda + 2G)\epsilon_{11} + \lambda\epsilon_{33} - 2G\alpha_{,22},\ \tau_{12} = 2G\,\epsilon_{12}$$

$$\sigma_2 = \lambda(\epsilon_{11} + \epsilon_{33}),\ \tau_{13} = 2G\epsilon_{13}$$

$$\sigma_3 = (\lambda + 2G)\epsilon_{33} + \lambda\epsilon_{11} - 2G\int_{-h}^{z} \epsilon_{23,2}dz,\ \tau_{23} = 2G\epsilon_{23}$$

(ϵ_{ij}) being the strain related to $U(F_1, F_3)$

Downloaded 03 May 2010 to 171.66.16.21. Redistribution subject to ASME license or copyright; see http://www.asme.org/terms/Terms_Use.cfm

N. Paydar
Assistant Professor of Mechanical Engineering,
Purdue University,
School of Engineering and Technology,
Indianapolis, IN. 46223
Mem. ASME

C. Libove
Professor of Mechanical and Aerospace Engineering,
Syracuse University,
Syracuse, NY 13244
Fellow ASME

Bending of Sandwich Plates of Variable Thickness

A small deflection theory, consisting of differential equations and a total potential energy expression, is presented for determining the stresses and deformations in variable thickness elastic sandwich plates symmetric about a middle surface. The theory takes into account the contribution of the face-sheet membrane forces (by virtue of their slopes) to the transverse shear. A finite-difference formulation of the stationary total potential energy principle is presented along with an illustrative application.

1 Introduction

In a previous paper (Paydar and Libove, 1986), a theory was presented for the stress analysis of sandwich plates for the case in which the planform is rectangular and the thickness variation is unidirectional. In the present paper, that work is extended to the case in which the thickness varies in both directions. The main feature of these analyses is that they take into account the contribution of the face-sheet membrane forces (by virtue of their inclinations) to the transverse shear. Thus they differ from alternate approaches (e.g., Huang and Alspaugh, 1974) which continue to use the constitutive equations of constant-thickness sandwich-plate theory but allow the plate elastic constants to vary in accordance with the local thickness. Paydar and Libove (1986) have shown that such an approach, which is quite acceptable for homogeneous plates of variable thickness, can lead to significant errors when applied to variable thickness sandwich plates with cores deformable in transverse shear.

There are relatively few papers dealing with the analysis of variable-thickness sandwich plates. Apart from their own work and that of Huang and Alspaugh, previously mentioned, the authors are aware of only one other relevant paper, that of Gupta and Jain (1982). The Gupta and Jain approach is, however, questionable because it leads to face-sheet stresses that are inconsistent with the assumption that the face sheets are membranes.

2 Description of Plate and Assumptions

Figure 1 shows an overall view of the plate under consideration. The core has a thickness variation that is assumed to be gradual in both x and y-directions. Since gradual thickness variation is the rule in practical cases, this assumption is not considered to be a serious limitation on the applicability of this theory. For simplicity, the plate is assumed to be symmetric about a middle surface, and the face sheets are assumed to be very thin compared to the core, and are treated as membranes. The core is assumed to be inextensible in the thickness direction, to carry only transverse shear stress on its vertical cross sections, and to be deformable in transverse shear. The elastic properties of the face sheets and the core are allowed to be orthotropic.

Loading on the plate may consist of the following components: a running vertical load $q(x,y)$ (force per unit of middle-surface area); moments $m_x(x,y)$ and $m_y(x,y)$ (moments per unit of middle-surface area in the x and y-directions, respectively); a pressure $P(x,y)$ on the upper surface and a suction of the same magnitude on the lower surface. This loading is the antisymmetric (and more interesting) portion of a more general loading presented by Paydar and Libove (1986).

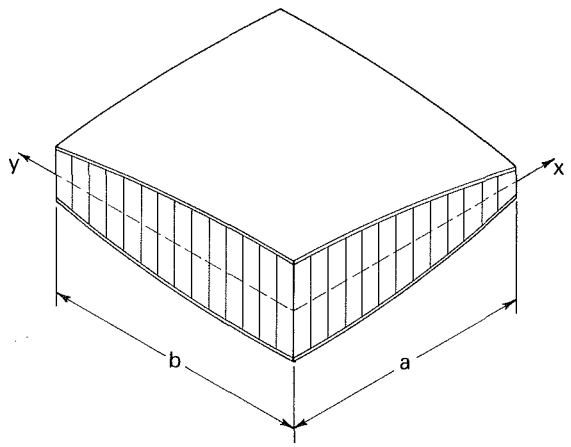


Fig. 1 Sandwich plate of variable thickness

Contributed by the Applied Mechanics Division for presentation at the Winter Annual Meeting, Chicago, IL, November 28 to December 2, 1988, of The American Society of Mechanical Engineers.

Discussion on this paper should be addressed to the Editorial Department, ASME, United Engineering Center, 345 East 47th Street, New York, NY 10017, and will be accepted until two months after final publication of the paper itself in the JOURNAL OF APPLIED MECHANICS. Manuscript received by ASME Applied Mechanics Division, April 27, 1987; final revision, January 25, 1988.

Paper No. 88-WA/APM-40.

Copyright © 1988 by ASME
Downloaded 03 May 2010 to 171.66.16.21. Redistribution subject to ASME license or copyright; see http://www.asme.org/terms/Terms_Use.cfm

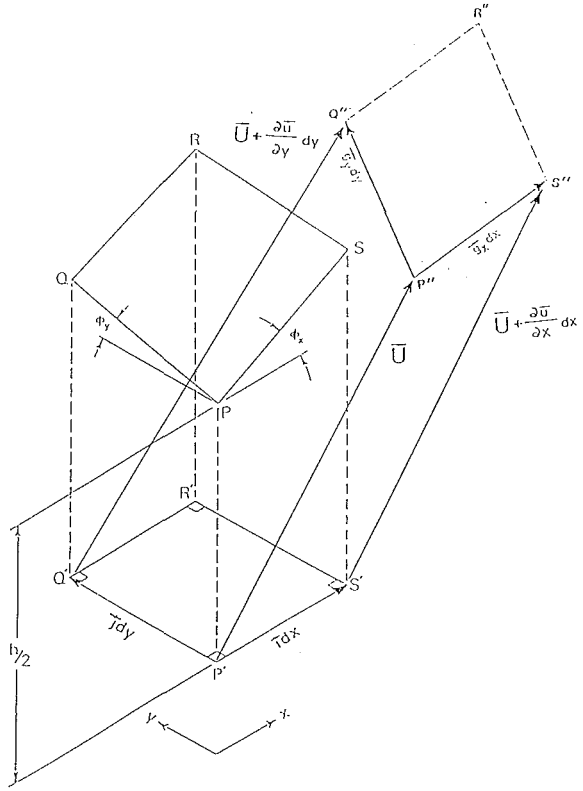


Fig. 2 Infinitesimal upper face-sheet element PQRS of undeformed plate and its projection $P'Q'R'S'$ on the middle surface

3 Face Sheet Strain Measures

Figure 2 shows an infinitesimal rectangular element $P'Q'R'S'$ of the middle surface of the unloaded sandwich plate. Vertical lines drawn upward from the corners of the element intersect the upper face sheet at P, Q, R, and S, and define a nonrectangular element $PQRS$ of the upper face sheet, having $P'Q'R'S'$ as its projection on the middle surface of the sandwich plate. In this analysis, the projected element $P'Q'R'S'$ is used as the reference element for face-sheet strain measures. Thus the face-sheet element $PQRS$, though stress-free, has initial strains (relative to the $P'Q'R'S'$ element). After the plate is loaded, element $PQRS$ will move to a new location $P''Q''R''S''$ (see Fig. 2) and will have new strains (relative to $P'Q'R'S'$). From these new strains we will subtract the initial strains, thus obtaining the stress-related strains in element $P''Q''R''S''$.

To determine the face-sheet strains and then the stress, we adopt the approach of Reissner (1953) and introduce the edge vectors $\mathbf{i}dx$ and $\mathbf{j}dy$ of the reference element $P'Q'R'S'$, and the edge vectors $\mathbf{g}_x dx$ and $\mathbf{g}_y dy$ of the corresponding face sheet element $P''Q''R''S''$ ($\mathbf{i}$ and $\mathbf{j}$ are orthogonal unit vectors, but $\mathbf{g}_x$ and $\mathbf{g}_y$ are neither orthogonal nor of unit magnitude). Any material point in the upper face sheet can be identified by its coordinates x and y in the unloaded plate. Its location after loading can be described by its position vector $\mathbf{u}(x,y)$ drawn from the point (x,y) in the middle surface. Letting $\bar{u}(x,y)$, $\bar{v}(x,y)$, and $\bar{w}(x,y)$, be the three Cartesian components of this position vector, we may write

$$\mathbf{u} = \bar{u}\mathbf{i} + \bar{v}\mathbf{j} + \bar{w}\mathbf{k} \tag{1}$$

The position vector of point p'' in particular will be denoted $\mathbf{U}$. From the vector polygons in Fig. 2, it then follows that

$$\mathbf{U} + \mathbf{g}_x dx = \mathbf{i}dx + (\mathbf{U} + \frac{\partial \mathbf{u}}{\partial x}dx)$$

$$\mathbf{U} + \mathbf{g}_y dy = \mathbf{j}dy + (\mathbf{U} + \frac{\partial \mathbf{u}}{\partial y}dy)$$

hence

$$\mathbf{g}_x = \mathbf{i} + \frac{\partial \mathbf{u}}{\partial x} \quad \text{and} \quad \mathbf{g}_y = \mathbf{j} + \frac{\partial \mathbf{u}}{\partial y} \tag{2}$$

or, using equation (1) to eliminate $\mathbf{u}$,

$$\mathbf{g}_x = \left(1 + \frac{\partial \bar{u}}{\partial x}\right)\mathbf{i} + \frac{\partial \bar{v}}{\partial x}\mathbf{j} + \frac{\partial \bar{w}}{\partial x}\mathbf{k}$$

$$\mathbf{g}_y = \frac{\partial \bar{u}}{\partial y}\mathbf{i} + \left(1 + \frac{\partial \bar{v}}{\partial y}\right)\mathbf{j} + \frac{\partial \bar{w}}{\partial y}\mathbf{k} \tag{3}$$

Strains $\bar{e}_x$, $\bar{e}_y$, and $\bar{\gamma}_{xy}$ of the face-sheet element $P''Q''R''S''$ relative to $P'Q'R'S'$ are then defined as follows

$$\begin{aligned} \bar{e}_x &= \frac{1}{2}(\mathbf{g}_x \cdot \mathbf{g}_x - 1) \\ \bar{e}_y &= \frac{1}{2}(\mathbf{g}_y \cdot \mathbf{g}_y - 1) \\ \bar{\gamma}_{xy} &= \mathbf{g}_x \cdot \mathbf{g}_y \end{aligned} \tag{4}$$

Elimination of $\mathbf{g}_x$ and $\mathbf{g}_y$ by means of equation (3) gives the following expressions for these strains in terms of $\bar{u}$, $\bar{v}$, and $\bar{w}$:

$$\bar{e}_x = \frac{\partial \bar{u}}{\partial x} + \frac{1}{2}\left[\left(\frac{\partial \bar{u}}{\partial x}\right)^2 + \left(\frac{\partial \bar{v}}{\partial x}\right)^2 + \left(\frac{\partial \bar{w}}{\partial x}\right)^2\right]$$

$$\bar{e}_y = \frac{\partial \bar{v}}{\partial y} + \frac{1}{2}\left[\left(\frac{\partial \bar{u}}{\partial y}\right)^2 + \left(\frac{\partial \bar{v}}{\partial y}\right)^2 + \left(\frac{\partial \bar{w}}{\partial y}\right)^2\right] \tag{5}$$

$$\bar{\gamma}_{xy} = \frac{\partial \bar{u}}{\partial y} + \frac{\partial \bar{v}}{\partial x} + \left[\frac{\partial \bar{u}}{\partial x}\frac{\partial \bar{u}}{\partial y} + \frac{\partial \bar{v}}{\partial x}\frac{\partial \bar{v}}{\partial y} + \frac{\partial \bar{w}}{\partial x}\frac{\partial \bar{w}}{\partial y}\right]$$

The initial strains of the upper face-sheet element (strains associated with the element $PQRS$, as measured with respect to the reference element $P'Q'R'S'$, shown in Fig. 2, correspond to the following components of the position vector $\mathbf{u}$:

$$\bar{u} = \bar{v} = 0, \quad \bar{w} = h/2$$

where $h(x,y)$ is the local thickness. Substitution of these values into equation (5) yields

$$\begin{aligned} \bar{e}_{x_{\text{initial}}} &= \frac{1}{8}\left(\frac{\partial h}{\partial x}\right)^2 \\ \bar{e}_{y_{\text{initial}}} &= \frac{1}{8}\left(\frac{\partial h}{\partial y}\right)^2 \\ \bar{\gamma}_{xy_{\text{initial}}} &= \frac{1}{4}\frac{\partial h}{\partial x}\frac{\partial h}{\partial y} \end{aligned} \tag{6}$$

The components of $\mathbf{u}$ for face-sheet points in the loaded sandwich plate will now be represented as follows

$$\bar{u} = u_f, \quad \bar{v} = v_f, \quad \bar{w} = h/2 + w_f$$

where the subscript f stands for "final," and u_f, v_f, and w_f are the displacements due to the application of load. The strains of face-sheet element $P''Q''R''S''$ (relative to $P'Q'R'S'$) are then given by equation (5) as

$$\bar{e}_{x_{\text{final}}} = \frac{\partial u_f}{\partial x} + \frac{1}{2}\left[\left(\frac{\partial u_f}{\partial x}\right)^2 + \left(\frac{\partial v_f}{\partial x}\right)^2 + \left(\frac{1}{2}\frac{\partial h}{\partial x} + \frac{\partial w_f}{\partial x}\right)^2\right]$$

Downloaded 03 May 2010 to 171.66.16.21. Redistribution subject to ASME license or copyright; see http://www.asme.org/terms/Terms_Use.cfm

$$\bar{e}_{y_{\text{final}}} = \frac{\partial v_f}{\partial y} + \frac{1}{2}\left[\left(\frac{\partial u_f}{\partial y}\right)^2 + \left(\frac{\partial v_f}{\partial y}\right)^2 + \left(\frac{1}{2}\frac{\partial h}{\partial y} + \frac{\partial w_f}{\partial y}\right)^2\right]$$

$$\bar{\gamma}_{xy_{\text{final}}} = \frac{\partial u_f}{\partial y} + \frac{\partial v_f}{\partial x} + \frac{\partial u_f}{\partial x}\frac{\partial u_f}{\partial y} + \frac{\partial v_f}{\partial x}\frac{\partial v_f}{\partial y} + \left(\frac{1}{2}\frac{\partial h}{\partial x} + \frac{\partial w_f}{\partial x}\right)\left(\frac{1}{2}\frac{\partial h}{\partial y} + \frac{\partial w_f}{\partial y}\right)$$

Retaining terms of only the first degree in the small displacements u_f, v_f, w_f, we obtain

$$\bar{e}_{x_{\text{final}}} = \frac{\partial u_f}{\partial x} + \frac{1}{2}\frac{\partial h}{\partial x}\frac{\partial w_f}{\partial x} + \frac{1}{8}\left(\frac{\partial h}{\partial x}\right)^2$$

$$\bar{e}_{y_{\text{final}}} = \frac{\partial v_f}{\partial y} + \frac{1}{2}\frac{\partial h}{\partial y}\frac{\partial w_f}{\partial y} + \frac{1}{8}\left(\frac{\partial h}{\partial y}\right)^2 \tag{7}$$

$$\bar{\gamma}_{xy_{\text{final}}} = \frac{\partial u_f}{\partial y} + \frac{\partial v_f}{\partial x} + \frac{1}{4}\frac{\partial h}{\partial x}\frac{\partial h}{\partial y} + \frac{1}{2}\frac{\partial h}{\partial x}\frac{\partial w_f}{\partial y} + \frac{1}{2}\frac{\partial h}{\partial y}\frac{\partial w_f}{\partial x}$$

The stress-related strains are then

$$\epsilon_x = \bar{e}_{x_{\text{final}}} - \bar{e}_{x_{\text{initial}}} = \frac{\partial u_f}{\partial x} + \frac{1}{2}\frac{\partial h}{\partial x}\frac{\partial w_f}{\partial x}$$

$$\epsilon_y = \bar{e}_{y_{\text{final}}} - \bar{e}_{y_{\text{initial}}} = \frac{\partial v_f}{\partial y} + \frac{1}{2}\frac{\partial h}{\partial y}\frac{\partial w_f}{\partial y}$$

$$\gamma_{xy} = \bar{\gamma}_{xy_{\text{final}}} - \bar{\gamma}_{xy_{\text{initial}}} = \frac{\partial u_f}{\partial y} + \frac{\partial v_f}{\partial x} + \frac{1}{2}\frac{\partial h}{\partial x}\frac{\partial w_f}{\partial y} + \frac{1}{2}\frac{\partial h}{\partial y}\frac{\partial w_f}{\partial x} \tag{8}$$

The infinitesimal displacements u_f and v_f are related to θ_x and θ_y (rotations of a vertical line element about its midpoint, in vertical planes parallel to x and $y-$ axes, respectively) by

$$u_f = (h/2)\theta_x, \quad v_f = (h/2)\theta_y$$

Elimination of u_f and v_f in equation (8) by means of the aforementioned relations and the use of w (representing transverse displacement, $w = -w_f$) leads to the following strain-displacement relations

$$\epsilon_x = \frac{h}{2}\frac{\partial \theta_x}{\partial x} - \frac{1}{2}\frac{\partial h}{\partial x}\left(\frac{\partial w}{\partial x} - \theta_x\right)$$

$$\epsilon_y = \frac{h}{2}\frac{\partial \theta_y}{\partial y} - \frac{1}{2}\frac{\partial h}{\partial y}\left(\frac{\partial w}{\partial y} - \theta_y\right)$$

$$\gamma_{xy} = \frac{h}{2}\left(\frac{\partial \theta_x}{\partial y} + \frac{\partial \theta_y}{\partial x}\right) - \frac{1}{2}\frac{\partial h}{\partial x}\left(\frac{\partial w}{\partial y} - \theta_y\right) - \frac{1}{2}\frac{\partial h}{\partial y}\left(\frac{\partial w}{\partial x} - \theta_x\right) \tag{9}$$

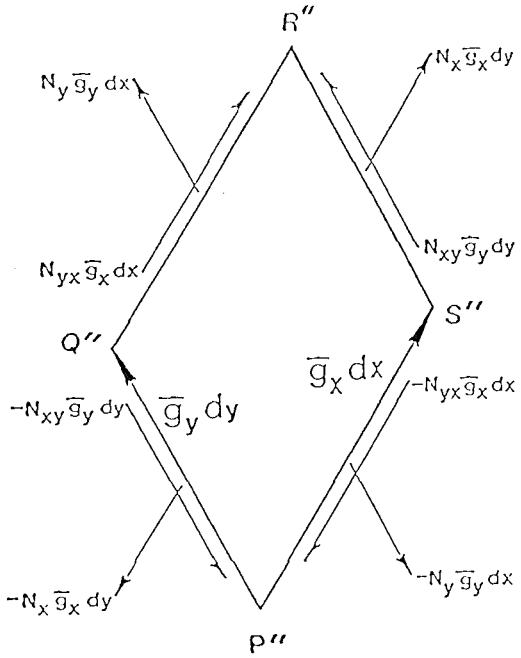


Fig. 3 Forces acting on edges of deformed face-sheet element

The corresponding strains in the lower face sheet are $-\epsilon_x$, $-\epsilon_y$, and $-\gamma_{xy}$.

4 Face-Sheet Stress Resultants

Considering the parallelogram $P''Q''R''S''$ of Fig. 2, which depicts an element of the upper face-sheet in its deformed state, and again following Reissner, one may represent the resultant forces on each side by means of two components as shown in Fig. 3.

It should be noted that the two components on any one edge are not mutually perpendicular. These components are taken parallel to $\mathbf{g}_x dx$ and $\mathbf{g}_y dy$ and, therefore, form an angle generally different from 90°. From the presence of the dimensions dx and dy as factors in the force components of Fig. 3, it is evident that $N_x\mathbf{g}_x$, $N_y\mathbf{g}_y$, $N_{xy}\mathbf{g}_y$, $N_{yx}\mathbf{g}_x$ are forces per unit width of the middle surface reference element. Since $\mathbf{g}_x$ and $\mathbf{g}_y$ are not quite unit vectors, the scalar quantities N_x, N_y, N_{xy}, N_{yx} are not quite the same as the magnitudes of these forces. In line with the terminology used by Reissner (1953), one could call N_x, etc., *pseudo-stress* resultants.

Equilibrium of moments about an axis perpendicular to the element $P''Q''R''S''$ requires that the pseudo-shear-stress resultants be equal; that is

$$N_{xy} = N_{yx} \tag{10}$$

Furthermore, it can be shown that the pseudo-stresses N_x, etc., are conjugate to strain ϵ_x, etc., in the sense that

$$N_x\delta\epsilon_x + N_y\delta\epsilon_y + \frac{1}{2}N_{xy}\delta\gamma_{xy} + \frac{1}{2}N_{yx}\delta\gamma_{xy}$$

is a true work increment per unit of undeformed middle surface area (Libove, 1973).

5 Stress-Strain Relations

The following linear orthotropic relationships will be assumed between the pseudo-stresses N_x, N_y, N_{xy}, N_{yx}, and the strains ϵ_x, ϵ_y, γ_{xy}

Downloaded 03 May 2010 to 171.66.16.21. Redistribution subject to ASME license or copyright; see http://www.asme.org/terms/Terms_Use.cfm

$$\begin{Bmatrix} N_x \\ N_y \\ N_{xy} \end{Bmatrix} = [E] \begin{Bmatrix} \epsilon_x \\ \epsilon_y \\ \gamma_{xy} \end{Bmatrix}$$

$$\begin{Bmatrix} N_x \\ N_y \\ N_{xy} \end{Bmatrix} = [E] \begin{Bmatrix} \epsilon_x \\ \epsilon_y \\ \gamma_{xy} \end{Bmatrix} = \begin{bmatrix} E_{11} & E_{12} & E_{16} \\ E_{21} & E_{22} & E_{26} \\ E_{61} & E_{62} & E_{66} \end{bmatrix} \begin{Bmatrix} \epsilon_x \\ \epsilon_y \\ \gamma_{xy} \end{Bmatrix} \tag{11}$$

The vertical shear stresses in the core are related to the core shear strains by

$$\begin{Bmatrix} \tau_{xz} \\ \tau_{yz} \end{Bmatrix} = [G] \begin{Bmatrix} \gamma_{xz} \\ \gamma_{yz} \end{Bmatrix} = \begin{bmatrix} G_{11} & G_{12} \\ G_{21} & G_{22} \end{bmatrix} \begin{Bmatrix} \gamma_{xz} \\ \gamma_{yz} \end{Bmatrix} \tag{12}$$

6 Total Potential Energy

A Strain Energy. Strain-energy density (per unit of undeformed middle surface area) of both face sheets is given by

$$U_{\text{faces}} = [N_x \;\; N_y \;\; N_{xy}] \begin{Bmatrix} \epsilon_x \\ \epsilon_y \\ \gamma_{xy} \end{Bmatrix}$$

Elimination of the pseudo-stresses in the foregoing equations by means of equation (11) gives

$$U_{\text{faces}} = \{\epsilon\}^T[\text{E}]\{\epsilon\}$$

where

$$\{\epsilon\}^T = \{\epsilon_x \;\; \epsilon_y \;\; \gamma_{xy}\}$$

The strain-energy density of the core per unit of undeformed middle surface area is given by

$$U_{\text{core}} = \frac{1}{2}\{\gamma\}^T[G]\{\gamma\}$$

where

$$\{\gamma\}^T = \{\gamma_{xy} \;\; \gamma_{yz}\}$$

Total strain energy, obtained by the addition of the strain energy of the face sheets and the strain energy of the core, is

$$U = \iint_A \{\epsilon\}^T[\text{E}]\{\epsilon\}dA + \frac{1}{2}\iint_A h\{\gamma\}^T[G]\{\gamma\}dA \tag{13}$$

B Potential Energy. The antisymmetric pressure P exerts a force of magnitude

$$P \sec\phi_x \sec\phi_y \, dx \, dy$$

on both the upper and the lower face sheet. It will be advantageous to break down these forces into a transverse force of magnitude $2P \, dx \, dy$ and moments ($Ph \tan\phi_x \, dx \, dy$) and ($Ph \tan\phi_y \, dx \, dy$) about the y and x-axes, respectively. Furthermore, by letting q^*, m_x^*, and m_y^* represent the net applied transverse loading and moments per unit middle surface area, to wit

$$q^* = q + 2P, \;\; m_x^* = m_x + Ph \tan\phi_x, \;\; m_y^* = m_y + Ph \tan\phi_y$$

one may write the following expression for the potential energy

$$V = -\iint_A (q^* w + m_x^* \theta_x + m_y^* \theta_y)dA \tag{14}$$

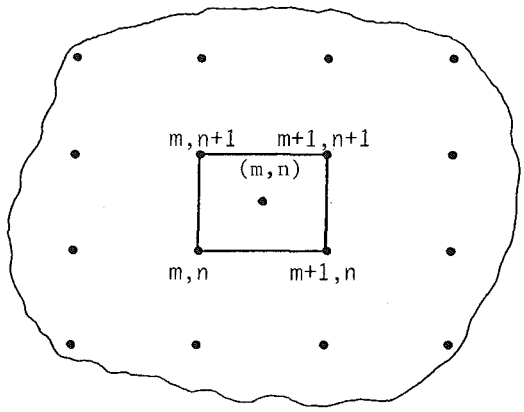


Fig. 4 Element (m,n) and the associated grid points

C Total Potential Energy. The Total Potential Energy (TPE), by definition, is the sum of the strain energy and the potential energy acquired by any prescribed loading.

Thus

$$\text{TPE} = U + V$$

or

$$\text{TPE} = \iint_A \{\epsilon\}^T[\text{E}]\{\epsilon\}dA + \frac{1}{2}\iint_A h\{\gamma\}^T[G]\{\gamma\}dA - \iint_A (q^* w + m_x^* \theta_x + m_y^* \theta_y)dA \tag{15}$$

7 Finite-Difference Energy Method

With the ultimate objective of implementing the stationary TPE principle, we imagine the plate being made up of a finite number of elements. Any element (m,n), shown in Fig. 4, will then be surrounded by four grid points, as shown. Replacing each integral in equation (15) by a summation of integrals over the (m,n) element, we write, without approximation

$$\text{TPE} = \sum_{m=1}^{M}\sum_{n=1}^{N}\iint_{A_{m,n}} \{\epsilon\}^T[\text{E}]\{\epsilon\}dA_{m,n} + \frac{1}{2}\sum_{m=1}^{M}\sum_{n=1}^{N}\iint_{A_{m,n}} h\{\gamma\}^T[G]\{\gamma\}dA_{m,n} - \sum_{m=1}^{M}\sum_{n=1}^{N}\iint_{A_{m,n}} (q^* w + m_x^* \theta_x + m_y^* \theta_y)dA_{m,n} \tag{16}$$

The integrands of the TPE expression will be evaluated at the geometric center of each element. The displacement variables w, θ_x, and θ_y in the integrand of the TPE will be approximated by the average of their values at the four corners of each element. Also, the derivatives of the displacement variable $\partial w/\partial x$, etc., will be approximated by

Downloaded 03 May 2010 to 171.66.16.21. Redistribution subject to ASME license or copyright; see http://www.asme.org/terms/Terms_Use.cfm

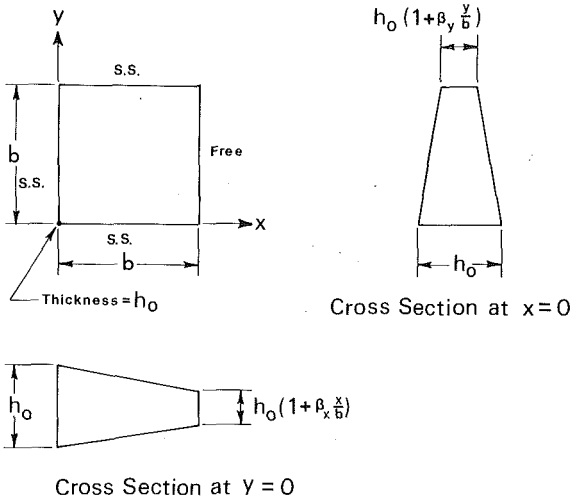


Fig. 5 Square sandwich plate of variable thickness

$$\frac{\partial w}{\partial x}=\frac{1}{2\Delta x}(w_{m+1,n+1}-w_{m,n+1}+w_{m+1,n}-w_{m,n})$$

etc. As a result of these approximations, the integrands of TPE become constants, and equation (16) then gives the following finite-difference approximation to the TPE

$$\text{TPE}=\sum_{m=1}^{M}\sum_{n=1}^{N}F_u(w_{m,n},\theta_{x_{m,n}},\theta_{y_{m,n}})$$

$$-\sum_{m=1}^{M}\sum_{n=1}^{N}F_p(w_{m,n},\theta_{x_{m,n}},\theta_{y_{m,n}}) \tag{17}$$

Making the TPE stationary with respect to each grid-point displacement variable, via the equations

$$\frac{\partial \text{TPE}}{\partial w_{m,n}}=0,\quad \frac{\partial \text{TPE}}{\partial \theta_{x_{m,n}}}=0,\quad \frac{\partial \text{TPE}}{\partial \theta_{y_{m,n}}}=0 \tag{18}$$

leads to the following matrix equation

$$[K]\{u\}=\{L\} \tag{19}$$

where $[K]$ is the stiffness matrix. It may be noted that $[K]$ is banded and symmetric. If any displacement variable is not subject to variation (i.e., is prescribed), the corresponding equation of the set (19) is to be omitted and replaced by an equation stating the prescribed value of that displacement variable.

8 Illustrative Application

In this section, we present the solution for a square sandwich plate with linear thickness variation in the x and y-directions. The plate is uniformly loaded by a running vertical pressure q (force per unit of middle surface area). Figure 5 shows the plate under consideration. It is simply supported along three edges, and its remaining edge is free. The thickness of the plate is given by

$$h=h_0(1+\beta_x\xi+\beta_y\eta)$$

where $\xi=x/b$, $\eta=y/b$, and β_x and β_y are taper coefficients. In this example, the face sheets are isotropic with Young's modulus E′ and a Poisson's ratio ν of 0.3, and the core is orthotropic with principal axes parallel to the x and y-directions and shear moduli of $G_{x''}$ and $G_{y''}$ in the xz and yz-planes, respectively. The parameter b/h_0, the ratio of the plate length to thickness at $\xi=\eta=0$, is taken to be 20. In the computations, 15 elements were used in the ξ and η-directions. To account for the simple support along the edges parallel to the x-axis, those equations of (18) that refer to $w_{m,n}$ and $\theta_{x_{m,n}}$ for grid points along those edges were replaced by the equations $w_{m,n}=\theta_{x_{m,n}}=0$. Similarly, the simple support along the edge coinciding with the y-axis requires that those equations of (19) referring to $w_{m,n}$ and $\theta_{y_{m,n}}$, for grid points along that edge, be replaced by $w_{m,n}=\theta_{y_{m,n}}=0$. The resulting set of equations (19) was then easily solved for the displacement variables at all the plate grid points.

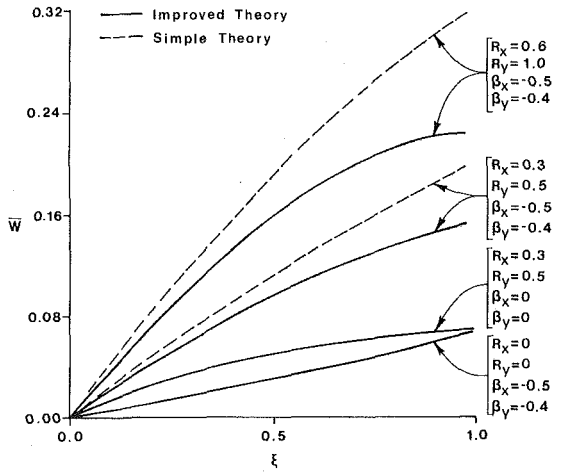


Fig. 6 Nondimensional deflection at $\eta=0.5$ as a function of ξ

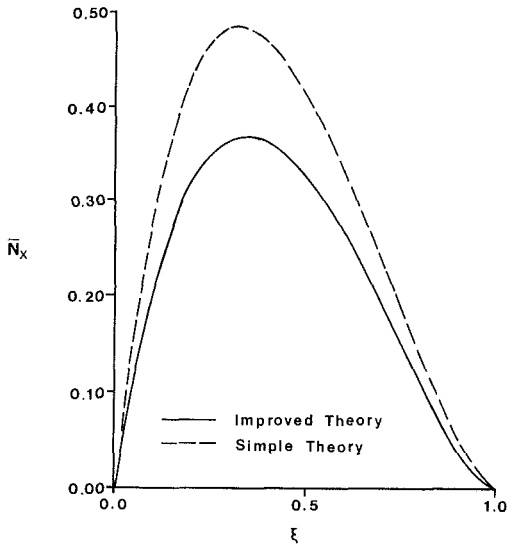


Fig. 7 Nondimensional face-sheet normal pseudo-stress along $\eta=0.5$ with $R_x=0.3$, $R_y=0.5$, $\beta_x=-0.5$, and $B_y=-0.4$

Some of the numerical results are shown in Figs. 6 and 7. Figure 6 shows the nondimensional deflection, defined as

$$\bar{w}=\frac{\text{E}'th_0^2}{2(1-\nu^2)qb^4},$$

at $\eta=0.5$ as a function of ξ for different values of β_x, β_y, R_x, and R_y. The latter two variables are defined by

$$R_x=\frac{\text{E}'th_0}{2(1-\nu^2)G_{x''}b^2},\qquad R_y=\frac{\text{E}'th_0}{2(1-\nu^2)G_{y''}b^2}$$

and will be recognized as dimensionless measures of the ratio of flexural stiffness to shear stiffness. ($R_x=0.6$ and $R_y=1$ correspond, for example, to core shear moduli of $G_{x''}=115$ MPa and $G_{y''}=69$ MPa in a plate with 0.005-m thick faces, E′ = 250 GPa, $h_0=0.025$ m, and $a=b=0.5$ m.) Figure 6 contains two sets of results: (*a*) Results obtained by present

Downloaded 03 May 2010 to 171.66.16.21. Redistribution subject to ASME license or copyright; see http://www.asme.org/terms/Terms_Use.cfm

("improved") theory; (*b*) Results based on the locally constant-thickness sandwich-plate theory (which we label "simple" theory for the lack of a better word). It is seen that the two theories agree closely or exactly, as they should, when $R_x = R_y = 0$ (core not deformable in transverse shear) or when $\beta_x = \beta_y = 0$ (uniform core thickness), but can differ appreciably when a plate with shear-deformable core is of variable thickness. Figure 7 shows the absolute values of the nondimensional face-sheet pseudo-stress $\bar{N}_x = N_x/(qb)$ at $\eta = 0.5$ as a function of ξ for $R_x = 0.3$, $R_y = 0.5$, $\beta_x = -0.5$, and $\beta_y = -0.4$. It will be noted that the simple theory overestimates the maximum normal pseudo-stress by about 36 percent.

9 Conclusion

A small deflection theory is presented for the stresses and deformations in variable-thickness elastic sandwich plates that are symmetric about a middle surface. In this theory, the face sheets are treated as membranes. The variable thickness core is assumed to be inextensible in the thickness direction, and to be deformable in transverse shear.

Numerical comparisons showed that an alternative theory, based on the assumption that the constant-thickness constitutive equations are valid locally, can be appreciably in error, although such a theory is quite acceptable for homogeneous plates of variable thickness.

Acknowledgments

The related research was supported in part by the National Science Foundation under Grant CEE-81-19613.

References

Gupta, A. P., and Jain, M., 1982, "Axisymmetric Vibration of Annular Sandwich Plates of Linearly Varying Thickness," *Journal of Sound and Vibration*, Vol. 80, pp. 329–337.

Huang, S. N., and Alspaugh, D. W., 1974, "Minimum Weight Sandwich Beam Design," *AIAA Journal*, Vol. 12, pp. 1617–1618.

Libove, C., 1973, "On the Stiffness, Stresses, and Buckling Analysis of Corrugated Shear Webs," *Proceedings of the Second Specialty Conference on Cold-Formed Steel Structures, October 22–24*, published by the Department of Civil Engineering, University of Missouri-Rolla, pp. 259–301.

Paydar, N., 1985, "Stress Analysis of Variable Thickness Sandwich Plates of Rectangular Planform," PhD dissertation, Order No. DA8524435, University Microfilms International, Ann Arbor, MI.

Paydar, N., and Libove, C., 1986, "Stress Analysis of Sandwich Plates with Unidirectional Thickness Variation," ASME JOURNAL OF APPLIED MECHANICS, Vol. 53, pp. 609–613.

Reissner, E., 1953, "On a Variational Theorem for Finite Elastic Deformations," *Journal of Mathematics and Physics*, Vol. 32, pp. 129–135.

Downloaded 03 May 2010 to 171.66.16.21. Redistribution subject to ASME license or copyright; see http://www.asme.org/terms/Terms_Use.cfm

Buckling of Locally Loaded Isotropic, Orthotropic, and Composite Cylindrical Shells

Wei Xiao
Visiting Scholar.

Shun Cheng
Professor.

Department of Engineering Mechanics,
University of Wisconsin—Madison,
Madison, WI 53706

This paper incorporates an analysis of the stability of orthotropic or isotropic cylindrical shells subjected to external pressure applied over all or part of their surfaces. An eighth-order governing equation for buckling of orthotropic, isotropic, and composite cylindrical shells is deduced. This governing differential equation can facilitate the analysis and enable us to resolve the buckling problem. The formulas and results, deduced for the first time in this paper, may be readily applied in determining critical loads for local loading of orthotropic, isotropic, and composite cylindrical shells.

Introduction

The problem of loss of stability of cylindrical shells due to pressure applied on part of their surfaces has arisen in recent years because of its importance in applications. However, even in the case of isotropic cylindrical shells, publications on such stability problems are very limited (Krysko and Kolomoets, 1981*a*). As for orthotropic or composite cylindrical shells, the governing equations are more complicated than those for isotropic shells. These complicated equations hamper the analysis, and hence, no problems of stability loss in such shells subjected to loads applied on part of their surfaces have been analyzed in the literature. It is noted that studies of stability problems in heterogeneous aeolotropic cylindrical shells by a number of authors (Cheng and Ho, 1963, Ho and Cheng, 1963, Lei and Cheng, 1969) all deal with loads uniformly applied over the shell's entire surface. Recently, accurate and simple governing equations for orthotropic or composite cylindrical shells have been developed by Cheng and He (1984*a*). These equations, with practically the same accuracy as those complicated equations known in earlier literature, can facilitate the analysis of cylindrical shells and enable us to obtain for the first time, the simple formulas and results that applications often require. The following cases are treated in the paper:

(*A*) External pressure uniformly applied on part of the length of the cylinder,

(*B*) External pressure uniformly and symmetrically applied over strips along the generator.

Critical loads are determined for both cases and also for the special case of cylinders subjected to uniformly distributed external pressure. Numerical results (critical loads) calculated from the governing equations deduced herein are obtained and compared with that obtained from equations known in the literature for isotropic cylinders. Comparisons have also been made among the results obtained from the governing equations of various orders of accuracy deduced in the paper.

Contributed by the Applied Mechanics Division for publication in the JOURNAL OF APPLIED MECHANICS.

Discussion on this paper should be addressed to the Editorial Department, ASME, United Engineering Center, 345 East 47th Street, New York, NY 10017, and will be accepted until two months after final publication of the paper itself in the JOURNAL OF APPLIED MECHANICS. Manuscript received by ASME Applied Mechanics Division, May 19, 1987; final revision, February 1, 1988.

Basic Equations

Let a and h be the radius of the midsurface of the shell and the wall thickness of the shell, respectively; x, y, z, the axial, circumferential, and radial coordinates; α, β, the dimensionless midsurface coordinates along lines of curvatures ($\alpha = x/a$, $\beta = y/a$); and u, v, w the three displacement components of the midsurface of the shell in the axial, circumferential, and radial directions, respectively. Let K_1, K_2 be the extensional rigidity and D_1 and D_2, the flexural rigidity, defined as follows

$$K_1 = \frac{E_1 h}{1-\nu_1\nu_2},\ K_2 = \frac{E_2 h}{1-\nu_1\nu_2},\ D_1 = \frac{h^2}{12}K_1,\ D_2 = \frac{h^2}{12}K_2 \quad (1)$$

Let

$$k = \frac{E_2}{E_1},\ k_1 = \frac{G(1-\nu_1\nu_2)}{E_1} \quad (2)$$

in which E_1, E_2 are the moduli of elasticity along the principal directions α and β, respectively; G the shear modulus that characterizes the change of angles between principal directions α and β; $\nu_1 = \nu_{\beta\alpha}$ the Poisson's ratio that characterizes the decrease in α-direction due to tension applied in β-direction; and $\nu_2 = \nu_{\alpha\beta}$, the Poisson's ratio that characterizes the decrease in β-direction due to tension applied in α-direction. The governing differential equation for orthotropic and composite cylindrical shells is derived by Cheng and He (1984*b*)

$$L\bar{L}w = \frac{a^4}{D_1}L_0 Z \quad (3)$$

in which $\bar{L}$ is the complex conjugate linear differential operator of L; Z represents normal surface load per unit area;

Copyright © 1988 by ASME
Downloaded 03 May 2010 to 171.66.16.21. Redistribution subject to ASME license or copyright; see http://www.asme.org/terms/Terms_Use.cfm

L represents, in the order of their accuracy, the following four linear differential operators

$$L=\nabla_0^4 + (K-2\sqrt{k})\frac{\partial^4}{\partial\alpha^2\partial\beta^2}+k\nabla^2+i\left[\frac{1}{c_1}\frac{\partial^2}{\partial\alpha^2}\right. \tag{3a}$$

$$+ c_1\left(k_3\frac{\partial^4}{\partial\alpha^4}+k_4\frac{\partial^4}{\partial\alpha^2\partial\beta^2}\right.$$

$$\left.\left.+ k_5\frac{\partial^4}{\partial\beta^4}+k_5\frac{\partial^2}{\partial\beta^2}+k_6\frac{\partial^2}{\partial\alpha^2}\right)\right]$$

$$L=\nabla_0^4 + k\nabla^2+\frac{i}{c_1}\frac{\partial^2}{\partial\alpha^2} \tag{3b}$$

$$L=\nabla_0^4 + k\frac{\partial^2}{\partial\beta^2}+\frac{i}{c_1}\frac{\partial^2}{\partial\alpha^2} \tag{3c}$$

$$L=\nabla_0^4 + \frac{i}{c_1}\frac{\partial^2}{\partial\alpha^2} \tag{3d}$$

and

$$L_0=\left[\frac{\partial^4}{\partial\alpha^4}+\frac{1}{k_1}(k-2\nu_1k_1-\nu_1^2)\frac{\partial^4}{\partial\alpha^2\partial\beta^2}+k\frac{\partial^4}{\partial\beta^4}\right] \tag{3e}$$

in which

$$K=\frac{k}{2k_1}(1-\nu_1\nu_2)+2k_1,\ k_2=6k+4\nu_1(K-4k_1)-8\nu_1^2$$

$$k_3=\nu_1-k,\ k_4=\frac{1}{2}(k_2-2kK-2k),\ k_5=kK-(k-\nu_1)$$

$$k_6=\frac{1}{2}(4k-k^2-3\nu_1^2),$$

$$\nabla_0^2=\frac{\partial^2}{\partial\alpha^2}+\sqrt{k}\frac{\partial^2}{\partial\beta^2},\ \nabla^2=\frac{\partial^2}{\partial\alpha^2}+\frac{\partial^2}{\partial\beta^2} \tag{4}$$

$$c_1=\frac{c}{\sqrt{k(1-\nu_1\nu_2)}},\ i=\sqrt{-1},\ c^2=\frac{h^2}{12a^2}$$

In dealing with lateral buckling of cylindrical shells under external pressure one should consider the projection of the middle surface forces on the z-axis owing to the change of curvature. This result is

$$Z=-qa\eta_\beta=-\frac{q}{a}\left(\frac{\partial^2 w}{\partial\beta^2}+w\right) \tag{5}$$

in which q is the external lateral pressure and η_β the change of curvature (bending deformation). The details of the derivation are given in the text by Timoshenko (1936*a*). One way to verify the preceding expression (5) is by comparing the moment equation of equilibrium, (Cheng and He, 1984*c*), in which the load term Z is presented, with the corresponding equation for buckling of cylindrical shells under external lateral load (there is no Z term), derived in the text by Timoshenko (1936*b*, p. 447, equation (*a*)). By means of this comparison, the Z in the equation of equilibrium (Cheng and He, 1984*d*) can be determined; it is given by expression (5). With this Z, the governing equation for buckling of orthotropic, composite, and isotropic cylindrical shells may be written as

$$[L\bar{L}+\frac{a^3}{D_1}L_0\ q(\frac{\partial^2}{\partial\beta^2}+1)]w=0 \tag{6}$$

Problem 1 – External Pressure Applied on Part of the Length of the Cylinder

Figure 1 shows the distribution of the external pressure applied on part of the length l_0 of the cylinder. The following

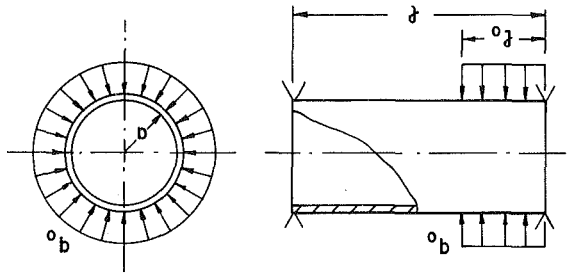


Fig. 1 External pressure applied on part of the length of the cylinder

boundary conditions for simply supported cylinders are considered

$$w=0,\ M_\alpha=0,\ N_\alpha=0,\ v=0$$

at $\alpha=0$ and $\alpha=l/a$. The external pressure may be written in a Fourier series

$$q=q_0\sum_{p=0}^{\infty}s_p\cos\frac{p\pi\alpha}{\eta},\quad (p=0,1,2,\ldots) \tag{7}$$

in which

$$\eta=\frac{l}{a},\ s_0=\frac{l_0}{l},\ s_p=\frac{2}{p\pi}\sin\frac{p\pi l_0}{l}$$

The boundary conditions are satisfied by taking

$$w=\cos n\beta\sum_{m-1,2,3,\ldots.}^{\infty}\phi_m\sin\lambda\alpha,\ (n=1,2,3,\ldots) \tag{8}$$

in which $\lambda=m\pi/\eta$ and m is the number of half-wavelengths axially, and n is the number of half-wavelengths circumferentially. The components of displacement u and v may be obtained from w (Cheng and He, 1984*e*). Substituting the expressions q and w from equations (7) and (8) into the stability equation (6) with L given by equation (3*a*) and observing that

$$\sum_{p=0}^{\infty}s_p\cos\frac{p\pi\alpha}{\eta}\sum_{m=1}^{\infty}\phi_m\sin\lambda\alpha$$

$$=\frac{1}{2}\sum_{p=0}^{\infty}\sum_{m=1}^{\infty}s_p\phi_m\left[\sin\frac{(m+p)\pi\alpha}{\eta}+\sin\frac{(m-p)\pi\alpha}{\eta}\right]$$

$$=\frac{1}{2}\sum_{m=1}^{\infty}\left(\sum_{t=1}^{m}\phi_ts_{m-t}+\sum_{t=m}^{\infty}\phi_ts_{t-m}-\sum_{t=1}^{\infty}\phi_ts_{t+m}\right)\sin\lambda\alpha$$

yields an equation which is satisfied if the coefficient of $\cos n\beta\sin\lambda\alpha$ vanishes, i.e.,

$$\left\{[\lambda^4+K\lambda^2n^2+k(n^4-\lambda^2-n^2)]^2+\left[-\frac{\lambda^2}{c_1}\right.\right.$$

$$\left.\left.+c_1(k_3\lambda^4+k_4\lambda^2n^2+k_5n^4-k_5n^2-k_6\lambda^2)\right]^2\right\}\phi_m+$$

$$+\frac{q_0a^3}{2D_1}(1-n^2)\left[\lambda^4+\frac{1}{k_1}(k-2\nu_1k_1-\nu_1^2)\lambda^2n^2+kn^4\right]$$

$$\left\{\sum_{t=1}^{m}\phi_ts_{m-t}+\sum_{t=m}^{\infty}\phi_ts_{t-m}-\sum_{t=1}^{\infty}\phi_ts_{t+m}\right\}=0 \tag{9}$$

When $n=1$, the second term in equation (9) vanishes. The

Downloaded 03 May 2010 to 171.66.16.21. Redistribution subject to ASME license or copyright; see http://www.asme.org/terms/Terms_Use.cfm

physical meaning of $n=1$ is that it corresponds to a rigid-body displacement as may be shown from the expressions of displacement. Hence, we take $n=2,3,4,\ldots$.

Introducing

$$Q=\frac{2D_1}{q_0a^3},\ R_m=\left\{[\lambda^4+K\lambda^2n^2+k(n^4-\lambda^2-n^2)]^2\right.$$

$$\left.+\left[\frac{-1}{c_1}\lambda^2+c_1(k_3\lambda^4+k_4\lambda^2n^2+k_5n^4-k_5n^2-k_6\lambda^2)\right]^2\right\}\Big/$$

$$(1-n^2)[\lambda^4+\frac{1}{k_1}(k-2\nu_1k_1-\nu_1^2)\lambda^2n^2+kn^4] \tag{10}$$

equation (9) may be written as

$$\phi_mQR_m+\sum_{t=1}^{m}\phi_ms_{m-t}+\sum_{t=m}^{\infty}\phi_ts_{t-m}-\sum_{t=1}^{\infty}\phi_ts_{t+m}=0 \tag{11}$$

When each of the last two terms in equation (11) is written as the sum of two parts, equation (11) becomes

$$\phi_m(QR_m+2S_0-S_{2m})+\sum_{t=1}^{m-1}\phi_t(s_{m-t}-s_{m+t})$$

$$+\sum_{t=m+1}^{\infty}\phi_t(s_{t-m}-s_{t+m})=0,\ (m=1,2,3,\ldots,$$

$$n=2,3,4,\ldots) \tag{12}$$

For a definite value of m, equation (12) is an algebraic equation in ϕ_m, having coefficients QR_m and s_p. Hence, equation (12) is a set of infinitely many algebraic equations with infinitely many unknowns ϕ_m. Solution ϕ_m exists if, and only if, the determinant of the coefficients of ϕ_m vanishes. This determinant, which possesses a symmetric structure, is as follows

$$\begin{vmatrix} QR_1+2s_0-s_2 & s_1-s_3 & s_2-s_4 & s_3-s_5 & \cdots\cdots \\ s_1-s_3 & QR_2+2s_0-s_4 & s_1-s_5 & s_2-s_6 & \cdots\cdots \\ s_2-s_4 & s_1-s_5 & QR_3+2s_0-s_6 & s_1-s_7 & \cdots\cdots \\ s_3-s_5 & s_2-s_6 & s_1-s_7 & QR_4+2s_0-s_8 & \cdots\cdots \\ \cdots & \cdots & \cdots & \cdots & \cdots\cdots \end{vmatrix}=0 \tag{13}$$

Critical loads q_0 $(=q_{cr})$ may be easily determined from equation (13). Illustrative examples are provided in the paper.

When the differential operator L, given by any one of the three equations (3*b–d*), is used in equation (6), the operator L_0 in the same equation (6) should be

$$L_0=\nabla_0^2$$

which is obtained by applying $\sqrt{k}=2k_1+\nu_1$, equation (4), to the coefficient $(1/k_1)$ $(k-2\nu_1k_1-\nu_1^2)$ in the operator (3*e*). The simplest governing equation of equation (6) for stability analysis of orthotropic cylindrical shells under external pressure is

$$[\nabla_0^8+\frac{1}{c_1^2}\frac{\partial^4}{\partial\alpha^4}+\frac{a^3}{D_1}\nabla_0^4\,q\left(\frac{\partial^2}{\partial\beta^2}+1\right)]w=0 \tag{14}$$

The determinant (13) corresponding to equation (14) remains the same except that the following R_m should be used in (13)

$$R_m=\frac{(\lambda^2+\sqrt{k}\,n^2)^4+\frac{1}{c_1^2}\lambda^4}{(1-n^2)(\lambda^2+\sqrt{k}\,n^2)^2} \tag{15}$$

(*A*) A Special Case – A Cylinder Under Uniformly Distributed External Pressure. Let $l_0=l$, then $s_0=1$ and $s_p=0$ $(p\neq 0)$ as seen from equation (7). In this case, all the off-diagonal elements in the determinant (13) vanish, and the existence of solutions for the set of infinitely many algebraic equations (13) requires that the determinant (13) vanishes, i.e.

$$(QR_1+2)\ (QR_2+2)\ (QR_3+2).....=0 \tag{16}$$

or

$$QR_m+2=0,\ (m=1,2,3,\ldots.),\ (n=2,3,4\ldots)$$

which yields

$$\frac{q_0a^3}{D_1}=\left\{[\lambda^4+K\lambda^2n^2+k(n^4-\lambda^2-n^2)]^2\right.$$

$$\left.+\left[\frac{-\lambda^2}{c_1^2}+c_1\ (k_3\lambda^4+k_4\lambda^2n^2+k_5n^4-k_5n^2-k_6\lambda^2)\right]^2\right\}\Big/$$

$$\left\{(n^2-1)[\lambda^4+\frac{1}{k_1}(k-2\nu_1k_1-\nu_1^2)\lambda^2n^2+kn^4]\right\} \tag{17}$$

It may be shown that a minimum value of q_0 is obtained when m has its smallest value; namely, $m=1$ (hence, $\lambda=a\pi/l$). As a consequence, a circular cylindrical shell under external pressure buckles into a single half-wavelength in the axial direction. When the simplest equation (14) is used, we obtain, instead of equation (17), the following buckling load q_0

$$\frac{q_0a^3}{D_1}=\frac{\left[\left(\frac{a\pi}{l}\right)^2+\sqrt{k}\,n^2\right]^4+\frac{1}{c_1^2}\left(\frac{a\pi}{l}\right)^4}{\left[\left(\frac{a\pi}{l}\right)^2+\sqrt{k}\,n^2\right]^2(n^2-1)} \tag{18}$$

In order to compare the accuracy of equation (18) with the more accurate equation (17), we consider the example

$$k=1,\ 0.5,\ 0.113;\ l/a=1\sim 100;\ h/a=0.01;$$
$$a=12.8\text{ cm};\ \nu_1=0.0165;\ \nu_2=0.014 \tag{19}$$

and compute the critical loads from equations (17) and (18). The results are shown in the logarithmic plot of Fig. 2. Computer results show that the error between equation (17) and equation (18) is less than 6 percent for $l/a\leq 3$. Hence formula (18), because of its simplicity, may be employed in calculating the critical load for short cylinders. However, when l/a increases, the discrepancy of the two equations also increases.

As the length increases ($l/a\geq 100$), the curves of Fig. 2 obtained from equations (17) and (18) approach a horizontal asymptote, giving the buckling load for a cylinder of infinite length. For the case of isotropic cylinders ($k=1$), the asymptotic value is $q_{cr}=3D_1/a^3$, as shown in Fig. 2. This value, obtained by substituting $\lambda=0$ and $n=2$ into equation (17), agrees with that given by Flugge (1967*a*, p. 433). It also coincides with the critical load of an isotropic circular ring (Timoshenko, 1936*c*, p. 218). The coincidence may be interpreted as follows: If a cylinder is long, its central part is little influenced by its end conditions, and hence, behaves much like a circular ring.

For moderate-length cylinders, it may be assumed that

Downloaded 03 May 2010 to 171.66.16.21. Redistribution subject to ASME license or copyright; see http://www.asme.org/terms/Terms_Use.cfm

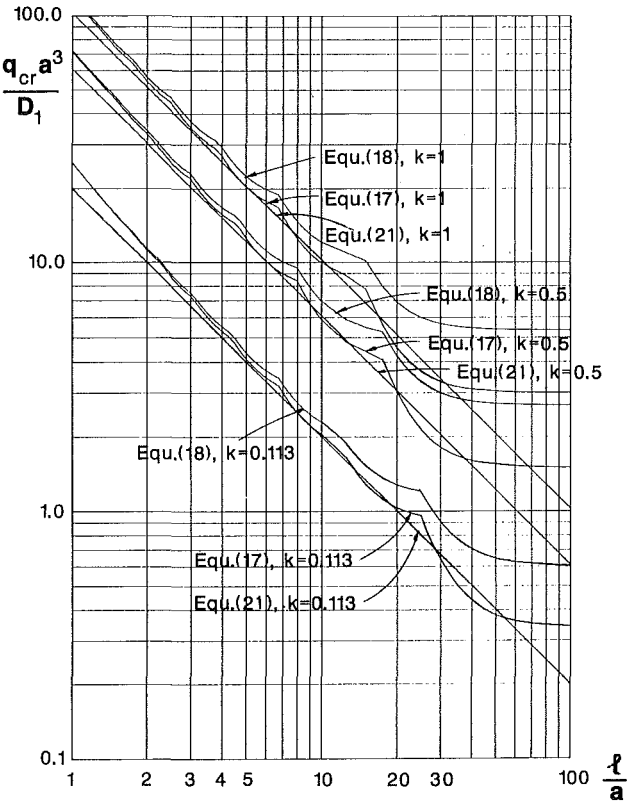


Fig. 2 Comparison of equations (17), (18), and (21)

$(\pi a/nl)^2 << \sqrt{k}$ and $(1/n)^2 << 1$, as used by Gerard (1962) for isotropic cylinders. In this case, equation (18) reduces to

$$\frac{q_0 a^3}{D_1} = \frac{1}{k}\left(\frac{\pi a}{l}\right)^2 \left[k^2\psi^2 + \frac{\psi^{-6}}{c_1^2}\left(\frac{l}{\pi a}\right)^4\right] \tag{20}$$

in which $\psi = nl/\pi a$. Upon minimizing equation (20), $\partial q_0/\partial\psi = 0$, the value of ψ is obtained. Using this ψ, we obtain from equation (20) the following critical load for moderate-length cylinders

$$q_{cr} = \frac{4\pi(1-\nu_1\nu_2)^{1/4} D_1 k^{3/4}}{3^{3/4} a^2 l\, c^{1/2}} \tag{21}$$

Again considering the previous example (19) and applying the preceding formula (21), we obtain three straight lines for the three different values of k, $k = 1$, 0.5 and 0.113 as shown in Fig. 2. It may be observed that in a certain interval of l/a, the solutions of equation (17) and equation (21) are very close. For example, when $k = 1$, $3 \le l/a \le 10$, the discrepancy between equation (17) and equation (21) is less than 5 percent. Hence, from a practical standpoint, the simple formula (21) can be used to estimate the critical loads for moderate-length cylinders. When l/a increases, the number (n) of half-wavelengths circumferentially decreases; thus the condition of equation (21), namely, $1/n^2 << 1$, cannot be satisfied, and equation (21) becomes invalid.

In the case of isotropic cylinders under external pressure distributed uniformly on the entire surface, the preceding formula (21) becomes

$$q_{cr} = \frac{2\pi\, Eh^2}{3\sqrt{6}(1-\nu^2)^{3/4} a\, l}\sqrt{\frac{h}{a}} \tag{22}$$

This result agrees with the result derived by Krysko and Kolomoets (1981*b*) using a quite different approach.

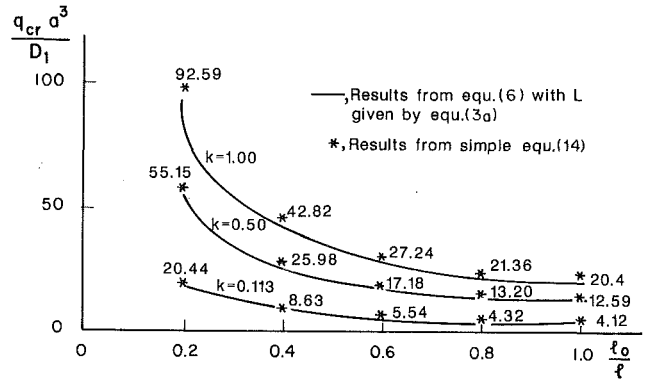


Fig. 3 External pressure applied on part of the length of the cylinder

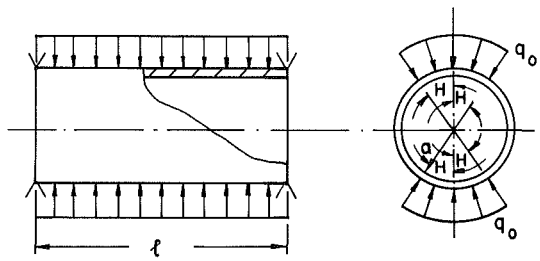


Fig. 4 External pressure applied on part of the circumference of the cylinder

However, the fact that the formula (22) is valid only for moderate-length cylinders is not addressed and entirely overlooked in their approach.

(*B*) General Case – A Cylinder Under External Pressure Applied on Part of Its Length. In the general case, the off-diagonal elements in the determinant (13) do not vanish. However, the value of s_p, equation (7), decreases rapidly as $p(p = 0,1,2,...)$ increases. Hence, only a few terms and equations in the determinant (13) are needed to obtain accurate solutions. Again we consider the same example (19) but with a specified ratio $l/a = 5$. Calculate the critical loads for $k = 1$, 0.5 and 0.113 from equation (6) with L given by equation (3*a*) and also from equation (14). Numerical results are given in Fig. 3 as calculated from these two equations. The dots in Fig. 3 are obtained from equation (14). It is seen that critical loads q_{cr} calculated from the simple equation (14) are always slightly greater than that from equation (6), with L given by equation (3*a*).

Problem 2 – External Pressure Applied on Part of the Circumference of the Cylinder

Figure 4 shows the distribution of the external pressure applied on part of the circumference of a simply supported cylinder. The external pressure is expressed in the following Fourier series

$$q = q_0 \sum_{p=0,2,4...}^{\infty} s_p \cos n\beta \tag{23}$$

in which

$$s_0 = \frac{2H}{\pi},\quad s_p = \frac{4}{\pi p}\sin pH \quad (p = 2,4,6,...)$$

and H (in radians) represents the part of the circumference of the cylinder subjected to external pressure (Fig. 4). The boundary conditions are satisfied by taking

Downloaded 03 May 2010 to 171.66.16.21. Redistribution subject to ASME license or copyright; see http://www.asme.org/terms/Terms_Use.cfm

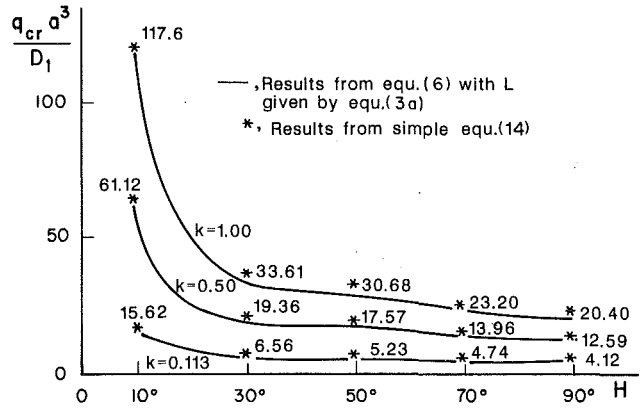


Fig. 5 External pressure applied on part of the circumference of the cylinder

$$w = \sin \lambda\alpha \sum_{n=2,3,4,\ldots}^{\infty} \phi \sin n\beta \tag{24}$$

in which $\lambda = (m\pi/\eta)$, $(m = 1,2,3\ldots)$. We note that in equation (24), $n = 1$ has been omitted since it represents rigid-body displacement as explained in Problem 1. By substituting equations (23) and (24) into the governing equation (6) and following the same procedures as in solving the first problem, the same determinant (13) is obtained except that the first row and the first column of the determinant are dropped out. This is due to the fact that, for the present problem, $n = 1$ is not needed in equation (24). We further note that expression (10) for R_m remains the same, except that R_m becomes R_n, since in the present problem n is not a fixed number ($n = 2,3,4\ldots$) and in contrast to the first problem, m is not a fixed number. In the special case, when the entire surface of the cylinder is under uniformly distributed pressure, i.e., $H = \pi/2$, $s_0 = 1$ and $s_p = 0$ ($p = 1,2,3,\ldots$), the same equation (17) for q_{cr} is obtained. We take the same example (19), $l/a = 5$, $h/a = 0.01$, $a = 12.8$ cm, $\nu_1 = 0.0165$, $\nu_2 = 0.014$ as considered previously and calculate the critical load q_{cr} from the determinant (13). Numerical results are given in Fig. 5 and connected by curves. The dots shown in Fig. 5 are obtained from the simple equation (14). As in the case of the first problem, critical loads q_{cr} calculated from the simple equation (14) are always slightly greater than that from the more accurate equation (6) with L given by equation (3*a*).

Conclusion and Comparison

The results and formulas deduced in the paper may be readily applied in determining critical loads for orthotropic or isotropic shells under external pressure acting on part of their surfaces. In order to investigate the accuracy of governing equation (6) deduced herein for buckling of orthotropic or isotropic cylinderical shells, the following example for isotropic shells under uniformly distributed pressure is considered

$$l/a = 1 \sim 100,\ a = 12.8 \text{ cm},\ h = 0.04434 \text{ cm},$$
$$E = 2 \times 10^6 \text{ kg/cm}^2,\ \nu = 0.3.$$

The critical loads calculated from equation (17), deduced from equation (6), are compared with that calculated from the corresponding equation (VII-20) given by Flugge (1967*b*, p. 432). Results show that the difference between the two equations are negligibly small and, when plotted, the two sets of curves almost coincide. This result is expected since the governing equation (6) is obtained from equation (3) and the accuracy of equation (3) has been established in the literature (Cheng and He, 1984*f*).

A considerable number of experiments have been done on buckling of isotropic cylinderical shells under uniform lateral pressure. References to those experiments can be found in the literature (Timoshenko, 1936*d*, p. 453). A study of the effect of imperfections on the magnitude of the critical pressure was made by Donnell (1956). It was shown that imperfections do not produce so great a reduction in critical pressure as was found for the case of axial compression. This explains why theory and experimentation agree better for lateral pressure than for axial compression.

References

Cheng, S., and He, F. B., 1984, "Theory of Orthotropic and Composite Cylindrical Shells, Accurate and Simple Fourth-Order Governing Equations," ASME JOURNAL OF APPLIED MECHANICS, Vol. 51, pp. 736–744.

Cheng, S., and Ho, B. P. C., 1963, "Stability of Heterogeneous Aeolotropic Cylindrical Shells Under Combined Loading," *AIAA Journal*, Vol. 1, No. 4, pp. 892–898.

Donnell, L. H., 1956, "Effect of Imperfections on Buckling of Thin Cylinders Under External Pressure," ASME JOURNAL OF APPLIED MECHANICS, Vol. 23, No. 4, pp. 569–575.

Flugge, W., 1967, *Stress in Shells*, Springer-Verlag, Berlin, pp. 432–433.

Gerard, G., 1962, *Introduction to Structural Stability Theory*, McGraw-Hill Book Co., Inc., pp. 129–131.

Ho, B. P. C., and Cheng, S., 1963, "Some Problems in Stability of Heterogeneous Aeolotropic Cylindrical Shells Under Combined Loading," *AIAA Journal*, Vol. 1, No. 7, pp. 1603–1607.

Krysko, V. A., and Kolomoets, A. A., 1981, "Stability of Local Loading of a Cylindrical," *Soviet Applied Mechanics*, Vol. 17, No. 10, pp. 86–92.

Lei, M. M., and Cheng, S., 1969, "Buckling of Composite and Homogeneous Isotropic Cylindrical Shells Under Axial and Radial Loading," *ASME* JOURNAL OF APPLIED MECHANICS, Vol. 36, pp. 791–798.

Timoshenko, S., 1936, *Theory of Elastic Stability*, McGraw-Hill Book Co., Inc., pp. 445–453.

Downloaded 03 May 2010 to 171.66.16.21. Redistribution subject to ASME license or copyright; see http://www.asme.org/terms/Terms_Use.cfm

Hui Li
Research Assistant.

J. P. Dempsey
Associate Professor.
Mem. ASME

Department of Civil and Environmental Engineering,
Clarkson University,
Potsdam, NY 13676

Unbonded Contact of a Square Plate on an Elastic Half-Space or a Winkler Foundation

The unbonded frictionless receding contact problem of a thin plate placed under centrally symmetric vertical loading while resting on an elastic half-space or a Winkler foundation is solved in this paper. The problem is transformed into the solution of two-coupled integral-series equations over an unknown contact region. The problem is nonlinear by virtue of unilateral contact and therefore needs to be solved iteratively. Special attention is given to the edge and corner contact pressure singularities for the plate on the elastic half-space. Comparison is made with other relevant numerical results available.

Introduction

The unbonded frictionless receding contact problem of a thin square plate placed under centrally symmetric vertical loading while resting on an elastic half-space or a Winkler foundation is solved in this paper. The combination of Navier solutions and Levy solutions is used to satisfy the governing differential equations, the equilibrium condition and the plate boundary conditions. Boussinesq's fundamental solution (1885) for the surface displacement of an elastic half-space due to a vertical point load is used to define the total surface displacement for an, as yet unknown, contact pressure distribution. Displacement compatibility between the plate and foundation, as well as the requirement that the foundation be tensionless, reduces the problem to the solution of two-coupled integral-series equations. The latter displacement and contact pressure inequalities make the problem nonlinear, and hence the contact region and pressure distribution are found by iteration. The corner and edge contact pressure singularities for a plate on an elastic half-space need special consideration. The contact treated in this paper can be characterized as *receding*, as identified by Dundurs (1975), since the contact surface within the loaded configuration is contained within the initial contact surface. A general feature of smooth receding contact solutions in linear elastostatics is for the extent of a receding contact to be independent of the level of loading. Moreover, if uplift is to occur, the change from initial contact (the flat plate initially has all of its surface in contact) to the contact in the loaded configuration takes place discontinuously.

Theoretical investigations into the contact behavior of plates resting on elastic foundations have been motivated to a considerable extent by the need in civil engineering to design mat and raft foundations, flexible column footings, and pavement slabs (Hooper, 1978). The earliest application of the finite element method to the analysis of rectangular plates on elastic foundations by Cheung and Zienkiewicz (1965) was followed by a great many related investigations most of which ignored nonlinear effects due to separation or uplifting between the plate and the supporting medium (Rajapakse and Selvadurai, 1986). The studies of these nonlinear effects using the finite element method include, among others, Cheung and Nag (1968), Svec (1974), Ascione and Grimaldi (1984), and Ascione and Olivito (1985). A theoretical treatment can be found in the paper by Villaggio (1983). Experimental work on the title problem is also scarce; Vint and Elgood (1935) loaded rectangular steel plates resting on a nest of springs and measured deflections, while Murphy (1937) loaded rectangular steel plates (resting on a layer of rubber) by corner, edge and central concentrated loads.

Basic Equations

A thin square plate of side length a in unbonded frictionless contact with an elastic foundation is subjected to a centrally symmetric load $q(x, y)$ and an unknown support reaction $p(x, y)$, Fig. 1. The governing equation for the plate deflection, $w_p(w, y)$, is given by

$$D\nabla^4 w_p(x,y) = q(x,y) - p(x,y), \tag{1}$$

where the flexural rigidity of the plate D equals $E_p h^3/12(1 - \nu_p^2)$ in which h is the thickness of the plate, while E_p and ν_p are the modulus of elasticity and the Poisson's ratio of the plate, respectively. For the symmetric square plate with four free edges, the boundary conditions of zero slope and zero vertical force at centerlines and zero moment and zero vertical force at edges have to be satisfied, viz.

Contributed by the Applied Mechanics Division for presentation at the Winter Annual Meeting, Chicago, IL, November 28 to December 2, 1988, of The American Society of Mechanical Engineers.

Discussion on this paper should be addressed to the Editorial Department, ASME, United Engineering Center, 345 East 47th Street, New York, N.Y. 10017, and will be accepted until two months after final publication of the paper itself in the JOURNAL OF APPLIED MECHANICS. Manuscript received by ASME Applied Mechanics Division, July 14, 1987; final revision, December 14, 1987.
Paper No. 88-WA/APM-28.

Copyright © 1988 by ASME
Downloaded 03 May 2010 to 171.66.16.21. Redistribution subject to ASME license or copyright; see http://www.asme.org/terms/Terms_Use.cfm

$$w_{p,x}=0, \quad \text{for} \quad x=a/2, \quad 0\le y\le a; \quad (2a)$$

$$w_{p,xxx}+(2-\nu_p)w_{p,xyy}=0, \quad \text{for} \quad x=a/2, \quad 0\le y\le a; \quad (2b)$$

$$w_{p,yy}+(2-\nu_p)w_{p,xx}=0, \quad \text{for} \quad y=0, \quad 0\le x\le a; \quad (2c)$$

$$w_{p,yyy}+(2-\nu_p)w_{p,xxy}=0, \quad \text{for} \quad y=0, \quad 0\le x\le a; \quad (2d)$$

$$w_p(x,y)=w_p(y,x). \quad (2e)$$

Vertical force equilibration of the plate also requires that

$$\int_0^a\int_0^a q(x,y)dxdy=\iint_\Omega p(x,y)dxdy, \quad (3)$$

where Ω is the unknown contact region and the contact pressure is zero outside the region. In general, the boundary condition that the corner forces must equal zero has also to be enforced. However, for the symmetric loading conditions considered here, the corner forces must point either all upward or all downward and thus they must be zero if the equilibrium condition (3) and the condition (2*d*) of zero edge forces are both satisfied. Therefore, the condition of zero corner forces is not needed.

In the paper, the medium supporting the plate is modeled either as an elastic half-space or as a Winkler foundation. For the elastic half-space under a distributed load $p(x, y)$, the surface displacement $w_f(x, y)$ follows from the fundamental vertical point load solution provided by Boussinesq (1885); integration over the loaded area gives

$$w_f(x,y)=\frac{1-\nu_f^2}{\pi E_f}\int_0^a\int_0^a\frac{p(u,v)dudv}{\sqrt{(x-u)^2+(y-v)^2}}, \quad (4)$$

where E_f and ν_f are the modulus of elasticity and Poisson's ratio for the foundation, respectively. For a Winkler foundation

$$w_f(x,y)=p(x,y)/k_f, \quad (5)$$

where k_f is the stiffness of the Winkler foundation.

In addition to the foregoing equations, the compatibility conditions between the plate and the half-space must also be considered. Since the contact is unilateral, the support reaction is either compressive or zero. These can be written as, with Ω denoting the contact region

$$w_f(x,y)=w_p(x,y), \quad p(x,y)>0, \quad \text{for} \quad (x,y)\in\Omega; \quad (6a,b)$$

$$w_f(x,y)>w_p(x,y), \quad p(x,y)=0, \quad \text{for} \quad (x,y)\notin\Omega. \quad (6c,d)$$

Formulation

The solution of the governing equation (1) can be expressed in the following as the combination of $w_1(x, y)$, $w_2(x, y)$, the particular solutions due to the support reaction and the load, respectively, $w_3(x, y)$, the complementary solution, and δ, the corner deflection

$$w_p(x,y)=w_1(x,y)+w_2(x,y)+w_3(x,y)+\delta, \quad (7)$$

where, with $\alpha_k = k\pi/\alpha$

$$\{w_1(x,y);w_2(x,y)\}=\frac{a^4}{\pi^4 D}\sum_{m=1,3,}^{\infty}\sum_{n=1,3,}^{\infty}\frac{\{a_{mn};b_{mn}\}}{(m^2+n^2)^2}\sin\alpha_m x\ \sin\alpha_n y, \quad (8a,b)$$

$$w_3(x,y)=a\sum_{m=1,3,}^{\infty}A_m\{r_m(x,y)+r_m(y,x)\}, \quad (9)$$

in which

$$\{a_{mn};b_{mn}\}=\frac{4}{a^2}\int_0^a\int_0^a\{p(x,y);q(x,y)\}\sin\alpha_m x\ \sin\alpha_n y\ dxdy. \quad (10a,b)$$

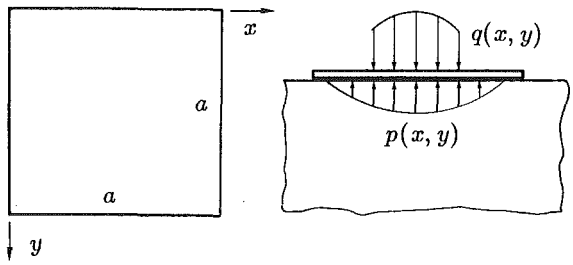


Fig. 1 Square plate on an elastic half-space

The Levy-type series solution in (9) requires that $\nabla^4 r_m = 0$, which, on satisfying the boundary conditions (2*a–c*), leads to the expression for $r_m(x, y)$ in (13*e*). Equation (2*e*) has already been satisfied by the particular form of $w_p(x, y)$ in (7). The remaining boundary condition (2*d*) becomes an equation to determine the unknown constants A_m, (m = 1, 3, . . .). The variable x contained within the equation can be removed by using orthogonality: multiply the both sides by $(1/a)$ sin $(k\pi x/a)$, (k = 1, 3, . . .), and integrate from 0 to a with respect to x. Then (11) is derived after substituting (10*a*) into the equation. Equation (12) can be derived from the compatibility equations (6*a*, *d*) upon substitution of (4), (7)–(10*a*). Then the resulting coupled integral-series equations are

$$\sum_{m=1,3,}^{\infty}A_m\mathcal{G}_{mk}+\frac{a}{D}\iint_\Omega p(u,v)f_k(u,v)dudv=\mathcal{H}_k, \quad k=1,3,\ldots \quad (11)$$

$$\frac{1-\nu_f^2}{\pi E_f}\iint_\Omega\frac{p(u,v)dudv}{\sqrt{(x-u)^2+(y-v)^2}}+\frac{a^2}{D}\iint_\Omega p(u,v)g(x,y;u,v)dudv$$

$$-a\sum_{m=1,3,}^{\infty}A_m\{r_m(x,y)+r_m(y,x)\}=w_2(x,y)+\delta, \quad x,y\in\Omega \quad (12)$$

where δ_{mk} is the Kronecker delta, $\zeta_p = (1 - \nu_p)/(3 + \nu_p)$, $\eta_p = (1 - \nu_p)(3 + \nu_p)$, $\lambda_p = (1 - \nu_p)/2$, $\beta_m = m\pi/2$, and

$$f_k(u,v)=\frac{4\sin\alpha_k u}{\eta_p\pi^4}\sum_{n=1,3,}^{\infty}\frac{n^3+(2-\nu_p)k^2n}{(k^2+n^2)^2}\sin\alpha_n v, \quad (13a)$$

$$g(x,y;u,v)=\frac{4}{\pi^4}\sum_{m=1,3,}^{\infty}\sum_{n=1,3,}^{\infty}\frac{\sin\alpha_m x\ \sin\alpha_n y\ \sin\alpha_m u\ \sin\alpha_n v}{(m^2+n^2)^2}, \quad (13b)$$

$$\mathcal{G}_{mk}=\frac{-4\zeta_p k^3m^3}{\pi(m^2+k^2)^2}+\frac{\delta_{mk}m^3}{2}(\tanh\beta_m-\zeta_p\beta_m\operatorname{sech}^2\beta_m), \quad (13c)$$

$$\mathcal{H}_k=\frac{a^3}{\eta_p\pi^4 D}\sum_{n=1,3,}^{\infty}b_{kn}\frac{n^3+(2-\nu_p)k^2n}{(k^2+n^2)^2}, \quad (13d)$$

$$r_m(u,v)=\{\cosh(\beta_m-\alpha_m u)+\lambda_p\alpha_m u\ \sinh(\beta_m-\alpha_m u)+\lambda_p\beta_m\ \operatorname{sech}\beta_m\ \sinh\alpha_m u\}\operatorname{sech}\beta_m\ \sin\alpha_m v \quad (13e)$$

The contact problem has now been reduced to the solution of the coupled integral-series equations (11) and (12), along with (3) and (6*b*, *c*), for the unknown support reaction $p(x, y)$ and the extent of contact Ω. For a rigid plate, D approaches infinity; $\mathcal{H}_k$, $w_2(x, y)$ then tend to zero, and equation (11) gives $A_m \equiv 0$, (m = 1, 3, . . .). Therefore, equations (11) and (12)

Downloaded 03 May 2010 to 171.66.16.21. Redistribution subject to ASME license or copyright; see http://www.asme.org/terms/Terms_Use.cfm

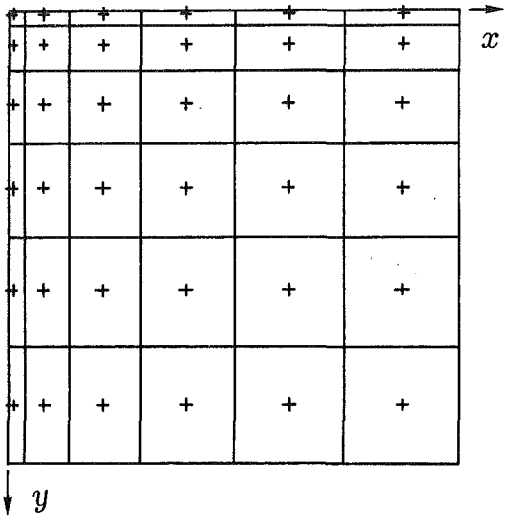


Fig. 2 Element division for a quarter plate with $N_0 = 12$

reduce to a single integral equation in the case of a rigid square indenter on a half-space.

Numerical Solution

Discretization and Integration. If the edges and the corners of the plate are in contact with the elastic half-space, the contact pressure is singular in these places. When the plate becomes rigid (the most singular case), the singularities are asymptotical to $\rho^{-0.5}$ and $\rho^{-\alpha}$ for the edges and corners, respectively. Rvachev (1959) derived that $\alpha = 0.686$; Bažant (1974) gave $\alpha = 0.704$; Borodachev (1976) gave $\alpha = 0.6996$; Morrison and Lewis (1976) gave $\alpha = 0.7034$. To evaluate (11) and (12) numerically, these singularities must be taken into account to ensure accuracy and fast convergence. Therefore, the plate is divided into a number of elements corresponding to Gauss-Chebyshev quadrature which treats the inverse-square-root singularities along the edge. The element division scheme is shown in Fig. 2 for a quarter plate with the number of elements in each direction, N_0, equaling 12. For the kth element from an edge, the distances from the edge to the upper-left corner and the center can be given, respectively, as

$$d_1 = \frac{a}{2}\left(1-\cos\frac{(k-1)\pi}{N_0}\right), \quad d_2 = \frac{a}{2}\left(1-\cos\frac{(2k-1)\pi}{2N_0}\right). \tag{14a,b}$$

Then the integration of contact pressure over each element is the same if the pressure distribution is $C/\sqrt{x(a-x)y(a-y)}$. The corner singularity is slightly overestimated. But the numerical error introduced by this overestimation is minimal.

The governing equations (11) and (12) are discretized by assuming that $p(x, y)$ is constant in each element, that the compatibility conditions hold at the center of each element, and that each infinite series may be truncated at the $(2M-1)$th term, to give

$$\sum_{m=1,3,}^{2M-1} A_m \mathfrak{S}_{mk} + \frac{1}{K}\sum_{j=1}^{N} P_j \mathfrak{F}_{kj} = \mathfrak{K}_k, \quad k = 1,3,\ldots 2M-1, \tag{15}$$

$$\sum_{j=1}^{N} \mathfrak{U}_{ij} P_j + \frac{1}{K}\sum_{j=1}^{N} \mathfrak{S}_{ij} P_j - \sum_{m=1,3,}^{2M-1} A_m \mathfrak{R}_{im} = \mathfrak{W}_{2i} + \Delta, \quad i = 1,2,\ldots N \tag{16}$$

where N is the number of elements considered and

$$P_j = p(u_j,v_j)(1-\nu_f^2)/\mathrm{E}_f, \quad \Delta = \delta/a, \tag{17a,b}$$

$$\mathfrak{R}_{im} = r_m(x_i,y_i) + r_m(y_i,x_i), \quad \mathfrak{W}_{2i} = w_2(x_i,y_i)/a, \tag{17c,d}$$

$$\{\mathfrak{F}_{kj};\mathfrak{S}_{ij}\} = \frac{1}{a^2}\int\int_{\mathrm{E}_j} \{f_k(u,v);g(x_i,y_i;u,v)\}\,dudv, \tag{17e,f}$$

$$\mathfrak{U}_{ij} = \frac{1}{a\pi}\int\int_{\mathrm{E}_j} \frac{dudv}{\sqrt{(u-x_i)^2+(v-y_i)^2}}; \tag{17g}$$

while K is the stiffness ratio defined as

$$K = D(1-\nu_f^2)/(a^3\mathrm{E}_f). \tag{18}$$

All terms in (15) and (16) are nondimensional. The summations over n within the terms and the integrations in (17) can all be evaluated analytically (Li and Dempsey, 1987).

Subelement Division. Another way to treat the singularities is to introduce a nonsingular function $\bar{p}(u, v)$ as

$$p(u,v) = \bar{p}(u,v)\Phi(u,v), \tag{19a}$$

where

$$\Phi(u,v) = \frac{a^{2\alpha}\{u(a-u)+v(a-v)\}^{1-\alpha}}{\sqrt{u(a-u)v(a-v)}}. \tag{19b}$$

$\bar{p}(u, v)$ is now well behaved since the singularities are explicitly included. After dividing the plate into elements and assuming that $\bar{p}(x, y)$ is constant in each element, each integral can be written as

$$I = \int\int_{\Omega} p(u,v)\Psi(x,y;u,v)\,dudv$$

$$= \sum_{j=1}^{N} \bar{p}(u_j,v_j)\int\int_{\mathrm{E}_j} \Phi(u,v)\Psi(x,y,u,v)\,dudv, \tag{20}$$

Each integral in (20) is evaluated by dividing the element E_j into N_s subelements E_k^j, $(k = 1, 2, \ldots N_s)$ and assuming $\Phi(u, v)$ to be a constant equal to its value at each subelememt center, $\Phi(u_k^j, v_k^j)$. Thus

$$I = \sum_{j=1}^{N} \frac{p(u_j,v_j)}{\Phi(u_j,v_j)}\left\{\sum_{k=1}^{N_s} \Phi(u_k^j,v_k^j)\int\int_{\mathrm{E}_k^j} \Psi(u,y;u,v)\,dudv\right\}. \tag{21}$$

Again, the remaining integrals can all be done analytically. The numerical accuracy increases as N_s increases since $\Phi(u, v)$ is a monotonic function in each element. There is no requirement for additional computer storage. For $N_s = 1$, the formulation is the same as that given in (17).

Computation Algorithm. Equations (15) and (16) are ready to be written into matrix form with two unknown vectors **A**, **P** containing A_m, $(m = 1, 3, \ldots, 2M-1)$, and P_j, $(j = 1, 2, \ldots, N)$, respectively. **A** can be eliminated by using the first matrix equation. Then the second equation and the equilibrium condition (3) are used to solve **P** and the corner displacement δ.

Since the problem is nonlinear, iteration has to be used. The following procedure is used in this paper. A similar procedure for the case of a uniform mesh was used by Ahmadi et al. (1983), for the contact of a cylinder on an elastic half-space.

1 Assume a contact region Ω;
2 Solve **P** and δ for the given contact region;
3 Check (6*b*) and, if necessary, find a new Ω which excludes the areas where the support reaction is in tension;
4 Finally, check (6*c*) and, if necessary, find a new Ω which includes the areas where the plate is in contact with the foundation, i.e., $w_p(x, y) \geq w_f(x, y)$.

Because the load and deflection are symmetric, they need to be calculated only over one eighth of the plate, e.g., over an

Downloaded 03 May 2010 to 171.66.16.21. Redistribution subject to ASME license or copyright; see http://www.asme.org/terms/Terms_Use.cfm

Table 1 Displacement of a rigid plate W_r

$$W_r = w_p a E_f/(1-\nu_f^2)P_0$$

N_0	$N_s=1$	$N_s=9$	$N_s=25$	$N_s=49$
8	.867744	.868703	.868196	.868031
16	.867801	.868050	.867922	.867880
24	.867818	.867929	.867872	.867853
32	.867824	.867886	.867854	.867843
48	.867828	.867855	.867841	.867836

Table 2 Corner displacement Δ

$$\Delta = \delta a E_f/(1-\nu_f^2)P_0,\ N_0 = 24,$$
$$R = 1,\ K_n = 0.0001 \times 2^{n-1}$$

	$N_s=1$	$N_s=49$		$N_s=1$	$N_s=49$
K_1	−4.063	−4.158	K_7	.3663	.3657
K_2	−2.512	−2.534	K_8	.5189	.5188
K_3	−1.442	−1.460	K_9	.6439	.6438
K_4	−.6917	−.7057	K_{10}	.7383	.7383
K_5	−.1907	−.1961	K_{11}	.7977	.7977
K_6	.1452	.1429	K_{12}	.8313	.8313

area of $0 \le x \le a/2$, $0 \le y \le x$. This saves computer time and storage. The matrices are rearranged each time to eliminate or add unknown variables and equations in order to conform with (6*a*, *d*). But the matrix elements need to be calculated only once.

Winkler Foundation. The contact problem of a plate on a Winkler foundation can be solved by just following the procedure for an elastic half-space. The two coupled integral-series equations derived are identical to (11) and (12), except that the first term of the second equation is replaced by $p(x, y)/k_f$. The problem is much simpler for the Winkler foundation since there are no contact pressure singularities. The whole plate is divided into a number of elements and the pressure is assumed constant in each element. Uniform division is preferred in this case. Recalling the definition of the Winkler foundation (5), it is necessary to replace (17*a*), (17*g*), and (18) by, respectively,

$$P_j = p(u_j, v_j)/ak_f, \quad \mathfrak{A}_{ij} = \delta_{ij}, \quad K = D/(a^4 k_f). \tag{22}$$

Implementation: A Uniform and a Concentrated Load

In this section, some useful results are provided for the most common loading cases: combinations of centrally concentrated load P_0 and a uniform load q_0, which may include the self-weight. From (10*b*), b_{mn} can be given as

$$b_{mn} = \frac{16q_0}{\pi^2 mn} + \frac{4P_0}{a^2} \sin\beta_m \sin\beta_n, \quad m,n = 1,3, \ldots \tag{23}$$

Then $\mathfrak{C}_k$ and $w_2(x, y)$ in (11) and (12) can be evaluated for the given b_{mn}. Other loading conditions, like multiple concentrated loads, locally distributed loads, and combinations thereof, merely result in different expressions for b_{mn}, $\mathfrak{C}_k$, and $w_2(x, y)$.

The ratio of concentrated load to the total load is defined as

$$R = P_0/(P_0 + q_0 a^2). \tag{24}$$

The contact pressure and displacements can be calculated for any given R and K. The Poisson's ratio of the plate, ν_p, appears in the boundary conditions in addition to the one contained in the plate stiffness, D. Therefore, it also has the influence over the numerical results. However, it has been found numerically that this influence is slight: For the most sensitive cases, $R = 1$, and $K \approx 0.0256$, 0.0128, 0.0064 for the center pressure, center displacement of an elastic half-space and the center pressure of a Winkler foundation, respectively, these values increase or decrease 3 percent, 2 percent, 2.5 percent as

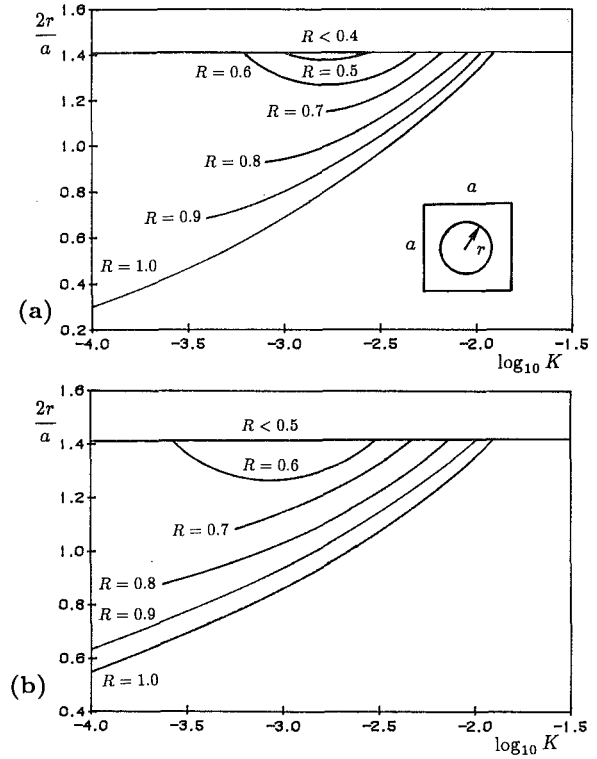


Fig. 3 Contact radii (*a*) a square plate on an elastic half-space; (*b*) a square plate on a Winkler Foundation

ν_p changes from 0.3 to 0.1 or from 0.3 to 0.5. So $\nu_p = 0.3$ is used and its influence is neglected from hereon.

Two methods have been tried for a plate on an elastic half-space as described previously: based on, respectively, the approximations that $p(x, y)$ or $\bar{p}(x, y)$ is constant in each element. Comparison is made in Table 1 for the displacement of a rigid plate on an elastic half-space, $W_r = w_p a E_f/(1-\nu_f^2)P_0$, with $\alpha = 0.696$ and different subelement numbers. It is interesting to note that values obtained by the first method ($N_s = 1$ in Table 1) and by the second method give, respectively, the upper and lower bounds for the limiting value which may be extrapolated as $W_r = 0.8677831$. This confirms the numerical accuracy. Though both methods converge rapidly and uniformly, the convergence of the first method is better. Comparison has also been made for flexible plates in Table 2 for the corner displacement, δ. The two methods give almost identical values for stiffer plates. Differences become slightly larger as the plate becomes increasingly flexible. For increasing plate flexibility, the first method is again better since the pressure singularities disappear as the edges move out of contact ($K \le 0.0032$). Based on these studies, the first method, which assumes $p(x, y)$ is constant in each element, is used for all of the calculations in the following with $N_0 = 24$. To further check this procedure, comparisons were made with contact pressure distributions obtained by Mullen et al. (1980), for the case of a rigid plate; very good agreement was found.

The values of contact pressure and displacement are calculated in each element center. The region out of contact is indicated by zero contact pressure. It has been found that for many cases the contact regions can be treated as circles or parts of circles when the edges are in contact. Therefore, a contact radius r can be used conveniently to describe the contact regions for these circumstances as given in Fig. 3(*a*) for the elastic half-space and in Fig. 3(*b*) for the Winkler foundation. These figures reveal the general tendency of the problem and answer important questions: When are the edges in contact ($2r/a > 1$) and when does full contact occur ($2r/a = \sqrt{2}$)?

Downloaded 03 May 2010 to 171.66.16.21. Redistribution subject to ASME license or copyright; see http://www.asme.org/terms/Terms_Use.cfm

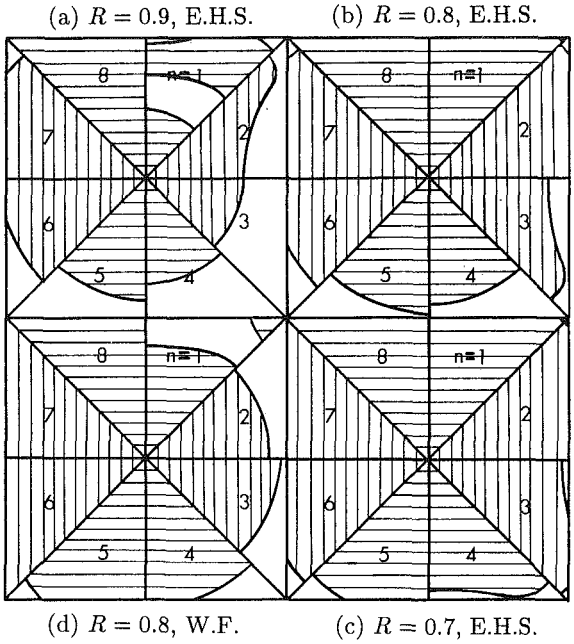


Fig. 4 Contact regions for a plate on an elastic half-space (E.H.S.) or a Winkler Foundation (W.F.). The stiffness ratio for each case (each octant) is given by $K_n = 0.0001 \times 2^{n-1}$.

The shapes of the contact regions become more complicated for very flexible plates with distributed loading and thus can no longer be taken as circular. These are indicated by the cutoff lines in Figs. 3(*a*, *b*). Contact regions for different foundations, stiffness ratios, and load ratios are shown in Fig. 4, in which each octant represents one combination. The increasingly large influence of the distributed load over the contact behavior of the very flexible plates is apparent.

Figures 5(*a*, *b*) show the contact pressure and the displacement at the plate center for an elastic half-space. Figure 5(*c*) shows the contact pressure and the center displacement for the Winkler foundation. The distributions are the same by the definition of Winkler foundation. The values at the center are obtained by extrapolation from the values on the diagonal line using the function $f(x) = a + b[(x/a) - 0.5]^2 + c[(x/a) - 0.5]^4$. The function is both smooth and symmetric at the plate center and is thus in compliance generally with the center deflection of a simply supported plate under a concentrated load. The exact distributions of pressure and displacement immediately under the concentrated load may need further study. But the accuracy of the figures given in this paper is good at least up to the measurability of these figures. Extrapolation results are better for stiffer plates because changes at the center are less dramatic.

It has been found that, surprisingly, uplift has a very small effect on the displacement and contact pressure at the plate center. The moderate nonlinearity due to uplift can be seen clearly from Fig. 6 for contact pressure. Similar diagrams can also be produced from Figs. 5(*b*, *c*) For the most extreme case in consideration, $K = 10^{-4}$ and $R = 1$, the central contact pressure reduces three percent and the displacement reduces two percent for the plate bonded to the half-space, while the reduction is six percent for the plate bonded to the Winkler foundation. This fact is important because it implies that superposition can be used even for the unilateral contact problem to determine the center displacements and contact pressure provided minor errors are acceptable.

Discussion

One difficult feature, historically, concerning the contact of a plate with an elastic half-space has been the contact pressure

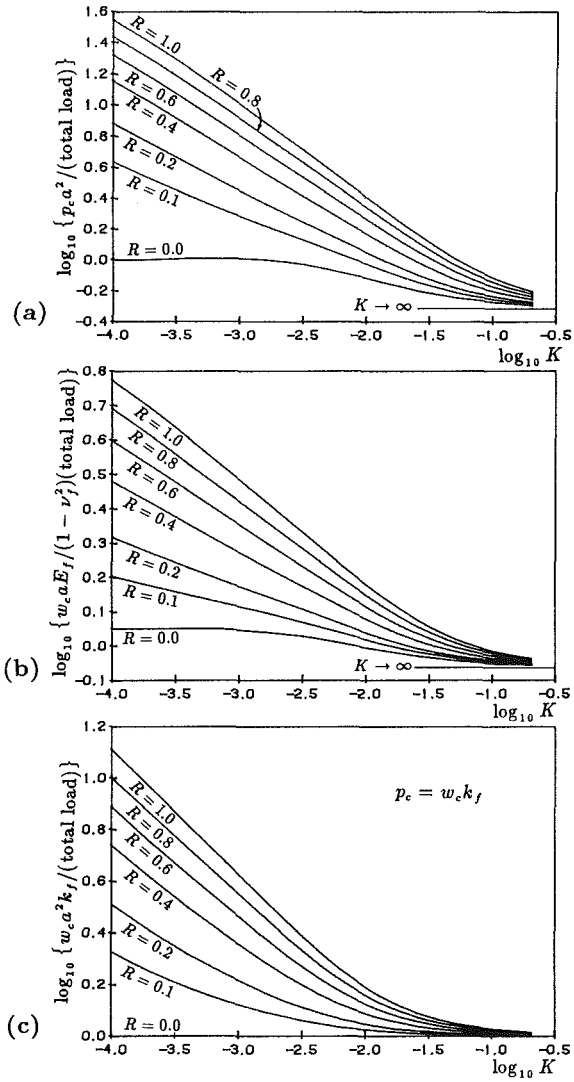


Fig. 5 (*a*) Center pressure for a plate on an elastic half-space; (*b*) center displacement for a plate on an elastic half-space; (*c*) center pressure and displacement for a plate on a Winkler Foundation

singularities along the edges and corners. The most studied case is the rigid plate on an elastic half-space. The treatment of the singularities can be found in papers by Rvachev (1959); Borodachev (1976); Morrison and Lewis (1976); Brothers et al. (1977); Mullan et al. (1980); Fabrikant (1986). To see the strong influence of the singularities on the numerical accuracy, the displacement of a rigid square plate on an elastic half-space, $W_r = w_p a E_f/(1 - \nu_f^2)P_0$, is again used. The upper bound can be given as the displacement of a circular indenter (Harding and Sneddon, 1945) with the same area and the lower bound is given by that of a circular indenter circumscribing the square (Brothers et al., 1977), viz., $\sqrt{\pi} > 2W_r > \sqrt{2}$. By considering the singularities, Fabrikant (1986) gives an approximate value: $W_r = 0.881$ using a one-term expression for the pressure; while Noble gave an extrapolated value of $W_r = 0.8673$ and obtained $W_r = 0.8695$ with an optimal element division of 6×6. In comparison, the following methods neglected the singularities: Gorbunov-Possadov and Serebrjanyi (1961) predicted $W_r = 0.88$ and obtained $W_r = 0.913$ with an eight-term polynomial contact pressure expansion; Conway and Farnham (1968) gave $W_r = 0.8977$ for 10×10 uniform division; Fraser and Wardle (1976) extrapolated $W_r = 0.87$, having obtained $W_r = 0.816, 0.841$ for 10×10, 20×20 meshes, respectively; finally, Rajapakse and Selvadurai (1986) claimed to obtain $W_r = 0.87$ for all 4×4, 6

Downloaded 03 May 2010 to 171.66.16.21. Redistribution subject to ASME license or copyright; see http://www.asme.org/terms/Terms_Use.cfm

Table 3 Central deflection (R = 1): comparison with R & S

	$w_c a E_f/(1-\nu_f^2)P_0$					
$K \times 10^3$	.833	1.30	8.33	13.0	83.3	130.
R & S**	2.89	2.65	1.59	1.42	0.98	0.91
bonded	3.18	2.78	1.59	1.41	.981	.942
unbonded	3.23*	2.82*	1.59†	1.41‡	.981‡	.942‡

* Corner and edge uplift, † corner uplift, ‡ full contact.
** Bonded, square.

Table 4 Central displacement and contact pressure (R = 1): comparison with A & O and A & G

	$w_c a E_f/(1-\nu_f^2)P_0$			$P_c a^2/P_0$		
$K \times 10^5$	9.82	29.5	98.2	9.82	29.5	98.2
A & O*	30.6	4.50	.754	81.8	34.1	14.7
A & G†	6.33	4.54	3.16	59.3	28.5	12.8
unbonded	6.00	4.41	3.06	35.6	20.2	10.3

* unbonded, square; † unbonded, circular.

× 6 and 8 × 8 meshes in Fig. 6 of their paper, but this is in contradiction with the other figures and $W_r = 0.913$ of equation (5) of the same paper. By examining the previously mentioned values and recalling those given in Table 1, the importance of considering the corner and edge singularities becomes apparent.

Another interesting case to examine is a flexible weightless plate with a concentrated load at the center. When the plate edges and corners are out of contact, the influence of the boundary shapes is small. Thus the results of weightless square plates and circular plates are comparable for certain flexibilities. The results obtained here for a square plate on an elastic half-space are in good agreement with the circular plate results: Contact radii by Gladwell and Iyer (1974) and contact radii, center displacement, center pressure by Ascione and Grimaldi (1984) using the finite element method. Ascione and Grimaldi (1984) also presented results for a plate on a Winkler foundation. But large numerical errors in their results are apparent if one attempts to correlate the values of the center displacement and contact pressures using governing relationship, $w_f(x, y) = p(x, y)/k_f$. It has also been found that, when the contact region is very small for small K-values, the contact radius approaches that of an infinitely large weightless plate under a concentrated load, for which Weitsman (1969) gave $2r/a = 7.373K^{1/3}$ and $2r/a = 5.70K^{1/4}$ for the elastic half-space and the Winkler Foundation, respectively. These two expressions are in fact the upper bounds for finite plates having arbitrary shapes.

The finite element method is a powerful tool used by many researchers in solving the plate contact problem. The method is useful in dealing with a wide range of problems like plates with irregular shapes or varying thickness and anisotropic, nonhomogeneous foundations. Some recent studies include papers by Fraser and Wardle (1976), Rajapakse and Selvadurai (1986) for bonded cases and by Svec (1974), Ascione and Grimaldi (1984), Ascione and Olivito (1985) for unbonded cases. These papers give extensive references to other related papers and, more importantly, provide some solutions for comparison. For a square plate under a uniform load on a half-space, the central displacements found in Fig. 3 of Fraser and Wardle's paper (1976), are in good agreement with the curve $R=0$ of Fig. 5(b) in this paper. For the square plate under a centrally concentrated load P_0, comparison is made in Table 3 (in notation of this paper) with results obtained by Rajapakse and Selvadurai (1986) (R & S) using athe Heterosis elements for bonded contact. The agreement is generally good except for very flexible plates where it appears the FEM made the plates too stiff. As mentioned previously, it can be seen

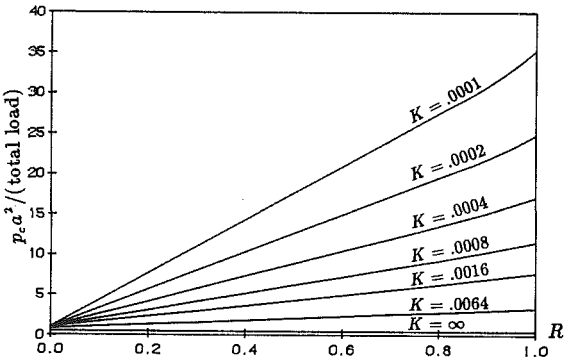


Fig. 6 Center pressure for a plate on an elastic half-space

that uplift affects the central contact pressure and displacement only slightly. Similar comparisons can also be made for an elastic half-space with the FEM results by Ascione and Olivito (1985) (A & O) for a square plate, and by Ascione and Grimaldi (1984) (A & G) for a circular plate since the plate is weightless and out of contact at edges. These are given in Table 4. There is a general agreement between the last two rows. Large differences exist between results by Ascione and Olivito (1985) and others, even though the paper predicted similar contact regions as the other two. Contact radii given by Svec (1974) for a square plate are too large for lower K-values in comparison to the others' results.

There are other methods to solve the plate-foundation problem, like solving the coefficients in trigonometric expansion of deflection by Chang and Hwang (1984) and solving the coefficients of a polynomial expansion for the contact pressure by Gorbunov-Possadov and Serebrjanyi (1961). But these methods are not suitable for the unilateral contact because of the difficulty in applying the condition $p(x, y) \geq 0$. Finally, for the bonded case and a concentrated load P_0 at the center of a plate on a Winkler foundation with $K = 10^{-4}$, Chang and Hwang (1984) used a 35-term trigonometric function expansion to give the center displacement as $w_c = 0.00125P_0a^2/D$. It has been found using the formulation in this paper that $w_c = 0.00122P_0a^2/D$ for the bonded case and $w_c = 0.00130P_0a^2/D$, $2r/a = 0.57$ for the associated unbonded case (which Chang and Hwang did not examine).

Acknowledgment

The second author (J. P. D.) would like to acknowledge that his interest in the class of problems treated in this paper was fostered during several discussions with L. M. Keer at the end of 1983.

References

Ahmadi, N., Keer, L. M., and Mura, T., 1983, "Non-Hertzian Contact Stress Analysis for an Elastic Half Space—Normal and Sliding Contact," *International Journal of Solids and Structures*, Vol. 19, pp. 357–373.

Ascione, L., and Grimaldi, A., 1984, "Unilateral Contact Between a Plate and an Elastic Foundation," *Meccanica*, Vol. 19, pp. 223–233.

Ascione, L., and Olivito, R. S., 1985, "Unbonded Contact of a Mindlin Plate on an Elastic Half-Space," *Meccanica*, Vol. 20, pp 49–58.

Bažant, Z. P., 1974, "Three-Dimensional Harmonic Functions Near Termination or Intersection of Gradient Singularity Lines: A General Numerical Method," *International Journal of Engineering Science*, Vol. 12, pp. 221–243.

Borodachev, N. M., 1976, "Contact Problem for a Stamp With a Rectangular Base," *PMM Journal of Applied Mathematics and Mechanics*, Vol. 40, pp. 505–512.

Boussinesq, J., 1885, *Application des Potentiels `a l'Etude de l'Equilibre et du Mouvement des Solides Elastiques*, Gauthier-Villars, Paris.

Brothers, P. W., Sinclair, G. B., and Segedin, C. M., 1977, "Uniform Indentation of the Elastic Half-Space by a Rigid Rectangular Punch," *International Journal of Solids and Structures*, Vol. 13, pp. 1059–1072.

Chang, F.-V., and Hwang, S.-M., 1984, "A Free Rectangular Plate on the Elastic Foundation," (in Chinese), *Applied Mathematics and Mechanics*, Vol. 5, pp. 345–353.

Downloaded 03 May 2010 to 171.66.16.21. Redistribution subject to ASME license or copyright; see http://www.asme.org/terms/Terms_Use.cfm

Cheung, Y. K., and Zienkiewicz, O. C., 1965, "Plates and Tanks on Elastic Foundations—An Application of the Finite Element Method," *International Journal of Solids and Structures*, Vol. 1, pp. 451–461.

Cheung, Y. K., and Nag, D. K., 1968, "Plates and Beams on Elastic Foundations—Linear and Non-Linear Behaviour," *Géotechnique*, Vol. 18, pp. 250–260.

Conway, H. D., and Farnham, K. A., 1968, "The Relationship Between Load and Penetration of a Rigid, Flat-Ended Punch of Arbitrary Cross Section," *International Journal of Engineering Science*, Vol. 6, pp. 489–496.

Dundurs, J., 1975, "Properties of Elastic Bodies in Contact," *The Mechanics of the Contact between Deformable Bodies*, De Pater, A. D., and Kalker, J. J., Eds., Delft University Press.

Fabrikant, V. I., 1986, "Flat Punch of Arbitrary Shape on an Elastic Half-Space," *International Journal of Engineering Science*, Vol. 24, pp. 1731–1740.

Fraser, R. A., and Wardle, L. J., 1976, "Numerical Analysis of Rectangular Rafts on Layered Foundation," *Géotechnique*, Vol. 26, pp. 613–630.

Gladwell, G. M. L., and Iyer, K. R. P., 1974, "Unbonded Contact Between a Circular Plate and an Elastic Half-Space," *Journal of Elasticity*, Vol. 4, pp. 115–130.

Gorbunov-Possadov, M. I., and Serebrjanyi, R. V., 1961, "Design of the Structures on Elastic Foundation," *Proceedings of the 5th Conference on Soil Mechanics and Foundation Engineering*, Vol. I, pp. 643–648.

Harding, J. W., and Sneddon, I. N., 1945, "The Elastic Stresses Produced by the Indentation of the Plane Surface of Semi-Infinite Elastic Body by a Rigid Punch," *Proceedings of the Cambridge Philosophical Society*, Vol. 41, pp. 16–26.

Hooper, J. A., 1978, "Foundation Interaction Analysis," *Developments in Soil Mechanics—1*, Scott, C. R., Ed., Chapter 5, pp. 149–211.

Li, H., and Dempsey, J. P., 1987, "Unbonded Contact of a Square Plate on an Elastic Half-Space or a Winkler Foundation," Department Report No. 87-10, Department of Civil and Environmental Engineering, Clarkson University.

Morrison, J. A., and Lewis, J. A., 1976, "Charge Singularity at the Corner of a Flat Plate," *SIAM Journal of Applied Mathematics*, Vol. 31, pp. 233–250.

Mullan, S. J., Sinclair, G. B., and Brothers, P. W., 1980, "Stresses for an Elastic Half-Space Uniformly Indented by a Rigid Rectangular Footing," *International Journal for Numerical and Analytical Methods in Geomechanics*, Vol. 4, pp. 277–284.

Murphy, G., 1937, "Stresses and Deflections in Loaded Rectangular Plates on Elastic Foundations," *Iowa Engineering Experiment Station Bulletin*, Vol. 36, No. 5, pp. 1–52.

Noble, B., 1960, "The Numerical Solution of the Singular Integral Equation for the Charge Distribution on a Flat Rectangular Lamina," *Symposium on the Numerical Treatment of Ordinary Differential Equations, Integral and Integro-Differential Equations, Proceedings of the Rome Symposium*, Sept. 20–24, 1960, Birkhäuser Verlag, Basel, pp. 530–543.

Rajapakse, R. K. N. D., and Selvadurai, A. P. S., 1986, "On the Performance of Mindlin Plate Elements in Modelling Plate-Elastic Medium Interaction: A Comparative Study," *International Journal for Numerical Methods in Engineering*, Vol. 23, pp. 1229–1244.

Rvachev, V. L., 1959, "The Pressure on an Elastic Half-Space of a Stamp With Wedge-Shaped Planform," *PMM Journal of Applied Mathematics and Mechanics*, Vol. 23, pp. 229–233.

Svec, O. J., 1974, "The Unbonded Contact Problem of a Plate on the Elastic Half Space," *Computer Methods in Applied Mechanics and Engineering*, Vol. 3, pp. 105–113.

Villaggio, P., 1983, "A Free Boundary Value Problem in Plate Theory," ASME JOURNAL OF APPLIED MECHANICS, Vol. 50, pp. 297–302.

Vint, J., and Elgood, W. N., 1935, "The Deformation of a Bloom Plate Resting on an Elastic Base When a Load is Transmitted to the Plate by Means of a Stanchion," *Philosophical Magazine, Series 7*, Vol. 19, pp. 1–21.

Weitsman, Y., 1969, "On the Unbonded Contact Between Plates and an Elastic Half Space," ASME JOURNAL OF APPLIED MECHANICS, Vol. 36, pp. 198–202.

Downloaded 03 May 2010 to 171.66.16.21. Redistribution subject to ASME license or copyright; see http://www.asme.org/terms/Terms_Use.cfm

Axisymmetric Free-Vibration Problems by Boundary Element Method

Hui-Ching Wang
Graduate Student.
Prasanta K. Banerjee
Professor.

Department of Civil Engineering,
State University of New York at Buffalo,
Buffalo, NY 14260

A new boundary-element formulation using particular integrals is developed for the free-vibration analysis of axisymmetric solids. The numerical results for a number of axisymmetric free-vibration problems are given and some of the results are compared with those obtained from Finite Element Method, Series Solution Method, or experimental method. Generally, agreement among all of these results is satisfactory.

I Introduction

Axisymmetric solids and structures are very often used by civil and mechanical engineers as cooling towers, domes, pipes, nozzles, and axle shafts, etc. Although the free-vibration problems of such structures have been investigated by many researchers using numerical methods such as the Finite-Difference Method and the Finite Element Method or analytical methods, no attempt has been made to date to analyze these problems by the Boundary Element Method (BEM).

The BEM has become a very powerful numerical tool in solving different types of engineering problems. One of its great benefits compared to other numerical methods is that the integration and discretization are only needed on boundary surface rather than on whole domain. The conventional boundary-element formulation for the free-vibration problem leads to a system of equations in which the frequency parameter is nonlinearly embedded within the kernel functions. These kernel functions themselves are either Henkel functions (in two-dimensions) or exponential functions (in three-dimensions) with complex arguments. In order to extract the eigenvalues of such a system, it is then necessary to use a determinant search technique which is enormously expensive.

It is also possible to cast the problem into a real variable form (exactly in the same form used in FEM) utilizing the static fundamental solution. Unfortunately, this leaves a volume integral involving the inertia force term. An internal discretization then becomes essential which of course is unsatisfactory. It is not surprising, therefore to find that the application of BEM to realistic problems of free-vibration analysis was somewhat limited until recently when alternative boundary-element procedures for plane problems were proposed by Nardini and Brebbia (1982) and Ahmad and Banerjee (1986). In both papers, the authors use global shape functions to express the inertia effect and use either divergence theorem (Nardini and Brebbia, 1982) or particular integral (Ahmad and Banerjee, 1986) so that only the boundary integrals independent of frequency are needed. In this paper, we extend the method by Ahmad and Banerjee to solving axisymmetric free vibration. First, their work is briefly reviewed here for three-dimensional problems.

Starting with the governing equation of harmonic free vibration for a homogeneous, isotropic body

$$(\lambda+\mu)u_{j,ij}+\mu u_{i,jj}+\rho\omega^2 u_i=0 \tag{1}$$

where λ and μ are Lame's constants, ρ is the density, and ω is the exciting frequency. They introduced an unknown fictitious global function ϕ and a known function C, to approximate the displacement field u in the inertia term as

$$u_i(x)=\sum_{m=1}^{\infty} C_{ik}(x,\xi^m)\phi_k(\xi^m) \tag{2}$$

where x is the field point, ξ^m is the point where the function ϕ is defined. Then the solution of equation (1) can be expressed as the sum of a complementary solution u_i^c satisfying

$$(\lambda+\mu)u^c_{j,ij}+\mu u^c_{i,jj}=0 \tag{3}$$

and a particular integral u_i^p satisfying

$$(\lambda+\mu)u^p_{j,ij}+\mu u^p_{i,jj}+\rho\omega^2\sum_{m=1}^{\infty} C_{ik}(x,\xi^m)\phi_k(\xi^m)=0 \tag{4}$$

If the function C is chosen as

$$C_{ik}(x,\xi^m)=\delta_{ik}(A-r) \tag{5}$$

where r is the distance between x and ξ^m and A is a constant, then one of the particular solutions of equation (4) can be found as

$$u_i^p=\rho\omega^2\sum_{m=1}^{\infty} D_{ik}(x,\xi^m)\phi_k(\xi^m) \tag{6}$$

and its corresponding surface traction via the stress-strain relations and the surface normal

Contributed by the Applied Mechanics Division for publication in the JOURNAL OF APPLIED MECHANICS.

Discussion on this paper should be addressed to the Editorial Department, ASME, United Engineering Center, 345 East 47th Street, New York, NY 10017, and will be accepted until two months after final publication of the paper itself in the JOURNAL OF APPLIED MECHANICS. Manuscript received by ASME Applied Mechanics Division, July 14, 1987; final revision, November 9, 1987.

Copyright © 1988 by ASME
Downloaded 03 May 2010 to 171.66.16.21. Redistribution subject to ASME license or copyright; see http://www.asme.org/terms/Terms_Use.cfm

$$t_i^p = \rho\omega^2 \sum_{m=1}^{\infty} T_{ik}(x,\xi^m)\phi_k(\xi^m) \tag{7}$$

where

$$D_{ik}(x,\xi^m) = \frac{1}{\mu}[(C_1 r - C_2 A)\delta_{ik} r^2 - C_3 y_i y_k r] \tag{8}$$

$$T_{ik}(x,\xi^m) = (C_4 r - C_5 A) y_k n_i + (C_6 r - 2C_2 A) y_i n_k + \left[(C_6 r - 2C_2 A)\delta_{ik} - 2C_3 \frac{y_i y_k}{r}\right] y_j n_j \tag{9}$$

where C_i are constants.

The boundary integral representation for equation (3) is

$$\alpha_{ij}(\xi) u_i^c(\xi) = \int_s [G_{ij}(x,\xi) t_i^c(x) - F_{ij}(x,\xi) u_i^c(x)] dS(x) \tag{10}$$

where G_{ij} and F_{ij} are the fundamental solutions in elastostatics (Banerjee and Butterfield, 1981). After a usual discretization of boundary S, the aforementioned equation can be written in the matrix form as

$$[G]\{t^c\} - [F]\{u^c\} = \{0\} \tag{11}$$

Substituting $u^c = u - u^p$ and $t^c = t - t^p$ into it, we have

$$[G]\{t\} - [F]\{u\} = [G]\{t^p\} - [F]\{u^p\} \tag{12}$$

Substituting (6) and (7) into (12) and using (2) to replace ϕ, the following equation can be derived

$$[G]\{t\} - [F]\{u\} = \rho\omega^2([G][T] - [F][D])[C]^{-1}\{u\} \tag{13}$$

if we take the same finite number of fictitious points, N, as that of discretized boundary nodes. By applying the appropriate free boundary conditions we obtain

$$[A]\{X\} - \rho\omega^2[B]\{X\} = \{0\} \tag{14}$$

where $\{X\}$ is unknown vector of boundary tractions and displacements. Through solving eigenvalues and eigenvectors of the foregoing equation, the natural frequencies of the system and the corresponding mode shapes can be found.

II Axisymmetric Boundary-Element Analysis

In axisymmetric free vibration, equation (13) is still valid. But for convenience, all the vectors and kernel matrices are expressed in cylindrical coordinates. The fundamental solutions of elastostatics in cylindrical coordinates as well as the semi-analytical method for evaluating the values of such kernel matrix by elliptical integrals have been explicitly described by Cruse, et al. (1977), Rizzo and Shippy (1979), Nigam (1979), Mayr, et al. (1980), Sarihan and Mukherjee (1982), and Henry, et al. (1987). In the present case, one additionally needs to evaluate the axisymmetric counterparts of kernels C, D and T.

Instead of using discretized form of fictitious densities C in equation (4), it is more appropriate to use a continuous distribution along θ-direction but discrete form on r-z plane, i.e.

$$u_i(x) = \sum_{m=1}^{\infty} \int_0^{2\pi} C'_{ik}(x,\xi^m)\phi_k(\xi^m) d\theta \tag{15}$$

where θ is the angle between points x and ξ^m.

Thus the particular solutions can also be expressed in the same way

$$u_i^p(x) = \rho\omega^2 \sum_{m=1}^{\infty} \int_0^{2\pi} D'_{ik}(x,\xi^m)\phi_k(\xi^m) d\theta \tag{16}$$

$$t_i^p(x) = \rho\omega^2 \sum_{m=1}^{\infty} \int_0^{2\pi} T'_{ik}(x,\xi^m)\phi_k(\xi^m) d\theta \tag{17}$$

instead of those in equations (6) and (7). Note that when transforming a line integral to an integral with respect to angle, one usually uses

$$dl = r_o d\theta \tag{18}$$

In equation (15), the radius r_o has been absorbed in the fictitious function ϕ term, so that it need not appear explicitly. Kernels C', D', and T' in the foregoing equations can be derived from those in Cartesian coordinates by using transformation

$$\begin{aligned} D'_{rr} &= D_{xx}\cos\theta + D_{xy}\sin\theta \\ D'_{rz} &= D_{xz} \\ D'_{zr} &= D_{zx} \\ D'_{zz} &= D_{zz} \end{aligned} \tag{19}$$

C' and T' also have similar transformation. The result of this transformation is given in the Appendix.

If a finite number of collocation points, N, is chosen, then the number of fictitious points is also chosen as N. But their distribution can be arbitrary as long as they are able to describe well the variation of the inertia term. For convenience, we choose the same nodal points for collocation and the location of fictitious density function ϕ.

III Numerical Treatment

The evaluation of static kernels G and F along a ring by using elliptical integrals have been described by Nigam (1979), Henry, et al., (1987), and accordingly they are not repeated here. For kernels C, D, and T, from equations (15)–(17), it is more efficient if one can analytically evaluate the following integrals

$$\int_0^{2\pi} \frac{1}{r} d\theta,\ \int_0^{2\pi} \frac{\cos\theta}{r} d\theta,\ \int_0^{2\pi} \frac{\cos^2\theta}{r} d\theta,\ \int_0^{2\pi} \frac{\cos^3\theta}{r} d\theta,$$

$$\int_0^{2\pi} r d\theta,\ \int_0^{2\pi} r\cos\theta\, d\theta,\ \int_0^{2\pi} r\cos^2\theta\, d\theta,$$

$$\int_0^{2\pi} r^3 d\theta,\ \int_0^{2\pi} r^3\cos\theta\, d\theta$$

where r is the distance between points x and ξ^m.

These integrals can be found in the similar manner to the procedure used in evaluating static kernels. The result can be expressed in terms of the elliptic integrals as follows

$$F_1 = \int_0^{2\pi} \frac{1}{r} d\theta = \frac{4K}{R}$$

$$F_2 = \int_0^{2\pi} \frac{\cos\theta}{r} d\theta = -\frac{4(2B_2 - B_1)}{R}$$

$$F_3 = \int_0^{2\pi} \frac{\cos^2\theta}{r} d\theta = \frac{4}{R}(4B_3 - 4B_2 + B_1)$$

$$F_4 = \int_0^{2\pi} \frac{\cos^3\theta}{r} d\theta = -\frac{4}{R}(8B_4 - 12B_3 + 6B_2 - B_1)$$

$$G_1 = \int_0^{2\pi} r d\theta = 4RE$$

$$G_2 = \int_0^{2\pi} r\cos\theta\, d\theta = 4mR(B_3 - B_2)$$

$$G_3 = \int_0^{2\pi} r\cos^2\theta\, d\theta = 2R[E - m(2B_4 - 3B_3 + B_2)]$$

$$H_1 = \int_0^{2\pi} r^3 d\theta = 2R^3[(2-m)E - m^2(B_3 - B_2)]$$

Downloaded 03 May 2010 to 171.66.16.21. Redistribution subject to ASME license or copyright; see http://www.asme.org/terms/Terms_Use.cfm

$$H_2 = \int_0^{2\pi} r^3 \cos\theta \, d\theta = mR^3[2(2-m)(B_3 - B_2) - E + m(2B_4 - B_3 + B_2)]$$

where

$$R = [(r_x + r_\xi)^2 + (z_x - z_\xi)^2]^{1/2}$$

$$E = \int_0^{\pi/2} \sqrt{1 - m \sin^2\theta} \, d\theta$$

the elliptical integral of first kind

$$K = \int_0^{\pi/2} \frac{1}{\sqrt{1 - m \sin^2\theta}} d\theta$$

the elliptical integral of second kind

$$m = \frac{4 r_x r_\xi}{R^2}$$

$$B_1 = \int_0^{\pi/2} \frac{d\theta}{\sqrt{1 - m \sin^2\theta}} = K$$

$$B_2 = \int_0^{\pi/2} \frac{\cos^2\theta d\theta}{\sqrt{1 - m \sin^2\theta}} = \frac{E - (1-m)K}{m}$$

$$B_3 = \int_0^{\pi/2} \frac{\cos^4\theta d\theta}{\sqrt{1 - m \sin^2\theta}} = \frac{2E(2m-1) + K(1-m)(2-3m)}{5m^2}$$

$$B_4 = \int_0^{\pi/2} \frac{\cos^6\theta \, d\theta}{\sqrt{1 - m \sin^2\theta}} = \frac{4(2m-1)C_3 + 3(1-m)C_2}{5m}$$

The series expansion for computing K and E can be seen in the book by Banerjee and Butterfield (1981).

If any of the collocation nodes is located on the Z-axis, the matrix $[C]$ becomes singular because the corresponding row in R-direction at this node becomes zero. Such difficulties can be eliminated by putting unit values in the diagonal terms of those rows. This somewhat arbitrary method works because all the fictitious densities ϕ in the R-direction are zero at nodes on the Z-axis. At each boundary node, either traction or displacement is specified except that at Z-axis traction boundary condition in R-direction must be specified to avoid a zero row appearing in the axisymmetric counterpart of matrix $[A]$ of equation (14). Traction in the R-direction is always zero at Z-axis unless there is a boundary discontinuity. If such a discontinuity of geometry does not exist, then we can specify either displacement or traction at Z-axis by replacing the corresponding zero element in matrix $[G]$ by any nonzero value which is then multiplied by zero traction. Another way to resolve this ambiguity is to delete its corresponding rows and columns from matrices $[A]$ and $[B]$.

As mentioned in the existing literature (Nardini and Brebbia, 1982; Ahmad and Banerjee, 1986) the use of internal points usually leads to faster rate of convergence. It may also be true for the axisymmetric free-vibration problems. If internal points are used, then formulation is modified as follows:

From equation (10), for internal points one can write

$$\{u^c\}_i = [G]_i\{t^c\}_b - [F]_i\{u^c\}_b \tag{20}$$

where subscript i denotes internal values and subscript b boundary values.

Substituting $u^c = u - u^p$ and $t^c = t - t^p$, it can be rewritten as

$$[G]_i\{t\}_b - [F]\{u\}_b - \{u\}_i = [G]_i\{t^p\}_b - [F]_i\{u^p\}_b - \{u^p\}_i \tag{21}$$

Using both boundary points and internal points to describe the inertia effects, equations (16) and (17) can be cast as

$$\{u^p\}_i = \rho\omega^2[D]_i\{\phi\}_{b+i} \tag{22a}$$

$$\{u^p\}_b = \rho\omega^2[D]_b\{\phi\}_{b+i} \tag{22b}$$

$$\{t^p\}_b = \rho\omega^2[T]_b\{\phi\}_{b+i} \tag{22c}$$

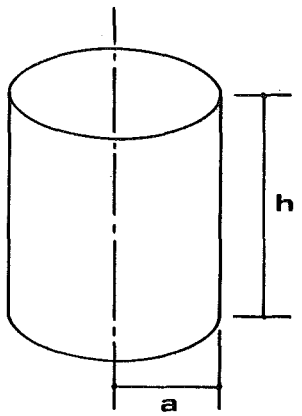


Fig. 1 Configuration of a solid cylinder

Substituting (22a–c) into (21), one obtains a system of equation for the interior points

$$[G]_i\{t\}_b - [F]_i\{u\}_b - \{u\}_i = \rho\omega^2([G]_i[T]_b - [F]_i[D]_b - [D]_i)\{\phi\}_{b+i} \tag{23}$$

Also for boundary points,

$$[G]_b\{t\}_b - [F]_b\{u\}_b = \rho\omega^2([G]_b[T]_b - [F]_b[D]_b)\{\phi\}_{b+i} \tag{24}$$

Combining two equations and using equation (15) to replace $\{\phi\}_{b+i}$ by $[C]^{-1}_{b+i}\{u\}_{b+i}$, one obtains

$$\begin{bmatrix} G_b \\ G_i \end{bmatrix}\{t\}_b - \begin{bmatrix} F_b & 0 \\ F_i & I \end{bmatrix}\begin{Bmatrix} u_b \\ u_i \end{Bmatrix} = \rho\omega^2\left(\left[\begin{bmatrix} G_b \\ G_i \end{bmatrix}[T]_b - \begin{bmatrix} F_b \\ F_i \end{bmatrix}[D]_b - \begin{bmatrix} 0 \\ D_i \end{bmatrix}\right][C]^{-1}_{b+i}\{u\}_{b+i}\right)$$

or

$$[G]_{b+i}\{t\}_b - [F]_{b+i}\{u\}_{b+i} = \rho\omega^2[M]_{b+i}\{u\}_{b+i} \tag{25}$$

where

$$[M]_{b+i} = \left(\left[\begin{bmatrix} G_b \\ G_i \end{bmatrix}[T]_b - \begin{bmatrix} F_b \\ F_i \end{bmatrix}[D]_b - \begin{bmatrix} 0 \\ D_i \end{bmatrix}\right][C]^{-1}_{b+i} \tag{26}$$

and I is identity matrix.

Note that although internal points are used in the foregoing collocation scheme, all integrals needed are still evaluated on the boundary only.

By incorporating the known values of boundary tractions and boundary displacements, the previous system of equation can be cast into

$$[A]\{X\} - \rho\omega^2[B]\{X\} = 0 \tag{27}$$

It should be noted that both matrices A and B are fully populated and nonsymmetric. Such a system cannot be guaranteed to provide real eigenvalues. It would be seen from the examples presented here that the eigenvalues of (26) in the present case are in fact real. The standard EISPACK developed at Argonne National Laboratory was used to extract the eigenvalues.

IV Verification of the Analysis

1 Convergence of the Analysis. To study the convergence of the proposed BEM formulation the axisymmetric free-vibration problem of a solid cylinder (Fig. 1) is investigated. The ratio between the length and the radius is 2.

Downloaded 03 May 2010 to 171.66.16.21. Redistribution subject to ASME license or copyright; see http://www.asme.org/terms/Terms_Use.cfm

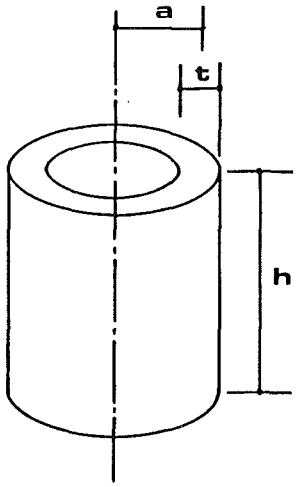


Fig. 2 Configuration of a hollow cylinder

The boundary condition is traction-free everywhere except that

$$u_z = 0 \quad \text{at} \quad z = 0$$

The convergence of the lowest 6 natural frequencies is shown in Table 1. The analytical result by Hutchinson (1986) using SSM is also given for comparison. All the frequencies are nondimensionized by using the multiplying factor $a/\sqrt{\mu/\rho}$. In this study, the number of elements or the number of internal points is increased in order to get the convergence. From Table 1, one can see that there is about 10 percent error in high modes when no internal points are used, even though relatively large number of boundary elements have been used. This is probably due to the inability of the global shape function to represent the more complex deformed shape. With the introduction of even modest number of internal points, the results improve dramatically (the maximum difference now is less than 1 percent). It is also important to note that in spite of the introduction of a very large number of interior nodes (which are clearly not necessary), the results remain quite stable. It can therefore be concluded that

(*i*) If enough boundary nodes have been used, then the best way to get a faster convergence is to add a few internal points principally because the deformed shape can be better represented by the global shape function $C(x,\xi)$, especially for higher modes.

(*ii*) The distribution of internal nodes does not appear to be critical and results remain stable even if an arbitrarily large number of interior points are used.

2 Comparison With FEM and SSM. The axisymmetric free vibration of a hollow cylinder (Fig. 2) of finite length has been investigated by Gladwell (1975) using FEM and by Hutchinson (1986) using SSM. The boundary condition is traction-free everywhere. Because of the symmetry of geometry in Z-direction, it is possible to analyze the problem by using just the upper half cylinder by introducing appropriate boundary conditions for the symmetric and axisymmetric modes at $z = h/2$, i.e.,

$u_z = 0$ for symmetric modes,

$u_r = 0$ for axisymmetric modes.

The comparison among the results by BEM and by other methods is shown in Table 2. Sufficient details of the FEM mesh used by Gladwell are not available. The mesh used in BEM has 20 quadratic boundary elements and 4 internal points which are uniformly distributed. If a thick cylinder is considered, then the use of such internal points becomes very important. On the other hand, internal points may not be needed for a thin cylinder. The maximum difference between the results by BEM and by SSM is 2.3 percent (1st symmetric mode for $H = 2$). The maximum difference between the results by BEM and by FEM is 2.2 percent (3rd symmetric mode for $H = 10$).

3 Comparison With Experimental Result. Having compared the results of the present analysis with a numerical method (FEM) and an analytic method (SSM), it would be interesting to compare the results with those given by an experimental method. McMahon (1964) carried out an experimental study on the natural frequencies of an isotropic elastic solid cylinder with free boundaries. The same problem is analyzed by BEM. The Poisson's ratio of 0.344 and the longitudinal wave velocity ($\sqrt{E/\rho}$) of 5150 m/sec was given for

Table 1 Convergence study of natural frequencies of a solid cylinder ($h/a = 2$)

MESH	1ST MODE	2ND MODE	3RD MODE	4TH MODE	5TH MODE	6TH MODE
3* + 0**	1.25	3.38	3.81	4.10	4.92	5.30
3 + 4	1.25	2.94	3.32	4.10	4.79	--
3 + 8	1.25	2.92	3.24	4.04	4.57	--
3 + 36	1.25	2.88	3.20	4.01	4.35	4.44
12 + 0	1.24	3.27	3.56	3.82	4.77	--
12 + 4	1.25	2.91	3.12	3.94	4.49	4.55
12 + 8	1.25	2.91	3.04	3.87	4.26	4.51
12 + 16	1.25	2.90	3.04	3.86	4.23	4.48
15 + 0	1.24	3.27	3.56	3.82	4.77	--
15 + 4	1.25	2.91	3.12	3.94	4.48	4.54
15 + 8	1.25	2.91	3.04	3.87	4.25	4.51
15 + 16	1.25	2.90	3.03	3.86	4.22	4.48
18 + 0	1.25	3.27	3.56	3.82	4.77	--
18 + 4	1.25	2.91	3.12	3.94	4.48	4.54
18 + 8	1.25	2.91	3.04	3.87	4.25	4.51
18 + 16	1.25	2.90	3.03	3.86	4.22	4.48
SSM	1.2470	2.9205	3.0296	3.8240	4.1854	4.4530

* = the number of quadratic boundary elements

** = the number of internal points

Table 2 Comparison of natural frequencies ($\omega' = \omega a/\sqrt{\mu/\rho}$) of a hollow tube ($t/a = 1.4$) for BEM, FEM (Gladwell, 1975), and SSM (Hutchinson, 1986)

		SYMMETRIC MODE			ANTI-SYMMETRIC MODE		
METHOD H=h/a	N	FEM	SSM	BEM	FEM	SSM	BEM
1	1	1.82	1.82	1.81	1.05	1.05	1.05
	2	4.26	4.26	4.27	3.13	3.13	3.12
	3	4.61	4.57	4.59	3.97	3.95	3.96
	4	5.26	5.25	5.21	5.71	5.69	5.74
	5	5.71	5.64	5.69			
2	1	1.72	1.68	1.72	1.43	1.43	1.42
	2	2.30	2.30	2.28	2.69	2.69	2.70
	3	2.83	2.83	2.83	3.71	3.70	3.69
	4	3.67	3.65	3.65	4.25	4.24	4.26
	5	4.19	4.18	4.22			
3	1	1.47	1.47	1.47	1.58	1.58	1.57
	2	1.79	1.79	1.78	2.21	2.21	2.21
	3	--	--	2.21	--	--	3.04
	4	--	--	3.09	--	--	3.46
	5	--	--	3.62			
4	1	1.19	1.19	1.19	1.64	1.63	1.62
	2	1.63	1.63	1.64	1.87	1.87	1.86
	3	2.07	2.06	2.05	2.67	2.66	2.68
	4	2.52	2.50	2.51	2.80	2.79	2.80
	5	3.30	3.23	3.29			
6	1	0.83	0.83	0.83	1.47	1.45	1.47
	2	1.63	1.63	1.61	1.67	1.67	1.64
	3	1.83	1.83	1.83	2.14	2.13	2.14
	4	2.07	2.06	2.05	2.22	2.22	2.23
	5	2.60	2.58	2.62			
8	1	0.63	0.63	0.63	1.19	1.19	1.19
	2	1.56	1.56	1.56	1.65	1.64	1.62
	3	1.66	1.66	1.63	1.83	1.83	1.83
	4	2.00	2.00	1.99	2.03	2.02	2.02
	5	2.13	2.12	2.13			
10	1	0.50	0.50	0.50	0.98	0.98	0.98
	2	1.37	1.37	1.37	1.61	1.60	1.60
	3	1.65	1.65	1.61	1.67	1.66	1.64
	4	1.82	1.82	1.83	1.97	1.97	1.97
	5	2.02	2.01	1.99			

Downloaded 03 May 2010 to 171.66.16.21. Redistribution subject to ASME license or copyright; see http://www.asme.org/terms/Terms_Use.cfm

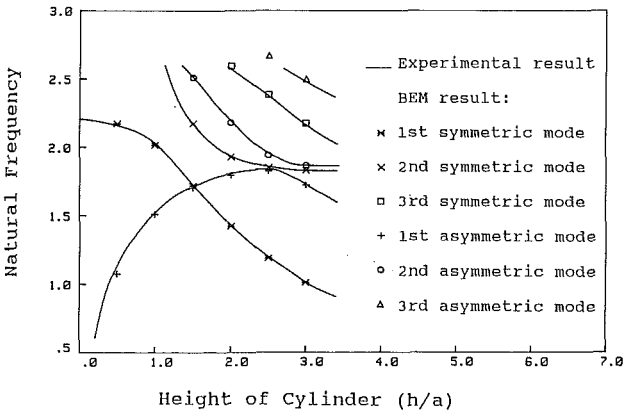


Fig. 3 Comparison between natural frequencies of hollow cylinder by BEM and by experimental method (McMahon)

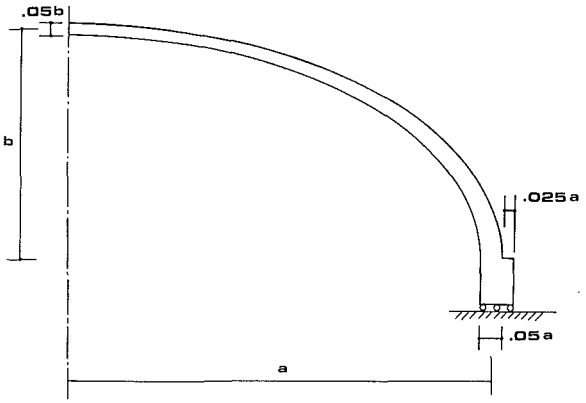


Fig. 4 Elliptic dome with a ring beam supported by rollers

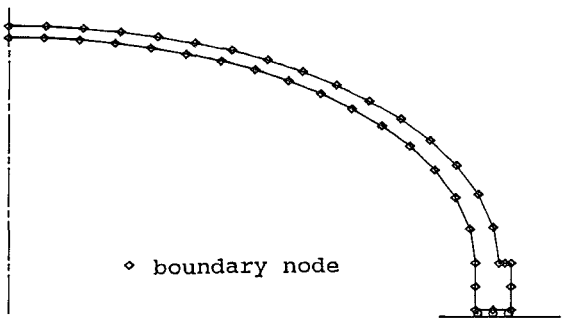


Fig. 5 Boundary-element model of the elliptic dome

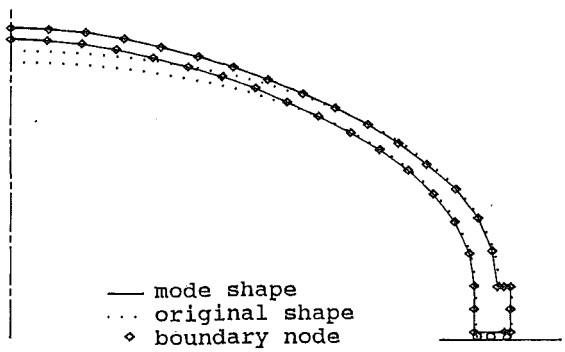


Fig. 6 First mode shape of the free vibration of the elliptic dome ($\omega a/\sqrt{E/\rho} = 0.8486$)

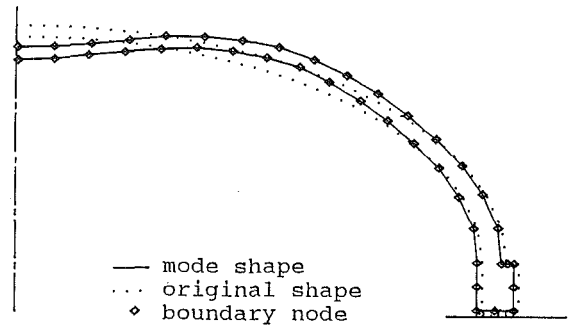


Fig. 7 Second mode shape of the free vibration of the elliptic dome ($\omega a/\sqrt{E/\rho} = 1.0808$)

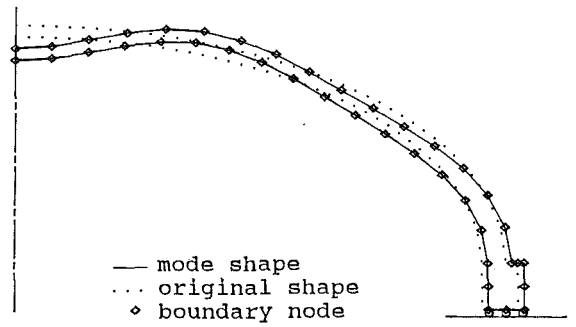


Fig. 8 Third mode shape of the free vibration of the elliptic dome ($\omega a/\sqrt{E/\rho} = 1.4858$)

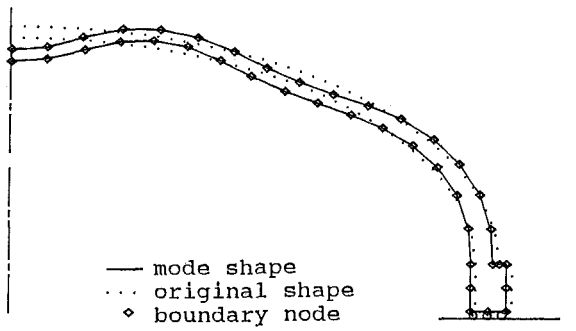


Fig. 9 Fourth mode shape of the free vibration of the elliptic dome ($\omega a/\sqrt{E/\rho} = 2.1422$)

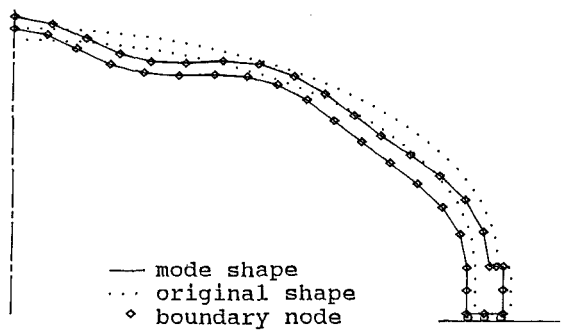


Fig. 10 Fifth mode shape of the free vibration of the elliptic dome ($\omega a/\sqrt{E/\rho} = 2.5166$)

aluminum. The results are expressed in terms of dimensionless frequency $\omega' = \omega a/\sqrt{E/\rho}$.

The theoretical BEM results which were obtained using 20 boundary elements and 13 internal nodes agree quite well with the experimental data for all ratios of height to radius of the cylinder (see Fig. 3).

Downloaded 03 May 2010 to 171.66.16.21. Redistribution subject to ASME license or copyright; see http://www.asme.org/terms/Terms_Use.cfm

4 Axisymmetric Free Vibration of an Elliptic Dome With a Ring Beam. An elliptic dome ($a/b=2$) is shown in Fig. 4, and the mesh used to solve this problem is shown in Fig. 5. It is interesting to note that although the dome is reasonably thin it can be analyzed as an axisymmetric solid by the BEM. The results are expressed in terms of the nondimensional frequency $\omega' = \omega a/\sqrt{E/\rho}$. The Poisson's ratio of the material was assumed to be 0.2. The first 5 mode shapes for this problem are shown in Figs. 6–10.

V Conclusion

The first application of BEM to axisymmetric free vibration of various solids is described. The method is verified by comparing the results with those obtained by other methods. It has been demonstrated that a real variable eigenvalue extraction method can be developed using the well-known method of particular integrals in the context of a BEM analysis.

References

Ahmad, S., and Banerjee, P. K., 1986, "Free Vibration Analysis by Boundary Element Method Using Particular Integrals," *Journal of Engineering Mechanics*, ASCE, Vol. 12, pp. 682–695.

Banerjee, P. K., and Butterfield, R., 1981, *Boundary Element Methods in Engineering Science*, McGraw-Hill, London and New York.

Cruse, T. A., Snow, D., and Wilson, R. B., 1977, "Numerical Solutions in Axisymmetric Elasticity," *Computers and Structures*, Vol. 7, pp. 445–451.

Gladwell, G. M. L., and Vijay, D. K., 1975, "Natural Frequencies of Free Finite-Length Circular Cylinders," *Journal of Sound and Vibration*, Vol. 42(3), pp. 387–397.

Henry, D. P., Pape, D. A., and Banerjee, P. K., 1987, "A New Axisymmetric BEM Formulation for Body Forces Using Particular Integrals," *Journal of Engineering Mechanics*, ASCE, Vol. 113, pp. 671–688.

Hutchinson, J. R., and El-Azhari, S. A., 1986, "Vibrations of Free Hollow Circular Cylinders," ASME JOURNAL OF APPLIED MECHANICS, Vol. 53, pp. 641–646.

Mayr, M., Drexler, W., and Kuhn, G., 1980, "A Semianalytical Boundary Integral Approach for Axisymmetric Elastic Bodies with Arbitrary Boundary Conditions," *International Journal of Solids and Structures*, Vol. 16, pp. 863–871.

McMahon, G. W., 1964, "Experimental Study of the Vibrations of Solid, Isotropic, Elastic Cylinders," *Journal of American Society of Acoustics*, Vol. 36, pp. 85–92.

Nardini, D., and Brebbia, C. A., 1982, "A New Approach to Free Vibration Analysis Using Boundary Elements," *Proceedings of the Fourth International Seminar, Southampton, England*, Ed. Brebbia, C. A., Spring-Verlag, pp. 313–326.

Nigam, R. K., 1979, "The Boundary Integral Equation Method for Elastoelastics Problems Involving Axisymmetric Geometry and Arbitrary Boundary Conditions," MS thesis, University of Kentucky.

Rizzo, F. J., and Shippy, D. J., 1979, "A Boundary Integral Approach to Potential and Elasticity Problems for Axisymmetric Bodies with Arbitrary Boundary Conditions," *Mechanics Research Communications*, Vol. 6, pp. 99–103.

Sarihan, V., and Mukherjee, S., 1982, "Axisymmetric Viscoplastic Deformation by the Boundary Element Method," *International Journal of Solids and Structures*, Vol. 18, pp. 1113–1128.

APPENDIX

Kernels C', D', and T' Expressed in Cylindrical Coordinates

$$C'_{rr} = (A-r)\cos\theta$$
$$C'_{rz} = C'_{zr} = 0$$
$$C'_{zz} = A - r$$

$$D'_{rr} = C_1 r^3 \cos\theta - C_2 A r^2 \cos\theta - C_3 r[-r_x r_\xi \cos^2\theta + (r_x^2 + r_\xi^2)\cos\theta - r_x r_\xi]$$
$$D'_{zr} = C_3 rz(r_x \cos\theta - r_\xi)$$
$$D'_{rz} = C_3 rz(r_x - r_\xi \cos\theta)$$
$$D'_{zz} = C_1 r^3 - C_2 A r^2 - C_3 Z^2 r$$
$$T'_{rr} = r\{-2C_6 n_r r_\xi \cos^2\theta + [(C_4 + 2C_6)n_r r_x + C_6 n_z Z]\cos\theta - C_4 n_r r_\xi\} - \frac{2C_3}{r}\{n_r r_x r_\xi^2 \cos^3\theta - [n_r r_\xi (r_x^2 + r_\xi^2) + (n_r r_x + n_z Z) r_x r_\xi]\cos^2\theta + [(n_r r_x + n_z Z)(r_x^2 + r_\xi^2) + n_r r_x r_\xi^2]\cos\theta - r_x r_\xi (n_r r_x + n_z Z)\} - A\{-4C_2 n_r r_\xi \cos^2\theta + [(C_5 + 4C_2)n_r r_x + 2C_2 n_z Z]\cos\theta - C_5 n_r r_\xi\}$$
$$T'_{zr} = r[(C_4 n_z r_x + C_6 n_r Z)\cos\theta - C_4 n_z r_\xi] + \frac{2C_3}{r} z\{n_r r_x r_\xi \cos^2\theta - [n_r (r_x^2 + r_\xi^2) + n_z Z r_x]\cos\theta + r_\xi (n_r r_x + n_z Z)\} - A[(C_5 n_z r_x + 2C_2 n_r Z)\cos\theta - C_5 n_z r_\xi]$$
$$T'_{rz} = r[-C_6 n_z r_\xi \cos\theta + (C_4 n_r Z + C_6 n_z r_x)] - \frac{2C_3}{r} Z[n_r r_\xi^2 \cos^2\theta - (2n_r r_x + n_z Z) r_\xi \cos\theta + (n_r r_x + n_z Z) r_x] - A[-2C_2 n_z r_\xi \cos\theta + (C_5 n_r Z + 2C_2 n_z r_x)]$$
$$T'_{zz} = r\{-C_6 n_r r_\xi \cos\theta + [(C_4 + 2C_6)n_z Z + C_6 n_r r_x]\} - \frac{2C_3}{r} z^2[-n_r r_\xi \cos\theta + (n_r r_x + n_z Z)] - A\{-2C_2 n_r r_\xi \cos\theta + [(C_5 + 4C_2)n_z Z + 2C_2 n_r r_x]\}$$

where A is the largest distance between two points of the body.

$$C_1 = \frac{12(1-\nu)-1}{144(1-\nu)\mu}$$
$$C_2 = \frac{1-2\nu}{4(2-3\nu)\mu}$$
$$C_3 = \frac{1}{48(1-\nu)\mu}$$
$$C_4 = \frac{6\nu - 1}{24(1-\nu)}$$
$$C_5 = \frac{\nu}{2-3\nu}$$
$$C_6 = \frac{5-6\nu}{24(1-\nu)}$$

n_r, n_z = components of normal vector at point ξ^m in r and z-directions, respectively
r = the distance between points $x(r_x, \theta_x, Z_x)$ and $\xi^m (r_\xi, \theta_\xi, Z_\xi)$
$Z = z_x - z_\xi$
$\theta = \theta_\xi - \theta_x$

Downloaded 03 May 2010 to 171.66.16.21. Redistribution subject to ASME license or copyright; see http://www.asme.org/terms/Terms_Use.cfm

K. J. Buhariwala
Senior Research Engineer.

J. S. Hansen
Professor.

Institute for Aerospace Studies,
University of Toronto,
4925 Dufferin Street,
Downsview, Ontario,
Canada, M3H 5T6

Construction of a Consistent Damping Matrix

A general method for constructing a material damping matrix in dynamical systems based on viscoelastic assumptions is presented. A generalization of the classical lamination theory, in particular, the consideration of viscoelasticity in the constitutive relation is considered. The discretized equations of motion for a laminated anisotropic viscoelastic plate using the finite-element method are derived. The mass, damping and stiffness matrices are completely defined and arise consistently in the formulation of motion equations. The technique is illustrated by calculating the mass, damping and stiffness matrices of a graphite-reinforced epoxy shell element. The eigenvalues are then calculated for the resulting eigenproblem.

1 Introduction

Energy dissipation is an important consideration in the study of stabilization and control of structures, as even limited dissipation can result in fundamentally different requirements. A particularly important form of energy dissipation in structures is material damping which is always present and is often either ignored or modeled crudely. The present paper is based on the premise that many material damping models currently used in the dynamical analysis are inadequate. The usual manner in which damping is incorporated in dynamical models is by first studying undamped models of the form

$$\underline{\mathbf{M}}\ddot{q} + \underline{\mathbf{K}}q = \underline{f}(t) \tag{1}$$

for suitable generalized coordinates $\underline{q}$ and generalized loading $\underline{f}$. Methods for constructing the system inertia matrix $\underline{\mathbf{M}}$ and the system stiffness matrix $\underline{\mathbf{K}}$, for structural systems are well documented; for example, reference may be made to Zienkiewicz (1977). In the usual procedure, material damping is accounted for by adding a linear viscous damping term $\underline{\mathbf{D}}\,\dot{q}$. The difficulty associated with this model

$$\underline{\mathbf{M}}\ddot{q} + \underline{\mathbf{D}}\dot{q} + \underline{\mathbf{K}}q = \underline{f}(t) \tag{2}$$

is that in writing (2), one rarely comes across an algorithm for constructing the system damping matrix $\underline{\mathbf{D}}$. Many studies involve quantifying the damping matrix from an experimentally measured data obtained from the dynamic behavior of the system. Hanagud, et al. (1984), Caravani, et al. (1977), Caravani and Thompson (1974) and Ibrahim (1982) describe techniques for identifying the damping matrix in such a manner. Quantifying the damping matrix from an experimentally measured set of data is unattractive however, since the damping matrix is not available at the design stage.

Hence, the present objective is to develop a general algorithm for constructing a consistent material damping matrix without knowledge obtained from the dynamic behavior of a system. As depicted in Fig. 1, the present work endeavors to strengthen the weak link in the dynamical modeling process by providing a damping matrix representation which is mathematically and physically as consistent as either the mass or stiffness matrices. In the development, it is shown that the motion equations are integro-differential in form rather than differential, (Hanagud, et al., 1984). The present interest is directed toward the use of laminated fiber-reinforced polymeric composite materials because of their

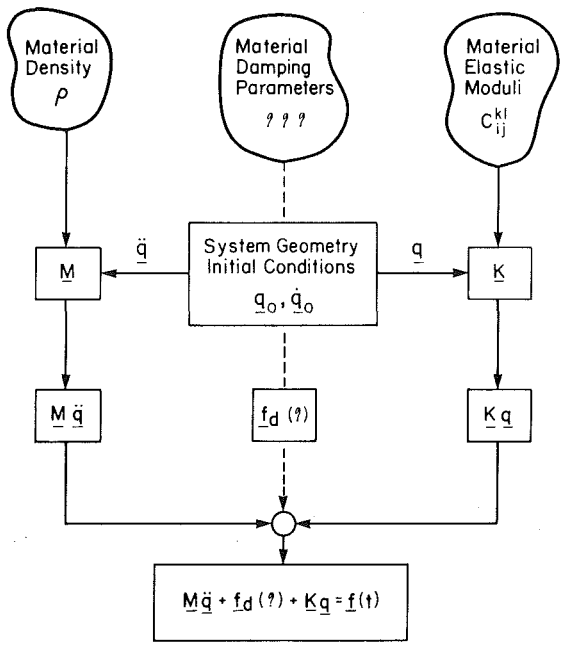


Fig. 1 Flow chart for a dynamical model

Contributed by the Applied Mechanics Division for publication in the JOURNAL OF APPLIED MECHANICS.

Discussion on this paper should be addressed to the Editorial Department, ASME, United Engineering Center, 345 East 47th Street, New York, NY 10017, and will be accepted until two months after final publication of the paper itself in the JOURNAL OF APPLIED MECHANICS. Manuscript received by ASME Applied Mechanics Division, May 21, 1986; final revision, October 6, 1987.

Copyright © 1988 by ASME
Downloaded 03 May 2010 to 171.66.16.21. Redistribution subject to ASME license or copyright; see http://www.asme.org/terms/Terms_Use.cfm

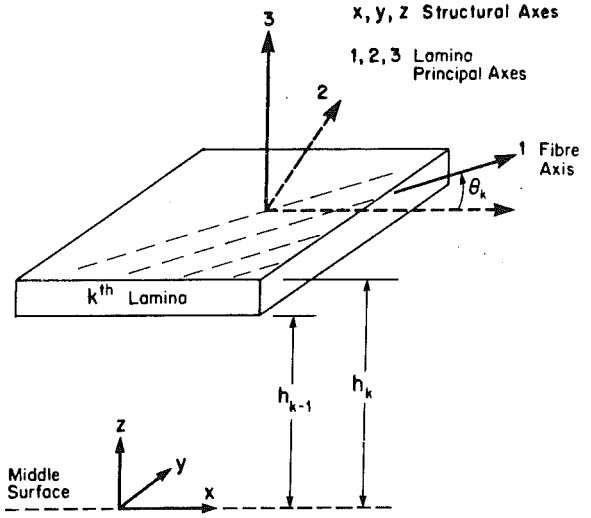


Fig. 2 Lamina relative to the structural axes

many advantages over conventional materials. Furthermore, since the polymeric matrix in composites is viscoelastic, the approach adopted is to model the composite as a viscoelastic material.

The anisotropic viscoelastic constitutive relation adopted in this work is presented in Section 2 while the model is specialized for an orthotropic lamina in Section 3. Stress and moment resultants in terms of the membrane, coupling and bending operators are presented in Section 4 for a laminate and these results are then used to develop the motion equation for a laminated circular cylindrical shell in Section 5. In Section 6, using the finite-element method, the discretized equations of motion are formulated for this shell and the algorithm for constructing the damping matrix is provided explicitly.

2 Linear Viscoelastic Constitutive Relation

In order to derive a consistent damping matrix in a manner analogous to a stiffness matrix using a finite element or a similar discretization procedure, we require a constitutive relation which accounts for the energy dissipated in a material. It is assumed that the material is viscoelastic, anisotropic and linear. The stress-strain relation that is adopted is given in an integral form and takes the form

$$\sigma_{ij}(t) = \int_0^t \sum_{k,l=1}^{3} G_{ij}^{kl}(\underline{r},t-\tau)\,\frac{\partial \epsilon_{kl}}{\partial \tau}\,d\tau + C_{ij}^{kl}(\underline{r})\epsilon_{kl} \tag{3}$$

$$G_{ij}^{kl}(\underline{r},t) = \int_0^\infty C_{ij}^{kl(*)}(\underline{r},\theta)\gamma(\theta)e^{-\theta t}d\theta \tag{4}$$

where $\gamma(\theta)$ is the relaxation density distribution function and C_{ij}^{kl} and G_{ij}^{kl} are symmetric in all four indices (when Onsager's relations apply), and are positive-semidefinite. Further details concerning this representation may be found in Buhariwala (1984).

3 Orthotropic Assumption

The stress-strain relations (3) and (4) apply to a viscoelastic material with an arbitrary degree of anisotropy. Here, the constitutive relations (3) and (4) take a simplified form, applicable for an orthotropic material. These relations will be applicable for each lamina and a laminate will consist of a stack of laminae with various ply orientations, as shown in Fig. 2.

For a material in a state of plane stress, the orthotropic, viscoelastic constitutive relation becomes

$$\underline{\sigma}_k = \int_0^t \underline{G}(t-\tau)\,\frac{\partial \underline{\epsilon}_k}{\partial \tau}\,d\tau + \underline{C}\,\underline{\epsilon}_k \tag{5}$$

$$\underline{\sigma}_k^T = [\sigma_1 \;\; \sigma_2 \;\; \sigma_{12}];\quad \underline{\epsilon}_k^T = \left[\epsilon_1 \;\; \epsilon_2 \;\; \frac{\gamma_{12}}{2}\right] \tag{6}$$

where γ_{12} is the engineering shear strain and

$$\underline{G}(t) = \int_0^\infty \begin{bmatrix} C_{11}^{(*)}(\theta) & C_{12}^{(*)}(\theta) & 0 \\ C_{12}^{(*)}(\theta) & C_{22}^{(*)}(\theta) & 0 \\ 0 & 0 & 2C_{66}^{(*)}(\theta) \end{bmatrix} \gamma(\theta)e^{-\theta t}d\theta \tag{7}$$

$$\underline{C} = \begin{bmatrix} C_{11} & C_{12} & 0 \\ C_{12} & C_{22} & 0 \\ 0 & 0 & 2C_{66} \end{bmatrix} \tag{8}$$

The indices in $\underline{G}(t)$ and $\underline{C}$ are ordered 1, 2 and 6 as usual in the analysis of composite materials. In general, the lamina principal axes (1,2) may not not be coincident with the structural axes (x,y) as is evident from Fig. 2. Thus the transformation relating the two axes with respect to the structural axes for the kth lamina, as defined by Ashton, et al. (1969) is

$$\begin{bmatrix} \sigma_1 \\ \sigma_2 \\ \sigma_{12} \end{bmatrix}_k = \underline{T}_k \begin{bmatrix} \sigma_{xx} \\ \sigma_{yy} \\ \sigma_{xy} \end{bmatrix}_k \tag{9}$$

and the transformation for the strain tensor is

$$\begin{bmatrix} \epsilon_1 \\ \epsilon_2 \\ \dfrac{\gamma_{12}}{2} \end{bmatrix}_k = \underline{T}_k \begin{bmatrix} \epsilon_{xx} \\ \epsilon_{yy} \\ \dfrac{\gamma_{xy}}{2} \end{bmatrix}_k \tag{10}$$

where the transformation matrix is

$$\underline{T}_k = \begin{bmatrix} m^2 & n^2 & 2mn \\ n^2 & m^2 & -2mn \\ -mn & mn & m^2-n^2 \end{bmatrix} \tag{11}$$

$$m = \cos(\theta_k) \;\text{ and }\; n = \sin(\theta_k)$$

In general, the fiber angle θ_k is different for each ply. Substituting the foregoing transformations (9) and (10) into (5) gives the general orthotropic lamina constitutive relation

$$\underline{\sigma} = \int_0^t \bar{\underline{\mathbf{G}}}(t-\tau)\,\frac{\partial \underline{\epsilon}}{\partial \tau}\,d\tau + \bar{\underline{\mathbf{C}}}\,\underline{\epsilon} \tag{12}$$

where the stress and strain vectors in the structural axes are

$$\underline{\sigma}^T = [\sigma_{xx} \;\; \sigma_{yy} \;\; \sigma_{xy}] \tag{13}$$

$$\underline{\epsilon}^T = [\epsilon_{xx} \;\; \epsilon_{yy} \;\; \gamma_{xy}] \tag{14}$$

and the entries of matrix $\bar{\underline{\mathbf{C}}}$ are given by

$$\begin{aligned} \bar{C}_{11} &= C_{11}m^4 + 2(C_{12}+2C_{66})m^2n^2 + C_{22}n^4 \\ \bar{C}_{22} &= C_{11}n^4 + 2(C_{12}+2C_{66})m^2n^2 + C_{22}m^4 \\ \bar{C}_{12} &= (C_{11}+C_{22}-4C_{66})m^2n^2 + C_{12}(m^4+n^4) \\ \bar{C}_{66} &= (C_{11}+C_{22}-2C_{12}-2C_{66})m^2n^2 + C_{66}(m^4+n^4) \\ \bar{C}_{16} &= (C_{11}-C_{12}-2C_{66})m^3n + (C_{12}-C_{22}+2C_{66})mn^3 \\ \bar{C}_{26} &= (C_{11}-C_{12}-2C_{66})mn^3 + (C_{12}-C_{22}+2C_{66})m^3n \end{aligned} \tag{15}$$

The entries of matrix $\bar{\underline{\mathbf{G}}}(t)$ are identical in form, with $\bar{G}_{ij}(t)$

Downloaded 03 May 2010 to 171.66.16.21. Redistribution subject to ASME license or copyright; see http://www.asme.org/terms/Terms_Use.cfm

replacing $\bar{C}_{ij}$ and $G_{ij}(t)$ replacing C_{ij}. It is observed that matrices $\underline{\bar{G}}(t)$ and $\underline{\bar{C}}$ are fully populated.

Stress vector can now be related to the displacement vector through the strain-displacement relation. The linear strain-displacement relation for a circular cylindrical shell of radius R, as shown in Fig. 3 (Langhaar, 1962) is

$$\underline{\epsilon} = \underline{\epsilon}^0 + z\,\underline{\kappa} \tag{16}$$

where

$$\underline{\epsilon}^{0T} = \left[\frac{\partial u^0}{\partial x} \quad \left(\frac{\partial v^0}{\partial y} + \frac{w}{R}\right) \quad \left(\frac{\partial u^0}{\partial y} + \frac{\partial v^0}{\partial x}\right)\right] \tag{17}$$

$$\underline{\kappa}^T = -\left[\frac{\partial^2 w}{\partial x^2} \quad \frac{\partial^2 w}{\partial y^2} \quad 2\frac{\partial^2 w}{\partial x \partial y}\right] \tag{18}$$

4 Laminate Constitutive Equations

The laminate constitutive equations can be obtained by summing over the laminae. Using (16) in (12), we obtain

$$\underline{\sigma}^{(k)} = \int_0^t \underline{\bar{G}}^{(k)}(t-\tau)\frac{\partial}{\partial \tau}[\underline{\epsilon}^0 + z\underline{\kappa}]^{(\kappa)} d\tau + \underline{\bar{C}}^{(k)}[\underline{\epsilon}^0 + z\underline{\kappa}]^{(k)} \tag{19}$$

The stress and moment resultants taken over M laminae can then be expressed as

$$\begin{bmatrix} N_{xx}(t) \\ N_{yy}(t) \\ N_{xy}(t) \\ \hline M_{xx}(t) \\ M_{yy}(t) \\ M_{xy}(t) \end{bmatrix} = \left[\begin{array}{c:c} \mathbf{A}(t) & \mathbf{B}(t) \\ \hdashline \mathbf{B}(t) & \mathbf{D}(t) \end{array}\right] \begin{bmatrix} \underline{\epsilon}^0 \\ \hline \underline{\kappa} \end{bmatrix} \tag{20}$$

where

$$\mathbf{A}(t) \triangleq \sum_{k=1}^{M} \left[\int_0^t \underline{\bar{G}}^{(k)}(t-\tau)\frac{\partial}{\partial \tau}(.)\,d\tau + \underline{\bar{C}}^{(k)}\right](h_k - h_{k-1}) \tag{21}$$

$$\mathbf{B}(t) \triangleq \frac{1}{2}\sum_{k=1}^{M} \left[\int_0^t \underline{\bar{G}}^{(k)}(t-\tau)\frac{\partial}{\partial \tau}(.)\,d\tau + \underline{\bar{C}}^{(k)}\right](h_k^2 - h_{k-1}^2) \tag{22}$$

$$\mathbf{D}(t) \triangleq \frac{1}{3}\sum_{k=1}^{M} \left[\int_0^t \underline{\bar{G}}^{(k)}(t-\tau)\frac{\partial}{\partial \tau}(.)\,d\tau + \underline{\bar{C}}^{(k)}\right](h_k^3 - h_{k-1}^3) \tag{23}$$

$\mathbf{A}(t)$, $\mathbf{B}(t)$ and $\mathbf{D}(t)$ are the membrane, coupling, and bending matrix-operators respectively. If all plies are assumed to obey Hooke's law, that is, when $\underline{G}(t) \equiv 0$, then the membrane, coupling and bending terms are no longer matrix operators, but simply the standard $\underline{\mathbf{A}}$, $\underline{\mathbf{B}}$ and $\underline{\mathbf{D}}$ matrices for composite materials.

5 Motion Equations

The motion equations for a thin laminated viscoelastic cylindrical shell, based on (20), is developed following the same procedure as in the case of elastic shells (Ashton and Whitney, 1970). The resulting equations are

$$\mathbf{A}_{11}\frac{\partial^2 u}{\partial x^2} + 2\mathbf{A}_{16}\frac{\partial^2 u}{\partial x \partial y} + \mathbf{A}_{66}\frac{\partial^2 u}{\partial y^2} + \mathbf{A}_{16}\frac{\partial^2 v}{\partial x^2} + (\mathbf{A}_{12} + \mathbf{A}_{66})\frac{\partial^2 v}{\partial x \partial y} + \mathbf{A}_{26}\frac{\partial^2 v}{\partial y^2} - \mathbf{B}_{11}\frac{\partial^3 w}{\partial x^3} - 3\mathbf{B}_{16}\frac{\partial^3 w}{\partial x^2 \partial y} - (\mathbf{B}_{12} + 2\mathbf{B}_{66})\frac{\partial^3 w}{\partial x \partial y^2} - \mathbf{B}_{26}\frac{\partial^3 w}{\partial y^3} + \frac{\mathbf{A}_{12}}{R}\frac{\partial w}{\partial x} + \frac{\mathbf{A}_{26}}{R}\frac{\partial w}{\partial y} = \rho\frac{\partial^2 u}{\partial t^2} \tag{24}$$

$$\mathbf{A}_{16}\frac{\partial^2 u}{\partial x^2} + (\mathbf{A}_{12} + \mathbf{A}_{66})\frac{\partial^2 u}{\partial x \partial y} + \mathbf{A}_{26}\frac{\partial^2 u}{\partial y^2} + \mathbf{A}_{66}\frac{\partial^2 v}{\partial x^2} + 2\mathbf{A}_{26}\frac{\partial^2 v}{\partial x \partial y} + \mathbf{A}_{22}\frac{\partial^2 v}{\partial y^2} - \mathbf{B}_{16}\frac{\partial^3 w}{\partial x^3} - (\mathbf{B}_{12} + 2\mathbf{B}_{66})\frac{\partial^3 w}{\partial x^2 \partial y} - 3\mathbf{B}_{26}\frac{\partial^3 w}{\partial x \partial y^2} - \mathbf{B}_{22}\frac{\partial^3 w}{\partial y^3} + \frac{\mathbf{A}_{26}}{R}\frac{\partial w}{\partial x} + \frac{\mathbf{A}_{22}}{R}\frac{\partial w}{\partial y} = \rho\frac{\partial^2 v}{\partial t^2} \tag{25}$$

$$\mathbf{D}_{11}\frac{\partial^4 w}{\partial x^4} + 4\mathbf{D}_{16}\frac{\partial^4 w}{\partial x^3 \partial y} + 2(\mathbf{D}_{12} + 2\mathbf{D}_{66})\frac{\partial^4 w}{\partial x^2 \partial y^2} + 4\mathbf{D}_{26}\frac{\partial^4 w}{\partial x \partial y^3} + \mathbf{D}_{22}\frac{\partial^4 w}{\partial y^4} - \mathbf{B}_{11}\frac{\partial^3 u}{\partial x^3} - 3\mathbf{B}_{16}\frac{\partial^3 u}{\partial x^2 \partial y} - (\mathbf{B}_{12} + 2\mathbf{B}_{66})\frac{\partial^3 u}{\partial x \partial y^2} - \mathbf{B}_{26}\frac{\partial^3 u}{\partial y^3} - \mathbf{B}_{16}\frac{\partial^3 v}{\partial x^3} - (\mathbf{B}_{12} + 2\mathbf{B}_{66})\frac{\partial^3 v}{\partial x^2 \partial y} - 3\mathbf{B}_{26}\frac{\partial^3 v}{\partial x \partial y^2} - \mathbf{B}_{22}\frac{\partial^3 v}{\partial y^3} - \frac{1}{R}\left(\mathbf{B}_{12}\frac{\partial^2 w}{\partial x^2} + 2\mathbf{B}_{26}\frac{\partial^2 w}{\partial x \partial y} + \mathbf{B}_{22}\frac{\partial^2 w}{\partial y^2}\right) + \rho\frac{\partial^2 w}{\partial t^2} = q \tag{26}$$

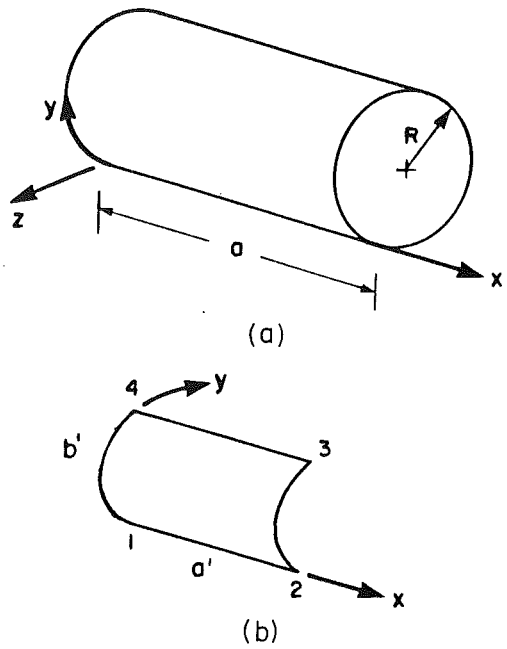


Fig. 3 Graphite-reinforced epoxy shell and cantilevered shell element

Downloaded 03 May 2010 to 171.66.16.21. Redistribution subject to ASME license or copyright; see http://www.asme.org/terms/Terms_Use.cfm

where q is the lateral pressure and ρ is the laminate density defined by

$$\rho \triangleq \sum_{k=1}^{M} \int_{h_{k-1}}^{h_k} \rho_0^{(k)} dz \tag{24}$$

Equations (24)–(26) are identical in form to those of laminated shells which obey the generalized Hooke's law, as can be seen by setting $G_{ij}(t) \equiv 0$, but now because of the definitions of **A**, **B** and **D**, (24)–(26) have the important embedded feature, namely, energy dissipation.

In order to obtain approximate solutions, these equations are discretized in space using the finite-element technique. Our approach was standard using bilinear Lagrange polynomial basis functions to model the spatial dependence of $u(x,y,t)$ and $v(x,y,t)$ while Hermite bicubics were used to model $w(x,y,t)$. The elements were therefore four noded rectangles with nodal degrees of freedom $(u_i, v_i, w_i, (w_x)_i, (w_y)_i, (w_{xy})_i)$ for the ith node. Complete details are presented in Buhariwala (1984).

Upon assembly of the element matrices, the resulting time-dependent equations are found to be integro-differential of the form

$$\underline{\mathbf{M}}\, \ddot{\underline{\mathbf{q}}}(t) + \int_0^t \underline{\mathbf{R}}(t-\tau) \frac{d\mathbf{q}(\tau)}{dt} d\tau + \underline{\mathbf{K}}\, \underline{\mathbf{q}}(t) = \underline{\mathbf{f}} \tag{28}$$

where $\underline{\mathbf{M}}$, $\underline{\mathbf{K}}$ are standard mass and stiffness matrices, $\underline{\mathbf{q}}$ is the vector of generalized coordinates (nodal degrees of freedom), $\underline{\mathbf{f}}$ is the forcing vector and $\underline{\mathbf{R}}(t)$ is the "damping" matrix.

The form of the damping matrix $\underline{\mathbf{R}}(t)$ as compared to the stiffness matrix $\underline{\mathbf{K}}$ is of considerable interest and importance for applications. It has been demonstrated (Buhariwala, 1984) that these matrices take the form

$$\underline{\mathbf{R}}(t) = \sum_{j=1}^{\alpha} \underline{\mathbf{R}}_j g_j(t) \tag{29}$$

and

$$\underline{\mathbf{K}} = \sum_{j=1}^{\alpha} \underline{\mathbf{K}}_j \tag{30}$$

where $\underline{\mathbf{R}}_j$ are constant matrices and

$$\underline{\mathbf{R}}_j \propto \underline{\mathbf{K}}_j, \quad j = 1, \alpha \tag{31}$$

Table 1 Decay distribution parameters

Distribution	α	β
Uniform	1.0	10^8
Cauchy	1.2	$\theta_0 = 0$
Normal	$\mu = 8$	$\sigma = 0.1$
Beta	4.2	3.6
Gamma	0.2	3.5
Exponential	0.01	–
Weibull	0.01	1.4
Maxwell	3.0	–

while $g_j(t)$ are time-varying scalar functions which depend on the material properties of the system.

The upper limit "α" in the summations (29) and (30) depends on system geometry and laminate considerations. For example:

$\alpha = 36$	for the general cylindrical shell laminate
$\alpha = 21$	symmetric, cylindrical shell laminate
$\alpha = 15$	balanced, symmetric, cylindrical shell laminate
$\alpha = 12$	balanced, symmetric flat laminate

The proportionality of $\underline{\mathbf{R}}_j$ and $\underline{\mathbf{K}}_j$ is useful from a finite-element point of view as it implies that the same computational algorithm can be applied to both. Thus an existing computer code which has been developed for a purely elastic structure ($\underline{\mathbf{M}}$, $\underline{\mathbf{K}}$ system) can be modified easily for the analysis of the corresponding viscoelastic structure ($\underline{\mathbf{M}}$, $\underline{\mathbf{R}}(t)$, $\underline{\mathbf{K}}$ system). However it should be noted that the aforementioned does not imply that $\underline{\mathbf{R}}(t)$ and $\underline{\mathbf{K}}$ are proportional as $\underline{\mathbf{R}}(t)$ has the inherent time-dependence defined by the $g_j(t)$. For example, $\underline{\mathbf{R}}(t)$ tends to zero for large time. The only aspect which remains to be specified is the material decay distribution function $\gamma(\theta)$ which is implicit in the $g_j(t)$.

6 Numerical Example

In this section, we calculate the eigenvalues of a graphite-epoxy composite shell element using Jacobi's root perturbation method. The development of this method for the viscoelastic problem is presented in Buhariwala (1984) as an extension of the work by Aubrun (1980). The discretized motion equation takes the form of (28) where, for the present geometry and laminate

$$\underline{\mathbf{R}}(t) = \sum_{i=1}^{15} \underline{\mathbf{R}}_i\, g_i(t) \tag{32}$$

The corresponding eigenproblem is

$$(p^2\underline{\mathbf{M}} + p\tilde{\underline{\mathbf{R}}}(p) + \underline{\mathbf{K}})\underline{\nu} = \underline{0} \tag{33}$$

The eigenvalues using the Jacobi root perturbation method are calculated for the following geometrical and material parameters

$$\begin{aligned} a' &= 0.254 \text{ m} && \text{(10 in.) axial length} \\ b' &= 0.239 \text{ m} && \text{(9.4 in.) circumferential length} \\ R &= 0.154 \text{ m} && \text{(6 in.) radius} \\ h &= 5.08 \times 10^{-4} \text{ m} && \text{(0.02 in.) laminate thickness} \\ \rho &= 1605 \text{ kg/m}^3 && \text{(0.058 lbs/in.}^3\text{) laminate density} \end{aligned} \tag{34}$$

for a balanced symmetric $(+\theta, -\theta)_s$ laminate with edge 1-4 fixed; see Fig. 3(*b*). The parameters chosen for the decay distribution functions $\gamma(\theta)$ are given in Table 1.

Smith (1981) has determined $C_{ij}^{(s)}$ and C_{ij} for several relaxation constants ρ for an othotropic graphite-reinforced epoxy. These coefficients are tabulated in Table 2. From these data, the functional relationship $C_{ij}^{*}(\theta)$ can be obtained by performing a least-squares fit to log $C_{ij}^{(s)}$ and log ρ_s for $\rho_s = 25$, 250, 2500, 2.5×10^4 and 2.5×10^5. This gives the variation in the norm of real part of the eigenvalues

Table 2 $C_{ij} = 10^b\, \rho^m$, $\theta = 1/\rho$

	C_{11}	C_{22}	C_{12}	C_{66}	Pa. (Psi)
y intercept, b	7.26416 (3.42567)	7.93455 (3.78942)	6.91463 (3.07607)	7.54510 (3.70658)	
Slope, m	0.082126 (0.082136)	0.086329 (0.086329)	0.14194 (0.104212)	0.071959 (0.071964)	
Correlation coefficient	0.8558	0.8143	0.5907	0.9377	

Downloaded 03 May 2010 to 171.66.16.21. Redistribution subject to ASME license or copyright; see http://www.asme.org/terms/Terms_Use.cfm

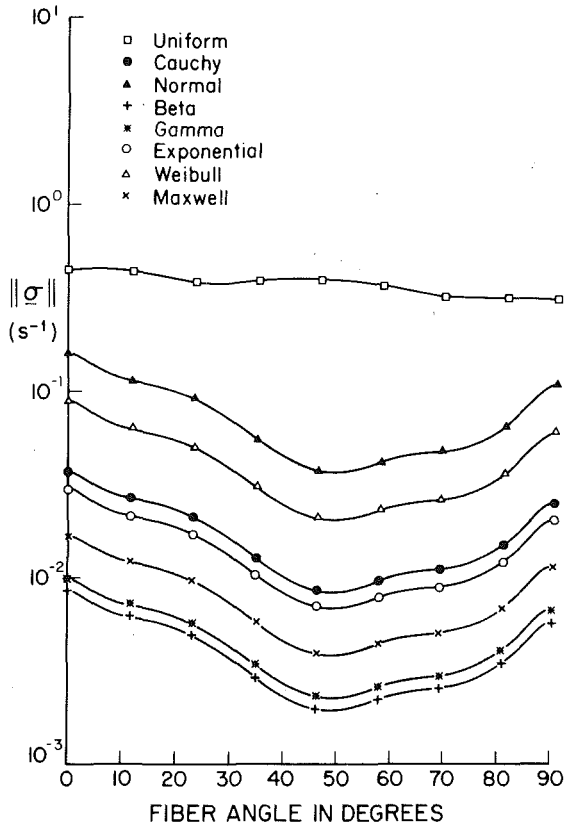


Fig. 4 Plot of the norm of the real part of the eigenvalue versus fiber angle for various distributions

$$\|\underline{\sigma}\| = \left(2\sum_{i=1}^{12} \underline{\sigma}_i^2\right)^{1/2} \tag{35}$$

as a function of the fiber angle θ is shown in Fig. 4. All distributions except the uniform distribution exhibit the same functional relationship and vary over three cycles of the logarithmic scale. A plot $\|\underline{\sigma}\|$ versus fiber angle would be useful to a designer, as one could incorporate the optimal damping characteristic in a structure. Of course, a more general optimization would involve maximizing $\|\sigma\|$ over the fiber angles $\theta_1, \theta_2, \ldots, \theta_M$ associated with each of the plies in a laminate.

7 Conclusion

We have demonstrated explicitly an algorithm for constructing a material damping matrix using the finite-element method. The assumptions made in the formulation of the damping matrix are: (1) The material is viscoelastic; (2) The stress-strain and strain-displacement relations are linear. The damping matrix is constructed in a manner analogous to the stiffness matrix; thus an existing computer code, which analyzes an elastic structure, can be easily modified to analyze a corresponding viscoelastic structure. The motion equations are no longer differential, but rather integro-differential in form, as depicted in the flowchart, Fig. 5.

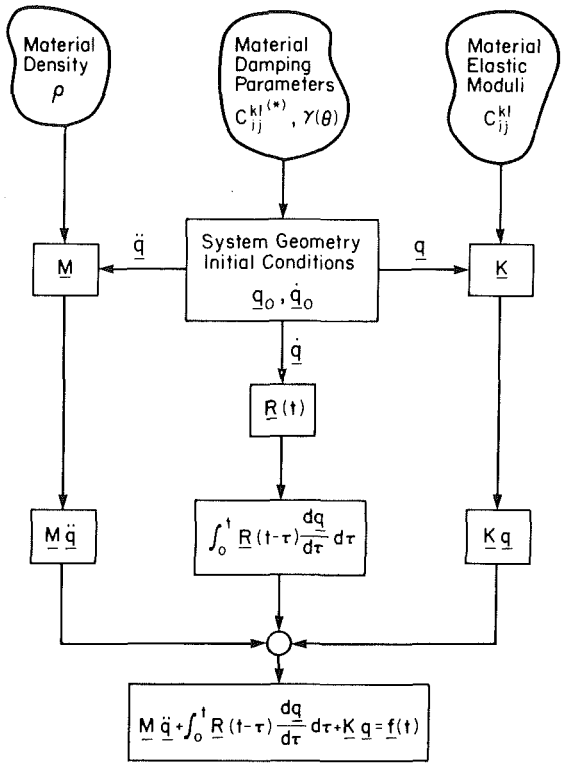


Fig. 5 Flowchart for a dynamical viscoelastic model (compare with Fig. 1)

References

Ashton, J. E., Halpin, J. C., and Petit, P. H., 1969, *Primer on Composite Materials: Analysis*, Technomic Publication, p. 19.

Ashton, J. E., and Whitney, J. M., 1970, *Theory of Laminated Plates*; Progress in Materials Science Series, Vol. IV, Technomic Publishing Co., Inc.

Aubrun, J. N., 1980, "Theory of the Control of Structures by Low Authority Controllers," ASME *Journal of Guidance and Control*, Vol. 3, No. 5, pp. 444-451.

Buhariwala, K. J., 1984, "Dynamics of Viscoelastic Structures," PhD thesis, Institute for Aerospace Studies, University of Toronto, Toronto, Ontario, Canada.

Caravani, P., and Thompson, W. T., 1974, "Identification of Damping Coefficients in Multidimensional Linear Systems," ASME JOURNAL OF APPLIED MECHANICS, Vol. 41, No. 2, pp. 379-382.

Caravani, P., Watson, M. L., and Thompson, W. T., 1977, "Recursive Least-Squares Time Domain Identification of Structural Parameters," ASME JOURNAL OF APPLIED MECHANICS, Vol. 44, No. 1, pp. 135-140.

Hanagud, S., Meyyappa, M., Cheng, Y. P., and Craig, J. I., 1984, "Identification of Structural Dynamic Systems with Nonproportional Damping," *AIAA/ASME/ASCE/AHS 25th Structures, Structural Dynamics and Materials Conference, Proceedings*, Part 2, pp. 283-291.

Ibrahim, S. R., "Dynamic Modeling of Structures from Measured Complex Modes," *AIAA/ASME/ASCE/AHS 23rd Structures, Structural Dynamics and Materials Conference, New Orleans, LA, Proceedings*, Part 2, pp. 564-573.

Langhaar, H. L., 1962, *Energy Methods in Applied Mechanics*, John Wiley and Sons, Inc.

Smith, B. A. W., 1981, "Polymer Matrix Composite Materials in Simulated Space Environment: Ultraviolet and Vacuum Effects," MASc thesis, Institute for Aerospace Studies, University of Toronto, Ontario, Canada.

Zienkiewicz, O. C., 1977, *The Finite Element Method*, 3rd Ed., McGraw-Hill Book Co., London, England.

Downloaded 03 May 2010 to 171.66.16.21. Redistribution subject to ASME license or copyright; see http://www.asme.org/terms/Terms_Use.cfm

R. Subbiah
Project Engineer,
Stress Technology, Inc.,
Rochester, NY 14623
Mem. ASME

A. S. Kumar
Postdoctoral Fellow.

T. S. Sankar
Professor.
Mem. ASME

Department of Mechanical Engineering,
Concordia University,
Montreal, Canada, H3G 1M8

Transient Dynamic Analysis of Rotors Using the Combined Methodologies of Finite Elements and Transfer Matrix

A new approach is proposed to predict the dynamic behavior of rotor-bearing systems in time domain using the combined methodologies of finite elements and transfer matrices. This approach makes use of the finite element method to model symmetric shafts and then transforms the system properties to transfer matrix mode. The formulation provides flexibility to include both linear and nonlinear system models, often encountered in rotor dynamic applications. Few example rotor cases had been studied and the results were compared with those obtained using finite element method. This establishes that considerable savings in computational effort can be achieved without losing any accuracy.

Introduction

Transfer matrix approach had been adopted by many researchers in the past (Lund, 1974; Rao, 1983) to solve rotor-dynamic problems in the frequency domain. While this approach is adequate to study the steady state behavior of the rotor, sometimes, it is important to obtain the information concerning the instantaneous behavior of the subsystems, especially for those regions close to the rotor instability condition. Under this situation, a time domain approach will be most appropriate to obtain the system informations precisely. Towards this, a combined time domain finite element transfer matrix method, namely Transient Property Transfer Approach (TPTA), is introduced here.

At the current state of rotor dynamic technology, the finite element method (FEM) is the only validated tool available for nonlinear time domain analysis (Ruhl et al., 1972; Nelson et al., 1976). For large rotor systems, however, the use of finite element method leads to prohibitively higher computation time and costs. In order to minimize this, a continuing effort is made by various researchers to limit the dynamic degrees of freedom without reducing the accuracy of the results. Of these, the combined finite element transfer matrix technique introduced by Dokainish (1972) is of importance since it results in an exact condensation of matrix size without any loss of accuracy. In recent years, other researchers (Chiatti et al., 1979; Mucino et al., 1981; Ohga et al., 1983; Degan et al., 1985) have improved and generalized this methodology for other applications. Inspite of this, because of the nature of transfer matrix relations used in the formulation, the use of this combined methodology is still limited to linear frequency domain analysis only. Moreover, a rotor system supported on hydrodynamic bearings is nonconservative, nonsymmetric, and possibly nonlinear due to the asymmetric cross coupled stiffness and damping properties of the oil film bearings. Thus, the Dokainish's combined finite element transfer matrix methodology, as it is, cannot be directly used for rotor-dynamic applications. Under these circumstances, it will be more appropriate to develop a combined finite element transfer matrix method.

In this respect the Discrete Time Transfer Matrix Method (DT-TMM), introduced recently by Kumar et al. (1986) for general structural dynamics response calculations, is of importance. They showed that with the use of appropriate time marching numerical integration algorithms, the application of transfer matrix methods can be extended to time domain and nonlinear analysis of dynamic systems. Following this, Subbiah et al. (1987) applied this method for transient nonlinear rotor dynamic applications and found that even for a simple rotor system the response results obtained using finite element method and discrete time transfer matrix method showed little discrepancy. The reason for such discrepancy can be attributed to the fact that the transfer matrix model for a shaft section is formulated using cantilever beam theory whereas the finite element model is developed with consistent property of the system (Archer, 1963). This observation led to the development of the present work wherein, following the strategy used by Dokainish, the finite element methodology and discrete time transfer matrix methodology are combined. This formulation provides flexibility to include both linear and nonlinear system models, often encountered in rotor-dynamic applications.

In the following sections the formulation of the proposed

Contributed by the Applied Mechanics Division for publication in the JOURNAL OF APPLIED MECHANICS.

Discussion on this paper should be addressed to the Editorial Department, ASME, United Engineering Center, 345 East 47th Street, New York, NY 10017, and will be accepted until two months after final publication of the paper itself in the JOURNAL OF APPLIED MECHANICS. Manuscript received by ASME Applied Mechanics Division, June 29, 1987; final revision, November 13, 1987.

Copyright © 1988 by ASME
Downloaded 03 May 2010 to 171.66.16.21. Redistribution subject to ASME license or copyright; see http://www.asme.org/terms/Terms_Use.cfm

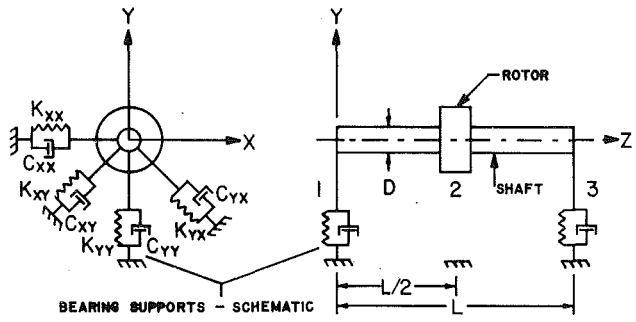


Fig. 1 Model rotor system

combined methodology is first presented. A comparison of the response results obtained using the proposed method with those obtained using finite element method is also carried out to establish the validity of the method.

Theory

Finite Element Formulation. Consider the three station rotor model which is discretized into shaft, disk and bearing elements as shown in Fig. 1. Based on this finite element model the matrix equations of motion for the element 1 with nodes 1 and 2 can be written as (Nelson et al., 1976):

$$[M^e]\{\ddot{q}(t)\}+[C^e]\{\dot{q}(t)\}+[K^e]\{q(t)\}=\{F(t)\} \tag{1}$$

where M^e, C^e and K^e are the element mass, damping and stiffness matrices (8×8), respectively, and are defined as,

$$M^e=\begin{bmatrix} m_{11} & m_{12} \\ m_{21} & m_{22} \end{bmatrix} \quad C^e=\begin{bmatrix} c_{11} & c_{12} \\ c_{21} & c_{22} \end{bmatrix} \quad K^e=\begin{bmatrix} k_{11} & k_{12} \\ k_{21} & k_{22} \end{bmatrix}$$

and the generlized force and displacement vectors (8×1) are given by

$$\{F(t)\}=\{f_1\,|f_2\}^T,$$

and

$$\{q(t)\}=\{x_1,\theta_1,y_1,\phi_1\,|x_2,\theta_2,y_2,\phi_2\}^T.$$

Similarly, the matrix equations of motion for all the elements in the model, including the point elements at unbalance locations, bearing locations, etc., can be derived. In the conventional finite element method these component element equations of motions are assembled into a large global matrix equation of motion which is then solved using any suitable time marching integration scheme.

Discrete Time Transfer Matrix Method Formulation. The DT-TMM (Kumar et al., 1986) is based on the assumption that at any given time instant, say, t_i, the acceleration and velocity in any given degree of freedom, say, q_n of subsystem n, can be expressed as a linear function of the displacement q_n with reasonable accuracy. That is,

$$\ddot{q}_n(t_i)=A_n(t_i)q_n(t_i)+B_n(t_i) \tag{2}$$

$$\dot{q}_n(t_i)=D_n(t_i)q_n(t_i)+E_n(t_i) \tag{3}$$

Derivation of these types of relationships can generally be carried out based on truncated Taylor series as given below.

The starting point for most of the numerical integration schemes used in structural response analysis is the truncated Taylor series of order 3. That is,

$$q_n(t_i)=q_n(t_{i-1})+\Delta T\dot{q}_n(t_{i-1})+\frac{\Delta T^2}{2}\ddot{q}_n(t_{i-1})+\frac{\Delta T^3}{6}\dddot{q}_n(t_{i-1}) \tag{4}$$

where interval $\Delta T = (t_i - t_{i-1})$. Different integration schemes with varying sophistication and accuracy are then derived by replacing the derivatives in equation (4) by finite differences. Here, one of the simplest finite difference schemes available is chosen to explain the methodology. In addition, it is assumed that the acceleration is constant during the time interval $(t_i - t_{i-1})$ and is equal to the average of the acceleration values at t_i and t_{i-1}. Thus,

$$\ddot{q}_n=a=\frac{\ddot{q}_n(t_i)+\ddot{q}_n(t_{i-1})}{2} \tag{5}$$

$$\dddot{q}_n=0 \tag{6}$$

$$\dot{q}_n=a\Delta T=\frac{\ddot{q}_n(t_i)+\ddot{q}_n(t_{i-1})}{2}\Delta T \tag{7}$$

Substitution of these relationships into equation (4) results in,

$$q_n(t_i)=q_n(t_{i-1})+\Delta T\dot{q}_n(t_{i-1})+\Delta T^2\frac{\ddot{q}_n(t_i)+\ddot{q}_n(t_{i-1})}{4} \tag{8}$$

which can be rewritten in the form equation (2), as,

$$\ddot{q}_n(t_i)=A_n(t_i)q_n(t_i)+B_n(t_i) \tag{9}$$

where

$$A_n(t_i)=\frac{4}{\Delta T^2} \tag{10}$$

and

$$B_n(t_i)=-A_n(t_i)\left[q_n(t_{i-1})+\Delta T\dot{q}_n(t_{i-1})+\frac{\Delta T^2}{4}\ddot{q}_n(t_{i-1})\right] \tag{11}$$

Similarly, by substituting equation (9) into equation (7), it can be rewritten in the form of equation (3), as,

$$\dot{q}_n(t_i)=D_n(t_i)q_n(t_i)+E_n(t_i) \tag{12}$$

where

$$D_n(t_i)=\frac{2}{\Delta T} \tag{13}$$

and

$$E_n(t_i)=-D_n(t_i)\left[q_n(t_{i-1})+\frac{\Delta T}{2}\dot{q}_n(t_{i-1})\right] \tag{14}$$

From equations (10), (11), (13), and (14), it can be seen that the coefficients $A_n(t_i)$, $B_n(t_i)$, $D_n(t_i)$, and $E_n(t_i)$ are all functions of the system properties at time t_i, and the response quantities $q_n(t_{i-1})$, $\dot{q}_n(t_{i-1})$, and $\ddot{q}_n(t_{i-1})$ at the previous time instant which are all known at time instant t_i. Thus, the coefficients $A_n(t_i)$, $B_n(t_i)$, $D_n(t_i)$, and $E_n(t_i)$ are all definable for any subsystem n for the time interval $(t_i - t_{i-1})$. It should be noted that the simple finite difference scheme and the constant average acceleration assumption used here in the formulation are only for explanatory purposes. Instead, any of the many more accurate and commonly available numerical integration procedures can be used.

The coefficients A_n, B_n, D_n, and E_n for various commonly used integrating procedures are tabulated by Kumar et al., (1986). They developed and employed this technique to replace the time derivative quantities in the subsystem equations of motion. The resulting relationships were then rewritten as transfer relations leading to discrete time transfer matrix of each subsytem. Then, following the conventional transfer matrix solution procedure, they computed the overall transfer matrix and solved for the unknown state vector quantities by applying the proper boundary conditions. For details refer to Kumar et al., (1986). This novel approach led to the development of a useful transient analysis tool for large dynamic systems. However, subsequent application of this technique to rotor dynamic analysis (Subbiah et al., 1987) showed that the lumped parameter characteristics and the massless cantilever beam theory used in this formulation led to some errors in response calculations. In order to eliminate this source of error the following methodology is proposed.

Downloaded 03 May 2010 to 171.66.16.21. Redistribution subject to ASME license or copyright; see http://www.asme.org/terms/Terms_Use.cfm

Transient Property Transfer Approach (TPTA) Formulation. The formulation of TPTA, as given below, combines the finite element formulation and the discrete time transfer matrix formulation. Consider the element matrix equation of motion given by the equation (1) at time $t = t_i$.

$$[M^e]\{\ddot{q}(t_i)\} + [C^e]\{\dot{q}(t_i)\} + [K^e]\{q(t_i)\} = \{F(t_i)\} \quad (15)$$

Substitution of the equations (2) and (3) into equation (15) will result in,

$$[M^e]\{A_n(t_i)q_n(t_i) + B_n(t_i)\} + [C^e]\{D_n(t_i)q_n(t_i) + E_n(t_i)\} + [K^e]\{q(t_i)\} = \{F(t_i)\} \quad (16)$$

or

$$[[M^e]A_n(t_i) + [C^e]D_n(t_i) + [K^e]]\{q_n(t_i)\} + [M^e]\{B_n(t_i)\} + [C^e]\{E_n(t_i)\} = \{F(t_i)\} \quad (17)$$

Expansion of this equation in terms of submatrices gives,

$$\begin{bmatrix} K_{11} & K_{12} & v_1 \\ K_{21} & K_{22} & v_2 \\ 0 & 0 & 1 \end{bmatrix} \begin{Bmatrix} q_1 \\ q_2 \\ 1 \end{Bmatrix} = \begin{Bmatrix} f_1 \\ f_2 \\ 1 \end{Bmatrix} \quad (18)$$

where,

$$K_{11} = m_{11}A_n + c_{11}D_n + k_{11}$$
$$K_{12} = m_{12}A_n + c_{12}D_n + k_{12}$$
$$K_{21} = m_{21}A_n + c_{21}D_n + k_{21}$$
$$K_{22} = m_{22}A_n + c_{22}D_n + k_{22}$$
$$v_1 = m_{11}B_1 + m_{12}B_2 + c_{11}E_1 + c_{12}E_2$$
$$v_2 = m_{21}B_1 + m_{22}B_2 + c_{21}E_1 + c_{22}E_2.$$

Equation (18) can then be rewritten in terms of left and right nodal displacements and forces such that,

$$\begin{Bmatrix} q_2 \\ f_2 \\ 1 \end{Bmatrix} = \begin{bmatrix} -K_{12}^{-1}K_{11} & K_{12}^{-1} & s_1 \\ K_{21} - K_{22}K_{12}^{-1}K_{11} & K_{22}K_{12}^{-1} & s_2 \\ 0 & 0 & 1 \end{bmatrix} \begin{Bmatrix} q_1 \\ f_1 \\ 1 \end{Bmatrix} \quad (19)$$

where

$$s_1 = -K_{12}^{-1}(m_{11}B_1 + m_{12}B_2 + c_{11}E_1 + c_{12}E_2)$$
$$s_2 = -K_{22}K_{12}^{-1}(m_{11}B_1 + m_{12}B_2 + c_{11}E_1 + c_{12}E_2) + m_{21}B_1 + m_{22}B_2 + c_{21}E_1 + c_{22}E_2$$

or

$$\{u\}_2^L = [S]\{u\}_1^R \quad (20)$$

Thus, for an uniform shaft element with nodes 1 and 2, the matrix $[S]$ in equation (20) gives the transfer matrix and vector $\{u\}$ gives the state vector. Similarly, starting from point element equations of motion, the following point element transfer matrix relation can be derived, such that,

$$\{u\}_1^R = [P]\{u\}_1^L. \quad (21)$$

The transfer matrix $[T]$ for a general rotor-bearing finite element can then be formulated by combining equations (20) and (21). That is,

$$\{u\}_2^L = [T]\{u\}_1^L \quad (22)$$

where

$$[T] = [S][P].$$

Repetitive application of the transfer matrix relation (22) results in the following transfer relation for the entire rotor-bearing system:

$$\{u\}_n^L = [T]_n[T]_{n-1} \ldots\ldots [T]_2[T]_1\{u\}_1^L \quad (23)$$

With the application of proper boundary conditions and the initial conditions corresponding to time $t = t_{i-1}$, the unknown generalized displacements and forces at the left end of the rotor can be solved for. Knowing this, at time $t = t_i$, the displacements at all the subsequent nodes can be obtained with the use of the equation (23). The nodal displacements at subsequent time instants (i.e., $t = t_{i+1}$ onwards) can be solved for by repetitively following the same steps.

In the foregoing formulation, the model has been obtained by the transfer system properties and hence this approach is named as transient property transfer approach (TPTA). Equations (18) and (19) correspond to Dokainish's (1972) frequency domain finite element transfer matrix formulation.

It should be noted that , as with the discrete time transfer matrix formulation, the TPTA can be used with any suitable time marching integration scheme which can be rewritten in the form of equations (2) and (3). In this study, the well known Houbolt's algorithm is used. This selection is based on the detailed sensitivity tests carried out by Subbiah et al., (1987). They tested different time marching algorithms (Bathe et al., 1976; Kumar et al., 1986) with different rotor configurations and concluded that for rotor dynamic applications the Houbolt's algorithm provides required high stability and rapid convergence even with a time step of ΔT = period/30.

Table 1 Details of the rotor-bearing system shown in Fig. 1

Type of bearings	Plain cylindrical
Bearing diameter (m)	0.0254
Bearing L/D ratio	1.0
Viscosity of oil at 25.5 degree C (N.s/m^2)	0.024
Disk mass (kg)	11.82
Disk diameter (m)	0.2032
Disk eccentricity (m)	0.001
Shaft diameter (m)	0.022
Total length of rotor (m)	0.5105
Modulus of elasticity for the shaft material (N/m^2)	2.145×10^{11}

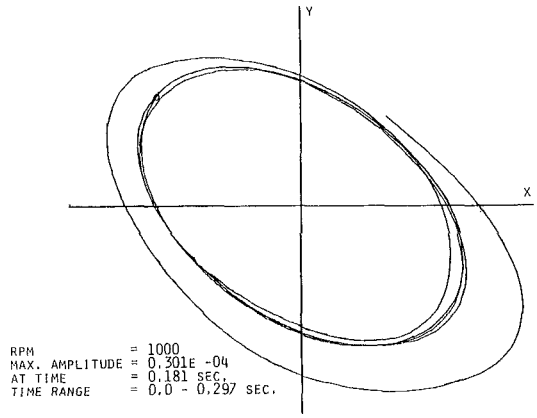


Fig. 2 Orbital response of rotor at bearing location (TPTA)

Results and Discussion

The TPTA has been used to study the dynamic response of a single rotor system supported on fluid film bearing which is shown in Fig. 1. The details of the rotor are given in Table 1. The transient orbital response obtained by the present investigation has been compared with those obtained using finite element method. In all the test cases considered, the number of elements, the type of elements, and the time step used are all kept the same for both the TPTA and the finite element approach. And as mentioned earlier, Houbolt's method is employed here as the integrating procedure. Coincidentally, the finite element code used, namely ANSYS, also employs Houbolt's method for integration. The initial conditions required to start the analysis are obtained using $A_n = -\omega^2$, and $B_n = D_n = E_n = 0$. This helps to reach steady state condi-

Downloaded 03 May 2010 to 171.66.16.21. Redistribution subject to ASME license or copyright; see http://www.asme.org/terms/Terms_Use.cfm

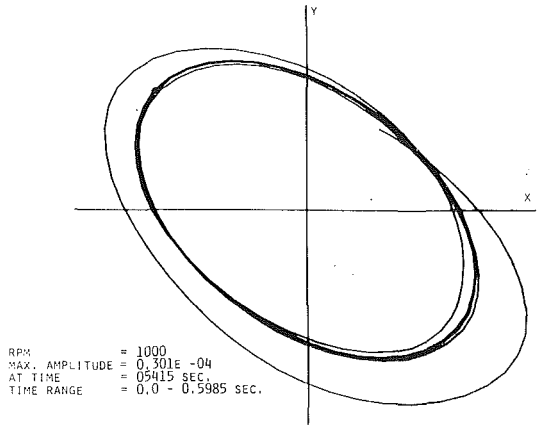


Fig. 3 Orbital response of rotor at bearing location (FEM)

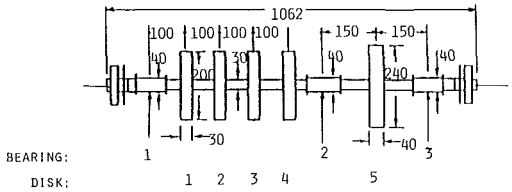


Fig. 4 Five-disk and three-bearing rotor (Kikuchi, 1970)

tions fast, resulting in considerable savings in computation time.

The orbital plots obtained for the rotor, using the present method and the finite element method, are shown in Figs. 2 and 3 for a rotor speed of 1000 rpm. The steady state of the rotor has been obtained within 5 cycles in both the cases. The discrepancy between these two results is almost negligible. In order to demonstrate the applicability of this approach to multi-span rotor-bearing system analysis, the multi rotor model of Kikuchi (1970) has been studied using the present approach. This rotor system consists of five disks and three bearings as shown in Fig. 4. The results obtained for this rotor using TPTA and finite element approach shows negligible discrepancy. Hence, only one such orbital plot obtained by TPTA is shown in Fig. 5. Finally, the nonlinear bearing model developed by Hashish et al. (1982a, 1982b), has been adapted to study dynamic response of the single rotor system shown in Fig. 1 and the nonlinear orbital response is shown in Fig. 6. For small amplitude motions, the total orbital amplitude in Fig. 6 closely corresponds to the linear result as shown already in Fig. 2.

The computational efficiency of TPTA is not appreciable in comparison with finite element approach when smaller rotor systems were studied. However, in the case of larger systems, the TPTA will lead to smaller computational effort. For example, in the case of Kikuchi's rotor, the computational time on a PRIME 950 comptuer was worked out to be 5.37 CPU minutes for TPTA and 7.35 CPU minutes for FEM.

Conclusions

1 A transient property transfer approach has been developed to study the linear and nonlinear dynamic behavior of complex rotor-bearing systems in both space and time using the combined methodologies of FEM, transfer matrix method and time marching numerical integration techniques.
2 The method presented in this investigation is capable of accommodating other subsystems such as pedestals, foundations, and mechanical couplings, etc.

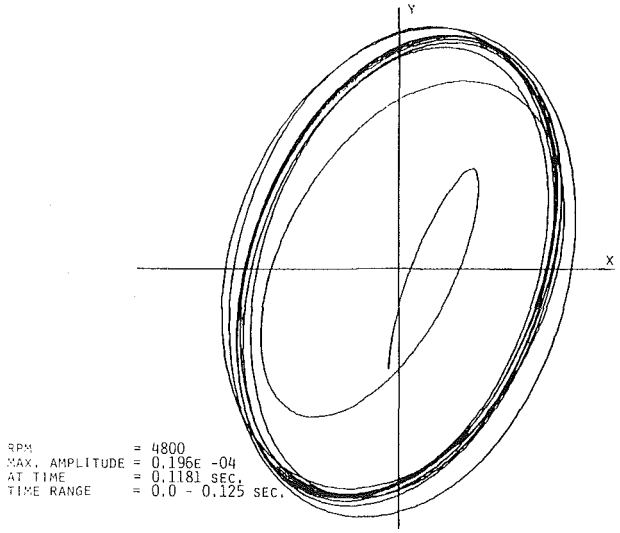


Fig. 5 Orbital response of Kikuchi rotor at disk location #4 (TPTA)

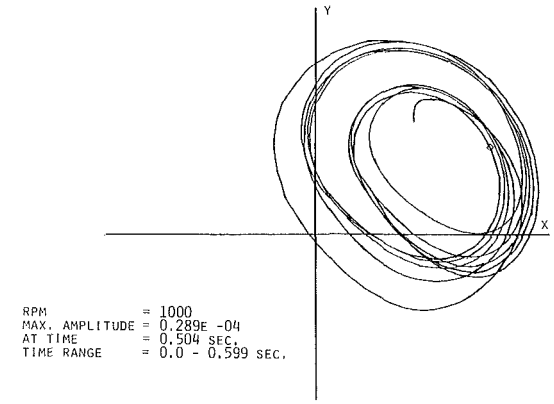


Fig. 6 Nonlinear orbital response of rotor at bearing location (TPTA)

3 The gyroscopic effects can be easily included in the model. System nonlinearities due to asymmetric shafts, nonlinear bearings and random pedestal motions can be studied by including their effects appropriately in the system model.
4 The method not only provides an excellent correlation with the finite element method, but also handles small and manageable forms of matrices and, hence, the computer effort is reduced to the largest extent possible.

Acknowledgments

The authors would like to thank STI for providing computer facilities to run a few test cases for the present investigation. The encouragement given by Dr. N. F. Rieger during the course of this investigation is appreciated and duly acknowledged.

References

Archer, J. S., 1963, "Consistent Mass Matrix of Distributed Mass Systems," *Proceedings of the ASCE, Journal of Structual Division*, Vol. 89, ST4, p. 161.

Bathe, K. J., and Wilson, E. L., 1976, *Numerical Methods in Finite Element Analysis*, Prentice-Hall, Englewood Cliffs, New Jersey.

Chiatti, G., and Sestieri, A., 1979, "Analysis of Static and Dynamic Structural Problems by a Combined Finite Element-Transfer Matrix Method," *Journal of Sound and Vibration*, Vol. 67, No. 1, pp. 35–42.

Degen, E. E., Shephard, M. S., and Loewy, R. G., 1985, "Combined Finite Element Transfer-Matrix Method Based on a Mixed Formulation," *Computers and Structures*, Vol. 20, pp. 173–180.

Dokainish, M. A., 1972, "A New Approach for Plate Vibrations: Combina-

Downloaded 03 May 2010 to 171.66.16.21. Redistribution subject to ASME license or copyright; see http://www.asme.org/terms/Terms_Use.cfm

tion of Transfer Matrix and Finite-Element Technique," ASME *Journal of Engineering for Industry*, Vol. 94, pp. 526–530.

Hashish, E., Sankar, T. S., and Osman, M. O. M., 1982a, "Finite Journal Bearing with Nonlinear Stiffness and Damping – Part I: Improved Mathematical Models," ASME *Journal of Mechanical Design*, Vol. 104, No. 2, pp. 397–405.

Hashish, E., Sankar, T. S., and Osman, M. O. M., 1982b, "Finite Journal Bearing with Nonlinear Stiffness and Damping – Part II: Stability Analysis," ASME *Journal of Mechanical Design*, Vol. 104, No. 2, pp. 406–411.

Kikuchi, K., 1970, "Analysis of Unbalance Vibration of Rotating Shaft System with Many Bearings and Disks," *Bulletin of JSME*, Vol. 13, No. 61, pp. 864–872.

Kumar A. Selva, and Sankar, T. S., 1986, "A New Transfer Matrix Method for Response Analysis of Large Dynamic Systems," *Computers and Structures*, Vol. 23, No. 4, pp. 545–552.

Lund, J. W., 1974, "Stability and Damped Critical Speeds of a Flexible Rotor in Fluid Film Bearings," ASME *Journal of Engineering for Industry*, Vol. 96, pp. 509–517.

Mucino, V. H., and Pavelic, V., 1981, "An Exact Condensation Procedure for Chain-like Structures Using a Finite Element-Transfer Matrix Approach," ASME *Journal of Mechanical Design*, Vol. 103, pp. 295–303.

Nelson, H. D., and McVaugh, J. M., 1976, "The Dynamics of Rotor-Bearing Systems Using Finite Elements," ASME *Journal of Engineering for Industry*, Vol. 98, pp. 593–600.

Ohga, M., Shigematsu, T., and Hara, T., 1983, "Structural Analysis by a Combined Finite Element-Transfer Matrix Method," *Computers and Structures*, Vol. 17, No. 3, pp. 321–326.

Rao, J. S., 1983, *Rotor Dynamics*, Wiley Eastern Ltd., New Delhi.

Ruhl, R. L., and Booker, J. F., 1972, "A Finite Element Model for Distributed Parameters Turborotor Systems," ASME *Journal of Engineering for Industry*, Vol. 94, pp. 126–132.

Subbiah, R., and Rieger, N. F., 1987, "On the Transient Analysis of Rotor-Bearing Systems," *Proc. of Rotating Machinery Dynamics*, Vol. II, pp. 525–536. Also accepted for publication in the ASME *Journal of Vibration, Acoustics, Stress, and Reliability in Design*.

Downloaded 03 May 2010 to 171.66.16.21. Redistribution subject to ASME license or copyright; see http://www.asme.org/terms/Terms_Use.cfm

A Fast Eigenfunction Approach for Computing Spinning Disk Deflections

Kevin A. Cole
Magnetic Recording Systems,
Eastman Kodak Company,
Rochester, NY 14621

Richard C. Benson
Associate Professor,
Department of Mechanical Engineering,
University of Rochester,
Rochester, NY 14627
Mem. ASME

Due to a complicated spectrum of natural modes of vibration, flexible spinning disks are very sensitive to transverse loading, and deflections have been difficult to compute. Developed in this paper is an efficient technique for determining the forced response from space fixed loads. Using an eigenfunction expansion, we are able to identify, a priori, *those modes which are most important to the overall response. By ignoring unimportant modes we are able to coverge upon a numerical solution with a speed that is orders of magnitude faster than other commonly used techniques.*

Introduction

Current computer applications make widespread use of "floppy-disk" drive units. Disks used in these systems deform easily when subjected to transverse loads and their behavior under these conditions must be understood to facilitate proper design.

The literature on flexible spinning disks is extensive. In an early study, Lamb and Southwell (1921) examined the frequencies and modes of free vibration for a complete disk. Both bending stresses and in-plane stresses due to rotation were considered. Later, Eversman and Dodson (1969) investigated the same problem with an interior clamp. Correlation to the earlier work in limiting cases was shown to be excellent.

More recently, the near-membrane case has been studied by Benson and Bogy (1978, 1983). In these papers, an arbitrarily positioned transverse load was applied to the flexible spinning disk. It was shown through an eigenvalue study that a membrane cannot in general support an arbitrary load. Thus it was concluded that bending terms are required in the governing differential equation if steady-state solutions are to be obtained. Further work was directed toward developing methods for solving the resulting highly sensitive equations.

Work of Greenberg (1978) and Adams (1980) is directed specifically toward floppy-disk analysis with system interactions with the read/write head considered. Both include plate-bending terms in the governing differential equation of the disk. Both also treat the effect of the read/write head using the steady-state Reynolds equation for gas-lubricated compressible bearings. In each case, correlation to experimental data is good.

Ono and Maeno (1986) investigated the dynamic behavior of both a nonspinning and a spinning flexible 3.5-in. floppy disk in the presence of a point contact head. Resonant modes of vibration were studied and correlation made to experimental results. Agreement between the two was improved if a small amount of initial negative stress in the circumferential direction was included. Disk nonflatness was considered and found to significantly affect the response.

In a recently reported study, Adams (1987) has shown that there exist certain critical speeds at which the spinning disk is incapable of supporting arbitrary spatially fixed loads even with bending stiffness included in the problem. This is shown to occur at speeds relevant in the operation of floppy disks. By adding the effect of an elastic foundation, it is shown that these speeds can be raised. Adams (1980, 1987) uses an elastic foundation as a model for the hydrodynamic effects between the disk and a nearby baseplate.

In the present work, a two-stage process is developed for the computation of spinning-disk deflections. We are interested in the steady response to space-fixed, transverse loads. We use eigenfunctions in a bilinear series expansion to construct the Green's function for concentrated loading. Deflections for general loading are then computed through the classical convolution integral with the Green's function. The eigenfunction approach has as its principal benefit the ability to know, in advance, which modes will dominate disk deflections. We use this knowledge to avoid singular conditions, and to order the series expansion so that it converges with the fewest terms.

Problem Formulation

The system of interest is an elastic, isotropic, homogeneous, spinning disk. We wish to compute the deflection caused by

Contributed by the Applied Mechanics Division for presentation at the Winter Annual Meeting, Chicago, IL, November 28 to December 2, 1988, of The American Society of Mechanical Engineers.

Discussion on this paper should be addressed to the Editorial Department, ASME, United Engineering Center, 345 East 47th Street, New York, N.Y. 10017, and will be accepted until two months after final publication of the paper itself in the JOURNAL OF APPLIED MECHANICS. Manuscript received by ASME Applied Mechanics Division, September 28, 1987.

Paper No. 88-WA/APM-26.

Copyright © 1988 by ASME
Downloaded 03 May 2010 to 171.66.16.21. Redistribution subject to ASME license or copyright; see http://www.asme.org/terms/Terms_Use.cfm

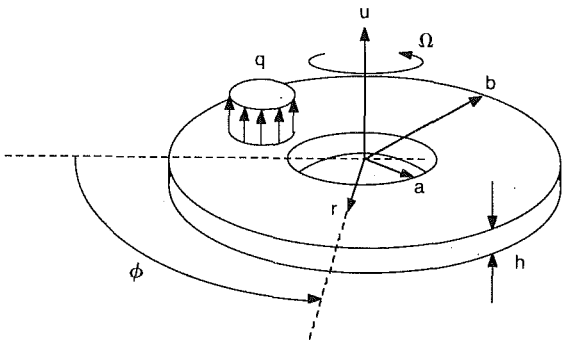


Fig. 1 Disk geometry

steady, space-fixed, transverse loads. Figure 1 and the following list define the variables

$$\begin{aligned} a &= \text{radius of the clamped inner edge} \\ b &= \text{radius of the free outer edge} \\ h &= \text{disk thickness (much less than } b) \\ \Omega &= \text{spin rate} \\ \mathrm{E} &= \text{modulus of elasticity} \\ \nu &= \text{Poisson ratio} \\ \rho &= \text{mass per unit volume} \\ a \le r \le b &= \text{radial polar coordinate} \\ -\eta < \Phi \le \eta &= \text{angular polar coordinate (space-fixed)} \\ q(r, \Phi) &= \text{transverse load} \\ u(r, \Phi) &= \text{transverse displacement} \end{aligned} \tag{1}$$

The problem is then nondimensionalized as follows

$$w = u/b, \quad \zeta = r/b, \quad \kappa = a/b$$

$$Q = 8q/[\rho\Omega^2 b^2 h(3+\nu)]$$

$$\alpha = 2Eh^2/[3\rho\Omega^2 b^4(3+\nu)(1-\nu^2)]$$

$$\beta = \left(\frac{1-\nu}{3+\nu}\right)\left[\frac{(3+\nu)-(1+\nu)\kappa^2}{(1+\nu)+(1-\nu)\kappa^2}\right]\kappa^2 \tag{2}$$

Following Benson and Bogy (1978, 1983), we compute the disk displacement by means of a convolution integral

$$w(\zeta, \Phi) = \int_\kappa^1 \int_{-\pi}^{\pi} G(\zeta, \xi, \Phi - \Psi) Q(\xi, \Psi)\, \xi d\xi d\Psi \tag{3}$$

where $G(\zeta, \xi, \Phi - \Psi)$ is the Green's function representing the displacement at point (ζ, Φ) due to a unit, concentrated load at point (ξ, Ψ). The Green's function is expanded in a cosine series

$$G(\zeta, \xi, \Phi - \Psi) = \sum_{n=0}^{\infty} G_n(\zeta, \xi) \cos[n(\Phi - \Psi)] \tag{4}$$

with radial functions $G_n(\zeta, \xi)$ satisfying the following differential equations

$$\begin{aligned} L_n[G_n(\zeta, \xi)] &= \alpha \frac{d^4 G_n}{d\zeta^4} + 2\alpha\zeta^{-1}\frac{d^3 G_n}{d\zeta^3} \\ &+ [(\zeta^2 - 1) + \beta(1 - \zeta^{-2}) - \alpha(1 + 2n^2)\zeta^{-2}]\frac{d^2 G_n}{d\zeta^2} \\ &+ [(3\zeta - \zeta^{-1}) + \beta(\zeta^{-1} + \zeta^{-3}) + \alpha(1 + 2n^2)\zeta^{-3}]\frac{dG_n}{d\zeta} \\ &- n^2[(3 - \zeta^{-2}) + \beta(\zeta^{-2} + \zeta^{-4}) + \alpha(4 - n^2)\zeta^{-4}]G_n \\ &= \delta(\zeta - \xi)/(C_n \eta); \quad n = 0,1,2,\ldots \end{aligned} \tag{5}$$

clamped boundary conditions

$$G_n = 0, \quad \frac{dG_n}{d\zeta} = 0 \text{ at } \zeta = \kappa \tag{6}$$

and free-edge boundary conditions

$$\frac{d^2 G_n}{d\zeta^2} + \nu\frac{dG_n}{d\zeta} - \nu n^2 G_n = 0$$

$$\frac{d^3 G_n}{d\zeta^3} + \frac{d^2 G_n}{d\zeta^2} - [1 + (2-\nu)n^2]\frac{dG_n}{d\zeta} + (3-\nu)n^2 G_n = 0;$$

$$\text{at } \zeta = 1. \tag{7}$$

In equation (5), δ is the Dirac delta function, and C_n is a coefficient with values

$$C_0 = 2, \quad C_1 = C_2 = C_3 = \ldots = 1 \tag{8}$$

Applying equations (3)–(7) yields the disk displacement in the context of linear, classical plate theory.

Bilinear Expansion in Eigenfunctions

Here we depart from the approach of Benson and Bogy (1978, 1983) where the radial mode Green's functions were computed directly by numerical integration. Instead, we seek an alternative approach using eigenfunctions. Let $\mathrm{E}_{mn}(\zeta)$ and λ_{mn} be the eigenfunctions and eigenvalues for the differential operator L_n

$$L_n[\mathrm{E}_{mn}(\zeta)] = \lambda_{mn}\mathrm{E}_{mn}(\zeta) \tag{9}$$

The boundary conditions are the same as (6) and (7) with E_{mn} replacing G_n. The second subscript, $m = 0,1,2,\ldots$, is added in recognition of the fact that, for each n, there will be an infinite number of solutions to equation (9). Physically, n is the number of nodal diameters and m is the number of nodal circles in the solution in the eigenfunction.

Next, we define an inner product and a norm for functions on the interval $\kappa < \zeta < 1$.

$$\langle f, g \rangle = \int_\kappa^1 f(\zeta) g(\zeta)\, \zeta d\zeta \tag{10}$$

$$\|f\| = \langle f, f \rangle^{1/2} \tag{11}$$

One can demonstrate that the differential operator L_n is self-adjoint

$$\langle L_n[f], g \rangle = \langle f, L_n[g] \rangle \tag{12}$$

which guarantees that the eigenfunctions are orthogonal (Stakgold 1969)

$$\langle \mathrm{E}_{mn}, \mathrm{E}_{ij} \rangle = 0 \text{ if } \lambda_{mn} \neq \lambda_{ij}. \tag{13}$$

Consider an expansion of the G_n in eigenfunctions

$$G_n(\zeta, \xi) = \sum_{m=0}^{\infty} A_{mn}(\xi)\mathrm{E}_{mn}(\zeta), \tag{14}$$

where the coefficients $A_{mn}(\xi)$ are to be determined. It follows that

$$\begin{aligned} \langle L_n[G_n(\zeta, \xi)], E_{mn}(\zeta) \rangle &= \langle \delta(\zeta - \xi)/(C_n \pi), E_{mn}(\zeta) \rangle \\ &= E_{mn}(\xi)/(C_n \pi). \end{aligned} \tag{15}$$

Due to the self-adjointness of L_n, we may also write

$$\begin{aligned} \langle L_n[G_n(\zeta, \xi)], E_{mn}(\zeta) \rangle &= \langle G_n(\zeta, \xi), L_n[\mathrm{E}_{mn}(\zeta)] \rangle \\ &= \left\langle \sum_{k=0}^{\infty} A_{kn}(\xi)\mathrm{E}_{kn}(\zeta), \lambda_{mn}\mathrm{E}_{mn}(\zeta) \right\rangle \\ &= \sum_{k=0}^{\infty} A_{kn}(\xi)\lambda_{mn}\langle \mathrm{E}_{kn}, \mathrm{E}_{mn} \rangle = A_{mn}(\xi)\lambda_{mn}\|\mathrm{E}_{mn}\|^2. \end{aligned} \tag{16}$$

Downloaded 03 May 2010 to 171.66.16.21. Redistribution subject to ASME license or copyright; see http://www.asme.org/terms/Terms_Use.cfm

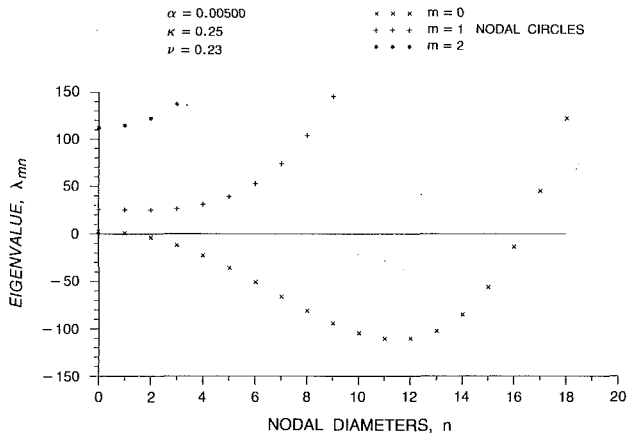


Fig. 2 Eigenvalue spectrum, $\alpha = 0.00500$

Equation (15) and (16) leads to

$$A_{mn}(\xi) = E_{mn}(\xi)/[C_n \pi \lambda_{mn} ||E_{mn}||^2]. \tag{17}$$

We then normalize the eigenfunctions

$$N_{mn}(\xi) = E_{mn}(\xi)/||E_{mn}|| \tag{18}$$

and use equations (4), (14), (17), and (18) to construct the desired eigenfunction expansion for $G(\zeta, \xi, \Phi - \Psi)$

$$G(\zeta, \xi, \Phi - \Psi) = \sum_{n=0}^{\infty} \sum_{m=0}^{\infty} \frac{\cos [n(\Phi - \Psi)]}{C_n \pi \lambda_{mn}} N_{mn}(\xi) N_{mn}(\zeta) \tag{19}$$

Observe the presence of λ_{mn} in the denominator of (19). As $C_n = 1$ or 2, and the eigenfunctions have been normalized, it is the eigenvalue which becomes the single determinator of the importance of a given mode in the Green's function expansion. We exploit this fact by computing the eigenfunctions and eigenvalues, in advance, and then ranking modes by the smallness of $|\lambda_{mn}|$

$$|\lambda_{m_1 n_1}| < |\lambda_{m_2 n_2}| < |\lambda_{m_3 n_3}| < \ldots \tag{20}$$

We then reorder the summation of equation (19) to

$$G(\zeta, \xi, \Phi - \Psi) = \sum_{i=1}^{I} \frac{\cos [n_i(\Phi - \Psi)]}{C_{ni} \eta \lambda_{m_i n_i}} N_{m_i n_i}(\xi) N_{m_i n_i}(\zeta) \tag{21}$$

In practice, we truncate summation (21) at some index, $i = I$, when the eigenvalues surpass a predetermined multiple, R, of the most fundamental mode, $\lambda_{m_1 n_1}$

$$|\lambda_{m_I n_I}| < R|\lambda_{m_1 n_1}| < |\lambda_{m_{I+1} n_{I+1}}|. \tag{22}$$

To find eigenvalues, we use the method of Barasch and Chen (1972). The method, in brief, consists of the following steps. A value λ is chosen and two displacement functions are generated.

The first has boundary values

$$E = \frac{dE}{d\zeta} = \frac{d^3E}{d\zeta^3} = 0, \quad \frac{d^2E}{d\zeta^2} = 1 \text{ at } \zeta = \kappa \tag{23}$$

and the second has boundary values

$$E = \frac{dE}{d\zeta} = \frac{d^2E}{d\zeta^2} = 0, \quad \frac{d^3E}{d\zeta^3} = 1 \text{ at } \zeta = \kappa \tag{24}$$

The differential equation

$$L_n[E] = \lambda E \tag{25}$$

generates subsequent values on $\kappa \le \zeta \le 1$. The requirements $E = 0$ and $dE/d\zeta = 0$ at $\zeta = \kappa$ follow from the inner clamp conditions. The choices for $d^2E/d\zeta^2$ and $d^3E/d\zeta^3$ are nonphysical, but will lead to nontrivial displacement functions. The question is whether a linear combination of these functions can satisfy the free-edge boundary conditions. Only for discrete values, $\lambda = \lambda_{mn}$, will this be possible. We use standard matrix techniques and a Newton/Raphson interaction to find these eigenvalues.

Table 1 Representative spin stiffnesses

	FLOPPY DISKS			HARD DISKS	
Radius (mm)	102.0	66.7	44.5	177.8	177.8
Thickness (mm)	0.076	0.076	0.076	2.03	4.06
Spin Rate (1/s)	188.5	188.5	188.5	377.0	377.0
Mass Density ($N\text{-}s^2/m^4$)	1400.	1400.	1400.	2700.	2700.
Elastic Modulus (MN/m^2)	3800.	3800.	3800.	70000.	70000.
Poisson Ratio	0.23	0.23	0.23	0.35	0.35
SPIN STIFFNESS	0.0009	0.005	0.025	0.17	0.68

Results

There are two principal advantages of the eigenfunction expansion approach. The first is improved computation speed through the use of well-defined eigenfunctions. The second is a clear understanding of disk resonances and parameter sensitivity by knowledge of the eigenvalues. To illustrate the approach, refer to Fig. 2. This shows the spectrum of eigenvalues for a spinning disk with typical parameters.

$$\alpha = 0.005, \ \beta = 0.0368, \ \kappa = 0.25, \ \nu = 0.23 \tag{26}$$

These parameters are taken from Table 1 where specifications are provided for several commercial disk storage devices. The first three columns are for computer "floppy" disks while the last two are for computer "hard" disks.

Each symbol in Fig. 2 represents a discrete eigenvalue. These follow general curves corresponding to 0, 1, and 2 nodal circles. The number of nodal diameters is plotted along the abscissa and the eigenvalue is plotted along the ordinate. As noted earlier in equation (19), the smallness of the eigenvalue is of primary importance in the disk response. With reference to Fig. 2, the most important modes are those for which the eigenvalue falls closest to the horizontal line through zero. An advantage of this approach is that important modes can be ordered by inspection. In this case, the ten most important are

$$(m_i, n_i) = (0,0),(0,1),(0,2),(0,3),(0,16)(0,4),(1,0),(1,1)(1,2),(1,3). \tag{27}$$

It is then a simple matter to use just these eigenvalues and eigenfunctions to construct the Green's function. Figure 3 shows such a construction for a unit load located at $\xi = 0.8$. The same deflection was generated using the numerical approach of Benson and Bogy (1978). Computation by the present technique was three-orders-of-magnitude faster. The increased speed should prove important in the analysis of more intricate systems where the disk must be equilibrated with other components (e.g., air loads, read/write head interactions, etc.).

Consider further, the eigenvalue spectrum of Fig. 2. The set of eigenvalues corresponding to zero nodal circles twice crosses the zero line. This occurs between 1 and 2 nodal diameters and again between 16 and 17 nodal diameters. This means that higher-ordered modes could become important in the disk response. This is consistent with the findings of Ben-

Downloaded 03 May 2010 to 171.66.16.21. Redistribution subject to ASME license or copyright; see http://www.asme.org/terms/Terms_Use.cfm

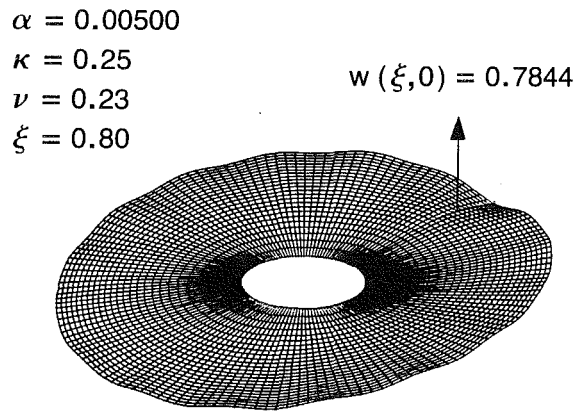


Fig. 3 Point load deflection, $\alpha = 0.00500$

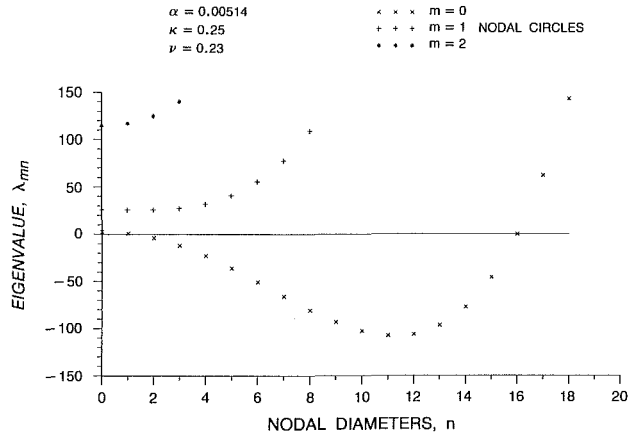


Fig. 4 Eigenvalue spectrum, $\alpha = 0.00514$

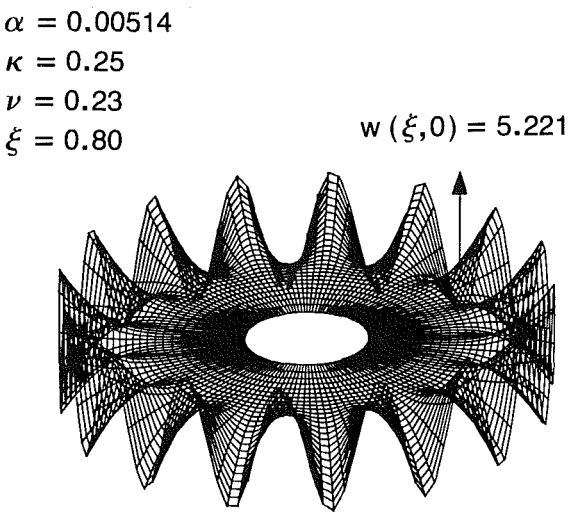


Fig. 5 Point load deflection, $\alpha = 0.00514$

son and Bogy (1978) where typically low-ordered modes and a higher-ordered "wave" mode were seen to dominate the disk response.

For the example ordering of equation (27), it is seen that most of the deflection is composed of modes having few nodal circles and nodal diameters. An exception is the high-order (0,16) wave mode. Its influence can be seen in Fig. 3 although it is relatively small compared to the first four modes. If, however, a slight modification to the spin stiffness is made, then the wave contribution changes. With α increased to 0.00514 (a 1.4 percent increase in the disk spin rate), then the eigenvalue spectrum of Fig. 4 results. It is nearly identical to

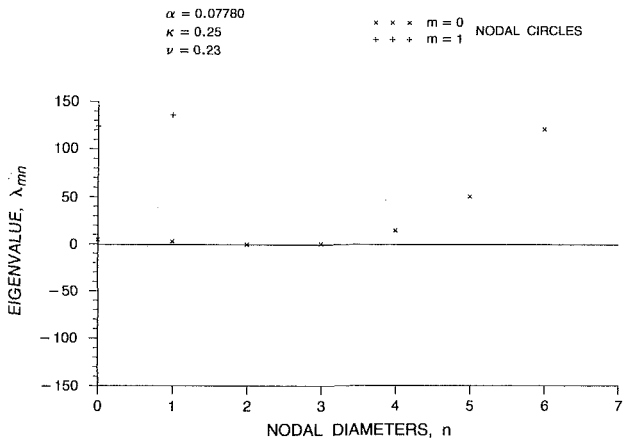


Fig. 6 Eigenvalue spectrum, $\alpha = 0.07780$

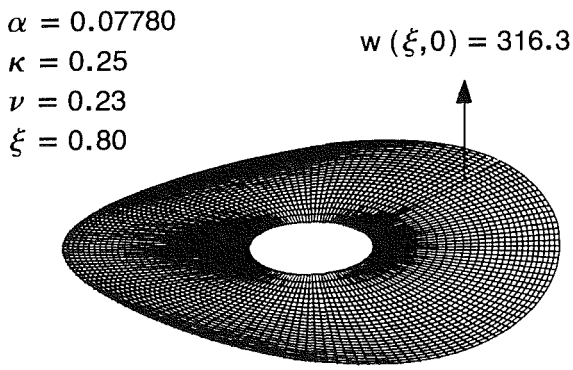


Fig. 7 Point load deflection, $\alpha = 0.07780$

the spectrum of Fig. 2 except that the (0, 16) eigenvalue is moved very close to the horizontal axis. We expect the Green's function to be dominated by this mode and Fig. 5 shows this to indeed be the case. It is worth noting that this near-resonant case was computed with the same ease as the preceeding case. Such would not be true if we tried to compute the Green's function directly. With the present eigenfunction expansion, however, even the most singular responses are composed of well-defined functions.

Clearly, other parameter changes could bring about similar resonant behavior in the disk. Plots in the form of Figs. 2 and 4 are very useful for assessing the effect of a given change. For example, continued increase in the spin stiffness would bring mode (0,15) into resonance, then mode (0,14), etc. Eventually, all modes would be above the zero eigenvalue line and the disk could not be made to resonate. Figures 6 and 7 show this critical case. It occurs for mode (0, 2) at $\alpha = 0.0778$. This compares well to a natural frequency study by Adams (1987). Converting his lowest natural frequency to our nondimensionalization gives $\alpha = 0.0793$. Looking again at Table 1, we see typical commercial floppy disks have spin stiffnesses in the "unsafe" region. Hard disks are "safe."

A contrasting example is provided by a value of α small enough to bring modes with one nodal circle into resonance. This first occurs for $\alpha = 0.0195$. Results are presented in Figs. 8 and 9. The ten most important modes for this Green's function expansion are

$$(m_i, n_i) = (1,9)(1,8),(0,1),(1,7),(0,0),(1,10),(0,2),(1,6),(1,5),(1,11). \tag{28}$$

Terms with one nodal circle clearly dominate the deflection seen in Fig. 9.

Finally, we consider a case for something other than a point

Downloaded 03 May 2010 to 171.66.16.21. Redistribution subject to ASME license or copyright; see http://www.asme.org/terms/Terms_Use.cfm

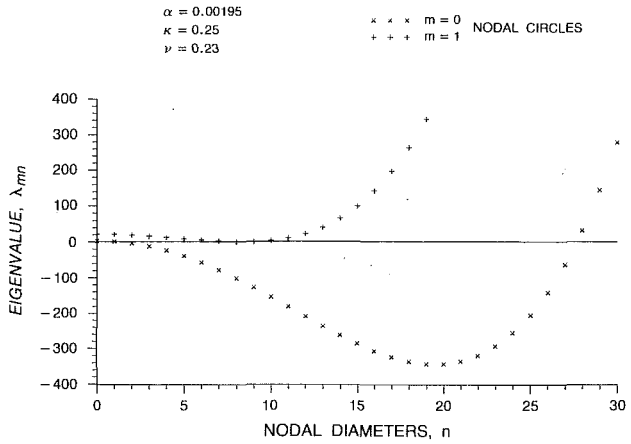


Fig. 8 Eigenvalue spectrum, $\alpha = 0.00195$

load. When distributed loads are considered, it is typical for authors to separate the load in coordinate variables, (e.g., Adams (1980) and White (1984). This technique restricts consideration to loads falling only on polar coordinate patches. No such restriction applies to the convolution integral of equation (3). As an example, we consider the following load which is distributed over a small circle on the disk. It has a magnitude over the circle given by

$$Q(\zeta,\Phi)=\frac{2}{\pi}\frac{1}{\zeta_0}\left\{2\left(\frac{\zeta}{\zeta_0}\right)\cos\Phi-\left(\frac{\zeta}{\zeta_0}\right)^2\right\} \tag{29}$$

where the center of the circle is located at $\zeta = \zeta_0$ and $\Phi = 0$. It is a simple matter to numerically integrate equation (3) to get the resulting deflection. We plot the response over a quarter of the disk in Fig. 10. The resultant force from the pressure distribution in equation (29) is equal to one. The disk parameters are identical to those considered in Figs. 2 and 3. We found the displacements were nearly the same, as would be expected.

Summary

In this paper, eigenfunction expansions have been used to study the basic behavior of flexible spinning disks. A two-stage process was developed. First, the eigenfunctions are summed in a bilinear series to create a Green's function for concentrated loading. Deflections are then computed through a convolution integral on the Green's function and the general load function.

The eigenvalues computed as part of this procedure provide valuable physical insight, and aid computational efficiency. By ranking the eigenvalues, from smallest to greatest by absolute value, we are able to optimize the bilinear series so that the modes are summed in order of importance. This reduces convergence times by orders of magnitude in comparison to typical series solutions which progress only by modal index, i.e., increasing numbers of nodal circles and diameters. The speed of the bilinear series convergence will benefit larger system studies involving flexible spinning disks.

An examination of the eigenvalues also permits us to determine, in advance, if the disk is near-resonance, and to make

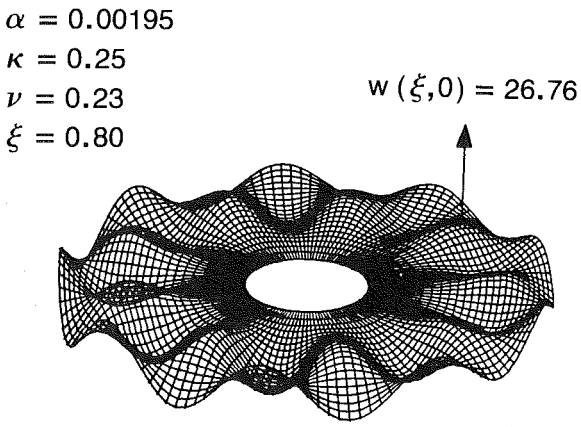


Fig. 9 Point load deflection, $\kappa = 0.00195$

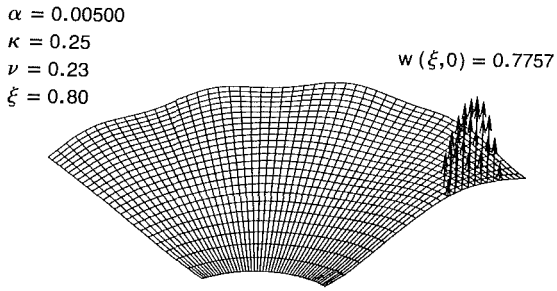


Fig. 10 Patch load deflection, $\kappa = 0.00500$

appropriate parameteric changes to avoid such a condition. Even in near-singular conditions, deflections are computed through well-behaved eigenfunctions.

References

Adams, G. G., 1980, "Analysis of the Flexible Disk/Head Interface," *ASME Journal of Lubrication Technology*, Vol. 102, No. 1, Jan., pp. 86–90.

Adams, G. G., 1987, "Critical Speeds for a Flexible Spinning Disk," *International Journal of Mechanical Sciences*, to appear.

Barasch, S., and Chen, Y., 1972, "On the Vibration of a Rotating Disk," ASME Journal of Applied Mechanics, Vol. 39, No. 4, Dec., pp. 1143–1144.

Benson, R.C., and Bogy, D. B., 1978, "Deflection of a Very Flexible Spinning Disk Due to a Stationary Transverse Load," ASME Journal of Applied Mechanics, Vol. 45, No. 3, Sept., pp. 636–642.

Benson, R.C., 1983, "Observations on the Steady-State Solution of an Extremely Flexible Spinning Disk With a Transverse Load," ASME Journal of Applied Mechanics, Vol. 50, No. 3, Sept., pp. 525–530.

Eversman, W., and Dodson, R. O., 1969, "Free Vibrations of a Centrally Clamped Spinning Circular Disk," *AIAA Journal*, Vol. 7, No. 10, Oct., pp. 2010–2012.

Greenberg, H. J., 1978, "Flexible Disk-Read/Write Head Interface," *IEEE Trans Magnetics.*, Vol. Mag-14, No. 5, Sept. pp. 336–338.

Lamb, H., and Southwell, R. V., 1921, "The Vibrations of a Spinning Disk," *Proceedings of the Royal Society, London*, Vol. 99, pp. 272–280.

Ono, K., and Maeno, T., 1986, "Theoretical and Experimental Investigation on Dynamic Characteristics of a 3.5-Inch Flexible Disk Due to a Point Contact," ASLE SP-21, pp. 144–151.

Stakgold, I., 1969, *Boundary Value Problems of Mathematical Physics Volumes I and II*, The Macmillian Co., Toronto.

White, J. W., 1984, "On the Design of Low Flying Heads for Floppy Disk Magnetic Recording," ASLE SP-16, pp. 126–131.

Downloaded 03 May 2010 to 171.66.16.21. Redistribution subject to ASME license or copyright; see http://www.asme.org/terms/Terms_Use.cfm

S. T. Ariaratnam

W.-C. Xie

Solid Mechanics Division,
Faculty of Engineering,
University of Waterloo,
Waterloo, Ontario, Canada, N2L 3G1

Stochastic Sample Stability of Oscillatory Systems

A method of obtaining a sufficient almost-sure asymptotic stability condition for second-order, linear oscillatory systems with an ergodic damping coefficient is presented. In this method, the probabilistic property of the derivative process of the damping coefficient is taken into account. A sufficient condition for almost-sure asymptotic stability is derived and numerical results are presented for the case of a Gaussian noise coefficient. The results are found to be an improvement over previously available results for oscillatory systems with stochastic damping.

Introduction

The almost-sure (a.s.) asymptotic stability of the trivial solution of the second-order system of the form

$$\ddot{x}+2[\zeta+f(t)]\dot{x}+[1+g(t)]x=0,$$

where $f(t)$, $g(t)$ are ergodic random processes, has attracted intensive study in the last three decades. Kozin and Wu (1973) took into account the distributional properties of the coefficient processes and obtained sufficient a.s. asymptotic stability boundaries numerically, which enabled them to obtain much sharper results than those obtained by Infante (1968), who considered only the mean and the variance of the coefficient processes. It is known, however, that knowledge of more statistical information on the processes $f(t)$ and $g(t)$ should enable one to get sharper, sufficient a.s. asymptotic stability boundaries. In this paper, we shall apply a transformation that brings the derivative process of $f(t)$, $\dot{f}(t)$, into account. It is shown that for oscillatory systems, i.e., $0<\zeta\leq 1$, the a.s. asymptotic stability boundaries can be significantly enlarged for Gaussian excitation. Numerical results and comparison with previous results are presented.

The results are of importance in the study of the dynamic stability of lightly damped elastic structures. In particular, the transverse vibration of a long rectangular panel in a randomly fluctuating supersonic flow field (with Mach number near unity) can be described by such a second-order stochastic differential equation.

Formulation

Let us consider the second-order system

$$\ddot{x}+2[\zeta+f(t)]\dot{x}+x=0, \tag{1}$$

where $f(t)$ is an ergodic process with zero mean value.

In order to bring in the influence of the derivative process, $\dot{f}(t)$, of the process $f(t)$, we seek a transformation of the form

$$x=y\exp\{-\zeta t-F(t)\}, \tag{2}$$

where

$$F(t)=\int_0^t f(\tau)d\tau.$$

Substituting equation (2) into (1) leads to

$$\ddot{y}+\{(1-\zeta^2)+[-2\zeta f(t)-f^2(t)-\dot{f}(t)]\}y=0. \tag{3}$$

For notational convenience, equation (3) can be written as

$$\ddot{y}+[c+\phi(t)]y=0, \tag{4}$$

where

$$c=1-\zeta^2,$$

$$\phi(t)=-2\zeta f(t)-f^2(t)-\dot{f}(t), \tag{5}$$

or, in the state equation form,

$$\dot{y}_1=y_2,$$

$$\dot{y}_2=-[c+\phi(t)]y_1. \tag{6}$$

It may be noted that in equation (3) the damping term has been removed, which is a significant change, since for this case the norm of y, $\|y\|$, may be taken in the very simple form given by

$$\|y\|^2=V(y)=y^TAy, \tag{7}$$

where A is a positive definite matrix of the form

$$A=\begin{bmatrix}\alpha^2 & 0\\ 0 & 1\end{bmatrix}, \tag{8}$$

where $\alpha>0$ is to be determined.

The time derivative of V along the trajectories of equation (6) yields

$$\dot{V}(y)=y^TBy, \tag{9}$$

where

Contributed by the Applied Mechanics Division for publication in the JOURNAL OF APPLIED MECHANICS.

Discussion on this paper should be addressed to the Editorial Department, ASME United Engineering Center, 345 East 47th Street, New York, N.Y. 10017, and will be accepted until two months after final publication of the paper itself in the JOURNAL OF APPLIED MECHANICS. Manuscript received by ASME Applied Mechanics Division, August 4, 1987; final version, November 9, 1987.

Copyright © 1988 by ASME

Downloaded 03 May 2010 to 171.66.16.21. Redistribution subject to ASME license or copyright; see http://www.asme.org/terms/Terms_Use.cfm

$$B=\begin{bmatrix} 0 & \alpha^2-c-\phi(t) \\ \alpha^2-c-\phi(t) & 0 \end{bmatrix}. \tag{10}$$

Therefore, since A, B are real symmetric matrices, and A is positive definite,

$$\frac{\dot{V}}{V}=\frac{y^TBy}{y^TAy}\leq\lambda(BA^{-1}), \tag{11}$$

where λ is the maximum eigenvalue of BA^{-1}, i.e., λ is the maximum root of the determinantal equation

$$|B-\lambda A|=0. \tag{12}$$

From equation (11),

$$V[y(t)]\leq V_0\exp\left\{\int_0^t\lambda(\tau)d\tau\right\}.$$

where $V_0=V[y(0)]$. Since $\|y\|^2=V$,

$$\|y\|^2\leq\|y_0\|^2\exp\left\{\int_0^t\lambda(\tau)d\tau\right\},$$

$$=\|y_0\|^2\exp\left\{t\cdot\frac{1}{t}\int_0^t\lambda(\tau)d\tau\right\}. \tag{13}$$

When $t\to\infty$,the right-hand side of (13) goes to

$$\|y_0\|^2\exp\{tE[\lambda(t)]\}$$

with probability 1 (w.p.1) for ergodic process $f(t)$.

Then, from equation (2), we have w.p.1 as $t\to\infty$,

$$\begin{aligned}|x|^2&=|y_1|^2\exp\{-2\zeta t-2F(t)\},\\ &\leq\|y\|^2\exp\{-2\zeta t-2F(t)\},\\ &\leq\|y_0\|^2\exp\{tE[(t)]-2\zeta t-2F(t)\},\\ &=\|y_0\|^2\exp\{t[E[\lambda(t)]-2\zeta-2E[f(t)]]\},\\ &=\|y_0\|^2\exp\{t[E[\lambda(t)]-2\zeta]\},\end{aligned}$$

where $|\cdot|$ denotes the absolute value.

Therefore, for large t, w.p.1

$$|x|\leq\|y_0\|\exp\left\{\frac{t}{2}[-2\zeta+E[\lambda(t)]]\right\}. \tag{14}$$

Letting

$$\lambda^*=\frac{1}{2}\{-2\zeta+E[\lambda(t)]\},$$

a sufficient condition for a.s. asymptotic stability of the trivial solution of equation (1) is given by

$$\lambda^*<-\epsilon,\quad\epsilon>0,$$

or

$$-2\zeta+E[\lambda(t)]<-\epsilon. \tag{15}$$

Substituting for matrices A, B from equations (8) and (10) into equation (12), one obtains

$$|B-\lambda A|=\begin{vmatrix} -\lambda\alpha^2 & \alpha^2-c-\phi(t) \\ \alpha^2-c-\phi(t) & -\lambda \end{vmatrix}=0.$$

Therefore, the eigenvalues are given by

$$\lambda^2=\frac{[\alpha^2-c-\phi(t)]^2}{\alpha^2},$$

the maximum eigenvalue being

$$\lambda=\left|\frac{\alpha^2-c-\phi(t)}{\alpha}\right|. \tag{16}$$

Substituting equation (16) into (15), it follows that the trivial solution of equation (1) is asymptotically stable w.p.1 if

$$-2\zeta+E\left[\left|\frac{\alpha^2-c-\phi(t)}{\alpha}\right|\right]<-\epsilon,\quad\epsilon>0.$$

or

$$-2\zeta\alpha+E[|\alpha^2-c-\phi(t)|]<-\epsilon,\quad\epsilon>0. \tag{17}$$

Substituting for $\phi(t)$ from equation (5) into (17) yields the sufficient stability condition

$$-2\zeta\alpha+E[|\alpha^2+\zeta^2-1+2\zeta f+f^2+\dot{f}|]<-\epsilon,\quad\epsilon>0. \tag{18}$$

If the probabilistic properties of both the processes $f(t)$ and $\dot{f}(t)$ are employed, much sharper sufficient a.s. asymptotic stability boundaries can be obtained. In the following, improved stability boundaries are presented for the case of an ergodic Gaussian coefficient.

Example

System with Ergodic Gaussian Coefficients. Since it is known that $E[f(t)\dot{f}(t)]=0$ and $\dot{f}(t)$ is also a Gaussian process, one may assume that

$$p(f,\dot{f})=\frac{1}{2\pi\sigma_f\sigma_{\dot{f}}}\exp\left\{-\frac{f^2}{2\sigma_f^2}-\frac{\dot{f}^2}{2\sigma_{\dot{f}}^2}\right\}, \tag{19}$$

so that for any integrable function $F(f,\dot{f})$,

$$E[F(f,\dot{f})]=\int_{-\infty}^{+\infty}df\int_{-\infty}^{+\infty}F(f,\dot{f})p(f,\dot{f})d\dot{f}. \tag{20}$$

By the change of variables $\xi=f/\sqrt{2}\sigma_f$, $\eta=\dot{f}/\sqrt{2}\sigma_{\dot{f}}$, equation (20) becomes

$$\begin{aligned}&\pi E[F(f,\dot{f})]=I\\ &=\int_{-\infty}^{+\infty}\exp(-\xi^2)d\xi\int_{-\infty}^{+\infty}F(\xi,\eta)\exp(-\eta^2)d\eta.\end{aligned} \tag{21}$$

The double integral can be calculated numerically by the double Gauss-Hermite integration formula (see, e.g., Davis and Rabinowitz, 1967)

$$I\approx\sum_{i=1}^{n}W_i\sum_{j=1}^{n}W_jF(\xi_i,\eta_j), \tag{22}$$

where ξ_i, ξ_j $(i,j=1,2,\ldots,n)$ are the n zeros of the Hermite polynomial

$$\begin{aligned}H_n(z)&=(-1)^n\exp(z^2)\frac{d^n}{dz^n}[\exp(-z^2)],\\ &=\sum_{k=0}^{[n/2]}\frac{(-1)^k n!}{k!(n-2k)!}(2z)^{n-2k}\end{aligned}$$

and the coefficients W_i, W_j $(i,j=1,2,\ldots,n)$ are of the form

$$W_k=\frac{2^{n+1}n!\sqrt{\pi}}{[H_{n+1}(z_k)]^2}.$$

Therefore, the sufficient asymptotic stability boundary given by (18) becomes

$$\begin{aligned}&\pi E[|\alpha^2+\zeta^2-1+\sqrt{2}\sigma_{\dot{f}}\eta+2(\sigma_f\xi)^2\\ &\qquad+2\sqrt{2}\zeta\sigma_f\xi|]-2\pi\zeta\alpha=0,\end{aligned} \tag{23}$$

where the first term of the left-hand side is a double Gauss-Hermite integral with the integrand

$$F(\xi,\eta)=|\alpha^2+\zeta^2-1+\sqrt{2}\sigma_{\dot{f}}\eta+2(\sigma_f\xi)^2+2\sqrt{2}\zeta\sigma_f\xi|.$$

In order to obtain the best possible condition, the parameter α is considered to be not only a function of damping ζ but also a function of σ_f and $\sigma_{\dot{f}}$. For a given damping ζ, a value of σ_f is first specified (starting from 0.0, and increasing in steps of 0.2). The parameter α is now varied (increasing in steps of 0.05) and the nonlinear equation (23) is solved to get $\sigma_{\dot{f}}$. Then, corresponding to a certain α, the maximum of $\sigma_{\dot{f}}$ (with respect

Downloaded 03 May 2010 to 171.66.16.21. Redistribution subject to ASME license or copyright; see http://www.asme.org/terms/Terms_Use.cfm

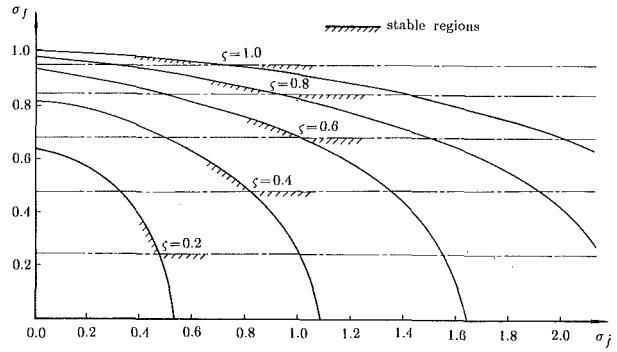


Fig. 1 Regions of almost-sure asymptotic stability for $\ddot{x}+2[\zeta+f(t)]\dot{x}+x=0$

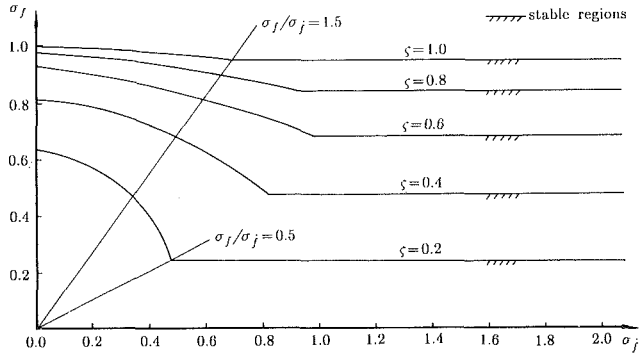


Fig. 2 Improved regions of almost-sure asymptotic stability for $\ddot{x}+2[\zeta+f(t)]\dot{x}+x=0$

to some $\sigma_{\dot{f}}$) is chosen. The results of the numerical computation are shown in Fig. 1 by the solid curves.

To compare the present result with that of Kozin and Wu (1973), which is a sufficient asymptotic stability condition without taking $\sigma_{\dot{f}}$ into account, their result is represented by the dotted lines in Fig. 1. It is obvious that, for a certain value of the damping coefficient ζ, within some region of $\sigma_{\dot{f}}$ the present result is better. However, beyond this region, the present result is not as good as theirs. Combining these two results, one can obtain an improved sufficient a.s. asymptotic stability boundary, which is shown in Figs. 2 and 3.

From Figs. 2 and 3, it is obvious that for small damping $\zeta \leq 1$ it is possible to enlarge the sufficient a.s. asymptotic stability boundary; the smaller the values of the damping ζ and $\sigma_{\dot{f}}$, the better the present results. Unfortunately, for $\zeta > 1$ it seems that better results cannot be obtained by the present approach. These results are therefore constrained for systems with small damping, i.e., oscillatory systems.

In order to examine the effective domain of the improved results, we assume that $f(t)$ is the response of a single degree of freedom system subjected to Gaussian white noise excitation. For a second-order system

$$\ddot{f}(t)+2\gamma\nu_0\dot{f}(t)+\nu_0^2 f(t)=F(t),$$

where $F(t)$ is a Gaussian white noise process with spectral density $\Phi_{FF}(\omega)=\Phi_0$, then (see, e.g., Lin, 1976) $\sigma_f^2=\pi\Phi_0/2\gamma\nu_0^3$, $\sigma_{\dot{f}}^2=\pi\Phi_0/2\gamma\nu_0$, whence

$$\frac{\sigma_f}{\sigma_{\dot{f}}}=\frac{1}{\nu_0}. \tag{24}$$

Now, consider a second-order system of the form

$$\frac{d^2x}{ds^2}+2[\zeta+f(s)]\Omega_0\frac{dx}{ds}+\Omega_0^2 x=0, \tag{25}$$

where $f(s)$ is governed by

$$\frac{d^2f}{ds^2}+2\gamma\nu_0\frac{df}{ds}+\nu_0^2 f=F_0(s), \tag{26}$$

$F_0(s)$ being a Gaussian white noise process with mean $\mu_{F_0}=0$ and spectral density $\Phi_{F_0F_0}(\omega)=\Phi_0$. By changing the time scale through $t=\Omega_0 s$, equation (25) is transformed to the form of equation (1), namely

$$\frac{d^2x}{dt^2}+2(\zeta+f)\frac{dx}{dt}+x=0,$$

while equation (26) becomes

$$\frac{d^2f}{dt^2}+2\gamma\frac{\nu_0}{\Omega_0}\frac{df}{dt}+\left(\frac{\nu_0}{\Omega_0}\right)^2 f=\frac{F_0}{\Omega_0^2}$$

Therefore, from (24), one obtains

$$\frac{\sigma_f}{\sigma_{\dot{f}}}=\frac{\Omega_0}{\nu_0}. \tag{27}$$

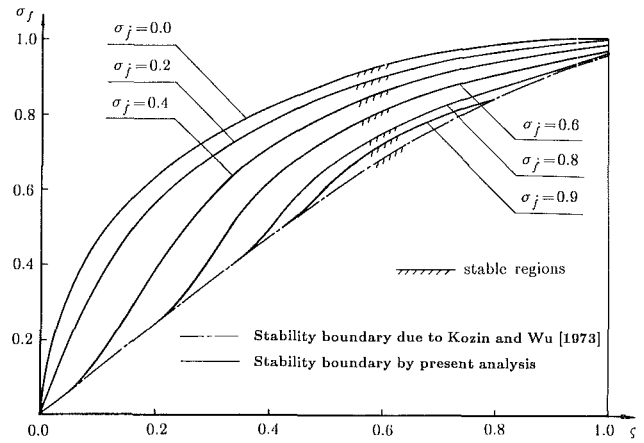


Fig. 3 Improved regions of almost-sure asymptotic stability for $\ddot{x}+2[\zeta+f(t)]\dot{x}+x=0$

From Fig. 2, it can be concluded that in the cases when $\zeta=0.2$ and $\Omega_0/\nu_0>0.5$, the improvement over the result of Kozin and Wu (1973) will be effective, and in the cases when $\zeta=0.4$, 0.6, 0.8, 1.0, the effective regions will roughly by $\Omega_0/\nu_0>0.6$, 0.7, 1.0, 1.5, respectively.

Conclusion

A method of obtaining a sufficient a.s. asymptotic stability condition for second-order oscillatory systems with an ergodic damping coefficient, which takes into account also the probabilistic property of the derivative process of the damping coefficient, has been presented. A sufficient condition for stability has been derived and numerical results have been presented for the case of a Gaussian noise coefficient. The results have been found to be an improvement over those of Kozin and Wu (1973) for systems with small mean damping coefficient.

Acknowledgment

This research was supported by the National Sciences and Engineering Research Council of Canada through Grant No. A-1815.

References

Davis, P. J. and Rabinowitz, P., 1967, *Numerical Integration*, Blaisdell Pub. Co., Massachusetts, Chapter 3.

Infante, E. F., 1968, "On the Stability of Some Linear Nonautonomous Systems," ASME JOURNAL OF APPLIED MECHANICS, Vol. 35, pp. 7–12.

Kozin, F. and Wu, C.-M., 1973, "On the Stability of Linear Stochastic Differential Equations," JOURNAL OF APPLIED MECHANICS, Vol. 40, pp. 87–92.

Lin, Y. K., 1976, *Probabilistic Theory of Structural Dynamics*, McGraw-Hill, Inc., New York, Chapter 5.

Downloaded 03 May 2010 to 171.66.16.21. Redistribution subject to ASME license or copyright; see http://www.asme.org/terms/Terms_Use.cfm

B. H. Tongue
Assistant Professor.
Department of Mechanical Engineering,
University of California,
Berkeley, CA 94720
Assoc. Mem. ASME

K. Gu
Graduate Research Assistant.
School of Mechanical Engineering,
Georgia Institute of Technology,
Atlanta, GA 30332
Student Mem. ASME

Interpolated Cell Mapping of Dynamical Systems[1]

A method is proposed to efficiently determine the basins of attraction of a nonlinear system's different steady-state solutions. The phase space of the dynamical system is spacially discretized and the continuous problem in time is converted to an iterative mapping. By means of interpolation procedures, an improvement in the system accuracy over the Simple Cell Mapping technique is achieved. Both basins of attraction for a representative nonlinear system and characteristic system trajectories are generated and compared to exact solutions.

Introduction

One of the central characteristics of nonlinear systems is that different initial conditions can potentially lead to more than one steady-state solution (Hagedorn, 1981 and Nayfeh, 1979). Given this fact, the problem immediately arises as to how one can determine which solution will occur for a given initial state. In recent years, various researchers have addressed this concern (Blair and Loud, 1960; Hayashi Ueda and Kawakami, 1969; Ueda, 1979; Guckenheimer and Holmes, 1983).

Hayashi (1964) utilized a hybrid analytical-numerical approach to obtain the domains of attraction of a given response. Initially, a harmonic balance procedure was utilized in order to identify the fixed points corresponding to a given periodic solution. The Poincaré iterates (Poincaré, 1892) of a number of points in the neighborhood of those fixed points with saddle-type singularities were used as initial points for backward time integrations in order to determine the stable manifolds that converge on the saddle singularity. These manifolds define the boundaries of the basins of attraction for each stable fixed point (periodic solution).

Hsu, Yee, and Cheng (1977) investigated a related idea in which the fixed point itself is surrounded by a closed locus of points. These points are all used as initial conditions for backward time integrations. These iterates then define the perimeter of a subset of the total basin of attraction for the fixed point. As time is integrated further, this subset more and more closely approximates the actual basin of attraction. The locus of the points at a given time will indicate also the position of the manifolds (basin boundaries).

Continued investigated into the topic of global analysis led Hsu to develop the Simple Cell Mapping (SCM) technique (Hsu, 1980; Hsu and Guttalu, 1980). The essential element in this analysis was the decision to discretize the actual phase space within which the system exists. The method first requires that an array of cells be overlayed on a given region of phase space. The center of each cell is used as the initial point for a time integration. This integration can be for a small time (leading to a transient analysis) or for a time equal to the system forcing period (leading to a Poincaré Map). The fixed amount of time that the integration involves is represented as Δ. Once this series of integrations has been completed, no additional integrations are needed. In order to determine the time evolution of the system, the array of cells is used as the basis of an iterative mapping. If a trajectory ends in a particular cell, it is assumed that the next segment of time evolution ($\Delta < t \leq 2\Delta$) proceeds with the center of the new cell serving as the initial point of this segment of the trajectory. In this way, an initial point is mapped to different cells in phase space every Δ s.

More recently, Hsu (1982) has introduced a more sophisticted analysis based upon a statistical study of an array of initial points that lie within each of the individual cells. This method involves a good deal of computation and leads to a probabilistic description of the system. Basically, the end trajectory of each of the array of points within a cell is recorded and the relative probability of a given cell mapping onto another cell is calculated by determining what fraction of the points ended within the target cell. This information can be used in the context of Markov Chain theory to determine steady-state trajectories. This variation of the Simple Cell Method is termed Generalized Cell Mapping (GCM). Hsu (1977), Hsu, Guttalu, and Zhu (1982) and Hsu and Kim (1985) present further explanations and applications of these techniques.

The ease of implementation and interpretation of the Simple Cell Mapping technique and the relative complexity of the Generalized Cell Mapping technique led the present author to

[1]This work was supported by the National Science Foundation, Grant No. MSM-8451186 and the Army Research Office, Contract No. 22557-EG.

Contributed by the Applied Mechanics Division for presentation at the Winter Annual Meeting, Chicago, IL, November 28 to December 2, 1988, of THE AMERICAN SOCIETY OF MECHANICAL ENGINEERS.

Discussion on this paper should be addressed to the Editorial Department, ASME, United Engineering Center, 345 East 47th Street, New York, N.Y. 10017, and will be accepted until two months after final publication of the paper itself in the JOURNAL OF APPLIED MECHANICS. Manuscript received by ASME Applied Mechanics Division, November 26, 1986; final revision, October 16, 1987.

Paper No. 88-WA/APM-17.

Copyright © 1988 by ASME
Downloaded 03 May 2010 to 171.66.16.21. Redistribution subject to ASME license or copyright; see http://www.asme.org/terms/Terms_Use.cfm

seek a method that combined some of the advantages of both methods. The technique that has been devised is termed Interpolated Cell Mapping (ICM). The rationale behind ICM is discussed in the following section.

ICM Method: Development

As discussed in the preceding section, the set of trajectories for all cells in the phase array defines a mapping of the discretized phase space from a time t to $t+\Delta$. In this way, the problem of integrating all the trajectories for a set length of time is reduced to that of repeatedly iterating the system's map. When analyzing the resultant motions, one quickly sees that a finite number of possibilities exists for the behavior of an individual trajectory. Clearly, a given trajectory can map off the array or stay within it. If it maps off the array, it is recorded as a point having no attractor within the array, even though the actual trajectory might eventually migrate back. If the trajectory stays within the array, it can be classified as periodic or transient according to whether or not it is part of a repeating pattern of cells. Further details of this kind of classification can be found in Hsu (1980).

For the purpose of this paper, the following definitions will be used:

(1) $T_n = n\Delta$, where Δ is the discretization interval;
(2) The ijth cell in the array is denoted by C_{ij};
(3) M^{ij} defines the mapping of the ijth cell (M^{ij} a 2×2 matrix);
(4) $M_1^{ij}(0) \equiv M^{ij}(1,1)$ is the x_1-coordinate of the center of C_{ij};
(5) $M_2^{ij}(0) \equiv M^{ij}(2,1)$ is the x_2-coordinate of the center of C_{ij};
(6) $M_1^{ij}(\Delta) \equiv M^{ij}(1,2)$ is the x_1-coordinate after Δ s;
(7) $M_2^{ij}(\Delta) \equiv M^{ij}(2,2)$ is the x_2-coordinate after Δ s.

These definitions hold for second-order systems. The mapping procedure can be generalized to consider higher-order systems, although this topic is not pursued in this paper.

The initial conditions for M^{ij} are

$$M_1^{ij}(0) = \frac{\Delta x_1}{2} + (i-1)\Delta x_1 + x_{1_0} \tag{1}$$

$$M_2^{ij}(0) = \frac{\Delta x_2}{2} + (j-1)\Delta x_2 + x_{2_0} \tag{2}$$

These definitions are graphically illustrated in Fig. 1.

The Simple Cell Method can easily be represented in terms of the aforementioned definitions. Assume that the trajectory starting in the center of cell C_{ij} ends in cell C_{kl} after Δ s and that the trajectory beginning in the center of cell C_{kl} ends in cell C_{mn} after the same time interval. Then, according to the Simple Cell Method, the cell C_{ij} maps into the cell C_{mn} after 2Δ s, by way of cell C_{kl}.

The trajectory of a given point is represented in the following way; I_1 represents the trajectory from T_0 to T_1; I_2 represents the trajectory from T_1 to T_2, etc. Under the SCM technique, each of these I's are identical to one of the already determined mappings, M. Thus a complete trajectory over n time intervals can be represented as

$$I_{1n} = [I_1, I_2, \ldots, I_{n-1}, I_n] \tag{3}$$

where each I_i is in fact a mapping M^{ij}. The total mapping over n periods is then given by $I_n \circ I_{n-1} \circ \ldots \circ I_2 \circ I_1$.

For the case just described, the terminal cell C_{mn} is found from

$$C_{mn} = I_2 \circ I_1(C_{ij})$$

where

$$I_1 = M^{ij} \quad \text{and} \quad I_2 = M^{kl}.$$

The shortcoming of this analysis lies in the nature of the transition from the end one iteration, I_i and the beginning of the next iteration, I_{i+1}. In general, the trajectory will not stop precisely at the center of each cell. Therefore, the iteration, which is based upon a trajectory starting at the cell's midpoint, involves a finite error in position and velocity

$$0. \le \text{position error} \le \frac{\Delta x_1}{2} \tag{4}$$

$$0. \le \text{velocity error} \le \frac{\Delta x_2}{2} \tag{5}$$

This error occurs at the beginning of every iteration and affects an individual trajectory in the manner shown in Fig. 2.

For an infinitesimal cell size, these errors go to zero. As the cell size increases, the errors become more and more serious. Recognition of this problem led the author to develop the Interpolated Cell Mapping (ICM) technique.

The first way in which ICM differs from SCM involves the fact that the actual location of each terminal point in the integrations is recorded, not just the cell within which the terminal point lies. To begin the iteration procedure, the relative position at $t=\Delta$ of a trajectory's terminal position is determined with respect to the centers of the four cells forming the vertices of a rectangle about the terminal point (C_{22}, C_{23}, C_{32}, and C_{33} in Fig. 1). The position at $t = 2\Delta$ is found by interpolating between the final locations of the trajectories emanating from the C_{ij}'s. Figure 1 illustrates how an initial point A maps to the new position B. The mapping involved is M^{11} and it is seen that $M_1^{11}(0) = x_{1_0} + \Delta x_1/2$; $M_2^{11}(0) = x_{2_0} + \Delta x_2/2$; $M_1^{11}(\Delta) = x_{1_B}$; $M_2^{11}(\Delta) = x_{2_B}$. The cell centers that surround the point B are those associated with C_{22}, C_{23}, C_{32},

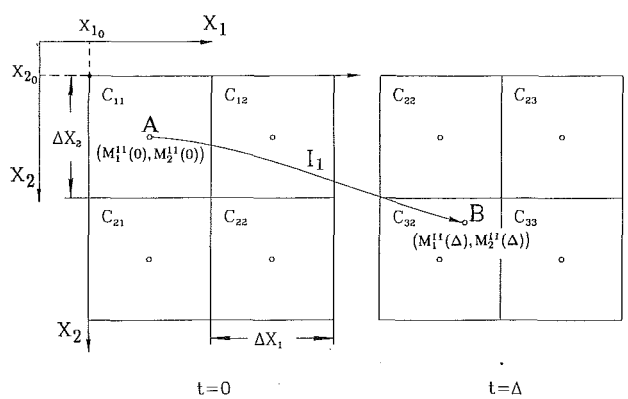


Fig. 1 Cell mapping, $t=0$ to $t=\Delta$

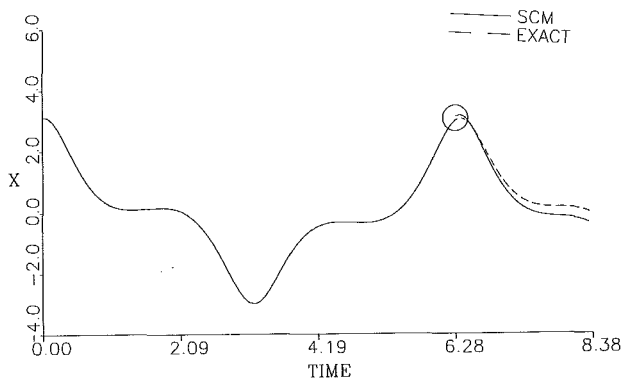


Fig. 2 Trajectory comparison, SCM versus exact integration

Downloaded 03 May 2010 to 171.66.16.21. Redistribution subject to ASME license or copyright; see http://www.asme.org/terms/Terms_Use.cfm

and C_{33}. In order to determine the position of the point B after Δ s, the corresponding positions of the surrounding center images must be used. The terminal coordinates of the surrounding centers are simply given by $M^{22}(\Delta)$, $M^{23}(\Delta)$, $M^{32}(\Delta)$, and $M^{33}(\Delta)$. The relative position of the point B to its surrounding centers is shown in Fig. 3. It is displaced a distance x_{1_H} to the right from the leftmost center and a distance x_{2_v} up from the lowermost center. Denote the ratio $x_{1_H}/\Delta x_1$ as α and the ratio $x_{2_v}/\Delta x_2$ as β. After an additional Δ s, the relative positions have changed to those shown in Fig. 3. The position that the trajectory occupies after Δ s is given by the intersection of the two line segments (a, b)-(e, f) and (c, d)-(g, h).

The coordinates (a, b), (c, d), (e, f), and (g, h) are found from the relations

$$a = \alpha[M_1^{33}(\Delta) - M_1^{32}(\Delta)] + M_1^{32}(\Delta) \tag{6}$$

$$b = \alpha[M_2^{33}(\Delta) - M_2^{32}(\Delta)] + M_2^{32}(\Delta) \tag{7}$$

$$c = \beta[M_1^{22}(\Delta) - M_1^{32}(\Delta)] + M_1^{32}(\Delta) \tag{8}$$

$$d = \beta[M_2^{22}(\Delta) - M_2^{32}(\Delta)] + M_2^{32}(\Delta) \tag{9}$$

$$e = \alpha[M_1^{23}(\Delta) - M_1^{22}(\Delta)] + M_1^{22}(\Delta) \tag{10}$$

$$f = \alpha[M_2^{23}(\Delta) - M_2^{22}(\Delta)] + M_2^{22}(\Delta) \tag{11}$$

$$g = \beta[M_1^{23}(\Delta) - M_1^{33}(\Delta)] + M_1^{33}(\Delta) \tag{12}$$

$$h = \beta[M_2^{23}(\Delta) - M_2^{33}(\Delta)] + M_2^{33}(\Delta) \tag{13}$$

The lines defined by the line segments (a, b)-(e, f) and (c, d)-(g, h) are represented by the equations

$$x_2 = u^1 x_1 + v^1 \tag{14}$$

and

$$x_2 = u^2 x_1 + v^2 \tag{15}$$

respectively.

The coefficients u^1, u^2, v^1, and v^2 are given by

$$\begin{pmatrix} u^1 \\ v^1 \end{pmatrix} = \frac{1}{(a-e)} \begin{pmatrix} 1 & -1 \\ -e & a \end{pmatrix} \begin{pmatrix} b \\ f \end{pmatrix} \tag{16}$$

$$\begin{pmatrix} u^2 \\ v^2 \end{pmatrix} = \frac{1}{(c-g)} \begin{pmatrix} 1 & -1 \\ -g & c \end{pmatrix} \begin{pmatrix} d \\ h \end{pmatrix} \tag{17}$$

The coordinates of the intersection of the two lines, (x_1^i and x_2^i), are given by

$$x_1^i = \left(\frac{v^2 - v^1}{u^1 - u^2}\right) \tag{18}$$

and

$$x_2^i = \left(\frac{u^1 v^2 - u^2 v^1}{u^1 - u^2}\right) \tag{19}$$

The foregoing analysis provides a clear picture of what the interpolation routine involves. In actual calculation, the following equivalent results are actually used

$$x_1^i = (1-\alpha)(1-\beta)a + \alpha(1-\beta)g + (1-\alpha)\beta c + \alpha\beta e \tag{20}$$

$$x_2^i = (1-\alpha)(1-\beta)b + \alpha(1-\beta)h + (1-\alpha)\beta d + \alpha\beta f \tag{21}$$

In the preceding analysis, it was assumed that each line segment had a finite slope and that the two lines possessed an intersection. It is clear that degenerate or ill-conditioned cases can occur and that these must be handled separately. For instance, if (a, b)-(e, f) defined a vertical line, then equation (16) no longer holds, due to the singularity induced by the term $1/a - e$. The solution for the intersection in this case is quite easily found to be

$$x_1^i = a \tag{20a}$$

and

$$x_2^i = au^2 + v^2. \tag{21a}$$

Extending the trajectory simply involves a repeated application of the interpolation technique. The ICM method will lead to a trajectory like that shown in Fig. 4. Note that there is no longer a step discontinuity in both the displacement and velocity at each time step; also note the close match between the exact and the interpolated response. Although the ICM generated trajectory will certainly diverge from the exact response eventually, the improvement due to the ICM method is apparent.

Under the ICM technique, the total trajectory is again expressible in the form of equation (3). However, the individual trajectory segments, I_i, are no longer equal to any individual mapping M^{ij}, but are derived from four separate mappings via the interpolation procedure. Therefore, the individual segments of a given total trajectory are unique to that particular trajectory and will not occur in any other trajectory.

Only a modest computational penalty is incurred by implementing ICM as opposed to SCM since the same amount of numerical integration is required. The additional cost involves the interpolation that determines each new terminal position.

Since the trajectory is continuous, the criteria for periodic motions is the same as for an exact integration. The actual position of the trajectory in phase space is examined at regular intervals. For the Poincaré map, these intervals would correspond to the forcing period. If the mapped trajectory passes within 10^{-3} of a previously mapped position, then the motion is considered to be periodic. If the trajectory has shown no periodicity within 20 iterates, then the motion is considered to be chaotic.

This is quite different than the criteria in the SCM procedure. Under SCM, a periodic response is indicated by a repeating pattern of cells. The highest period that can be sustained is clearly equal to the total number of cells in the cell array. Thus a chaotic motion can only be indicated by a periodic response in which the period is relatively long. The use of ICM, on the other hand, places no explicit restriction on the length of the period that can be observed. Of course the com-

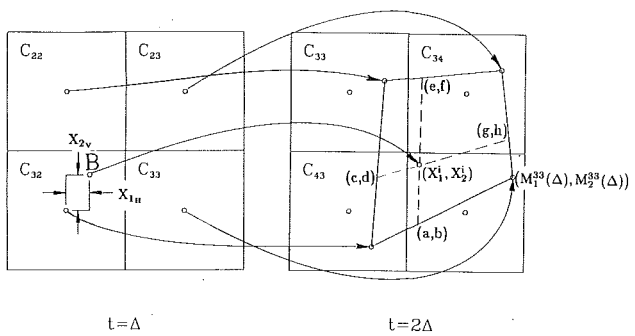


Fig. 3 Interpolated cell procedure, $t = \Delta$ to $t = 2\Delta$

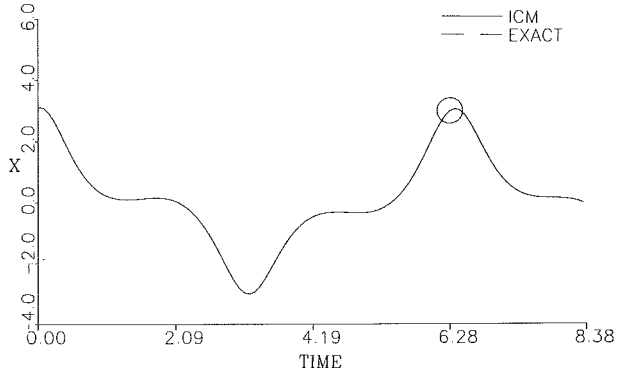


Fig. 4 Trajectory comparison, ICM versus exact integration

Downloaded 03 May 2010 to 171.66.16.21. Redistribution subject to ASME license or copyright; see http://www.asme.org/terms/Terms_Use.cfm

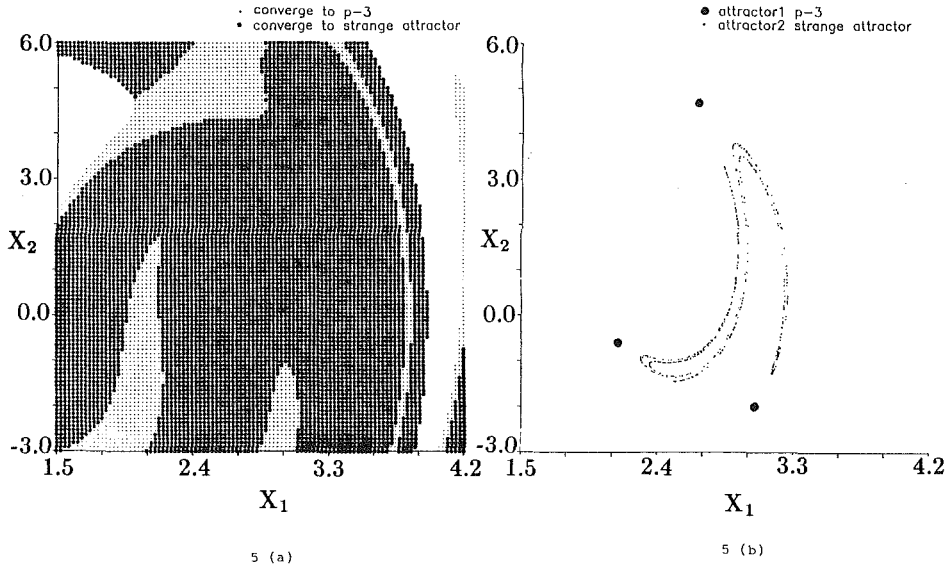


Fig. 5 Direct integration: initial condition map and attractors

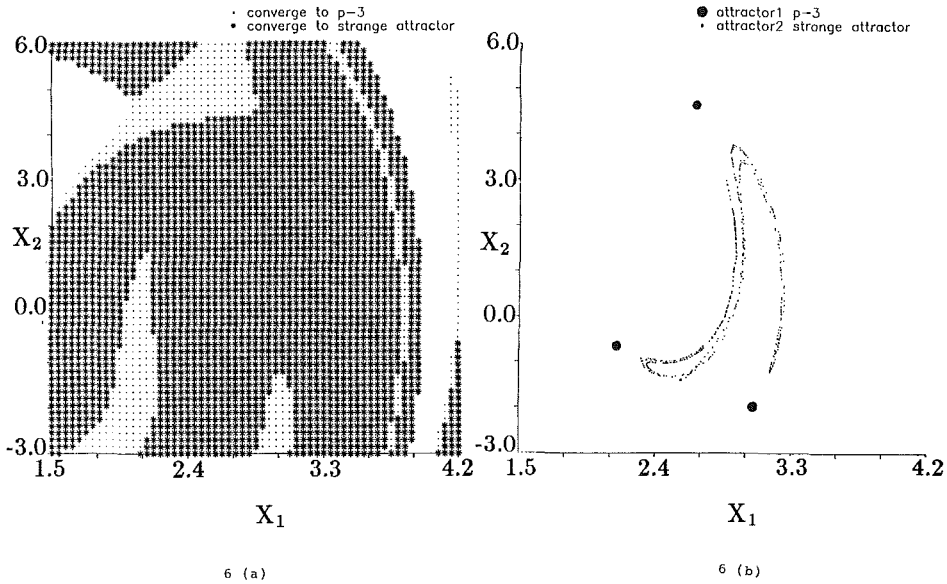


Fig. 6 ICM, 61 by 61 cells: initial condition map and attractors

puter's own finite word length will place a limit on the length of time that a nonperiodic response can exist. A chaotic response will exhibit the classical characteristic of not exactly repeating for as long as the iteration continues, up until the numerical computer itself imposes periodicity because of its limited precision. It should be noted that for any modern computer, the length of time that an integrated trajectory can remain nonperiodic is extremely long.

Results

In order to highlight the ICM method, a series of plots have been generated that apply to the system described by the Duffing's equation (Duffing, 1918)

$$\ddot{x}+0.02\dot{x}+0.25x+x^3=8.5\cos(t) \tag{22}$$

which can be represented in state form as

$$\frac{d}{dt}\begin{pmatrix}x_1\\x_2\end{pmatrix}=\begin{pmatrix}x_2\\-0.02x_2-0.25x_1-x_1{}^3+8.5\cos(t)\end{pmatrix} \tag{23}$$

The Duffing's equation has been extensively studied in the past (Guckenheimer and Holmes, 1983; Minorsky, 1983; Moon, 1980, for instance) because it is a simple system that supports a wide variety of nonlinear responses. This particular set of parameters was also examined by Hsu (1987) for the case of a Generalized Cell Mapping.

The region of phase space to be examined is defined by

$$1.5\le x_1\le 4.2$$
$$-3.0\le x_2\le 6.0$$

This particular system can support both a steady-state period three motion as well as chaotic oscillations. Thus each trajectory will either leave the phase array, lead to (or immediately be part of) a period three motion, or lead to chaos. For reference purposes, Fig. 5 represents an "exact" solution in the sense that each cell trajectory was continuously integrated until the response either left the phase array or went to a steady-state condition. No phase space discretization was involved, and thus, for each trajectory, this represents the limit of the spatial discretization size going to zero. Implicit in the preceding comment are the approximations introduced by the limited word length of the numerical computer. Figures 6–9 illustrate SCM and ICM for different discretizations. Thus the accuracy in determining the regions of global attrac-

Downloaded 03 May 2010 to 171.66.16.21. Redistribution subject to ASME license or copyright; see http://www.asme.org/terms/Terms_Use.cfm

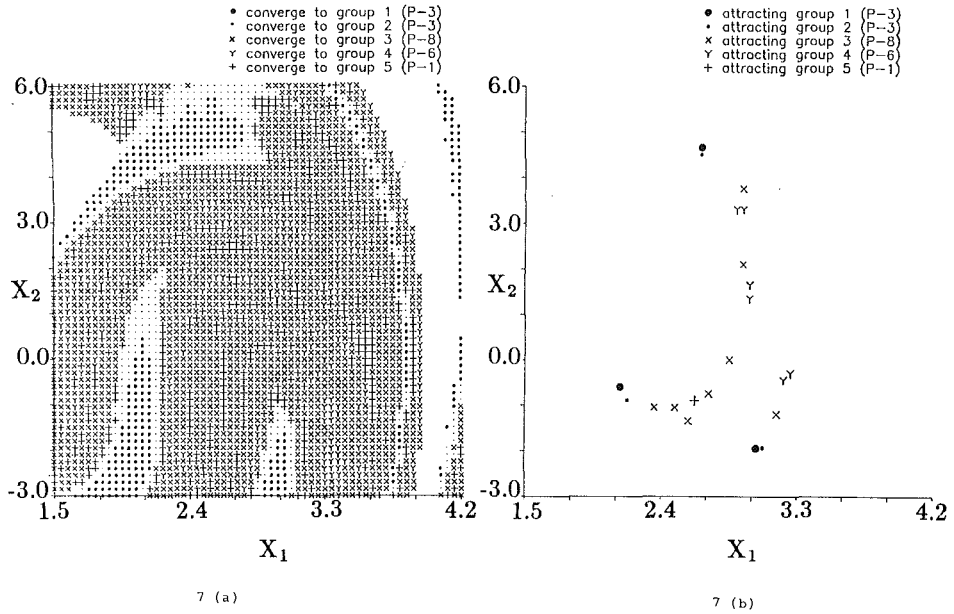


Fig. 7 SCM, 61 by 61 cells: initial condition map and attractors

tion can easily be assessed. The CPU time required was also recorded, thereby giving a sense of the relative computation involved in the two methods.

Figure 5(*a*) shows that the points in the phase space are divided into three main types: Those that map out of the space (blank regions), those that approach a period three orbit (dots), and those that lead to a chaotic response (stars). The actual Poincaré maps of the attractors are illustrated in Fig. 5(*b*).

Figure 6(*a*) shows the results of using ICM with a cell array of dimension 61×61 (discretization of $\Delta x_1 = 0.04426$ and $\Delta x_2 = 0.14754$). The match between this plot and the exact solution, Fig. 5(*a*), is extremely good. Within the limits of the discretization itself, no difference is discernible in the boundaries of the period three, chaotic, and "no-return" motions. Figure 6(*b*) shows that the attractors generated by the ICM technique are essentially identical with the actual attractors as shown in Fig. 5(*b*).

Figure 7(*a*) displays the results of applying SCM for the same level of discretization. In this case, only the most coarse features of the basins of attraction are uncovered. The positions of the basin boundaries are distorted and a large number of spurious data points have been recorded. These spurious readings take the form of period 1, period 6, and two period 3 motions within the region that actually supports only nonperiodic motions. The responses that correspond to chaotic motion are indicated by period 1, 6, and 8 responses, reinforcing the previous observation that SCM is not capable of indicating chaotic motions, only periodic motions of a relatively high period. The Poincaré sections of the attractors are shown in Fig. 7(*b*). It can be seen that the period 1, 6, and 8 responses occur within the portion of phase space that is actually occupied by the system's strange attractor.

It is quite interesting to note that the cells in the basin of attraction of one of the period three groups (indicated by small dots) surround the basins of attraction of the other period three group (indicated by large dots). This same kind of boundary region is found by Hsu (1987) through the use of a generalized cell mapping. In his paper, Hsu refers to these regions as points that are cells of the boundary set of the zeroth level or the multiple-domicile cells of the zeroth level. They are not considered to be a part of the period three or the chaotic regions. It is mentioned that the width of this region should decrease if the cell size is diminished.

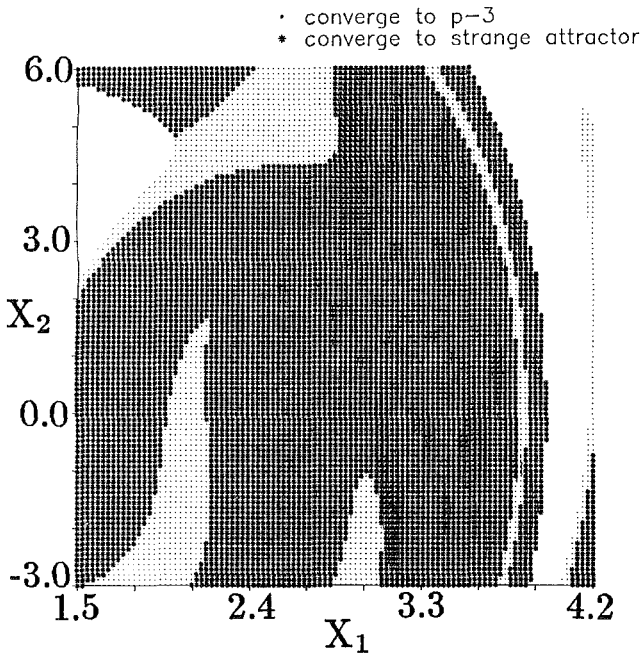


Fig. 8 ICM, 101 by 101 cells: initial condition map

The physical meaning of these cells is readily ascertained from the SCM plot to be two distinct basins of attraction for two distinct period three responses, Fig. 7(*a*, *b*). The large group falls within the region occupied by the period three attracting set of the exact response and the surrounding group is simply an artifact of the SCM method. Both period three groups taken together give a rough approximation of the basin of attraction of the actual three period group (shown in Figs. 5 and 6) but the chaotic-periodic boundary is in error to an observable degree.

This observation points out another advantage of the ICM technique, namely, its ability to generate the basins of attraction for the chaotic attractor and the period three attractor without generating an additional, and spurious, attractor.

Figure 8 illustrates the result of using ICM with a phase array of dimension 101×101 (discretization of $\Delta x_1 = 0.02673$ and $\Delta x_2 = 0.08911$). The basin boundaries of Figs. 5 and 8 are almost indistinguishable to the limits of the cell size.

Downloaded 03 May 2010 to 171.66.16.21. Redistribution subject to ASME license or copyright; see http://www.asme.org/terms/Terms_Use.cfm

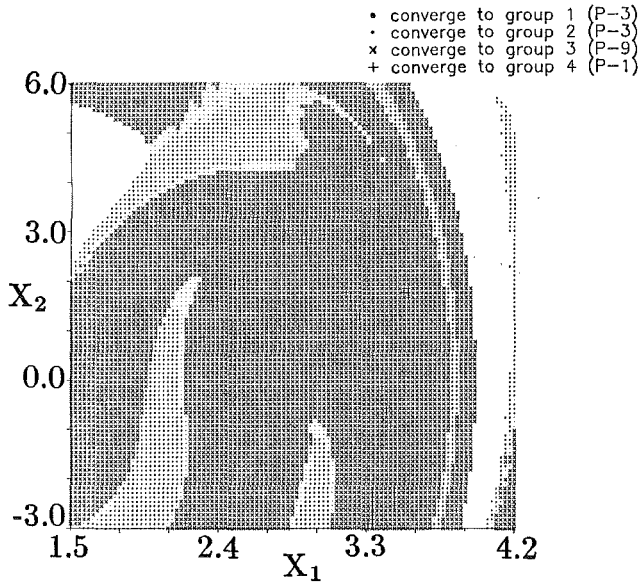


Fig. 9 SCM, 101 by 101 cells: initial condition map

Using SCM, Fig. 9, gives a much improved basin determination over the coarser discretization, although the results are still noticeably inferior to those obtained with ICM. Clearly, the indicated basin of attraction for the period three motions are distorted from the exact results. As in the previous case, the basins of attraction for the chaotic motion also are contaminated with spurious period 1 and period 3 motions. At this level of discretization, chaos is indicated by a period nine response. The bulk of this plot consists of four main behavior types: Points that map out the boundaries, one group of period three motions, a different group of period three motions, and a chaotic response (indicated by a period one and a period nine motion). This figure again illustrates the phenomenon of the period three region surrounded by another period three region and in fact is quite similar to the plot obtained by Hsu. In particular, the "tail" of the top attracting region of the period three attractor (dots) is generated by both the SCM as well as the GCM technique.

The easiest way to indicate the relative efficiencies of the two approaches is to record the relative CPU time that was required, as shown in Table 1.

The computational penalty of using ICM as opposed to SCM is seen to be on the order of seven percent. This is due to the fact that the bulk of the cost involves numerically integrating the trajectories of each point for one forcing cycle, and this cost is common to both methods. The small increase in cost is a small price to pay for the greatly improved accuracy of the ICM method. Furthermore, once the complete phase plot is constructed, one can obtain transient time characterizations of the motion at almost no additional cost.

Conclusions

The Interpolated Cell Mapping technique has been shown to provide a substantial gain in accuracy over the Simple Cell Mapping method with only a small increase in cost and complexity. The method allows a much closer approximation to a system's continuous trajectory to be computed and permits very accurate determinations of the basins of attraction for a given system's steady-state responses. Since the continuous trajectory is well approximated with this method, one is free to perform transient analyses on the system's response. One example of such an analysis would be a determination of the system's Lyapunov exponents (Wolf, 1985) from the continuous trajectory of a point initially slightly perturbed from a steady-state attractor. Once the initial cell mapping has been determined, such an analysis is extremely inexpensive to perform.

Table 1

	CPU Time Required	
Array size	ICM	SCM
61×61	106	100
101×101	107	100

To conclude, the technique produces accurate basins of attraction for a nonlinear system and avoids the pitfall present in both SCM and GCM of creating spurious basins of attraction that have no basis in the actual system.

References

Blair, K. W., and Loud, W. S., 1960, "Periodic Solutions of $\ddot{x} + c\dot{x} + g(x) = Ef(t)$ under Variation of Certain Parameters," *J. Soc. Ind. Appl. Math.*, Vol. 8, pp. 74–101.

Duffing, G., 1918, *Erzwungene Schwingungen bei veranderlicher Eigenfrequenz und ihre technisch Bedeutung*, Sammlung Vieweg, Braunschweig.

Guckenheimer, J., and Holmes, P. J., 1983, *Nonlinear Oscillations, Dynamical Systems, and Bifurcations of Vector Fields*, Springer-Verlag, New York, Berlin, Heidelberg, Tokyo.

Guttalu, R. S., and Hsu, C. S., 1984, "A Global Analysis of a Non-Linear System Under Parametric Excitation," *Journal of Sound and Vibration*, Vol. 97, No. 3, pp. 399–427.

Hagedorn, P., 1981, *Nonlinear Oscillations*, Clarendon Press.

Hayashi, C., 1964, *Nonlinear Oscillations in Physical Systems*, McGraw-Hill Book Co.

Hayashi, C., Ueda, Y., and Kawakami, H., 1969, "Transformation Theory as Applied to the Solutions of Non-Linear Differential E' of the Second Order," *International Journal of Non-Linear Mechanics*, Vol. 4, pp. 235–255.

Hsu, C. S., Yee, H. C., and Cheng, W. H., 1977, "Determination of Global Regions of Asymptotic Stability for Difference Dynamical Systems," ASME *Journal of Applied Mechanics*, Vol. 44, No. 1, March, pp. 147–153.

Hsu, C. S., 1977, "On Nonlinear Parametric Excitation Problems," *Advances in Applied Mechanics*, Vol. 17, pp. 245–299.

Hsu, C. S., 1980, "A Theory of Cell-to-Cell Mapping Dynamical Systems," ASME JOURNAL OF APPLIED MECHANICS, Vol. 47, No. 4, December, pp. 931–939.

Hsu, C. S. and Guttalu, R. S., 1980, "An Unraveling Algorithm for Global Analysis of Dynamical Systems: An Application of Cell-to-Cell Mappings," ASME JOURNAL OF APPLIED MECHANICS, Vol. 47, No. 4, December, pp. 940–948.

Hsu, C. S., Guttalu, R. S., and Zhu, W. H., 1982, "A Method of Analyzing Generalized Cell Mappings," ASME JOURNAL OF APPLIED MECHANICS, Vol. 49, No. 4, December, pp. 885–894.

Hsu, C. S., 1982, "A Probabilistic Theory of Nonlinear Dynamical Systems Based on the Cell Space Concept," ASME JOURNAL OF APPLIED MECHANICS, Vol. 49, No. 4, December, pp. 895–902.

Hsu, C. S., and Kim, M. C., 1985, "Statistics of Strange Attractors by Generalized Cell Mapping," *Journal of Statistical Physics*, Vol. 38, pp. 735–761.

Hsu, C. S., and Chiu, H. M., 1987, to appear in the *Journal of Sound and Vibration*, April.

Minorsky, N., 1983, *Nonlinear Oscillations*, Krieger Publishing Co.

Moon, F. C., 1980, "Experiments on Chaotic Motions of a Forced Nonlinear Oscillator: Strange Attractors," ASME JOURNAL OF APPLIED MECHANICS, Vol. 47, No. 3, September, pp. 638–644.

Nayfeh, A. H., and Mook, D. T., *Nonlinear Oscillations*, New York: Wiley Inters.

Poincaré, H., 1952, *Les Methodes nouvelles de la mécanique céleste*, Vol. 1, 1892, English Translation: "New Methods of Celestial Mechanics," Vol. 3, NASA Technical Translation, TTF-452, 1967 Inc., New York.

Tongue, B. H., 1987, "Characteristics of Numerical Simulations of Chaotic Systems," to appear in the ASME JOURNAL OF APPLIED MECHANICS.

Ueda, Y., 1979, "Randomly Transitional Phenomena in the System Governed by Duffing's Equation," *Journal of Statistical Physics*, Vol. 2, No. 2, pp. 181–197.

Wolf, A., 1985, "Determining Lyapunov Exponents from a Time Series," *Physica*, Vol. 16D, pp. 285–317.

Downloaded 03 May 2010 to 171.66.16.21. Redistribution subject to ASME license or copyright; see http://www.asme.org/terms/Terms_Use.cfm

Experimental Investigation of Liquid Sloshing Under Parametric Random Excitation

R. A. Ibrahim
Professor,
Department of Mechanical Engineering,
Wayne State University,
Detroit, MI 48202
Mem. ASME

R. T. Heinrich
Associate Design Engineer,
LTV,
Aircraft Products Group,
Dallas, TX

This paper presents an experimental investigation of the random parametric excitation of a dynamic system with nonlinear inertia. The experimental model is a rigid circular tank partially filled with an incompressible inviscid liquid. The random responses of the first antisymmetric and symmetric sloshing modes are considered for band-limited random excitations. These include the means, mean squares, and probability density functions of each sloshing mode. The response of the liquid-free surface is found to be a stationary process for test durations exceeding ten minutes. The time-history response records reveal four response characteristic regimes. Each regime takes place within a certain range of excitation spectral density level. An evidence of the jump phenomenon, which was predicted theoretically by using the non-Gaussian closure scheme, is also reported. Comparisons with analytical results, derived by three different approaches, are given for the first antisymmetric sloshing mode.

Introduction

The past two decades have witnessed an increasing progress in the mathematical theory of random processes and stochastic differential equations. This progress has motivated a number of engineers to develop new stochastic stability theorems (Kushner, 1967, and Kozin, 1969) and to derive closed-form solutions for the response probability density of special classes of nonlinear systems (Caughey, 1971, 1986). These developments and others have recently been documented in a research monograph by Ibrahim (1985). It is noteworthy to mention that these efforts involved a number of controversies (Gray and Caughey, 1965) and contradictions (Ariaratnam, 1980). For example, the coefficients of the Fokker-Planck equation of a system, driven by a Gaussian "physical" white noise, will be different if the same system is driven by the "formal" derivative of the Brownian motion process. Gray and Caughey (1965) treated these two "apparent" identical problems and clarified the main differences. The coefficients of the Fokker-Planck equation depend mainly on whether the random coefficient to the next-to-the-highest derivative is a physical white noise or an increment Brownian motion process. Another contradiction observed in the literature was reported by Ariaratnam (1980) who showed that the mean-square stability boundary, as obtained by the Gaussian closure scheme, is half the stability boundary derived by using the Stratonovich stochastic averaging. In an attempt to resolve this contradiction, Ibrahim, et al. (1985), employed a non-Gaussian closure which resulted in a jump phenomenon in the response statistics. This jump phenomenon is believed to be first known in the area of random vibration and occurs at a critical excitation level.

In view of the observed contradictions in the analytical results, the authors have been motivated to undertake an experimental approach. The experimental investigation is believed to be very valuable for several reasons. The first is to verify the validity of the analytical predictions pertaining to the mean-square stability, jump phenomenon, and response statistics. The second is to observe any new response characteristics not predicted theoretically. The third is that experimental investigations usually provide more physical insight and understanding of various response characteristics that may or may not be predicted theoretically. The scarcity of experimental investigations seems to be due to the difficulties involved in verifying a number of theoretical requirements. For example, definitions of stochastic stability involve numbers that should be made arbitrarily small during the experiment, which is practically unrealistic (Bolotin, 1984).

To the authors' knowledge, three experimental investigations were reported in the literature. Dalzell (1967) conducted a series of tests to measure the spectral density of the liquid-free surface under narrow and wide-band random excitations. Under wide-band excitation, an abrupt transition between harmonic and subharmonic responses was observed when the excitation root-mean-square acceleration was reduced. An important feature was that low level harmonic response to random Gaussian excitation was nearly Gaussian. However, when large amplitude subharmonic response was excited, the

Contributed by the Applied Mechanics Division for presentation at the Winter Annual Meeting, Chicago, IL, November 28 to December 2, 1988, of The American Society of Mechanical Engineers.

Discussion on this paper should be addressed to the Editorial Department, ASME, United Engineering Center, 345 East 47th Street, New York, N.Y. 10017, and will be accepted until two months after final publication of the paper itself in the JOURNAL OF APPLIED MECHANICS. Manuscript received by ASME Applied Mechanics Division, September 26, 1986; final revision, October 19, 1987.

Paper No. 88-WA/APM-23.

Copyright © 1988 by ASME
Downloaded 03 May 2010 to 171.66.16.21. Redistribution subject to ASME license or copyright; see http://www.asme.org/terms/Terms_Use.cfm

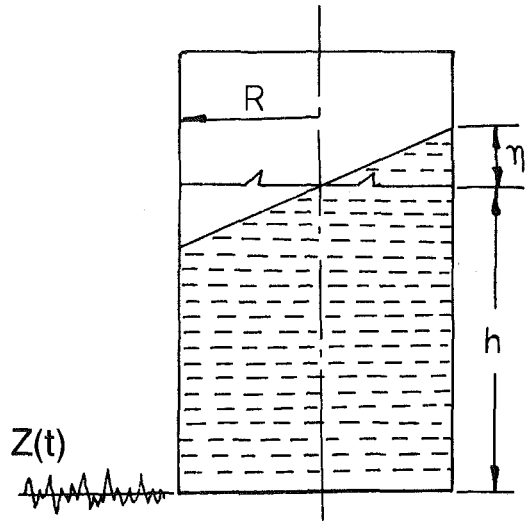


Fig. 1 Schematic diagram of a liquid tank under vertical random excitation

probability distribution changed abruptly into a double-exponential distribution. Unfortunately, Dalzell did not report the influence of liquid damping on the response or stability, which would help in correlating his results with the analytical ones. However, he described his findings as a "stab in the dark" in the absence of theoretical background. Baxter and Evan-Iwanowski (1975) conducted a series of laboratory tests to observe and measure the nonlinear parametric response of an elastic column subjected to random axial loading. The measured probability density was found to have a remarkable peak near zero amplitudes for all excitation bandwidths. Unfortunately, Baxter and Evan-Iwanowski (1975) did not compare their experimental results with those predicted by Baxter (1971) who used a stochastic averaging approach. It was Roberts (1980) who compared the measured and predicted mean-square stability boundaries of a vertical beam supported by a horizontal beam. The predicted stability boundaries were obtained by using the Gaussian closure scheme and a perturbation approach. The analytical results were in a fair agreement with the measured ones when the natural frequencies are in the immediate vicinity of the internal resonance condition.

The system, chosen for the present experimental investigation, is shown in Fig. 1, which is a circular rigid container partially filled with incompressible fluid and subjected to random parametric excitation. This system has been examined analytically by Ibrahim and Soundararajan (1983, 1985) by three different analytical methods. These were the Gaussian and non-Gaussian closure schemes and the Stratonovich stochastic averaging method. The three methods gave different stability boundaries. In particular, the non-Gaussian closure scheme predicted the occurrence of a jump in the response statistical moments at a critical excitation level. The experimental investigation will consider the excitation of the first antisymmetric and symmetric sloshing modes separately. The measured results will be compared with those predicted theoretically.

Analytical Background

This section provides a brief analytical background of the nonlinear response of the liquid-free surface under parametric random excitation as obtained by Ibrahim and Soundararajan (1983, 1985) who employed three different approaches. Based on the assumption that the liquid is incompressible, inviscid and initially irrotational the liquid-free surface motion of mode mn in a circular cylindrical container subjected to parametric random acceleration $\ddot{Z}(t)$ is governed by the differential equation

$$A''_{mn} + 2\zeta_{mn}A'_{mn} + [1+\xi''(\tau)]A_{mn}(1 - K_1A_{mn} - K_2A^2_{mn}) + K_3A'^2_{mn} + K_4A_{mn}A''_{mn} + K_5A_{mn}A'^2_{mn} + K_6A^2_{mn}A''_{mn} = 0 \quad (1)$$

where $A_{mn} = a_{mn}/R$;

a_{mn} is the liquid wave height amplitude of the sloshing mode mn,

R is the tank radius,

a prime denotes differentiation with respect to the nondimensional time parameter $\tau = \omega_{mn}t$,

ω_{mn} is the natural frequency of the sloshing mode mn,

ζ_{mn} is the damping ratio and $\xi''(\tau) = \ddot{Z}(t)/g$

The coefficients K_i provide a measure of the relative order of magnitude of the nonlinear terms in equaton (1). For example, for the first antisymmetric sloshing mode $K_2 = 29.21$, $K_5 = 1.5015$, and $K_6 = 0.2084$ when $h/a = 1.0$, where h is the fluid depth. The coefficients K_i are given for certain number of sloshing modes by Ibrahim and Soundararajan (1983). Equation (1) represents the nonlinear modeling of any mode mn and does not include nonlinear coupling with another mode. Nonlinear interaction of three different modes has been treated for the case of harmonic parametric excitation by Dodge, et al. (1965).

It is possible to treat the response as a Markov process if the parametric random excitation $\xi''(\tau)$ is approximated as a physical white noise $W(\tau)$. In order to generate the Markov vector, the acceleration term A''_{mn} associated with the nonlinear inertia expression $(K_4A_{mn}A''_{mn} + K_6A^2_{mn}A''_{mn})$ must be removed by successive elimination. The elimination process will result in quadratic, cubic, and higher-order terms. Keeping terms up to cubic order and introducing the coordinate transformation $A_{mn} = X_1$, and $A'_{mn} = X_2$, equation (1) may be written in the state vector form

$$\begin{aligned} X'_1 &= X_2, \\ X'_2 &= -2\zeta_{mn}X_2 + C_1X_1X^2_2 + C_2X^2_2 + C_3\zeta_{mn}X^2_1X_2 \\ &\quad + C_4\zeta_{mn}X_1X_2 - \{1+W(\tau)\}(X_1 - C_6X^2_1 - C_5X^3_1) \end{aligned} \quad (2)$$

where the new coefficients C_i are related to K_i.

A general differential equation of the response statistical moments was derived by using the It_{δ} stochastic calculus or the Fokker-Planck equation (Ibrahim, 1985). For the Markov state vector (2), this equation is

$$\begin{aligned} m'_{k,l} &= km_{k-1,l+1} + l\{-2\zeta_{mn}m_{k,l} + C_1m_{k+1,l+1} \\ &\quad + C_2m_{k,l+1} + C_3\zeta_{mn}m_{k+2,l} + C_4\zeta_{mn}mm_{k+1,l} \\ &\quad + C_5m_{k+3,l-1} + C_6m_{k+2,l-1} - m_{k+1,l-1}\} \\ &\quad + l(l-1)D\{m_{k+2,l-2} - 2C_6m_{k+3,l-2} + C_7m_{k+4,l-2}\} \end{aligned} \quad (3)$$

where

$$m_{k,l} = \int_{-\infty}^{\infty}\int X^k{}_1X'^l{}_2p(X,\tau)dX_1dX_2$$

and $2D$ is the spectral density of the white noise $W(\tau)$.

It is seen that equation (3) constitutes an infinite coupled set of first-order differential equations; that is, the moment equation of order n, $(n = k+l)$ contains moment terms of order $n+1$ and $n+2$. These equations were closed via Gaussian and non-Gaussian closure schemes. The mean-square response according to the Gaussian closure solution is

$$E[X^2_1] = \{(D/2\zeta_{mn}) - 1\}/\{C_{11}[(D/2\zeta_{mn}) - C_{12}]\} \quad (4)$$

where

$$C_{11} = 6C_5 - 3C_6{}^2 - C_1 \quad \text{and} \quad C_{12} = (1/C_{11})(0.5C_3 + 3C_5)$$

Downloaded 03 May 2010 to 171.66.16.21. Redistribution subject to ASME license or copyright; see http://www.asme.org/terms/Terms_Use.cfm

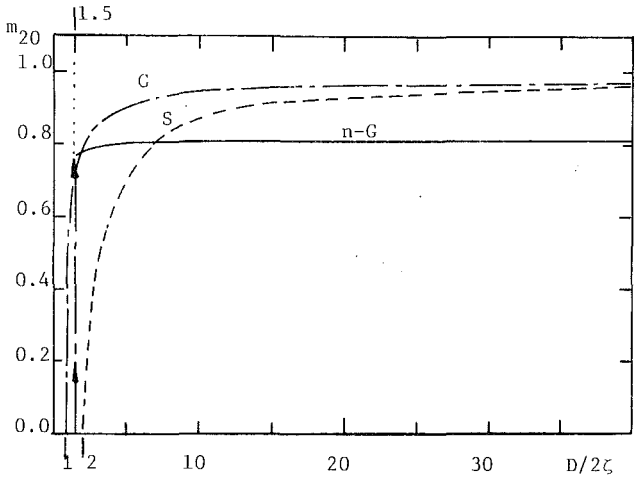


Fig. 2 Comparison of mean-square responses as obtained by non-Gaussian closure (n – G); Gaussian closure (G), and Stratonovich stochastic averaging (S), for $\zeta = 0.1$

The non-Gaussian closure soluton was obtained numerically and is plotted in Fig. 2 for the first antisymmetric sloshing mode. Figure 2 also shows the Gaussian solution (4) and the mean-square response as obtained by using the Stratonovich stochastic averaging method. The Stratonovich method yields a closed-form solution given by the expression

$$E[X^2{}_1] = (\zeta_{mn}/D)\,(D/2\zeta_{mn} - 2)D^*{}_{\mu\nu}/\sqrt{2n_3} \tag{5}$$

where

$$D^*{}_{\mu\nu} = D_{-\mu}(n_2/\sqrt{2n_3})/D_{-\nu}(n_2/\sqrt{2n_3});$$

$D_{-\mu}(\ )$ or $D_{-\nu}(\ )$ is the parabolic cylindrical function known as Whittaker's function (Abramowitz and Stegen, 1972),

$n_2 = (\zeta_{mn}/D)\,|0.5C_3 + 4C_7|$;
$n_3 = 0.75C^2{}_7 - 0.25(\zeta_{mn}/D)\,(8C_8 - C_3C_7)$,
$C_7 = 0.5(C^2{}_6 - 2C_5)$; $C_8 = 0.3125C^2{}_5$.

The three solutions give different mean-square boundary conditions. It is seen that the Gaussian closure solution is consistent with the condition of asymptotic stability of mean square

$$D/2\zeta_{mn} < 1 \tag{6}$$

On the other hand, the Stratonovich averaging solution agrees with the sample stability condition (stability with probability one)

$$D/2\zeta_{mn} < 2 \tag{7}$$

The non-Gaussian closure solution is emanated at a critical excitation level where a jump in the mean-square response takes place. This critical level is somewhere between $1 < D/2\zeta_{mn} < 2$.

Experimental Investigation

Experimental Model and Equipment. The experimental model is a plexiglass cylindrical tank of 0.096-m internal diameter and 0.0029-m wall thickness. The tank is mounted on the armature of a Caldyne model A88 electrodynamic shaker. The shaker thrust is 445 N and provides 0.0254-m (1 in.) peak-to-peak stroke. The shaker is powered by a Ling Electronics Model RA-250 power supply and receives a random signal through a GenRad Type 1381 Random Noise Generator. The random signal is filtered to a desired bandwidth with a Krohn-Hite Model 3343 Variable Electronic Filter. The filtered signal is amplified via a Calex Model 176 Instrument Amplifier. Figure 3 shows a schematic diagram of the instrumentation used in this investigation.

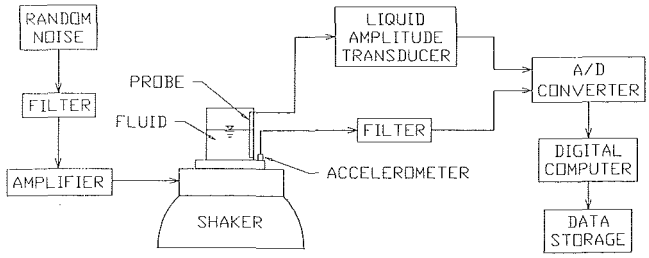


Fig. 3 Block diagram of experimental equipment

The liquid-free surface amplitude is measured by a pair of resistance wires. To measure the antisymmetric sloshing mode, eight transducers are installed around the circumference of the tank. One of these transducers is selected to measure the liquid wave height once the liquid wave orientation is identified at the beginning of each test. The symmetric sloshing mode is measured by another pair of wires located at the tank center. The excitation is measured by using a PCB Piezotronic Model 302A02 accelerometer mounted on the shaker platform. The excitation and liquid response signals are read and converted into 12 bit binary numbers by using a Data Translation DT-3752 Intelligent Analog Peripheral. This A/D converter is inserted in an expansion slot of an IBM System 9001 computer and appears as a block of memory to the computer. The computer controls the A/D converter through a FORTRAN program to perform the sampling process of both excitation and response signals and to convert them into a binary number on a floppy disk.

The tank is filled with water to a 1-dia depth. Preliminary free oscillation tests are first conducted to measure the damping ratio of the first antisymmetric mode. The first symmetric sloshing mode is developed by exciting the tank sinusoidally, then stopping the shaker, and measuring the subsequent liquid-free surface motion. The measured natural frequencies and damping ratios of the two modes are:

$$f_{11} = 3.0 \text{ Hz}, \quad \zeta_{11} = 0.0063$$
$$f_{01} = 4.4 \text{ Hz}, \quad \zeta_{01} = 0.0127$$

The main tests are conducted by selecting the following central frequencies d_c and bandwidths Δf for the two sloshing modes:

$f_c = 6$ Hz, $\Delta f = 1.5$ for the first antisymmetric mode

$f_c = 8.8$ Hz, $\Delta f = 0.5$ Hz for the first symmetric mode.

The statistical parameters of the response and excitation signal are estimated after the digital data are converted into physical units.

Experimental Observations and Time-History Responses. The first antisymmetric sloshing mode is excited by a band-limited random excitation at different levels of excitation spectral density. Both harmonic and subharmonic oscillations are observed but the harmonic response is less common and characterized by small amplitudes. When subharmonic liquid motion begins, the positive and negative free surface amplitudes are observed to be unequal. The linear liquid response is observed during small free surface oscillations. In most cases the nonlinear liquid response is more prominent than the linear motion.

Depending on the level of the excitation spectral density $D/2\zeta_{mn}$, the liquid-free surface response can be divided into four regimes. These four regimes are shown in Figs. 4 and 5 for the first antisymmetric and first symmetric sloshing modes, respectively. These figures also show samples of time-history responses of 30 s test duration for each excitation region. These regimes are as follows:

Downloaded 03 May 2010 to 171.66.16.21. Redistribution subject to ASME license or copyright; see http://www.asme.org/terms/Terms_Use.cfm

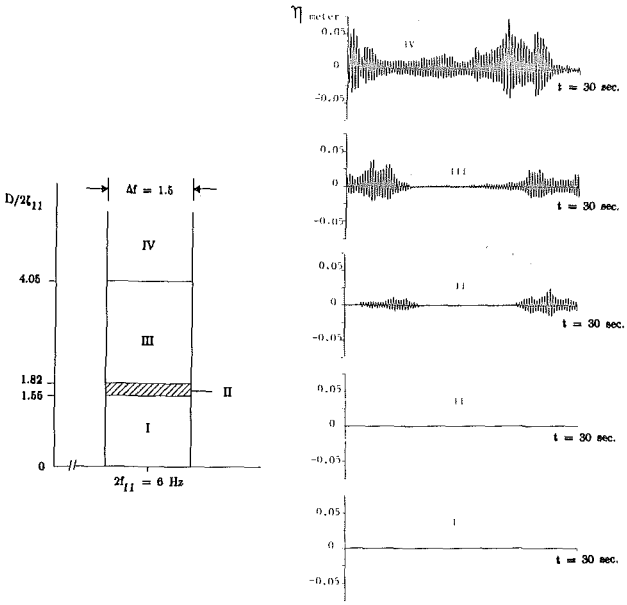


Fig. 4 Regimes of time-history responses of the first antisymmetric sloshing mode

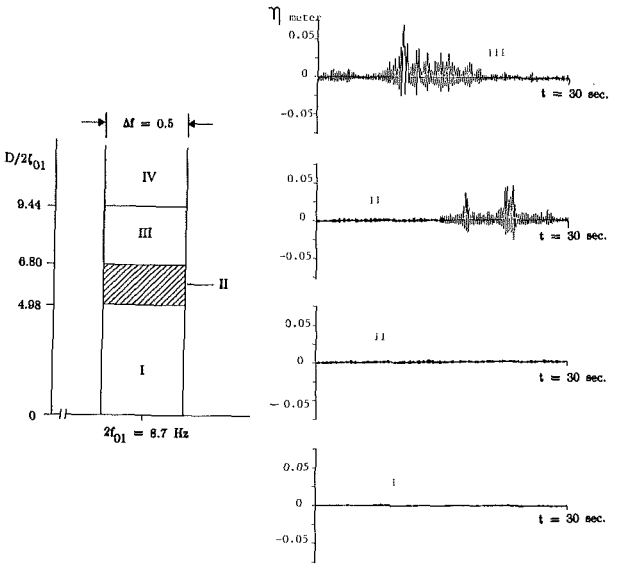


Fig. 5 Regimes of time-history responses of the first symmetric sloshing mode

Region I: Zero Liquid Motion. This range of excitation spectral density does not result in any liquid motion mainly because the liquid damping force prevents any liquid motion. The excitation ranges for the two modes are, respectively

$$0 < D/2\zeta_{11} < 1.55, \quad 0 < D/2\zeta_{01} < 4.98$$

This region was predicted analytically by Ibrahim and Soundararajan (1983, 1985); however, different ranges of the excitation levels predicted by other approaches were reported.

Region II: Uncertain Zero Motion. This is an uncertain region since the liquid-free surface may or may not oscillate under the excitation ranges

$$1.55 < D/2\zeta_{11} < 1.82, \quad 4.98 < D/2\zeta_{01} < 6.8$$

A corresponding regime, known as undeveloped sloshing was predicted by Ibrahim and Soundararajan (1983) which is characterized differently by very small motion of the liquid-free surface within an excitation level

$$2 < D/2\zeta_{mn} < 4.$$

Region III: Partially Developed Sloshing. This regime is characterized by undeveloped sloshing where significant liquid-free surface motion occurs for a certain period of time and then ceases for another period of time. At higher excitation levels, the time period of liquid motion exceeds the time period of zero motion. The excitation levels of this region for the two modes are, respectively

$$1.82 < D/2\zeta_{11} < 4.05, \quad 6.8 < D/2\zeta_{01} < 9.44$$

The analytical results of the partially developed sloshing indicated that the response is characterized by finite random motion with the excitation level defined by the region $4 < D/2\zeta_{mn} < \infty$. However, the present investigation qualitatively agrees with the observations reported by Baxter (1971) and Roberts (1980) who conducted similar tests on elastic elements.

The authors observed the development of circular motion of a central spike for the case of first symmetric mode excitation. Occasionally, the spike is displaced from the center of the tank and precesses in a way that preserves the azimuthal symmetry in a time-average sense. This motion was first reported by Gollub and Meyer (1983) who studied the amplitude dependence on the precession frequency under harmonic parametric excitation.

Region IV: Fully Developed Sloshing. This region exhibits continuous random liquid motion for all excitation levels exceeding the aforementioned ranges. When the first symmetric sloshing mode is excited, other higher sloshing modes are excited as well. This is why the bandwidth of the symmetric mode excitation is narrowed. The same observation of the interaction of the first symmetric mode with other modes was also reported by Dalzell (1967). With regard to the first antisymmetric mode, another nonlinear phenomenon is observed; that is, the nodal diameter rotates in clockwise and then counter-clockwise directions. It is obvious that this phenomenon will cause deviations from theoretical results.

It may be noticed that there are no upper limits defined in this region since the maximum shaker output is limited. If a more powerful shaker were used and the excitation spectral density is allowed to increase, the mean-square response may achieve a constant value as predicted theoretically. However, above a certain excitation level, there could be a "chaotic" sloshing where other modes may be excited or the spatial structure of the free-surface flow becomes disordered. The disordered structure of the free-surface flow under relatively large harmonic excitation amplitude was experimentally observed by Gollub and Meyer (1983). Their measurements showed a sequence of symmetry-braking instabilities leading to a chaotic state.

Figures 4 and 5 show that the liquid-free response does not have zero mean response. For the two sloshing modes considered and for small liquid amplitudes, the positive and negative displacements are essentially the same. However, for relatively higher excitation levels the positive amplitude is significantly greater than the negative ones which indicates that the liquid-free surface motion is nonlinear. The four regimes of the liquid-free surface response are mainly governed by the type of the sloshing mode under consideration and system parameters.

In order to examine the stationarity of the response process, several tests are conducted at the same excitation level and "almost" identical graphs are obtained for the mean and mean square of the wave height. These graphs (not shown) reveal that the liquid-free surface random motion is essentially stationary (in the wide sense) for test durations exceeding 600 s.

Mean and Mean-Square Responses. Figures 6 and 7 show

Downloaded 03 May 2010 to 171.66.16.21. Redistribution subject to ASME license or copyright; see http://www.asme.org/terms/Terms_Use.cfm

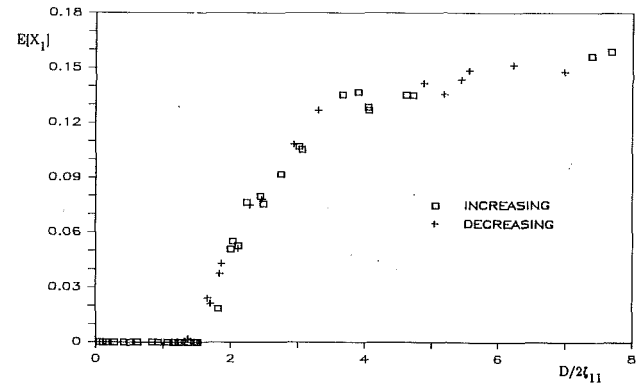


Fig. 6 Dependence of the mean value of the first antisymmetric sloshing mode on the excitation spectral density level

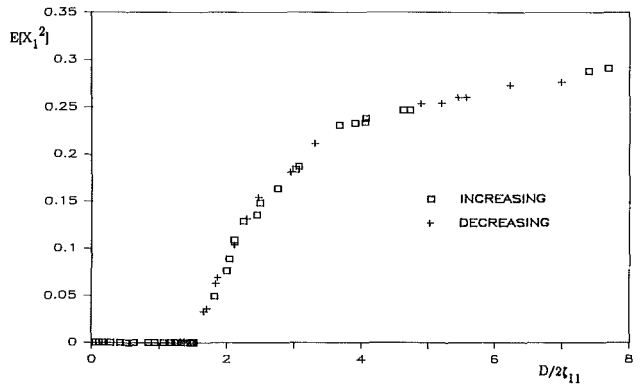


Fig. 7 Dependence of the mean square of the first antisymmetric sloshing mode on the excitation spectral density level

the mean and mean square of the first antisymmetric sloshing mode as a function of the excitation spectral density level $D/2\zeta_{11}$. The square and cross points are obtained when the excitation level is increasing and decreasing, respectively. It is seen that the values of the mean and mean-square responses remain zero up to a critical excitation level above which the free surface begins to oscillate. Because of the shaker limitations, it was not possible to increase the excitation level above the range given in Figs. 6 and 7. It may be observed that the uncertain sloshing region is included in the zero-response region.

The mean-square response of the first symmetric sloshing mode is shown in Fig. 8. This figure shows the uncertain sloshing region and another region where other higher sloshing modes are excited and interact with the first symmetric mode.

The measured mean-square response of the first antisymmetric sloshing mode is compared in Fig. 9 with those predicted by Ibrahim and Soundararajan (1983, 1985). The theoretical results were obtained by using Gaussian and non-Gaussian closure schemes and the Stratonovich stochastic averaging method. It is seen that the jump where the liquid-free surface begins to slosh is seen to be less evident than the jump level predicted by using the non-Gaussian closure scheme (Ibrahim and Soundararajan, 1985). However, the critical excitation level at which jump occurs is seen to be in a good agreement with the mean-square stability boundary predicted by the non-Gaussian closure solution. The observed differences between the measured and predicted mean squares for excitation levels greater than the critical level are attributed to two main sources. The first is due to the rotational effect of the nodal diameter about the vertical axis. This phenomenon causes the fluid wave height transducers to detect smaller liquid amplitude than the maximum amplitude when the free surface is shifted from the transducer location. The second is

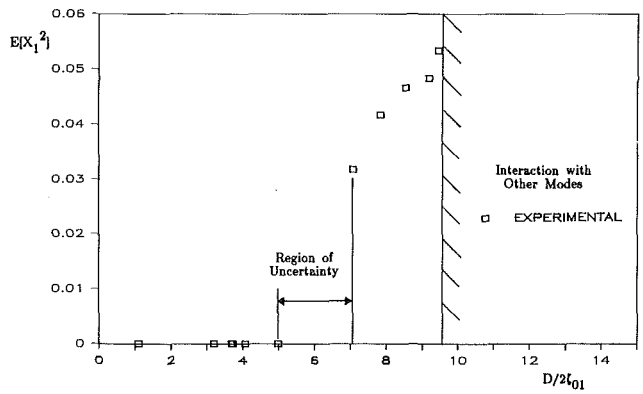


Fig. 8 Dependence of the mean square of the first symmetric sloshing mode on the excitation spectral density

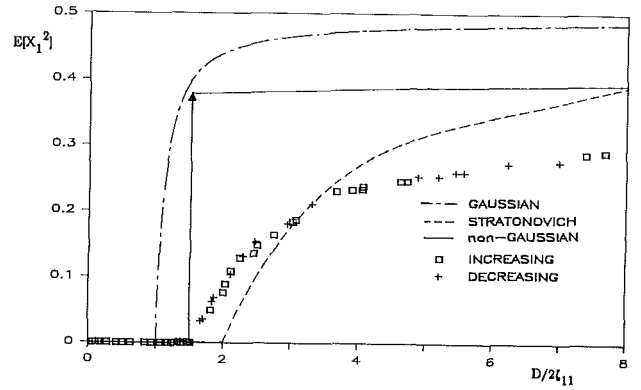


Fig. 9 Comparison of measured and predicted mean-square responses of the first antisymmetric sloshing mode

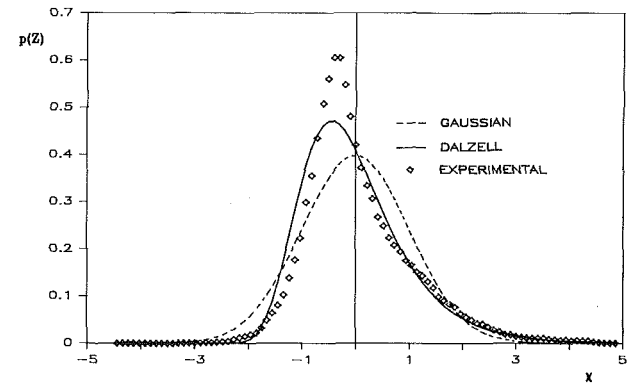


Fig. 10 Comparison of measured probability density with Dalzell and Gaussian Densities (first antisymmetric sloshing mode)

due to the fact that the bandwidths of experimental and theoretical random excitations are not the same. The analytical results are based on a wide-band random process while the experimental excitation is a band-limited random process.

Probability Functions. Figure 10 shows the measured probability density function of the first antisymmetric sloshing mode for an excitation level $D/2\zeta_{11} = 7.39$. The dotted curve represents the Gaussian probability density curve. The figure also includes a comparison with those results obtained by Dalzell (1967) shown by the solid curve. Dalzell obtained his probability functions by using a least-square curve fit of the raw probability estimates which resulted in a double-exponential distribution. The double-exponential probability distribution and density functions are defined as, respectively,

$$P(Z) = (\pi/\sqrt{6}) \exp \{ -\exp (-Z) \},$$

Downloaded 03 May 2010 to 171.66.16.21. Redistribution subject to ASME license or copyright; see http://www.asme.org/terms/Terms_Use.cfm

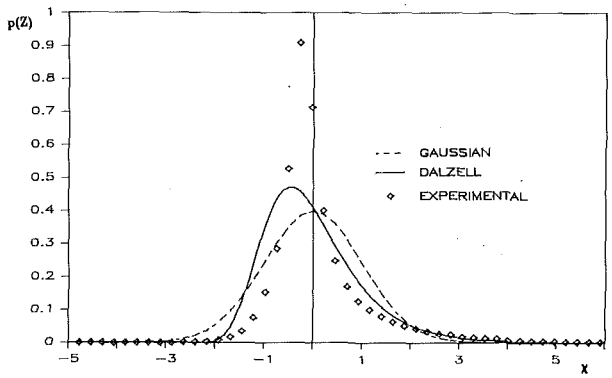


Fig. 11 Comparison of measured probability density with Dalzell and Gaussian densities (first symmetric sloshing mode)

and

$$P(Z) = (\pi/\sqrt{6}) \exp \{-Z - \exp(-Z)\} \quad (8)$$

where $Z = (\pi/\sqrt{6})\chi + \gamma$; γ is the Euler constant 0.577215665; $\chi = \{X - E[X]\}/\sigma$ and σ is the rms fluid elevation.

The double-exponential density function gives a moderately good fit for most of the experimental results except the region which is close to mean value of the liquid elevation. The probability density of the first symmetric sloshing mode corresponding to an excitation level $D/2\zeta_{01} = 9.43$ is shown in Fig. 11. The dotted curve represents the Gaussian probability density function while the solid curve is due to Dalzell's double-exponential curve. The double-exponential function yields a tolerable fit to Dalzell's results in most reponse amplitudes; however, it does not exhibit a peak which is measured in the present investigation.

Conclusions and Discussion

The liquid-free surface dynamic response, in a circular cylindrical tank, to random parametric excitation is investigated experimentally. Statistical response parameters, such as, mean, mean square, and probability density function are estimated from response sample records based on the fact that the response processes are verified to be stationary. These response parameters are determined for various excitation spectral density levels. The excitations are selected to be band-limited with central frequency equivalent to twice the natural frequency of the sloshing mode in question. The first antisymmetric and symmetric sloshing modes are considered.

The liquid-free surface motion experiences harmonic and subharmonic responses. The subharmonic motion is observed to be more predominant. For the case of first antisymmetric sloshing mode excitation, it is found that small liquid response is characterized by a linear planar motion; that is, the positive and negative liquid elevations are equal. Under relatively large excitation levels, the liquid-free surface experiences nonlinear, nonplanar motion. That is the nodal diameter rotates in the clockwise and counterclockwise directions. Depending on the level of the excitation spectral density, the liquid-free surface motion takes one of four response regimes. These are the zero-liquid motion region, the uncertain response region (where the liquid may or may not oscillate), partially developed sloshing regime, and fully developed sloshing. These four regions are identified for the first antisymmetric sloshing mode; however, for the first symmetric sloshing mode, the fourth region is observed to be mixed with other sloshing modes.

The results are compared with theoretical predictions. It is found that the experimental results confirm the occurrence of the jump phenomenon predicted by using the non-Gaussian closure scheme. The critical excitation level at which jump occurs is found to be in good agreement with the non-Gaussian closure solution for the case of antisymmetric sloshing mode. This important observation is believed to resolve a contradiction reported in the literature pertaining to different results of mean-square stability boundaries derived by different analytical approaches. The stationary mean-square response is found to be less than the predicted results obtained by Gaussian and non-Gaussian closures and the Stratonovich averaging method for relatively higher excitation levels. This difference is mainly attributed to the fact that the peak wave height experiences swirl motion around the tank centerline. In this case, the reported measurements do not represent the true wave amplitude except during those periods where the wave height transducer is located at 90-deg from the nodal diameter. Another important factor is that the theoretical results are based on the assumption that the excitation is a wide-band random process while, in the present experimental investigation, the excitation is a band-limited random process.

The measured probability density function of the liquid response is found to be non-Gaussian for those regions of large subharmonic motion. This non-normality is a result of nonlinear motion of the liquid-free surface. The system investigated is mainly governed by cubic nonlinear inertia forces and with nonlinear parametric terms. Theoretically, this type of nonlinarity brings the system response into a bounded limit cycle. Theoretical results showed that the response mean square reaches an asymptotic constant value in the region of fully developed sloshing. Because of the shaker limitation, it was not possible to verify this result.

The authors have recently conducted a series of exploratory tests under sinusoidal parametric excitation for the two sloshing modes with the purpose of observing the development of chaotic sloshing. The excitation amplitude is increased gradually until the maximum limit is reached. For the excitation of the first symmetric sloshing mode, the chaotic motion is observed. An important feature which distinguishes the random sloshing from deterministic chaotic motion is that the random response is characterized by a narrow-band process while the chaotic motion involves several modes and may constitute a narrow as well as wide-band frequency spectra. We may recall that, in the random test, the excitation level was not increased above the level at which other modes start to attend. In this case, if the random excitation spectral level is allowed to increase, we may observe chaotic sloshing. In connection with chaotic sloshing, one should refer to the experimental investigations of Ciliberto and Gollub (1984, 1985*a*,*b*) and Gollub and Meyer (1983). Their model consists of a fluid layer in a circular tank with depth-to-radius ratio $h/R = 0.16$ for which the sloshing natural frequency is strongly dependent on h/R. A major difference between the present model and that used by Gollub, et al., is that $h/R = 1$ for which the sloshing frequency is almost independent of the flulid depth. Gollub, et al., measured the regions of parametric instability of two sloshing modes: $mn = (4, 3)$ and (7, 2). Above the stability boundaries, the fluid surface oscillates at half the driving frequency in a single stable mode. However, they observed another region of mode competition, in which the fluid surface can be described as a superposition of the (4, 3) and (7, 2) modes with amplitudes having a slowly varying envelope. These slow variations can be either periodic or chaotic.

At the intersection of the two boundaries of the two modes both modes oscillate simultaneously. Careful inspection of the stability diagram of Ciliberto and Gollub (1985*b*) reveals that the onset of chaotic and periodic regions takes place in the vicinity of combination parametric resonance, i.e., $f_0 = f_{4,3} + f_{7,2}$, where f_0 is the excitation frequency, and $f_{4,3}$ and $f_{7,2}$ are the sloshing frequencies of modes (4,3) and (7,2), respectively.

Downloaded 03 May 2010 to 171.66.16.21. Redistribution subject to ASME license or copyright; see http://www.asme.org/terms/Terms_Use.cfm

Acknowledgment

This research is supported by a grant from the National Science Foundation under Research Grant No. MSME 8796342, for which the authors are very grateful. The authors would like to thank Prof. D. Jordan of Texas Tech for helping in programming the A/D converter. Professor F. Moon of Cornell University directed the attention of the first author to the chaotic sloshing experiments which are still in progress.

References

Abramowitz, M., and Stegen, I. A., 1972, *Handbook of Mathematical Functions with Formulas, Graphs and Mathematical Tables*, Chapter 19, Dover Publications, New York.

Ariaratnam, S. T., 1980, "Bifurcation in Nonlinar Stochastic Systems," in *New Developments in Nonlinear Problems in Dynamics*, Ed., Holmes, P.H., SIAM, Philadelphia, pp. 470–474.

Baxter, G. K., 1971, "The Nonlinear Response of Mechanical Systems to Parametric Random Excitation," PhD dissertation, University of Syracuse, New York.

Baxter, G. K., and Evan-Iwanowski, R. M., "Response of a Column in Random Vibration Tests," *ASCE J. Struct. Div.*, Vol. 101, pp. 1749–1761.

Bolotin, V. V., 1984, *Random Vibrations of Elastic Systems*, Martinus Nijhoff Publishers, The Netherlands.

Caughey, T. K., 1971, "Nonlinear Theory of Random Vibration," in *Advances in Applied Mechanics*, Ed., Yih, C. S., Vol. 11, pp. 209–243, Academic Press, New York.

Caughey, T. K., 1986, "Exact Solution in the Theory of Nonlinear Random Vibration and Their Applications," a lecture presented at the 23rd Annual Meeting of the Society of Engineering Science, August 25–27, State University of New York at Buffalo.

Ciliberto, S., and Gollub, J. P., 1984, "Pattern Competition leads to Chaos," *Physical Review Letters*, Vol. 52, No. 11, pp. 922–925.

Ciliberto, S., and Gollulb, J. P., 1985*a*, "Phenomological Model of Chaotic Mode Competition in Surface Waves," *IL Nuovo Cimento*, Vol. 6D, No. 4, pp. 309–316.

Ciliberto, S., and Gollub, J. P., 1985*b*, "Chaotic Mode Competition in Parametrically Forced Surface Waves," *Journal of Fluid Mechanics*, Vol. 158, pp. 381–398.

Dalzell, J. F., 1967, "Exploratory Studies of Liquid Behavior in Randomly Excited Tanks: Longitudinal Excitation," Southwest Research Institute, San Antonio, Report No. 1.

Dodge, F. T., Kana, D. D., and Abramson, H. N., 1965, "Liquid Surface Oscillations in Longitudinally Excited Rigid Cylindrical Containers," *AIAA Journal*, Vol. 3, No. 4, pp. 685–695.

Gollub, J. P., and Meyer, W., 1983, "Symmetry-Breaking Instabilities on a Fluid Surface," *Physica* 6D, pp. 337–346.

Gray, A. H., Jr., and Caughey, T. K., 1965, "A Controversy in Problems Involving Random Parametric Excitation," *Journal of Math. and Phys.*, Vol. 44, No. 3, pp. 288–296.

Ibrahim, R. A., 1985, *Parametric Random Vibration*, John Wiley & Sons, New York.

Ibrahim, R. A., and Soundararajan, A., 1983, "Nonlinear Parametric Liquid Sloshing Under Wide Band Random Excitation," *Journal of Sound and Vibration*, Vol. 91, No. 1, pp. 119–134.

Ibrahim, R. A., and Soundararajan, A., 1985, "An Improved Approach for Random Parametric Response of Dynamic Systems with Nonlinear Inertia," *International Journal of Nonlinear Mechanics*, Vol. 20, No. 4, pp. 309–323.

Ibrahim, R. A., Soundararajan, A., and Heo, H., 1985, "Stochastic Response of Nonlinear Dynamic Systems Based on a Non-Gaussian Closure," ASME JOURNAL OF APPLIED MECHANICS Vol. 52, No. 4, pp. 965–970.

Kozin, F., 1969, "A Survey of Stability of Stochastic Systems," *Automatica*, Vol. 5, pp. 95–112.

Kushner, H. J., 1967, *Stochastic Stability and Control*, Academic Press, New York, 1967.

Roberts, J. W., 1980, "Random Excitation of a Vibratory System with Autoparametric Interaction," *Journal of Sound and Vibration*, Vol. 69, pp. 101–116.

Downloaded 03 May 2010 to 171.66.16.21. Redistribution subject to ASME license or copyright; see http://www.asme.org/terms/Terms_Use.cfm

A Practical One-Parameter Integral Method for Laminar Incompressible Boundary Layer Flow With Transpiration

L. C. Thomas

W. L. Amminger

Mechanical Engineering Department,
King Fahd University of
Petroleum and Minerals,
Dhahran 31261, Saudi Arabia

A practical one-parameter polynomial type integral method is developed in this paper for laminar incompressible plane and thin axisymmetric boundary layer flow with transpiration and pressure gradient. The method features the use of approximations for the velocity distribution that are based on second and third order polynomial approximations for the distribution in shear stress. These approximations are used to develop solutions to the integral momentum equation for similar and nonsimilar flows. The accuracy of the method is generally within about 3 percent, except near separation where the error can reach 10 to 15 percent. The range of conditions for which the method applies covers a fairly wide range of blowing and suction rates and pressure gradients which encompasses plane and axisymmetric stagnation flows and extends to separation. Because of its fundamental nature, the approach provides a basis for generalization to heat and mass transfer and turbulent flow, and provides a framework for the development of more accurate multiple parameter integral methods for transpired boundary layer flow.

Introduction

The Pohlhausen (1921) method is the best known and simplest approximate integral approach for analyzing laminar incompressible two-dimensional plane and thin axisymmetric boundary layer flow over impermeable surfaces. This one-parameter method involves the use of a 4th order polynomial approximation for the velocity distribution of the form

$$U=2\,\xi-2\,\xi^3+\xi^4+\frac{\Lambda}{6}(\xi-3\,\xi^2+3\,\xi^3-\xi^4) \tag{1}$$

where $U = u/U_\infty$, $\xi = y/\delta$ and $\Lambda = (\delta^2/\nu)\ (dU_\infty/dx)$, together with the integral momentum equation,

$$\frac{f_x}{2}=\frac{1}{r_o}\frac{d}{dx}(r_o\delta_2)+\frac{\delta_2}{U_\infty}\frac{dU_\infty}{dx}(2+H)-V_o \tag{2a}$$

or

$$\frac{1}{r_o^2}\frac{U_\infty}{\nu}\frac{d}{dx}(r_o\delta_2)^2=F_2=2[S-\lambda(2+H)-\Omega_2] \tag{2b}$$

where the displacement and momentum thicknesses are defined by

$$\delta_1=\int_o^\infty (1-U)dy \tag{3}$$

and

$$\delta_2=\int_o^\infty U(1-U)dy \tag{4}$$

and $H = \delta_1/\delta_2$, $S = \tau_o\delta_2/\mu\ U_\infty$, and $\Omega_2 = -v_o\delta_2/\nu = 0$ for no transpiration. The accuracy of the Pohlhausen polynomial method is within about 3 percent for accelerating flows with values of the pressure gradient parameter Λ in the range 0 to 12, but degenerates to values of the order of 20 percent to 30 percent for adverse pressure gradient flows near separation. Interestingly, the use of the simpler third order polynomial approximation

$$U=\frac{3}{2}\,\xi-\frac{1}{2}\,\xi^3+\frac{\Lambda}{4}(\xi-2\,\xi^2+\xi^3) \tag{5}$$

in place of equation (1) for adverse pressure gradients generally provides an accuracy of between 3 to 10 percent up to the point of separation. Consequently, the accuracy of a composite third and fourth order polynomial type integral solution approach is comparable to the accuracy of one-parameter approaches of Thwaites (1949a), Timman (1949), Howarth (1938), Waltz (1941), and Launder (1964).

The Pohlhausen method has also been adapted to boundary layer flow with suction by Torda (1952) and Prandtl (1935).

Contributed by the Applied Mechanics Division for presentation at the Winter Annual Meeting, Chicago, IL, November 28 to December 2, 1988, of the American Society of Mechanical Engineers.

Discussion on this paper should be addresed to the Editorial Department, ASME, United Engineering Center, 345 East 47th Street, New York, N.Y. 10017, and will be accepted until two months after final publication of the paper itself in the JOURNAL OF APPLIED MECHANICS. Manuscript received by ASME Applied Mechanics Division, March 10, 1986; final revision, April 15, 1987. Paper No. 88-WA/APM-15.

Copies of this paper will be available until March, 1990.

Copyright © 1988 by ASME
Downloaded 03 May 2010 to 171.66.16.21. Redistribution subject to ASME license or copyright; see http://www.asme.org/terms/Terms_Use.cfm

Other one-parameter integral methods have been developed for laminar boundary layer flow with transpiration by Schlichting (1943), Thwaites (1949b), Trunkenbrodt (1956), and Mangler (1948). However, the methods by Thwaites and Schlichting are applicable to suction but not blowing, and none of these early one-parameter methods have provided a basis for generalization to heat transfer and turbulent flow. The objective of this paper is to develop a fundamental and general one-parameter integral method for incompressible laminar boundary layer flow with blowing or suction.

Analysis

Because of approximate similarities that generally exist within boundary layers, the traditional boundary layer approximations can be supplemented by approximations for the distributions in dimensionless shear stress for a broad range of applications. These supplementary boundary layer approximations for stress provide a basis for establishing useful approximations for distributions in the velocity.

Following this approach, the distribution in shear stress τ_{xy} is required to satisfy the familiar fundamental Couette law (Schlichting, 1979; White, 1974),

$$\frac{\tau_{xy}}{\tau_o} = 1 + \beta_\delta \xi + B_M U \tag{6}$$

in the region near the wall, where $\beta_\delta = \delta/\tau_o\ (dP/dx)$ and $B_M = \rho v_o U_\infty/\tau_o$, and the physical constraints

$$\frac{\partial \tau_{xy}}{\partial y} = 0 \quad \text{and/or} \quad \tau_{xy} = 0 \qquad \text{at } y = \delta \tag{7-10}$$

$$\frac{\partial U}{\partial y} = 0 \quad \text{and} \quad U = 1$$

at the outer edge of the boundary layer. An Nth order polynomial type approximation that satisfies these requirements is obtained by writing

$$\frac{\tau_{xy}}{\tau_o} = \sum_{n=0}^{N} a_n \xi^n + B_M U \tag{11}$$

The coefficients a_n are summarized in Table 1 for simple second ($N = 2$) and third ($N = 3$) order one-parameter approximations. (Higher order ($N = 4, 5, 6.$.) one-parameter approximations are readily developed by the use of higher order constraints at the wall and outer edge of the boundary layer. However, comparisons with exact solutions indicate that the simpler second and third (and fourth) order approximations are generally no less accurate than higher order approximations.)

Equation (11) is put into a convenient dimensionless form by writing

$$\frac{\tau_{xy}\delta}{\mu U_\infty} = Mo_\delta \sum_{n=0}^{N} a_n \xi^n - \Omega U \tag{12}$$

or

$$\frac{\tau_{xy}\delta}{\mu U_\infty} = Mo_\delta \sum_{n=0}^{N} \alpha_n \xi^n + \Lambda \sum_{n=0}^{N} \beta_n \xi^n + \Omega \sum_{n=0}^{N} \gamma_n \xi^n - \Omega U \tag{13}$$

where

$$a_n = \alpha_n - \beta_n \beta_\delta - \gamma_n B_M \tag{14}$$

and

$$Mo_\delta = \frac{\tau_o \delta}{\mu U_\infty} \tag{15}$$

$$\Lambda = \frac{\delta^2}{\nu}\frac{dU_\infty}{dx} = -Mo_\delta \beta_\delta \tag{16}$$

$$\Omega = -\frac{v_o \delta}{\nu} = -Mo_\delta B_M \tag{17}$$

The coefficients α_n, β_n, and γ_n are listed in Table 2.

The velocity distribution is expressed in terms of the Newton law of viscous stress,

$$\frac{\tau_{xy}\delta}{\mu U_\infty} = \frac{dU}{d\xi} \tag{18}$$

Equations (12) and (18) are combined to obtain

$$\frac{dU}{d\xi} + \Omega U = Mo_\delta \sum_{n=0}^{N} a_n \xi^n \tag{19}$$

for the general Nth order approximation. Introducing the integration factor $e^{\Omega\xi}$ and setting $U = 0$ at $\xi = 0$ and $U = 1$ at $\xi = 1$, the solution to this equation for $\Omega \neq 0$ takes the form (Appendix)

$$U = \sum_{n=0}^{N} C_n \xi^n - C_o e^{-\Omega\xi} \tag{20}$$

where

$$C_n = Mo_\delta \sum_{m=n}^{N} a_m j_{nm}(\Omega)$$

$$= Mo_\delta \sum_{m=n}^{N} \alpha_m j_{nm}(\Omega) + \Lambda \sum_{m=n}^{N} \beta_m j_{nm}(\Omega) + \Omega \sum_{m=n}^{N} \gamma_m j_{nm}(\Omega) \tag{21}$$

$$Mo_\delta = \frac{M_o + M_1\, e^{-\Omega}}{M_2 + M_3\, e^{-\Omega}} \tag{22}$$

$$j_{nm}(\Omega) = \frac{(-1)^{m-n} m!}{\Omega^{m-n+1} n!} \tag{23}$$

and $M_o = 1 - \sum_{n=0}^{N}\sum_{m=n}^{N} (\beta_m \Lambda + \gamma_m \Omega) j_{nm}(\Omega)$, $M_1 = -\sum_{n=0}^{N} (\beta_n \Lambda + \gamma_n \Omega) j_n(\Omega)$, $M_2 = \sum_{n=0}^{N}\sum_{m=n}^{N} \alpha_m j_{nm}(\Omega)$ and $M_3 = \sum_{n=0}^{N} \alpha_n j_n(\Omega)$.

These results provide the basis for establishing relationships for the displacement and momentum thicknesses in terms of Ω and Λ; that is,

$$\frac{\delta_1}{\delta} = \int_o^1 (1-U)\,d\xi = \int_o^1 \left(1 - \sum_{n=0}^{N} C_n \xi^n + C_o e^{-\Omega\xi}\right) d\xi$$

$$= 1 - \sum_{n=0}^{N} \frac{C_n}{n+1} - \frac{C_o}{\Omega}(e^{-\Omega} - 1) \tag{24}$$

Table 1 Coefficients a_n

N	a_o	a_1	a_2	a_3
2	1	β_δ	$-1-\beta_\delta-B_M$	$\frac{}{2+\beta_\delta+2\,B_M}$
3	1	β_δ	$-3-2\beta_\delta-3B_M$	

Table 2 Coefficients α_n, β_n, and γ_n

N	α_0	α_1	α_2	α_3	β_0	β_1	β_2	β_3	γ_0	γ_1	γ_2	γ_3
2	1	0	−1	−	0	−1	1	−	0	0	1	−
3	1	0	−3	2	0	−1	2	−1	0	0	3	−2

Downloaded 03 May 2010 to 171.66.16.21. Redistribution subject to ASME license or copyright; see http://www.asme.org/terms/Terms_Use.cfm

Table 3 Coefficients b_n and c_n

N	b_1	b_2	b_3	b_4	c_1	c_2	c_3	c_4
2	3/2	0	−1/2	–	1/4	−1/2	1/4	–
3	2	0	−2	1	1/6	−1/2	1/2	−1/6

Table 4 Coefficients ℓ_n and m_n

N	ℓ_0	ℓ_1	m_0	m_1	m_2
2	0.3750	−0.020833	0.13929	−0.0017857	−0.00059524
3	0.3	−0.008333	0.11746	−0.0010582	−0.0001103

and

$$\frac{\delta_2}{\delta}=\int_o^1 U(1-U)d\xi$$

$$=\sum_{n=0}^{N}\frac{C_n}{1+n}+\frac{C_o}{\Omega}(e^{-\Omega}-1)+\frac{C_o^2}{2\Omega}(e^{-2\Omega}-1)$$

$$+2\,C_o\sum_{n=0}^{N}C_nJ_n(-\Omega)-\sum_{n=0}^{N}\sum_{i=0}^{N}\frac{C_n\,C_i}{n+i+1} \tag{25}$$

where

$$J_o(-\Omega)=\int_o^1 e^{-\Omega\xi}d\xi=\frac{e^{-\Omega}-1}{-\Omega} \tag{26}$$

$$J_n(-\Omega)=\int_o^1 \xi^n e^{-\Omega\xi}d\xi=\frac{e^{-\Omega}}{-\Omega}-\frac{n}{-\Omega}J_{n-1}(-\Omega) \tag{27}$$

In the limiting case for which $\Omega = 0$, the solution to equation (19) is

$$U=Mo_\delta\sum_{n=0}^{N}\frac{a_n}{n+1}\,\xi^{n+1} \tag{28}$$

or

$$U=Mo_\delta\sum_{n=0}^{N}\frac{\alpha_n}{n+1}\,\xi^{n+1}+\Lambda\sum_{n=0}^{N}\frac{\beta_n}{n+1}\,\xi^{n+1} \tag{29}$$

Setting $U = 1$ at $\xi = 1$, an expression is obtained for Mo_δ of the form

$$Mo_\delta=\frac{1-\Lambda\sum_{n=0}^{N}\frac{\beta_n}{n+1}}{\sum_{n=0}^{N}\frac{\alpha_n}{n+1}}=b_1+c_1\Lambda \tag{30}$$

where

$$b_1=\frac{1}{\sum_{n=0}^{N}\frac{\alpha_n}{n+1}},\quad c_1=-\frac{\sum_{n=0}^{N}\frac{\beta_n}{n+1}}{\sum_{n=0}^{N}\frac{\alpha_n}{n+1}} \tag{31, 32}$$

Combining equations (29) and (30), the approximation for U takes the convenient form

$$U=\sum_{n=1}^{N+1}C_n\xi^n \tag{33}$$

where

$$C_n=b_n+\Lambda\,c_n \tag{34}$$

and

$$b_n=\frac{\alpha_{n-1}}{n}\,b_1,\quad c_n=\frac{\alpha_{n-1}}{n}\,c_1+\frac{\beta_{n-1}}{n} \tag{35, 36}$$

The coefficients b_n and c_n are listed in Table 3 for $N = 2$ and $N = 3$. Equation (33) corresponds to equation (5) for $N = 2$ and to the Pohlhausen equation, equation (1), for $N = 3$. Using equation (33) for U, relationships are obtained for the displacement and momentum thicknesses of the form

$$\frac{\delta_1}{\delta}=\int_o^1\left(1-\sum_{n=1}^{N+1}b_n\xi^n-\Lambda\sum_{n=1}^{N+1}c_n\xi^n\right)d\xi$$

$$=\ell_o+\ell_1\Lambda \tag{37}$$

and

$$\frac{\delta_2}{\delta}=\int_o^1\left[\sum_{n=1}^{N+1}b_n\xi^n+\Lambda\sum_{n=1}^{N+1}c_n\xi^n\right]$$

$$\left[1-\sum_{n=1}^{N+1}b_n\xi^n-\Lambda\sum_{n=1}^{N+1}c_n\xi^n\right]d\xi$$

$$=m_o+m_1\Lambda+m_2\Lambda^2 \tag{38}$$

where the coefficients ℓ_n and m_n are listed in Table 4.

Returning to the general analysis, the parameters Mo_δ, δ_1/δ and δ_2/δ can be efficiently computed as a function of Λ and Ω by the use of nested do-loops or by the use of the relations listed in Table 5. The accompanying integral parameters can be obtained from the relations

$$S=Mo_\delta\frac{\delta_2}{\delta},\quad H=\frac{\delta_1/\delta}{\delta_2/\delta},\quad \lambda=\Lambda\left(\frac{\delta_2}{\delta}\right)^2$$

$$\Omega_2=\Omega\frac{\delta_2}{\delta},\quad F_2=2[S-\lambda(2+H)-\Omega_2] \tag{39}$$

These results provide a basis for establishing effective approximate integral solutions for similar and nonsimilar laminar boundary layer flow with transpiration and pressure gradient.

Similar Flow. Similar boundary layer flows are characterized by constant values of the integral parameters Λ, Ω, S, H, λ, Ω_2, and F_2 and, for the range of conditions considered in this paper, by a free-stream velocity distribution of the form

$$U_\infty=C\,x^m=C\,x^{\beta/(2-\beta)} \tag{40}$$

where C, m, and β are constant. Holding the integral parameters constant and using equation (40) to represent U_∞, the solution to equation (2) for similar plane flow is given by

$$\delta_2^2=\frac{F_2}{1-m}\,\frac{\nu x}{U_\infty} \tag{41}$$

Using this result, the parameters λ and Ω_2 are expressed in terms of m and v_o/U_∞ by

$$\lambda=\frac{\delta_2^2}{\nu}\,\frac{dU_\infty}{dx}=\frac{F_2}{1-m}\,\frac{x}{U_\infty}\,\frac{dU_\infty}{dx}=\frac{m}{1-m}\,F_2 \tag{42}$$

and

$$\Omega_2=-\frac{v_o\delta_2}{\nu}=-\frac{v_o}{\nu}\sqrt{\frac{F_2}{1-m}\,\frac{\nu x}{U_\infty}}=-BP\sqrt{\lambda+F_2} \tag{43}$$

where the blowing parameter BP is defined as

$$BP=\frac{v_o}{U_\infty}\sqrt{\mathrm{Re}_x} \tag{44}$$

Rearranging, expressions are obtained for m and BP in terms of the integral parameters of the form

Downloaded 03 May 2010 to 171.66.16.21. Redistribution subject to ASME license or copyright; see http://www.asme.org/terms/Terms_Use.cfm

Table 5(*a*) Integral relations for transpired flow: $N = 2$

$$M_0 = \frac{\Omega}{2-\Omega}\left[2-\frac{2}{\Omega}+\frac{\Lambda}{\Omega}\left(1-\frac{2}{\Omega}\right)\right]$$

$$M_1 = \frac{\Omega}{2-\Omega}\left[\frac{2}{\Omega}+\frac{\Lambda}{\Omega}\left(1+\frac{2}{\Omega}\right)\right]$$

$$M_2 = \frac{\Omega}{2-\Omega}\left[\frac{2}{\Omega}\left(1-\frac{1}{\Omega}\right)\right]$$

$$M_3 = \frac{\Omega}{2-\Omega}\left(-1+\frac{2}{\Omega^2}\right)$$

$$C_0 = \frac{1}{\Omega}\left[Mo_\delta\left(1-\frac{2}{\Omega^2}\right)+\frac{\Lambda}{\Omega}\left(1+\frac{2}{\Omega}\right)+\frac{2}{\Omega}\right]$$

$$C_1 = \frac{1}{\Omega}\left[\frac{2}{\Omega}\,Mo_\delta-\Lambda\left(1+\frac{2}{\Omega}\right)-2\right]$$

$$C_2 = \frac{1}{\Omega}\left(-\,Mo_\delta+\Lambda+\Omega\right)$$

$$\frac{\delta_1}{\delta} = 1-C_0\left(1-\frac{1}{\Omega}+\frac{e^{-\Omega}}{\Omega}\right)-\frac{C_1}{2}-\frac{C_2}{3}$$

$$\frac{\delta_2}{\delta} = I_1 - I_2$$

$$I_1 = C_0\left(1-\frac{1}{\Omega}-\frac{e^{-\Omega}}{\Omega}\right)+\frac{C_1}{2}+\frac{C_2}{3}$$

$$I_2 = C_0^2\left[1+\frac{2}{\Omega}(e^{-\Omega}-1)-\frac{1}{2\Omega}(e^{-2\Omega}-1)\right]$$

$$+2\,\frac{C_0}{\Omega}\,e^{-\Omega}\left(C_1+C_2+\frac{2\,C_2}{\Omega}\right)$$

$$+C_0C_1+\frac{C_0C_2}{3}+\frac{C_1^2}{3}+\frac{C_1C_2}{2}+\frac{C_2^2}{5}$$

Table 5(*b*) Integral relations for transpired flow: $N = 3$

$$M_0 = \frac{\Omega^2}{12-\Omega^2}\left[\frac{6}{\Omega}-\frac{12}{\Omega^2}+\Lambda\left(\frac{2}{\Omega^2}-\frac{6}{\Omega^3}\right)\right]$$

$$M_1 = \frac{\Omega^2}{12-\Omega^2}\left[\frac{6}{\Omega}+\frac{12}{\Omega^2}+\Lambda\left(\frac{1}{\Omega}+\frac{4}{\Omega^2}+\frac{6}{\Omega^3}\right)\right]$$

$$M_2 = \frac{\Omega^2}{12-\Omega^2}\left(\frac{6}{\Omega^2}-\frac{12}{\Omega^3}\right)$$

$$M_3 = \frac{\Omega^2}{12-\Omega^2}\left(-1+\frac{6}{\Omega^2}+\frac{12}{\Omega^3}\right)$$

$$C_0 = \frac{1}{\Omega}\left[Mo_\delta\left(1-\frac{6}{\Omega^2}-\frac{12}{\Omega^3}\right)\right.$$

$$\left.+\Lambda\left(\frac{1}{\Omega}+\frac{4}{\Omega^2}+\frac{6}{\Omega^3}\right)+\frac{6}{\Omega}+\frac{12}{\Omega^2}\right]$$

$$C_1 = \frac{1}{\Omega}\left[Mo_\delta\left(\frac{6}{\Omega}+\frac{12}{\Omega^2}\right)-\Lambda\left(1+\frac{4}{\Omega}+\frac{6}{\Omega^2}\right)-6-\frac{12}{\Omega}\right]$$

$$C_2 = \frac{1}{\Omega}\left[Mo_\delta\left(-3-\frac{6}{\Omega}\right)+\Lambda\left(2+\frac{3}{\Omega}\right)+6+3\,\Omega\right]$$

$$C_3 = \frac{1}{\Omega}(2\,Mo_\delta-\Lambda-2\,\Omega)$$

$$\frac{\delta_1}{\delta} = 1-C_0\left(1-\frac{1}{\Omega}+\frac{e^{-\Omega}}{\Omega}-\frac{C_1}{2}-\frac{C_2}{3}-\frac{C_3}{4}\right)$$

$$\frac{\delta_2}{\delta_1} = I_1 - I_2$$

$$I_1 = C_0\left(1-\frac{1}{\Omega}+\frac{e^{-\Omega}}{\Omega}\right)+\frac{C_1}{2}+\frac{C_2}{3}+\frac{C_3}{4}$$

$$I_2 = C_0C_1+\frac{2}{3}\,C_0C_2+\frac{C_0C_3}{2}+\frac{C_1^2}{3}$$

$$+\frac{C_1C_2}{2}+\frac{2}{5}\,C_1C_3+\frac{C_2^2}{5}+\frac{C_2C_3}{3}+\frac{C_3^2}{7}$$

$$-12\,\frac{C_0C_3}{\Omega^4}-4\,\frac{C_0C_2}{\Omega^3}-2\,\frac{C_0C_1}{\Omega^2}$$

$$+\frac{2}{\Omega}\,C_0C_3\,e^{-\Omega}\left(1+\frac{3}{\Omega}+\frac{6}{\Omega^2}+\frac{6}{\Omega^3}\right)$$

$$+\frac{4}{\Omega^3}\,C_0C_2\,e^{-\Omega}+\frac{2}{\Omega}\,C_0C_2\,e^{-\Omega}\left(1+\frac{2}{\Omega}\right)$$

$$+\frac{2}{\Omega^2}\,C_0C_1\,e^{-\Omega}(1+\Omega)$$

$$+C_0\left[1+\frac{2}{\Omega}(e^{-\Omega}-1)-\frac{1}{2\Omega}(e^{-2\Omega}-1)\right]$$

$$m = \frac{\lambda}{\lambda+F_2}, \quad BP = -\sqrt{\frac{1-m}{F_2}}\,\Omega_2 = -\frac{\Omega_2}{\sqrt{\lambda+F_2}} \tag{45, 46}$$

and, the friction factor is represented by

$$\frac{f_x}{2}\sqrt{\mathrm{Re}_x} = S\sqrt{\frac{1-m}{F_2}} = \frac{S}{\sqrt{\lambda+F_2}} \tag{47}$$

With the integral parameters known as a function of Λ and Ω, equations (44)–(47) can be used to calculate m, β, BP and $f_x/2\sqrt{\mathrm{Re}_x}$ for similar plane flow.

For the case of axisymmetric stagnation flow the radius of curvature r_o is equal to x and U_∞ is given by equation (40) with $m = 1$, such that the solution to equation (2) becomes

$$\delta_2^2 = \frac{F_2}{2}\,\frac{\nu x}{U_\infty} \tag{48}$$

It follows that

$$\lambda = \frac{F_2}{2}\,m = \frac{F_2}{2} \tag{49}$$

Downloaded 03 May 2010 to 171.66.16.21. Redistribution subject to ASME license or copyright; see http://www.asme.org/terms/Terms_Use.cfm

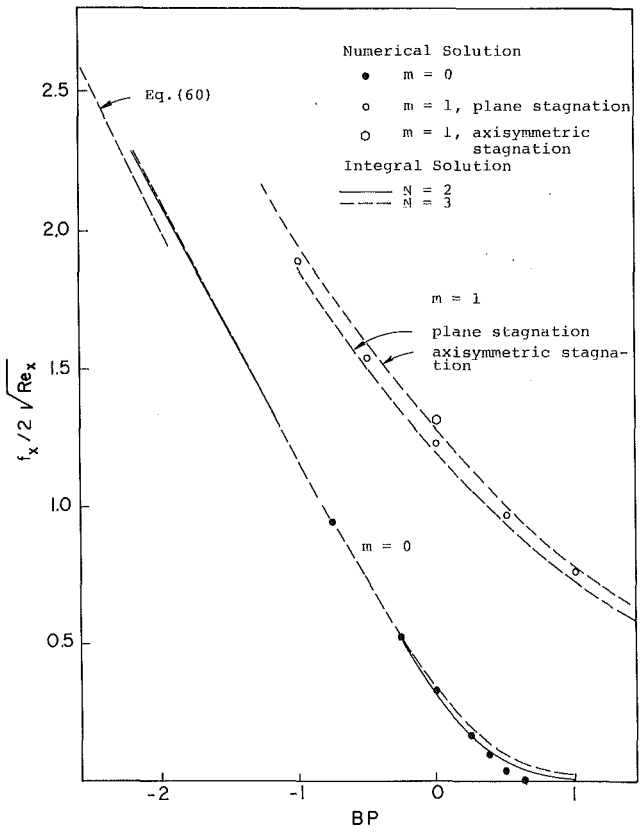


Fig. 1 Calculations for friction factor for similar transpired boundary layer flow

$$BP = -\sqrt{\frac{2}{F_2}}\,\Omega_2 \tag{50}$$

$$\frac{f_x}{2}\sqrt{\mathrm{Re}_x} = \sqrt{\frac{2}{F_2}}\,S \tag{51}$$

Nonsimilar Flow. For nonsimilar boundary layer flow, the integral momentum equation can be solved by finite difference methods. To develop a noniterative numerical solution applicable to plane and thin axisymmetric flows, equation (2) is written as

$$\frac{U_\infty}{\nu}\frac{d\delta_2}{dx} = \frac{U_\infty}{\nu}\frac{d}{dx}\left(\delta\frac{\delta_2}{\delta}\right) = \frac{F_2}{2\delta_2} - \mathrm{Re}_{\delta_2}\frac{1}{r_o}\frac{dr_o}{dx} \tag{52}$$

or

$$\frac{U_\infty}{\nu}\frac{d\delta}{dx/L} = \frac{L}{\delta}G_2 \tag{53}$$

where

$$G_2 = \left(\frac{\delta}{\delta_2}\right)^2\left[\frac{F_2}{2} - \frac{\mathrm{Re}_{\delta_2}}{r_o}\frac{dr_o}{dx/L} - \frac{\mathrm{Re}_\delta^2(\delta_2/\delta)}{U_oL/\nu}\frac{d}{dx/L}\left(\frac{\delta_2}{\delta}\right)\right] \tag{54}$$

Using a simple forward difference scheme, equation (53) is put into the form

$$\delta_{i+1} = \delta_i + \left(\frac{\nu}{U_\infty}G_2\right)_i\frac{\Delta x}{L} \tag{55}$$

or in terms of Re_δ,

$$\mathrm{Re}_{\delta_{i+1}} = \frac{U_{\infty i+1}}{U_{\infty i}}\left(\mathrm{Re}_\delta + G_2\frac{\Delta x}{L}\right)_i \tag{56}$$

where $i = 1, 2, 3, \ldots$ The parameters Λ and Ω are expressed

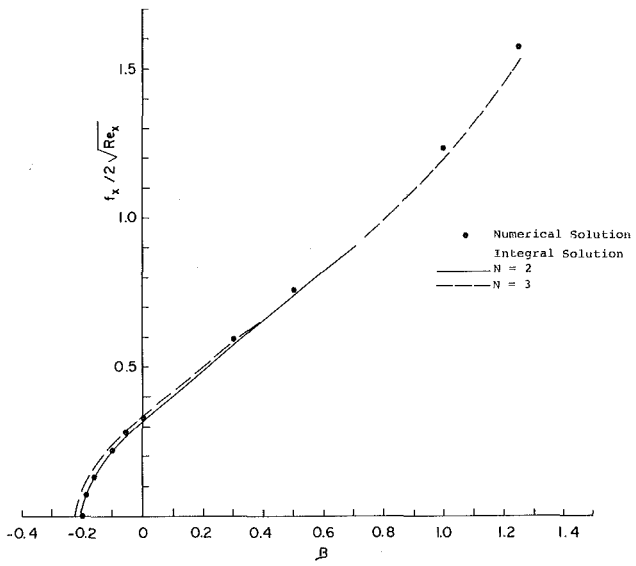


Fig. 2 Calculations for friction factor for similar boundary layer flow with pressure gradient

in terms of Re_δ by

$$\Lambda = \frac{\mathrm{Re}_\delta^2\, m}{\mathrm{Re}_x} \quad \text{and} \quad \Omega = -\frac{v_o}{U_\infty}\mathrm{Re}_\delta \tag{57, 58}$$

With Λ and Ω known at station $i + 1$, the integral parameters S, H, λ, Ω_2, and F_2 can be computed and the friction factor f_x can be obtained from

$$\frac{f_x}{2} = \frac{S}{(\delta_2/\delta)\mathrm{Re}_\delta} \tag{59}$$

Results

Solution results obtained by means of the one-parameter integral approach developed above are now presented for standard Falkner-Skan similar wedge flows with β in the range -0.2 to 2 and for several familiar nonsimilar flows.

Second and third order integral solution results for friction factor f_x are compared with exact similarity solutions for transpired flow with uniform free-stream velocity ($m = 0$) and nontranspired flow with pressure gradient in Figs. 1 and 2, respectively. As indicated in the introduction, the accuracy of the standard Pohlhausen ($N = 3$) method for nontranspired flow ranges from about 3 percent for accelerating flows in the range $0 \leqslant \Lambda \leqslant 12$ ($0 \leqslant \beta \leqslant 2$) to 20 to 30 percent (or 12 percent relative to β) near separation.[1] The accuracy of the solution results for $N = 2$ near separation is within 10 percent (or 3.5 percent relative to β). For the transpired flow case, the error in the solution varies from 0 percent for strong suction ($BP \gtrsim -3$) to 23 percent for blowing near separation with $N = 3$, and from 0 percent for strong suction to 14 percent near separation with $N = 2$. For values of BP less than about -3, the solution for f_x is accurately correlated by

$$\frac{f_x}{2}\sqrt{\mathrm{Re}_x} = -BP \tag{60}$$

or

$$\frac{f_x}{2} = -\frac{v_o}{U_\infty} \tag{61}$$

[1] The accuracy of the calculations for f_x is given relative to the friction factor for uniform free stream velocity flow $f_x(o)$; that is,

$$\text{relative error} = \frac{|f_x - f_{xe}| - |f_x(o) - f_{xe}(o)|}{f_{xe} + f_{xe}(o)}$$

where f_{xe} represents the exact similarity solution.

Downloaded 03 May 2010 to 171.66.16.21. Redistribution subject to ASME license or copyright; see http://www.asme.org/terms/Terms_Use.cfm

The results for these two basic cases suggest the accuracy for a simple polynomial type one-parameter integral method for boundary layer flow with transpiration and pressure gradient can be enhanced by setting $N = 3$ for moderate to strong acceleration and $N = 2$ for mild acceleration and adverse pressure gradients.

Approximate integral solution calculations for f_x are also shown in Fig. 1 for transpired boundary layers associated with plane and axisymmetric stagnation flow. The accuracy of these calculations is within about 3 percent. The variation in Λ with BP is correlated by

$$\Lambda = 7.052 + 2.748\ BP + 1.051\ BP^2 + 0.172\ BP^3 + 0.07733\ BP^4 \quad (62)$$

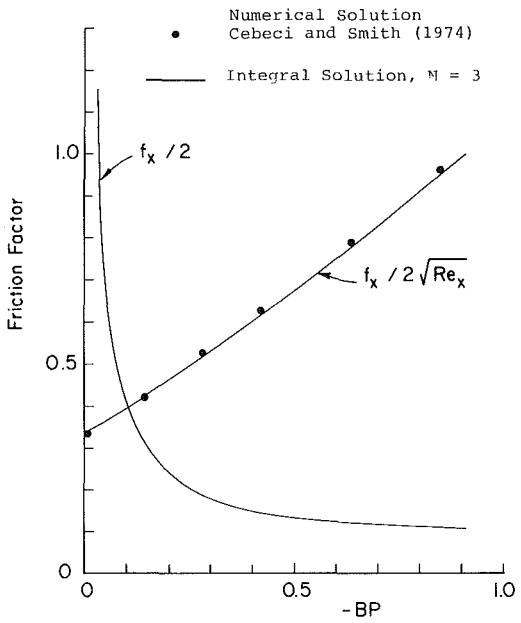


Fig. 3 Calculations for friction factor for nonsimilar boundary layer flow with uniform suction ($v_0/U_\infty = -0.1$) and uniform free-stream velocity

for plane stagnation flow, and by

$$\Lambda = 4.714 + 1.926\ BP + 0.6257\ BP^2 + 0.1212\ BP^3 + 0.007758\ BP^4 \quad (63)$$

for axisymmetric stagnation flow. These similarity solution results provide a means of establishing the starting conditions for analyzing nonsimilar two-dimensional boundary layer flow over curved surfaces.

To illustrate the capability of the approach for nonsimilar conditions, consideration is given to the classic cases of asymptotic suction flow with uniform free-stream velocity and plane flow over a circular cylinder.

Asymptotic suction boundary layers are associated with uniform negative values of the dimensionless transpiration rate v_o/U_∞ and are characterized by values of the friction factor that asymptotically approach equation (61) as x increases. Calculations for friction factor obtained by the third order integral method are compared in Fig. 3 with numerical solution results of Cebeci and Smith (1974). The calculations obtained by the two methods are within 1 percent, except very near the origin where the difference is about 3 percent.

To develop solutions for plane flow over a circular cylinder, the free-stream velocity is represented by a correlation developed by Hiemenz (1911)

$$\frac{U_\infty}{U_o} = 1.814\left(\frac{x}{R_o}\right) - 0.2710\left(\frac{x}{R_o}\right)^3 - 0.04710\left(\frac{x}{R_o}\right)^5 \quad (64)$$

for actual conditions, and by

$$\frac{U_\infty}{U_o} = 2 \sin \frac{x}{R_o} \quad (65)$$

for ideal potential flow, where R_o represents the cylinder radius and x represents the arc length measured from the stagnation point. Because the conditions associated with this flow range from stagnation to separation, the composite integral method is used with $N = 3$ for moderate acceleration and $N = 2$ for mild acceleration and deceleration. Integral and numerical calculations for friction factor obtained for the actual and potential flows with $v_o = 0$ are compared in Fig. 4. The accuracy of the composite integral calculations is within

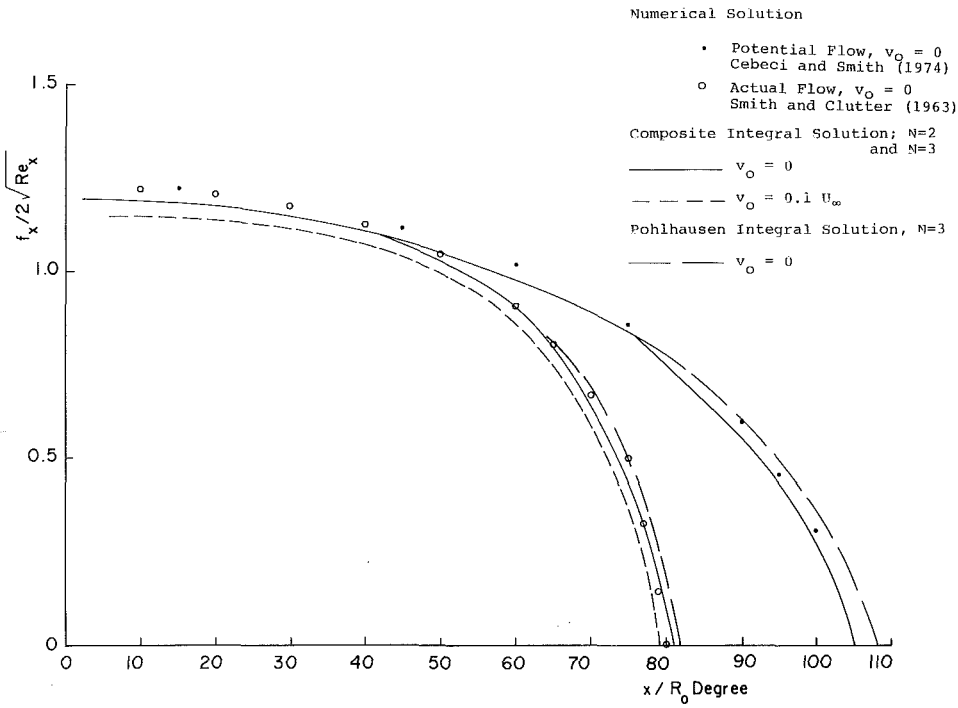


Fig. 4 Calculations for friction factor for nonsimilar boundary layer flow over a circular cylinder

Downloaded 03 May 2010 to 171.66.16.21. Redistribution subject to ASME license or copyright; see http://www.asme.org/terms/Terms_Use.cfm

about 3 percent from stagnation to separation as compared to 3 to 17 percent for the Pohlhausen method ($N = 3$). To see the effect of transpiration, calculations for friction factor are also shown in Fig. 4 for the case of actual flow over a circular cylinder with blowing. As would be expected, blowing results in lower values of the friction factor f_x and an earlier separation point. Suction produces the opposite effect.

The calculations presented in this paper were first obtained using BASIC programming and an Apple MacIntosh. Calculations were later made using FORTRAN programming and an IBM 360. The computer time per run for flow over a circular cylinder using the noniterative approach associated with equation (53) is 20 s for the MacIntosh and 0.1 s for the mainframe IBM.

Conclusion

A one-parameter polynomial type integral method has been developed for laminar incompressible boundary layer flow with transpiration and pressure gradient. In this approach, second and third order boundary layer approximations for the distribution in stress τ_{xy} have been used to establish approximations for the velocity distribution for transpired flows of the form of equation (20), where the coefficients C_n and associated parameter Mo_δ are expressed in terms of the parameters Λ and Ω by equations (21) and (22). For boundary layer flows with no transpiration, the velocity distribution is approximated by equation (33), where C_n and Mo_δ are given by equations (34) and (30). Using these equations for U, relations have been developed for δ_1/δ and δ_2/δ and related integral parameters S, H, λ, Ω_2, and F_2 which are readily evaluated by nested numerical computations. These relations have been used to develop solutions to the integral momentum equation, equation (2), for similar and nonsimilar flows. For $N = 3$ and $\Omega = 0$, the method reduces to the familiar Pohlhausen approach.

The accuracy of the method is generally about 3 percent, except in the vicinity of separation where the error can reach 10 to 15 percent. This level of accuracy is achieved by the use of a composite approximation for U with $N = 3$ for moderate to strong acceleration and $N = 2$ for mild acceleration and adverse pressure gradients. Although the third order polynomial approximation breaks down for very strongly accelerated flows with values of Λ greater than about 12 (depending on the value of Ω), the range of conditions for which the method applies covers a fairly wide range of pressure gradients which encompasses plane and axisymmetric stagnation flows and extends to separation. Furthermore, the approach is quite versatile in that it applies to plane and thin axisymmetric flows and can be extended to heat transfer and turbulent flow, and provides a framework for the development of more accurate multi-parameter integral methods for transpired boundary layer flow. Consequently, this method may prove to be very useful in design work for boundary layer flows with transpiration and pressure gradient.

Acknowledgment

We wish to acknowledge the support of King Fahd University of Petroleum and Minerals for this work.

References

Cebeci, T., and Smith, A. M. O., 174, *Analysis of Turbulent Boundary Layers*, Academic Press, New York.

Hiemenz, K., 1911, "Die Grenzschicht an Einem in den Gliech Formigen Flussigkeitsstrom Eingetanchten Geraden Kreiszylinder," Thesis Gottingen 1911, *Dinglers Polytech. Journal*, Vol. 326, p. 321.

Howarth, L.,1938, "On the Solution of the Laminar Boundary Layer Equations," *Proceedings Royal Society*, Vol. A 164, pp. 547-579.

Kays, W. M., and Crawford, M. E., 1980, *Convective Heat and Mass Transfer*, McGraw-Hill.

Launder, B. E., 1964, "An Improved Pohlhausen-Type Method of Calculating the Two-dimensional Laminar Boundary Layer in a Pressure Gradient," ASME *Journal of Heat Transfer*, Vol. 86, p. 360.

Mangler, W., 1948, "Special Exact Solutions," *Monographs Aerodynamische Versuchsanstalt Zu Goltingen*, Section 1.2.

Pohlhausen, E., 1921, "Der Warmeaustausch Weischen Festen Korpern und Flussigkeiten mit Kleiner Reibung and Kleiner Warmeleitung," *Zeitschrift fur Angewandte Mathematik und Mechankik*.

Prandtl, L., 1935, "The Mechanics of Viscous Fluids," *Aerodynamic Theory*, Vol. 3, Springer, Berlin, pp. 34-208.

Schlichting, H., 1943, "Ein Naherungsverfahren zur Berechnung der Laminaren Grenzschicht mit Absaungung bei Beliebiger Korperform," Berlin Institute Aeronautical Technical Hochschule, Braunschweig, No. 43/13.

Schlichting, H., 1979, *Boundary Layer Theory*, 7th ed., McGraw-Hill, New York.

Smith, A. M. O., and Clutter, D. W., 1963, "Solution of the Incompressible Laminar Boundary-Layer Equations," *Journal Aerospace Science*, Vol. 26, p. 229.

Thwaites, B., 1949a, "Approximate Calculation of the Laminar Boundary Layer," *Aeronautical Quarterly*, Vol. 1, pp. 245-280.

Thwaites, B., 1949b, "The Development of Laminar Boundary Layers Under Conditions of Continuous Suction, Part II: Approximate Methods of Solution," *Report Aeronautical Research Council*, London, No. 12699.

Timman, R., 1949, "A One-parameter Method for the Calculation of Laminar Boundary Layers," *Report Transactions National Luchtv Laboratory*, Amsterdam, Vol. 15, pp. F29-F45.

Torda, T. P., 1952, "Boundary Layer Control by Continuous Surface Suction or Injection," *Journal Mathematical Physics*, Vol. 31, pp. 206-213.

Trucknebrodt, E., 1956, "Ein Einfaches Naherungsverfahren zum Berechnen der Laminaren Reibungsschicht mit Absaugung, *Forschung Ingenieus Wesen*, Vol. 22, pp. 147-157.

Walz, A., 1941, Ein Neuer Ansatz fur das Geschwindigkeitsprofil der Laminaren Reibungsschicht, *Berlin Lilienthal-Gesellschaft fur Luftfahrtforschung*, No. 141, pp. 8-12.

White, F. M., 1974, *Viscous Fluid Flow*, McGraw Hill Book Company, New York.

APPENDIX

The solution to equation (19) is written as

$$U = Mo_\delta \left[\sum_{n=0}^{N} a_n J_n(\Omega\xi) \right] e^{-\Omega\xi} \tag{A-1}$$

where

$$J_n(\Omega\xi) = \int_o^\xi \xi^n e^{\Omega\xi} d\xi = \frac{\xi^n}{\Omega} e^{\Omega\xi} - \frac{n}{\Omega} J_{n-1}(\Omega\xi)$$

$$= e^{\Omega\xi} \left[\sum_{m=0}^{n} \frac{(-1)^{n-m} n!}{\Omega^{n-m+1} m!} \xi^m \right] + \frac{(-1)^{n+1} n!}{\Omega^{n+1}}$$

$$= e^{\Omega\xi} \sum_{m=0}^{n} j_{mn}(\Omega) \xi^m + j_n(\Omega) \tag{A-2}$$

and

$$j_{mn}(\Omega) = \frac{(-1)^{n-m} n!}{\Omega^{n-m+1} m!}, \quad j_n(\Omega) = \frac{(-1)^{n+1} n!}{\Omega^{n+1}} \tag{A-3, 4}$$

Substituting for $J_n(\Omega\xi)$ in equation (A-1), the solution for U becomes

$$U = Mo_\delta \left(\sum_{n=0}^{N} a_n \sum_{m=0}^{n} j_{mn}(\Omega) \xi^m + \sum_{n=0}^{N} a_n j_n(\Omega) e^{-\Omega\xi} \right) \tag{A-5}$$

or, after rearranging the order of the double summation,

$$U = Mo_\delta \left(\sum_{n=0}^{N} \sum_{m=n}^{N} a_m j_{nm}(\Omega) \xi^n + \sum_{n=0}^{N} a_n j_n(\Omega) e^{-\Omega\xi} \right) \tag{A-6}$$

This result provides the basis for equation (20).

To develop a relationship between Mo_δ and the parameters Λ and Ω, equation (20) is put into the form

Downloaded 03 May 2010 to 171.66.16.21. Redistribution subject to ASME license or copyright; see http://www.asme.org/terms/Terms_Use.cfm

$$U = Mo_\delta \left(\sum_{n=0}^{N} \sum_{m=n}^{N} \alpha_m j_{nm}(\Omega)\xi^n + \sum_{n=0}^{N} \alpha_n j_n(\Omega) e^{-\Omega\xi} \right)$$
$$+ \sum_{n=0}^{N} \sum_{m=n}^{N} (\beta_m \Lambda + \gamma_m \Omega) j_{nm}(\Omega)\xi^n$$
$$+ \sum_{n=0}^{N} (\beta_n \Lambda + \gamma_n \Omega) j_n(\Omega) e^{-\Omega\xi} \qquad (A\text{-}7)$$

Setting $U = 1$ at $\xi = 1$ and solving for Mo_δ,

$$Mo_\delta = \frac{1 - \left[\sum_{n=0}^{N} \sum_{m=n}^{N} (\beta_n \Lambda + \gamma_m \Omega) j_{nm}(\Omega) + \sum_{n=0}^{N} (\beta_n \Lambda + \gamma_n \Omega) j_n(\Omega) e^{-\Omega} \right]}{\sum_{n=0}^{N} \sum_{m=n}^{N} \alpha_m j_{nm}(\Omega) + \sum_{n=0}^{N} \alpha_n j_n(\Omega) e^{-\Omega}} \qquad (A\text{-}8)$$

which leads to equation (22).

Downloaded 03 May 2010 to 171.66.16.21. Redistribution subject to ASME license or copyright; see http://www.asme.org/terms/Terms_Use.cfm

Effect of Entrance Region on Laminar Startup Flow in Pipes

H. I. Andersson
Professor.
Mem. ASME

R. Kristoffersen
Research Assistant.

Division of Applied Mechanics,
Norwegian Institute of Technology,
N-7034 Trondheim-NTH, Norway

The ultimate effects of the entrance region on startup flow are considered by one-dimensional steady-state analysis. By roughly accounting for the entrance loss, semiempirical formulas for the average velocity and the hydrodynamic entrance length in terms of a startup flow parameter and an entrance effect coefficient are provided. The startup flow parameter $M = gHD^4/2048\nu^2L^2$ is identified as the fundamental parameter of the problem. While Szymanski's solution is recovered in the long pipe limit, i.e., $M \to 0$, the steady-state volume flux through short pipes ($M > 0.05$) is significantly reduced due to entrance region effects.

Introduction

The classical solution of Szymanski (1932) for the startup flow in circular pipes has been verified experimentally by Letelier and Leutheusser (1976) for long pipes. While Szymanski took the pressure gradient, and thus the forcing function of the system, as being constant, Otis (1985) recently recognized that a portion of the total head must be utilized to establish the kinetic head as the flow accelerates. To account for this effect, Otis introduced the dimensionless startup flow parameter

$$M = \frac{1}{2048}\,\frac{gHD^4}{(\nu L)^2} \tag{1}$$

where ν is the kinematic viscosity and D, H and L are defined in Fig. 1. For M-values of the order of unity, Otis observed that the startup time period and the steady-state velocity were significantly reduced as compared with the Szymanski-solution.

Szymanski (1932) and Otis (1985) both neglected the axial flow development in the entrance region of the pipe and considered the flow as being fully developed in space. In many instances of technological importance, however, ducts and pipes are short, and the crucial question arises: How does entrance flow influence on the startup flow phenomena?

While the effects of the axial variation of the velocity profile have been discarded in the previous analyses of the startup problem, the steady-state entrance region flow has received considerable attention throughout the years; see, for example, the extensive monograph by Shah and London (1978). However, the enhanced intricacy of the entrance region, arising from the nonlinear convective terms in the Navier-Stokes equations, makes even the steady-state flow more cumbersome to investigate.

In the unsteady case, the startup flow is governed by the time-dependent axisymmetric Navier-Stokes equations, from which detailed numerical solutions can be obtained by finite-difference or finite-element methods. As a first approach, however, we resort to one-dimensional analysis. Moreover, from physical intuition it can be anticipated that the streamwise extension of the entrance region is monotonically increasing with time, until the steady-state flow field has been established. To this end, we consider a one-dimensional formulation for steady-state pipe flow, in which the existence of the entrance region is accounted for by an entrance loss coefficient. The resulting steady-state volume flux will then reflect the ultimate entrance effects on the transient startup flow. The steady-state results will thereby provide important guidance for experimental as well as numerical investigations of the transient flow problem.

Theoretical Model

The establishment of laminar flow in the pipe shown schematically in Fig. 1 is governed by the time-dependent Navier-Stokes equations. The transient flow following the sudden opening of a downstream valve tends to a steady state which depends on the effective pressure difference

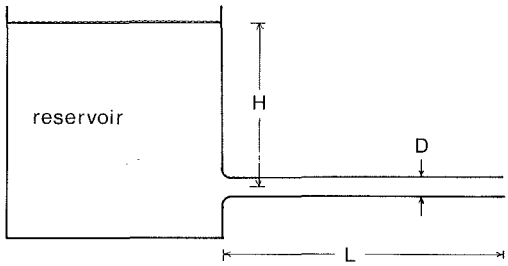


Fig. 1 Schematic representation of the flow configuration

Contributed by the Applied Mechanics Division for presentation at the Winter Annual Meeting, Chicago, IL, November 28 to December 2, 1988, of THE AMERICAN SOCIETY OF MECHANICAL ENGINEERS.

Discussion on this paper should be addressed to the Editorial Department, ASME, United Engineering Center, 345 East 47 Street, New York, NY 10017, and will be accepted until two months after final publication of the paper itself in the JOURNAL OF APPLIED MECHANICS. Manuscript received by ASME Applied Mechanics Division, March 9, 1987; final revision, February 1, 1988.

Paper No. 88-WA/APM-39.

Copyright © 1988 by ASME
Downloaded 03 May 2010 to 171.66.16.21. Redistribution subject to ASME license or copyright; see http://www.asme.org/terms/Terms_Use.cfm

$$p_o - p_{\text{atm}} = \rho g H - \frac{1}{2}\alpha_o \rho U^2 \tag{2}$$

which remains to drive the flow through the pipe. Here, U denotes the cross-sectional average velocity, α is the kinetic energy correction factor which accounts for the variation of the axial velocity across the pipe section, and the subscript o signifies the entrance cross section of the pipe.

In engineering practice, it is customary to express the steady-state pressure drop in pipes and ducts in terms of the Darcy-Weisbach friction factor f for fully developed flow. While equation (2) represents the conservation of mechanical energy from the constant-level reservoir to the pipe entrance, the overall pressure drop from the entrance to the exit is commonly written as

$$p_o - p_{\text{atm}} = \left(f\frac{L}{D} + k\right)\frac{1}{2}\rho U^2 \tag{3}$$

Here, k is an entrance loss coefficient which accounts for the effects of flow development. More specifically, k should account for the change in velocity profile between the entrance and exit, and for the increased wall shear stress in the entrance region relative to that of fully developed flow.

The Darcy-Weisbach friction factor f for fully developed laminar flow in a circular tube, i.e.

$$f = \frac{64}{UD/\nu} \tag{4}$$

is exactly derived from the Navier-Stokes equations in introductory texts on fluid mechanics, e.g., Olson (1980), and has also been verified experimentally. Now, since equations (2) and (3) express the same pressure drop, they can be combined to give a quadratic equation in U, which readily can be solved to give

$$U = \frac{1}{32}\frac{gHD^2}{\nu L}\frac{\sqrt{1+8ME}-1}{4ME} \tag{5}$$

where

$$E \equiv (k+\alpha_o)/2 \tag{6}$$

and M is the startup flow parameter defined in equation (1). The resulting average velocity (5) is conveniently expressed in dimensionless form as

$$U^+ \equiv \frac{U}{U_s} = \frac{\sqrt{1+8ME}-1}{4ME} \tag{7}$$

where the velocity scale

$$U_s \equiv \frac{1}{32}\frac{gHD^2}{\nu L} \tag{8}$$

is recognized as the steady-state average velocity in the Szymanski problem. It can readily be verified that the Szymanski solution, i.e., $U^+ = 1$, is recovered from equation (7) in the limit $M \to 0$, i.e., for long pipes.

In the recent analysis of Otis (1985), fully developed flow conditions were assumed to prevail throughout the pipe. Thus, with $k = 0$ and $\alpha_o = 2.0$ in the present context, E becomes equal to unity and the previous result reduces to the steady-state solution derived by Otis.

Semiempirical Considerations

If the liquid in the reservoir in Fig. 1 is tranquil and the pipe entrance is nicely rounded, the velocity of liquid entering the pipe will be nearly uniform, i.e., $\alpha_o \approx 1.0$. Furthermore, the entrance loss coefficient k is assumed constant in most engineering calculations. Since M and U_s are given by geometrical and physical characteristics only, the steady-state velocity U is completely determined by equation (7).

In numerous technological applications, however, pipes and ducts are short, and the variation of k in the entrance region should be taken into account. The increased pressure drop near the pipe entrance has been considered by several authors, for instance by White (1974) and Shah and London (1978). An apparent friction factor

$$c_{f,\text{app}} \equiv \frac{p_o - p_{\text{atm}}}{\frac{1}{2}\rho U^2}\cdot\frac{D}{4L} \tag{9}$$

is sometimes related to the total pressure drop over the pipe length L. The entrance loss coefficient introduced in equation (3) can then be expressed as

$$k = 4L^+\left(c_{f,\text{app}}\ \text{Re} - \frac{f}{4}\ \text{Re}\right) \tag{10}$$

where

$$\text{Re} \equiv UD/\nu \tag{11}$$

$$L^+ \equiv L/D\ \text{Re} = 1/64MU^+ \tag{12}$$

are the diameter Reynolds number and dimensionless pipe length, respectively. Here, $f/4$ is recognized as the Fanning friction factor for fully developed flow. It should be noted that, according to its definition (12), L^+ can take any positive value depending on the desired flow rate, the fluid property ν and the pipe size (D and L).

The apparent friction factor defined in equation (9) and the entrance loss coefficient in equation (10) both depend on the length of the actual pipe. Bender (1969) established an approximate formula for the apparent friction factor in the entry region. One of the constants was later modified by Shah (1978) with the following result

$$c_{f,\text{app}}\cdot\text{Re} = \frac{3.44}{(L^+)^{1/2}} + \frac{1.25/(4L^+)+16-3.44/(L^+)^{1/2}}{1+0.00021(L^+)^{-2}} \tag{13}$$

Normally, the apparent friction factor $c_{f,\text{app}}$ is given as a function of the axial coordinate, say, x, in order to account for the total pressure drop from the inlet $x = 0$ to an arbitrary position x. In the present context, the total pressure drop over the entire pipe length L is required. Accordingly, x has been replaced by L in the Bender-Shah formula (13).

The entrance loss coefficient k can now be accurately determined from equations (10) and (13) for any pipe length, including the extreme cases

$$k \to 13.76(L^+)^{1/2} - 64L^+ \quad \text{as} \quad L^+ \to 0 \tag{14a}$$

$$k \to 1.25 \quad \text{as} \quad L^+ \to \infty \tag{14b}$$

These expressions are derived as asymptotic limits in the extreme cases as the dimensionless pipe length L^+ tends to zero and infinity, respectively. Equation (14a) may thus be considered a fair approximation to the Bender-Shah formula (13) for short pipes, but its accuracy is decreasing with increasing pipe lengths. If L^+ is equal to 0.001, for example, equation (14a) gives $k = 0.371$ while equation (13) gives $k = 0.375$; i.e., equation (14a) approximates equation (13) to within 1.1 percent for dimensionless lengths up to 0.001. For $L^+ = 0.0001$ the deviation is reduced to 0.04 percent.

Finally, it should be emphasized that the dimensionless length L^+, according to its definition (12), depends on the resulting velocity U^+. Thus, for a specified value of the startup parameter M, U^+ has to be obtained iteratively from equations (7), (10), and (13). In the long pipe limit, however, k tends to a constant value (14b) and equation (7) reduces to an explicit solution for the steady-state average velocity.

Downloaded 03 May 2010 to 171.66.16.21. Redistribution subject to ASME license or copyright; see http://www.asme.org/terms/Terms_Use.cfm

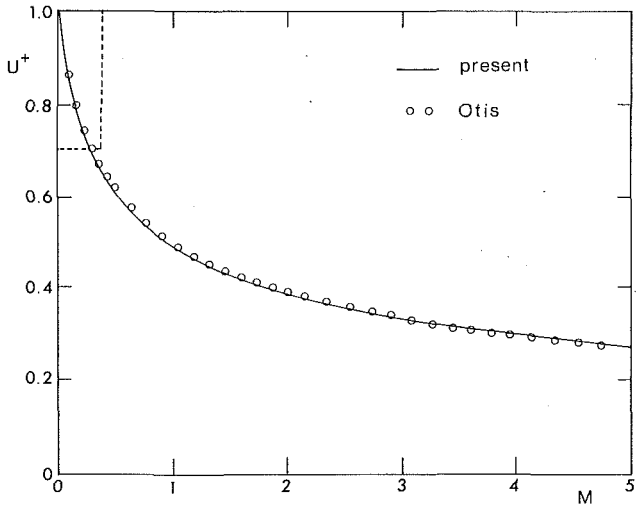


Fig. 2 Effect of startup flow parameter M on the steady-state average velocity; the rectangle in the upper left-hand corner of the figure is enlarged in Fig. 4

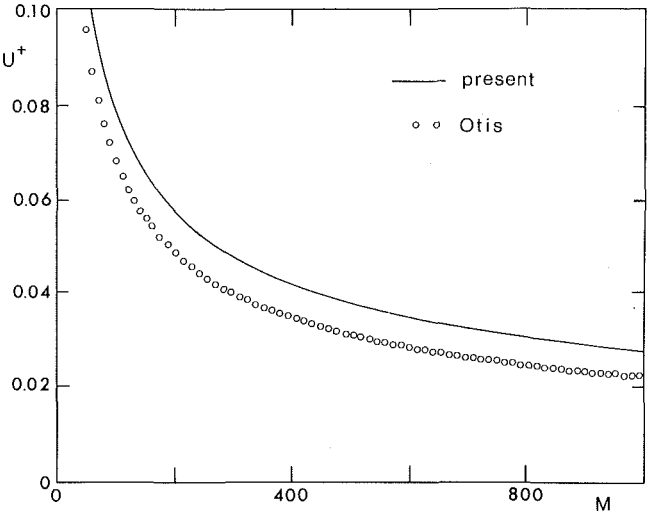


Fig. 3 Ultimate average velocity in shorter pipes

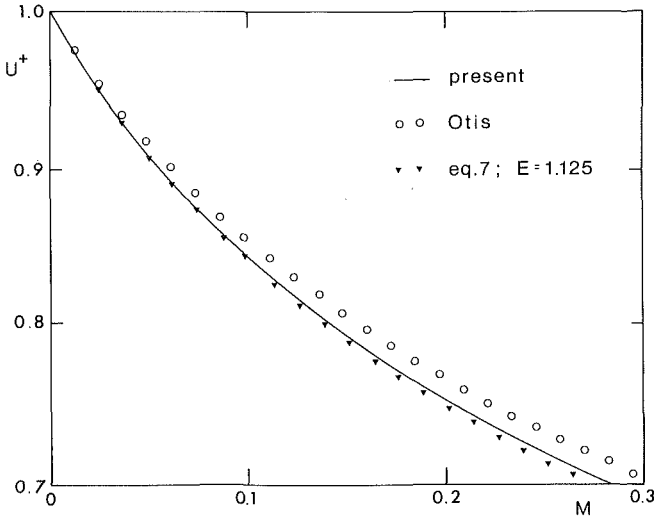


Fig. 4 Ultimate average velocity in long pipes

Results and Discussions

Considering uniform inflow conditions the upstream kinetic energy correction factor α_o becomes equal to unity. The resulting steady-state average velocity is shown in Fig. 2 (solid line) for moderate values of the startup parameter M. The axial variation of the entrance effect coefficient E defined in equation (6) has been accounted for by using equation (10) and the Bender-Shah formula (13). The explicit solution derived by Otis (1985); i.e., equation (7) with E constant and equal to unity, has been plotted for comparison (symbols).

While Otis neglected the axial flow development at the entrance, Fig. 2 demonstrates that the inclusion of the entrance effects slightly modifies Otis' solution. The surprisingly small difference between the results can be explained in terms of the entrance effect coefficients E, which is defined as the algebraic mean value of the entrance loss coefficient and the upstream kinetic energy correction factor. While $k = 0$ in Otis' analysis, the excess pressure drop in the entrance region is accounted for in the present solution ($k > 0$), but the reduction of the total driving head in equation (2) is lower for the uniform entrance flow ($\alpha_o = 1$) than for the fully developed profile ($\alpha_o = 2$) considered by Otis (1985). The close correspondance between the present results and Otis' solution in Fig. 2 indicates that the higher available driving head is used to overcome most of the excess pressure drop in the entrance region.

For higher values of the startup flow parameter, i.e., $M \gg 1$, the entrance loss coefficient k decreases according to equation (14*a*) and the entrance effect coefficient E tends to its asymptotic value 0.5. Figure 3 shows that the average steady-state velocity is significantly lower than the corresponding Szymanski solution $U^+ = 1$.

In the long pipe limit, i.e., $M \to 0$, on the other hand, k tends to the constant value (14*b*), which represents the total effect of the entire entrance region on the pressure drop. This asymptotic value of k, which is used in engineering calculations, has been determined analytically, numerically and experimentally. Among the earlier proposals compared by Lundgren, et al. (1964), the asymptotic k-value ranges from 1.08 to 1.41. Bender (1969) obtained theoretically $k = 1.25$, which approximates a mean of experimental and numerical values, and the same limiting value is obtained from the modified formula (13) due to Shah (1978).

For long pipes, k becomes constant and equation (7) reduces to an explicit expression for the steady-state average velocity. Figure 4 demonstrates that equation (7) with $E = 1.125$, which corresponds to $k = 1.25$, closely approximates the more accurate solution obtained iteratively using equations (7), (10), and (13). It should be noticed that Fig. 4 is nothing else than an enlargement of the upper left-hand part of Fig. 2, in which a third solution has also been plotted. The surprisingly small deviation between Otis' solution and the present formulation for small values of M in Fig. 2 has been magnified by the choice of scale of the vertical axis in Fig. 4. It can thus be observed that Otis' solution, which corresponds to $E = 1.0$, gives a slightly higher mean velocity than the present analysis for the lower M-values.

An essential feature of the present analysis is that the results cover the complete range of pipe lengths, i.e., the entire range of M-values, while the validity of Otis' analysis is restricted to pipes in which the length of the entrance region is short compared with the overall pipe length. Accordingly, the hydrodynamic entrance length L_e becomes an important length scale in the problem.

The flow in the downstream part of the pipe can be defined as fully developed (in the hydrodynamic sense) provided that k has reached its asymptotic value to within 98 percent at the pipe exit. According to this definition and the approximate formula (13), the exit flow is hydrodynamically fully developed if the dimensionless length of the pipe L^+ exceeds the dimensionless entrance length

Downloaded 03 May 2010 to 171.66.16.21. Redistribution subject to ASME license or copyright; see http://www.asme.org/terms/Terms_Use.cfm

$$L_e^+ = 0.38 \tag{15}$$

Otherwise the flow is still developing at the pipe exit.

In a long pipe, such that the flow is fully developed at the exit, an estimate for the hydrodynamic entrance length can be derived from equation (15) using the present solution (7) for the average velocity. The entrance length can then be written as

$$L_e/L = 6.08(\sqrt{1+8ME}-1)/E \tag{16}$$

The present formula is meaningful only if $L > L_e$, and the entrance loss coefficient k has therefore been approximated by its asymptotic value (14*b*). Thus the entrance effect coefficient E defined in equation (6) becomes constant and equal to 1.125. Equation (16) demonstrates that the entrance region occupies a greater part of the pipe as the startup flow parameter M increases. In the particular case

$$M_{cr} = 0.045 \tag{17}$$

the entrance region extends to the pipe exit. The solution (16) is therefore valid only for M-values below the critical value (17).

Various estimates for the hydrodynamic entrance length L_e^+ have been proposed in the literature. White (1974), for instance, considered the streamwise variation of k predicted by Schmidt and Zeldin (1969), and estimated L_e^+ to about 0.08. Based on the unrealistic assumption of an inviscid core flow along the axis, McComas (1967) and Olson (1980) proposed the substantially shorter entry region $L_e^+ \approx 0.026$. If the hydrodynamic entrance length is defined as the pipe length required for the flow to achieve a maximum velocity of 99 percent of the fully developed magnitude, typical values of L_e^+ are between 0.05 and 0.06, see Shah and London (1978).

In the present analyis, we have obtained a substantially larger dimensionless entrance length (0.38) than the commonly accepted values about 0.06. This difference may be due to the criterion on which L_e is based or to the approximate Bender-Shah formula (13). Most investigators have defined the hydrodynamic entrance length as the pipe length required to achieve a flow rate (or, alternatively, a centerline velocity) of 98 percent or 99 percent of its fully developed magnitude; see, for instance, Shah and London (1978). The choice of definition of L_e will certainly have some influence on its value. However, White's (1974) estimate 0.08 was based on the streamwise variation of k. The dimensionless entrance length (15), which is more than 6 times larger than customarily accepted, cannot be explained in terms of the criterion for L_e used in the present analysis.

The explanation of the present result (15) should accordingly be sought in the Bender-Shah formula. The closed-form expression (13) is intended to cover the complete range of L^+-values. The leading term for small L^+; i.e., the first term on the right-hand side, represents an excellent curve-fit to the experimental data of Shapiro, et al. (1954) for $L^+ < 0.001$. The constants in the second term were estimated by Shah (1978) in order to provide the least rms error when compared with numerical results for $L^+ < 0.09$. The accuracy of the resulting formula (13) is thus typically within 2–3 percent over the entire range of L^+-values. If the Bender-Shah formula underpredicts the apparent friction factor by, for example, 2 percent next to the fully developed flow region, the corresponding underprediction of the slowly developing k may result in a significant overestimation of L_e. It can thus be concluded that the Bender-Shah formula, which accurately correlates data for the apparent friction factor, nevertheless fails in estimating the hydrodynamic entrance length with reasonable accuracy.

It may therefore be worthwhile to emphasize that the present analysis and the results displayed in Figs. 2–4 do not depend on the entrance length. The estimate (15) for L_e^+ has been obtained as a secondary result of the analysis, and has only been used in the derivation of equations (16) and (17).

Otis (1985) recently neglected the existence of the entrance region, and presented detailed results like velocity profiles and wall shear stress for some different values of M up to 5. According to the preceding arguments, however, his analysis is strictly valid in the asymptotic limit $M \to 0$ only, but the results can be considered a fair approximation to reality for small values of M. For larger M-values, on the other hand, axial flow development takes place over the entire pipe, and Otis' assumption of fully developed flow is hardly reasonable.

The startup parameter M defined in equation (1) is obviously the crucial parameter in the present analysis. It is therefore important to notice that M can be expressed as the ratio between two different time scales, i.e.

$$M = \frac{1}{64}\,\frac{D^2/\nu}{L/U_s} \tag{18}$$

Here, U_s denotes the steady-state average velocity in the Szymanski problem, equation (8), and the denominator therefore represents a typical time-scale for streamwise convection. The numerator in equation (18), on the other hand, is the time-scale for flow establishment in the Szymanski solution and, hence, represents cross-stream diffusion. Small values of M therefore correspond to cases in which the radial diffusion of momentum is a significantly faster process than the axial transport through the pipe. The opposite conclusion can be applied for short pipes, while the critical M-value in equation (17) represents a flow in which both processes occur at the same rate.

Besides the startup flow parameter M, the steady-state flow is also dependent upon the Reynolds number. While this Reynolds number effect has been neglected in the present analysis, the accurate finite-difference computations of Schmidt and Zeldin (1969) demonstrates that the asymptotic k-value is slightly reduced (from 1.397 to 1.346) as Re increases from 100 to 500. Thus, according to equation (7), the ultimate average velocity is expected to decrease slightly as the Reynolds number is increased.

Concluding Remarks

The previous analysis represents the simplest approach to an examination of the startup effects on the ultimate steady-state entrance region flow in pipes. The main findings can be summarized as follows:

1 The head required to the local acceleration of the fluid significantly reduces the steady-state velocity as compared with the classical solution due to Szymanski. The ultimate volume flux is further reduced by entrance region effects.

2 The startup flow parameter M introduced by Otis is identified as the fundamental parameter in the problem, and the magnitude of M provides an efficient criterion for separating short pipes from the longer ones.

3 It is demonstrated that Otis' analysis is valid for long pipes only, and that Szymanski's solution is recovered in the long pipe limit, i.e., $M \to 0$ as $L \to \infty$.

4 When the entrance region extends over a substantial part of the pipe, the startup effect becomes more important, and the axial flow development cannot be neglected.

5 The present analysis can readily be extended to laminar flow in ducts of arbitrary cross sections.

References

Bender, E., 1969, "Druckverlust bei Laminarer Strömung im Rohreinlauf," *Chemie-Ingenieur Technik*, Vol. 11, pp. 682–686.

Letelier, S., M. F., and Leutheusser, H. J., 1976, "Skin Friction in Unsteady Pipe Flow," *ASCE Journal of the Hydraulics Division*, Vol. 102, pp. 41–56.

Lundgren, T. S., Sparrow, E. M., and Starr, J. B., 1964, "Pressure Drop Due

Downloaded 03 May 2010 to 171.66.16.21. Redistribution subject to ASME license or copyright; see http://www.asme.org/terms/Terms_Use.cfm

to the Entrance Region in Ducts of Arbitrary Cross Section," ASME *Journal of Basic Engineering*, Vol. 86, pp. 620–626.

McComas, S. T., 1967, "Hydrodynamic Entrance Lengths for Ducts of Arbitrary Cross Section," ASME *Journal of Basic Engineering*, Vol. 89, pp. 847–850.

Olson, R. M., 1980, *Essentials of Engineering Fluid Mechanics*, 4th Ed., Harper & Row, New York.

Otis, D. R., 1985, "Laminar Start-Up Flow in a Pipe," ASME JOURNAL OF APPLIED MECHANICS, Vol. 52, pp. 706–711.

Schmidt, F. W., and Zeldin, B., 1969, "Laminar Flows in Inlet Sections of Tubes and Ducts," *American Institute of Chemical Engineers Journal*, Vol. 15, pp. 612–614.

Shah, R. K., 1978, "Correlation for Laminar Hydrodynamic Entry Length Solutions for Circular and Non-Circular Ducts," ASME *Journal of Fluids Engineering*, Vol. 100, pp. 177–179.

Shah, R. K., and London, A. L., 1978, *Laminar Flow Forced Convection in Ducts*, Academic Press, New York.

Shapiro, A. H., Siegel, R., and Kline, S. J., 1954, "Friction Factor in the Laminar Entry Region of a Smooth Tube," *Proceedings of the Second U.S. National Congress of Applied Mechanics*, pp. 733–741.

Szymanski, F., 1932, "Quelques Solutions Exactes des Equations de l'Hydrodynamique du Fluide Visqueux dans le Case d'un Tube Cylindrique," *Journal des Mathematiques Pures et Appliquees*, Vol. 11, pp. 67–107.

White, F. M., 1974, *Viscous Fluid Flow*, McGraw-Hill, New York.

Downloaded 03 May 2010 to 171.66.16.21. Redistribution subject to ASME license or copyright; see http://www.asme.org/terms/Terms_Use.cfm

Journal of Applied Mechanics

Brief Notes

A Brief Note is a short paper that presents a specific solution of technical interest in mechanics but which does not necessarily contain new general methods or results. A Brief Note should not exceed 1500 words *or equivalent* (a typical one-column figure or table is equivalent to 250 words; a one line equation to 30 words). Brief Notes will be subject to the usual review procedures prior to publication. After approval such Notes will be published as soon as possible. The Notes should be submitted to the Technical Editor of the JOURNAL OF APPLIED MECHANICS. Discussions on the Brief Notes should be addressed to the Editorial Department, ASME, United Engineering Center, 345 East 47th Street, New York, N. Y. 10017, or to the Technical Editor of the JOURNAL OF APPLIED MECHANICS. Discussions on Brief Notes appearing in this issue will be accepted until two months after publication. Readers who need more time to prepare a Discussion should request an extension of the deadline from the Editorial Department.

Stress Concentration Around a Pair of Circular Holes in a Hydrostatically Stressed Elastic Sheet

R. W. Zimmerman[1]

Kienzler and Duan (1987) have recently derived a simple and compact expression for the hoop stresses around a circular hole in an infinite sheet subjected to a given loading. Their results allow one to find the hoop stresses at the hole boundary in terms of the stresses that would exist in the sheet in the absence of the hole, without having to solve for the entire state of stress throughout the body. The purpose of this note is to show how their result can also be used to find approximate expressions for hoop stresses in a sheet containing a pair of holes. It will be seen that in this particular (and nontrivial) problem, fairly accurate results can be obtained, with essentially no calculations required.

To illustrate this, I take the initial stress state to be the state that exists in a hydrostatically stressed sheet that already contains a single hole, and then use the result of Kienzler and Duan to find an approximate expression for the maximum stress concentration at the boundary of the second hole. The results are only approximate, since the perturbed stress field that is implicit in Kienzler and Duan's theorem causes nonzero (and hence incorrect) stresses on the boundary of the original hole. However, it will be seen that the predicted maximum stress concentration is within 10 percent of the exact value for holes which are as close as one-tenth of a hole diameter.

Following the notation of Kienzler and Duan, I will denote the initial stress state that would exist in the absence of the second hole as σ^0_{ij}, and the perturbed stresses caused by the presence of the second hole by σ^1_{ij}. The total stress field is the sum of these two, and is written without a superscript. It will be helpful to consider two polar coordinate systems, (r_1, ϕ_1) and (r_2, ϕ_2), centered on the first and second hole, respectively (see Fig. 1). Kienzler and Duan show that the hoop stress on the boundary of the second hole is given by

$$\sigma_{\phi_2\phi_2} = K + 2[\sigma^0_{\phi_2\phi_2} - \sigma^0_{r_2r_2}], \tag{1}$$

where $K = \frac{1}{2\pi}\int_0^{2\pi} [\sigma^0_{\phi_2\phi_2} + \sigma^0_{r_2r_2}]d\phi_2$. (2)

If the sheet is subjected to a hydrostatic tension at infinity, the initial stress state is

$$\sigma^0_{r_1r_1} = P[1 - (a/r_1)^2], \tag{3}$$

$$\sigma^0_{\phi_1\phi_1} = P[1 + (a/r_1)^2], \tag{4}$$

where a is the radius of each hole. In the general case, the main nontrivial computation needed to find the hoop stresses would be the evaluation of the integral that defines K. For this particular problem the integrand is simply equal to $2P$; since the integrand is an invariant (the mean normal stress), there is no need to transform the stresses to the (r_2, ϕ_2) coordinate system. Hence, K is readily found to equal $2P$.

To find the hoop stresses at arbitrary points on the hole boundary, the stresses from equations (3, 4) would have to be transformed into the (r_2, ϕ_2) coordinate system. The maximum stress, however, occurs at the point which is closest to the neighboring hole, where the two coordinate systems essentially coincide. As an example, therefore, I will determine the hoop stress only at the points labelled A and B in Fig. 1, for which

$$2(\sigma^0_{\phi_2\phi_2} - \sigma^0_{r_2r_2}) = 4P\,(a/r_1)^2. \tag{5}$$

Since r_1 is measured from the center of hole 1, its value at points A and B is $\lambda \pm a$, where λ is the distance between the centers of the holes. Therefore,

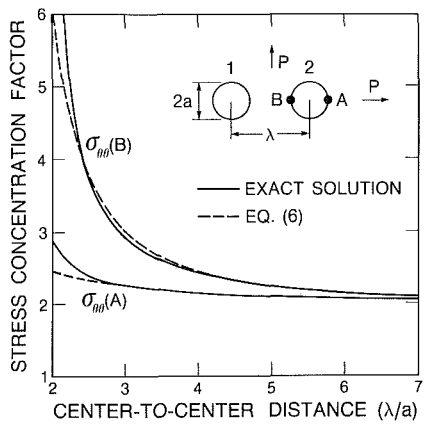


Fig. 1

[1]Department of Mechanical Engineering, University of California, Berkeley, CA 94720.

Manuscript received by ASME Applied Mechanics Division, December 14, 1987; final revision, February 29, 1988.

Copyright © 1988 by ASME
Downloaded 03 May 2010 to 171.66.16.21. Redistribution subject to ASME license or copyright; see http://www.asme.org/terms/Terms_Use.cfm

$$\sigma_{\phi_2\phi_2}(\text{at } A \text{ or } B) = 2P + 4P\left[\frac{a^2}{(\lambda \pm a)^2}\right]$$

$$= P\left[2 + \frac{4a^2}{(\lambda \pm a)^2}\right]. \quad (6)$$

In Fig. 1, these expressions are compared to the exact values that were found by Ling (1948) in the form of very complicated and slowly convergent series. Note that the values from equation (6) are very accurate as long as the edges of the holes are not closer than about one-tenth of a diamater. It is also worth noting that when $\lambda = 2.2$, for example, 14 terms of Ling's series solution would be needed to achieve the same 10 percent accuracy as does equation (6)!

References

Ling, C. B., 1948, "On the Stresses in a Plate Containing Two Circular Holes," *Journal of Applied Physics*, Vol. 19, pp. 77–82.

Kienzler, R., and Duan, Z. P., 1987, "On the Distribution of Hoop Stresses Around Circular Holes in Elastic Sheets," ASME JOURNAL OF APPLIED MECHANICS, Vol. 54, pp. 110–114.

On the Theory of Gyroelasticity

G. M. T. D'Eleuterio[2]

Introduction

A new and general theory of the dynamics of gyroelastic vehicles has been recently developed (D'Eleuterio and Hughes, 1984, 1987; D'Eleuterio, 1985; Hughes and D'Eleuterio, 1986). A "gyroelastic vehicle" is a free *elastic* body containing *gyricity*, that is, containing an arbitrary distribution of stored angular momentum as might arise from momentum-exchange devices; imagine, for example, a large flexible spacecraft with a number of strategically located control gyros or momentum wheels providing attitude and shape control. The analysis was conducted using a continuum approach in which the gyricity distribution, as well as the mass and stiffness properties of the vehicle, was assumed continuous.

This approach proves to be quite convenient from a mathematical standpoint. The equation of motion for a gyroelastic continuum can be derived from Newtonian mechanics and verified using Hamilton's (extended) principle (D'Eleuterio and Hughes, 1984). Owing to the continuum nature of the problem, and in the interest of completeness, we shall show here that the equation of motion can also be obtained from the "balance equations" of continuum mechanics (Eringen, 1967, 1970; Fung, 1965).

Equation of Motion

Let us consider a continuous gyroelastic body fixed at some point to a rigid base as shown in Fig. 1. (For explanatory purposes, the following development deals with constrained bodies; however, the extension to free vehicles can be had with a mere reinterpretation of some symbols.) The gyricity distribution is represented, in component form, by h_i and is constant relative to a local reference frame at x_j, x_j being the spatial coordinates of the body. The mass density is denoted by σ. The momentum balance is governed by

$$t_{ji,\,j} + f_i - \sigma\ddot{u}_i = 0 \quad (1)$$

where u_i is the displacement of the body, f_i is the external force (per volume) distribution and t_{ji} is the stress tensor. Note that

$$(\bullet)_{,\,j} = \frac{\partial(\bullet)}{\partial x_j} \quad (2)$$

(Indicial tensor notation will be used throughout.)

The presence of gyricity in the body results in body moments which render the stress tensor *asymmetric*. The skew-symmetric part of the stress tensor is revealed by the balance of angular momentum

$$t_{ij} - t_{ji} + \epsilon_{ijk}\tau_k = 0 \quad (3)$$

where τ_k is the body moment (per volume) acting on the structure and ϵ_{ijk} is the third-order permutation tensor. Equation (3) is usually written as

$$\tau_k + \epsilon_{ijk}t_{ij} = 0 \quad (4)$$

but (3) will serve us better. Now τ_k contains one component due to gyricity and one due to external torques g_k,

$$\tau_k = \epsilon_{klm}h_l\dot{\alpha}_m + g_k \quad (5)$$

where $\alpha_m = \frac{1}{2}\,\epsilon_{mnp}u_{p,n}$ is the local rotational displacement. Thus,

$$\tau_k = \tfrac{1}{2}\epsilon_{klm}\epsilon_{mnp}h_l\dot{u}_{p,n} + g_k \quad (6)$$

This leads to

$$t_{ij} - t_{ji} + \tfrac{1}{2}\epsilon_{ijk}\epsilon_{klm}\epsilon_{mnp}h_l\dot{u}_{p,n} + \epsilon_{ijk}g_k = 0 \quad (7)$$

upon substitution into (3).

In continuing our derivation, it will be imperative to separate the stress tensor t_{ij} into its symmetric and skew-symmetric parts as follows:

$$t_{ij} = \tfrac{1}{2}(t_{ij} + t_{ji}) + \tfrac{1}{2}(t_{ij} - t_{ji}) \quad (8)$$

The skew-symmetric portion can be had from (7). The symmetric part can be related to strain by the generalized Hooke's law:

$$\tfrac{1}{2}(t_{ij} + t_{ji}) = E_{ijkl}e_{kl} \quad (9)$$

where

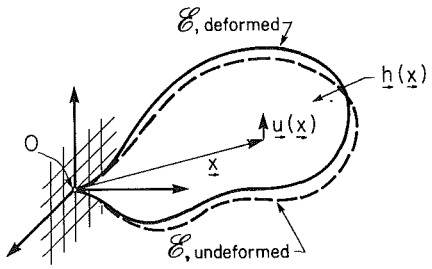
$$e_{kl} = \tfrac{1}{2}(u_{k,l} + u_{l,k}) \quad (10)$$

is the strain tensor and E_{ijkl}, the tensor of "Young's moduli," possesses the usual symmetries, i.e.,

$$E_{ijkl} = E_{jikl} = E_{ijlk} = E_{klij} \quad (11)$$

Using (7)–(10) in (1) eventually gives

$$\sigma\ddot{u}_i - \tfrac{1}{4}\epsilon_{ijk}\epsilon_{klm}\epsilon_{mnp}\left(h_l\dot{u}_{p,n}\right)_{,\,j} - \left(E_{ijkl}u_{l,k}\right)_{,\,j} = f_i + \tfrac{1}{2}\epsilon_{ijk}g_{k,\,j} \quad (12)$$



Cantilevered at O

Fig. 1 A gyroelastic continuum

[2]University of Toronto, Institute for Aerospace Studies, 4925 Dufferin Street, Downsview, Ontario, M3H 5T6, Canada.

Manuscript received by ASME Applied Mechanics Division, October 30, 1985, final revision, February 5, 1988.

Downloaded 03 May 2010 to 171.66.16.21. Redistribution subject to ASME license or copyright; see http://www.asme.org/terms/Terms_Use.cfm

$$\sigma_{\phi_2\phi_2}(\text{at } A \text{ or } B) = 2P + 4P\left[\frac{a^2}{(\lambda \pm a)^2}\right]$$

$$= P\left[2 + \frac{4a^2}{(\lambda \pm a)^2}\right]. \quad (6)$$

In Fig. 1, these expressions are compared to the exact values that were found by Ling (1948) in the form of very complicated and slowly convergent series. Note that the values from equation (6) are very accurate as long as the edges of the holes are not closer than about one-tenth of a diamater. It is also worth noting that when $\lambda = 2.2$, for example, 14 terms of Ling's series solution would be needed to achieve the same 10 percent accuracy as does equation (6)!

References

Ling, C. B., 1948, "On the Stresses in a Plate Containing Two Circular Holes," *Journal of Applied Physics*, Vol. 19, pp. 77–82.

Kienzler, R., and Duan, Z. P., 1987, "On the Distribution of Hoop Stresses Around Circular Holes in Elastic Sheets," ASME JOURNAL OF APPLIED MECHANICS, Vol. 54, pp. 110–114.

On the Theory of Gyroelasticity

G. M. T. D'Eleuterio[2]

Introduction

A new and general theory of the dynamics of gyroelastic vehicles has been recently developed (D'Eleuterio and Hughes, 1984, 1987; D'Eleuterio, 1985; Hughes and D'Eleuterio, 1986). A "gyroelastic vehicle" is a free *elastic* body containing *gyricity*, that is, containing an arbitrary distribution of stored angular momentum as might arise from momentum-exchange devices; imagine, for example, a large flexible spacecraft with a number of strategically located control gyros or momentum wheels providing attitude and shape control. The analysis was conducted using a continuum approach in which the gyricity distribution, as well as the mass and stiffness properties of the vehicle, was assumed continuous.

This approach proves to be quite convenient from a mathematical standpoint. The equation of motion for a gyroelastic continuum can be derived from Newtonian mechanics and verified using Hamilton's (extended) principle (D'Eleuterio and Hughes, 1984). Owing to the continuum nature of the problem, and in the interest of completeness, we shall show here that the equation of motion can also be obtained from the "balance equations" of continuum mechanics (Eringen, 1967, 1970; Fung, 1965).

Equation of Motion

Let us consider a continuous gyroelastic body fixed at some point to a rigid base as shown in Fig. 1. (For explanatory purposes, the following development deals with constrained bodies; however, the extension to free vehicles can be had with a mere reinterpretation of some symbols.) The gyricity distribution is represented, in component form, by h_i and is constant relative to a local reference frame at x_j, x_j being the spatial coordinates of the body. The mass density is denoted by σ. The momentum balance is governed by

$$t_{ji,\,j} + f_i - \sigma\ddot{u}_i = 0 \quad (1)$$

where u_i is the displacement of the body, f_i is the external force (per volume) distribution and t_{ji} is the stress tensor. Note that

$$(\bullet)_{,\,j} = \frac{\partial(\bullet)}{\partial x_j} \quad (2)$$

(Indicial tensor notation will be used throughout.)

The presence of gyricity in the body results in body moments which render the stress tensor *asymmetric*. The skew-symmetric part of the stress tensor is revealed by the balance of angular momentum

$$t_{ij} - t_{ji} + \epsilon_{ijk}\tau_k = 0 \quad (3)$$

where τ_k is the body moment (per volume) acting on the structure and ϵ_{ijk} is the third-order permutation tensor. Equation (3) is usually written as

$$\tau_k + \epsilon_{ijk}t_{ij} = 0 \quad (4)$$

but (3) will serve us better. Now τ_k contains one component due to gyricity and one due to external torques g_k,

$$\tau_k = \epsilon_{klm}h_l\dot{\alpha}_m + g_k \quad (5)$$

where $\alpha_m = \frac{1}{2}\,\epsilon_{mnp}u_{p,n}$ is the local rotational displacement. Thus,

$$\tau_k = \tfrac{1}{2}\epsilon_{klm}\epsilon_{mnp}h_l\dot{u}_{p,n} + g_k \quad (6)$$

This leads to

$$t_{ij} - t_{ji} + \tfrac{1}{2}\epsilon_{ijk}\epsilon_{klm}\epsilon_{mnp}h_l\dot{u}_{p,n} + \epsilon_{ijk}g_k = 0 \quad (7)$$

upon substitution into (3).

In continuing our derivation, it will be imperative to separate the stress tensor t_{ij} into its symmetric and skew-symmetric parts as follows:

$$t_{ij} = \tfrac{1}{2}(t_{ij} + t_{ji}) + \tfrac{1}{2}(t_{ij} - t_{ji}) \quad (8)$$

The skew-symmetric portion can be had from (7). The symmetric part can be related to strain by the generalized Hooke's law:

$$\tfrac{1}{2}(t_{ij} + t_{ji}) = E_{ijkl}e_{kl} \quad (9)$$

where

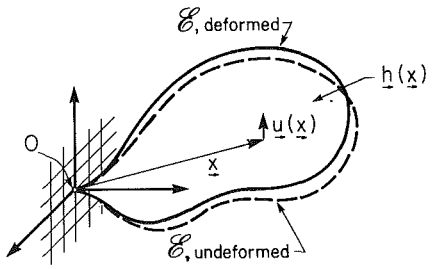
$$e_{kl} = \tfrac{1}{2}(u_{k,l} + u_{l,k}) \quad (10)$$

is the strain tensor and E_{ijkl}, the tensor of "Young's moduli," possesses the usual symmetries, i.e.,

$$E_{ijkl} = E_{jikl} = E_{ijlk} = E_{klij} \quad (11)$$

Using (7)–(10) in (1) eventually gives

$$\sigma\ddot{u}_i - \tfrac{1}{4}\epsilon_{ijk}\epsilon_{klm}\epsilon_{mnp}\,(h_l\dot{u}_{p,n})_{,\,j} - (E_{ijkl}u_{l,k})_{,\,j} = f_i + \tfrac{1}{2}\epsilon_{ijk}g_{k,\,j} \quad (12)$$



Cantilevered at O

Fig. 1 A gyroelastic continuum

[2]University of Toronto, Institute for Aerospace Studies, 4925 Dufferin Street, Downsview, Ontario, M3H 5T6, Canada.

Manuscript received by ASME Applied Mechanics Division, October 30, 1985, final revision, February 5, 1988.

Copyright © 1988 by ASME
Downloaded 03 May 2010 to 171.66.16.21. Redistribution subject to ASME license or copyright; see http://www.asme.org/terms/Terms_Use.cfm

This equation of motion, although notationally different, is the same as that obtained in earlier derivations. The appropriate natural and forced boundary conditions must, of course, accompany (12).

Summary

Using a Newtonian approach, the equation of motion for a gyroelastic body was shown to be, in matrix-operator form,

$$\mathfrak{M}\ddot{\mathbf{u}} + \mathcal{G}\dot{\mathbf{u}} + \mathcal{K}\mathbf{u} = \mathbf{f} + \tfrac{1}{2}\nabla^{\times}\mathbf{g} \tag{13}$$

where

$$\mathfrak{M} \triangleq \sigma \underline{1}$$
$$\mathcal{G} \triangleq -\tfrac{1}{4}\nabla^{\times}\mathbf{h}^{\times}\nabla^{\times} \tag{14}$$

and $\underline{1}$ is the identity operator. Also, $(\bullet)^{\times}$ denotes the (3×3) skew-symmetric matrix associated with the vector cross product and hence $\nabla^{\times}$ represents the curl operator. The mass operator $\mathfrak{M}$ is symmetric and positive-definite. For a constrained body, the stiffness operator $\mathcal{K}$ is both symmetric and positive-definite as well; however, for a free vehicle, it is symmetric and positive-semidefinite. The gyricity operator $\mathcal{G}$ is skew-symmetric.

Expanding $\mathfrak{M}$ and $\mathcal{G}$ from (14) in component form, we have

$$\{\mathfrak{M}\}_{ij} = \sigma\delta_{ij}$$
$$\{\mathcal{G}\}_{ij} = -\tfrac{1}{4}\epsilon_{ijk}\epsilon_{klm}\epsilon_{mnp}\left(h_l(\bullet)_{,n}\right)_{,j} \tag{15}$$

which are indeed the forms that appear in (12). Furthermore, comparing (13) with (12), we can identify the stiffness operator as

$$\{\mathcal{K}\}_{il} = -\left(E_{ijkl}(\bullet)_{,k}\right)_{,j} \tag{16}$$

Thus, it has been shown that the equation for a gyroelastic body can also be derived from the principles of continuum mechanics.

In arriving at (12), we have obtained as lagniappe an alternate proof of the equivalent force distribution for a torque distribution, viz.,

$$f_i^{(e)} = \tfrac{1}{2}\epsilon_{ijk}g_{k,j} \tag{17}$$

This relationship had been proven previously using physical considerations.

Acknowledgments

The author wishes to thank Professor Peter C. Hughes for his helpful comments. This work was supported by the Natural Sciences and Engineering Research Council (NSERC) of Canada.

References

D'Eleuterio, G. M. T., and Hughes, P. C., 1984, "Dynamics of Gyroelastic Continua," ASME JOURNAL OF APPLIED MECHANICS, Vol. 106, No. 2, pp. 415–422.

D'Eleuterio, G. M. T., and Hughes, P. C., 1987, "Dynamics of Gyroelastic Spacecraft," *AIAA Journal of Guidance, Control and Dynamics*, Vol. 10, No. 4, pp. 401–405; also presented at AIAA/ASME/ASCE/AHS 26th Structures, Structural Dynamics and Materials Conference, April 15–17, 1985, Orlando, Florida.

D'Eleuterio, G. M. T., 1985, "Dynamics of Gyroelastic Vehicles," Fifth VPI & SU/AIAA Symposium on Dynamics and Control of Large Structures, June 12–14, Blacksburg, Virginia.

Eringen, A. C., 1967, *Mechanics of Continua*, Wiley.

Eringen, A. C., 1970, "Balance Laws of Micromorphic Mechanics," *Int. Journal of Engineering Science*, Vol. 8, pp. 819–828.

Fung, Y. C., 1965, *Foundations of Solid Mechanics*, Prentice-Hall.

Hughes, P. C., and D'Eleuterio, G. M. T., 1986, "Modal Parameter Analysis of Gryoelastic Continua," ASME JOURNAL OF APPLIED MECHANICS, Vol. 108, No. 4, pp. 918–924.

Inverse Problem Solutions Via Plate Theory With Applications to Position and Force Sensing

P. P. Lin[3] and P. Datseris[4]

Introduction

Theory of plates is employed to solve inverse problems in elasticity with specific applications to position and force sensing. The term "inverse problems" implies the determination of position, distribution and magnitude of loads applied by an object on an elastic element, if strains are known at several locations of the element. Both analytical and numerical methods are presented. The analytical method presented is limited to rectangular plates having two opposite edges simply supported and uniform distribution in the loaded region.

Inverse problems for different types of loading conditions are solved and simulated by computer (Lin, 1985). By assuming that strains at some locations are known, computer simulation results obtained by both analytical and numerical techniques are compared with exact solutions. The results thus obtained are quite good (Lin and Datseris, 1986). Finally, strains were measured to verify the inverse problem solutions.

Forward Plate Problem Solution

1 Plate Configuration. The forward plate problem is defined by assuming that the loading conditions for the plate are known in advance. A thin rectangular plate with two opposite edges simply supported, the third edge free, and the fourth edge built-in, was chosen so that the plate can be used as a position and force sensor attached on a robot gripper, for instance. The ratio of the thickness to any smallest lateral discussion was chosen under 0.1 to meet the assumptions of thin plates.

The governing differential equation of the plate subjected to lateral loads is (Szilard, 1974).

$$(\partial^4 w/\partial x^4) + 2(\partial^4 w/\partial x^2\partial y^2) + (\partial^4 w/\partial y^4) = P_z(x,y)/D \tag{1}$$

where $P_z(x,y)$ is the force per unit area in the Z direction and the plate is initially in XY plane.

The deflection of the plate under any lateral load can be obtained by combining the solution for the plate with all edges simply supported, with a solution to satisfy boundary conditions where the edges are not simply supported (Timoshenko, 1959). Thus, the total deflection of the plate is assumed to consist of two parts, as follows:

$$W = W_1 + W_2 \tag{2}$$

where W_1 represents the deflection of the plate with all sides simply supported in a form of single trigonometric series which satisfies the simply supported boundary conditions in the X direction

$$W_1 = \sum_{m=1}^{\infty} H_m \sin(m\pi X/a) \tag{3}$$

and W_2 is represented by the series suggested by M. Levy for the case of a rectangular plate with two opposite edges not simply supported

[3]Assistant Professor, Mechanical Engineering, Cleveland State University, Cleveland, OH 44115.

[4]Associate Professor, Mechanical Engineering and Applied Mechanics Dept., University of Rhode Island, Kingston, RI 02881.

Manuscript received by ASME Applied Mechanics Division, February 23, 1987; final revision, December 9, 1987.

Downloaded 03 May 2010 to 171.66.16.21. Redistribution subject to ASME license or copyright; see http://www.asme.org/terms/Terms_Use.cfm

This equation of motion, although notationally different, is the same as that obtained in earlier derivations. The appropriate natural and forced boundary conditions must, of course, accompany (12).

Summary

Using a Newtonian approach, the equation of motion for a gyroelastic body was shown to be, in matrix-operator form,

$$\mathfrak{M}\ddot{\mathbf{u}} + \mathcal{G}\dot{\mathbf{u}} + \mathcal{K}\mathbf{u} = \mathbf{f} + \tfrac{1}{2}\nabla^{\times}\mathbf{g} \tag{13}$$

where

$$\mathfrak{M} \triangleq \sigma \underline{1}$$
$$\mathcal{G} \triangleq -\tfrac{1}{4}\nabla^{\times}\mathbf{h}^{\times}\nabla^{\times} \tag{14}$$

and $\underline{1}$ is the identity operator. Also, $(\bullet)^{\times}$ denotes the (3×3) skew-symmetric matrix associated with the vector cross product and hence $\nabla^{\times}$ represents the curl operator. The mass operator $\mathfrak{M}$ is symmetric and positive-definite. For a constrained body, the stiffness operator $\mathcal{K}$ is both symmetric and positive-definite as well; however, for a free vehicle, it is symmetric and positive-semidefinite. The gyricity operator $\mathcal{G}$ is skew-symmetric.

Expanding $\mathfrak{M}$ and $\mathcal{G}$ from (14) in component form, we have

$$\{\mathfrak{M}\}_{ij} = \sigma\delta_{ij}$$
$$\{\mathcal{G}\}_{ij} = -\tfrac{1}{4}\epsilon_{ijk}\epsilon_{klm}\epsilon_{mnp}\left(h_l(\bullet)_{,n}\right)_{,j} \tag{15}$$

which are indeed the forms that appear in (12). Furthermore, comparing (13) with (12), we can identify the stiffness operator as

$$\{\mathcal{K}\}_{il} = -\left(E_{ijkl}(\bullet)_{,k}\right)_{,j} \tag{16}$$

Thus, it has been shown that the equation for a gyroelastic body can also be derived from the principles of continuum mechanics.

In arriving at (12), we have obtained as lagniappe an alternate proof of the equivalent force distribution for a torque distribution, viz.,

$$f_i^{(e)} = \tfrac{1}{2}\epsilon_{ijk}g_{k,j} \tag{17}$$

This relationship had been proven previously using physical considerations.

Acknowledgments

The author wishes to thank Professor Peter C. Hughes for his helpful comments. This work was supported by the Natural Sciences and Engineering Research Council (NSERC) of Canada.

References

D'Eleuterio, G. M. T., and Hughes, P. C., 1984, "Dynamics of Gyroelastic Continua," ASME JOURNAL OF APPLIED MECHANICS, Vol. 106, No. 2, pp. 415–422.

D'Eleuterio, G. M. T., and Hughes, P. C., 1987, "Dynamics of Gyroelastic Spacecraft," *AIAA Journal of Guidance, Control and Dynamics*, Vol. 10, No. 4, pp. 401–405; also presented at AIAA/ASME/ASCE/AHS 26th Structures, Structural Dynamics and Materials Conference, April 15–17, 1985, Orlando, Florida.

D'Eleuterio, G. M. T., 1985, "Dynamics of Gyroelastic Vehicles," Fifth VPI & SU/AIAA Symposium on Dynamics and Control of Large Structures, June 12–14, Blacksburg, Virginia.

Eringen, A. C., 1967, *Mechanics of Continua*, Wiley.

Eringen, A. C., 1970, "Balance Laws of Micromorphic Mechanics," *Int. Journal of Engineering Science*, Vol. 8, pp. 819–828.

Fung, Y. C., 1965, *Foundations of Solid Mechanics*, Prentice-Hall.

Hughes, P. C., and D'Eleuterio, G. M. T., 1986, "Modal Parameter Analysis of Gryoelastic Continua," ASME JOURNAL OF APPLIED MECHANICS, Vol. 108, No. 4, pp. 918–924.

Inverse Problem Solutions Via Plate Theory With Applications to Position and Force Sensing

P. P. Lin[3] and P. Datseris[4]

Introduction

Theory of plates is employed to solve inverse problems in elasticity with specific applications to position and force sensing. The term "inverse problems" implies the determination of position, distribution and magnitude of loads applied by an object on an elastic element, if strains are known at several locations of the element. Both analytical and numerical methods are presented. The analytical method presented is limited to rectangular plates having two opposite edges simply supported and uniform distribution in the loaded region.

Inverse problems for different types of loading conditions are solved and simulated by computer (Lin, 1985). By assuming that strains at some locations are known, computer simulation results obtained by both analytical and numerical techniques are compared with exact solutions. The results thus obtained are quite good (Lin and Datseris, 1986). Finally, strains were measured to verify the inverse problem solutions.

Forward Plate Problem Solution

1 Plate Configuration. The forward plate problem is defined by assuming that the loading conditions for the plate are known in advance. A thin rectangular plate with two opposite edges simply supported, the third edge free, and the fourth edge built-in, was chosen so that the plate can be used as a position and force sensor attached on a robot gripper, for instance. The ratio of the thickness to any smallest lateral discussion was chosen under 0.1 to meet the assumptions of thin plates.

The governing differential equation of the plate subjected to lateral loads is (Szilard, 1974).

$$(\partial^4 w/\partial x^4) + 2(\partial^4 w/\partial x^2\partial y^2) + (\partial^4 w/\partial y^4) = P_z(x,y)/D \tag{1}$$

where $P_z(x,y)$ is the force per unit area in the Z direction and the plate is initially in XY plane.

The deflection of the plate under any lateral load can be obtained by combining the solution for the plate with all edges simply supported, with a solution to satisfy boundary conditions where the edges are not simply supported (Timoshenko, 1959). Thus, the total deflection of the plate is assumed to consist of two parts, as follows:

$$W = W_1 + W_2 \tag{2}$$

where W_1 represents the deflection of the plate with all sides simply supported in a form of single trigonometric series which satisfies the simply supported boundary conditions in the X direction

$$W_1 = \sum_{m=1}^{\infty} H_m \sin(m\pi X/a) \tag{3}$$

and W_2 is represented by the series suggested by M. Levy for the case of a rectangular plate with two opposite edges not simply supported

[3]Assistant Professor, Mechanical Engineering, Cleveland State University, Cleveland, OH 44115.

[4]Associate Professor, Mechanical Engineering and Applied Mechanics Dept., University of Rhode Island, Kingston, RI 02881.

Manuscript received by ASME Applied Mechanics Division, February 23, 1987; final revision, December 9, 1987.

Copyright © 1988 by ASME
Downloaded 03 May 2010 to 171.66.16.21. Redistribution subject to ASME license or copyright; see http://www.asme.org/terms/Terms_Use.cfm

$$W_2 = \sum_{m=1}^{\infty} Y_m(Y)\sin(m\pi X/a) \tag{4}$$

(Nadai, 1915) has introduced the solution of the above equation in the form of hyperbolic function:

$$Y_m(Y) = A_m\cosh(m\pi Y/a) + B_m(m\pi Y/a)\sinh(m\pi Y/a) + C_m\sinh(m\pi Y/a) + D_m(m\pi Y/a)\cosh(m\pi Y/a) \tag{5}$$

The constants A_m, B_m, C_m and D_m can be determined from the boundary conditions at four edges. For a specific m value, A_m, B_m, C_m and D_m are all in terms of H_m.

Upon obtaining all H_m, the total deflection is determined. The load at any location in the plate can then be computed by employing the equation of the plate. In addition, the bending moments and twisting moments can also be calculated. The total deflection for each specified m value is expressed as

$$W_m = [H_m + A_m\cosh(m\pi Y/a) + B_m(m\pi Y/a) + C_m\sinh(m\pi Y/a) + D_m(m\pi Y/a)\cosh(m\pi Y/a)]\sin(m\pi X/a) \tag{6}$$

Inverse Plate Problem Solution

1 Analytical Method. The analytical inverse solution is presented in this section. In most cases it is satisfactory to consider only the first few terms of sine series due to fast convergence, since all the coefficients A_m, B_m, C_m, and D_m are in terms of H_m, which can then be factored out for a specific value of m. In the case of using the first four terms, four unknowns H_1, H_2, H_3 and H_4 are to be determined. Thus, four independent strains in X or Y direction should be measured in order to generate four linearly independent equations. Note that

$$\epsilon_x = -Z(\partial^2 W/\partial X^2) \tag{7}$$

$$\epsilon_y = -Z(\partial^2 W/\partial Y^2) \tag{8}$$

Employing the first four terms, for example, gives

$$\epsilon_x = -Z\sum_{m=1}^{4}(\partial^2 W_m/\partial X^2) \tag{9}$$

$$\epsilon_y = -Z\sum_{m=1}^{4}(\partial^2 W_m/\partial Y^2) \tag{10}$$

where m is a number starting at 1, and z is the distance in Z direction perpendicular to the plate from the middle surface to the bottom surface of the plate. In this case, Z is $h/2$, since strain gages are placed on the bottom surface of the plate. H_1, H_2, H_3 and H_4 can then be solved by the following set of equations:

$$\epsilon_x(X_n, Y_n) = -Z\sum_{m=1}^{4}[\partial^2 W_m(X_n, Y_n)/\partial X^2]$$

or

$$\epsilon_y(X_n, Y_n) = -Z\sum_{m=1}^{4}[\partial^2 W_m(X_n, Y_n)/\partial Y^2] \tag{11}$$

where (X_n, Y_n) represents locations or positions in the planar coordinate of the plate and $n = 1,2,3,4$.

The basic idea for solving the inverse problem is to solve for all the numerical coefficients H_m provided that H_m can be factored out.

Note that the first eight terms of sine series should be used for obtaining the inverse solution with less than ten percent error according to the results of computer simulation.

Several cases are examined in the following for a plate with side lengths a and b in X and Y directions, respectively.

Case (a): Partial load distributed over the plate from

$X = 0$ to a and from $Y = Y_1$ to Y_2 $(0 < Y_1 < Y_2 < b)$

Case (b): Partial load distributed over the plate from

$X = X_1$ to X_2 $(0 < X_1 < X_2 < a)$ and from $Y = Y_1$ to Y_2 $(0 < Y_1 < Y_2 < b)$

The expressions of H_m are the same for case (a) and case (b), but the numerical values of m are different. In other words, the expression for H_m is determined only by the distribution of the applied load in Y direction, while the distribution of the load in X direction determines the numerical values of H_m.

Case (c): Partial load with an inclined angle theta with respect to Y-axis

This problem can be solved by imagining an infinitesimal increment from Y_1 to Y_2. It should be noted that the loaded area remains almost the same with this approximation. H_m in this case is no longer a constant for each specific value of m. It is a function of the location in Y direction.

In this case, only part of H_m, say H_m', remains constant and will be factored out.

$$H_m = H_m' H_m'' \tag{12}$$

After all H_m' are solved, H_m'' corresponding to each specified location are premultiplied by H_m' to obtain the real value of H_m.

2 Numerical Method. Among the numerical techniques, the finite difference method is used. In applying this method, the derivatives in the differential equation under consideration are replaced by differential quantities at some selected points. If high accuracy in the finite difference solution of plate problems is required, improved finite difference techniques should be applied which takes more mesh points in the vicinity of the pivotal point.

Determination of Position and Distribution of an Applied Load

The position and distribution of an applied load can be determined by examining the strain distributions in the X and Y directions. Strains are measured from the bottom surface of the thin plate. The results thus obtained in comparison with the exact position and distribution can be seen in (Lin and Datseris, 1986).

Conclusions and Future Work

The analytical method presented is limited to uniform distribution over a loaded region, while the numerical method can be applied to non-uniform loading distributions. Future work includes the extension of this work to non-uniform loading distribution using the analytical method. Moreover, this work can be extended to solve inverse problems with any other boundary conditions.

One of the specific applications of the inverse plate problem solutions is the position and force sensing for a robot gripper. This problem is important because the loading condition when a gripper holds an object is always unknown. The inverse solution in this case includes the determination of position, distribution and magnitude of the contact force between the object and the gripper.

References

Lin, P., 1985, "Gripper-Based Position/Force Sensor Design and Robot Hand Motion Control During Assembly," Doctoral Dissertation, Mechanical Engineering and Applied Mechanics, University of Rhode Island, pp. 42–57.

Downloaded 03 May 2010 to 171.66.16.21. Redistribution subject to ASME license or copyright; see http://www.asme.org/terms/Terms_Use.cfm

Lin, P. P. and Datseris, P., 1986, "Development of a Position and Force Sensor for Robotic Applications," *Proceedings of 1986 IEEE International Conference on Robotics and Automation*, Vol. 3, Apr. 7-10, pp. 1798-1805.

Nadai, A., 1915, "Die Formanderungen und die Spannungen von Rechteckigen Elastichen Pattern," Forsch A. D. Gebiete D. Ingenieurwesens, Berlin, Nos. 170 and 171.

Szilard, R., 1974, *Theory and Analysis of Plates*, New Jersey, Prentice Hall, pp. 36-42.

Timoshenko, S. and Woinowsky-Krieger, S., 1959, *Theory of Plates and Shells*, Second Edition, McGraw-Hill, New York, pp. 113-114.

Unstable Elastic Materials and the Viscoelastic Response of Bars in Tension[5]

R. Abeyaratne[6] and J. K. Knowles[7]

Some homogeneous elastic materials are capable of sustaining finite equilibrium deformations with discontinuous strains. For materials of this kind, the energetics of isothermal, quasi-static motions may differ from those conventionally associated with elastic behavior. When equilibrium states involving strain jumps occur during such motions, the rate of increase of stored energy in a portion of the body may no longer coincide with the rate of work of the external forces present. In general, energy balance now includes an additional effect due to the presence of moving strain discontinuities. As a consequence, the macroscopic response of the body may be dissipative. This fact makes it possible to model certain types of inelastic behavior in solids with the help of such "unstable" elastic materials; see, for example, Abeyaratne and Knowles (1987a,b,c).

The purpose of the present note is to illustrate behavior of this kind with the help of an especially simple example involving the extensional deformations of a bar treated as a one-dimensional continuum. The bar is composed of an unstable elastic material of the type considered by Ericksen (1975). We show that the force-elongation relation (or "macroscopic response") of the bar during a quasi-static motion may be viscoelastic when a moving strain jump is present, even though the underlying constitutive law is elastic in the sense that, at each particle, the present stress is determined by the present strain.

Consider an elastic bar which, in the reference configuration, occupies the interval $[0,L]$ of the x-axis and has constant cross-sectional area A. In a deformation, the particle at x is carried to $y=x+u(x)$, where u is the displacement. We assume that u is continuous on $[0,L]$, and that $u'(x)$ exists and is continuous for $0\leq x\leq s$ and $s\leq x\leq L$, but $u'(s+)$ and $u'(s-)$ may differ; here $0<s<L$. If $x\neq s$, the strain at x is $\epsilon(x)=u'(x)$. It is required that $\epsilon(x)>-1$ for $x\neq s$, so that the mapping $x\rightarrow y$ is invertible. We take the left end of the bar to be fixed, so that $u(0)=0$.

Suppose that the material is elastic with strain energy per unit reference volume $W(\epsilon)$. The nominal stress response function is then

$$\hat{\sigma}(\epsilon)=W'(\epsilon), \tag{1}$$

so that the nominal stress in the bar at particle x is $\sigma(x)=\hat{\sigma}(\epsilon(x))$. We shall be concerned with the special "trilinear" stress response function given by

$$\hat{\sigma}(\epsilon)=\begin{cases}\mu\epsilon\ , & -1<\epsilon\leqq\epsilon_M,\\ \dfrac{\mu\epsilon_M}{\epsilon_m-\epsilon_M}(\epsilon_m+\epsilon_M-2\epsilon), & \epsilon_M\leqq\epsilon\leqq\epsilon_m,\\ \mu(\epsilon-\epsilon_0), & \epsilon_m\leqq\epsilon<\infty.\end{cases} \tag{2}$$

The graph of $\hat{\sigma}(\epsilon)$ is shown in Fig. 1, where the meanings of the constants μ, ϵ_M, ϵ_m and $\epsilon_0=\epsilon_M+\epsilon_m$ are made clear. One may think of the material as exhibiting three phases: the first phase is represented by the rising branch of the stress-strain curve through the origin, the third phase corresponds to the final rising branch, and the declining portion of the curve represents an unstable intervening second phase. In the present case, the first and third phases are both associated with the same modulus μ.

In the absence of body force, the bar will be in equilibrium if the nominal stress $\sigma(x)$ satisfies

$$\sigma(x)=\sigma=\text{constant},\quad 0\leqq x\leqq L. \tag{3}$$

A deformation with a strain discontinuity of the kind described above will correspond to an equilibrium state if it is of the form

$$u(x)=\begin{cases}\epsilon_1 x, & 0\leqq x\leqq s,\\ \epsilon_2 x+(\epsilon_1-\epsilon_2)s, & s\leqq x\leqq L,\end{cases} \tag{4}$$

where the strains ϵ_1 and ϵ_2 are constant and such that

$$\hat{\sigma}(\epsilon_1)=\hat{\sigma}(\epsilon_2)=\sigma. \tag{5}$$

We shall be concerned here only with those deformations of the form (4) in which

$$-\epsilon_M\leqq\epsilon_1\leqq\epsilon_M,\quad \epsilon_m\leqq\epsilon_2\leqq\epsilon_M+\epsilon_0, \tag{6}$$

so that only phases one and three are represented. For an equilibrium state of this kind, the total energy stored in the bar is

$$E=AW(\epsilon_1)s+AW(\epsilon_2)(L-s). \tag{7}$$

Now suppose that the bar is in a quasi-static motion during which, at each instant t, the displacement $u(x,t)$ is of the form (4), with $s=s(t)$, $\epsilon_1=\epsilon_1(t)$ and $\epsilon_2=\epsilon_2(t)$. The restrictions (5) and (6) are to hold for all t, with $\sigma=\sigma(t)$. Assume that $s(t)$, $\epsilon_1(t)$ and $\epsilon_2(t)$ are continuous and piecewise continuously differentiable in t. During such a motion, the energy $E(t)$ is given by (7) with ϵ_1, ϵ_2, and s now functions of time. A direct calculation gives

$$\dot{E}(t)=F(t)\dot{\delta}(t)+A[-f(t)]\dot{s}(t), \tag{8}$$

where $F(t)=\sigma(t)A$ is the force,

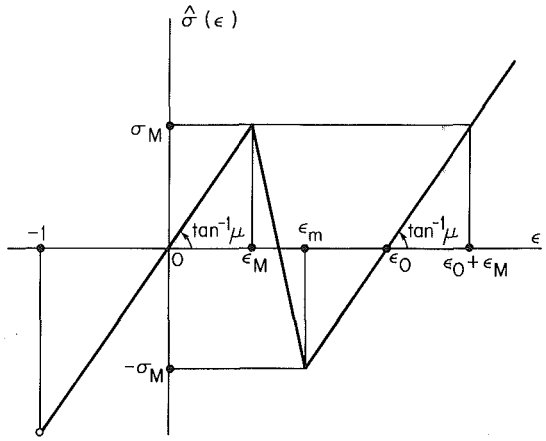


Fig. 1 Stress response function

[5]The results reported here were obtained in the course of an investigation supported in part by the U.S. Office of Naval Research under Contract N00014-87-K-0117.

[6]Department of Mechanical Engineering, Massachusetts Institute of Technology, Cambridge, MA 02139.

[7]Division of Engineering and Applied Science, California Institute of Technology, Pasadena, CA 91125.

Manuscript received by ASME Applied Mechanics Division, November 10, 1987.

Downloaded 03 May 2010 to 171.66.16.21. Redistribution subject to ASME license or copyright; see http://www.asme.org/terms/Terms_Use.cfm

Lin, P. P. and Datseris, P., 1986, "Development of a Position and Force Sensor for Robotic Applications," *Proceedings of 1986 IEEE International Conference on Robotics and Automation*, Vol. 3, Apr. 7-10, pp. 1798-1805.

Nadai, A., 1915, "Die Formanderungen und die Spannungen von Rechteckigen Elastichen Pattern," Forsch A. D. Gebiete D. Ingenieurwesens, Berlin, Nos. 170 and 171.

Szilard, R., 1974, *Theory and Analysis of Plates*, New Jersey, Prentice Hall, pp. 36-42.

Timoshenko, S. and Woinowsky-Krieger, S., 1959, *Theory of Plates and Shells*, Second Edition, McGraw-Hill, New York, pp. 113-114.

Unstable Elastic Materials and the Viscoelastic Response of Bars in Tension[5]

R. Abeyaratne[6] and J. K. Knowles[7]

Some homogeneous elastic materials are capable of sustaining finite equilibrium deformations with discontinuous strains. For materials of this kind, the energetics of isothermal, quasi-static motions may differ from those conventionally associated with elastic behavior. When equilibrium states involving strain jumps occur during such motions, the rate of increase of stored energy in a portion of the body may no longer coincide with the rate of work of the external forces present. In general, energy balance now includes an additional effect due to the presence of moving strain discontinuities. As a consequence, the macroscopic response of the body may be dissipative. This fact makes it possible to model certain types of inelastic behavior in solids with the help of such "unstable" elastic materials; see, for example, Abeyaratne and Knowles (1987a,b,c).

The purpose of the present note is to illustrate behavior of this kind with the help of an especially simple example involving the extensional deformations of a bar treated as a one-dimensional continuum. The bar is composed of an unstable elastic material of the type considered by Ericksen (1975). We show that the force-elongation relation (or "macroscopic response") of the bar during a quasi-static motion may be viscoelastic when a moving strain jump is present, even though the underlying constitutive law is elastic in the sense that, at each particle, the present stress is determined by the present strain.

Consider an elastic bar which, in the reference configuration, occupies the interval $[0,L]$ of the x-axis and has constant cross-sectional area A. In a deformation, the particle at x is carried to $y=x+u(x)$, where u is the displacement. We assume that u is continuous on $[0,L]$, and that $u'(x)$ exists and is continuous for $0\leq x\leq s$ and $s\leq x\leq L$, but $u'(s+)$ and $u'(s-)$ may differ; here $0<s<L$. If $x\neq s$, the strain at x is $\epsilon(x)=u'(x)$. It is required that $\epsilon(x)>-1$ for $x\neq s$, so that the mapping $x\rightarrow y$ is invertible. We take the left end of the bar to be fixed, so that $u(0)=0$.

Suppose that the material is elastic with strain energy per unit reference volume $W(\epsilon)$. The nominal stress response function is then

$$\hat{\sigma}(\epsilon)=W'(\epsilon), \tag{1}$$

so that the nominal stress in the bar at particle x is $\sigma(x)=\hat{\sigma}(\epsilon(x))$. We shall be concerned with the special "trilinear" stress response function given by

$$\hat{\sigma}(\epsilon)=\begin{cases}\mu\epsilon\ , & -1<\epsilon\leq\epsilon_M,\\ \dfrac{\mu\epsilon_M}{\epsilon_m-\epsilon_M}(\epsilon_m+\epsilon_M-2\epsilon), & \epsilon_M\leq\epsilon\leq\epsilon_m,\\ \mu(\epsilon-\epsilon_0), & \epsilon_m\leq\epsilon<\infty.\end{cases} \tag{2}$$

The graph of $\hat{\sigma}(\epsilon)$ is shown in Fig. 1, where the meanings of the constants μ, ϵ_M, ϵ_m and $\epsilon_0=\epsilon_M+\epsilon_m$ are made clear. One may think of the material as exhibiting three phases: the first phase is represented by the rising branch of the stress-strain curve through the origin, the third phase corresponds to the final rising branch, and the declining portion of the curve represents an unstable intervening second phase. In the present case, the first and third phases are both associated with the same modulus μ.

In the absence of body force, the bar will be in equilibrium if the nominal stress $\sigma(x)$ satisfies

$$\sigma(x)=\sigma=\text{constant},\ 0\leq x\leq L. \tag{3}$$

A deformation with a strain discontinuity of the kind described above will correspond to an equilibrium state if it is of the form

$$u(x)=\begin{cases}\epsilon_1 x, & 0\leq x\leq s,\\ \epsilon_2 x+(\epsilon_1-\epsilon_2)s, & s\leq x\leq L,\end{cases} \tag{4}$$

where the strains ϵ_1 and ϵ_2 are constant and such that

$$\hat{\sigma}(\epsilon_1)=\hat{\sigma}(\epsilon_2)=\sigma. \tag{5}$$

We shall be concerned here only with those deformations of the form (4) in which

$$-\epsilon_M\leq\epsilon_1\leq\epsilon_M,\ \epsilon_m\leq\epsilon_2\leq\epsilon_M+\epsilon_0, \tag{6}$$

so that only phases one and three are represented. For an equilibrium state of this kind, the total energy stored in the bar is

$$E=AW(\epsilon_1)s+AW(\epsilon_2)(L-s). \tag{7}$$

Now suppose that the bar is in a quasi-static motion during which, at each instant t, the displacement $u(x,t)$ is of the form (4), with $s=s(t)$, $\epsilon_1=\epsilon_1(t)$ and $\epsilon_2=\epsilon_2(t)$. The restrictions (5) and (6) are to hold for all t, with $\sigma=\sigma(t)$. Assume that $s(t)$, $\epsilon_1(t)$ and $\epsilon_2(t)$ are continuous and piecewise continuously differentiable in t. During such a motion, the energy $E(t)$ is given by (7) with ϵ_1, ϵ_2, and s now functions of time. A direct calculation gives

$$\dot{E}(t)=F(t)\dot{\delta}(t)+A[-f(t)]\dot{s}(t), \tag{8}$$

where $F(t)=\sigma(t)A$ is the force,

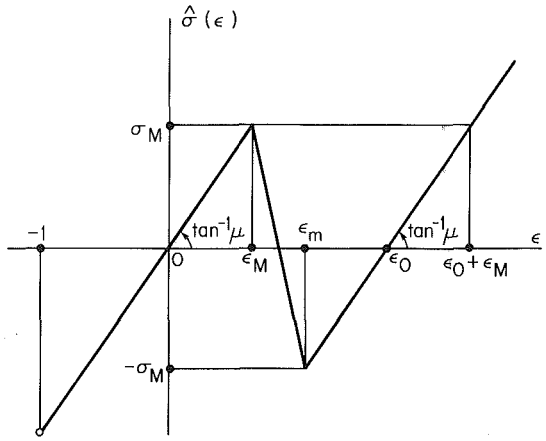


Fig. 1 Stress response function

[5]The results reported here were obtained in the course of an investigation supported in part by the U.S. Office of Naval Research under Contract N00014-87-K-0117.

[6]Department of Mechanical Engineering, Massachusetts Institute of Technology, Cambridge, MA 02139.

[7]Division of Engineering and Applied Science, California Institute of Technology, Pasadena, CA 91125.

Manuscript received by ASME Applied Mechanics Division, November 10, 1987.

Copyright © 1988 by ASME
Downloaded 03 May 2010 to 171.66.16.21. Redistribution subject to ASME license or copyright; see http://www.asme.org/terms/Terms_Use.cfm

$$\delta(t) = u(L,t) = \epsilon_1(t)s(t) + \epsilon_2(t)(L - s(t)) \tag{9}$$

is the elongation of the bar at time t, and $f(t)$ is given by

$$f(t) = W(\epsilon_2(t)) - W(\epsilon_1(t)) - \sigma(t)(\epsilon_2(t) - \epsilon_1(t)). \tag{10}$$

The first term on the right in (8) is the rate of work of the force acting on the end $x = L$ of the bar. The second term may be interpreted as the rate of work done by a fictitious "traction" $f(t)$ in moving the strain discontinuity at $x = s(t)$. For the stress-strain relation (2), one finds using (1), (6) and (10) that

$$f(t) = -\epsilon_0\sigma(t). \tag{11}$$

If the motion takes place isothermally, the second law of thermodynamics requires that $\dot{E} - F\dot{\delta}$ be nonnegative; thus the motion must be such that

$$f(t)\dot{s}(t) \geqq 0. \tag{12}$$

Because of (5) and (6), specifying the history of the stress acting on the bar determines $\epsilon_1(t)$ and $\epsilon_2(t)$, but leaves undetermined the location $s(t)$ of the strain jump, and therefore the elongation history $\delta(t)$ of (9) as well.

In formulas (7) and (9), one may regard s as an "internal variable" akin to those arising in microstructural theories of plasticity; see, for example, Rice (1971). This suggests that, by analogy with such theories, the constitutive description of the material should be augmented by relating the fictitious traction $f(t)$ to the velocity of the moving discontinuity $\dot{s}(t)$. One form that such a "kinetic relation" might take is

$$\dot{s}(t) = V(f(t)), \tag{13}$$

where V is a function determined by the material. Using (11), one infers from (13) that

$$\dot{s}(t) = V(-\epsilon_0\sigma(t)). \tag{14}$$

Note from (12) that every admissible V must be such that $V(f)f \geqq 0$.

Let $\gamma(t) = \delta(t)/L$ be the *relative* elongation of the bar. The relation between γ and F—the macroscopic response of the bar—may now be determined as follows. Using (2) and (6) in (9) yields

$$\delta(t) = \epsilon_0[L - s(t)] + \sigma(t)L/\mu, \tag{15}$$

from which, with the help of (14), one finds the nonlinear viscoelastic relation

$$\dot{\gamma}(t) = \dot{F}(t)/\mu A - \epsilon_0 V(-\epsilon_0 F(t)/A)/L. \tag{16}$$

If in particular the kinetic response function V is specified through $V(f) = f/\nu$, where ν is a positive constant, (13) provides a linearly "viscous" kinetic relation between f and $\dot{s}$. The macroscopic response relation (16) specializes to

$$\dot{\gamma}(t) = \dot{F}(t)/\mu A + \epsilon_0^2 F(t)/\nu LA. \tag{17}$$

This is precisely the form of the response relation characteristic of the so-called "Maxwell" spring-dashpot model of elementary viscoelasticity. Other forms of macroscopic response can be obtained by replacing (13) by a more general kinetic relation.

A more extensive discussion of the one-dimensional theory of quasi-static motions of bars composed of unstable elastic materials may be found in Abeyaratne and Knowles (1987c).

References

Abeyaratne, R. and Knowles, J. K., 1987a, "Non-elliptic Elastic Materials and the Modeling of Elastic-plastic Behavior for Finite Deformation," *Journal of the Mechanics and Physics of Solids*, Vol. 35, pp. 343–365.

Abeyaratne, R. and Knowles, J. K., 1987b, "Non-elliptic Elastic Materials and the Modeling of Dissipative Mechanical Behavior: An Example," *Journal of Elasticity*, Vol. 18, pp. 227–278.

Abeyaratne, R. and Knowles, J. K., 1987c, "On the Dissipative Response due to Discontinuous Strains in Bars of Unstable Elastic Material," Technical Report No. 1, ONR Contract N00014-87-K-0117, California Institute of Technology, September, 1987; to appear in *International Journal of Solids and Structures.*

Ericksen, J. L., 1975, "Equilibrium of Bars," *Journal of Elasticity*, Vol. 5, pp. 191–201.

Rice, J. R., 1971, "Inelastic Constitutive Relations for Solids: An Internal Variable Theory and its Application to Metal Plasticity," *Journal of the Mechanics and Physics of Solids*, Vol. 19, pp. 433–455.

Diffusion of Self-Equilibrating End Loads in Elastic Solids

D. Durban[8] and W. J. Stronge[9]

Introduction

The classical Papkovich-Fadle eigenfunction analysis for axial diffusion of self-equilibrating end loads, in plane strain linear elasticity, predicts exponential decay of the form exp $(-kz/h)$ where $z \geq 0$ is the axial coordinate, h-half thickness, and k is any root of the associated eigenvalue equation. The lowest rate of axial decay for an elastic solid at small strains is governed by the *first symmetric eigenfunction* with $k_1 = 2.1061 + i\,1.1254$. The next term, in order of increasing magnitude of Re $\{k\}$, is given by the first antisymmetric eigenfunction with $k_2 = 3.7488 + i\,1.3843$. These values of k, as well as the higher roots, are determined by the transcendental equations $\sin 2k \pm 2k = 0$ where the $(+)$ and $(-)$ signs correspond to symmetric and antisymmetric eigenfunctions, respectively.

A recent paper by Abeyaratne, Horgan and Chung (1985) has addressed the plane strain end effect problem within the framework of finite strain elasticity. The authors consider an incrementally self-equilibrating end disturbance imposed on a uniformly stretched strip. The axial decay rate is again exponential but the eigenvalue k is now dependent on the magnitude of initial stretch. Furthermore, the variation of k with the initial stretch displays considerable sensitivity to the form of the strain energy function. Unfortunately, that study has been restricted to the subspace of symmetric eigenfunctions so it reveals only part of the complete picture.

The main purpose of the present note is to demonstrate that the smallest decay rate (which provides a bound on the validity of Saint-Venant's principle) can be associated with the *first antisymmetric eigenfunction*. It is necessary, therefore, to examine the *complete space* of eigenfunctions (i.e., symmetric and antisymmetric) allowing for competition among the corresponding eigenvalues over the entire range of prestrain and material parameters.

The basic setting is similar to that of Abeyaratne, Horgan and Chung (1985), though we differ in the solution method and follow the Hill and Hutchinson (1975) stream function formulation. The material is assumed to be hyperelastic and incompressible. Specific examples are illustrated for the Mooney-Rivlin model and for a power-law solid. A few related topics are discussed and some general results are presented.

Formulation of the Problem

A semi-infinite strip of rectangular cross section (Fig. 1) is uniformly stretched under plane strain conditions. The current axial stress is $\sigma_z = \sigma$ and the principal stretches are $\lambda_z = \lambda$ and $\lambda_x = \lambda^{-1}$. The deformed thickness is denoted by $2h$ and the faces $x = \pm h$ are stress free. Note that $h = H/\lambda$ where H is the original undeformed thickness.

[8]Department of Aeronautical Engineering, Technion, Haifa 32000, Israel.

[9]Department of Engineering, University of Cambridge, Trumpington Street, Cambridge CB2 1PZ, England.

Manuscript received by ASME Applied Mechanics Division, August 25, 1987.

Downloaded 03 May 2010 to 171.66.16.21. Redistribution subject to ASME license or copyright; see http://www.asme.org/terms/Terms_Use.cfm

$$\delta(t) = u(L,t) = \epsilon_1(t)s(t) + \epsilon_2(t)(L - s(t)) \tag{9}$$

is the elongation of the bar at time t, and $f(t)$ is given by

$$f(t) = W(\epsilon_2(t)) - W(\epsilon_1(t)) - \sigma(t)(\epsilon_2(t) - \epsilon_1(t)). \tag{10}$$

The first term on the right in (8) is the rate of work of the force acting on the end $x = L$ of the bar. The second term may be interpreted as the rate of work done by a fictitious "traction" $f(t)$ in moving the strain discontinuity at $x = s(t)$. For the stress-strain relation (2), one finds using (1), (6) and (10) that

$$f(t) = -\epsilon_0\sigma(t). \tag{11}$$

If the motion takes place isothermally, the second law of thermodynamics requires that $\dot{E} - F\dot{\delta}$ be nonnegative; thus the motion must be such that

$$f(t)\dot{s}(t) \geqq 0. \tag{12}$$

Because of (5) and (6), specifying the history of the stress acting on the bar determines $\epsilon_1(t)$ and $\epsilon_2(t)$, but leaves undetermined the location $s(t)$ of the strain jump, and therefore the elongation history $\delta(t)$ of (9) as well.

In formulas (7) and (9), one may regard s as an "internal variable" akin to those arising in microstructural theories of plasticity; see, for example, Rice (1971). This suggests that, by analogy with such theories, the constitutive description of the material should be augmented by relating the fictitious traction $f(t)$ to the velocity of the moving discontinuity $\dot{s}(t)$. One form that such a "kinetic relation" might take is

$$\dot{s}(t) = V(f(t)), \tag{13}$$

where V is a function determined by the material. Using (11), one infers from (13) that

$$\dot{s}(t) = V(-\epsilon_0\sigma(t)). \tag{14}$$

Note from (12) that every admissible V must be such that $V(f)f \geqq 0$.

Let $\gamma(t) = \delta(t)/L$ be the *relative* elongation of the bar. The relation between γ and F—the macroscopic response of the bar—may now be determined as follows. Using (2) and (6) in (9) yields

$$\delta(t) = \epsilon_0[L - s(t)] + \sigma(t)L/\mu, \tag{15}$$

from which, with the help of (14), one finds the nonlinear viscoelastic relation

$$\dot{\gamma}(t) = \dot{F}(t)/\mu A - \epsilon_0 V(-\epsilon_0 F(t)/A)/L. \tag{16}$$

If in particular the kinetic response function V is specified through $V(f) = f/\nu$, where ν is a positive constant, (13) provides a linearly "viscous" kinetic relation between f and $\dot{s}$. The macroscopic response relation (16) specializes to

$$\dot{\gamma}(t) = \dot{F}(t)/\mu A + \epsilon_0^2 F(t)/\nu LA. \tag{17}$$

This is precisely the form of the response relation characteristic of the so-called "Maxwell" spring-dashpot model of elementary viscoelasticity. Other forms of macroscopic response can be obtained by replacing (13) by a more general kinetic relation.

A more extensive discussion of the one-dimensional theory of quasi-static motions of bars composed of unstable elastic materials may be found in Abeyaratne and Knowles (1987c).

References

Abeyaratne, R. and Knowles, J. K., 1987a, "Non-elliptic Elastic Materials and the Modeling of Elastic-plastic Behavior for Finite Deformation," *Journal of the Mechanics and Physics of Solids*, Vol. 35, pp. 343–365.

Abeyaratne, R. and Knowles, J. K., 1987b, "Non-elliptic Elastic Materials and the Modeling of Dissipative Mechanical Behavior: An Example," *Journal of Elasticity*, Vol. 18, pp. 227–278.

Abeyaratne, R. and Knowles, J. K., 1987c, "On the Dissipative Response due to Discontinuous Strains in Bars of Unstable Elastic Material," Technical Report No. 1, ONR Contract N00014-87-K-0117, California Institute of Technology, September, 1987; to appear in *International Journal of Solids and Structures.*

Ericksen, J. L., 1975, "Equilibrium of Bars," *Journal of Elasticity*, Vol. 5, pp. 191–201.

Rice, J. R., 1971, "Inelastic Constitutive Relations for Solids: An Internal Variable Theory and its Application to Metal Plasticity," *Journal of the Mechanics and Physics of Solids*, Vol. 19, pp. 433–455.

Diffusion of Self-Equilibrating End Loads in Elastic Solids

D. Durban[8] and W. J. Stronge[9]

Introduction

The classical Papkovich-Fadle eigenfunction analysis for axial diffusion of self-equilibrating end loads, in plane strain linear elasticity, predicts exponential decay of the form exp $(-kz/h)$ where $z \geq 0$ is the axial coordinate, h-half thickness, and k is any root of the associated eigenvalue equation. The lowest rate of axial decay for an elastic solid at small strains is governed by the *first symmetric eigenfunction* with $k_1 = 2.1061 + i\,1.1254$. The next term, in order of increasing magnitude of Re $\{k\}$, is given by the first antisymmetric eigenfunction with $k_2 = 3.7488 + i\,1.3843$. These values of k, as well as the higher roots, are determined by the transcendental equations $\sin 2k \pm 2k = 0$ where the $(+)$ and $(-)$ signs correspond to symmetric and antisymmetric eigenfunctions, respectively.

A recent paper by Abeyaratne, Horgan and Chung (1985) has addressed the plane strain end effect problem within the framework of finite strain elasticity. The authors consider an incrementally self-equilibrating end disturbance imposed on a uniformly stretched strip. The axial decay rate is again exponential but the eigenvalue k is now dependent on the magnitude of initial stretch. Furthermore, the variation of k with the initial stretch displays considerable sensitivity to the form of the strain energy function. Unfortunately, that study has been restricted to the subspace of symmetric eigenfunctions so it reveals only part of the complete picture.

The main purpose of the present note is to demonstrate that the smallest decay rate (which provides a bound on the validity of Saint-Venant's principle) can be associated with the *first antisymmetric eigenfunction*. It is necessary, therefore, to examine the *complete space* of eigenfunctions (i.e., symmetric and antisymmetric) allowing for competition among the corresponding eigenvalues over the entire range of prestrain and material parameters.

The basic setting is similar to that of Abeyaratne, Horgan and Chung (1985), though we differ in the solution method and follow the Hill and Hutchinson (1975) stream function formulation. The material is assumed to be hyperelastic and incompressible. Specific examples are illustrated for the Mooney-Rivlin model and for a power-law solid. A few related topics are discussed and some general results are presented.

Formulation of the Problem

A semi-infinite strip of rectangular cross section (Fig. 1) is uniformly stretched under plane strain conditions. The current axial stress is $\sigma_z = \sigma$ and the principal stretches are $\lambda_z = \lambda$ and $\lambda_x = \lambda^{-1}$. The deformed thickness is denoted by $2h$ and the faces $x = \pm h$ are stress free. Note that $h = H/\lambda$ where H is the original undeformed thickness.

[8]Department of Aeronautical Engineering, Technion, Haifa 32000, Israel.

[9]Department of Engineering, University of Cambridge, Trumpington Street, Cambridge CB2 1PZ, England.

Manuscript received by ASME Applied Mechanics Division, August 25, 1987.

Copyright © 1988 by ASME

Downloaded 03 May 2010 to 171.66.16.21. Redistribution subject to ASME license or copyright; see http://www.asme.org/terms/Terms_Use.cfm

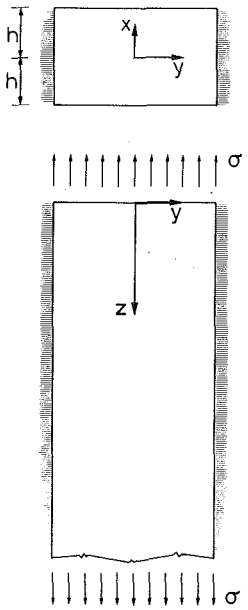


Fig. 1 Semi-infinite rectangular strip in uniform stretch under plane-strain conditions. The current thickness is 2*h*.

Assume now that an instantaneous self-equilibrating surface disturbance is imposed over the end $z = 0$. The perturbed stress-rate and strain-rate fields within the body are governed by the constitutive relations

$$\overset{\nabla}{\sigma}_x - \overset{\nabla}{\sigma}_z = 2\mu^*(\epsilon_x - \epsilon_z), \quad \overset{\nabla}{\tau}_{xz} = 2\mu\gamma_{xz} \tag{1}$$

and the incompressibility constraint

$$\epsilon_x + \epsilon_z = 0 \tag{2}$$

Here, $(\sigma_x, \sigma_z, \tau_{xz})$ are the Cauchy stress components, $(\overset{\nabla}{\ })$ stands for the objective Jaumann rate, $(\epsilon_x, \epsilon_z, \gamma_{xz})$ are the components of the Eulerian strain rate, and the instantaneous moduli (μ, μ^*) are related to the strain energy function $W(\lambda)$ by (Hill and Hutchinson, 1975)

$$2\mu = \frac{\lambda^4 + 1}{\lambda^4 - 1}\,\sigma, \qquad 4\mu^* = \mu\,\frac{d\sigma}{d\lambda}, \quad \sigma = \lambda\,\frac{dW}{d\lambda} \tag{3}$$

Let (u, w) be the (x, z) components of the perturbed velocity field. It is convenient then to introduce, via (2), a stream function $\phi(x, z)$ such that $u = \phi_{,z}$ and $w = -\phi_{,x}$. The strain rate components follow as

$$\epsilon_x = \phi_{,xz}, \quad \gamma_{xz} = -\frac{1}{2}(\phi_{,xx} - \phi_{,zz}), \quad \epsilon_z = -\phi_{,xz} \tag{4}$$

and, similarly, the components of the spin tensor become

$$\omega_{xz} = -\omega_{zx} = -\frac{1}{2}(\phi_{,xx} + \phi_{,zz}) \tag{5}$$

The two rate-equilibrium equations

$$\overset{\nabla}{\sigma}_{x,x} + (\overset{\nabla}{\tau}_{xz} - \omega_{xz}\sigma)_{,z} = 0 \tag{6a}$$

$$(\overset{\nabla}{\tau}_{xz} - \gamma_{xz}\sigma)_{,x} + (\overset{\nabla}{\sigma}_z - \epsilon_z\sigma)_{,z} = 0 \tag{6b}$$

can now be conjoined to produce, with the aid of (1) and (4)–(5), the single fourth order partial differential equation

$$(2\mu - \sigma)\phi_{,xxxx} + 4(2\mu^* - \mu)\phi_{,xxzz} + (2\mu + \sigma)\phi_{,zzzz} = 0 \tag{7}$$

This equation is supplemented by the stress-free boundary conditions at $x = \pm h$. The rate form of these conditions is $\overset{\nabla}{\sigma}_x = 0$ and $\overset{\nabla}{\tau}_{xz} - \gamma_{xz}\,\sigma = 0$ or, in terms of the stream function,

$$(2\mu - \sigma)\phi_{,xxx} + (8\mu^* - 2\mu - \sigma)\phi_{,xzz} = 0 \quad \text{at } x = \pm h \tag{8}$$

$$\phi_{,xx} - \phi_{,zz} = 0 \quad \text{at } x = \pm h \tag{9}$$

Equations (7)–(9) determine the eigenfunctions which can be used to solve the nonhomogeneous boundary value problem for surface data at $z = 0$ (provided that the eigenfunction set is complete). Here, however, we focus attention on the eigenfunction space itself in order to establish the axial rate of diffusion of the end loads.

Solution and Examples

A representative eigensolution of (7) can be written as

$$\phi = f(x)\exp\left(-k\,\frac{z}{h}\right) \quad \text{with } \mathrm{Re}\{k\} > 0 \tag{10}$$

where $f(x)$ is given by

$$f(x) = C_1\sin\left(\Gamma_1 k\frac{x}{h}\right) + C_2\sin\left(\Gamma_2 k\frac{x}{h}\right), \quad \text{for symmetric}[10] \text{ eigenfunctions,} \tag{11}$$

$$f(x) = C_1\cos\left(\Gamma_1 k\frac{x}{h}\right) + C_2\cos\left(\Gamma_2 k\frac{x}{h}\right), \quad \text{for antisymmetric eigenfunctions,} \tag{12}$$

C_1, C_2 are integration constants and

$$\Gamma_1 = X + iY, \qquad \Gamma_2 = X - iY \tag{13}$$

with

$$X^2 = \frac{1}{2}\left(\sqrt{\frac{2\mu+\sigma}{2\mu-\sigma}} - \frac{2\mu - 4\mu^*}{2\mu-\sigma}\right),$$

$$Y^2 = \frac{1}{2}\left(\sqrt{\frac{2\mu+\sigma}{2\mu-\sigma}} + \frac{2\mu - 4\mu^*}{2\mu-\sigma}\right) \tag{14}$$

Compliance with the boundary conditions (8)–(9) leads to the transcendental eigenvalue equations

$$P\sin(2Xk) \pm Q\sinh(2Yk) = 0 \tag{15}$$

where the (+) and (−) signs correspond to symmetric and antisymmetric eigenfunctions, respectively, and

$$P = Y\left(4\mu^* - \sigma + \sigma\sqrt{\frac{2\mu-\sigma}{2\mu+\sigma}}\right), \quad Q = X\left(4\mu^* - \sigma - \sigma\sqrt{\frac{2\mu-\sigma}{2\mu+\sigma}}\right) \tag{16}$$

The eigenvalues k are determined by (15), for a given strain energy function, at any stress (strain) level. [The proof that each eigenfunction (10) is associated with a self-equilibrating end disturbance is straightforward though lengthy.]

Mooney-Rivlin Material. Consider, as a first example, the Mooney-Rivlin material

$$W = \frac{1}{2}\,\mu_0(\lambda^2 + \lambda^{-2} - 1) \text{ with } \mu = \mu^* = \frac{1}{2}\,\mu_0(\lambda^2 + \lambda^{-2}),$$
$$\text{and } \sigma = \mu_0(\lambda^2 - \lambda^{-2}) \tag{17}$$

It is known that, with (17), ellipticity of the governing equation (7) is maintained at any stretch. Equations (15) admit now the simple forms

$$4\tan(k) - \lambda^2(\lambda^2 + \lambda^{-2})^2\tan(\lambda^2 k) = 0 \quad \text{(symmetric eigenfunctions)} \tag{18}$$

$$4\tan(\lambda^2 k) - \lambda^2(\lambda^2 + \lambda^{-2})^2\tan(k) = 0 \quad \text{(antisymmetric eigenfunctions)} \tag{19}$$

[10] Eigenfunctions have been termed "symmetric" or "antisymmetric" according to the pattern of the corresponding perturbed stress-rate and strain-rate fields.

Downloaded 03 May 2010 to 171.66.16.21. Redistribution subject to ASME license or copyright; see http://www.asme.org/terms/Terms_Use.cfm

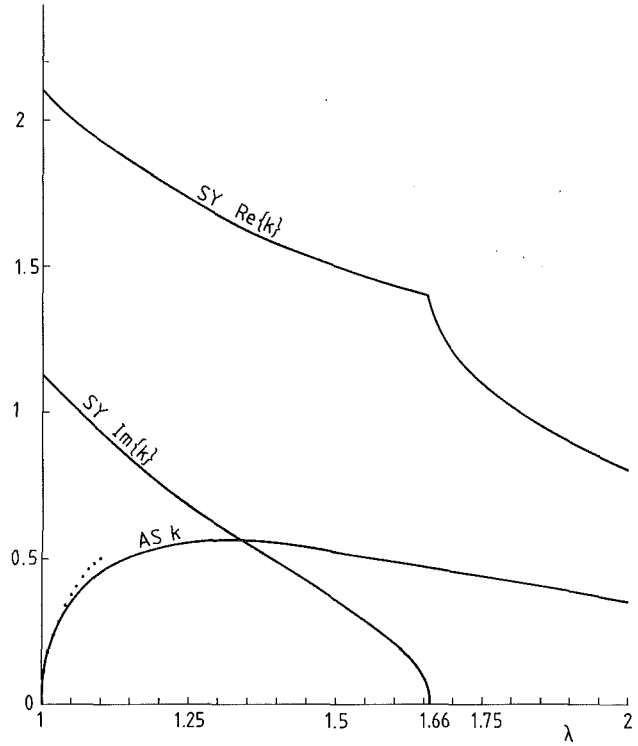


Fig. 2 *First eigenvalues $k(\lambda)$ for the Mooney-Rivlin material with* uniform stretch λ. SY - symmetric eigenfunctions, AS - antisymmetric eigenfunctions. The dotted line shows the small strain approximation (20) for the AS eigenfunctions.

The variation of the first roots (those with smallest real part) of (18)-(19) as a function of the uniform stretch λ is shown in Fig. 2. The results for the first symmetric eigenvalue are in complete agreement with those of Abeyaratne, Horgan and Chung, (1985). Starting with the linear elastic value at $\lambda = 1$, the decay rate k remains complex up to $\lambda \approx 1.66$ where it becomes purely real. For large stretches k approaches the asymptote π/λ^2.

Much lower decay rates, however, are associated with the *first antisymmetric eigenfunction*. Here, the first root of (19) is *real for all* $\lambda > 1$ and for small values of stretch (i.e., $\lambda - 1 = \Delta \ll 1$) it is given essentially by

$$k \approx \sqrt{\frac{3(\lambda^4-1)}{3\lambda^4+1}} \approx \sqrt{3\Delta} \tag{20}$$

It is worth mentioning that the *second* antisymmetric root agrees, at the limit of $\lambda = 1$, with the corresponding linear elastic value. At high levels of stretch k approaches the asymptote $\pi/2\lambda^2$.

Power Law Material with Softening Modulus. Our next example is that of the power law material with

$$\sigma = \sigma_0 (ln\ \lambda)^{1/n} \quad n \geq 1 \tag{21}$$

The eigenvalue equations (15) are now

$$\sqrt{n\frac{\lambda^2+1}{\lambda^2-1}\,ln\,\lambda - 1}\left(n\frac{\lambda^2-1}{\lambda^2}\,ln\,\lambda - 1\right) \times \sin\left[\sqrt{\frac{\lambda^4-1}{n\,ln\,\lambda} - (\lambda^2-1)^2}\;k\right]$$
$$\pm\sqrt{1-n\frac{\lambda^2-1}{\lambda^2+1}\,ln\,\lambda}\left(n\frac{\lambda^2+1}{\lambda^2}\,ln\,\lambda - 1\right) \times sinh\left[\sqrt{(\lambda^2+1)^2 - \frac{\lambda^4-1}{n\,ln\,\lambda}}\;k\right] = 0 \tag{22}$$

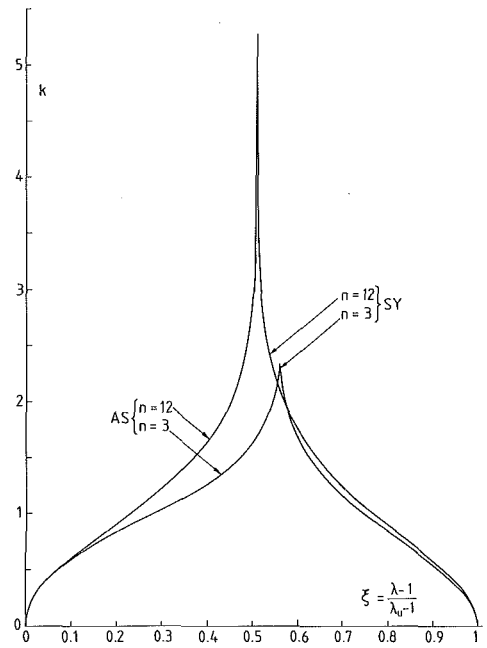


Fig. 3 *First eigenvalues $k(\lambda)$ for the power-law material with* uniform stretch λ. SY - symmetric eigenfunctions, AS - antisymmetric eigenfunctions. $\lambda_u = \exp(1/n)$ is the stretch at ultimate load. Here all values of k are real numbers. The peak value for large n is $k_p \approx (\pi/2)\sqrt{n}$.

Sample calculations for the first eigenvalues, as evaluated from (22), are shown in Fig. 3 for $n = 3$ and $n = 12$. A convenient measure of deformation is given by $\xi = (\lambda - 1)/(\lambda_u - 1)$ where $\lambda_u = \exp(1/n)$ is the uniform stretch at ultimate (maximum) axial tension. This load is attained when $\sigma = 4\mu^*$, well below failure of ellipticity. Indeed, using (4.5) of (Hill and Hutchinson, 1975), it can be verified that ellipticity holds as long as the inequality

$$n\frac{\lambda^2-1}{\lambda^2+1}\,ln\,\lambda < 1 \tag{23}$$

is not violated. Simple algebraic reasoning shows that (23) is valid for any stretch in the range $1 \leq \lambda \leq \lambda_u$.

The first eigenvalue (smallest decay rate) is always real for $1 \leq \lambda \leq \lambda_u$. This smallest k is associated with an antisymmetric eigenfunction when the tensile stretch is small and a symmetric eigenfunction when the stretch is near λ_u. The eigenfunction with the smallest decay rate changes at a stretch λ_p where, from (22),

$$n(\lambda_p^2+1)(ln\,\lambda_p) - \lambda_p^2 = 0 \tag{24}$$

At λ_p the antisymmetric and symmetric branches of k meet in a sharp peak (see Fig. 3) where the decay rate k_p is a maximum,

$$k_p = \pi\left[\frac{\lambda_p^4-1}{n\,ln\,\lambda_p} - (\lambda_p^2-1)^2\right]^{-1/2} \tag{25}$$

For large values of the softening parameter n where $\lambda_p - 1 = \Delta_p \ll 1$, we find from (24) that $\Delta_p \approx 1/2n$ (i.e., about half the strain at the ultimate load) and (25) gives essentially $k_p \approx (\pi/2)\sqrt{n}$.

For very small strains the first eigenvalue (antisymmetric eigenfunction) can be approximated by

$$k \approx \sqrt{\frac{6n\,ln\,\lambda}{3\lambda^4 - 1 - n(\lambda^4+1)ln\,\lambda}} \approx \sqrt{3n\Delta} \tag{26}$$

Downloaded 03 May 2010 to 171.66.16.21. Redistribution subject to ASME license or copyright; see http://www.asme.org/terms/Terms_Use.cfm

When n is large, $\xi \approx n\Delta$ so that (26) becomes $k \approx \sqrt{3\xi}$; this is similar to (20).

The smallest root of (22) increases with stretch up to λ_p and then decreases towards zero as the ultimate load is approached (Fig. 3). Near λ_n we have again an asymptotic expansion, viz,

$$k \approx \sqrt{\frac{6(1-n\ ln\ \lambda)}{2n\ ln\ \lambda-(1-n\ ln\ \lambda)\left(\lambda^4+1-\dfrac{\lambda^4-1}{n\ ln\ \lambda}\right)}} \approx \sqrt{3n\left(1-\frac{\lambda}{\lambda_u}\right)} \tag{27}$$

For large values of n we get from (27) that $k \approx \sqrt{3(1-\xi)}$ indicating—along with earlier results and numerical observations—that as n increases the k versus ξ curves of Fig. 3 become more and more symmetric with respect to the center line $\xi = 1/2$.

Conclusions

In addition to the constitutive sensitivity of the smallest decay rate (k), and the importance of considering the complete space of eigenfunctions, there are a few more interesting observations that emerge from our study: To begin with, the lowest eigenvalues shown in Figs. 2–3 are all real and they predict a purely exponential, non-oscillatory decay of the first eigenfunctions in contrast to the complex roots for the linear elastic solid.

Secondly, it appears that there is almost no diffusion of the antisymmetric end disturbance at low values of stretch. The asymptotic relations of (20) and (26) show clearly that $k \to 0$ as $\lambda \to 1$ (and $\Delta \to 0$). A more general result, derived from the antisymmetric branch of (15), for small strains, reads $k^2 \approx 3\sigma/4\mu_0^*$ where μ_0^* is the ground state (at zero strain) value of modulus μ^*. This low rate of decay when the strains are small is not predicted by the linear theory of elasticity, and can be described as a *critical second order effect*.

For the power law material, slow diffusion of the end effect also is predicted as the load approaches its ultimate value (Fig. 3). This is in agreement with the bifurcation study of Hill and Hutchinson (1975), since k from (27) becomes, for $\lambda > \lambda_u$, a purely imaginary number, reflecting the oscillatory nature of the bifurcation eigenmodes. Note that no bifurcation away from the primary orthogonal path exists for the Mooney-Rivlin material.

Finally, for the power law material around the antisymmetric/symmetric eigenfunction transition at $\lambda = \lambda_p$, there is a narrow band of stretch with a high rate of diffusion (Fig. 3). At large values of n this needle-shaped region is extraordinarily sharp and can perhaps be described as a *Saint-Venant spike*. Similar results have recently been obtained by the authors in a related study of strain hardening elastoplastic materials, Durban and Stronge (1988).

Acknowledgment

One of us (DD) wishes to express his thanks for the kind hospitality of the Cambridge University Engineering Department, during the sabbatical year 1986/7. Part of this work has been supported by the V.P.R.-Aeronautical Engineering Research Fund, Technion, Haifa.

References

Abeyaratne, R., Horgan, C. O., and Chung, D.-T., 1985, "Saint-Venant End Effects for Incremental Plane Deformations of Incompressible Nonlinearity Elastic Materials," ASME Journal of Applied Mechanics, Vol. 52, pp. 847–852.

Durban, D., and Stronge, W. J., 1988, "Diffusion of Self Equilibrating End Loads in Plain Strain Plasticity," *I. Tech. Phys. Solids,* to be published.

Hill, R., and Hutchinson, J. W., 1975, "Bifurcation Phenomena in the Plane Tension Test," *J. Mech. Phys. Solids*, Vol. 23, pp. 239–264.

Transversely Isotropic Medium with a Rigid Spheroidal Inclusion Under an Axial Pull

A. H. Zureick[1]

Introduction

Selvadurai (1976) presented a three-dimensional axisymmetric solution, exact within elastostatics, to the problem of a rigid spheroidal inclusion embedded in an infinite isotropic elastic medium and subjected to an axial pull. This problem has applications to both composite materials and soil mechanics. The present paper constitutes the transversely isotropic counterpart of Selvadurai's problem.

Fundamental Formulae

Consider a homogeneous transversely isotropic elastic medium occupying a region of the three-dimensional space referred to a fixed cylindrical coordinate system (r, θ, z) in which the z-axis coincides with the material axis of symmetry. It can be shown that in the absence of body forces, solutions of three-dimensional axisymmetric problems can be found in terms of two quasi-harmonic potential functions $\phi_\alpha\ (r, z)$, $(\alpha = 1, 2)$, which are the solutions of

$$\left(\frac{\partial^2}{\partial r^2}+\frac{1}{r}\frac{\partial}{\partial r}+\nu_\alpha^2\frac{\partial^2}{\partial z^2}\right)\phi_\alpha=0, \quad (\alpha=1, 2), \tag{1}$$

where $\nu_1{}^2$ and $\nu_2{}^2$ are the roots of the equation

$$c_{11}c_{44}\nu^4+[c_{13}(2c_{44}+c_{13})-c_{11}c_{33}]\nu^2+c_{33}c_{44}=0 \tag{2}$$

The roots $\nu_1{}^2$ and $\nu_2{}^2$ are either real or complex conjugate depending on the values of the elastic constants c_{11}, c_{13}, c_{33}, and c_{44}. It is also specified that ν_1 and ν_2 always have positive real parts. The displacement and stress components for the axisymmetric problem can be expressed as follows (Lekhnitskii, 1981):

$$u_r=\frac{\partial\phi_1}{\partial r}+\frac{\partial\phi_2}{\partial r}, \tag{3}$$

$$u_z=k_1\frac{\partial\phi_1}{\partial z}+k_2\frac{\partial\phi_2}{\partial z}, \tag{4}$$

$$\sigma_{rr}=-c_{44}\left[(1+k_1)\frac{\partial^2\phi_1}{\partial z^2}+(1+k_2)\frac{\partial^2\phi_2}{\partial z^2}\right] -\frac{2c_{66}}{r}\left[\frac{\partial\phi_1}{\partial r}+\frac{\partial\phi_2}{\partial r}\right], \tag{5}$$

$$\sigma_{zz}=c_{44}\left[\nu_1^2(1+k_1)\frac{\partial^2\phi_1}{\partial z^2}+\nu_2^2(1+k_2)\frac{\partial^2\phi_2}{\partial z^2}\right], \tag{6}$$

$$\sigma_{\theta\theta}=-c_{44}\left[(1+k_1)\frac{\partial^2\phi_1}{\partial z^2}+(1+k_2)\frac{\partial^2\phi_2}{\partial z^2}\right] -2c_{66}\frac{\partial^2}{\partial r^2}(\phi_1+\phi_2), \tag{7}$$

$$\sigma_{rz}=c_{44}\left[(1+k_1)\frac{\partial^2\phi_1}{\partial r\partial z}+(1+k_2)\frac{\partial^2\phi_2}{\partial r\partial z}\right]. \tag{8}$$

where the parameters k_1 and k_2 are defined by

$$k_\alpha=\frac{c_{11}\nu_\alpha^2-c_{44}}{c_{13}+c_{44}}, \quad (\alpha=1, 2). \tag{9}$$

[1]Assistant Professor, School of Civil Engineering, Georgia Institute of Technology, Atlanta, GA 30332.

Manuscript received by ASME Applied Mechanics Division, August 4, 1987; final revision, February 12, 1988.

Downloaded 03 May 2010 to 171.66.16.21. Redistribution subject to ASME license or copyright; see http://www.asme.org/terms/Terms_Use.cfm

When n is large, $\xi \approx n\Delta$ so that (26) becomes $k \approx \sqrt{3\xi}$; this is similar to (20).

The smallest root of (22) increases with stretch up to λ_p and then decreases towards zero as the ultimate load is approached (Fig. 3). Near λ_n we have again an asymptotic expansion, viz,

$$k \approx \sqrt{\frac{6(1-n\ ln\ \lambda)}{2n\ ln\ \lambda-(1-n\ ln\ \lambda)\left(\lambda^4+1-\dfrac{\lambda^4-1}{n\ ln\ \lambda}\right)}} \approx \sqrt{3n\left(1-\frac{\lambda}{\lambda_u}\right)} \tag{27}$$

For large values of n we get from (27) that $k \approx \sqrt{3(1-\xi)}$ indicating—along with earlier results and numerical observations—that as n increases the k versus ξ curves of Fig. 3 become more and more symmetric with respect to the center line $\xi = 1/2$.

Conclusions

In addition to the constitutive sensitivity of the smallest decay rate (k), and the importance of considering the complete space of eigenfunctions, there are a few more interesting observations that emerge from our study: To begin with, the lowest eigenvalues shown in Figs. 2–3 are all real and they predict a purely exponential, non-oscillatory decay of the first eigenfunctions in contrast to the complex roots for the linear elastic solid.

Secondly, it appears that there is almost no diffusion of the antisymmetric end disturbance at low values of stretch. The asymptotic relations of (20) and (26) show clearly that $k \to 0$ as $\lambda \to 1$ (and $\Delta \to 0$). A more general result, derived from the antisymmetric branch of (15), for small strains, reads $k^2 \approx 3\sigma/4\mu_0^*$ where μ_0^* is the ground state (at zero strain) value of modulus μ^*. This low rate of decay when the strains are small is not predicted by the linear theory of elasticity, and can be described as a *critical second order effect*.

For the power law material, slow diffusion of the end effect also is predicted as the load approaches its ultimate value (Fig. 3). This is in agreement with the bifurcation study of Hill and Hutchinson (1975), since k from (27) becomes, for $\lambda > \lambda_u$, a purely imaginary number, reflecting the oscillatory nature of the bifurcation eigenmodes. Note that no bifurcation away from the primary orthogonal path exists for the Mooney-Rivlin material.

Finally, for the power law material around the antisymmetric/symmetric eigenfunction transition at $\lambda = \lambda_p$, there is a narrow band of stretch with a high rate of diffusion (Fig. 3). At large values of n this needle-shaped region is extraordinarily sharp and can perhaps be described as a *Saint-Venant spike*. Similar results have recently been obtained by the authors in a related study of strain hardening elastoplastic materials, Durban and Stronge (1988).

Acknowledgment

One of us (DD) wishes to express his thanks for the kind hospitality of the Cambridge University Engineering Department, during the sabbatical year 1986/7. Part of this work has been supported by the V.P.R.-Aeronautical Engineering Research Fund, Technion, Haifa.

References

Abeyaratne, R., Horgan, C. O., and Chung, D.-T., 1985, "Saint-Venant End Effects for Incremental Plane Deformations of Incompressible Nonlinearity Elastic Materials," ASME Journal of Applied Mechanics, Vol. 52, pp. 847–852.

Durban, D., and Stronge, W. J., 1988, "Diffusion of Self Equilibrating End Loads in Plain Strain Plasticity," *I. Tech. Phys. Solids,* to be published.

Hill, R., and Hutchinson, J. W., 1975, "Bifurcation Phenomena in the Plane Tension Test," *J. Mech. Phys. Solids*, Vol. 23, pp. 239–264.

Transversely Isotropic Medium with a Rigid Spheroidal Inclusion Under an Axial Pull

A. H. Zureick[1]

Introduction

Selvadurai (1976) presented a three-dimensional axisymmetric solution, exact within elastostatics, to the problem of a rigid spheroidal inclusion embedded in an infinite isotropic elastic medium and subjected to an axial pull. This problem has applications to both composite materials and soil mechanics. The present paper constitutes the transversely isotropic counterpart of Selvadurai's problem.

Fundamental Formulae

Consider a homogeneous transversely isotropic elastic medium occupying a region of the three-dimensional space referred to a fixed cylindrical coordinate system (r, θ, z) in which the z-axis coincides with the material axis of symmetry. It can be shown that in the absence of body forces, solutions of three-dimensional axisymmetric problems can be found in terms of two quasi-harmonic potential functions $\phi_\alpha\ (r, z)$, $(\alpha = 1, 2)$, which are the solutions of

$$\left(\frac{\partial^2}{\partial r^2}+\frac{1}{r}\frac{\partial}{\partial r}+\nu_\alpha^2\frac{\partial^2}{\partial z^2}\right)\phi_\alpha=0, \quad (\alpha=1, 2), \tag{1}$$

where $\nu_1{}^2$ and $\nu_2{}^2$ are the roots of the equation

$$c_{11}c_{44}\nu^4+[c_{13}(2c_{44}+c_{13})-c_{11}c_{33}]\nu^2+c_{33}c_{44}=0 \tag{2}$$

The roots $\nu_1{}^2$ and $\nu_2{}^2$ are either real or complex conjugate depending on the values of the elastic constants c_{11}, c_{13}, c_{33}, and c_{44}. It is also specified that ν_1 and ν_2 always have positive real parts. The displacement and stress components for the axisymmetric problem can be expressed as follows (Lekhnitskii, 1981):

$$u_r=\frac{\partial\phi_1}{\partial r}+\frac{\partial\phi_2}{\partial r}, \tag{3}$$

$$u_z=k_1\frac{\partial\phi_1}{\partial z}+k_2\frac{\partial\phi_2}{\partial z}, \tag{4}$$

$$\sigma_{rr}=-c_{44}\left[(1+k_1)\frac{\partial^2\phi_1}{\partial z^2}+(1+k_2)\frac{\partial^2\phi_2}{\partial z^2}\right] -\frac{2c_{66}}{r}\left[\frac{\partial\phi_1}{\partial r}+\frac{\partial\phi_2}{\partial r}\right], \tag{5}$$

$$\sigma_{zz}=c_{44}\left[\nu_1^2(1+k_1)\frac{\partial^2\phi_1}{\partial z^2}+\nu_2^2(1+k_2)\frac{\partial^2\phi_2}{\partial z^2}\right], \tag{6}$$

$$\sigma_{\theta\theta}=-c_{44}\left[(1+k_1)\frac{\partial^2\phi_1}{\partial z^2}+(1+k_2)\frac{\partial^2\phi_2}{\partial z^2}\right] -2c_{66}\frac{\partial^2}{\partial r^2}(\phi_1+\phi_2), \tag{7}$$

$$\sigma_{rz}=c_{44}\left[(1+k_1)\frac{\partial^2\phi_1}{\partial r\partial z}+(1+k_2)\frac{\partial^2\phi_2}{\partial r\partial z}\right]. \tag{8}$$

where the parameters k_1 and k_2 are defined by

$$k_\alpha=\frac{c_{11}\nu_\alpha^2-c_{44}}{c_{13}+c_{44}}, \quad (\alpha=1, 2). \tag{9}$$

[1]Assistant Professor, School of Civil Engineering, Georgia Institute of Technology, Atlanta, GA 30332.

Manuscript received by ASME Applied Mechanics Division, August 4, 1987; final revision, February 12, 1988.

Copyright © 1988 by ASME
Downloaded 03 May 2010 to 171.66.16.21. Redistribution subject to ASME license or copyright; see http://www.asme.org/terms/Terms_Use.cfm

Statement of Problem

Consider an infinite elastic transversely isotropic medium containing a rigid spheroidal inclusion whose surface is defined by

$$\frac{z^2}{a^2}+\frac{r^2}{b^2}=1, \tag{10}$$

where a and b are the two semi-axes of the spheroid. At the contact surface between the inclusion and the surrounding medium, perfect bonding is presupposed. When the inclusion is subjected to an axially symmetric load whose resultant is denoted by F, it will undergo a rigid displacement, δ, in the z-direction. Thus, the displacement boundary conditions at the spheroidal interface are

$$u_r=0, \quad u_z=\delta. \tag{11}$$

In addition to these boundary conditions, the displacement and stress components must vanish at sufficiently large distances from the inclusion. It is required to determine the displacement and stress fields throughout the medium as well as the load-deflection ($F-\delta$) relationship.

Analysis

Since the inclusion is spheroidal in shape, it is convenient to employ the spheroidal coordinate systems (η_α, γ_α, θ) defined through the following transformation (Chen, 1968, 1971)

$$r=C_\alpha(q_\alpha^2-1)^{1/2}(1-p_\alpha^2)^{1/2},$$
$$z=C_\alpha\nu_\alpha q_\alpha p_\alpha, \quad (\alpha=1,2), \tag{12}$$

where for Re $[C^2{}_\alpha] > 0$,

$$q_\alpha=\cosh\eta_\alpha, \quad p_\alpha=\cos\gamma_\alpha, \tag{13}$$

and for Re $[C^2{}_\alpha] < 0$,

$$q_\alpha=i\sinh\eta_\alpha, \quad p_\alpha=\cos\gamma_\alpha, \tag{14}$$

The parameters C_α are defined by

$$C_\alpha^2=\frac{a^2}{\nu_\alpha^2}-b^2. \tag{15}$$

Let ρ_α denote the value q_α on the spheroidal surface, then for $q_\alpha = \rho_\alpha$ equation (12) represents the spheroidal surface, and $p_1 = p_2 = z/a$. The potential functions for the problem at hand are chosen in the form

$$\phi_\alpha(r,z)=C_\alpha A_\alpha[P_1(p_\alpha)Q_1(q_\alpha)+Q_0(p_\alpha)+Lnr], \quad (\alpha=1,2), \tag{16}$$

in which the A_α are constants that can be determined from the boundary conditions at the spheroidal interface and P_n and Q_n ($n = 0, 1, 2, \ldots$) are the Legendre functions of the first and second kind, respectively, defined as follows:

$$P_1(p_\alpha)=p_\alpha, \tag{17}$$

$$Q_0(p_\alpha)=\frac{1}{2}\,Ln\,\frac{p_\alpha+1}{p_\alpha-1}, \tag{18}$$

$$Q_1(q_\alpha)=\frac{q_\alpha}{2}\,Ln\,\frac{q_\alpha+1}{q_\alpha-1}-1. \tag{19}$$

Substituting equation (16) into equations (3)-(4), the expressions for the displacement components take the form

$$u_r=\frac{1}{r}\sum_{\alpha=1}^{2}C_\alpha A_\alpha(1-p_\alpha), \tag{20}$$

$$u_z=\sum_{\alpha=1}^{2}\frac{k_\alpha A_\alpha}{\nu_\alpha}Q_0(q_\alpha). \tag{21}$$

At the spheroidal interface, equations (20)-(21) together with equation (11) give:

$$C_1A_1+C_2A_2=0, \tag{22}$$

$$\frac{k_1}{\nu_1}Q_0(\rho_1)A_1+\frac{k_2}{\nu_2}Q_0(\rho_2)A_2=\delta, \tag{23}$$

from which A_1 and A_2 are found to be

$$A_1=\frac{-\delta}{C_1D}, \quad A_2=\frac{\delta}{C_2D}, \tag{24}$$

where

$$D=\frac{k_2}{C_2\nu_2}Q_0(\rho_2)-\frac{k_1}{C_1\nu_1}Q_0(\rho_1). \tag{25}$$

It should be noted that equation (22) removes the singularity along the line $r = 0$ in equation (20). Taking into account equation (22), the displacement and stress component can then be written as follows:

$$u_r=-\frac{1}{r}\sum_{\alpha=1}^{2}C_\alpha A_\alpha p_\alpha, \tag{26}$$

$$u_z=\sum_{\alpha=1}^{2}\frac{k_\alpha A_\alpha}{\nu_\alpha}Q_0(q_\alpha), \tag{27}$$

$$\sigma_{rr}=c_{66}\sum_{\alpha=1}^{2}A_\alpha C_\alpha p_\alpha\left[\frac{2}{r^2}+\frac{c_{44}}{c_{66}}\,\frac{(1+k_\alpha)}{C_\alpha^2\nu_\alpha^2}\,\frac{1}{(q_\alpha^2-p_\alpha^2)}\right], \tag{28}$$

$$\sigma_{zz}=-c_{44}\sum_{\alpha=1}^{2}\frac{A_\alpha(1+k_\alpha)}{C_\alpha}\,\frac{p_\alpha}{(q_\alpha^2-p_\alpha^2)}, \tag{29}$$

$$\sigma_{rz}=-\frac{c_{44}}{r}\sum_{\alpha=1}^{2}\frac{A_\alpha(1+k_\alpha)}{\nu_\alpha}\,\frac{q_\alpha(1-p_\alpha^2)}{(q_\alpha^2-p_\alpha^2)}, \tag{30}$$

$$\sigma_{\theta\theta}=c_{66}\sum_{\alpha=1}^{2}-A_\alpha C_\alpha p_\alpha\left[\frac{2}{r^2}+\frac{2}{C_\alpha^2(q_\alpha^2-p_\alpha^2)}\right.$$
$$\left.-\frac{c_{44}}{c_{66}}\,\frac{(1+k_\alpha)}{C_\alpha^2\nu_\alpha^2}\,\frac{1}{(q_\alpha^2-p_\alpha^2)}\right]. \tag{31}$$

The force-displacement relationship can be conveniently calculated from the expression

$$F=\int_S\int(\sigma_{zz}n_z+\sigma_{rz}n_r)ds, \tag{32}$$

where S is the surface $q_\alpha = \rho_\alpha$ and n_z and n_r are the components of the unit normal directed away from the surrounding material. The n's may be evaluated from the expressions

$$n_r=\frac{a}{b}\,\frac{r}{\lambda}, \quad n_z=\frac{b}{a}\,\frac{z}{\lambda}, \tag{33}$$

in which

$$\lambda=\left(\frac{a^2}{b^2}r^2+\frac{b^2}{a^2}z^2\right)^{1/2}, \tag{34}$$

The result of integration of equation (32) can be easily obtained in the form

$$F=4\pi c_{44}\delta\,\frac{k_2-k_1}{\frac{k_2}{\nu_2C_2}Q_0(\rho_2)-\frac{k_1}{\nu_1C_1}Q_0(\rho_1)}. \tag{35}$$

Downloaded 03 May 2010 to 171.66.16.21. Redistribution subject to ASME license or copyright; see http://www.asme.org/terms/Terms_Use.cfm

Limiting Cases

For the limiting case of a rigid inclusion with elongated shape, the semi major axis of the spheroid is much greater than the semi minor axis. Thus the ratio b/a becomes small and equation (35) takes the form

$$F = 4\pi a \delta c_{44} \frac{k_2 - k_1}{k_1 Ln\left(\frac{b\nu_1}{2a}\right) - k_2 Ln\left(\frac{b\nu_2}{2a}\right)}, \tag{36}$$

where the second and higher order terms in b/a have been neglected.

For the limiting case of a rigid circular disk of radius b and infinitesimal thickness, the load deflection relationship can be directly obtained by taking the limit of equation (35) as $b/a \to \infty$. By so doing, we obtain

$$F = 8c_{44} b\delta \frac{k_2 - k_1}{\frac{k_2}{\nu_2} - \frac{k_1}{\nu_1}}. \tag{37}$$

When the medium is isotropic, then $c_{11} = c_{33} = 2(1-\nu)G/(1-2\nu)$, $c_{12} = c_{13} = 2\nu G/(1-2\nu)$ and $c_{44} = c_{66} = G$, where ν and G are Poisson's ratio and the shear modulus of the isotropic elastic medium, respectively. Consequently, $\nu_1 = \nu_2 = 1$ and equations (35)–(37) can then be reduced by a limiting process to the corresponding expressions obtained by Selvadurai (1976) for the isotropic problem.

Acknowledgment

The author wishes to express his thanks to Dr. S. M. Heinrich of Marquette University for his suggestions and general interest in the work and to the School of Civil Engineering at the Georgia Institute of Technology for financial assistance.

References

Chen, W. T., 1968, "Axisymmetric Stress Field Around Spheroidal Inclusions and Cavities in a Transversely Isotropic Materials," ASME JOURNAL OF APPLIED MECHANICS, Vol. 35, pp. 770–773.

Chen, W. T., 1971, "Elastic Analysis of an Axisymmetric Stress Field Perturbed by a Spheroidal Inhomogeneity," *Quart. Appl. Math.*, Vol. XXVIII, pp. 517–525.

Lekhnitskii, S. G., 1981, *Theory of Elasticity of an Anisotropic Body*, MIR Publishers, Moscow.

Selvadurai, A. P. S., 1976, "The Load-Deflection Characteristics of a Deep Rigid Anchor in an Elastic Medium," *Geotechnique*, Vol. 26, No. 4, pp. 603–612.

Downloaded 03 May 2010 to 171.66.16.21. Redistribution subject to ASME license or copyright; see http://www.asme.org/terms/Terms_Use.cfm

Journal of Applied Mechanics

Discussion

Exact Stationary-Response Solution for Second-Order Nonlinear Systems Under Parametric and External White-Noise Excitations[1]

M. F. Dimentberg[2]. The authors should be congratulated on their paper, which illustrates a systematic approach to the search of exact solutions for stationary probability densities of the responses of dynamic systems to combined external and parametric white-noise excitations.

The authors refer to the paper [8] by this writer, in which one such solution had first been obtained. The writer, indeed, had not shown in [8], how that solution had been attained. However, this was by no means "accidental" and, therefore, some clarifying remarks seem appropriate.

The solution for stationary amplitude probability density in a SDOF system with nonlinear damping and combined external and parametric random excitation had been obtained by this writer as far back as the 1970's by the approximate stochastic averaging method (*Soviet Appl. Mech.*, Vol. 11, No. 4, 1975, pp. 401–404). It is evident that if the exact solution does exist, it should result in such expression for stationary probability density of the amplitude, that coincides with the approximate one. Therefore, to obtain the exact solution one may express the known amplitude probability density in terms of displacement and velocity and then substitute it into Fokker-Planck equation for the original system. The latter would be satisfied exactly, only provided that the system's parameters are related in a certain special way; thus, the problem is reduced to algebraic equations for this specific subset of parameters, for which this exact solution is valid indeed. This way of looking for exact solutions, based on the use of the approximate stochastic averaging results is, indeed, of the inverse type, but seems to be rather systematic, although it differs from that adopted by the authors.

By the way, the seemingly unexpected result in Example 4 – Gaussian property of the response of nonlinearly damped system with combined external and parametric white-noise excitation in a certain special case – has a very clear physical interpretation. Whilst random parametric excitation tends to prolong the tails of response probability density, the (positive) damping nonlinearity tends to make them shorter. In the above special case these two effects cancel each other, leading to the same shape of response probability density as in linear SDOF system with purely external random excitation.

A more detailed discussion of these topics can be found in the forthcoming book by this writer entitled "Statistical Dynamics of Nonlinear and Time-Varying Systems," which will be published by the Research Studies Press in 1988.

Authors' Closure

Professor Dimentberg's discussion on our paper has provided additional insights into the behavior of nonlinear systems under combined external and parametric white-noise excitations. Determining the exact joint probability density of displacement and velocity indirectly by way of the probability density of the amplitude obtained from the approximate stochastic averaging method is indeed a very useful approach, and it may be applicable to some cases, for example, [8]. We take this opportunity to point out, however, that since restrictive relations between the system parameters and spectral densities of the excitations must be imposed to obtain exact solutions if parametric and external white-noise excitations are both present, a more important issue is how to obtain approximate solutions without such restrictions. In a recent investigation [17], we consider a system

$$\ddot{X}+\alpha\dot{X}+X=XW_1(t)+\dot{X}W_2(t)+W_3(t) \tag{1}$$

where $W_j(t)$ are correlated Gaussian white noises. Although example (1) is linear, the stationary joint probability of $X(t)$ and $\dot{X}(t)$ is not obtainable at the present time. An approximate solution for the amplitude can be obtained using the stochastic averaging method, and when converted to the joint probability density of $X(t)$ and $\dot{X}(t)$, we obtain

$$p_1(x_1, x_2)=C_1[4K_{33}+(K_{11}+3K_{22})(x_1^2+x_2^2)]^{-\sigma} \tag{2}$$

where

$$\sigma=\frac{2(\alpha+\pi k_{22})}{\pi(K_{11}+3K_{22})} \tag{3}$$

where K_{jj} is the spectral density of $W_j(t)$, and where x_1 and x_2 are possible values of $X(t)$ and $\dot{X}(t)$, respectively. However, using a generalized version of the present approach [18] and an equal energy dissipation criterion [17], we obtain another approximation,

$$p_2(x_1, x_2)=C_2\{1+\nu[(1-\pi K_{12})(x_1-x_{1,0})^2+x_2]\}^{-\delta} \tag{4}$$

where K_{ij} is the cross-spectral density of $W_i(t)$ and $W_j(t)$ and

$$\begin{aligned} x_{1,0} &= \frac{\pi K_{23}}{1-\pi K_{12}} \\ \nu &= \frac{K_{11}+3K_{22}(1-\pi K_{12})}{4(1-\pi K_{12})(K_{11}x_{1,0}^2+2K_{13}x_{1,0}+K_{33})} \end{aligned} \tag{5}$$

$$\delta = \frac{2(1-\pi K_{12})(\alpha+\pi K_{22})]}{\pi[K_{11}+3K_{22}(1-\pi K_{12})]} \tag{6}$$

It is of interest to note that p_2 contains the cross-spectral densities of the excitations whereas p_1 does not, and the stability

[1] By Y. Yong and Y. K. Lin, published in the June, 1987, issue of the ASME JOURNAL OF APPLIED MECHANICS, Vol. 54, pp. 414–418.

[2] Leading Scientist, Institute for Problems in Mechanics USSR Academy of Sciences, prospect Vernadskogo 101, Moscow, USSR.

Copyright © 1988 by ASME
Downloaded 03 May 2010 to 171.66.16.21. Redistribution subject to ASME license or copyright; see http://www.asme.org/terms/Terms_Use.cfm

conditions implied in examples (2) and (4) are very much different.

Whether p_1 or p_2 is a better approximation is not immediately clear. However, for the linear system (1) it is possible to derive a set of *exact* equations for the moments $E[X(t)]$, $E[\dot{X}(t)]$, $E[X^2(t)]$, $E[X(t)\dot{X}(t)]$, and $E[\dot{X}^2(t)]$. It can be shown that these equations are satisfied by the moments computed from p_2 but not from p_1 [17]. Therefore, the method of stochastic averaging, even though very versatile, should be used with care.

Finally, the "unexpected" results shown in example 4 in our paper is no longer unexpected. We have since found that different stochastic systems can indeed share an identical probability distribution. They are called equivalent stochastic systems [19]. When the associated Fokker-Planck equations are identical, the equivalent stochastic systems must share both the stationary probability distribution and the transient nonstationary probability distribution under identical initial conditions. Such systems are said to be stochastically equivalent in the strict sense. A wider class, referred to as the class of equivalent stochastic systems in the wide sense, also includes those sharing only the stationary probability distribution but having different Fokker-Planck equations.

Additional References

17 Cai, G. Q., and Lin, Y. K., 1988, "A New Approximate Solution Technique for Randomly Excited Nonlinear Oscillators" to appear in *International Journal of Nonlinear Mechanics*.

18 Lin, Y. K., Yong, Y., and Cai, G. Q., 1987, "Exact Solution for Nonlinear Systems Under Parametric and External White-Noise Excitations," *Stochastic Structural Mechanics, Lecture Notes in Engineering 31*, Edited by Y. K. Lin and G. I. Schueller, Springer-Verlag, New York, pp. 268-280.

19 Lin, Y. K., and Cai, G. Q., 1988, "Equivalent Stochastic Systems," to appear in ASME JOURNAL OF APPLIED MECHANICS.

Torsion of Cylinders With Shape Intrinsic Orthotropy[3]

J. G. Kennedy[4] and D. R. Carter.[4] It should be clarified that the central results stated by S. C. Cowin in (1987) had been established previously by Kennedy and Carter (1985a) and extensively cited by Kennedy et al., (1985b). A class of cylindrical orthotropy termed "circumferential" orthotropy is discussed in (1985a, 1985b) which is equivalent to the "shape intrinsic" orthotropy studied in (1987). It is shown explicitly in (1985a) that "an orthotropic shaft with circumferential planes of material symmetry tangent to the torsional stress lines which would occur if the shaft was (tranversely) isotropic (the defining property of circumferential orthotropy) will experience a torsional stress field identical to that which would occur if the shaft was (transversely) isotropic." Furthermore, " . . . the strain field is identical to that which would occur in an isotropic body having a shear modulus equal to G_{23} (the orthotropic shear modulus associated with the circumferential and longitudinal directions)." Consequently, in the presence of circumferential orthotropy, these results are identical to the central conclusion of Cowin that, "for a certain class of elastic cylinders with shape intrinsic orthotropy, the solution of the torsion problem is the same as the solution to the torsion problem for the isotropic cylinder of the same shape if the isotropic shear modulus G were replaced by the orthotropic shear modulus G_{iz} ($\equiv G_{23}$ above)." Furthermore, Cowin's discussion of the "experimental evaluation of the shear moduli for shape intrinsic orthotropy" uses one of the alternative experimental procedures discussed explicitly in (1985b).

It is unfortunate that Dr. Cowin overlooked these publications in the Biomechanics literature.

References

Cowin, S. C., 1987, "Torsion of Cylinders With Shape Intrinsic Orthotropy," ASME JOURNAL OF APPLIED MECHANICS, Vol. 54, pp. 778-782.

Kennedy, J. G., and Carter, D. R., 1985a, "Long Bone Torsion: I. Effects of Heterogeneity, Anisotropy and Geometric Irregularity," ASME *Journal of Biomechanical Engineering*, Vol. 107, pp. 183-188.

Kennedy, J. G., Carter, D. R., Caler, W. E., 1985b, "Long Bone Torsion: II. A Combined Experimental and Computational Method for Determining an Effective Shear Modulus," ASME *Journal of Biomechanical Engineering*, Vol. 107, pp. 189-191.

Author's Closure

It is unfortunate that I overlooked these publications. There are many reasons why I should have seen them and read them. I apologize to the authors for my oversight.

A verbal statement of the central argument in my paper extending the St. Venant solution for torsion of certain classes of shafts with shape intrinsic orthotropy does appear in the appendix of Kennedy and Carter (1985a). In my opinion that is the only original element in common between the two papers. I disagree with the opening statement in the above discussion by Kennedy and Carter. My paper, Cowin (1987), contains the following results not contained in Kennedy and Carter (1985a, b):

1. An explicit mathematical condition defining the class of cylinders with shape intrinsic orthotropy for which the solution to the torsion problem is the same as the solution to the torsion problem for the isotropic cylinder of the same shape if the isotropic shear modulus G were replaced by the orthotropic shear modulus G_{tz};
2. Examples of cylinders satisfying this condition;
3. A formula for the torque in a laminated shape intrinsic cylinder if each laminate has a different G_{tz} shear modulus.

The key equations of Kennedy and Carter (1985a), their equations (9) and (10), cannot be used to establish the explicit formulas given in my paper for the three results detailed above because their equations (9) and (10) are expressed in terms of arbitrary orthogonal curvilinear coordinates.

If I had seen the papers of Kennedy and Carter before I wrote my paper, Cowin (1987), I would still have written it, but it would have been slightly modified to account for their earlier argument. I think my paper is quite different from those of Kennedy and Carter (1985a, b) and I believe that readers interested in that subject would benefit from reading all three papers.

Finally, it should be noted that the principal equations used by Kennedy and Carter (1985a) in their argument, their equations (9) and (10), contain an error. The right hand side of both equations should be multiplied by the factor

$$\frac{1}{2h_1h_2}\left(\frac{\partial}{\partial q_1}(q_1h_1)+\frac{\partial}{\partial q_2}(q_2h_1)\right)$$

where h_1, h_2, q_1 and q_2 are identified by Kennedy and Carter (1985a).

[3] By S. C. Cowin, published in the December, 1987 issue of the ASME JOURNAL OF APPLIED MECHANICS, Vol. 54, No. 4, pp. 778-782.

[4] Graduate Student and Professor, respectively, Department of Mechanical Engineering, Stanford University, Stanford, CA 94305.

Downloaded 03 May 2010 to 171.66.16.21. Redistribution subject to ASME license or copyright; see http://www.asme.org/terms/Terms_Use.cfm

conditions implied in examples (2) and (4) are very much different.

Whether p_1 or p_2 is a better approximation is not immediately clear. However, for the linear system (1) it is possible to derive a set of *exact* equations for the moments $E[X(t)]$, $E[\dot{X}(t)]$, $E[X^2(t)]$, $E[X(t)\dot{X}(t)]$, and $E[\dot{X}^2(t)]$. It can be shown that these equations are satisfied by the moments computed from p_2 but not from p_1 [17]. Therefore, the method of stochastic averaging, even though very versatile, should be used with care.

Finally, the "unexpected" results shown in example 4 in our paper is no longer unexpected. We have since found that different stochastic systems can indeed share an identical probability distribution. They are called equivalent stochastic systems [19]. When the associated Fokker-Planck equations are identical, the equivalent stochastic systems must share both the stationary probability distribution and the transient nonstationary probability distribution under identical initial conditions. Such systems are said to be stochastically equivalent in the strict sense. A wider class, referred to as the class of equivalent stochastic systems in the wide sense, also includes those sharing only the stationary probability distribution but having different Fokker-Planck equations.

Additional References

17 Cai, G. Q., and Lin, Y. K., 1988, "A New Approximate Solution Technique for Randomly Excited Nonlinear Oscillators" to appear in *International Journal of Nonlinear Mechanics*.

18 Lin, Y. K., Yong, Y., and Cai, G. Q., 1987, "Exact Solution for Nonlinear Systems Under Parametric and External White-Noise Excitations," *Stochastic Structural Mechanics, Lecture Notes in Engineering 31*, Edited by Y. K. Lin and G. I. Schueller, Springer-Verlag, New York, pp. 268-280.

19 Lin, Y. K., and Cai, G. Q., 1988, "Equivalent Stochastic Systems," to appear in ASME JOURNAL OF APPLIED MECHANICS.

Torsion of Cylinders With Shape Intrinsic Orthotropy[3]

J. G. Kennedy[4] and D. R. Carter.[4] It should be clarified that the central results stated by S. C. Cowin in (1987) had been established previously by Kennedy and Carter (1985a) and extensively cited by Kennedy et al., (1985b). A class of cylindrical orthotropy termed "circumferential" orthotropy is discussed in (1985a, 1985b) which is equivalent to the "shape intrinsic" orthotropy studied in (1987). It is shown explicitly in (1985a) that "an orthotropic shaft with circumferential planes of material symmetry tangent to the torsional stress lines which would occur if the shaft was (tranversely) isotropic (the defining property of circumferential orthotropy) will experience a torsional stress field identical to that which would occur if the shaft was (transversely) isotropic." Furthermore, " . . . the strain field is identical to that which would occur in an isotropic body having a shear modulus equal to G_{23} (the orthotropic shear modulus associated with the circumferential and longitudinal directions)." Consequently, in the presence of circumferential orthotropy, these results are identical to the central conclusion of Cowin that, "for a certain class of elastic cylinders with shape intrinsic orthotropy, the solution of the torsion problem is the same as the solution to the torsion problem for the isotropic cylinder of the same shape if the isotropic shear modulus G were replaced by the orthotropic shear modulus G_{iz} ($\equiv G_{23}$ above)." Furthermore, Cowin's discussion of the "experimental evaluation of the shear moduli for shape intrinsic orthotropy" uses one of the alternative experimental procedures discussed explicitly in (1985b).

It is unfortunate that Dr. Cowin overlooked these publications in the Biomechanics literature.

References

Cowin, S. C., 1987, "Torsion of Cylinders With Shape Intrinsic Orthotropy," ASME JOURNAL OF APPLIED MECHANICS, Vol. 54, pp. 778-782.

Kennedy, J. G., and Carter, D. R., 1985a, "Long Bone Torsion: I. Effects of Heterogeneity, Anisotropy and Geometric Irregularity," ASME *Journal of Biomechanical Engineering*, Vol. 107, pp. 183-188.

Kennedy, J. G., Carter, D. R., Caler, W. E., 1985b, "Long Bone Torsion: II. A Combined Experimental and Computational Method for Determining an Effective Shear Modulus," ASME *Journal of Biomechanical Engineering*, Vol. 107, pp. 189-191.

Author's Closure

It is unfortunate that I overlooked these publications. There are many reasons why I should have seen them and read them. I apologize to the authors for my oversight.

A verbal statement of the central argument in my paper extending the St. Venant solution for torsion of certain classes of shafts with shape intrinsic orthotropy does appear in the appendix of Kennedy and Carter (1985a). In my opinion that is the only original element in common between the two papers. I disagree with the opening statement in the above discussion by Kennedy and Carter. My paper, Cowin (1987), contains the following results not contained in Kennedy and Carter (1985a, b):

1. An explicit mathematical condition defining the class of cylinders with shape intrinsic orthotropy for which the solution to the torsion problem is the same as the solution to the torsion problem for the isotropic cylinder of the same shape if the isotropic shear modulus G were replaced by the orthotropic shear modulus G_{tz};
2. Examples of cylinders satisfying this condition;
3. A formula for the torque in a laminated shape intrinsic cylinder if each laminate has a different G_{tz} shear modulus.

The key equations of Kennedy and Carter (1985a), their equations (9) and (10), cannot be used to establish the explicit formulas given in my paper for the three results detailed above because their equations (9) and (10) are expressed in terms of arbitrary orthogonal curvilinear coordinates.

If I had seen the papers of Kennedy and Carter before I wrote my paper, Cowin (1987), I would still have written it, but it would have been slightly modified to account for their earlier argument. I think my paper is quite different from those of Kennedy and Carter (1985a, b) and I believe that readers interested in that subject would benefit from reading all three papers.

Finally, it should be noted that the principal equations used by Kennedy and Carter (1985a) in their argument, their equations (9) and (10), contain an error. The right hand side of both equations should be multiplied by the factor

$$\frac{1}{2h_1h_2}\left(\frac{\partial}{\partial q_1}(q_1h_1)+\frac{\partial}{\partial q_2}(q_2h_1)\right)$$

where h_1, h_2, q_1 and q_2 are identified by Kennedy and Carter (1985a).

[3] By S. C. Cowin, published in the December, 1987 issue of the ASME JOURNAL OF APPLIED MECHANICS, Vol. 54, No. 4, pp. 778-782.

[4] Graduate Student and Professor, respectively, Department of Mechanical Engineering, Stanford University, Stanford, CA 94305.

Copyright © 1988 by ASME
Downloaded 03 May 2010 to 171.66.16.21. Redistribution subject to ASME license or copyright; see http://www.asme.org/terms/Terms_Use.cfm

Journal of Applied Mechanics

Book Reviews

Thermomechanical Coupling in Solids, edited by H. D. Bui and Q. S. Nguyen. IUTAM, North-Holland, Amsterdam, 1987.

REVIEWED BY T. MURA[1]

This IUTAM Symposium, dedicated to the memory of Jean Mandel, was held in the first week of September 1986, covering topics: thermodynamics of irreversible process, dissipative phenomena in plasticity and viscoplasticity in fracture and damage, behaviors of heterogeneous or complex media such as composites, woods and geomaterials, phase transformation, experimental techniques based on infrared thermography, cyclic leads, large deformation, numerical methods for coupled problems, etc. The topics are heterogeneous but unified in terms of thermomechanical couplings.

Some of the papers presented in this proceeding will be briefly reviewed here.

I. Müller simulated thermomechanical properties of materials with shape memory and proposed a model with the potential energy under a shear load and interfacial energy. Statistical mechanics of the model is discussed.

J. Kestin presented his recent work on metal plasticity as a problem in thermodynamics. He is interested in the fact that Volterra and Somigliana dislocations can be produced by fictitiously reversible processes of changing the internal state created by plastic deformation. In turn, this makes it possible to calculate entropy and Gibbs equations.

G. J. Dvorak's paper is "Thermomechanical deformation and coupling in elastic-plastic composite materials." He presented his recent discovery that spatially uniform stress and strain fields can be caused in certain heterogeneous media by simultaneous application of a uniform thermal change and uniform overall stress.

J. L. Lataillade presented the use of a standard infrared camera to measure the temperature evolution of a polymetric material during its dynamic plastic deformation.

M. P. Luong used infrared vibrothermography as a nondestructive technique to analyze the unstable crack propagation in concrete.

J. R. Barber and M. Comninou reviewed thermoelastic effects in fracture and discussed crack closure and thermal contact resistance.

P. Perzyna's paper concerns the influence of thermomechanical coupling on dynamic fracture of ductile solids.

M. Taya and T. Mori used the Eshelby method to evaluate dimensional change in metal matrix composites subjected to thermal cycling. At high temperature, the thermal stress relaxation occurs by first matrix creep and followed by the diffusion around the matrix-fiber interfaces. At low temperature, the thermal stress relaxation occurs by plastic deformation in the matrix. The theory is satisfactory with experimental measurements of the dimensional change.

F. D. Fisher et al. also investigated thermal cycling of hangers theoretically and experimentally. They found "unexpected phenomena" that this cyclic temperature loading leads to failure of the hangers by large cracks initiated internally, which differs from the chill cracks in casting dies, etc.

A. C. F. Locks and F. A. Leckie presented an internal state variable theory for the tertiary stage of creep responsible for the degradiation of the material.

J. B. Leblond et al. studied the anomalous plastic behavior of steels during phase transformations by using the Hill-Mandel theory and by the finite element method.

T. Inoue, Z. G. Wang and K. Miyao investigated the role of transformation plasticity in the carburized quenching process.

T. H. Lehmann presented thermomechanical coupling in large deformations particularly in bifurcation problems.

H. D. Bui, A. Ehrlacher, and Q. S. Nguyen studied the thermal effect due to thermomechanical coupling at the tip of a moving crack within the framework of classical thermodynamics. The crack tip is a heat source and its temperature singularity is discussed. The results are compared to experimental observations by infrared thermography.

C. Theodosiu gave an analysis of a set of viscoplastic constitutive equations for metals and alloys in the hot working range. The initial and boundary-value problems are solved by the 2-D finite element method for plane and axisymmetric viscoplasticity with consideration of thermal boundary conditions. The results are compared with experimental data.

A. R. S. Ponter and J. A. Scaife explored properties of a class of constitutive equations which model the high temperature creep of metals.

A First Look at Perturbation Theory, by James G. Simmonds and James E. Mann, Jr., Robert E. Krieger Publishing Company, Malabar, Florida, 1986. 144 Pages. $12.50.

REVIEWED BY J. LYELL SANDERS, JR.[2]

This small 136-page monograph is an excellent introduction to the subject for anyone who knows calculus through the level of an undergraduate course on ordinary differential equations. Some proofs are offered, but the emphasis is always on understanding rather than rigor. There are ample references to the literature for more in-depth treatment of a particular topic.

[1]Department of Civil Engineering, Northwestern University, Evanston, IL 60208.

[2]Division of Engineering and Applied Physics, Harvard University, Cambridge, MA 02138.

Copyright © 1988 by ASME
Downloaded 03 May 2010 to 171.66.16.21. Redistribution subject to ASME license or copyright; see http://www.asme.org/terms/Terms_Use.cfm

In their "first look" the authors have chosen not to discuss asymptotic methods as applied to definite integrals or partial differential equations, but nothing much has been left out as far as ordinary differential equations is concerned. A short list of the topics: Poincare's method, WKB approximation, Cole's two-variable method, Langer's method for turning point problems, and the subject of matched asymptotic expansions. The two-variable approach to Langer's results appears to be original.

There are a large number of exercises for sharpening the reader's wits and many helpful figures.

Stochastic Methods in Structural Dynamics, edited by G. I. Schueller and M. Shinozuka, Nijhoff, 1987. 218 Pages. Price: $76.50.

REVIEWED BY ROSS B. COROTIS[3]

This book is a collection of coordinated chapters presented by five different authors, each an outstanding expert in stochastic dynamics. Although relatively brief (under 200 pages) and introductory in tone, the material is actually covered quite rapidly and at an advanced level.

Chapter 1, by G. I. Schuëller, is a very quick overview of basic probability, reliability, stochastic processes, and process excursions. The chapter is a convenient review for those familiar with the field, but would be difficult to follow in a learning context. It contains an extensive bibliography of pertinent literature.

Chapter 2, also by Schuëller, is a brief (12 page) chapter providing an introduction to random vibration analysis of single and multi-degree-of-freedom linear systems. It includes a discussion of frequency domain (power spectral density) analysis and time-history analysis.

In Chapter 3, M. Shinozuka provides a rather formal coverage of stochastic processes for engineering purposes. Significant detail is provided on the physical and mathematical bases of autocorrelation and power spectral density functions, illustrated for a one-dimensional process. These relationships are then expanded to the more general case of a multidimensional stochastic field. Finally, a matrix formulation for a multivariate process is presented (the case of m stochastic fields, each described in n dimensions), with a limitation to homogeneous Gaussian field. The emphasis is on cross spectral density functions and their simulation, and the process is illustrated with a one-dimensional wind velocity record at $m = 3$ reference points.

Chapter 4, written by Y. K. Lin, discusses the use of Markov process theory as a tool appropriate for nonlinear random vibration problems. First a brief background is given of the Fokker-Planck equation and the development of the Itô equation. A section on approximations of physical processes by a Markov process introduces the concept of correlation time of the excitation. The method is derived for a linear first order system, and then generalized using Stratonovich's stochastic averaging method. An example of using Itô's differential equation for a system with nonlinear stiffness is presented. Finally, a procedure is described to derive statistical moments for problems in which the Fokker-Planck equation is not solvable. One particular scheme, cumulant-neglect closure, is given in some detail.

The use of approximate methods for nonlinear systems is approached by F. Casciati in Chapter 5. Limiting the discussion to systems with generalized restoring force, $g(\dot{u},u)$, the author focuses on response surface and equivalent linearization techniques for multi-degree-of-freedom systems subjected to Gaussian excitation. The former method is applicable to systems with random parameters, while the latter is applied to a deterministic system, with hysteresis. The method of equivalent linearization is applied to a finite element code for framed structures, as an example.

The final chapter is by A. H-S. Ang. It is somewhat more specific than the others, addressing a damage model for reinforced concrete buildings subjected to earthquake motion. The model, based on two previous papers with Y. J. Park, utilizes a damage index combining the effects of excessive deformation and cyclic loading. Element damages are combined to provide a building model, and a brief comparison is made with historic data from damaged buildings in past earthquakes.

This book is a valuable reference to a variety of advanced techniques for those involved in the area of stochastic structural dynamics.

[3]Professor, Department of Civil Engineering, Johns Hopkins University, Baltimore, MD 21218.

Copyright © 1988 by ASME
Downloaded 03 May 2010 to 171.66.16.21. Redistribution subject to ASME license or copyright; see http://www.asme.org/terms/Terms_Use.cfm

ERRATA

Errata on a discussion by E. Reissner published in the March 1988 issue of ASME JOURNAL OF APPLIED MECHANICS, Vol. 55, p. 250.

$$D\left\{1+\frac{2-\nu}{1-\nu}\,\frac{h^2}{10}\,\nabla^2\right\}\nabla^4 w=q \qquad (1)$$

Similarly, equation (4) should be read as

$$(Q_x,\ Q_y)=-D\left[\frac{\partial}{\partial x},\frac{\partial}{\partial y}\right]\left[\nabla^2 w+\frac{h^2}{10}\left(1+\frac{1}{1-\nu}\right)\nabla^4 w\right], \qquad (4)$$

Following equation (3), the sixth line

$$\partial\nabla^2\partial y). \ . \ .$$

should read

$$\partial\nabla^2 w/\partial y). \ . \ .$$

Copyright © 1988 by ASME
Downloaded 03 May 2010 to 171.66.16.21. Redistribution subject to ASME license or copyright; see http://www.asme.org/terms/Terms_Use.cfm